A MATCHED-HARMONIC CONFLUENCE APPROACH TO ROTOR LOADS PREDICTION WITH COMPREHENSIVE APPLICATION TO FLIGHT TEST

A Thesis
Presented to
The Academic Faculty

by

Chance C. McColl

In Partial Fulfillment
of the Requirements for the Degree
Doctor of Philosophy in the
School of Aerospace Engineering

Georgia Institute of Technology
December 2012

A MATCHED-HARMONIC CONFLUENCE APPROACH TO ROTOR LOADS PREDICTION WITH COMPREHENSIVE APPLICATION TO FLIGHT TEST

Approved by:

Professor Massimo Ruzzene, Advisor
School of Aerospace Engineering
Georgia Institute of Technology

Professor Lakshmi Sankar
School of Aerospace Engineering
Georgia Institute of Technology

Professor Mark Costello
School of Aerospace Engineering
Georgia Institute of Technology

Dr. Stephen Makinen, Ph.D.
Dynamics and Internal Acoustics
Sikorsky Aircraft Corporation

Professor Dewey Hodges
School of Aerospace Engineering
Georgia Institute of Technology

Date Approved: August 29, 2012

To my children, Faith and Carue

ACKNOWLEDGEMENTS

First and foremost, I wish to thank my advisor, Dr. Massimo Ruzzene, for his expertise and encouragement on this effort. In fact, it was Dr. Ruzzene who, back in 2008, encouraged me to pursue my Ph.D. at that point in my career. I am deeply indebted to him for this. I also wish to thank my thesis committee: Dr. Dewey Hodges, Dr. Lakshmi Sankar, and Dr. Mark Costello from Georgia Tech, as well as Dr. Stephen Makinen from Sikorsky Aircraft Company. It was most helpful to have such a team of experts available as resources to me throughout this effort.

This research is based on work funded by the US Navy through SBIR N08-021. Special thanks to the US Navy, NAVAIR Structures, PMA-261, as well as the SBIR Program Office. Specifically Nam Phan and Robert Hay at NAVAIR; I have learned much from both of them through the years.

Thanks to my fellow graduate student (and now college professor) Maria Chierichetti. Others at Georgia Tech deserve much thanks as well, including Dr. Marilyn Smith and Dr. Jeff Jagoda. Thanks to Dr. Olivier Bauchau as well.

Sikorsky Aircraft Company has been very helpful to me on this effort. In addition to Stephen Makinen, both Mark Davis and Jim Cycon have been invaluable resources to me. Also, Bob Kufeld at NASA Ames has been an incredible help to me, always quick to respond to my questions about the UH-60A Airloads Program. Bob also reviewed my thesis. Thanks, Bob!

All of this is possible through the generosity and understanding of those at the company I work for: Technical Data Analysis, Inc. (TDA) - the best place in the world to work. Thanks to Scott Bradfield, Bob Merrill, Dr. Nagaraja Iyyer, Patty Walk, Doug Algera, Chris Thaiss, Doug Palmer, Ty Connell, Felix Uzoukwu, Sara

Iacobucci, and Renzo Higa. A special thanks to Chris and Bob for their comments and feedback on this thesis.

On a personal note, I wish to thank my life-long best friend Dr. Jeff Rumiano; my sister, Lara Ward; my mother, Shirley McColl; and my father, Fred McColl. I think often about my brother, Ricky McColl, who passed away in 1991. He taught me much about living.

I dedicate this effort to my dear children, Faith and Carue. I love you both!

Lastly, a special thanks to my girlfriend, Pamela Chesser (I love you!).

I've heard it said that people come into our lives for a reason, bringing something we must learn. And we are led to those who help us most to grow, if we let them - and we help them in return. - Stephen Schwartz

TABLE OF CONTENTS

LIST OF TABLES

LIST OF FIGURES

LIST OF SYMBOLS OR ABBREVIATIONS

β	Blade flap angle (deg), positive blade tip up
δ_a	Lateral cyclic control
δ_e	Longitudinal cyclic control
δ_r	Directional cyclic control
μ	Advance ratio
Ω	Rotor angular speed (rpm, Hz, or rad/s), positive counter-clockwise rotation
ϕ	Aircraft Euler angle (roll; deg)
ψ	Rotor azimuth; zero for blade pointing aft; positive counter-clockwise
σ	Rotor solidity, defined as blade area divided by blade disk area; $n_b \mathrm{c}/\pi \mathrm{R}$
θ	Blade pitch (feathering) angle (deg), positive blade leading edge up
θ	Aircraft Euler angle (pitch; deg)
ζ	Blade lag angle (deg), positive counter-clockwise rotation
ANN	Artificial neural network
AOF	Aggregate objective function
AS	Aft servo load, lb
BVI	Blade-vortex interaction
CFD	Computational fluid dynamics
C_p	Aircraft power coefficient; $\mathrm{T}/\rho \mathrm{A}(\Omega R)^3$
CSD	Computational structural dynamics
C_t	Aircraft thrust coefficient; $\mathrm{T}/\rho \mathrm{A}(\Omega R)^2$
C_w	Aircraft weight coefficient; $\mathrm{W}/\rho \mathrm{A}(\Omega R)^2$
DLM	Direct loads measurement
DOF	Degree-of-freedom
$\dot{p}$	Aircraft roll acceleration (deg/s^2)

$\dot{q}$	Aircraft pitch acceleration (deg/s^2)
FE	Finite element
FS	Forward servo load, lb
FT	Fourier transform
HB	Harmonic balance
iP	i^{th}-per-rev response content
LCA	Load confluence algorithm
LLT	Lifting line theory
LS	Lateral servo load, lb
MDC	Multidisciplinary coupling
MOO	Multi-objective optimization
n_b	Number of blades
N_z	Aircraft cg normal acceleration (g)
p	Aircraft roll rate (deg/s)
P_i	Pushrod (pitch link) axial load for the i^{th} blade (F_x; lb), positive in tension
q	Aircraft pitch rate (deg/s)
r	Blade radial station, ft
R	Blade length, ft
SCF	Spectral centroid frequency (Hz or /rev)
SE	Blade edgewise (in-plane) bending moment (M_z, lag bending; in-lb), positive counter-clockwise
SHM	Structural health monitoring
SN	Blade flapwise bending moment (M_y, flatwise or normal bending; in-lb), positive blade tip up
ST	Blade torsional moment (M_x, in-lb), positive blade leading edge up
USN	United States Navy

SUMMARY

Future management of helicopter fleets will be more heavily based on individual component damage tracking and less on legacy usage monitoring (flight parameter-based) methods. This enhances health assessment capabilities by taking into account the actual loads on a component-by-component basis. However, accurate loads prediction in rotating frame components remains a challenge. Even with advanced computational fluid dynamics (CFD) techniques, prediction of the unsteady aerodynamic loads acting on the rotor blades is computationally intensive and problematic in terms of accurate loads prediction across the entire flight regime of the helicopter. High-speed flight can potentially introduce both shock and near-stall effects within a given rotor rotation. Low-speed flight can include blade-vortex interaction (BVI) effects, wherein flow from a given blade (vorticity loading from tip vortices) impinges upon the preceding blade, causing unsteady aerodynamic loading that is difficult to quantity and predict numerically. Vehicle maneuvering can produce significantly higher blade pitching moments than steady flight. All of these regimes combine to represent the loading history of the rotor system. Therefore, accurate loads prediction methods, in terms of matching peak-to-peak, magnitude, phase, as well as vibratory/harmonic content, are required that capture all flight regimes for all critical structural components.

This research focuses on the development of a loads prediction method, known as the Load Confluence Algorithm (LCA), and its application to the analysis of a large set of flight test data from the NASA/US Army UH-60A Airloads Program. The LCA combines measured response at a prescribed set of locations with a numerical model of the rotor system. For a given flight condition (steady flight, maneuvers,

etc.) the numerical simulation's predicted loads distribution is iteratively incremented (by harmonic) until convergence with measured loads is reached at the prescribed locations (control points). Predicted loads response at non-instrumented locations is shown to be improved as well, thus enhancing fatigue lifing methods for these components.

The procedure specifically investigates the harmonic content of the applied loads and the improved prediction of the harmonic components. The impact of the enhanced accuracy on loads predictions on component structural fatigue is illustrated by way of an example.

Results show that, for a limited sensor set (two 3-axis sensors per blade), blade loads are accurately predicted across a full range of flight regimes. Hub loads are best modeled using the pushrod as the control point. Results also show that load magnitude has a tremendous influence on damage, with a 25% over-estimation of vibratory load resulting in a damage factor of nearly 3. This research highlights the importance of accurate loads prediction for a rotorcraft life tracking program. Small inaccuracies in loads lead to dramatic errors in damage assessment.

CHAPTER I

INTRODUCTION

1.1 Overview

This research focuses on the development of a loads prediction method, known as the Load Confluence Algorithm (LCA), and its application to the analysis of a large set of flight test data from the NASA/US Army UH-60A Airloads Program [17, 50, 51]. The LCA combines measured response at a prescribed set of locations with a numerical model of the rotor system. For a given flight condition (steady flight, maneuvers, etc.) the numerical simulation's predicted loads distribution is iteratively incremented (by harmonic) until convergence with measured loads is reached at the prescribed locations (control points). Predicted loads response at non-instrumented locations is shown to be improved as well, thus enhancing fatigue lifing methods for these components.

1.2 The Importance of Accurate Rotor Loads Prediction

The importance of accurate rotor loads prediction is seen in practical application by the United States Navy's (USN) plans to transition from usage monitoring to individual component damage tracking, in order to improve aircraft structures' health assessments via better prediction of fatigue damage expended for each dynamic component and fatigue critical area [56]. To achieve this objective, the USN's focus is on (1) enhanced recognition accuracy for low-speed regimes, (2) improved individual aircraft loads/strain predictions, and (3) increased accuracy in serialization and tracking of fatigue-life-limited, flight-critical safety items. Of particular interest to the research presented herein is the ability to improve loads predictions for rotary

wing aircraft, especially in the rotating frame.

Hansford et al. [42], in a review of a workshop focusing on the correlation of vibratory hub load predictions (based on a series of aeroelastic codes, all using Lynx helicopter flight test measurements), stress the importance of accurate rotor loads prediction by noting that rotor vibratory loads are extremely critical in terms of rotor design, with vibration issues being a major reason for extended lead times and costs during the aircraft development phase. Hansford highlights how consistently accurate aircraft vibration prediction is very demanding from an analytical viewpoint and is considered by many to be a goal that is currently elusive, given that the prediction of hub vibratory loads in both amplitude and phase requires a detailed knowledge of the higher frequency spanwise and azimuthal blade loading actions.

Challenges for loads prediction in the rotating frame (e.g., blade bending, pushrod axial load, etc.) include the following: nonlinear aerodynamic effects, such as (1) shed vortices from the leading blade impinging upon subsequent blades in the flow (blade-vortex interaction, BVI); (2) large airload differentials with rotor azimuth (ψ) in high-speed forward flight (e.g., the advancing blade tip approaching transonic flow while the retreating blade has regions in a near-stall condition); and (3) complex changes in load response as a function of flight condition (hover, high-speed forward flight, maneuvering, etc.). Load transference effects and influence between the rotating and fixed frames of the system (e.g., pushrod harmonic load components coalescing when fed to the fixed frame) are also challenging. The dynamics of the system itself (as well as aeroelastic coupling between the elastic system's structural and aerodynamic responses) are not trivial to adequately model numerically. Lastly, CFD methods - while capable of addressing a number of the nonlinear aerodynamic effects outlined above - are computationally intensive and not yet practical for flight-by-flight loads mapping of an in-service rotorcraft. All of these challenges point to an opportunity to approach this rotor loads prediction problem from a new perspective - the Load

Confluence Algorithm (LCA) - which is the objective of this research effort.

1.3 Rotor Loads Nomenclature and Sign Conventions

This section introduces terminology as well as the sign convention adopted for rotor loads. According to Figure 1.1, rotor angular speed, Ω, is defined as positive counter-clockwise, blade pitch (feathering) angle (θ) is defined as positive blade leading edge up, blade flap angle (β) is defined as positive blade tip up, and blade lag angle (ζ) is defined as positive clockwise rotation (opposite the direction of blade angular rotation). Furthermore, let the blade torsional moment (M_x, or ST) be de-

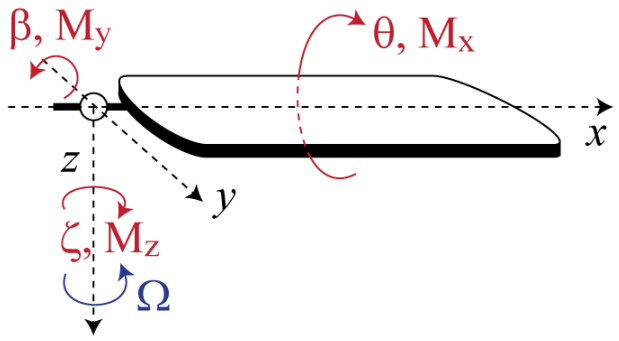

Figure 1.1: Blade sign convention.

fined as positive blade leading edge up, blade flapwise bending moment (M_y, or SN; sometimes referred to as flatwise bending or normal bending) as positive blade tip up, blade edgewise bending moment (M_z, or SE; sometimes referred to as lead-lag bending) as positive counter-clockwise, and blade pushrod (pitch link) axial load (F_x, or P_i) as positive in tension. Rotor response will often be referenced herein as a function of load contribution by harmonic of the rotor angular speed, Ω, with iP denoting the i^{th}-per-rev contribution to the load. Figure 1.2 shows the definition of rotor azimuth (ψ), the relative positions of the four UH-60A rotor blades, as well as the four quadrants of rotation (Q_1, Q_2, Q_3, and Q_4).

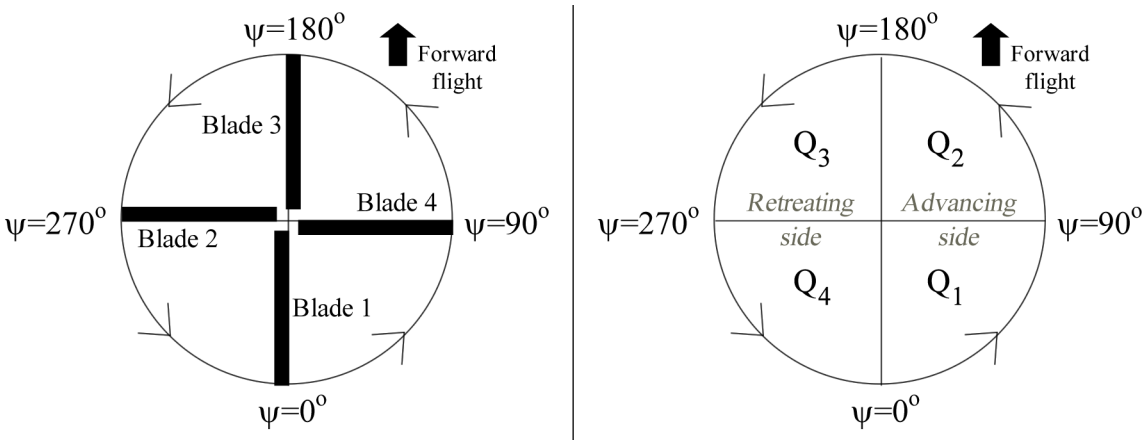

Figure 1.2: UH-60A blade position (left), quadrants of rotation (right).

1.4 Background; Related Research

This section provides an overview of relevant research and the subsequent applicability to this effort. These research areas will be broken into two distinct disciplines: (1) rotor loads identification and (2) rotor component fatigue and structural health monitoring (SHM).

1.5 Rotor Loads Identification

Ormiston [64] stated the following general trends one would hope to capture for accurate rotor loads prediction:

1. Blade torsional moment (ST) variations are most sensitive to advance ratio, μ; they are strongly driven by dynamic stall aerodynamics

2. Blade edgewise bending moment (SE) predictions are driven by the quality of the structural dynamics model

The following sections outline methods used for rotor loads estimation, with the objective of capturing these trends.

1.5.1 Flight Test Data Analysis; Multidisciplinary Coupling

There are several analyses aimed at direct observation of flight test results to understand the physics behind rotor loads behavior [53]. Additionally, numerical techniques are used to predict these behaviors. Multidisciplinary coupling (MDC) - combining CFD with computational structural dynamics (CSD) was developed and applied to address two key, unsolved problems in rotor airloads prediction: (1) azimuthal phase lag of advancing blade negative lift in high speed flight, and (2) under-prediction of blade pitching moments (torsional moment) over the entire speed range [15].

A range of research efforts have been performed based on the NASA/US Army UH-60A Airloads Program [17, 50, 51]. In a number of cases, measured UH-60A airloads were used to validate the structural model. Once validated, the predicted blade deformations are used to calculate airloads using CFD. This loose coupling method (*loose* in that it transfers airloads and blade deformations between CFD and CSD models once every rotor revolution) has been applied to a range of flight conditions to better understand the airloads and structural response (mainly the accurate prediction of blade airloads or blade bending and pushrod loads) across key points in the flight regime for the air vehicle (high-speed flight, high load maneuvers, etc.). One objective is better airloads prediction by tuning the CSD-generated elastic deformation of the blade prior to application of CFD-generated airloads. This is also known as the *mechanical airloads problem* [65], so named because it allows refinement of the structural response (response due to the application of measured (i.e., known airloads) separate from refinement of the aerodynamic response.

Chapter 3 will provide a more complete description of the NASA/US Army UH-60A Airloads Program. Section 4.6 will discuss and examine nine flight counters of interest (specific maneuvers or steady flight segments) to the research community from this test.

1.5.2 Loads Estimation Based on Fixed System Measurements

One area for improvement - and a departure from the pure numerical description of the problem outlined via multidisciplinary coupling (MDC) - is the use of fixed system measured kinematics and kinetics (acceleration, load, strain, etc.) to enhance load prediction. This could be via an approach such as rotating system component loads determined as a function of parameters measured in the fixed system via multiple regression techniques [38, 39]. In these references, air vehicle accelerations/rates, airspeed, mass, rate-of-climb, rotor angular speed (Ω), swashplate controls, and stabilator position were used to predict main rotor pushrod and blade normal bending vibratory loads. These fixed-system components were chosen because they are representative of other critical components of the rotating system.

Another method that has been explored is using fixed system flight response measurements to derive rotating system component loads via an artificial neural network (ANN; Cook et al. [28] and Flitter et al. [35]). In these references, ANNs are used to predict the loads in critical rotor dynamic components based on flight parameters that can be easily measured. The ANN learns the relationship between flight parameters (c.g. normal acceleration, pitch and roll characteristics, etc.) and component loads through exposure to a database of flight parameter records and corresponding loads histories taken from an instrumented helicopter undergoing standard maneuvers. After training, good correlation was found between the predictions of the ANN and the measurements. One concern with these approaches is the inability of fixed system measurements to predict rotating frame *reactionless* modal responses such as the $2P$ pushrod loads on a 4-bladed rotor. These loads are critical for pushrod loads prediction but are effectively canceled out in the rotating frame (i.e., for a 4-bladed rotor, blades 1 and 3 behave in a similar fashion; as do blades 2 and 4), and thus not detectable in fixed frame measurements. This is detailed in Chapter 6 of this thesis.

1.5.3 Direct Loads Measurement

An alternate approach is direct loads measurement (DLM) in the rotating frame. It seems natural to simply measure strain components in flight to monitor rotorcraft fatigue life. However, this approach has a number of difficulties. First, strain gage installation in rotating components is expensive and challenging, in terms of power, signal capture, and data transfer. Second, in view of such difficulties, it may be impractical to measure more than a small number of strain components. When few strain components are available, the accuracy of local strain predictions becomes questionable. Nevertheless, significant research has been devoted to the prediction of strain components based on the measurement of a few flight parameters or strains. For example, Bousman [14] developed a method to estimate blade normal airloads by using measured flapwise bending moments. In this work, the modal amplitudes were identified from the blade bending moments using the Strain Pattern Analysis Method. The application of the method was examined using simulated flap bending moment data that had been calculated from measured airloads for a full-scale CH-34 rotor in a wind tunnel. Bousman then compared the estimated airloads with the wind tunnel measurements. The effects of the number of measurements, the number of modes, and errors in the measurements and the blade properties were then examined. Bousman's effort has direct influence on the research at hand due to the following findings:

1. System identification techniques are suitable for application to rotor loads analyses due to the dominant periodic nature of the rotor system. System response may be realistically modeled as a function of modal response and rotor speed.

2. The fidelity of the predicted response is a function of the number of modes used in the load identification algorithm as well as the number of measurement stations.

   (a) The number of measurement stations must be equal to or greater than the

number of modes for the identification of the modal amplitudes.

(b) When errors are introduced into the data, redundancy in the number of measurement stations shows some improvement in the loads identification method.

3. Effects due to measurement error need to be considered.

(a) Calibration or scale errors will vary for each measurement station along the blade. They influence all harmonic load calculations.

(b) Static or zero offset errors only influence the calculation of the steady airload. These may be eliminated by looking only at vibratory response (mean removed).

(c) Random errors distributed in time may be present and are assumed to be reduced by averaging across larger time periods (or rotor rotations).

1.5.4 Inverse Methods for Load Identification

Inverse methods are approaches that recover the state of a system (be it displacement, load, etc.) based on a subset of state measurements. This is also referred to as *shape sensing*: the determination of a deformed shape (or system response) when it cannot be directly measured. For example, Foss et al. [36] and, later, Bogert et al. [13] investigated and implemented an algorithm for recovering a given structure's displacement field under arbitrary static loading using strain data determined at a limited number of discrete locations. This is of benefit in situations where a discrete set of strains may be measured but the displacement field itself is not directly known. The solution of this inverse problem is then based on a modal transformation, using the structure's deformation and strain modes, in conjunction with the discrete strain data, to recover the deformed shape. Bogert's effort is directly relevant to the work at hand because it uses modal analysis to relate strains to displacements. Also,

it highlights the efficiency of a modal-based solution, given that it is very efficient computationally, requiring only matrix multiplication once the transfer matrices have been formed. Given that modal characteristics of arbitrary structures may be easily formulated using finite element (FE) methods (formulation of generalized equations of motion; subsequent solution for eigenvalues and eigenvectors), it further highlights the advantages and ease of implementation of such modal-based methods.

Coates et al. [25], expanding on the quality function concept of Shkarayev et al. [75]; i.e., best fit loads match, developed an inverse interpolation method to identify in-flight loads based on real-time strain gage measurements. The loads match is based on a least-squares minimization of the error between calculated (FE-based) and measured strains. He compared predicted Fourier coefficients to sets of Fourier coefficients from a database based on historical or theoretical loads and a least-squares minimization was performed to determine which set of coefficients was the most probable solution.

Coates' effort defines the concept of load match by harmonic, according to the Fourier expansion of a given load quantity [26]. In this context, based on the assumption of periodicity of the solution relative to a given rotor angular speed, Ω (where the system period $= 2\pi/\Omega$), Fourier expansion of a given load quantity L results in the following.

$$L(t) = \underline{a}_0 + \sum_{j=1}^{H} (c_j \cos j\Omega t + s_j \sin j\Omega t) \tag{1.1}$$

where H is the retained number of harmonics of the forcing frequency used in the expansion. Additionally, Coates examined the variability/error in strain measurement and its effects on the regression analysis results as well as the importance of number of location of strain sensors. These effects will be discussed further herein. He frames the problem in the context of structural health monitoring (SHM), noting that a key problem is accurate, reliable, and real-time prediction of the applied loads, stresses, and displacements experienced in flight [26]. The implication is that, without accurate

loads, aircraft lifing exercises are inaccurate and of little value.

It should be noted that both Coates' and Bogert's efforts were based on static loading conditions. Coates notes the importance of cyclic loads for fatigue analysis. The research effort documented herein addresses cyclic loading.

1.5.5 Harmonic Balancing

The harmonic balance (HB) method may be defined as a time discretization based on a Fourier representation in time to take advantage of its periodic nature leading to spectral accuracy for loads' predictions on a per-harmonic basis [37]. The approach works for periodic systems with a well-defined fundamental frequency of the flow and a given number of its harmonics. It has been applied to pitching airfoils and wings [37] as well as turbomachinery [40, 76] and is ideally suited for rotor systems given the dominance of rotor loads content as a function of rotor angular speed.

1.6 Rotor Component Fatigue and Structural Health Monitoring

Accurate rotor loads estimation is best examined in the context of the end-use of the loads; i.e., application in an aircraft fleet's fatigue life management program. This entails individual component damage tracking [56], specifically: (1) accurate loads prediction for all critical components across the entire flight regime of the aircraft; (2) fatigue analysis for each component using these loads; and (3) a broader structural life management program for trending, forecasting, and decision making based on the results of these analyses. This can fall under the heading of Structural Health Monitoring, or SHM.

Metallic rotorcraft components are typically tracked using the Palmgren-Miner Linear Damage Accumulation Hypothesis [63, 68] to predict the time to crack initiation [33, 48]. This rule states that the crack onset occurs when the summation of life fractions reaches unity. The successful use of this rule requires proper handling

of cycle counting, over-strain effects, and local notch mean stress effects. The local strain approach is typically used, which focuses attention on the stresses and strains that occur locally at a stress concentration of interest, and uses a strain versus life curve instead of the typical S-N curve. This analysis method is discussed in greater detail and demonstrated by way of an example in Chapter 7.

Regardless of the computational methods used to assess component life, the greatest challenge lies in the assemblage of the usage spectra for the given component. This has historically been done based on assuming that certain maneuvers (flight regimes) are performed for defined periods of time. For the US Army, this method has been used to compute Calculated Retirement Time (CRT) of limited-life components [60]. This could lead to fatigue life-limited structural components being routinely removed, replaced, and retired well before reaching the number of flight hours determined by the manufacturer's calculated retirement times. This is due to conservative usage profiles being applied, in order to ensure high component reliability. Typical is the so-called *six-nine* reliability: a reliability level of 0.999999, based on a $\mu+3\sigma$ factor of safety applied to component lives [34]. Component reliability is driven by a number of factors, including acquisition of actual aircraft flight-by-flight loads and the accuracy of these loads. The absence of flight-by-flight loads would lead to a conservative estimate of what was missing. Inaccuracy of the loads used for fatigue assessment could drive the assessment in a conservative or unconservative direction, depending on whether loads are over-predicted or under-predicted.

Studies by Algera et al. [5] have categorized lifing methods into three categories:

1. Hours-based lifing: each component's CRT is preset to a number. Flight records are used to track component hours. Once the usage hours meet the published retirement time, the component is removed from service. This approach is simple to implement and track but must be very conservative since no actual usage variations are considered.

2. Regime-based lifing: using measured flight data, each flight usage is partitioned into regimes, each with a prescribed damage rate by component. Once these accumulated damages exceed some preset limit, the component is removed from service. This approach does account for the variation in aircraft usage, but still relies on predefined damage rates per regime, which in themselves may vary significantly. For example, a 2g maneuver could produce different load distributions, depending on the pilot's technique.

3. Direct loads measurement (DLM)-based lifing: direct loads measurement (e.g., strain gages installed at each critical component) is obviously the most realistic scenario and removes all conservatism from the fatigue analysis. DLM was discussed in greater detail above.

This reference estimates differences in life for the UH-60A main rotor shaft and pitch control horn of a factor of 2 to 5 between regime recognition and direct loads monitoring, with regime recognition being the more conservative of the two (i.e., lower life estimates). Rotorcraft damage tolerance and probabilistic-based lifing methodologies exist as well (e.g., [79] and [61], respectively) but will not be applied herein.

1.7 Motivations

The motivations for development of the LCA technology are as follows:

1. More accurate loads prediction results in improved service life estimation for fatigue-critical structural components. This expands the rotorcraft industry's ability to design, operate, and manage aircraft.

2. The LCA is an iterative, semi-empirical solution technique; it is expected to only require a small set of measurements to predict stresses throughout the structure. This is compatible with rotating system instrumentation sets currently being field tested by the USN [6].

3. It demonstrates robustness and accuracy across a range of flight regimes. This is consistent with the USN's SHM requirement for enhanced regime recognition accuracy [56].

4. It exhibits rapid computation time (relative to CFD).

5. The LCA is compatible with load alleviation and damage mitigation technologies: it matches loads on a per harmonic basis, thus accounting for all critical vibratory content.

From an industry perspective, this technology could serve a key purpose. The USN's engineering community recognizes the advantages of individual component damage tracking with the goal of enhancing health assessment capabilities. Improving individual aircraft loads/strain prediction is an important focus of this objective [56]. Direct loads-based usage tracking for fatigue-critical rotorcraft dynamic components provides insight into the actual load history of the component in question, offers the potential to extend component service life, and allow for part remediation through the acceptance of greater repair limits. Direct loads-based usage tracking can also prevent unnecessary maintenance actions, such as early retirement of the component, enhancing mission readiness and reducing maintenance costs. This presents the opportunity for significant maintenance cost savings as well as enhanced awareness of component structural health and improved safety.

1.8 Objectives

The objectives of this effort are to develop the load confluence algorithm and systematically apply it to a large, real-world flight test dataset, show its strengths in matching system response both at instrumented and mapped locations on the rotor structure, and show its limitations in reaching suitable loads matches. Additionally,

the objectives include advancing the understanding of rotor loads content by harmonic as well as the mechanics behind loads transference between the rotating and fixed frames (e.g., rotor system-to-control servos). Lastly, the impact of enhanced loads matching on rotor component fatigue lifing will be addressed.

1.9 Contributions

The following is a list of innovative contributions generated from this research.

1. Development of the Load Confluence Algorithm (LCA)
2. Systematic application of the LCA to UH-60A flight test data
3. Assessment, derivation, and understanding of rotor loads harmonic content as well as load transference between the rotating and fixed frames
4. Enhanced application and advancement of the use of real-world measurement for numerical model loads correction and matching
5. Advancing the knowledge base for rotor component fatigue lifing

1.10 Organization of the Work

This work is organized as follows. The Load Confluence Algorithm (LCA) methodology and numerical implementation in DYMORE [8] are provided in Chapter 2. Application of the LCA to the NASA/US Army UH-60A dataset is documented in Chapters 3 through 5. Chapter 6 addresses rotor load harmonic decomposition and load transference between the rotating and fixed frames. The impact of loads accuracy on rotor component structural fatigue life is documented in Chapter 7. Finally, Chapter 8 summarizes research conclusions and proposed future work.

CHAPTER II

THE LOAD CONFLUENCE ALGORITHM

2.1 Load Confluence Algorithm Overview

The Load Confluence Algorithm (LCA) is an iterative numerical method that combines modeling and measurement to improve CSD-based system response predictions (e.g., loads and stress predictions in mechanical systems). The overall approach is summarized as follows. A number of system response measurements are made at specified *control points* on a structure. These measurements - displacements, accelerations, strains, or forces and moments - are then used to identify the external forces and moments applied to the system. This *inverse method* for load identification [26] is performed in the modal domain for computational efficiency. These identified loads are then used to predict system response (e.g., loads or stresses) at all structural locations of interest - specifically at locations other than control points. These will be referred to as *mapped stations*. Applied loads are then iteratively incremented until predicted response matches measured response at the control points. The full response field - including response at mapped stations - is then known. Iteration is required because each incremental change to the system forcing function results in a change in system response. The true strength of the LCA is its ability to accurately predict system response at these mapped locations.

2.2 LCA Application to a Rotor System

For example, let the system be a rotor: specifically the rotor hub, controls, and blades. Force and moment measurements are made at prescribed locations, such as pushrod axial load and blade flapwise, torsional, and edgewise bending at two radial stations.

The LCA is then used to compute system response at all critical locations on the rotor system: pitch control horn, control servos, blade, etc.

The prediction of the aeroelastic response of a rotor system involves two main components. First, a structural dynamics tool that predicts the dynamic response of the rotor and dynamic components given the loads applied to the system, and second, a fluid dynamics tool that predict the unsteady aerodynamic loads applied to the blade given its configuration and velocity field. The first module of the LCA predicts the fully nonlinear dynamic response of the rotor system given the applied loads. In particular, the displacements, strains, or bending moments in the blades and rotating components are predicted. Due to model inaccuracy and uncertainty in the operating environment, the predicted response (e.g., strain), ϵ, will not necessarily match their measured counterparts, and a response discrepancy, $\Delta\epsilon$, is computed as the difference between the two. The second module is a linearized load identification algorithm that predicts a correction in the applied loads, ΔL, that should produce this $\Delta\epsilon$ strain. Proceeding in an iterative manner, the predicted strains can be made to match the measurements at the prescribed control points. Since the process is iterative in nature, the LCA can be linearized. A modal approximation to the dynamic behavior of the system provides a suitable base to the development of this algorithm. A CSD code such as DYMORE [8] may be used for the nonlinear analysis of the system. At convergence, a fully nonlinear solution is obtained, and the applied loads will create a response that closely approximates the actual strain field at the control points, with expectation for improvement at other non-instrumented (mapped) stations as well.

2.3 LCA Methodology

Consider a linear, undamped discrete system with n-degrees of freedom (DOF; e.g., n nodal displacements and/or rotations), such as a rotor blade rotating at constant angular speed Ω, subject to aerodynamic and inertial loading. The resulting equations

of motion are n coupled second-order ordinary differential equations:

$$\mathbf{M}\underline{\ddot{y}}(t) + \mathbf{K}\underline{y}(t) = \underline{F}(t) \tag{2.1}$$

where $\underline{y}(t)$ are the n system degrees of freedom, y_1, ..., y_n, $\mathbf{M}$ and $\mathbf{K}$ are, respectively, the finite element model (FEM)-derived mass and stiffness matrices of the system (both $n \times n$), and $\underline{F}(t)$ are the externally applied nodal loads, F_1, ..., F_n. The objective is to have a solution to these equations that is separable in time and of the following form.

$$\underline{y}(t) = \mathbf{\Phi}\underline{q}(t) \tag{2.2}$$

This form of the solution (obtained by a linear transformation) physically means that all coordinates (now $\underline{q}(t)$) perform synchronous motions and the system configuration does not change its shape during motion, only its amplitude [62]. $\underline{q}(t)$ are the m generalized (or modal) displacements, q_1, ..., q_m, and $\mathbf{\Phi}$ are the m eigenmodes.

Note that $m \leq n$ since the number of measurement stations must be equal to or greater than the number of modes for the proper identification of the modal amplitudes (Bousman [14]). By a similar change in variable, the external nodal forces $\underline{F}(t)$ may be expressed in terms of the external modal forces, λ_1, ..., λ_m.

$$\underline{F}(t) = \mathbf{M}\mathbf{\Phi}\underline{\lambda}(t) \tag{2.3}$$

The eigensolution is normalized such that:

$$\mathbf{\Phi}^T\mathbf{M}\mathbf{\Phi} = \mathbf{I} \tag{2.4}$$

Equation 2.1 may now be written as m uncoupled second-order equations in the modal domain [62] as:

$$\underline{\ddot{q}}(t) + diag(\omega_i^2)\underline{q}(t) = \underline{\lambda}(t) \tag{2.5}$$

where ω_i^2 are the eigenvalues of the system. Based on the assumption of periodicity of the solution relative to some fundamental harmonic Ω (e.g., rotor angular speed; see

Section 3.3.4), Fourier expansion of the modal displacements can be applied, resulting in the following.

$$\underline{q}(t) = \underline{q}_0 + \sum_{j=1}^{H} (\underline{q}_j \cos j\Omega t + \underline{r}_j \sin j\Omega t) \tag{2.6}$$

where H is the retained number of harmonics of the fundamental harmonic used in the expansion. The value of H is chosen such that the Fourier expansion provides a suitable representation of the actual periodic time series (see Figure 3.3 for an example). $\underline{q}_0$, $\underline{q}_j$, and $\underline{r}_j$ are the mean, Fourier cosine, and Fourier sine coefficients of $\underline{q}(t)$, respectively [30], and are defined as follows.

$$\underline{q}_0 = \frac{1}{2\pi} \int_0^{2\pi} \underline{q}(\psi)\, \mathrm{d}\psi \tag{2.7}$$

$$\underline{q}_j = \frac{1}{\pi} \int_0^{2\pi} \underline{q}(\psi)\, \cos(j\psi)\, \mathrm{d}\psi \tag{2.8}$$

$$\underline{r}_j = \frac{1}{\pi} \int_0^{2\pi} \underline{q}(\psi)\, \sin(j\psi)\, \mathrm{d}\psi \tag{2.9}$$

where azimuth, ψ, is related to time, t, as:

$$\psi = \Omega t \tag{2.10}$$

Fourier expansion of the external modal forces results in the following.

$$\underline{\lambda}(t) = \underline{\lambda}_0 + \sum_{j=1}^{H} (\underline{\lambda}_j \cos j\Omega t + \underline{\mu}_j \sin j\Omega t) \tag{2.11}$$

where $\underline{\lambda}_0$, $\underline{\lambda}_j$, and $\underline{\mu}_j$ are the mean, Fourier cosine, and Fourier sine coefficients of $\underline{\lambda}(t)$, respectively. Now equations 2.6 and 2.11 are inserted into 2.5. By harmonic balancing, the external modal forces, $\underline{\lambda}$, may be related to the modal displacements, $\underline{q}$, as:

$$\underline{\lambda}_0 = diag(\omega_i^2)\, \underline{q}_0 \tag{2.12}$$

$$\underline{\lambda}_j = diag(\omega_i^2 - j^2\Omega^2)\, \underline{q}_j \tag{2.13}$$

$$\underline{\mu}_j = diag(\omega_i^2 - j^2\Omega^2)\, \underline{r}_j \tag{2.14}$$

By a change in variable, the nodal response (be it nodal displacement, acceleration, strain, or force/moment; ϵ_1, ..., ϵ_n) is now expressed in terms of the modal displacements (q_1, ..., q_m) by means of the response (acceleration/strain/force/moment)-displacement matrix, $\mathbf{B}$ ($n \times m$).

$$\underline{\epsilon}(t) = \mathbf{B}\,\underline{q}(t) \tag{2.15}$$

In the special case where the objective is to solve for system nodal displacements, y, then $\mathbf{B}$ is the eigenmode matrix, $\mathbf{\Phi}$. In other cases, the desire may be to directly relate modal displacements to nodal accelerations, strains, forces, or moments. These time or spatial derivatives of the nodal displacements (scaled by the appropriate quantities, e.g., nodal mass for acceleration) are to be computed and incorporated into the $\mathbf{B}$ matrix for use herein. $\mathbf{B}$ will be referred to as the *strain-displacement matrix* for simplicity. Inversion of equation 2.15 via singular value decomposition (SVD) methods ([8], Section 18.9) yields the following.

$$\underline{q}(t) = \mathbf{B}^{+}\,\underline{\epsilon}(t) \tag{2.16}$$

where $\mathbf{B}^{+}$ ($m \times n$) is the Moore-Penrose pseudo-inverse [69] of the strain-displacement matrix, $\mathbf{B}$. Fourier expansion of the nodal strains results in the following.

$$\underline{\epsilon}(t) = \underline{\epsilon}_0 + \sum_{j=1}^{H} (\underline{\epsilon}_j \cos j\Omega t + \underline{\kappa}_j \sin j\Omega t) \tag{2.17}$$

where $\underline{\epsilon}_0$, $\underline{\epsilon}_j$, and $\underline{\kappa}_j$ are the mean, Fourier cosine, and Fourier sine coefficients of $\underline{\epsilon}(t)$, respectively. Now equation 2.17 is inserted into 2.16 and that result into equations 2.12 through 2.14. This yields the external modal forces, $\underline{\lambda}$, in terms of the Fourier expansion of the nodal response (e.g., strains), $\underline{\epsilon}$.

$$\underline{\lambda}_0 = diag(\omega_i^2)\,\mathbf{B}^{+}\,\underline{\epsilon}_0 \tag{2.18}$$

$$\underline{\lambda}_j = diag(\omega_i^2 - j^2\Omega^2)\,\mathbf{B}^{+}\,\underline{\epsilon}_j \tag{2.19}$$

$$\underline{\mu}_j = diag(\omega_i^2 - j^2\Omega^2)\,\mathbf{B}^{+}\,\underline{\kappa}_j \tag{2.20}$$

Expansion of 2.3 yields the desired result: the external force vector in terms of nodal loads, each of which has now been expressed in terms of nodal strains (by 2.18 - 2.20).

$$\underline{F}(t) = \mathbf{M}\mathbf{\Phi}\left(\underline{\lambda}_0 + \sum_{j=1}^{H}(\underline{\lambda}_j \cos j\Omega t + \underline{\mu}_j \sin j\Omega t)\right) \tag{2.21}$$

2.3.1 Application to a Numerical Time History Simulation

Say that the above approach is based on a finite element (FE)-based structure undergoing dynamic loading in a numerical time history simulation. The LCA could produce predicted loads or strains, $\underline{\epsilon}$, at a set of prescribed locations (*control points*) matching those obtained from an experiment (e.g., flight test-measured response). A similar set of equations to those presented above can be expressed for these measured strains, $\underline{\epsilon}^*$. Equations 2.18 through 2.20 can now be used to formulate external modal forces, $\underline{\lambda}^*$, in terms of these experimentally-measured nodal strains, as:

$$\underline{\lambda}_0^* = diag(\omega_i^2)\,\mathbf{B}^+\underline{\epsilon}_0^* \tag{2.22}$$

$$\underline{\lambda}_j^* = diag(\omega_i^2 - j^2\Omega^2)\,\mathbf{B}^+\underline{\epsilon}_j^* \tag{2.23}$$

$$\underline{\mu}_j^* = diag(\omega_i^2 - j^2\Omega^2)\,\mathbf{B}^+\underline{\kappa}_j^* \tag{2.24}$$

The difference between analysis and experiment at each of the n nodes, $\Delta\underline{\epsilon}$, may now be computed, as:

$$\Delta\underline{\epsilon} = \underline{\epsilon} - \underline{\epsilon}^* \tag{2.25}$$

From here $\Delta\underline{\lambda}$ could be computed and, thus, $\Delta\underline{F}$, which yields the change in external nodal loads required to produce the desired change in strain at each control point, as:

$$\Delta\underline{F}(t) = \mathbf{M}\mathbf{\Phi}\left(\Delta\underline{\lambda}_0 + \sum_{j=1}^{H}(\Delta\underline{\lambda}_j \cos j\Omega t + \Delta\underline{\mu}_j \sin j\Omega t)\right) \tag{2.26}$$

The total externally applied load vector can then be reassembled as:

$$\underline{F}(t^+) = \underline{F}(t) + \Delta\underline{F}(t) \tag{2.27}$$

where t^+ is the next timestep in the numerical simulation. This force vector is applied to the entire system, thus affecting the response at the prescribed *control points* as well as at all other mapped locations. This achieves the objective of loads correction across the entire structure. This approach is outlined in Figure 2.1.

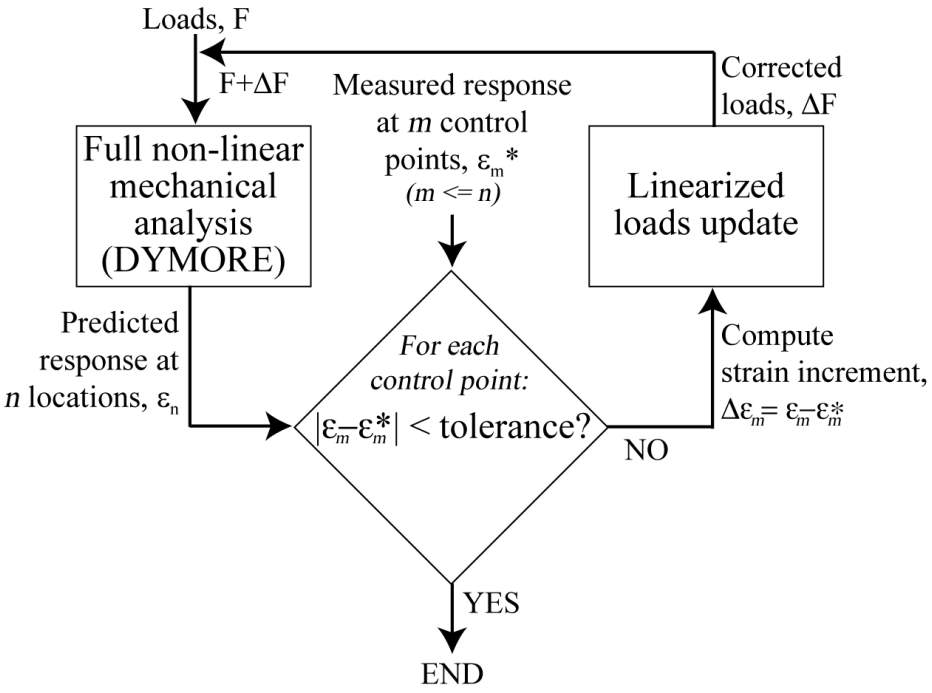

Figure 2.1: LCA overview.

The load confluence approach may be summarized as follows. In the modal domain, changes in the applied loads are related to changes in measured strains. The solution is then iterated until a best fit match between analytically-predicted and measured strains is reached. In this context, a best fit match is one that minimizes the error between analytically-predicted and measured strains across all critical locations.

2.3.2 Application in the Context of a Rotor System

In the context of a rotor system, a best fit match is one that minimizes the error between analytically-predicted and measured strains across all critical locations across all critical flight regimes. This could allow a simplified airload distribution to be

applied (e.g., lifting line theory (LLT) as opposed to more computationally-intensive CFD) and iteratively modified to reach a solution that matches measured response. As the iteration proceeds, the aerodynamic loads predicted by simplified LLT are progressively updated by corrections that shape both spatial and temporal distributions of the applied airloads to produce the measured strains. Thus, the method uses the measured strains to account for the inaccurate airloads predicted by the simplified aerodynamic models. The benefits include dramatic reduction in runtime and computational requirements for airload generation provided by simpler aerodynamic models. This may be more supportive of a rotorcraft life tracking system required to operate in near-real time.

This approach also bypasses the problems associated with uncertainty in the aircraft operating environment. Whereas overall flight parameters, such as airspeed, altitude, and gross weight, are recorded, many other parameters are not. Among them are gust speed and direction, turbulence levels, instantaneous weight and center-of-gravity location, pilot inputs, etc. The LCA will automatically correct for these factors, because it is based on actual measurements in the rotating system.

2.4 DYMORE Implementation

The LCA has been integrated into DYMORE (v.4), the details of which are presented in [22]. This implementation involves several interacting software modules. The first module defines the output signals to be used in the analysis. The user defines the location and nature of each signal to be used. A typical signal could be a particular component of strain or load (e.g., flapwise bending moment at a specific spanwise location along the blade). These signals must include all control points as well as all mapped locations to be used for loads estimation by the LCA. The second module defines the control points to be used by the LCA. For each defined signal to be used as a control point in the analysis, an experimental measurement is required.

Measurements are input in the form of Fourier coefficients for a given number of harmonics. The last module is the actual load confluence algorithm. Given the signals defined in the instrumentation package and the experimental measurements, the applied loads are modified to better match the given measurements at each control point. Corrections are applied iteratively throughout the duration of the simulation.

2.4.1 Experimental Data Import

The experimental data import defines a text file containing Fourier coefficients for a predefined number of harmonics for a prescribed set of signals (e.g., flapwise bending at $0.20R$; *SN20*) to be used by the LCA for loads estimation and correction. These inputs must include the following:

1. Experimental data file name and location
2. Signal name and definition

2.4.2 Confluence Definition

The confluence definition provides the list of signals to be used as control points by the LCA, along with the selected modes to be used in the solution, the start time for application of the LCA, and the period between LCA applications. These inputs must the following:

1. List of control points
2. LCA start time
3. Number of cycles between LCA applications
4. Selected modes to be used in analysis (equation 2.2)

2.5 Validation

In addition to application and validation with UH-60A flight test data (Chapters 3 through 5, herein), the LCA has been validated using well-controlled laboratory experiments. Specifically, tests were performed on a scale model rotor blade (Chierichetti et al. [22]) and a plate structure (Chierichetti et al. [23]).

2.5.1 Rotor Blade Test

The test specimen [22] was a straight, uniform blade of length 0.413 m, chord 0.07 m, and mass 178 kg. It was a NACA 0012 airfoil. The blade was excited by an LDS V201/3 electrodynamic shaker located at two-thirds span. The blade was clamped at its base. The response was characterized through velocity and displacement measurements recorded by a Polytec PSV-400 scanning laser vibrometer. In addition, strain measurements were performed at five locations along the blade span using five axial strain gages. The strain gages were placed within two-thirds of the span close to the root, where strains would be expected to reach higher values. For a 10 Hz excitation, the objective was to match response (blade curvature) at the blade root and blade tip between numerical simulation with the LCA applied and experiment. It was shown that in only three iterations the numerical response converged to the corresponding measured values, both in magnitude and phase.

2.5.2 Plate Test

Experiments were performed on an aluminum plate to demonstrate the validity of the LCA. The plate was rectangular, with dimensions of 0.25×0.46 m, and a thickness of 1.5 mm. The plate was partially cantilevered at its bottom edge and a concentrated force was applied through an LDS V201/3 electrodynamic shaker located at $x = 0.125$ m and $y = 0.355$ m from the lower left corner of the cantilevered plate. The velocity distribution over the plate surface was measured by a Polytec PSV-400 scanning laser vibrometer. The velocity field of the plate was integrated to obtain the

corresponding displacement distribution. The scanning laser vibrometer was set to take measurements at 209 points over the plate. This set of points was divided into two subsets: a small subset whose measurements were used by the LCA to identify the response, and a larger subset that was used to compare the full-field numerical predictions with the actual response of the plate.

The harmonic response of the plate was analyzed for different excitation frequencies. Results were presented in Reference [23] for two different excitations: 10 Hz and 20 Hz. Both the cases of an accurate initial load distribution (a concentrated load applied in the numerical solution at the test shaker location) and an inaccurate initial distribution (a concentrated load applied in the numerical solution at a different location than the test shaker location) were presented. The ability of the LCA to identify the full-field response of the structure was successfully demonstrated. The reconstructed response showed good agreement with experimental. The peak-to-peak error and phase difference between signals were reduced by more than 90%. Results showed that these improvements were also achieved at points not used as control points, thus validating the LCA's ability to provide valid mapped loads fields.

2.6 LCA Extension to Other CSD Codes

Though implemented in DYMORE, the intent of the LCA would be compatibility with other CSD codes, such as the US Army's Rotorcraft Comprehensive Analysis System (RCAS). This could proceed as one of the following two implementation methods:

1. Directly embed the LCA in RCAS at each timestep of the simulation.
   (a) This is the method used for DYMORE implementation.
   (b) This method would be difficult to implement since RCAS source code is not publicly available.

2. Develop the LCA as an iterative post-processor.

   (a) For each i^{th} timestep, output the RCAS-computed responses at each control point and compare with the experimental results.

   (b) Modify the RCAS airloads input, per Figure 2.1.

   (c) Restart RCAS at the next timestep, using these new LCA-modified airloads.

   (d) Continue until a best fit loads match is achieved.

   (e) This method would be easier to implement than method 1, but would add significant runtime.

CHAPTER III

UH-60A FLIGHT TEST ANALYSIS: SETUP AND MODEL DEVELOPMENT

This chapter details the systematic process applied to UH-60A flight test data for loads generation, comparison, and correction between experiment (flight test) and DYMORE-based LCA analysis.

3.1 NASA/US Army UH-60A Airloads Program Overview

The flight test phase of the NASA/US Army UH-60A Airloads Program [17, 19, 50, 51] was completed in February 1994. The objective of the program was to measure a comprehensive set of measured airloads and external loads in the rotating frame, as well as aircraft flight parameters and other fixed system measurements. This then allows the research community (as well as industry) opportunities to improve numerical simulations of rotor loads and system responses. Airloads were measured on one blade (hereafter *blade 1*) using 221 pressure transducers installed in nine radial arrays. Additionally, 21 transducers were installed in blade 3 (180 deg lag relative to blade 1) at nine radial stations to measure blade bending along the three axes: flapwise (normal) bending (SN), edgewise (in-plane) bending (SE), and torsional moment (ST). A total of 31 data flights were flown, totaling 57 flight hours.

Table 3.1 lists the first set of UH-60A flights used for analysis herein (flights 84 and 85, totaling 51 flight counters; [16, 19]). All flight counters from flights 84 through 116 (601 total flight counters) are examined in Section 4.7. Tables 3.2 through 3.4 list the measured parameters applied to this research effort. These parameters are a subset of the full instrumentation list from the test program. See Reference [19] for

the full listing. Figure 3.1 shows the blade instrumentation.

Table 3.1: UH-60A flights used for analysis.

Flight number	**Flight counters**	**Objective**	**Description**
84	22	Steady and maneuvering airloads	Level flight; accel/decel; hover
85	29	Steady and maneuvering airloads	Level flight; steady turns; roll reversals
Total:	**51**		

Table 3.2: Relevant aircraft, blade, and hub measurements.

Measurement group	**Number of sensors**	**Sample rate (per sec)**	**Filter frequency (Hz)**
Aircraft states and controls	42	209	36
Blade pressures	242	2142	550
Blade flapwise bending, edgewise bending, and torsional moment	21	357	110
Blade pitch (feather), flap, and lag angles	12	357	110
Blade pitch link (pushrod) and lag damper load	8	357	110
Blade flap and edge acceleration	20	357	110

Table 3.3: Relevant measured parameters (1 of 2).

TRENDS ID	**Description**	**Units**
ABCLOCK	Airborne clock	msec
AMU	Advance ratio (μ)	-
AZCGC	Normal acceleration at the cg	ft/s^2
AZIMUTH	Rotor azimuth (ψ)	deg
BE01	MR root edgewise bending (blade 3)	in-lb
CP	Coefficient of power (C_p)	-
CT	Coefficient of thrust (C_t)	-
GW	Aircraft gross weight	lb
HPB	Pressure altitude (boom)	ft
LATSTK	Control position (lateral; δ_a)	-
LONGSTK	Control position (longitudinal; δ_e)	-
MQIN	Main rotor shaft torque	in-lb
MRALSS	MR aft link load	lb
MRFLAP1,2,3,4	MR flap angle (blade 1,2,3,4; β)	deg
MRFLSS	MR fwd link load	lb
MRLAG1,2,3,4	MR lag angle (blade 1,2,3,4; ζ)	deg
MRLSS	MR lateral link load	lb
MRPITCH1,2,3,4	MR pitch angle (blade 1,2,3,4; θ)	deg
MRSTASC	MR stationary scissors load	lb
MTIP	Advancing tip Mach number (blade 1)	Mach
PEDAL	Control position (directional; δ_r)	-
PITCHATT	Pitch attitude (θ)	deg
PTCHRATE	Pitch rate (q)	deg/s
PTCHACC	Pitch acceleration ($\dot{q}$)	deg/s^2
ROLLATT	Roll attitude (ϕ)	deg
ROLLRATE	Roll rate (p)	deg/s
ROLLACC	Roll acceleration ($\dot{p}$)	deg/s^2
RPMMR	Rotor speed (Ω)	rpm
RQ10	MR torque	ft-lb
VCALB	Boom calibrated airspeed	kts

Table 3.4: Relevant measured parameters (2 of 2).

TRENDS ID	Description	Units
BN01	MR root normal (flapwise) bending	in-lb
BP10,20,30,40	MR pushrod load (blade 1,2,3,4)	lb
RL01,2,3,4	Lead-lag damper load (blade 1,2,3,4)	lb
RQ11	MR shaft bending	in-lb
RQ12	MR shaft upper bending	in-lb
SE01	Edgewise (in-plane) bending $0.113R$ (blade 3)	in-lb
SE20	Edgewise (in-plane) bending $0.20R$ (blade 3)	in-lb
SE30	Edgewise (in-plane) bending $0.30R$ (blade 3)	in-lb
SE40	Edgewise (in-plane) bending $0.40R$ (blade 3)	in-lb
SE50	Edgewise (in-plane) bending $0.50R$ (blade 3)	in-lb
SE60	Edgewise (in-plane) bending $0.60R$ (blade 3)	in-lb
SE70	Edgewise (in-plane) bending $0.70R$ (blade 3)	in-lb
SE80	Edgewise (in-plane) bending $0.80R$ (blade 3)	in-lb
SN01	Flapwise (normal) bending $0.113R$ (blade 3)	in-lb
SN20	Flapwise (normal) bending $0.20R$ (blade 3)	in-lb
SN30	Flapwise (normal) bending $0.30R$ (blade 3)	in-lb
SN40	Flapwise (normal) bending $0.40R$ (blade 3)	in-lb
SN50	Flapwise (normal) bending $0.50R$ (blade 3)	in-lb
SN60	Flapwise (normal) bending $0.60R$ (blade 3)	in-lb
SN70	Flapwise (normal) bending $0.70R$ (blade 3)	in-lb
SN80	Flapwise (normal) bending $0.80R$ (blade 3)	in-lb
SN90	Flapwise (normal) bending $0.90R$ (blade 3)	in-lb
ST30,50,70,90	Torsional moment $0.30R$-$0.90R$ (blade 3)	in-lb
CC1, CN1	Chordwise, normal force $0.225R$ (blade 1)	lb/in
CC2, CN2	Chordwise, normal force $0.400R$ (blade 1)	lb/in
CC3, CN3	Chordwise, normal force $0.550R$ (blade 1)	lb/in
CC4, CN4	Chordwise, normal force $0.675R$ (blade 1)	lb/in
CC5, CN5	Chordwise, normal force $0.775R$ (blade 1)	lb/in
CC6, CN6	Chordwise, normal force $0.865R$ (blade 1)	lb/in
CC7, CN7	Chordwise, normal force $0.920R$ (blade 1)	lb/in
CC8, CN8	Chordwise, normal force $0.965R$ (blade 1)	lb/in
CC9, CN9	Chordwise, normal force $0.990R$ (blade 1)	lb/in
CM1	Pitching moment $0.225R$ (blade 1)	in-lb/in
CM2	Pitching moment $0.400R$ (blade 1)	in-lb/in
CM3	Pitching moment $0.550R$ (blade 1)	in-lb/in
CM4	Pitching moment $0.675R$ (blade 1)	in-lb/in
CM5	Pitching moment $0.775R$ (blade 1)	in-lb/in
CM6	Pitching moment $0.865R$ (blade 1)	in-lb/in
CM7	Pitching moment $0.920R$ (blade 1)	in-lb/in
CM8	Pitching moment $0.965R$ (blade 1)	in-lb/in
CM9	Pitching moment $0.990R$ (blade 1)	in-lb/in

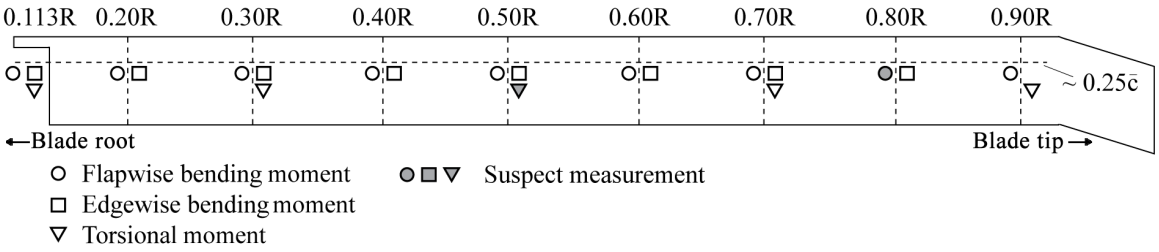

Figure 3.1: UH-60A blade 3 instrumentation for loads measurement.

3.2 UH-60A Flight Test Data: Known Issues

3.2.1 Data Issues and Discrepancies

Reference [66] describes known measured data discrepancies and anomalies in the UH-60A dataset. Issues of note to this research effort are listed in Table 3.5.

Table 3.5: Known UH-60A flight test data issues and discrepancies.

Issue	**Resolution**
Mean values of several load quantities considered erroneous	Mean removed from all load quantities; this was confirmed by Kufeld et al. [53]: "in most cases, the steady loading has been removed from the plots; the strain gages drifted during the test with the result that the steady terms are not reliable"
Uncertain pushrod stiffness (62,631 v. 187,792 lb/ft) [54]	The stiffer model was used, resulting in a blade first torsion modal frequency greater than $4P$
Small unidentified errors in the measured airloads resulting in discrepancies in the $1P$ flapping phase	Measured airloads are only used in the *mechanical airloads* solution (see Section 4.5 for analysis description)

3.2.2 Differences Between UH-60A Flight Test Rotor Blades

The test aircraft rotor blades were modified with embedded instrumentation: pressure transducers in blade 1; strain gages (loads transducers) in blade 3; along with the production blades 2 and 4. Given this, the question arises as to the expected similarity in response between blades. Kufeld et al. [41] describes a shake test performed on the UH-60A blades in a free-free configuration, where each blade was hung from bungee cords whose stiffness was lower than that of the blade. Free-free testing was selected over a clamped or pinned blade configuration due to ease of testing. The objective of the test was to compare natural frequencies for the different blades for each distinct modeshape. Conclusions from the test include the following:

1. There was up to 2.4% variability between the frequencies of the four production blades (i.e., material/manufacturing scatter)

2. There was a 2-4% reduction in modal frequency for the pressure blade (flight test blade 1); this is only slightly lower than the variance seen among production blades

3. The strain gage blade (blade 3) deviated less from the production average than did some of the standard blades

Table 3.6 lists the modal frequencies for the tested UH-60A blades [41]. Given these results, the analysis documented herein uses the production blade properties.

3.3 UH-60A Flight Test Data Analysis

The following sections detail the process through which UH-60A flight test counters are processed for use in numerical simulation for rotor loads prediction using the LCA.

Table 3.6: Model frequencies of the UH-60A blades tested.

Mode	Production blades (range; Hz)	Strain blade (Hz)	Pressure blade (Hz)
1st flapping	4.77 - 4.83	4.78	4.69
2nd flapping	12.74 - 13.01	12.74	12.46
3rd flapping	25.17 - 26.01	25.47	24.87
4th flapping	41.64 - 42.66	42.01	40.51
5th flapping	64.08 - 65.45	64.15	62.28
6th flapping	95.32 - 97.15	96.00	92.72
1st edgewise	25.84 - 26.38	25.60	26.00
2nd edgewise	69.12 - 70.31	69.12	67.37
1st torsion	45.51 - 46.61	45.56	44.49
2nd torsion	83.48 - 85.12	83.88	80.75
Blade weight (lb)	210.4 - 211.7	212.5	215.7

3.3.1 TRENDS Database Data Extraction

The parameters listed in Tables 3.3 and 3.4 are extracted from the TRENDS database at 357 Hz (the sample rate for the bending and torsional moments; Table 3.2) for each flight (and subsequent flight counters) listed in Tables 3.1 and 4.5. This requires re-sampling of certain other parameters. The mean is removed from each measured response (loads, blade angles), thus allowing analysis on the oscillatory (or *incremental*) response only. All data are then filtered in Matlab - first with a 50 Hz, 5-pole Butterworth low-pass filter to remove all higher frequency content from the response, then with a 1 Hz, 5-pole Butterworth high-pass filter to remove all lower frequency noise (and air vehicle rigid body effects) from the response. The targeted range of response is from $1P$ (4.3 Hz, the rotor angular speed) up to $6P$ (25.8 Hz).

3.3.2 Time Series Extraction

Per Reference [50], due to storage limitations, typically only five seconds of a 20-second steady flight condition were time-sliced and archived. Up to 45 seconds were retained for maneuvers or dynamic conditions due to the changing nature of the response with time. Reference [18] established that, for steady, level flight (e.g. c8534), the flight data are considered sufficiently steady to justify using only the first revolution (or cycle) for correlation purposes. Unless otherwise stated, the first cycle of each flight counter is used herein.

Due to the UH-60A torque offset (or hub offset), the blade lags the standard hub coordinate system (the reference for measured azimuth) by 7 degrees [52]. This lag is reconciled in the data to ensure accurate comparisons between analysis and experiment.

3.3.3 Consistent Sign Conventions with DYMORE

The UH-60A Airloads Program and DYMORE sign conventions for the blade are listed in Table 3.7 and shown in Figure 3.2. The measured UH-60A responses fed as input into the DYMORE LCA algorithm are adjusted accordingly. This means changing the sign on blade flapping and lag angles as well as flapping and edgewise bending moments. For consistent display with legacy published UH-60A analyses, all final results are transformed back into the UH-60A Airloads Program sign convention prior to display. All results documented herein will follow this UH-60A Airloads Program sign convention.

Table 3.7: Rotor blade sign conventions.

Quantity	**UH-60A Airloads Program**	**DYMORE**
x	Positive outboard	Positive outboard
y	Positive with decreasing azimuth ("aft")	Positive with increasing azimuth ("forward")
z	Positive down	Positive up
Pitch angle, θ	Positive leading edge up	Positive leading edge up
Flapping angle, β	Positive tip up	Positive tip down
Lag angle, ζ	Positive with decreasing azimuth ("aft")	Positive with increasing azimuth ("forward")
Torsional moment, ST (M_x)	Positive leading edge up	Positive leading edge up
Flapwise bending moment, SN (M_y)	Positive tip up	Positive tip down
Edgewise bending moment, SE (M_z)	Positive with decreasing azimuth ("aft")	Positive with increasing azimuth ("forward")

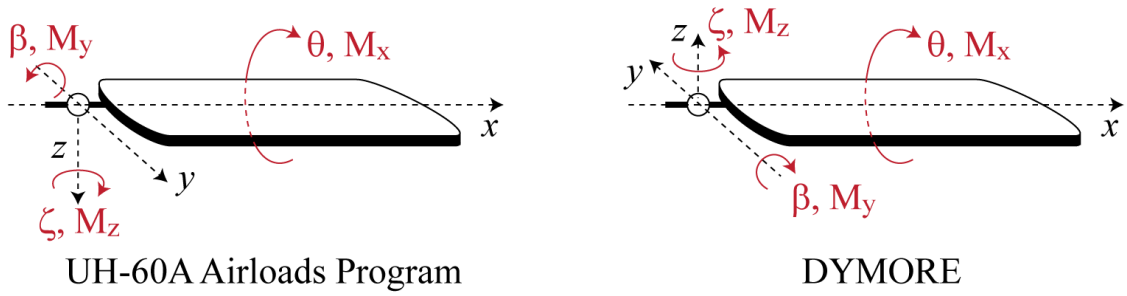

Figure 3.2: Rotor blade sign conventions.

3.3.4 Periodicity

Based on the assumption of periodicity of the solution relative to a given forcing frequency, Ω, Fourier expansion of the measured airloads, bending moments, etc. (ϵ) are applied and used in the DYMORE LCA analysis, resulting in the following.

$$\underline{\epsilon}(t) = \underline{a}_0 + \sum_{j=1}^{H} (\underline{c}_j \cos j\Omega t + \underline{s}_j \sin j\Omega t) \tag{3.1}$$

where H is the retained number of harmonics of the forcing frequency used in the expansion. In this analysis, H is set to 6 harmonics. This provides frequency content in the Fourier approximation up to 25.8 Hz ($\Omega = 4.3$ Hz). Figure 3.3 shows an overlay of one cycle of measured flapwise bending (SN70, top) and torsional moment (ST70, bottom) at $0.70R$ and the 6-harmonic Fourier approximation of each time series. As shown, a suitable match is obtained.

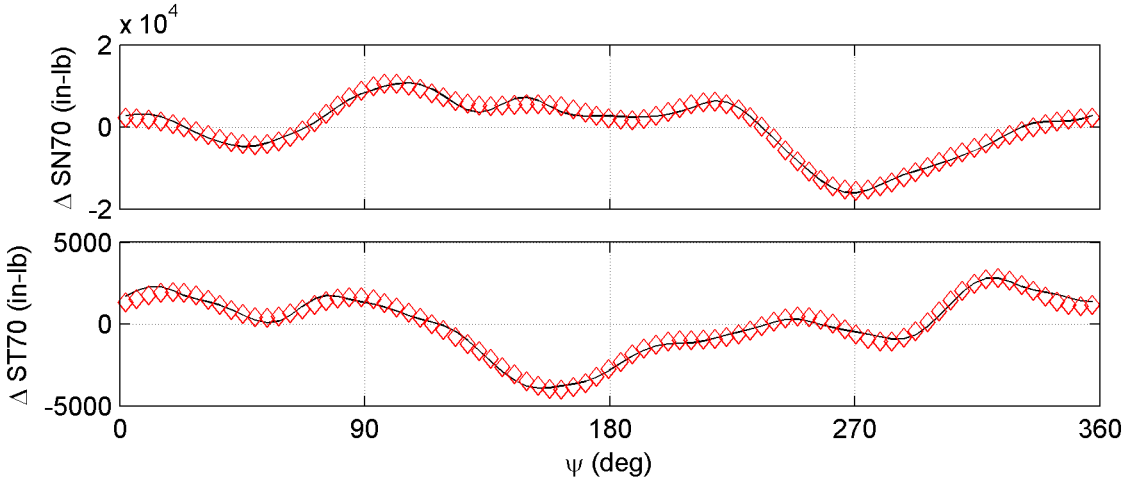

Figure 3.3: Fourier expansion for c8534 ($\mu = 0.368$); SN70 (top), ST70 (bottom).

Each flight counter contains time histories for all parameters listed in Tables 3.3 and 3.4. Each of these time histories is approximately 5-20 seconds in duration. To validate this assumption of system periodicity as a function of Ω, a Fourier Transform (FT) was performed on each flight counter for all flights for all blade loads measurements (flapwise bending moments at eight radial stations; torsional moments at four

radial stations; and edgewise bending moments at seven radial stations). Results for flights 84 and 85 are provided herein. Results for flights 88 through 116 are provided in Appendix A. Blade flapwise bending moment magnitude v. frequency response and advance ratio are shown in Figures 3.4 and 3.5. Blade torsional moment magnitude v. frequency response and advance ratio are shown in Figures 3.6 and 3.7. Blade edgewise bending moment magnitude v. frequency response and advance ratio are shown in Figures 3.8 and 3.9.

The following conclusions are reached. In most cases, the loads show relatively pure and distinct content at $1P$, $2P$, ..., with minimal *off-harmonic* content (e.g., load content at $5.5P$). For example, Figure 3.10 (top) shows load response v. harmonic for SN30, ST30, and SE30 for c8533 (μ=0.360). However, there are cases where there is appreciable off-harmonic content. The middle chart in this figure shows load response v. harmonic for SN30, ST30, and SE30 for c8431 (μ=0.103). The bottom chart in figure 3.10 shows load response v. harmonic for SN30, ST30, and SE30 for c11509 (μ=0.027). In both cases, there is loads content for SE30 between $5P$ and $6P$. For c8431, this is likely response due to blade-vortex interaction (BVI)-induced blade mode excitation. For c11509, effectively a hover condition, slight effects due to the presence of wind could result in non-harmonic response due to, for example, tail rotor tip vortices affecting the main rotor airflow field. This last point was brought up as a possible effect during an informal email correspondence between the author, W. Kufeld, and W. Bousman (June 2012). It should be noted that work by Ormiston and Martin [67] has shown that, for more extreme maneuvers (e.g., c11029, a high-speed pull-up maneuver), there can be significant off-harmonic content at the higher harmonics (5.8P in that case). For a given set of valid measurements, the actual physical explanation is secondary to the influence this off-harmonic content has on the LCA applied for loads correction. This will be discussed in Section 3.4. Table 3.8 summarizes the findings from this study for flights 84, 84, 88, 89, 90, 110, 115, and

Table 3.8: Findings by flight.

Flight	**Comments**
84	Sensor errors at SN80, ST50; off-harmonic content (between $5P$ and $6P$) more prevalent at SN90 (all μ) and SE (low μ)
85	Sensor errors at SN80, ST50, SE80; off-harmonic content (between $4P$, $5P$, and $6P$) more prevalent at SE (low μ)
88	Sensor errors at SN40/50/80/90, SE30/40/50/80
89	Sensor errors at SN40/50/80/90, SE40/50/80
90	Sensor errors at SN40/50/80/90, SE30/40/50/80
110	Sensor errors at SN80
115	Sensor errors at SN80; off-harmonic content (between $4P$, $5P$, and $6P$) more prevalent at SE (low μ)
116	Sensor errors at SN80

116. If a sensor is considered erroneous, it is excluded as a control point in the analysis.

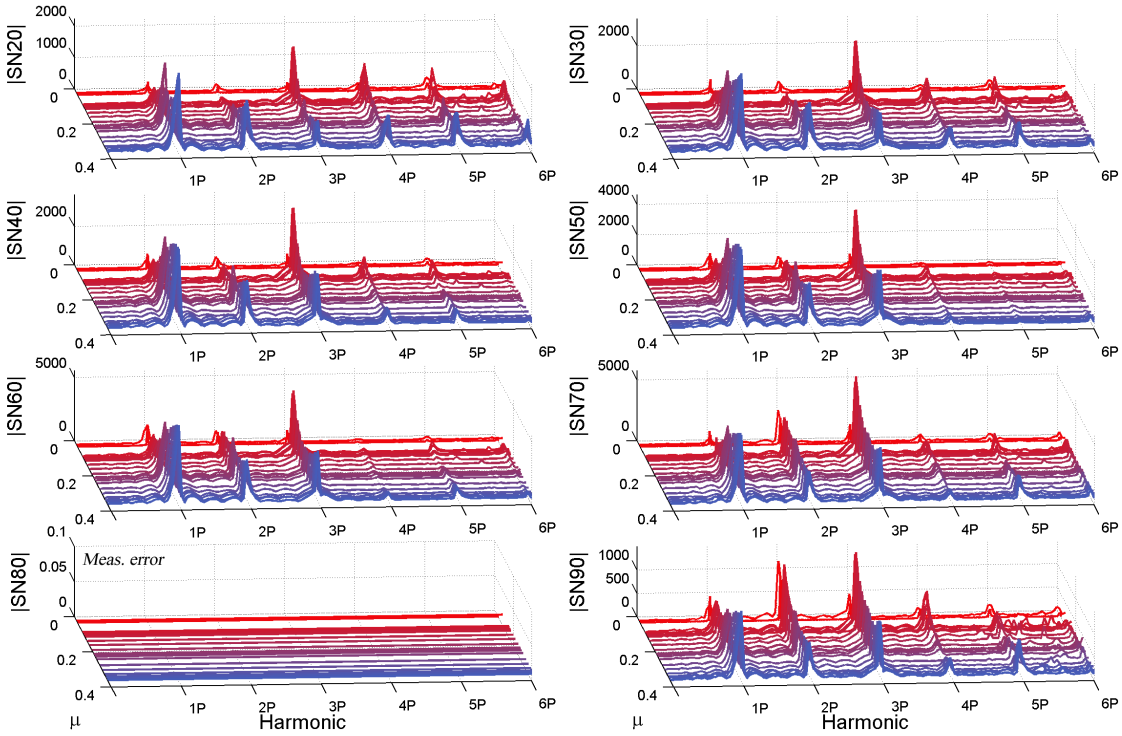

Figure 3.4: Blade flapwise bending moment v. advance ratio (flight 84).

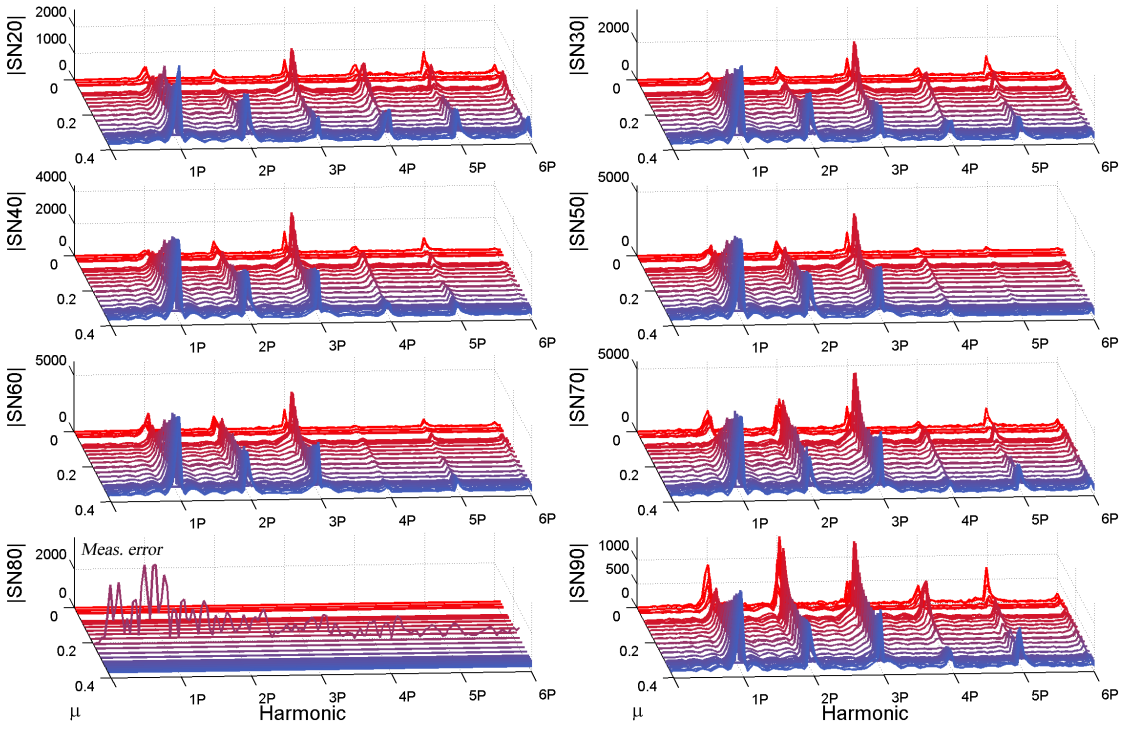

Figure 3.5: Blade flapwise bending moment v. advance ratio (flight 85).

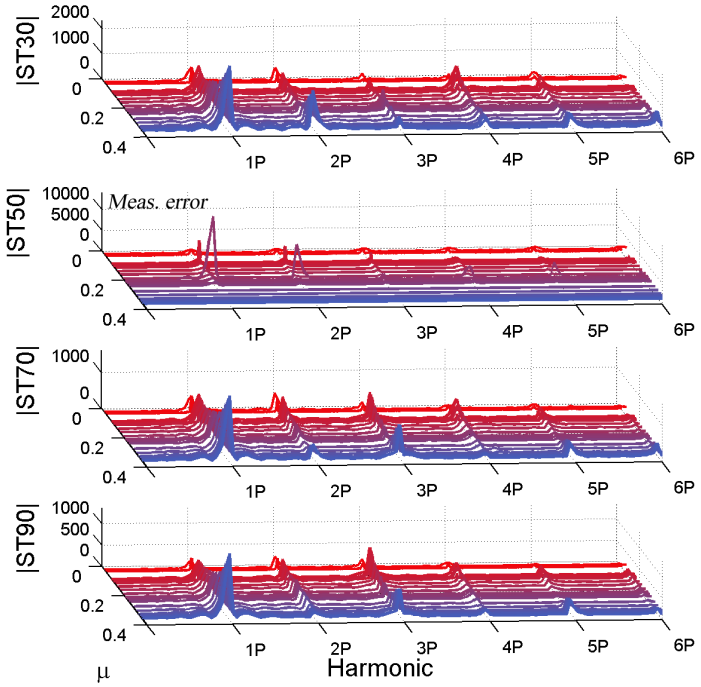

Figure 3.6: Blade torsional moment v. advance ratio (flight 84).

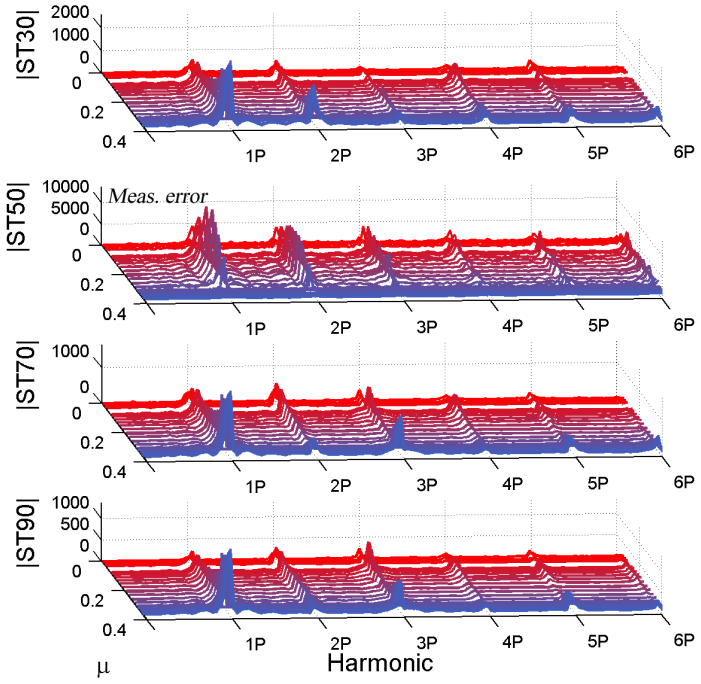

Figure 3.7: Blade torsional moment v. advance ratio (flight 85).

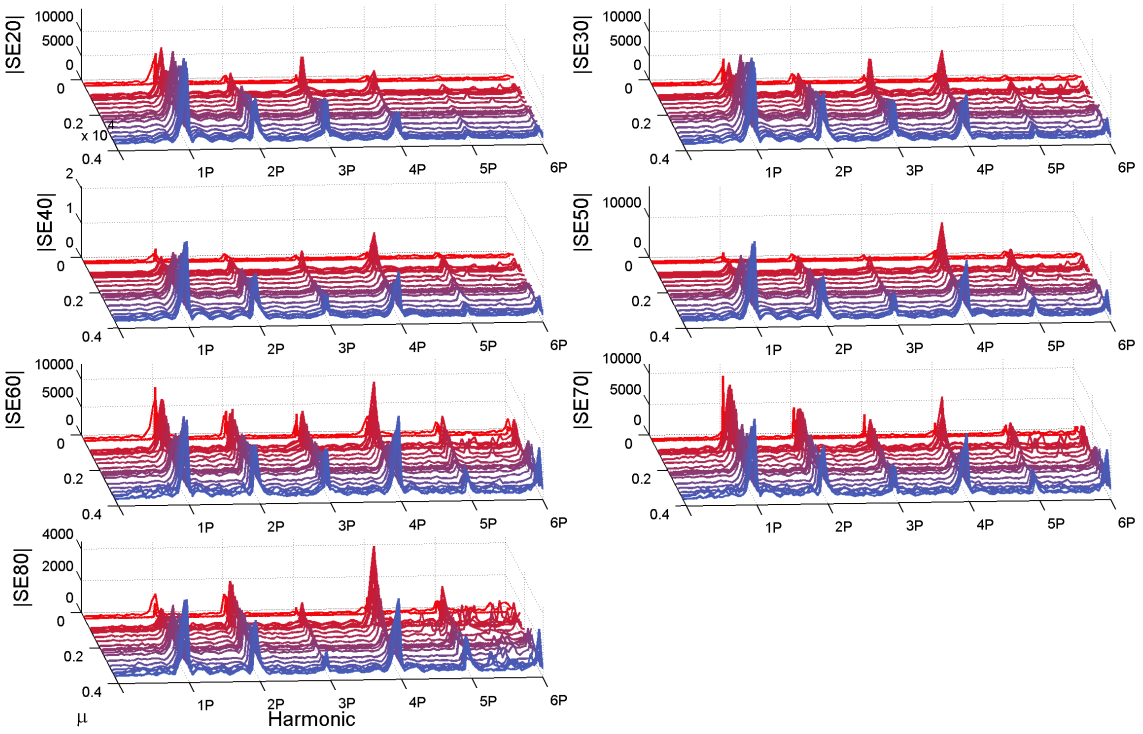

Figure 3.8: Blade edgewise bending moment v. advance ratio (flight 84).

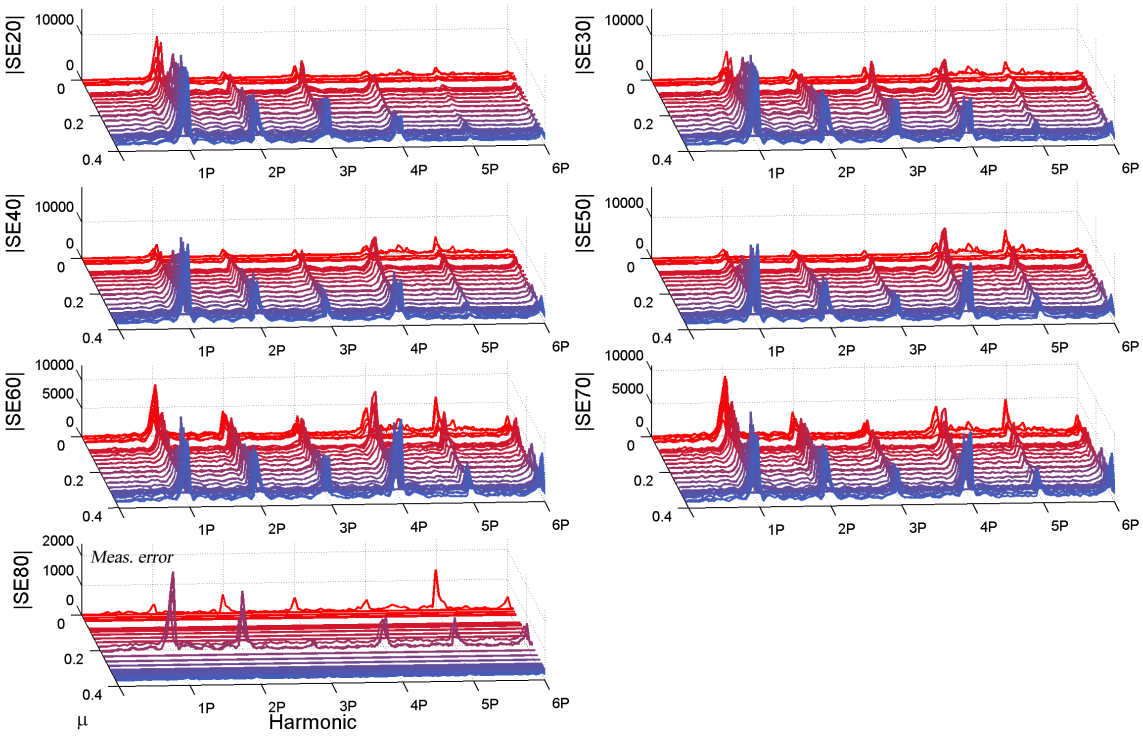

Figure 3.9: Blade edgewise bending moment v. advance ratio (flight 85).

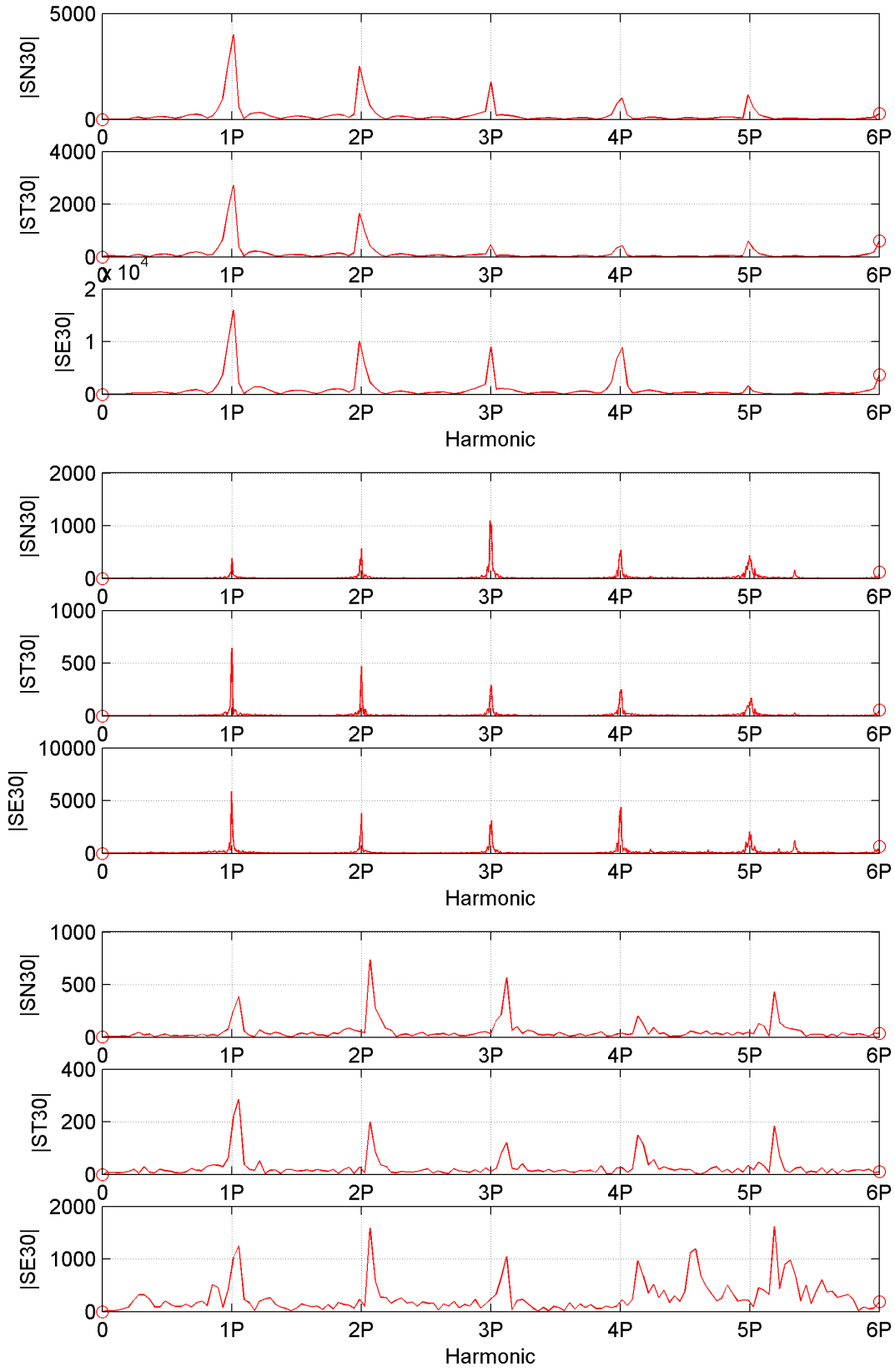

Figure 3.10: Blade bending, by harmonic: c8533, $\mu = 0.360$ (top); c8431, $\mu = 0.103$ (middle); c11509, $\mu = 0.027$ (bottom).

3.4 DYMORE UH-60A Numerical Model Development and Simulations

The success of multibody dynamics analysis tools (e.g., DYMORE [8]) stems from their accuracy and modeling flexibility. A given rotorcraft system can be modeled by an idealization process that identifies the mechanism components from within a large library of elements implemented in the code. Each element provides a basic functional building block, for example a rigid or flexible member, a hinge, a motor, etc. By assembling the various elements, it is then possible to construct a mathematical description of the mechanism with the required level of accuracy.

Of particular relevance to this effort is the ability of multibody dynamics formulations to provide rigorous modeling capabilities for rotorcraft dynamic components. Most comprehensive rotorcraft codes are based on a modal representation of the blade, assuming the hub to be rigid, and ignoring all control linkages. In contrast, multibody formulations are able to model all relevant hardware components, such as control linkages, hydraulic lead-lag dampers [12], or coupling with fuselage dynamics [11].

3.4.1 UH-60A Structural Model

The DYMORE UH-60A model used herein has been used in a number of legacy analyses (e.g., Abras et al. [4], Marpu et al. [57]). This model is based on the physical properties defined by Bousman and Maier [20]. The structural model involves four blades connected to the hub through blade root retention structures and lead-lag dampers. For this analysis, one blade is modeled and the responses of the other three blades are determined from phase-lagged mirrored images. The blade is discretized into thirteen cubic finite elements using the finite element-based multibody dynamics code described in [10]. The root retention structure, connecting the hub to the blade, was separated into three segments (Figure 3.11). The first segment, modeled by one

beam element, is attached to the hub. The flap, lead-lag, and pitch hinges of the blade are modeled by three revolute joints connecting the first two segments of the root retention structure. The physical characteristics of the elastomeric bearing are represented by springs and dampers in the joints to model the stiffness and energy dissipation characteristics of the elastomeric material. The last two segments, each modeled by two beam elements, are rigidly connected to each other and to the pitch control horn. Finally, the last segment is rigidly connected to the blade and damper horn. The pitch angle of the blade is set by the following control linkages: the swashplate, pushrod, and pitch horn. The pushrod, modeled by cubic beam elements, is attached to the rigid swashplate by means of a universal joint and to the rigid pitch control horn by a spherical joint. The damper arm and damper horn are modeled as rigid bodies. The lead-lag damper is modeled as a prismatic joint with its end points connected to the damper arm and horn. In the DYMORE model, swashplate

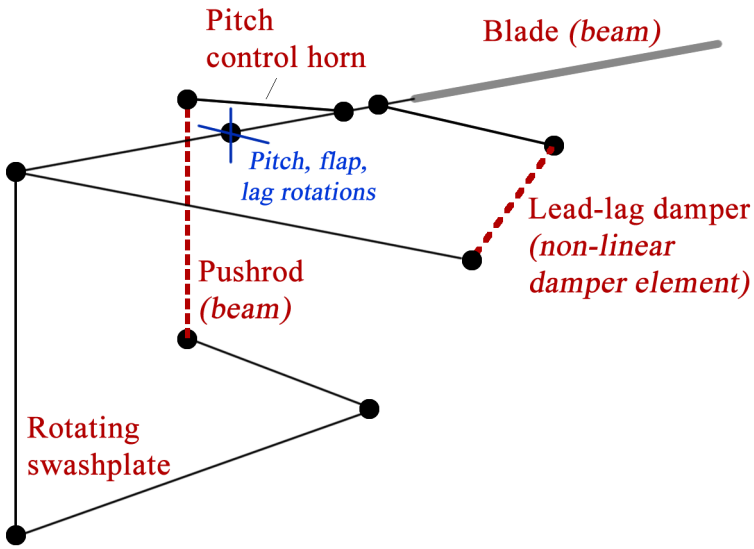

Figure 3.11: DYMORE UH-60A multibody dynamics formulation.

deflection (collective) and rotations (longitudinal and lateral cyclic) are prescribed; the blade root flap, pitch, and lag angles are then determined as a function of the swashplate configuration and the resulting motion of the pushrod. The UH-60A

experimental data directly provides these blade root angles, but not the position of the swashplate. An empirical solution was performed in DYMORE to develop the swashplate-to-blade root angle transfer functions. Each DYMORE simulation (one per flight counter) was then prescribed a swashplate configuration to produce the required blade root angles (specifically blade root pitch).

To define the structural model's modal characteristics, an eigensolution has been performed. The blade coupled modes are listed in Table 3.9 as well as shown in Figures 3.12 through 3.22. Table 3.9 also compares frequencies with those computed by Theodore [78].

Table 3.9: UH-60A rotating blade modes.

Mode number	**Frequency DYMORE Hz (/rev)**	**Frequency Ref. [78] /rev**	**Description**
1	1.12 (0.26)	0.27	Rigid lagging (in-plane)
2	4.45 (1.03)	1.04	Rigid flapping
3	12.13 (2.82)	2.82	2nd flapping
4	19.47 (4.53)	4.65	3rd flapping, 2nd lagging, 1st torsion
5	19.94 (4.64)	-	2nd lagging, 1st torsion
6	22.41 (5.21)	5.18	3rd flapping, 2nd lagging
7	33.29 (7.74)	7.89	4th flapping
8	47.23 (10.98)	-	5th flapping, 3rd lagging
9	48.46 (11.27)	-	5th flapping, 3rd lagging
10	60.73 (14.12)	-	5th flapping, 2nd torsion
11	68.22 (15.87)	-	6th flapping, 6th lagging, 2nd torsion

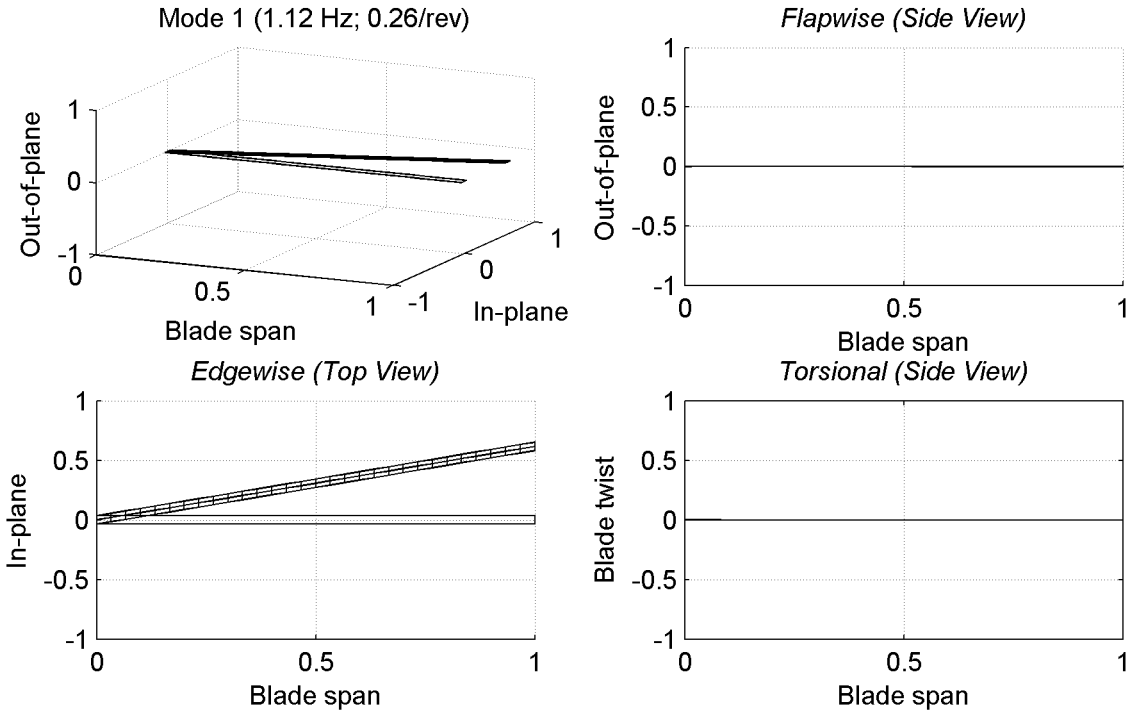

Figure 3.12: UH-60A rotating blade coupled mode 1: rigid lagging (in-plane; edgewise).

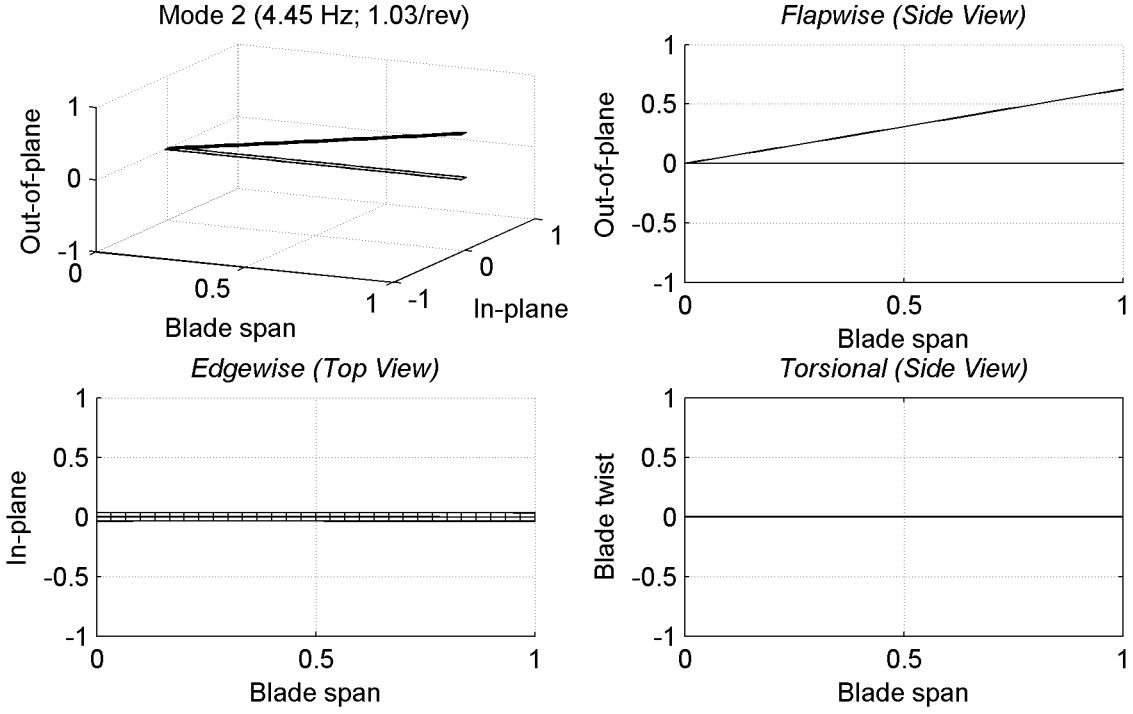

Figure 3.13: UH-60A rotating blade coupled mode 2: rigid flapping.

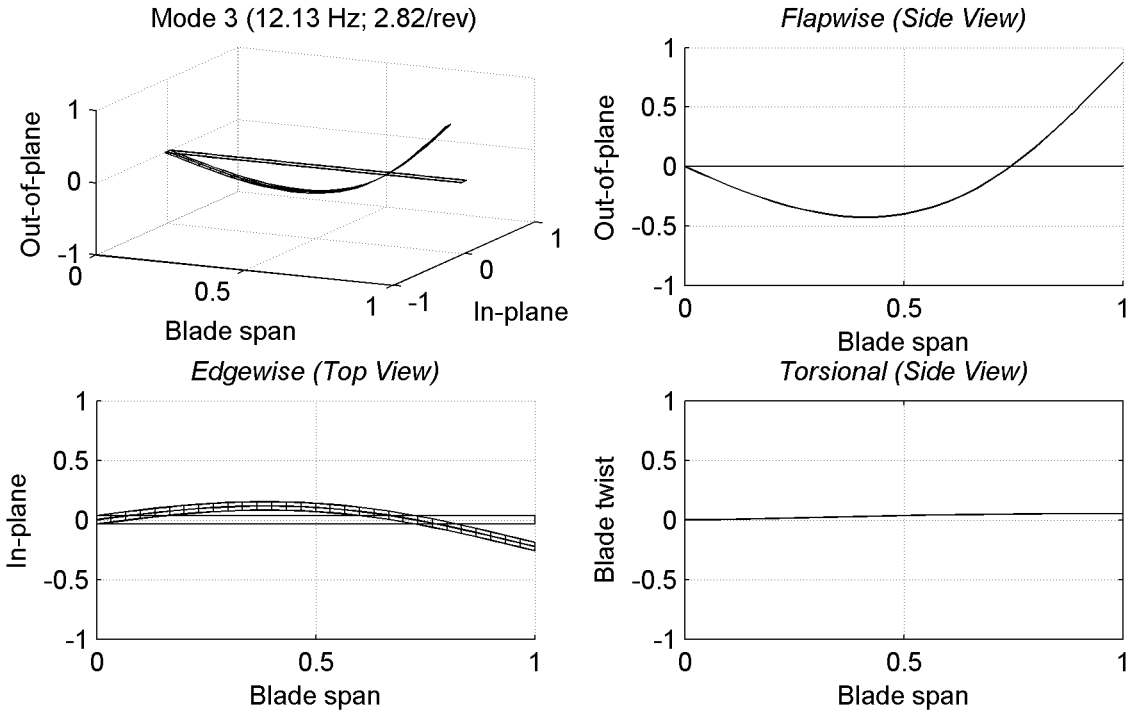

Figure 3.14: UH-60A rotating blade coupled mode 3: 2nd flapwise bending.

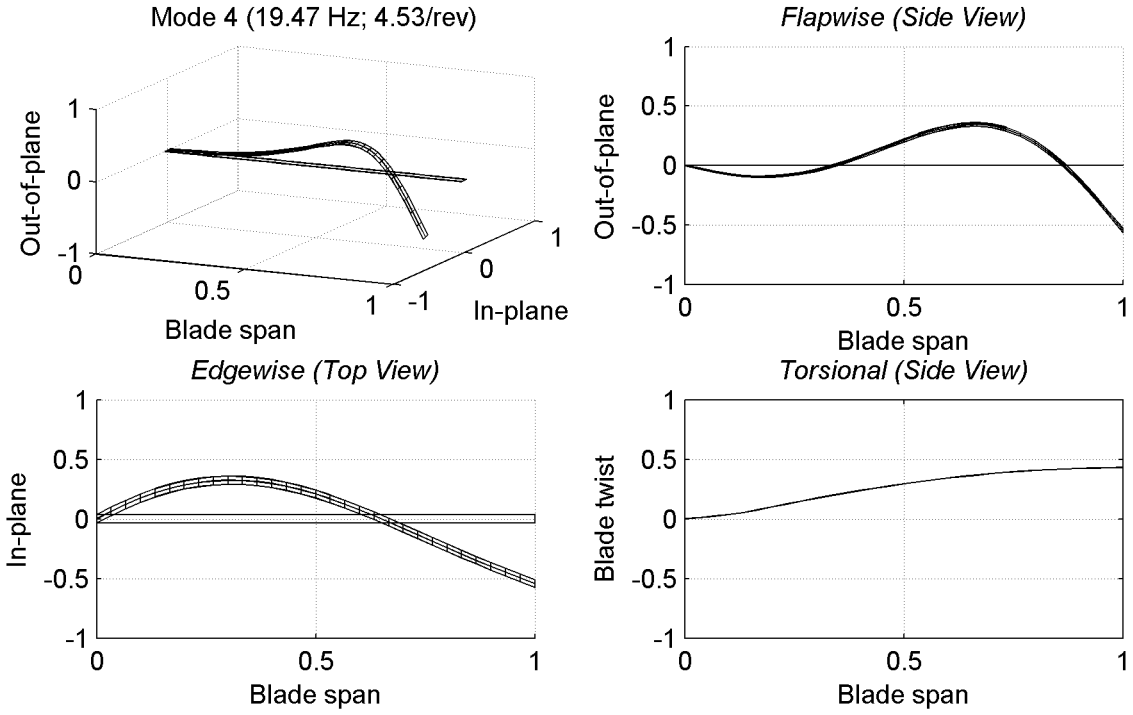

Figure 3.15: UH-60A rotating blade coupled mode 4: 3rd flapwise, 2nd edgewise, 1st torsion.

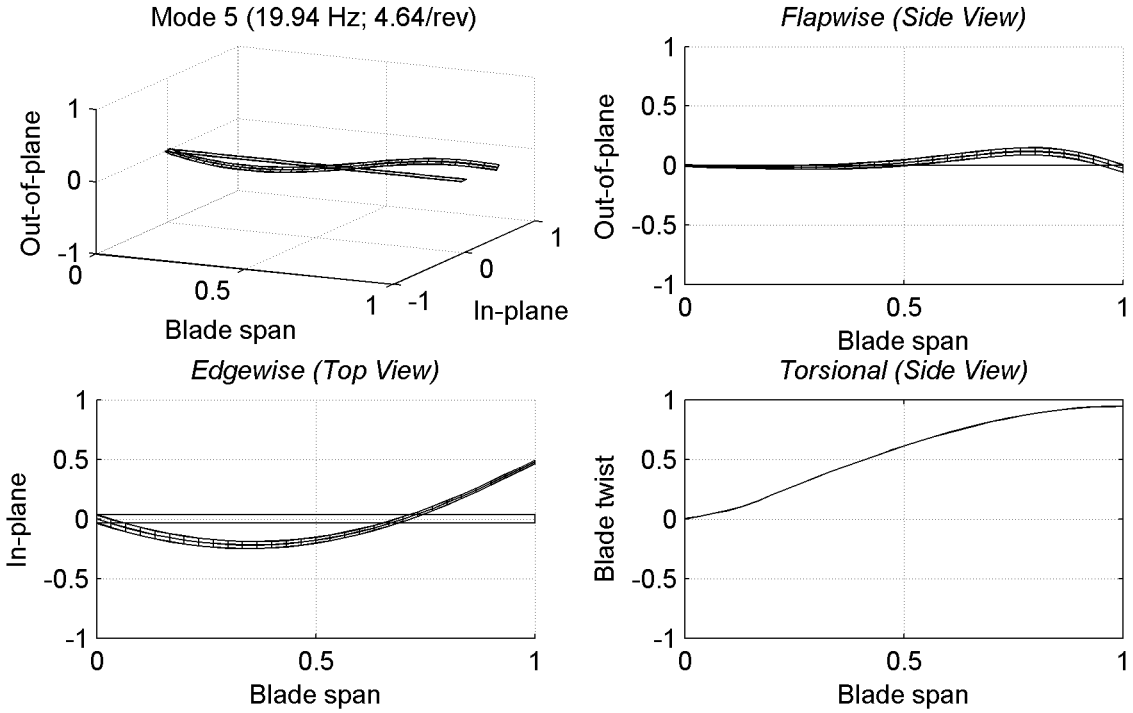

Figure 3.16: UH-60A rotating blade coupled mode 5: 2nd edgewise, 1st torsion.

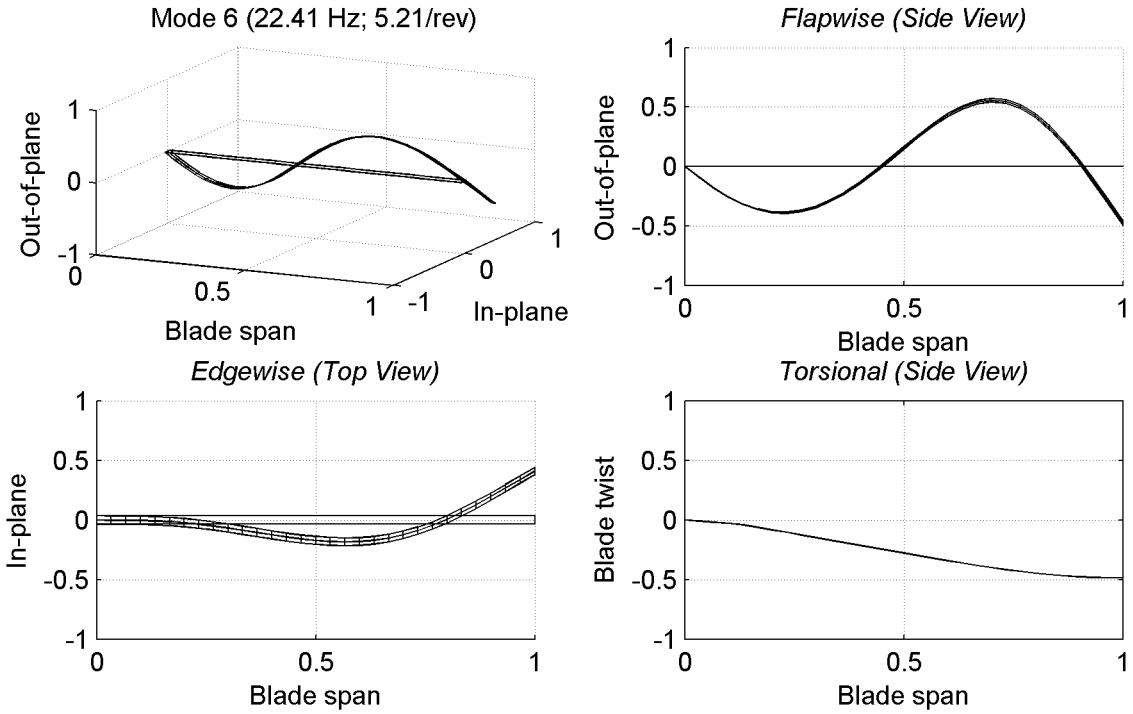

Figure 3.17: UH-60A rotating blade coupled mode 6: 3rd flapwise, 2nd edgewise.

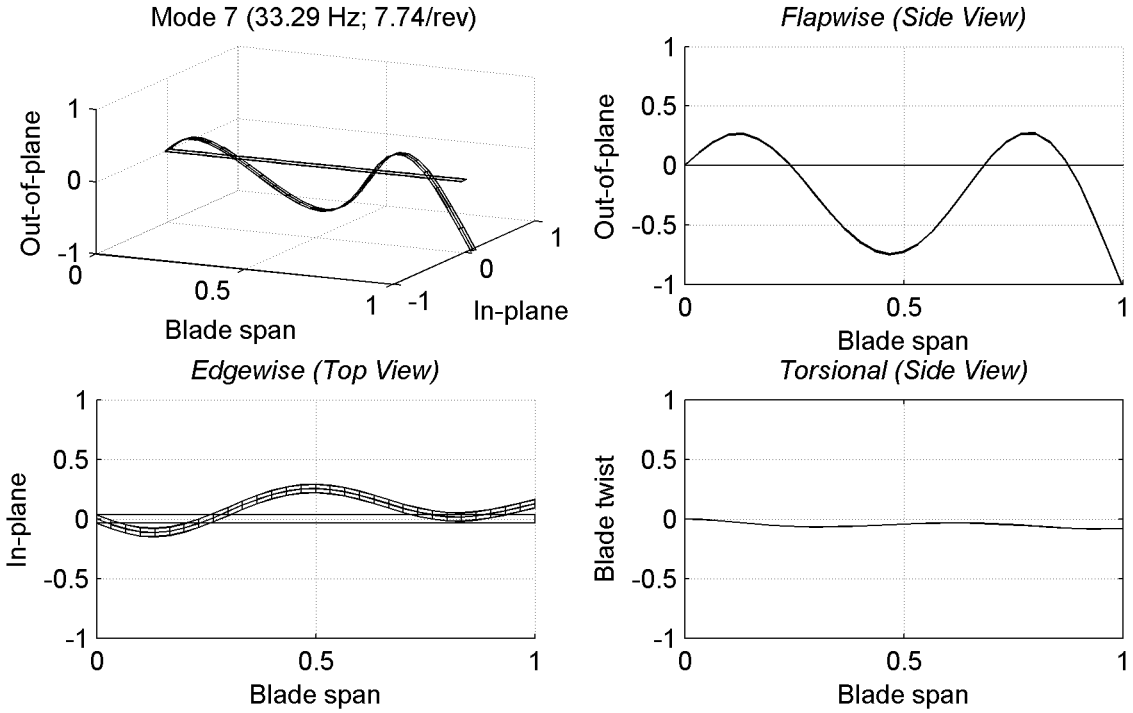

Figure 3.18: UH-60A rotating blade coupled mode 7: 4th flapwise.

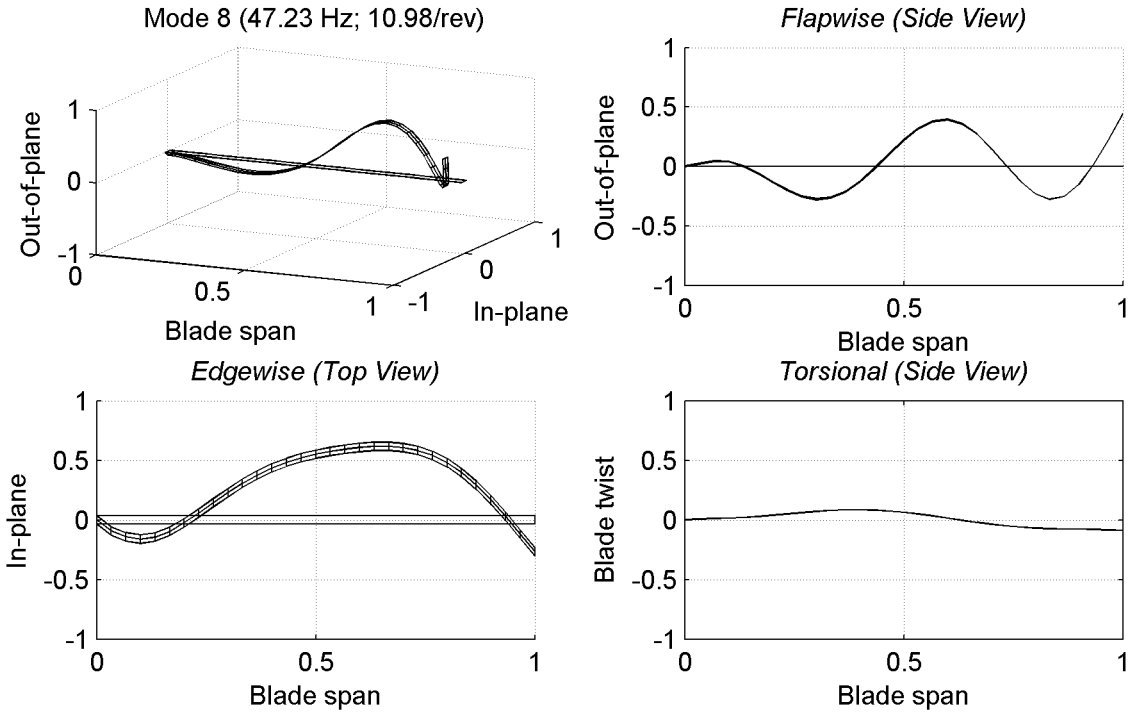

Figure 3.19: UH-60A rotating blade coupled mode 8: 5th flapwise, 3rd edgewise.

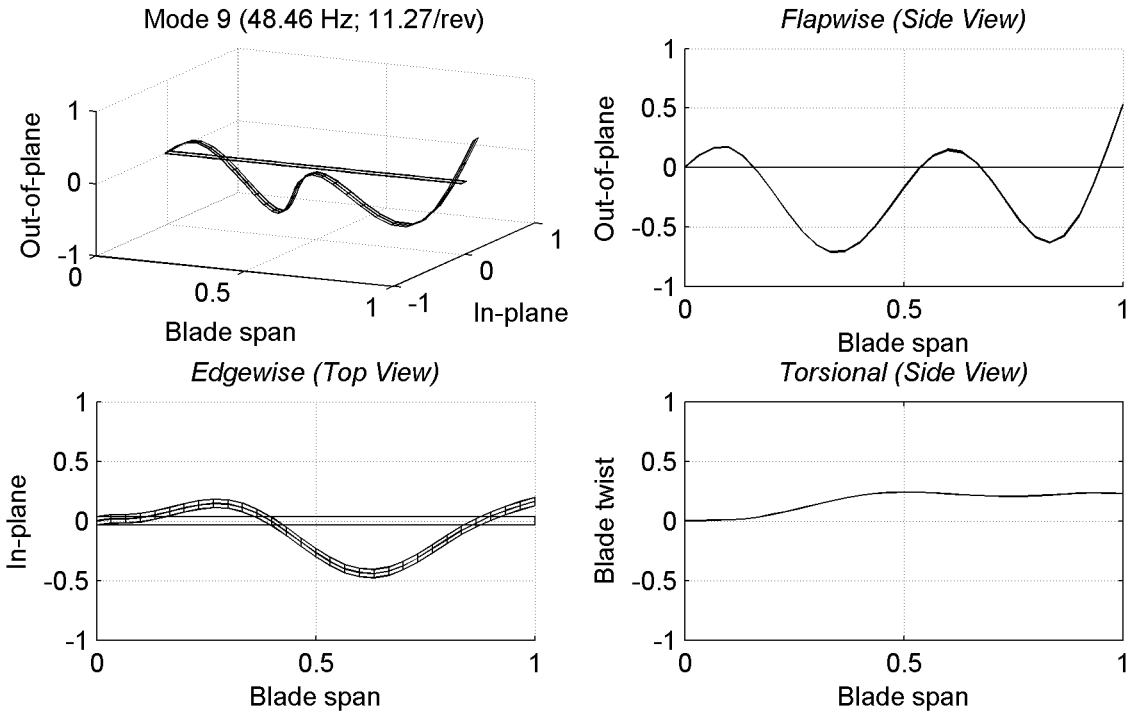

Figure 3.20: UH-60A rotating blade coupled mode 9: 5th flapwise, 3rd edgewise.

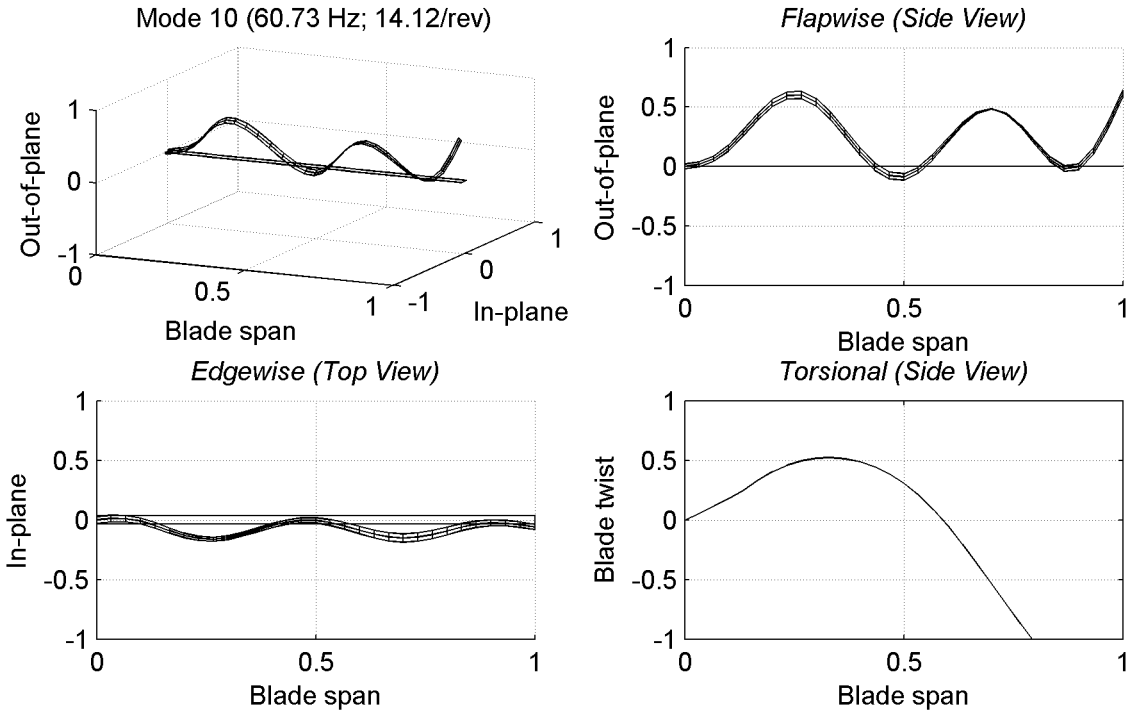

Figure 3.21: UH-60A rotating blade coupled mode 10: 5th flapwise, 2nd torsion.

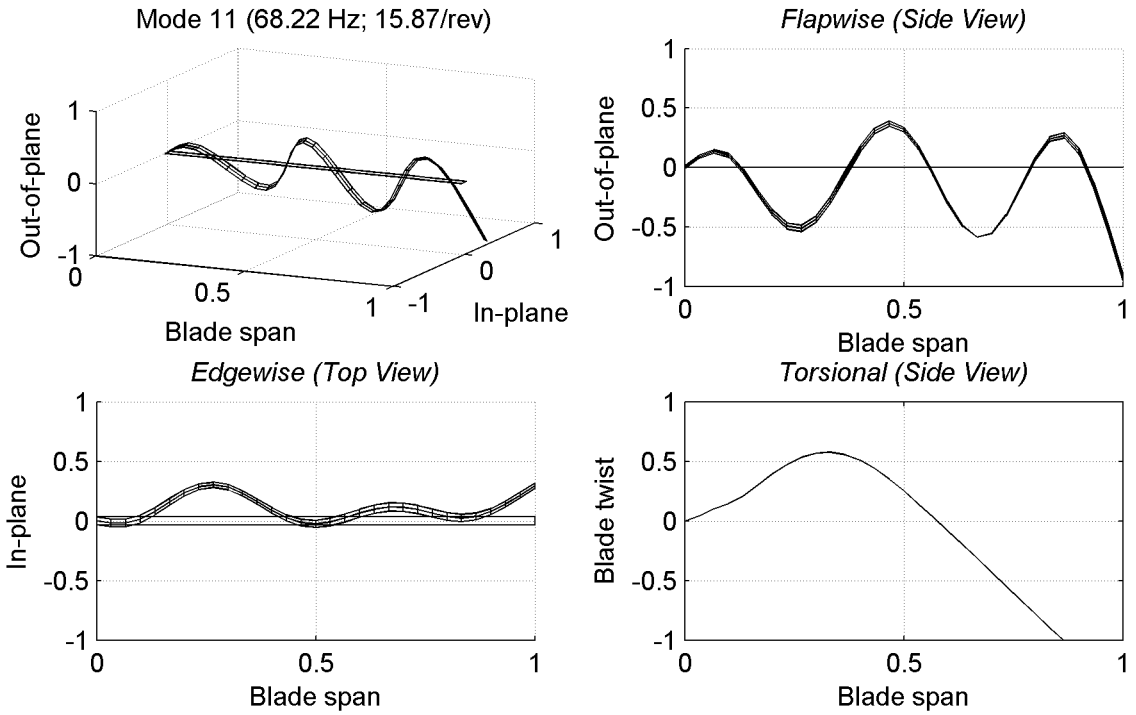

Figure 3.22: UH-60A rotating blade coupled mode 11: 6th flapwise, 6th edgewise, 2nd torsion.

The first flap and lag modes of an articulated rotor blade with a non-zero hinge offset may be approximated as follows (Leishman [55]):

$$\omega_{flap} = \left[1 + \frac{3e}{2(1-e)}\right]^{1/2} \Omega \tag{3.2}$$

$$\omega_{lag} = \left[\frac{3e}{2(1-e)}\right]^{1/2} \Omega \tag{3.3}$$

Where the hinge offset $e = 0.04659$ [43] and $\Omega = 4.3$ Hz for the UH-60A, resulting in an approximate first flapping mode of 4.45 Hz ($1.04P$) and first lag mode of 1.16 Hz ($0.27P$). These are identical to the full FE-based DYMORE solution (Table 3.9) for flapping and within 4% for the lag mode ($0.26P$).

3.4.2 UH-60A Aerodynamic Model

The aerodynamic model and aerodynamic process used within DYMORE for the UH-60A are described herein. This description is based on the DYMORE User's Manual [9]. Figure 3.23 shows the coordinate system and orientation of the airflow relative to the airfoil. For two-dimensional unsteady aerodynamic theories (used herein), the analysis focuses on flow components U_2 (tangential, U_T) and U_3 (perpendicular, U_P) in the plane of airfoil, ignoring the radial component U_1 (U_R). The flow velocity, V, is defined as the resultant of components U_2 and U_3, as follows.

$$V^2 = U_2^2 + U_3^2 \tag{3.4}$$

The flow velocity contains an inflow component (v) based on unsteady flow theory for a two-dimensional airfoil (see Reference [9], Section 11). That is, in simple terms:

$$U_3 = V \sin\alpha + v + \textit{blade dynamics...} \tag{3.5}$$

The two-dimensional unsteady aerodynamic behavior of airfoils used in this analysis is based on the work of Peters et al. [9, 70], wherein, for a thin airfoil in a two-dimensional inviscid, incompressible flow, the unsteady lift, drag, and moment are defined as distinct contributions due to separate steady and unsteady components. No flow separation effects are considered. Furthermore, the steady lift, drag, and pitching moment coefficients are corrected based on airfoil table lookups from steady wind tunnel measurements [80]. Per this reference, a critical assessment of the SC1095 [UH-60A airfoil cross section from $0.19R$ to $0.47R$ and $0.85R$ to $1.00R$] and SC1094R8 [UH-60A airfoil cross section from $0.50R$ to $0.82R$] airfoil data used on the UH-60 main rotor blade was performed across nine sources of wind tunnel data. From this, the most accurate representations of steady flow were extracted for use in analysis.

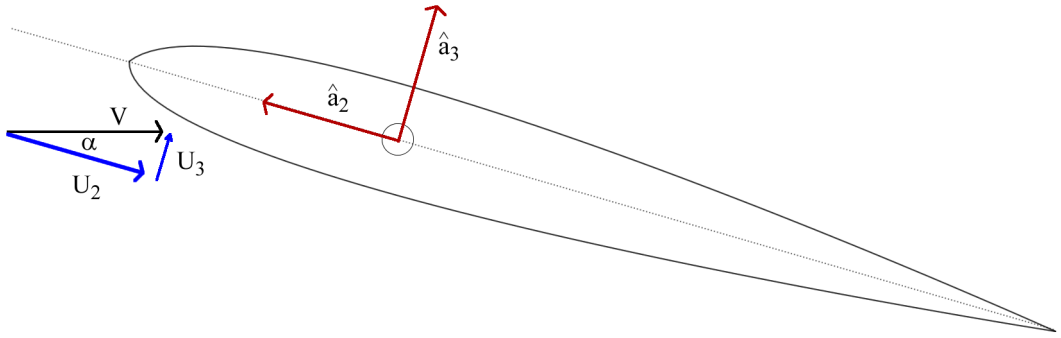

Figure 3.23: Coordinate system and orientation of the airflow relative to the airfoil.

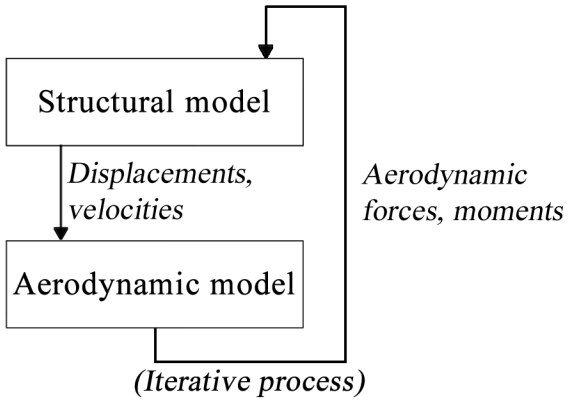

Figure 3.24: DYMORE: interplay between the structural and aerodynamic models.

The final wind tunnel-corrected representation of blade forces and moments due to aerodynamic loading are as follows (ignoring tip loss effects).

$$F_2 = \rho b V (c_l U_3 - c_d U_2) \tag{3.6}$$

$$F_3 = \rho b V (c_l U_2 + c_d U_3) + \rho \frac{b^2}{2} a_0 (\dot{U}_3 + U_2 q) \tag{3.7}$$

$$M_{1(c/4)} = 2\rho b^2 c_m V^2 - \rho a_0 \left[\frac{b^4}{16} \dot{q} + \frac{b^3}{4} (\dot{U}_3 + U_2 q) \right] \tag{3.8}$$

where ρ is air density, b is rotor blade semi-span, q is aircraft pitch rate, $\dot{q}$ is aircraft pitch acceleration, a_0 is airfoil lift curve slope, and c_l, c_d, and c_m are the wind tunnel test-derived lift, drag, and quarter-chord pitching moment coefficients, respectively. See Section 12 of Reference [9] for the full derivation of these terms.

Lifting line aerodynamics has limitations. Sitarama et al. [77] identified two main reasons for the inaccuracies in lifting line models. The first is the inability to resolve unsteady transonic effects (e.g., pitching moments caused by unsteady transonic flows) and second is the inability to accurately resolve the returning wake effects. As will be shown herein, in spite of these limitations, LLT is well-suited for this analysis. This is due to two reasons: (1) fast performance relative to CFD; (2) an effective enough *starting point* for the LCA to apply load corrections.

3.4.3 Simulation Procedure

For each flight counter, the following steps are implemented for simulation:

1. Define swashplate orientation to match measured blade pitch angle for prescribed flight counter
2. Define inflow model
3. Define density at altitude, far-field flow velocity, lift-curve slope
4. Define pointer to aerodynamic coefficients file (wind tunnel-derived steady lift, drag, pitching moment data)
5. For the *mechanical airloads* problem (Section 4.5), aerodynamics are superseded by experimentally-derived Fourier coefficients of blade normal force, chord force, and pitching moment (per unit span)

3.5 Summary

This chapter summarized the UH-60A Airloads Program, flight test data processing, and the systematic method with which this dataset will be used for analysis herein. It also detailed the DYMORE structural and aerodynamic model development process. Chapter 4 will apply this dataset and show the effects the LCA has on rotor loads prediction.

CHAPTER IV

UH-60A FLIGHT TEST ANALYSIS: COMPREHENSIVE RESULTS SUMMARY

4.1 Overview

The LCA has been applied to a range of UH-60A test cases [21, 58]. All relevant results are documented and discussed in this chapter. Figure 4.1 lists the flight counters examined, as a function of thrust coefficient (normalized by rotor solidity, σ) versus advance ratio, μ. One uniqueness of this effort is the exhaustive list of flight counters examined: 601 total flight counters across flights 84 through 116. The objective in each case is to match peak-to-peak load (per cycle) as well as magnitude and phase by harmonic. This includes load contributions due to $1P$, $2P$, etc. - up to all contributing frequencies: $6P$ for the UH-60A. This chapter addresses the following

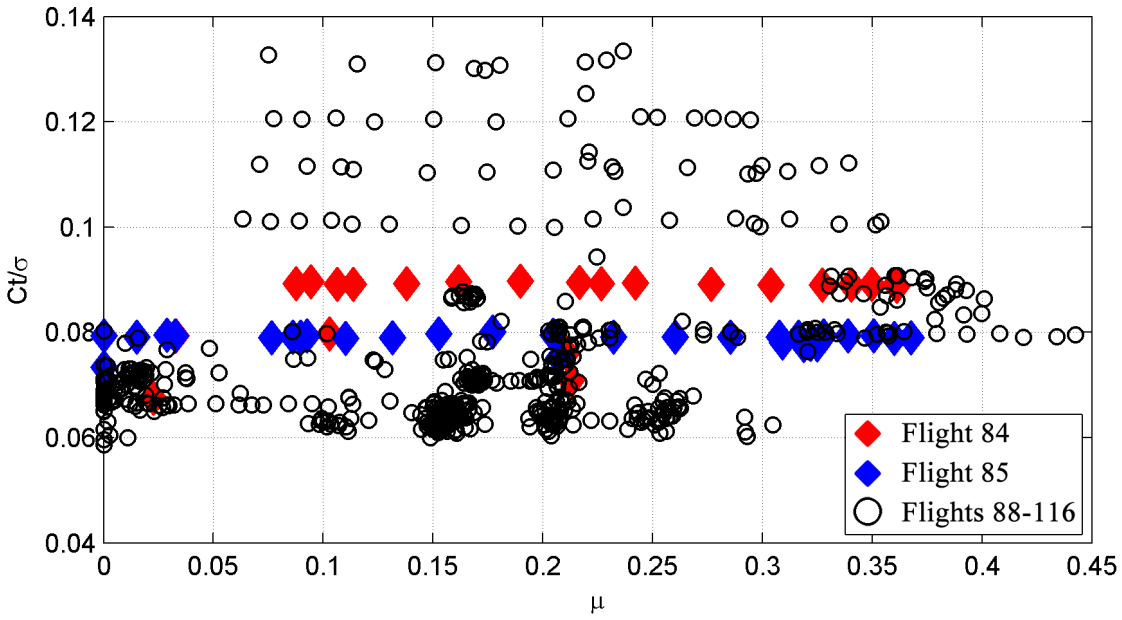

Figure 4.1: Flight counters examined for analysis; C_t/σ v. advance ratio, μ.

topics:

1. Definition of blade sensors and control points used for numerical rotor loads simulation (Section 4.2.1)
2. Definition of the *LCA score*, a metric used to quantify the quality of a given loads prediction (Section 4.2.2)
3. Listing of all LCA input settings for DYMORE-based simulation (Section 4.2.3)
   (a) Chapter 5 will show the results of sensitivity studies used to derive these LCA input settings.
4. Rotor loads simulation and LCA application for eight arbitrary UH-60A flight counters (Sections 4.3 and 4.4)
   (a) This includes the effects of different control point sets
5. Rotor loads simulation and LCA application for the *mechanical airloads* problem (Section 4.5)
6. Analysis of nine flight counters that have been of interest in legacy research efforts (Section 4.6)
7. Analysis of the first cycle of all flight counters for flights 84 through 116 (601 total flight counters) (Section 4.7)
   (a) The purpose is to show the robustness of the LCA across all flight regimes
8. Lag damper loads (Section 4.8)

4.2 LCA Setup

4.2.1 Blade Sensors

A blade sensor is a prescribed DOF at a given radial station at which blade loads are computed. SN is blade flapwise (normal) bending; ST is blade torsional moment;

and *SE* is blade edgewise bending. Each term is followed by a two-digit identifier for the radial station at which this load is computed. *SN20* is blade flapwise bending at $0.20R$; *SE70* is blade edgewise bending at $0.70R$. Figure 4.2 shows all UH-60A blade sensors available for use herein.

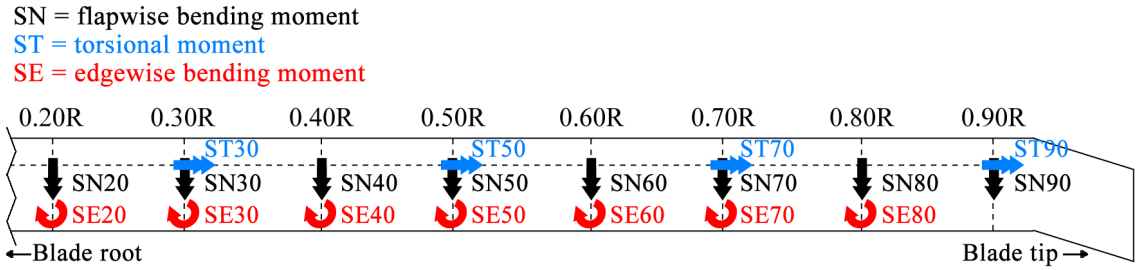

Figure 4.2: UH-60A blade sensors.

4.2.2 LCA Score

In order to compare different loads results, an objective metric has been defined to help determine the best match. This *LCA score* is defined as follows.

$$LCA\ score = median\left[\left(\frac{1}{C}\frac{1}{S}\frac{1}{H}\sum_{c=1}^{C}\sum_{s=1}^{S}\sum_{h=1}^{H}\left(\frac{\epsilon_{csh}-\epsilon^{*}_{csh}}{\epsilon^{*}_{csh}}\right)^{2}\right)^{1/2}\right] \tag{4.1}$$

where C is the number of flight counters examined, S is the number of control points, and H is the number of harmonics. In most cases, ϵ is defined as the set of [SN20/30/40/50/60/70/90, ST30/70/90, and SE20/30/40/50/60/70], for six harmonics, where SN20, etc. are defined in Figure 4.2. The intent is to optimize the solution to best match load response for flapwise bending, torsional moment, and edgewise bending across all dominant harmonics across all flight counters analyzed. The median is the point at which the dataset is divided into two equal halves [44]. It is an indicator of the central tendency of the data and accounts for the fact that, for certain flight counters and/or load stations, the experimental data may be erroneous (even zero), thus skewing any type of straight mean or variance calculation. These

invalid experimental data should not invalidate the quality of the loads match assessment. The value of the *LCA score* is unitless; it is effectively a least-squares error - a metric indicating the qualitative difference between analysis and test data. The lower the value, the better the aggregate loads match for that case.

4.2.3 Summary of Input Settings

The following LCA input settings were applied. Each of these parameters will be discussed and demonstrated in Chapter 5.

Table 4.1: LCA input settings.

Setting	**Value**
LCA application start point	4.0 sec
Duration of simulation	36.0 sec
LCA applications	Applied every 6 revolutions
Control points	16, 6, or 1 (Section 5.5)
Blade modes	Modes 3-10 (16 control points); 3-6,8,10 (6 control points); 10 (1 control point)
Harmonic scalar	[1.0, 1.0, 1.0, 0.5, 0.3, 0.3]

4.3 Rotor Loads Results: Radial, Azimuthal Load Distribution: Fully Instrumented Blades (16 Load Control Points)

This section provides detailed loads polar plots (load versus both radial station and azimuth) and time histories for the first cycle from eight arbitrarily-selected flight counters from flight 84, covering hover to high-speed flight. Polar plots are useful for assessing loads phasing as well as harmonic content (i.e., the number and azimuth location of different frequencies in the response). These flight counters, along with each associated C_w/σ, are listed in Table 4.2. In all cases, internally-generated (LLT;

Section 3.4.2) airloads are applied. Figure 4.3 shows the control points and mapped stations used in this simulation.

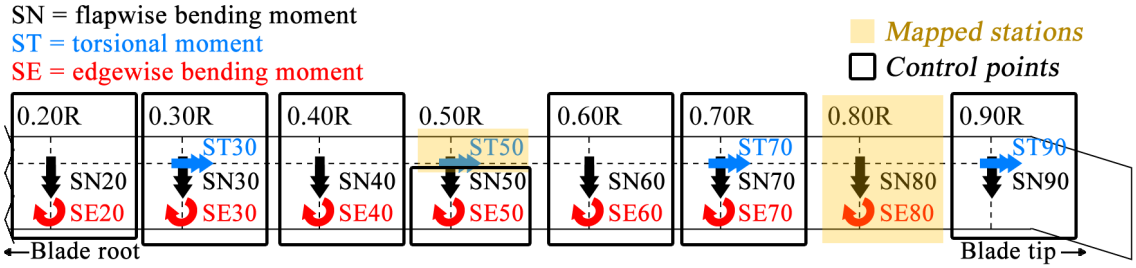

Figure 4.3: UH-60A blade control points and mapped stations.

Table 4.2: Eight flight counters of interest: flight 84.

Counter	μ	C_w/σ
8434	0.023	0.0674
8420	0.088	0.0892
8431	0.103	≈ 0.089
8417	0.114	0.0890
8415	0.162	0.0896
8412	0.211	≈ 0.089
8422	0.242	0.0892
8428	0.361	0.0887

Figures 4.4 and 4.5 show loads polar plots for flapwise bending moment as a range of increasing advance ratio. Figures 4.6 through 4.11 show time history plots for flapwise bending moment as a range of increasing advance ratio. A quick glance at the LLT prediction for flapwise bending reveals a dominant $1P$ effect, with one valley (trough) on the advancing side and one peak on the retreating side. Application of the LCA remedies this deficiency by accurately capturing the $2P$ and $3P$ effects (due to the presence of multiple stall events for steady, level flight). This is best

illustrated by the time history chart in Figure 4.8, showing a strong $5P$ presence in the load response inboard on the blade. The LCA accurately captures this effect. These higher harmonic effects are less influential at higher μ, leading LLT to provide a good *shape* of the load time history, though with an over-prediction in peak-to-peak magnitude and a phase lag (e.g., see Figure 4.11).

Figures 4.12 and 4.13 show loads polar plots for blade torsional moment as a range of increasing advance ratio. Figures 4.14 through 4.19 show time history plots for blade torsional moment as a range of increasing advance ratio. LLT predicts very little torsional moment response during hover. This is due to the fact that, in an idealized hover environment, very little change in blade pitching (and, thus, blade flapping) is required to hold the vehicle steady. However, in the real environment, there could be effects due to the presence of wind, rotor motion, tail rotor tip vortices impinging upon the main rotor blade, etc. that can lead to non-zero response in torsional moment. For forward speed flight in a BVI regime (e.g., c8431, $\mu = 0.103$; see Figure 4.16), there is significant $3P$ and $5P$ load content due to multiple stalls throughout a given rotor rotation. These are not captured by LLT but are accurately captured via application of the LCA. In all other flight regimes, there is strong $4P$ load content, due to aerodynamic excitation of the first flexible torsional moment mode of the blade ($\approx 4P$; $4.53P$ in the numerical simulation used herein). For ST90, the LLT continues to be problematic at matching the complex flow effects seen in the measured response. This leads to one of the conclusions of this effort that the LCA is most effective (and designed for) inboard (and, ultimately, hub) components. It is not an accurate predictor of high frequency (greater than $6P$) aerodynamic effects that are dominant near the blade tip.

Figures 4.20 and 4.21 show loads polar plots for edgewise bending moment as a range of increasing advance ratio. Figures 4.22 through 4.27 show time history plots for edgewise bending moment as a range of increasing advance ratio. Edgewise

bending is dominated by $1P$ through $4P$ harmonic content. LLT effectively predicts $1P$ content only. Application of the LCA remedies this discrepancy.

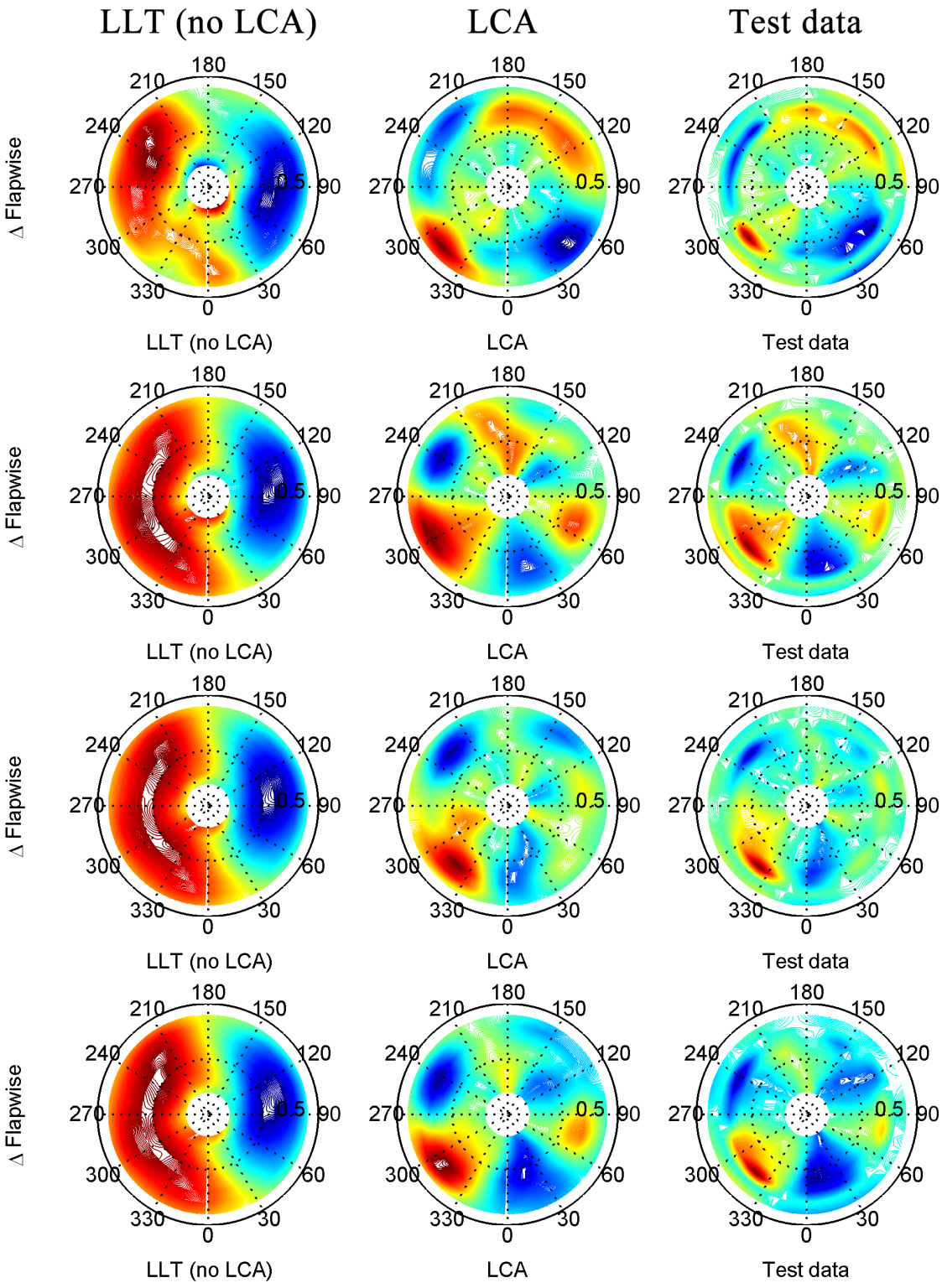

Figure 4.4: Flapwise bending moment: radial, azimuthal distribution; [flight counter, μ] = [8434, 0.023], [8420, 0.088], 8431, 0.103], [8417, 0.114] (top-to-bottom); red (peak), blue (valley).

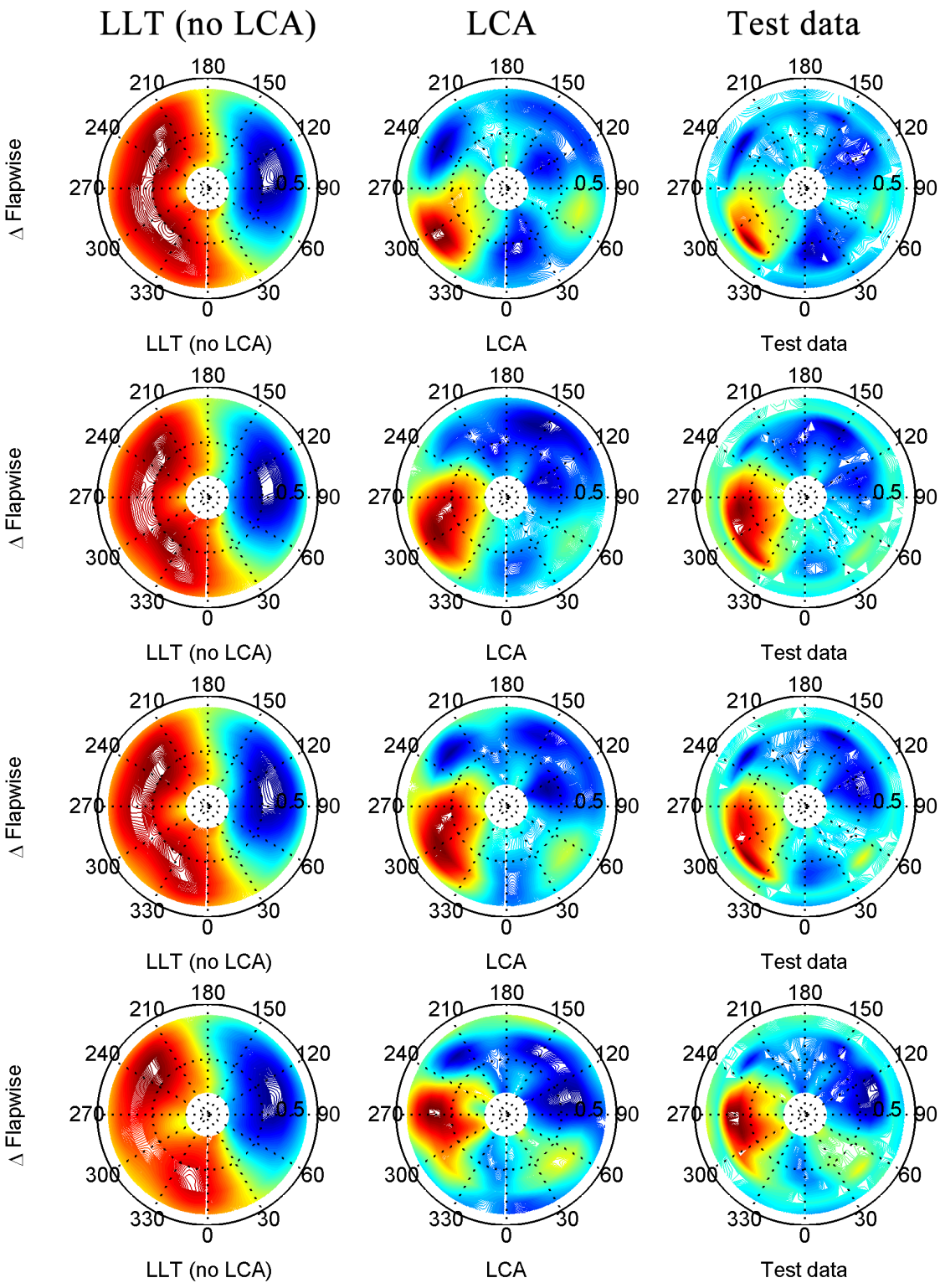

Figure 4.5: Flapwise bending moment: radial, azimuthal distribution; [flight counter, μ] = [8415, 0.162], [8412, 0.211], 8422, 0.242], [8428, 0.361] (top-to-bottom); red (peak), blue (valley).

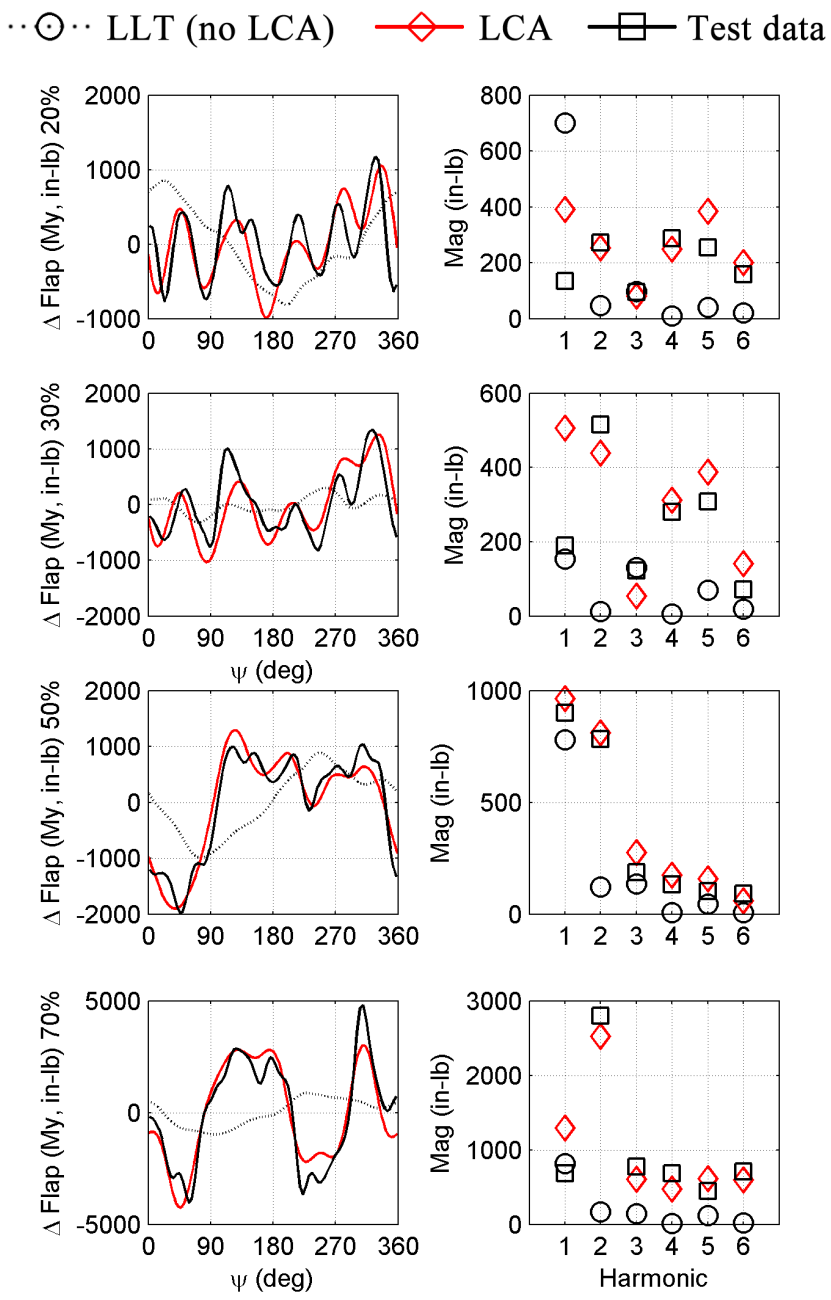

Figure 4.6: Flapwise bending moment: time history, load component by harmonic; [flight counter, μ] = [8434, 0.023]

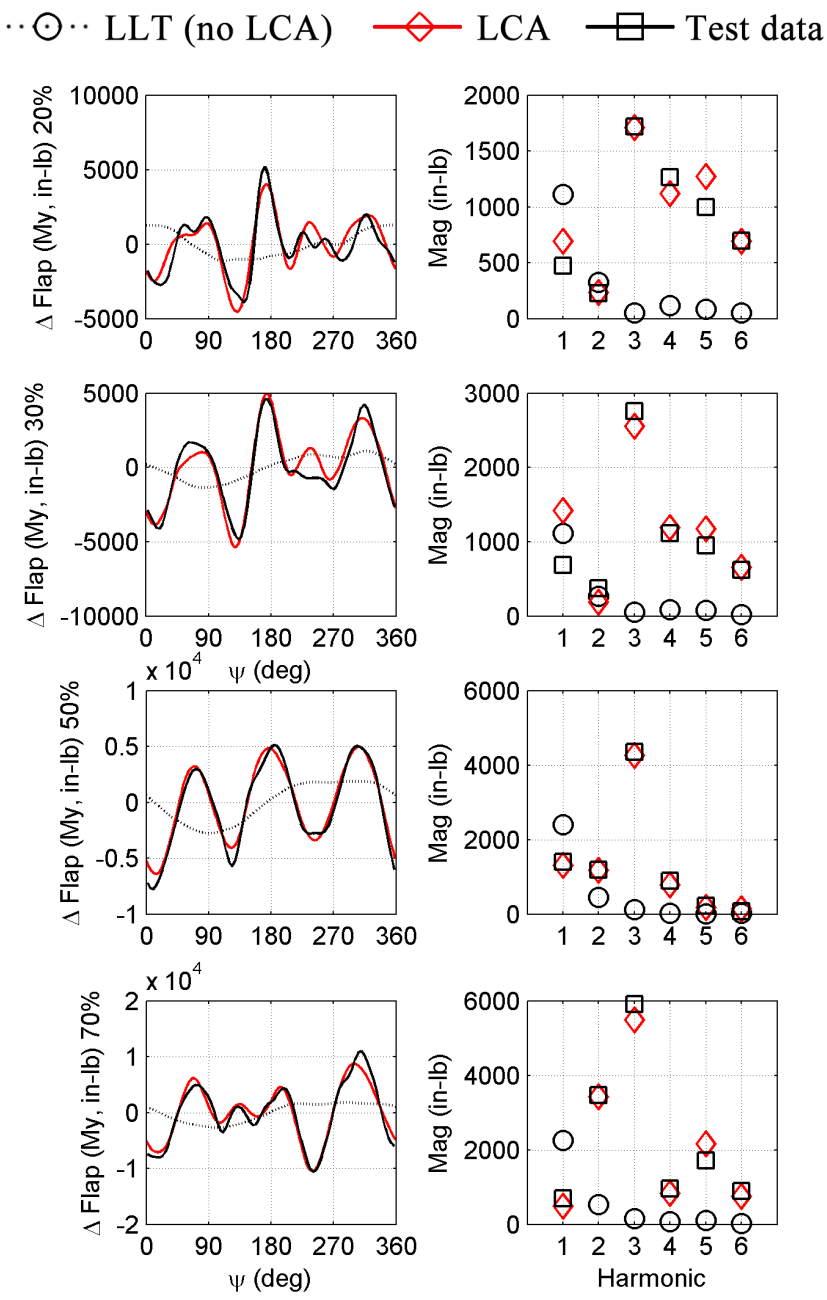

Figure 4.7: Flapwise bending moment: time history, load component by harmonic; [flight counter, μ] = [8420, 0.088]

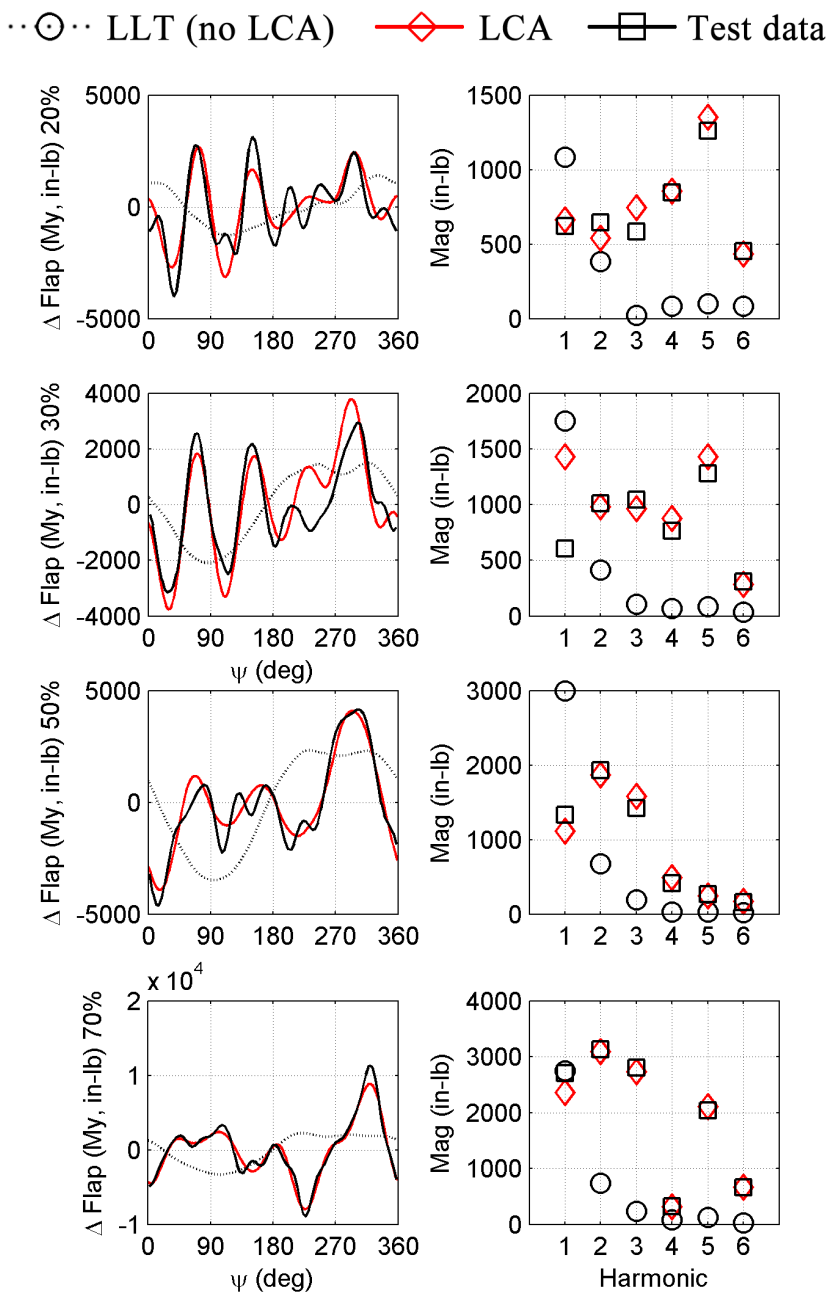

Figure 4.8: Flapwise bending moment: time history, load component by harmonic; [flight counter, μ] = [8431, 0.103]

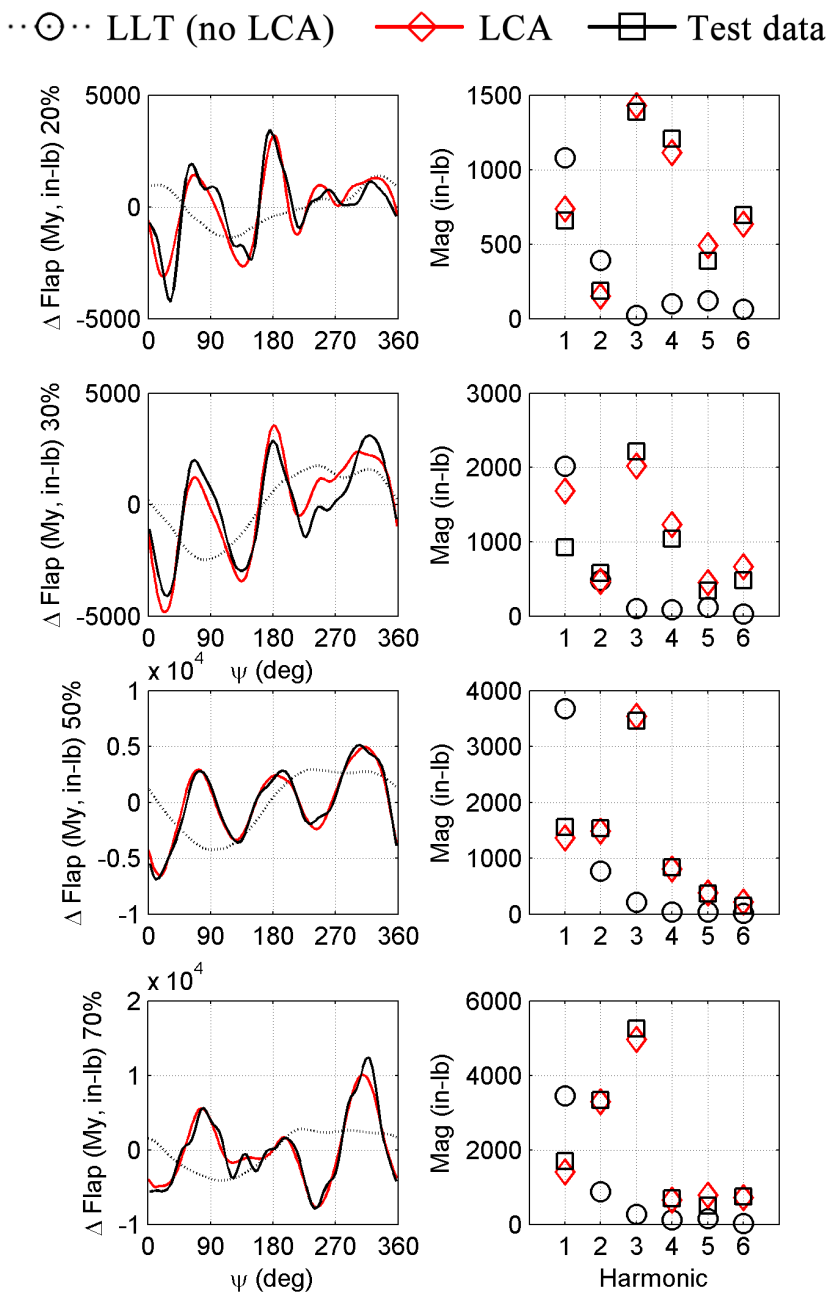

Figure 4.9: Flapwise bending moment: time history, load component by harmonic; [flight counter, μ] = [8417, 0.114]

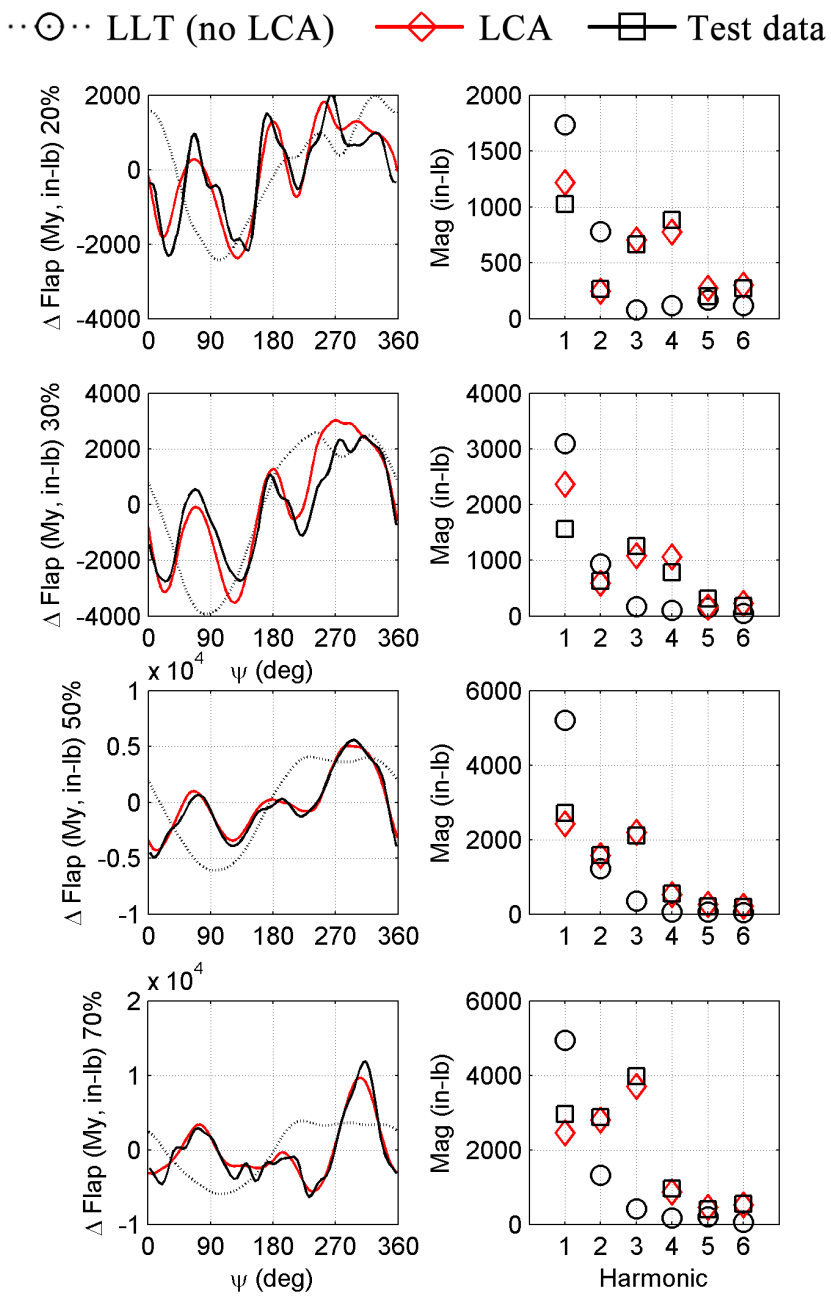

Figure 4.10: Flapwise bending moment: time history, load component by harmonic; [flight counter, μ] = [8415, 0.162]

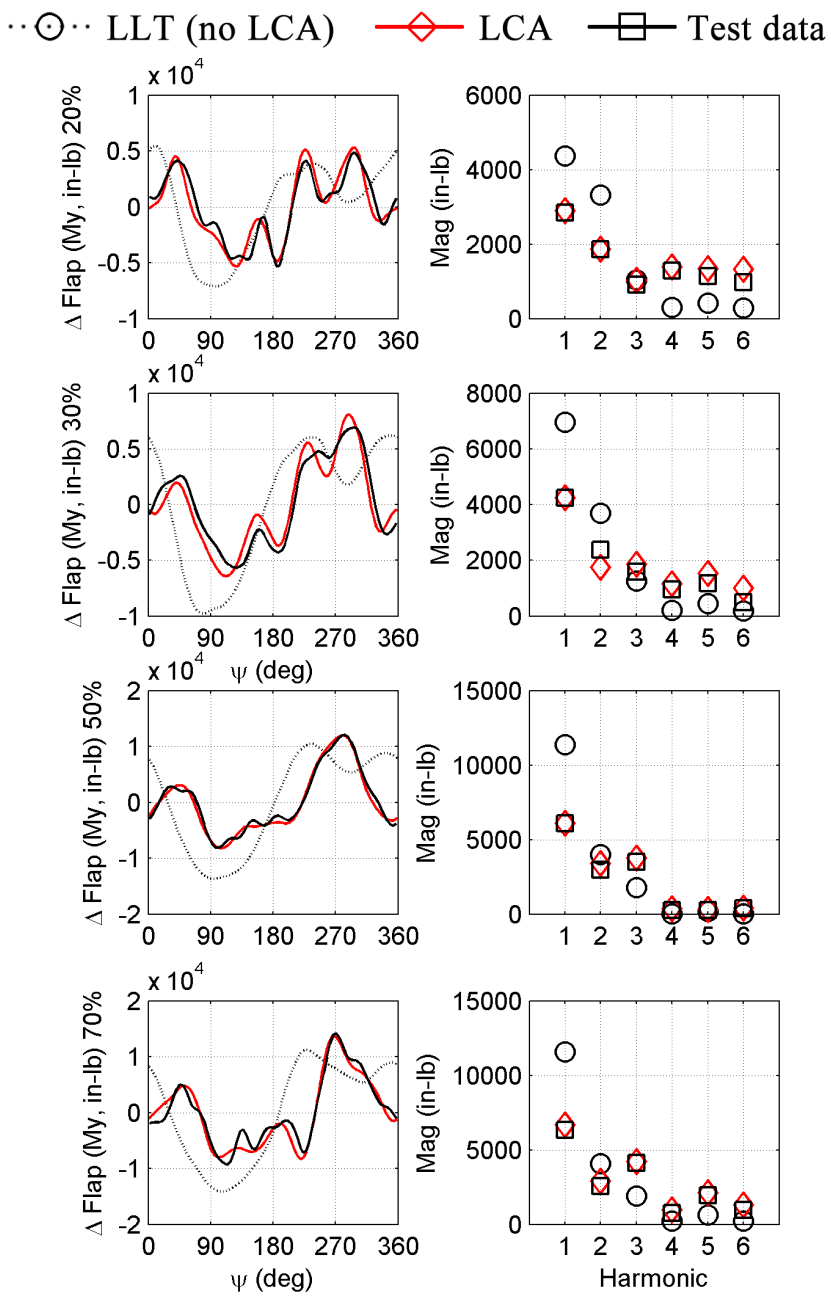

Figure 4.11: Flapwise bending moment: time history, load component by harmonic; [flight counter, μ] = [8428, 0.361]

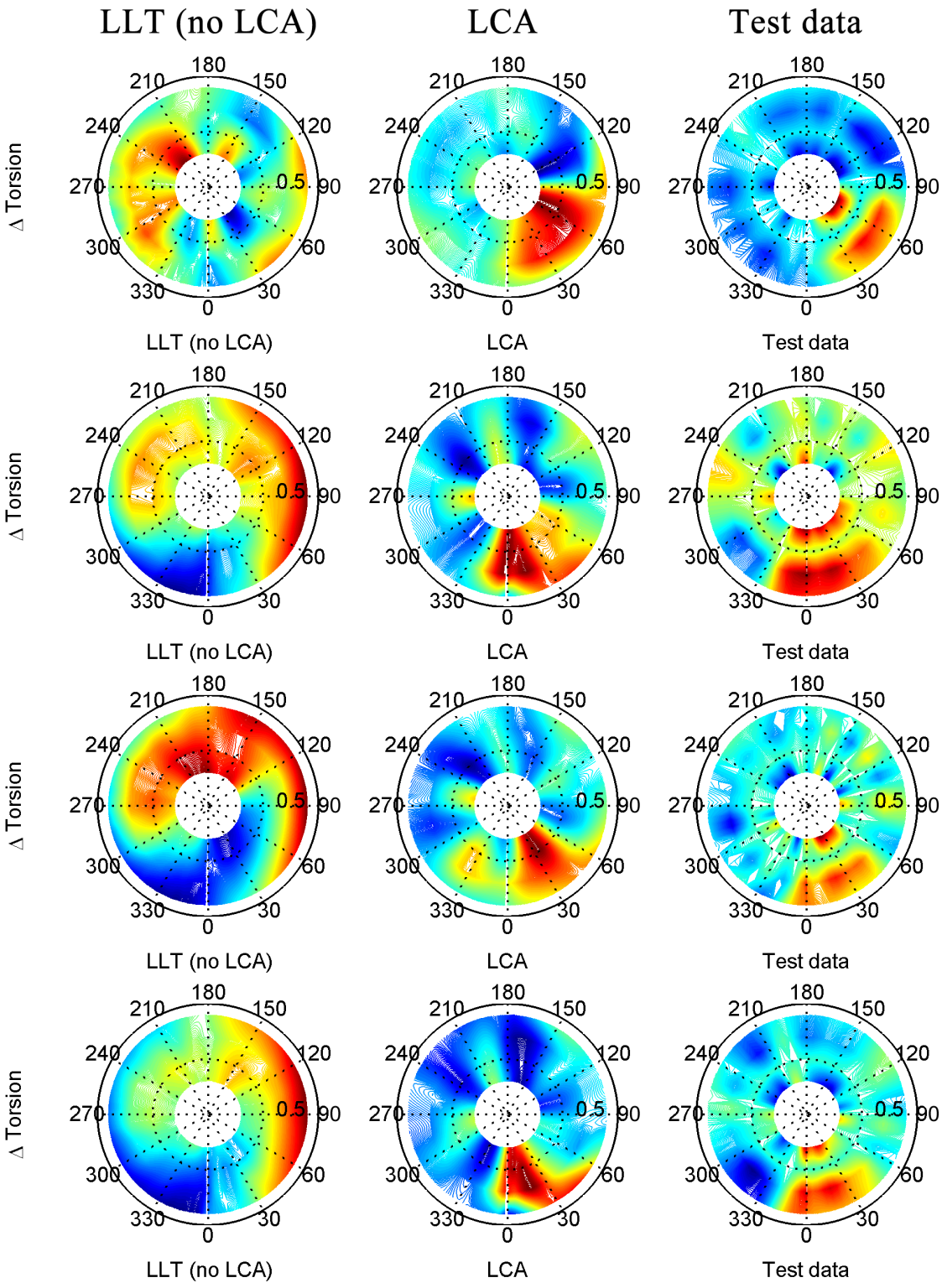

Figure 4.12: Torsional moment: radial, azimuthal distribution; [flight counter, μ] = [8434, 0.023], [8420, 0.088], 8431, 0.103], [8417, 0.114] (top-to-bottom); red (peak), blue (valley).

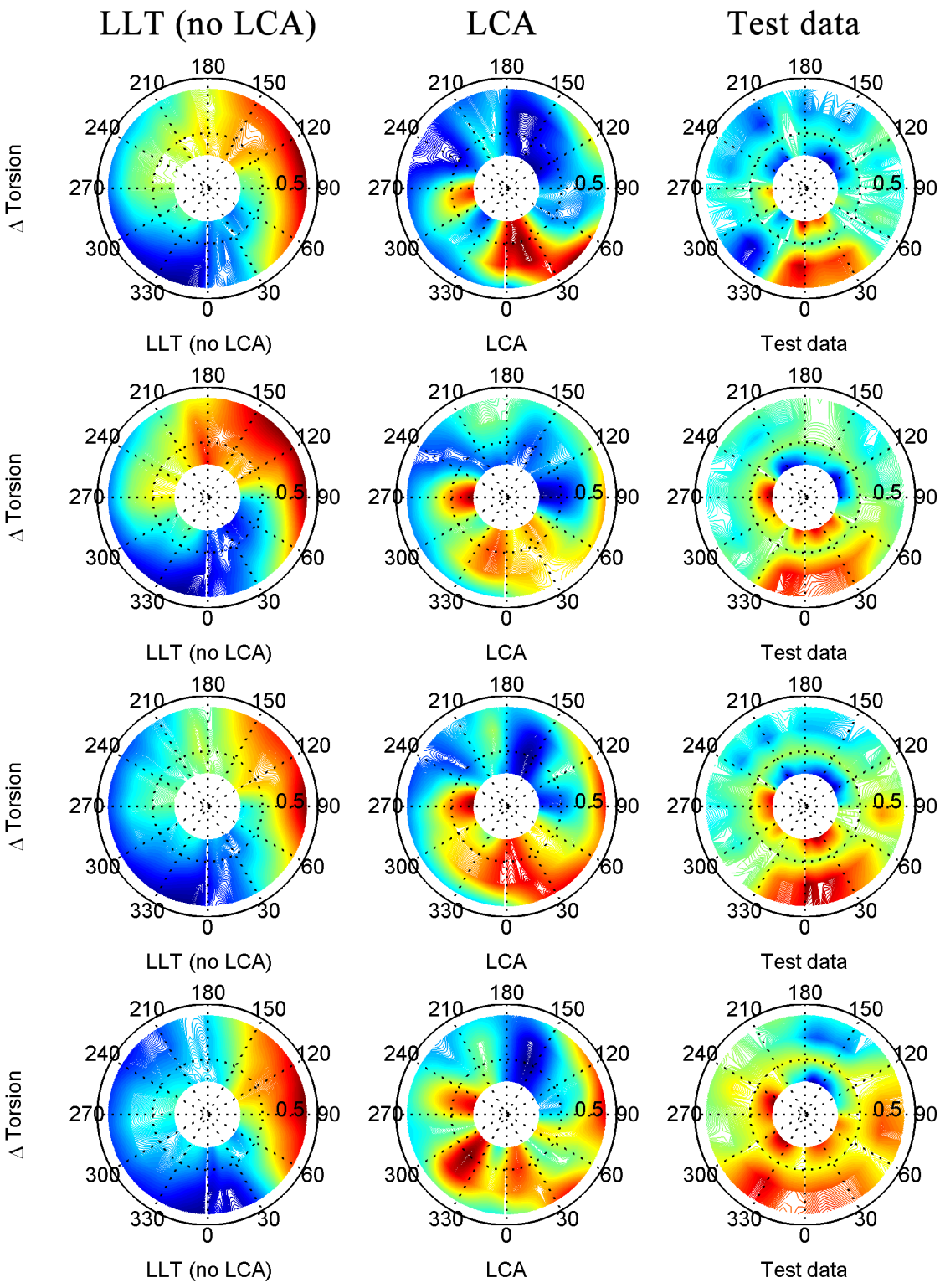

Figure 4.13: Torsional moment: radial, azimuthal distribution; [flight counter, μ] = [8415, 0.162], [8412, 0.211], 8422, 0.242], [8428, 0.361] (top-to-bottom); red (peak), blue (valley).

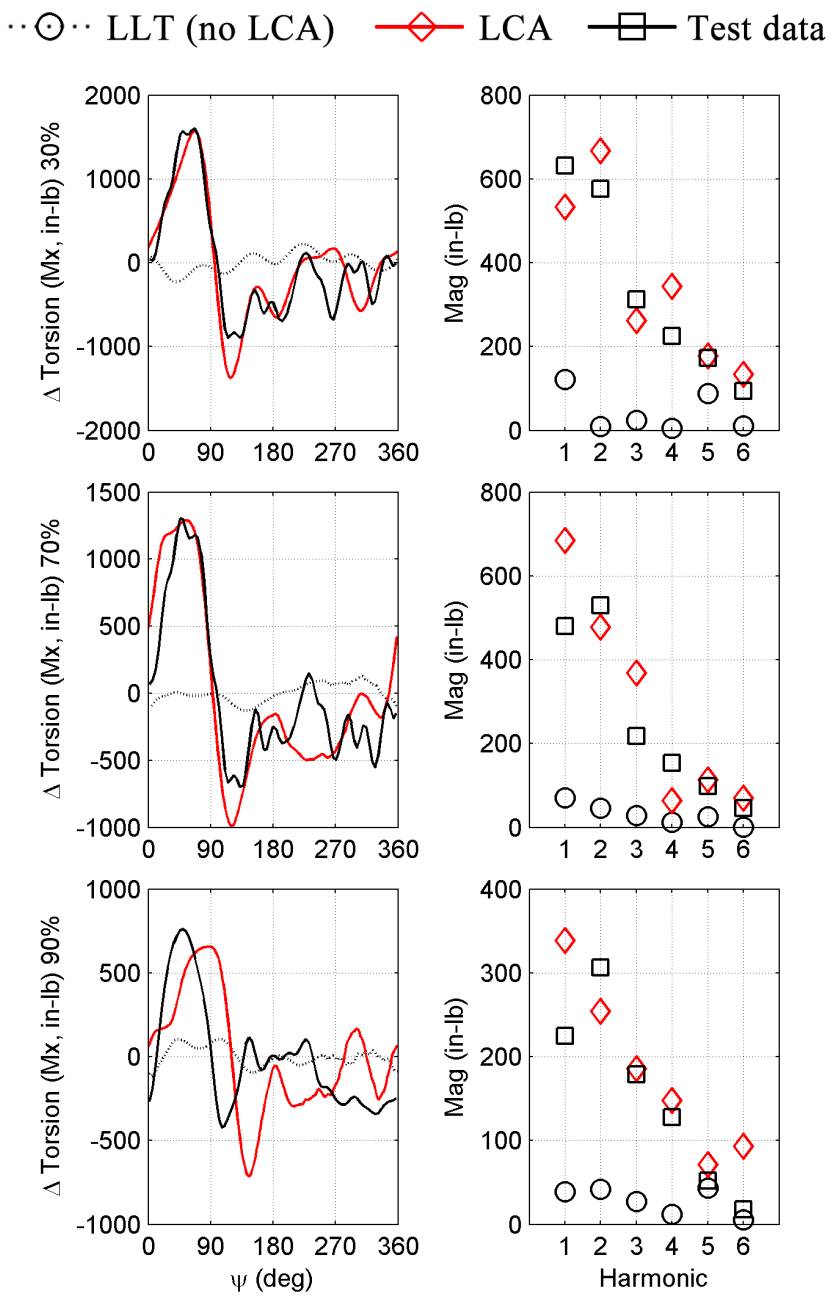

Figure 4.14: Torsional moment: time history, load component by harmonic; [flight counter, μ] = [8434, 0.023]

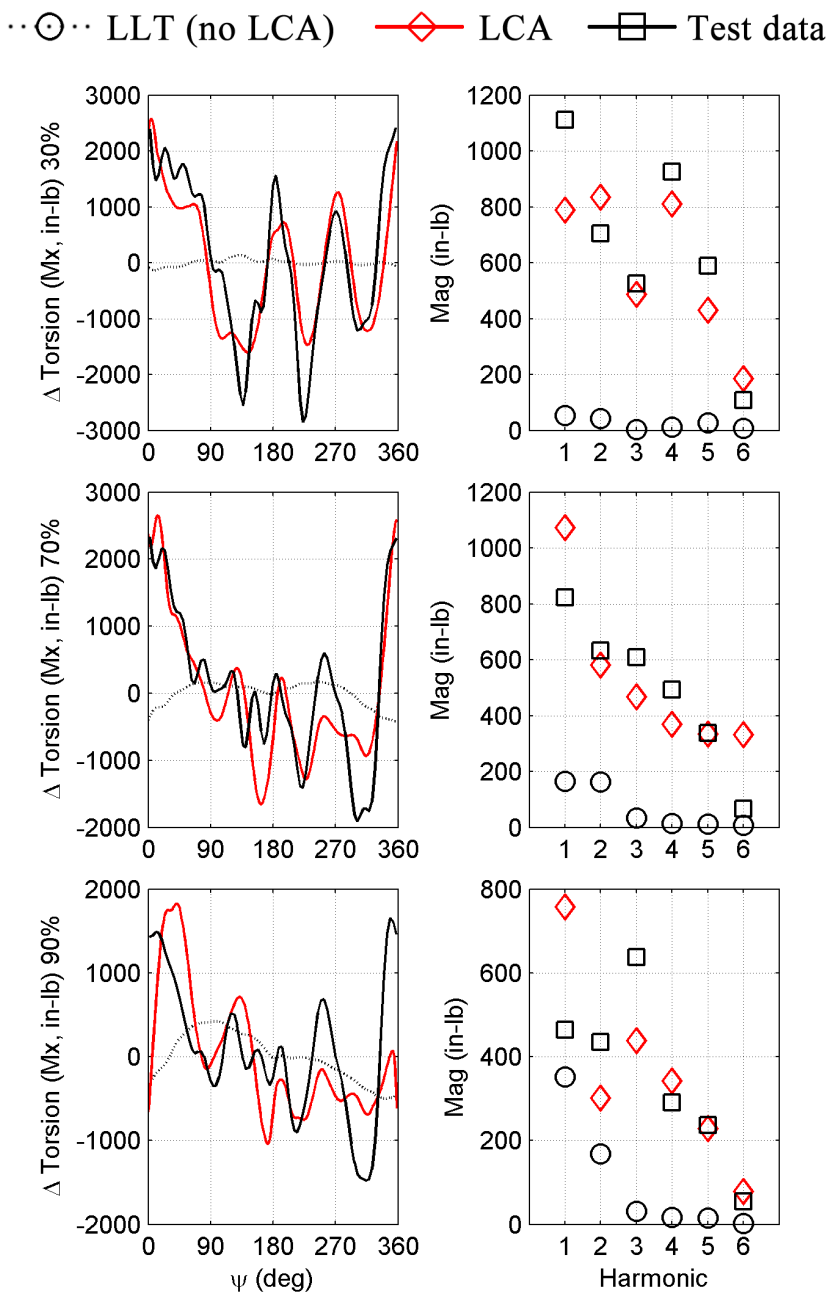

Figure 4.15: Torsional moment: time history, load component by harmonic; [flight counter, μ] = [8420, 0.088]

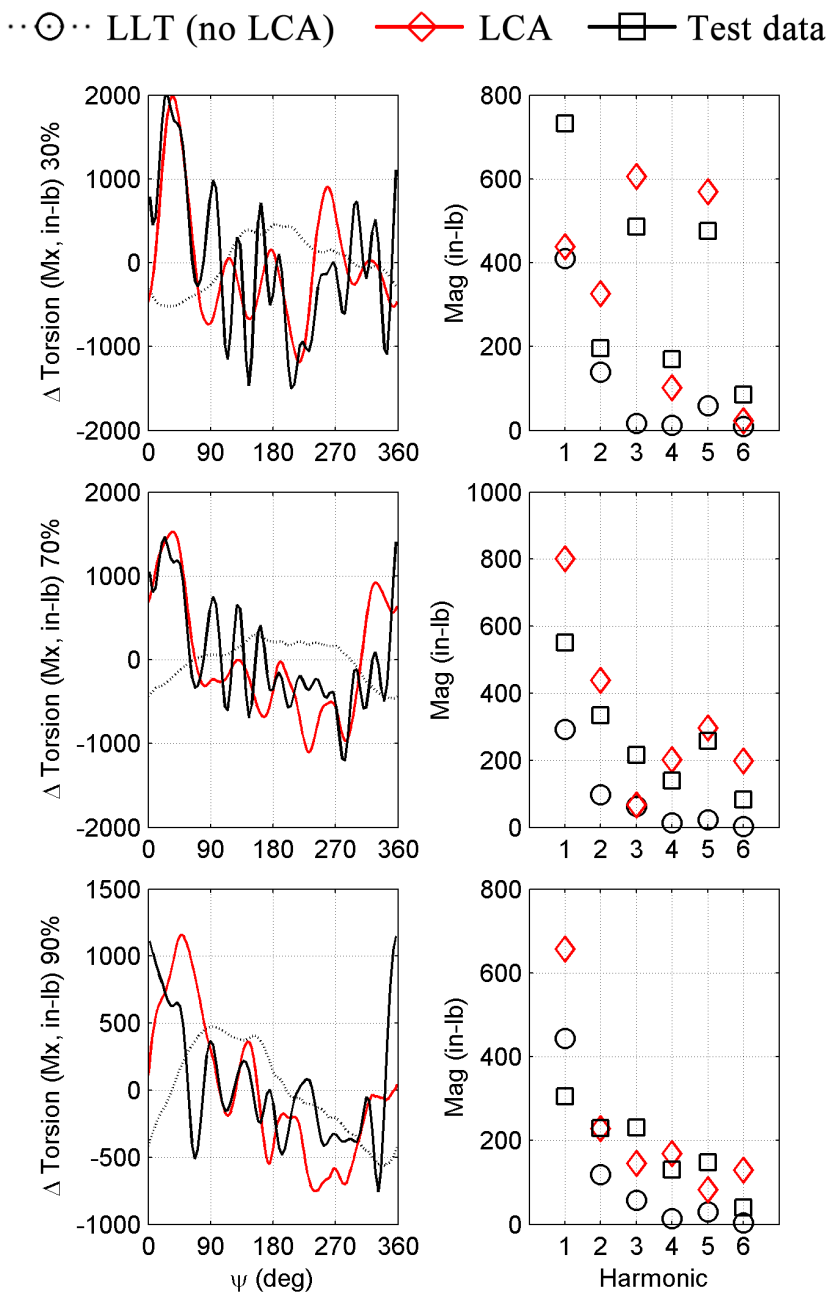

Figure 4.16: Torsional moment: time history, load component by harmonic; [flight counter, μ] = [8431, 0.103]

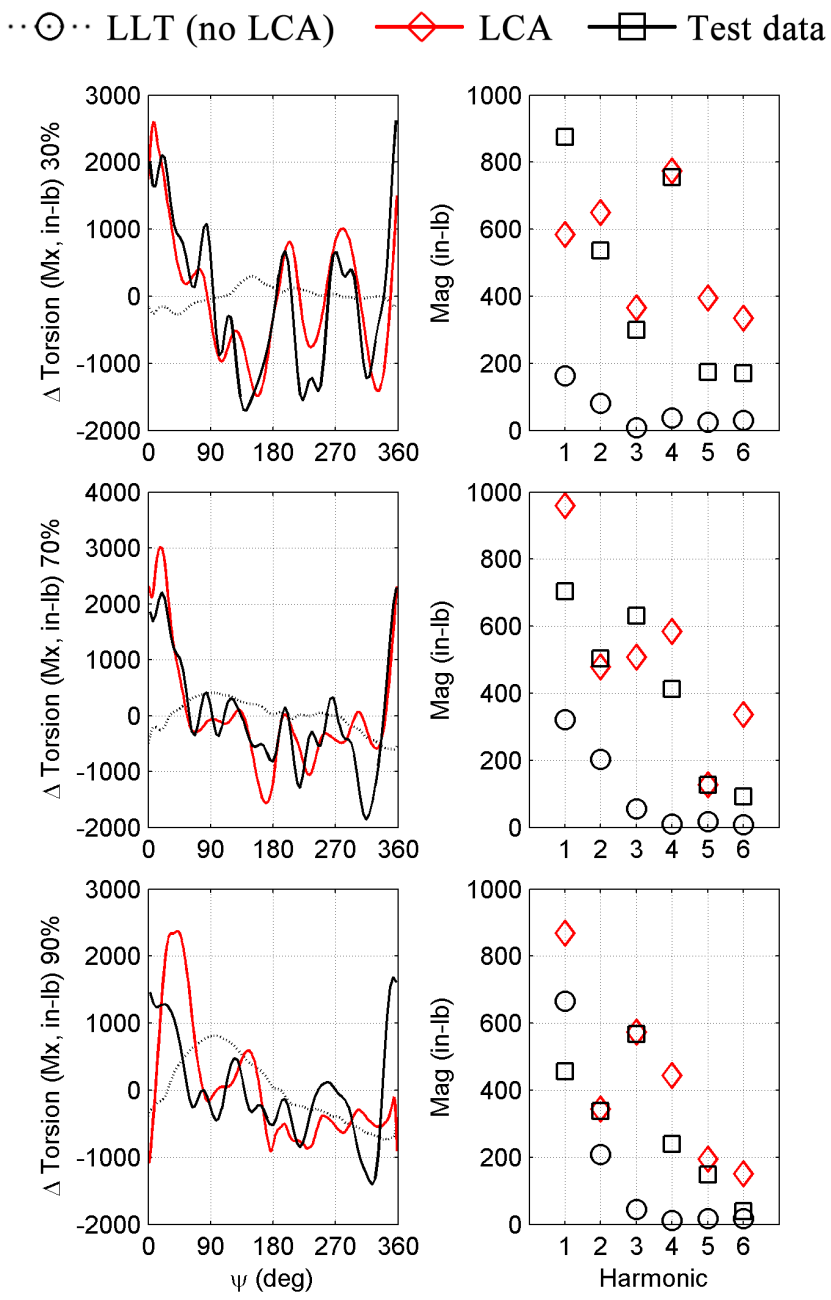

Figure 4.17: Torsional moment: time history, load component by harmonic; [flight counter, μ] = [8417, 0.114]

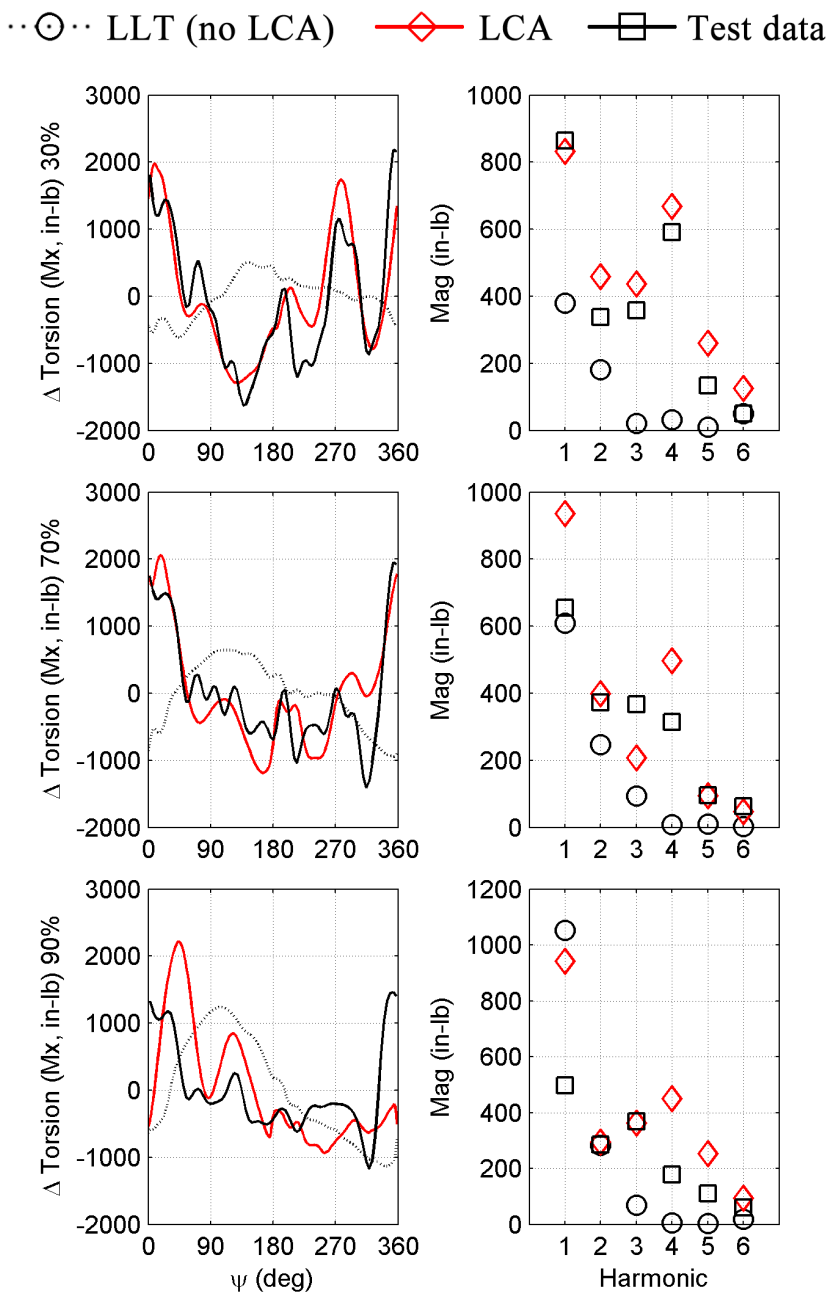

Figure 4.18: Torsional moment: time history, load component by harmonic; [flight counter, μ] = [8415, 0.162]

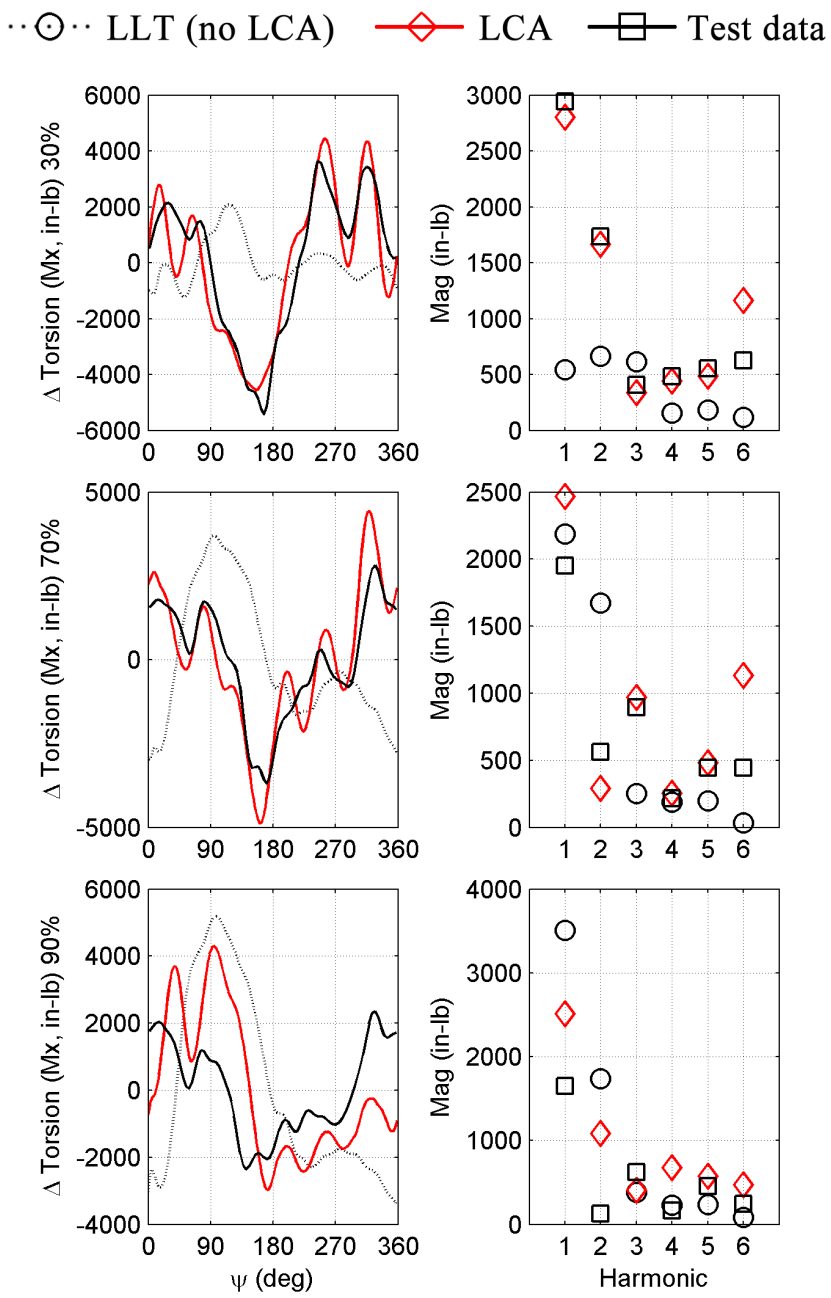

Figure 4.19: Torsional moment: time history, load component by harmonic; [flight counter, μ] = [8428, 0.361]

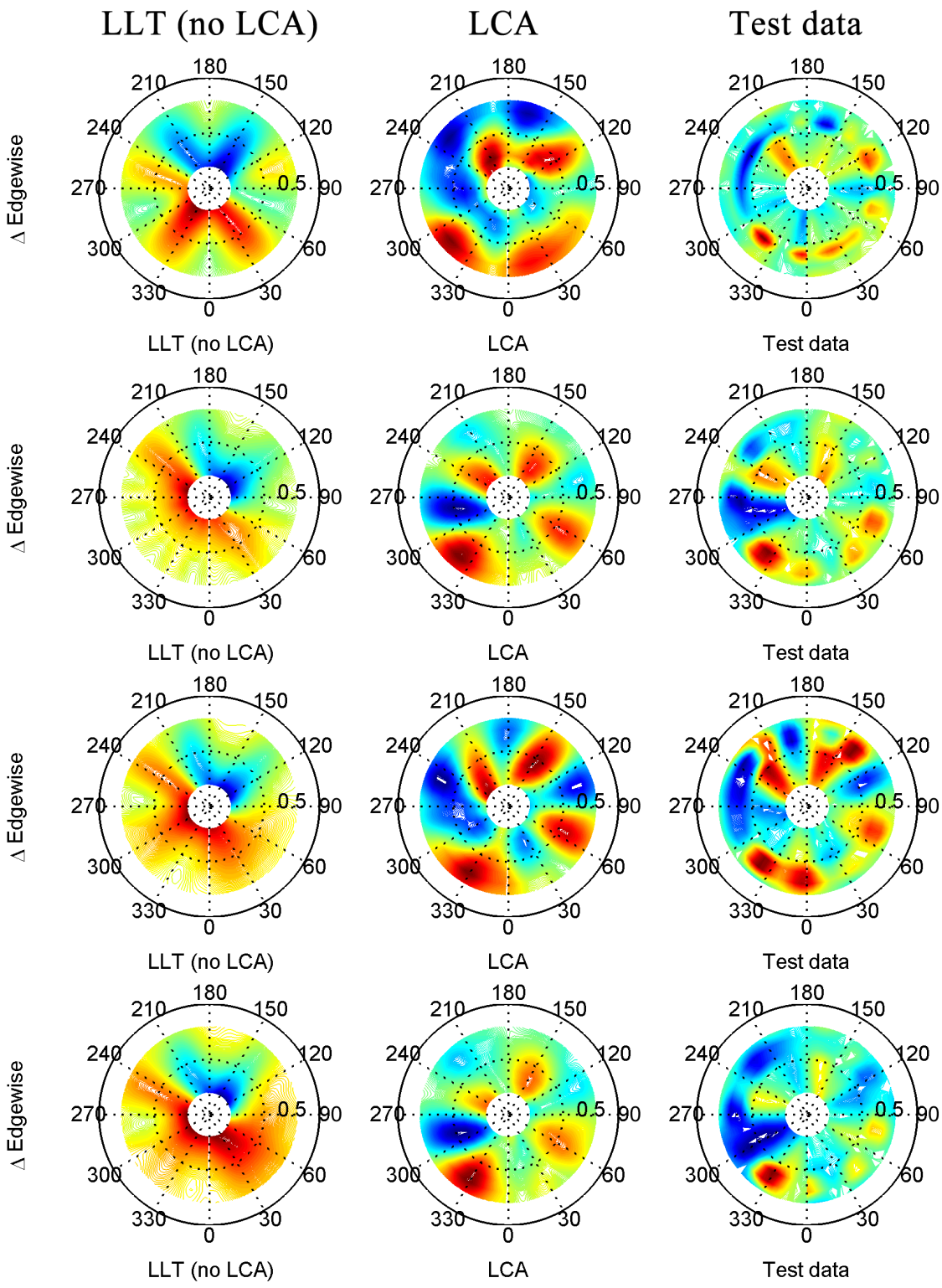

Figure 4.20: Edgewise bending moment: radial, azimuthal distribution; [flight counter, μ] = [8434, 0.023], [8420, 0.088], 8431, 0.103], [8417, 0.114] (top-to-bottom); red (peak), blue (valley).

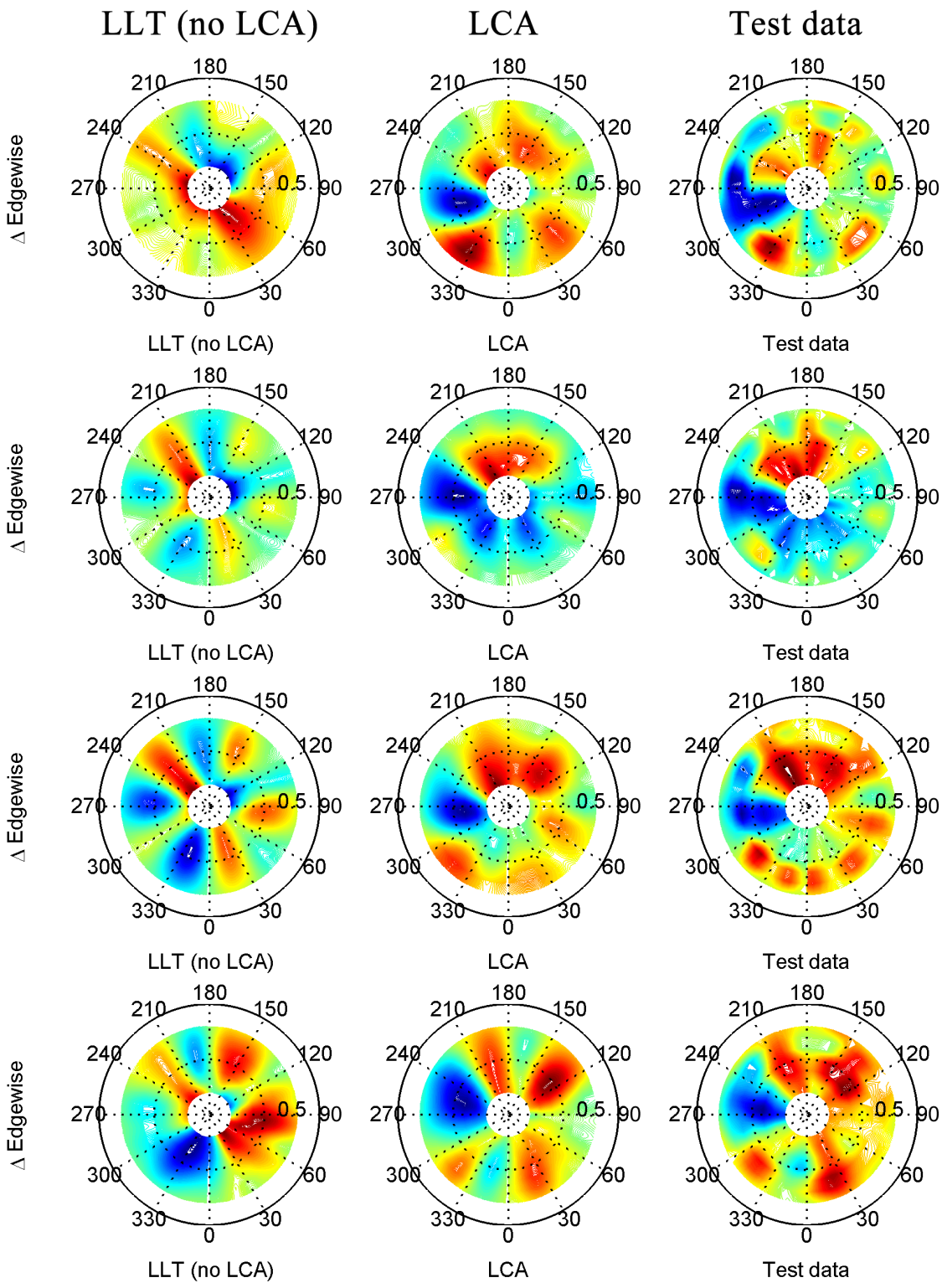

Figure 4.21: Edgewise bending moment: radial, azimuthal distribution; [flight counter, μ] = [8415, 0.162], [8412, 0.211], 8422, 0.242], [8428, 0.361] (top-to-bottom); red (peak), blue (valley).

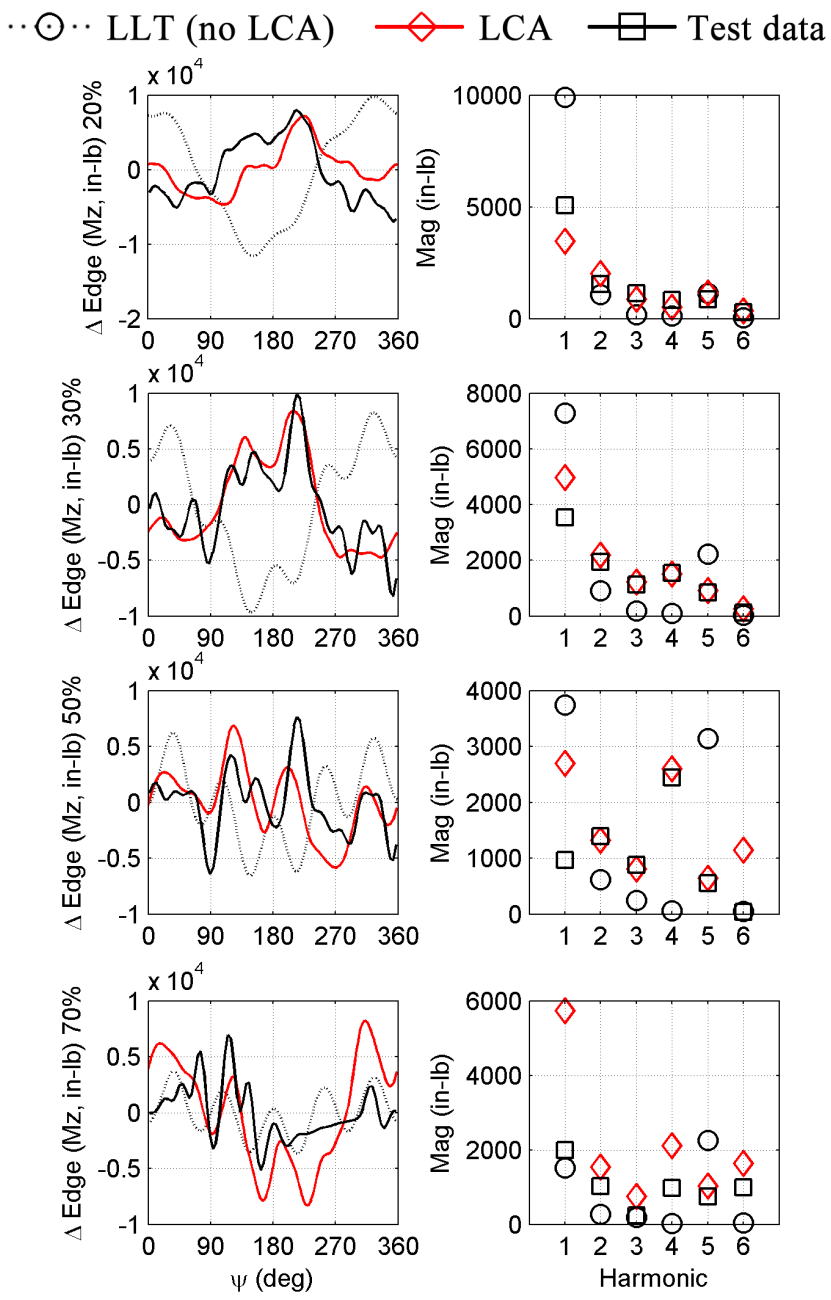

Figure 4.22: Edgewise bending moment: time history, load component by harmonic; [flight counter, μ] = [8434, 0.023]

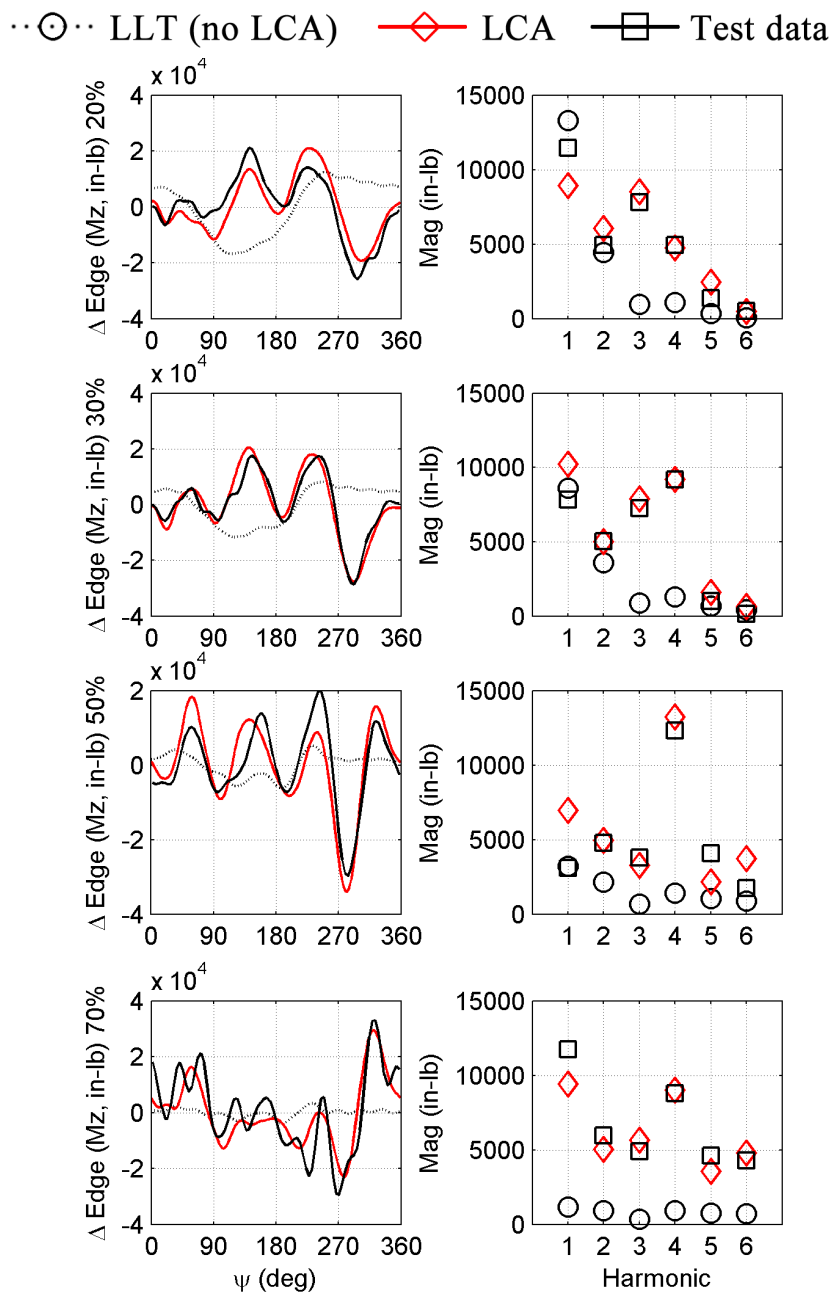

Figure 4.23: Edgewise bending moment: time history, load component by harmonic; [flight counter, μ] = [8420, 0.088]

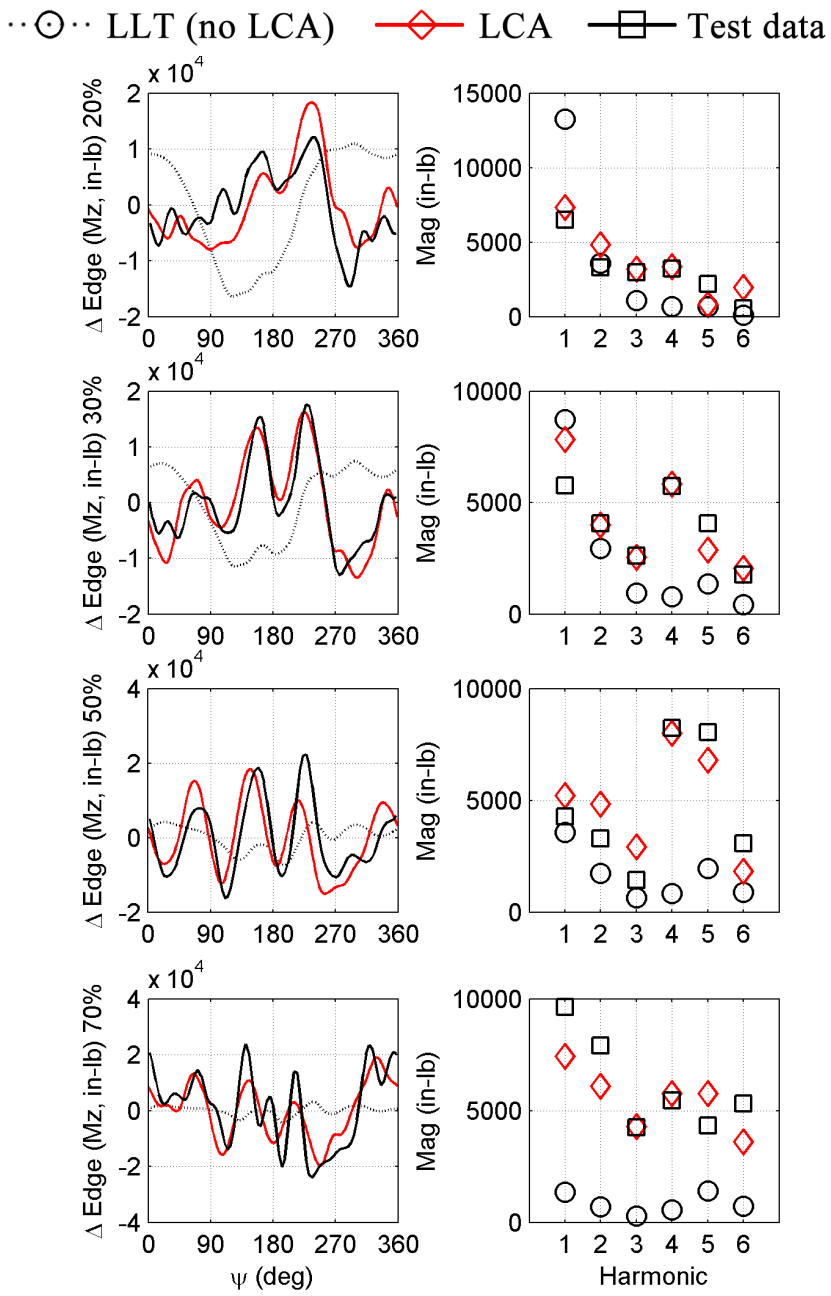

Figure 4.24: Edgewise bending moment: time history, load component by harmonic; [flight counter, μ] = [8431, 0.103]

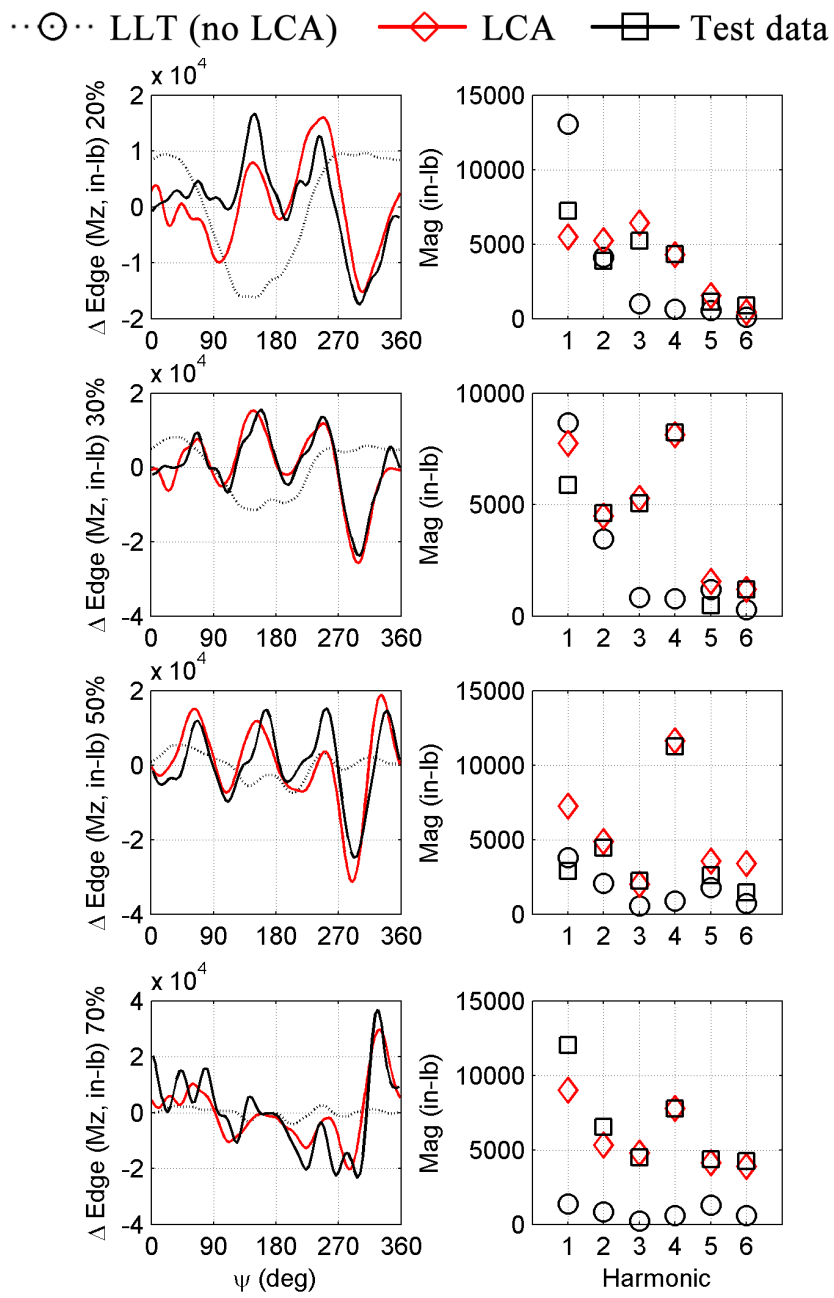

Figure 4.25: Edgewise bending moment: time history, load component by harmonic; [flight counter, μ] = [8417, 0.114]

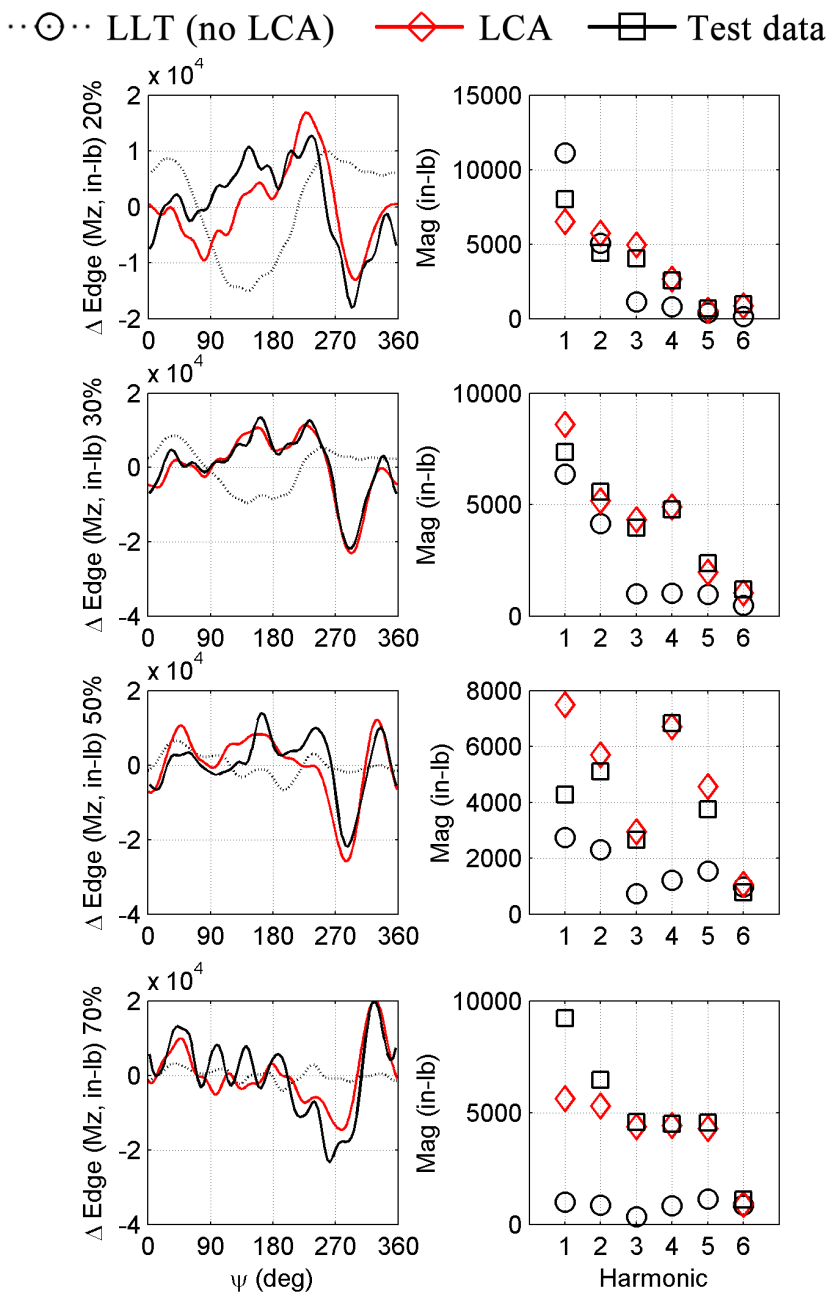

Figure 4.26: Edgewise bending moment: time history, load component by harmonic; [flight counter, μ] = [8415, 0.162]

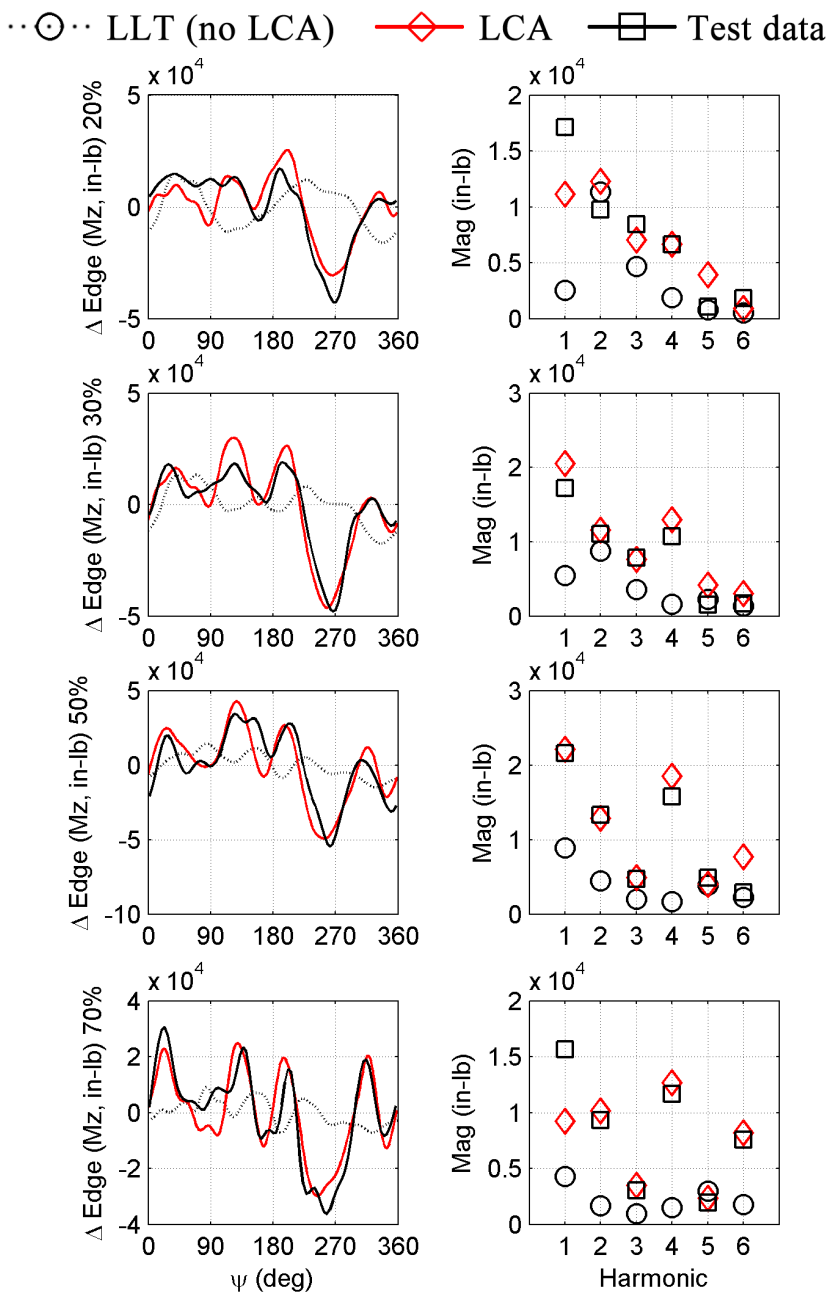

Figure 4.27: Edgewise bending moment: time history, load component by harmonic; [flight counter, μ] = [8428, 0.361]

4.4 *Rotor Loads Results: Radial, Azimuthal Load Distribution: Six Load Control Points (SN30/70, ST30/70, SE30/70)*

The following results are for a reduced set of control points. Internal (LLT) airloads are applied, but with six load control points (SN30/70, ST30/70, SE30/70). Results for $0.20R$, $0.50R$ (SN and SE) as well as $0.90R$ (ST) are *mapped* results based on load control points at $0.30R$ and $0.70R$. This method shows the validity of the LCA for loads prediction at non-instrumented locations. Figure 4.28 shows the control points and mapped stations used in this simulation.

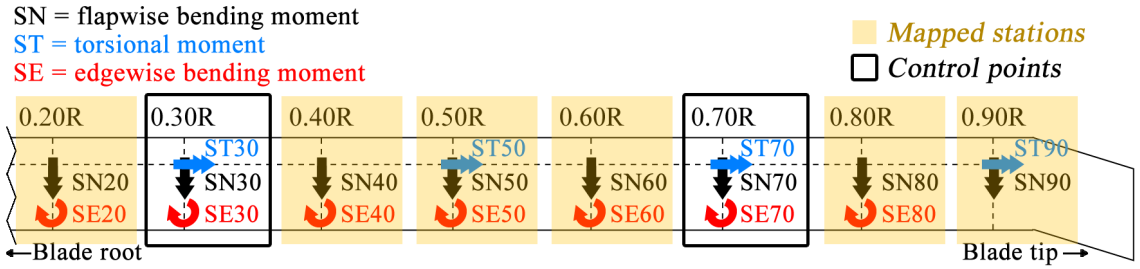

Figure 4.28: UH-60A blade control points and mapped stations.

Figures 4.29 and 4.30 show loads polar plots for flapwise bending moments as a range of increasing advance ratio. Figures 4.31 and 4.32 show loads polar plots for torsional moments as a range of increasing advance ratio. Figures 4.33 and 4.34 show loads polar plots for edgewise bending moments as a range of increasing advance ratio.

Results are similar to those in the previous section, showing that application of the LCA accurately captures the number of cycles, magnitude, and phasing of blade loads across μ - even at *mapped* locations (e.g., SN50).

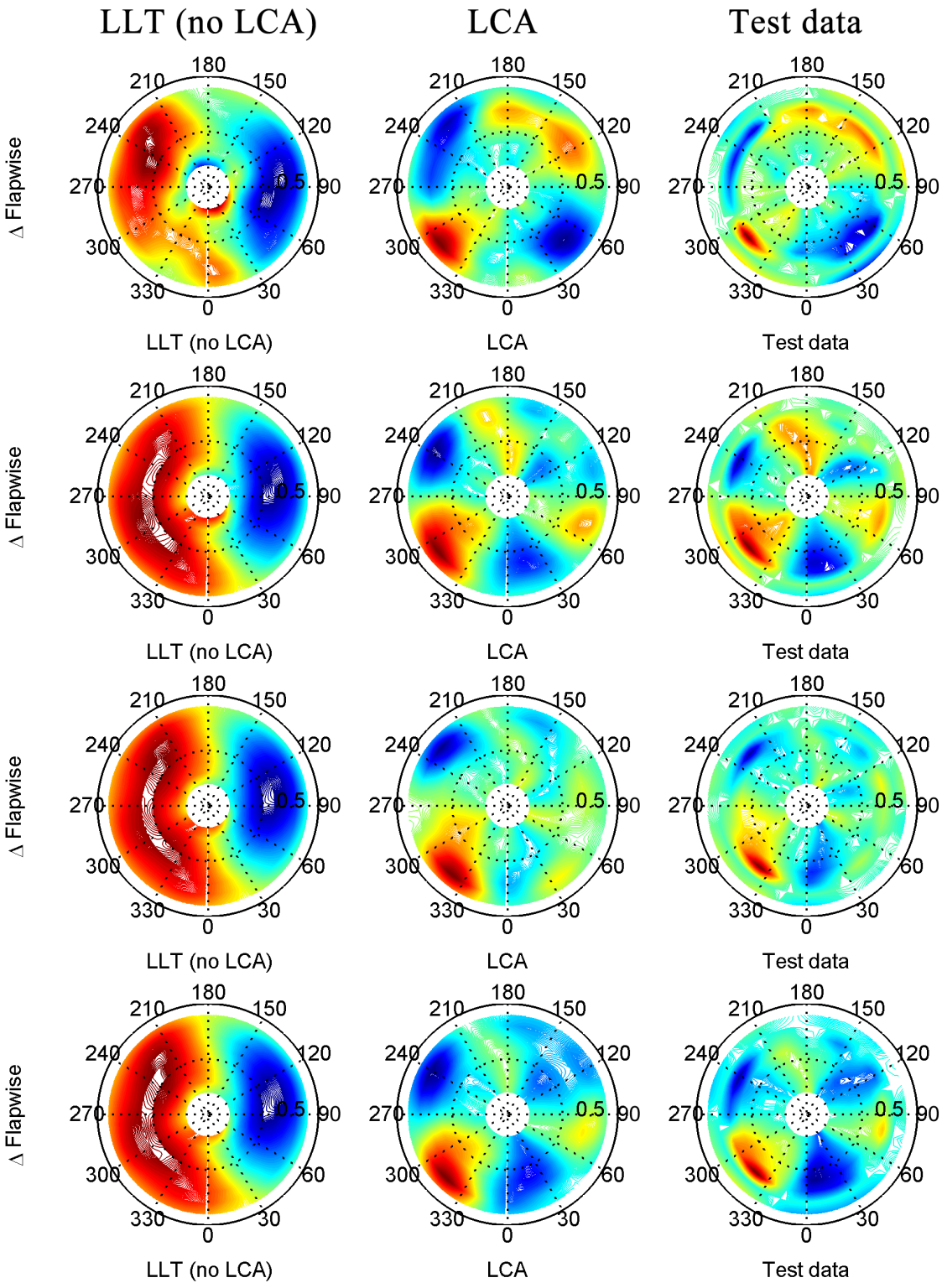

Figure 4.29: Flapwise bending moment: radial, azimuthal distribution; [flight counter, μ] = [8434, 0.023], [8420, 0.088], 8431, 0.103], [8417, 0.114] (top-to-bottom); red (peak), blue (valley).

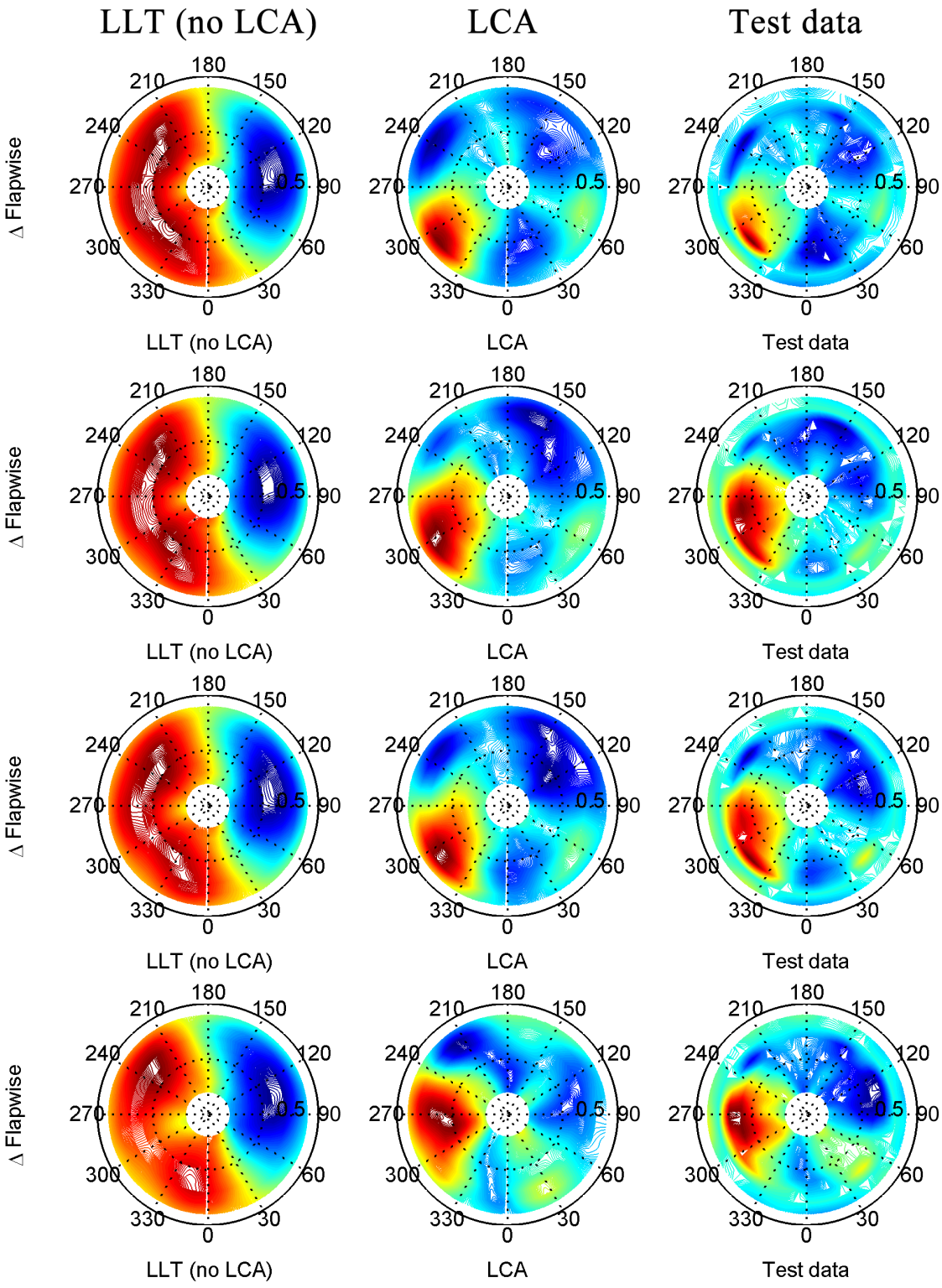

Figure 4.30: Flapwise bending moment: radial, azimuthal distribution; [flight counter, μ] = [8415, 0.162], [8412, 0.211], 8422, 0.242], [8428, 0.361] (top-to-bottom); red (peak), blue (valley).

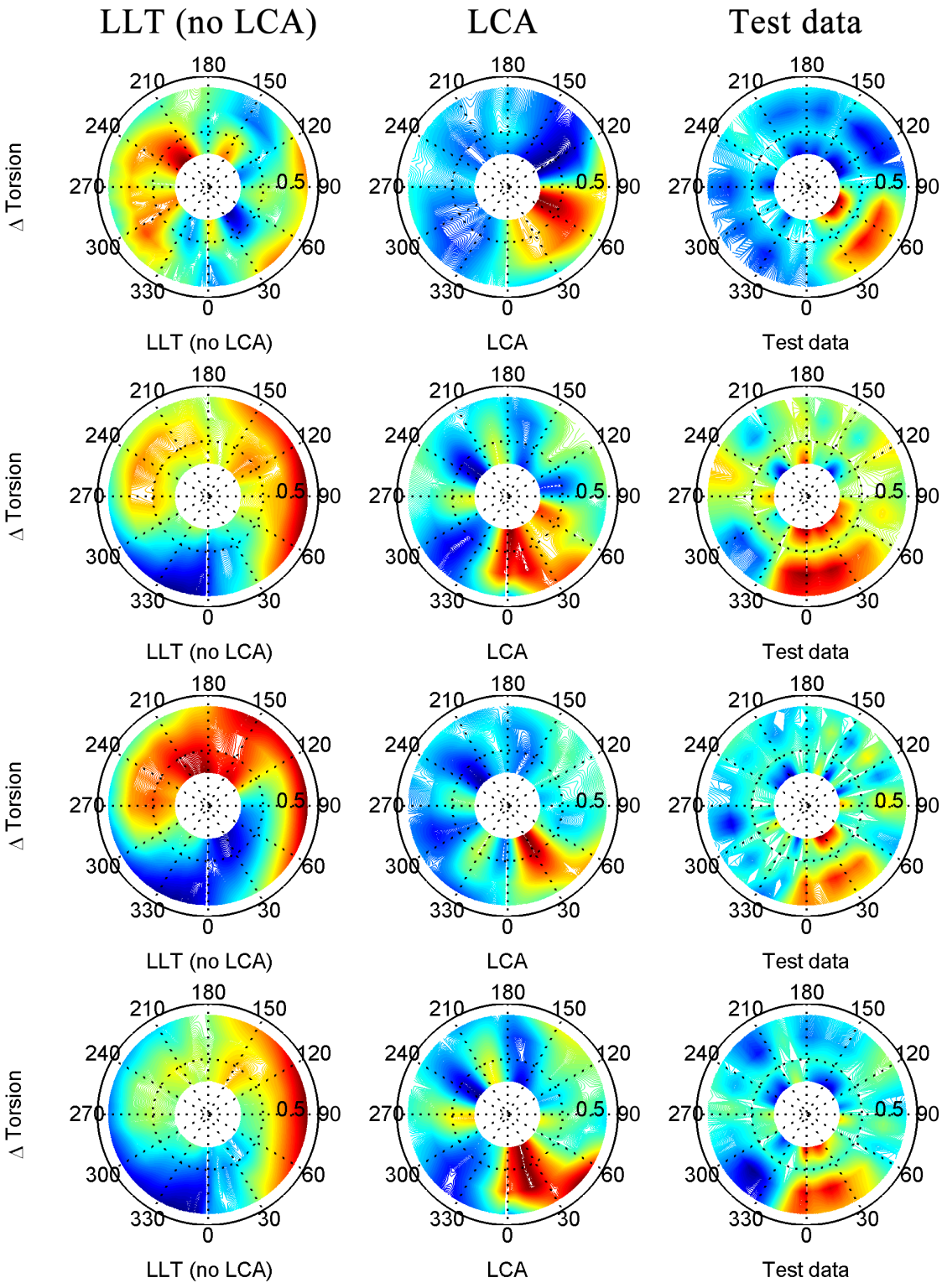

Figure 4.31: Torsional moment: radial, azimuthal distribution; [flight counter, μ] = [8434, 0.023], [8420, 0.088], 8431, 0.103], [8417, 0.114] (top-to-bottom); red (peak), blue (valley).

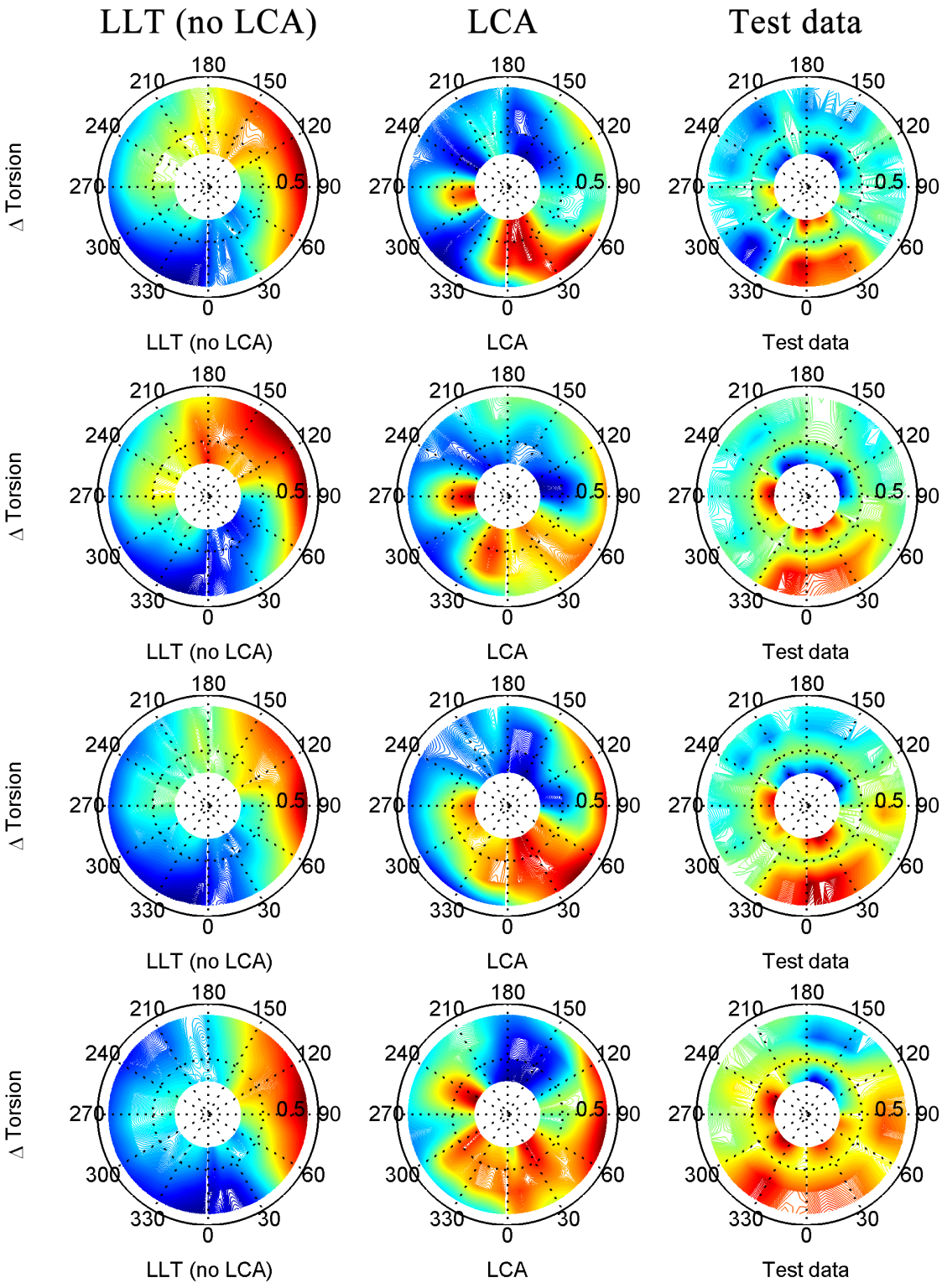

Figure 4.32: Torsional moment: radial, azimuthal distribution; [flight counter, μ] = [8415, 0.162], [8412, 0.211], 8422, 0.242], [8428, 0.361] (top-to-bottom); red (peak), blue (valley).

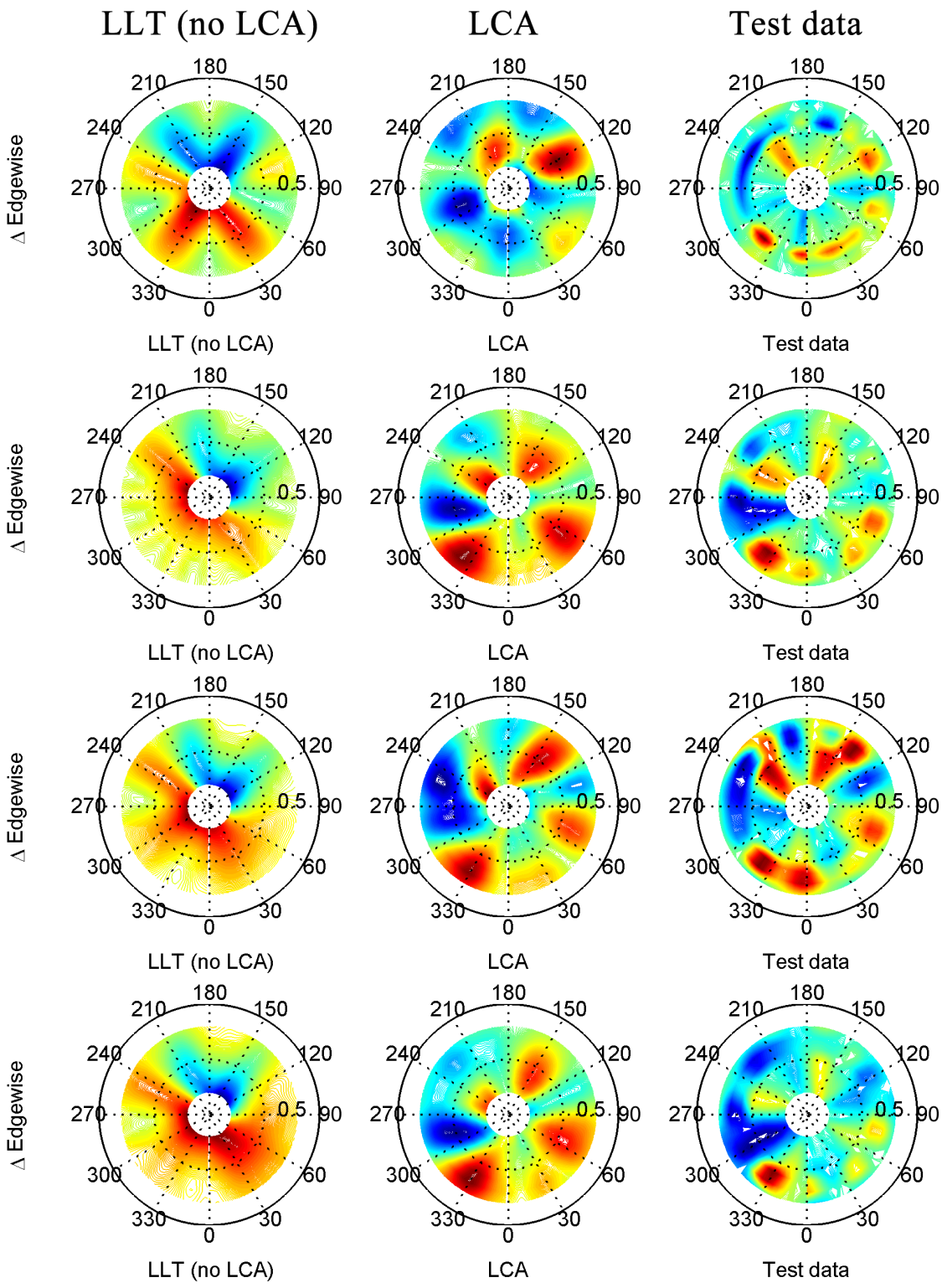

Figure 4.33: Edgewise bending moment: radial, azimuthal distribution; [flight counter, μ] = [8434, 0.023], [8420, 0.088], 8431, 0.103], [8417, 0.114] (top-to-bottom); red (peak), blue (valley).

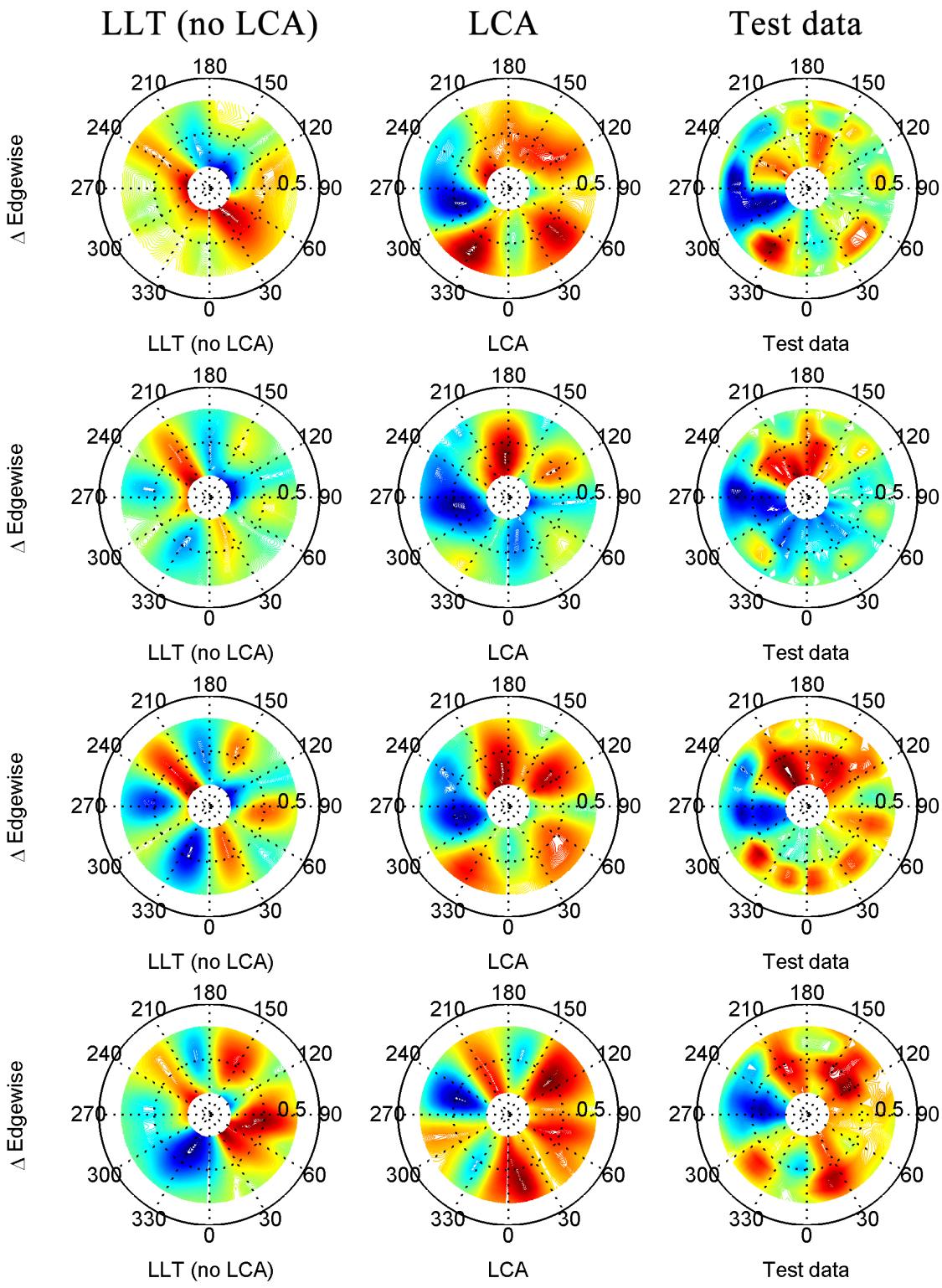

Figure 4.34: Edgewise bending moment: radial, azimuthal distribution; [flight counter, μ] = [8415, 0.162], [8412, 0.211], 8422, 0.242], [8428, 0.361] (top-to-bottom); red (peak), blue (valley).

4.5 Mechanical Airloads Problem

Now the so-called *mechanical airloads* problem [65] is examined. In this case, measured airloads from the UH-60A Airloads Program are fed into the DYMORE LCA simulation. This is effectively a test of the quality of the simulation's structural dynamics, since the airloads are known. These cases are run for the first sensor set (16 blade loads), modes 3-10, and harmonic scalars = [1.0, 1.0, 1.0, 0.5, 0.3, 0.3]. Figure 4.35 shows the control points and mapped stations used in this simulation. Flights 84 and 85 (51 flight counters) were examined.

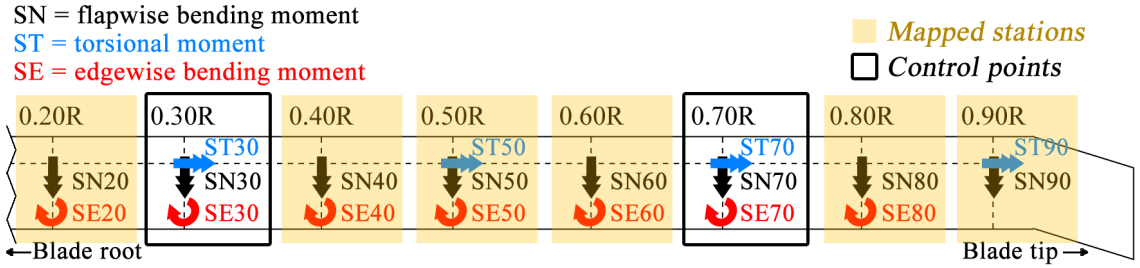

Figure 4.35: UH-60A blade control points and mapped stations.

In addition to the baseline mechanical airloads case, sensitivity of the LCA to the quality/magnitude of the initial airloads is examined. Table 4.3 lists the cases that were run as well as the *LCA scores* for each of these runs. Interestingly enough, the solutions all converge to close to the same response. This is a very encouraging result, showing that the quality of the initial airloads solution is of low importance.

Figures 4.36 and 4.37 show that LLT does an adequate job at predicting flapwise bending (including BVI effects at $\mu \approx 0.09$). Application of the LCA improves these results further, especially outboard on the blade. For torsional moments (Figures 4.38 and 4.39), LLT shows similar trends as for flapwise bending moments, though with a number of aberrant data points for certain flight counters. Application of the LCA is most notable in its improvement of the loads match at ST90, though still deficient in magnitude relative to measured response.

Table 4.3: Mechanical airloads: airloads cases.

Case	**Rationale**	**LCA score**
No LCA	-	0.170
Measured airloads	Baseline *mechanical airloads* problem	0.068
50% airloads	How well will the LCA converge if airloads are under-predicted by half?	0.063
200% airloads	How well will the LCA converge if airloads are over-predicted by 100%?	0.075
c8534 airloads	How well will the LCA converge if the airloads have the right "harmonic shape" (i.e., they look like a single measured flight case)?	0.075
Zero airloads	How well will the LCA converge if zero airloads are applied?	0.084

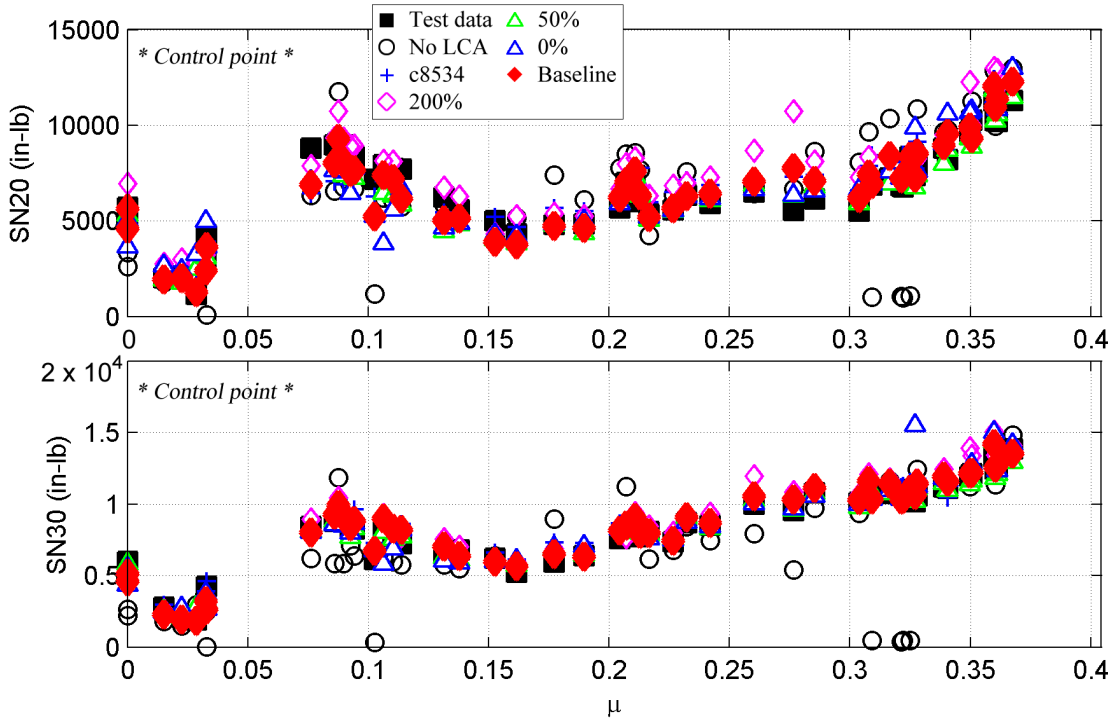

Figure 4.36: Peak-to-peak loads matching: mechanical airloads: SN20, SN30.

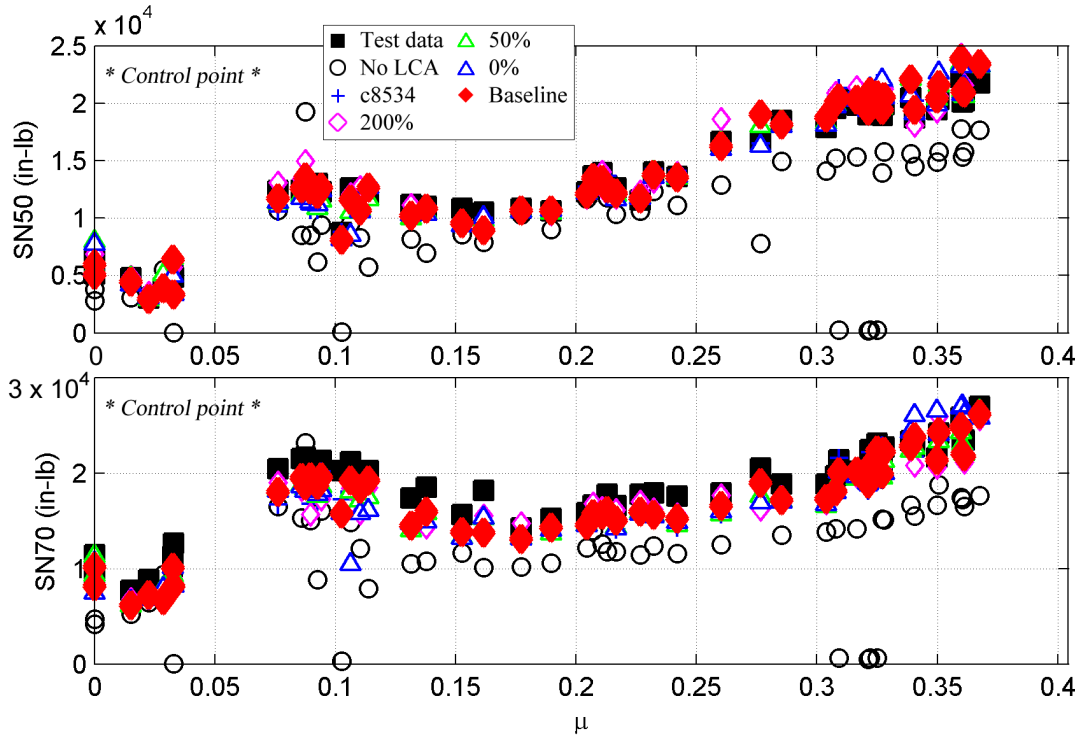

Figure 4.37: Peak-to-peak loads matching: mechanical airloads: SN50, SN70.

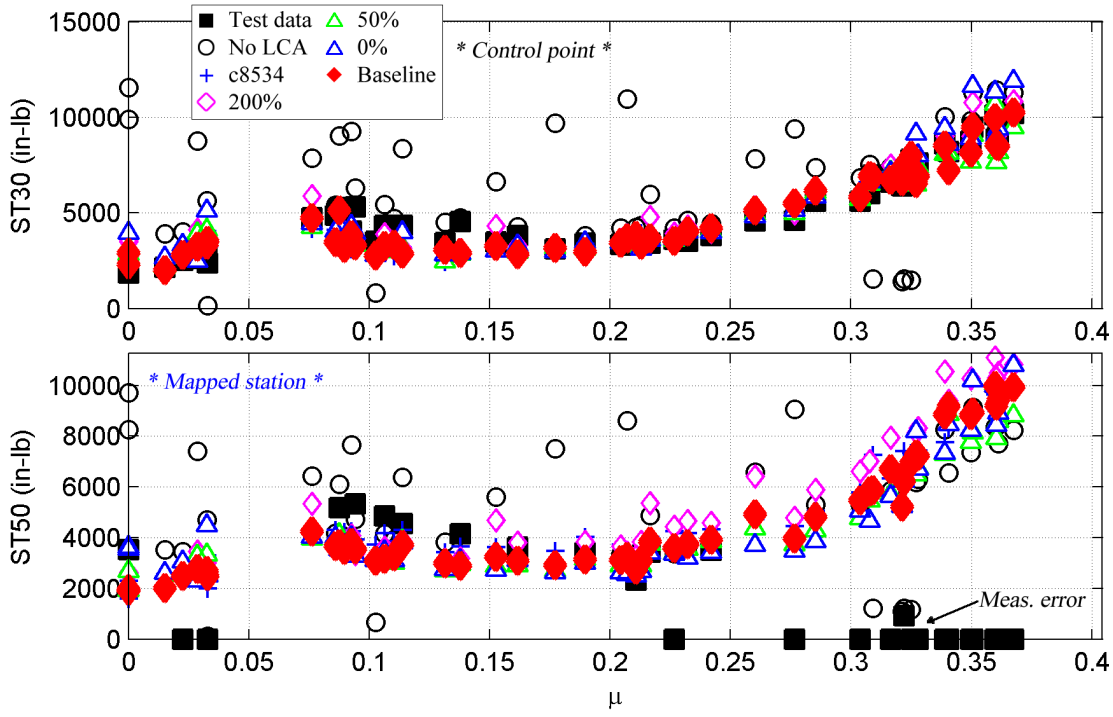

Figure 4.38: Peak-to-peak loads matching: mechanical airloads: ST30, ST50.

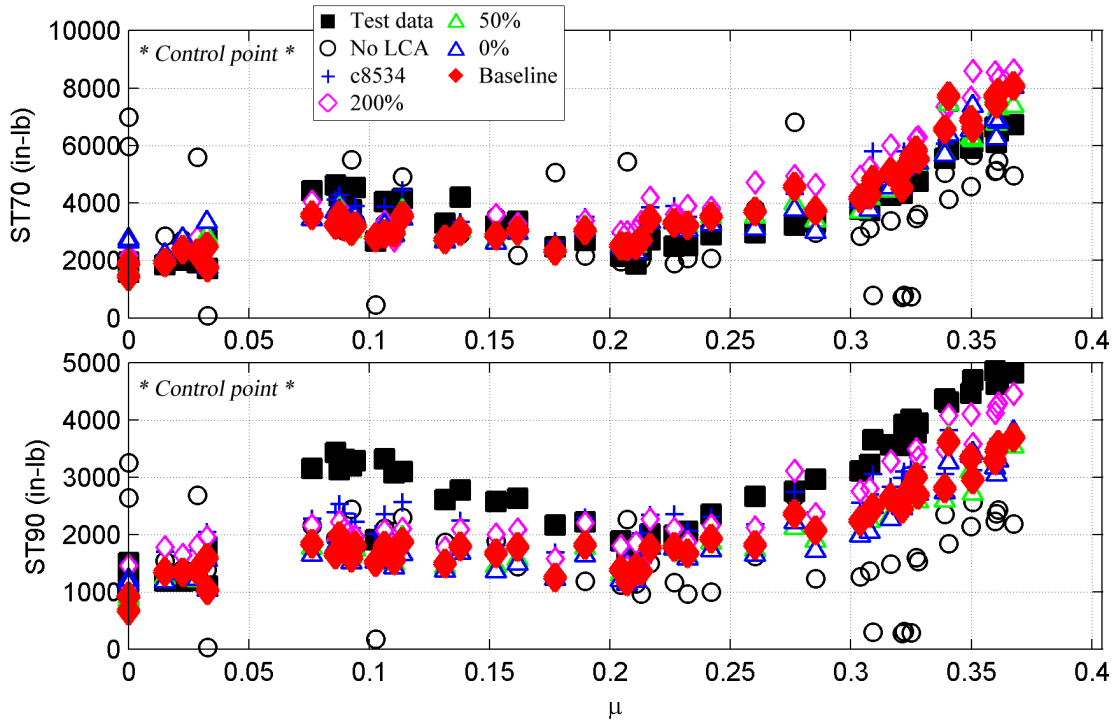

Figure 4.39: Peak-to-peak loads matching: mechanical airloads: ST70, ST90.

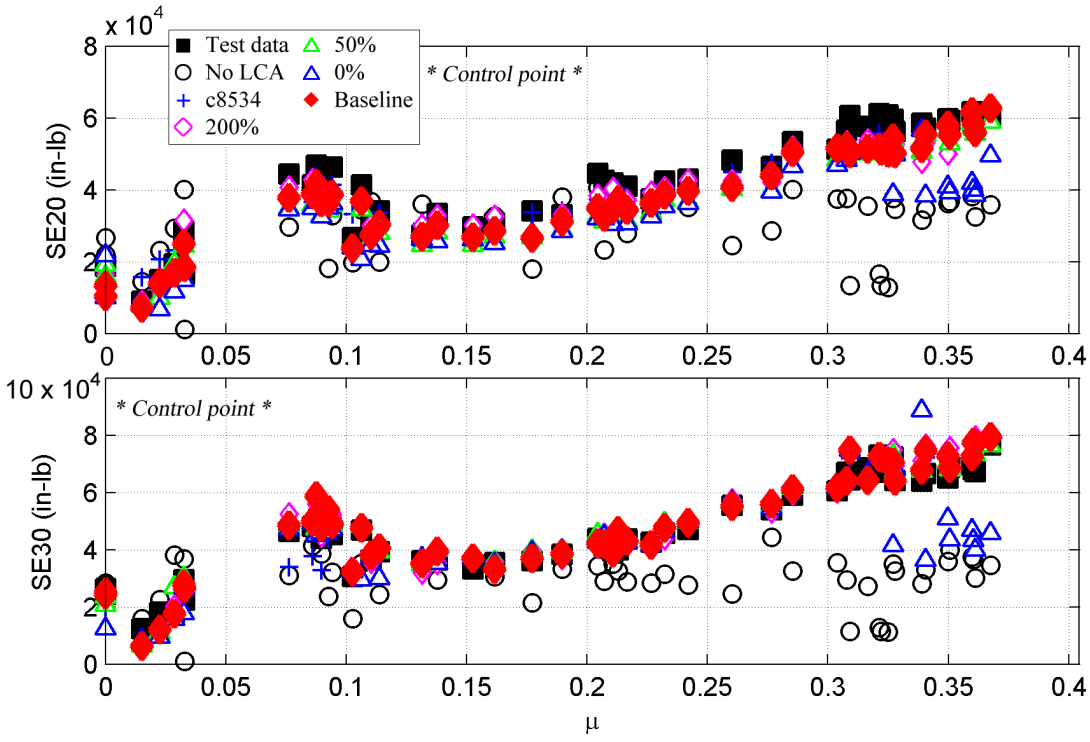

Figure 4.40: Peak-to-peak loads matching: mechanical airloads: SE20, SE30.

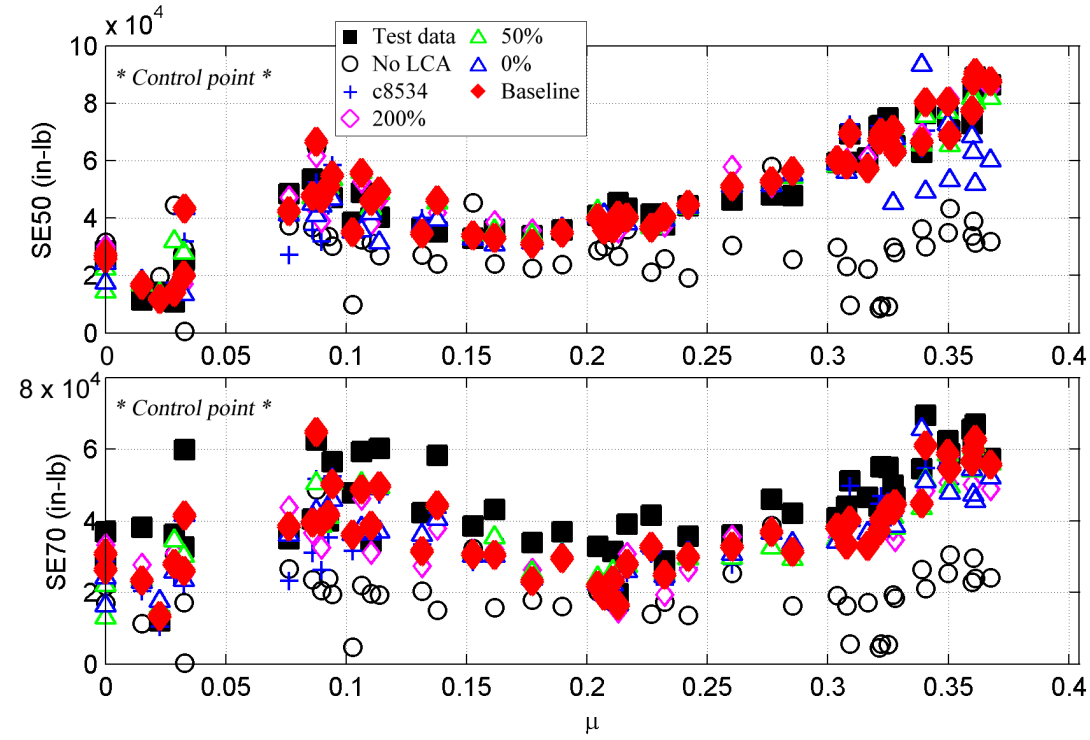

Figure 4.41: Peak-to-peak loads matching: mechanical airloads: SE50, SE70.

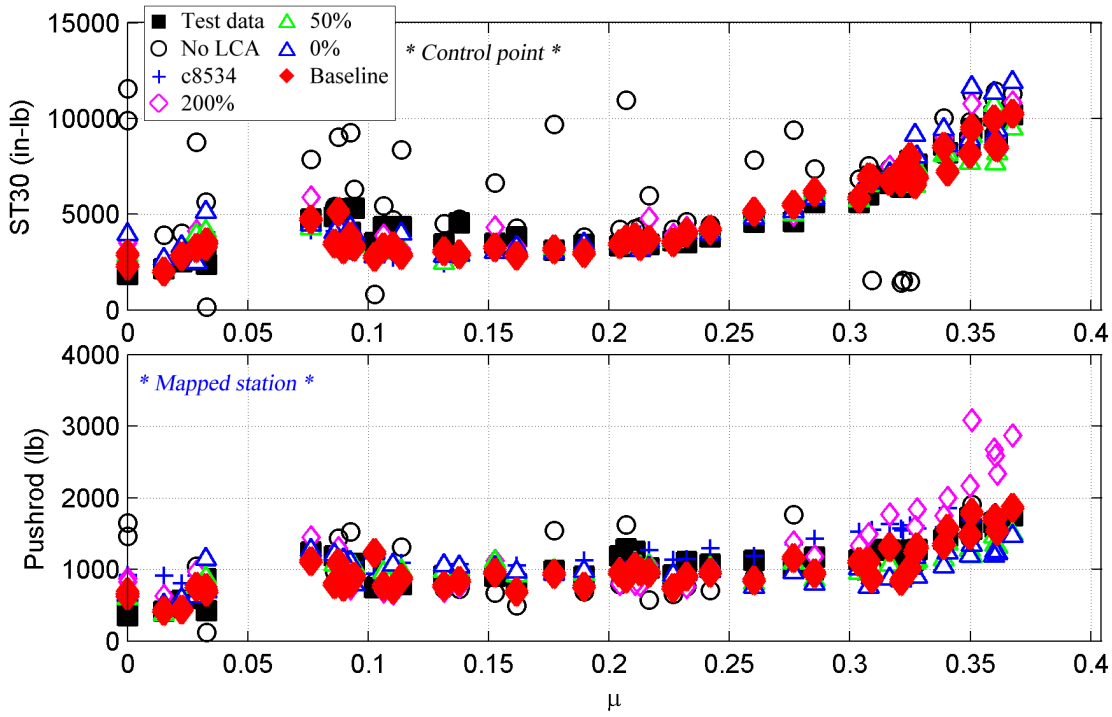

Figure 4.42: Peak-to-peak loads matching: mechanical airloads: ST30, pushrod.

4.6 Nine Detailed Flight Counters of Interest

This section discusses nine flight counters that have been of interest in legacy research efforts by other individuals and organizations. Table 4.4 lists these flight counters from legacy MDC-based analyses. Flight counters noted with an asterisk (*) will be examined in detail using the LCA. All LCA-generated results are for internal (LLT) airloads with six load control points (SN30/70, ST30/70, SE20/70). Note that SE20 is used as a control point rather than SE30 due to invalid measured edgewise bending for flights 89 and 90 (Table 3.8). Figure 4.43 shows the control points and mapped stations used in this simulation.

Table 4.4: Flight counters of interest.

Flight counter	**Description**	μ	C_w/σ	**Reference(s)**
8424	Moderate speed level flight	0.304	0.0889	[4]
8529	Level flight; BVI	0.317	0.0789	[53]
8534*	High-speed forward flight; high vibration regime	0.368	0.0788	[4, 24, 27, 45, 71, 72]
8927*	Pull-up maneuver	0.277	≈ 0.11	[53]
8930	Pushover maneuver	0.213	≈ 0.11	[53]
9017*	Dynamic stall (moderate speed, high thrust)	0.236	0.1335	[24, 29, 45, 71, 72]
11029	Pull-up maneuver	≈ 0.31	≈ 0.08	[1, 2, 77]
11679*	Diving turn	0.393	0.1437	[57]
11680*	Diving turn	0.388	0.1219	[57]

Flight counters noted with an asterisk (*) are examined in detail using the LCA

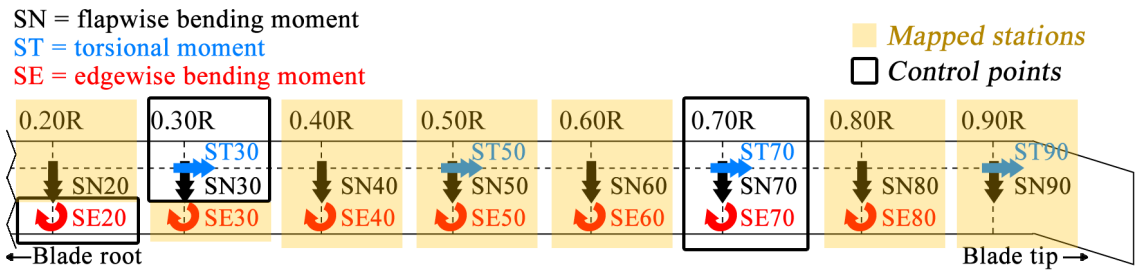

Figure 4.43: UH-60A blade control points and mapped stations.

4.6.1 Moderate speed flight: c8424

Abras et al. [4] performed a coupled CFD/CSD solution (FUN3D and OVERFLOW/DYMORE) for c8424, a moderate speed level flight counter. They observed differences in prediction between analysis and experiment for blade bending.

4.6.2 BVI: c8529

c8529 was studied by Kufeld et al. [53]. This level flight, mid-thrust flight counter exhibited some slight BVI effects on both the advancing and retreating sides of the rotor. As in high-speed flight, there was a reduction in lift in Q2 near the blade tip. This is due to swashplate cyclic orientation combined with inherent negative blade twist with span and is required for roll balance.

4.6.3 High-speed flight: c8534

High-speed flight is one of the highest vibration regimes. Datta et al. [29] quantify these vibrations as due to large elastic twist deformations due to transonic pitching moments. Ho et al. [45] performed a coupled CFD/CSD solution (CAMRAD II/RCAS) for c8534. They observed that, for high-speed flight, the advancing blade lift and, thus pitching moment are negative outboard at $r/R = 0.675$ to 0.965 [77]. This is due to the large forward velocity ($r\Omega + V_\infty$ at $\psi = 90^o$) paired with a large nose down blade motion (thus negative angle-of-attack) and the requirement that

lift is balanced across all sides of the rotor (thus, no aerodynamic-induced rolling or pitching moments in steady, level flight).

Sitarama et al. [77] observed minimal returning wake effects for this high-speed case due to the wake's convection away from the rotor system in the horizontal direction. They also observed that, due to the large difference in the aerodynamic loading distributions on the advancing and retreating side of the rotor disk (negative lift on advancing side; positive lift on retreating side), the wake geometry shows asymmetrical roll-up aft of the main rotor.

c8534 is effectively a steady flight throughout its 17 cycles, as noted by Bousman [18] and shown in Figures 4.44 through 4.50. These figures show peak-to-peak loads for blade flapwise bending, torsional, and edgewise bending moments (as well as pushrod load) for the 17 cycles of this flight counter. Figures 4.51 through 4.60 show load magnitudes by harmonic for these cycles as well. The response is steady, so cycle 1 is examined in detail (Figures 4.61 through 4.64).

Application of the LCA matches prediction for flapwise bending fairly effectively across all cycles, with several deviations, most notably SN70 (Figure 4.45). The reason for this is not well understood at this time. One solution would be to average the LCA loads solution across a range of cycles rather than based on a single cycle; using averaging as an error minimization technique [14]. This would be easy to do for steady flight, though it would require *a priori* knowledge of the steadiness of the flight counter. As in the SE30/70 case described above, this SE20/70 case over-predicts edgewise bending. This is due to an over-prediction of $1P$ and $5P$ content.

Overall, the loads match is acceptable. This is highlighted in the loads polar plot of Figure 4.61 as well as the time history plots in Figures 4.62 through 4.64.

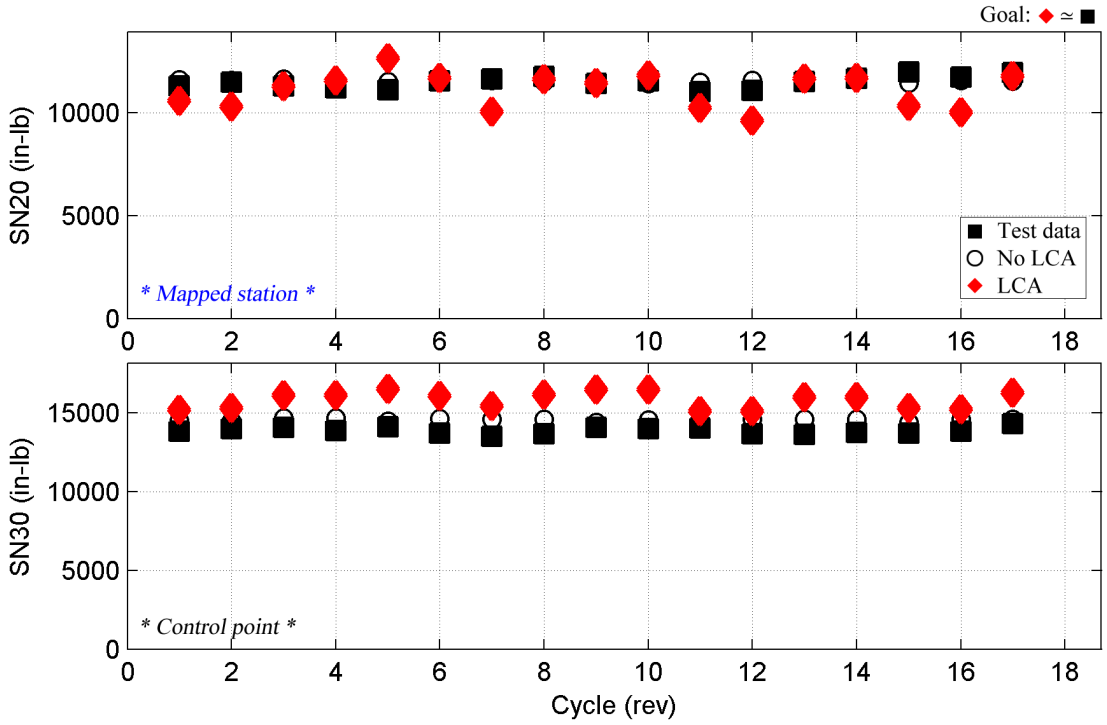

Figure 4.44: Peak-to-peak loads matching: all cycles of c8534: SN20, SN30.

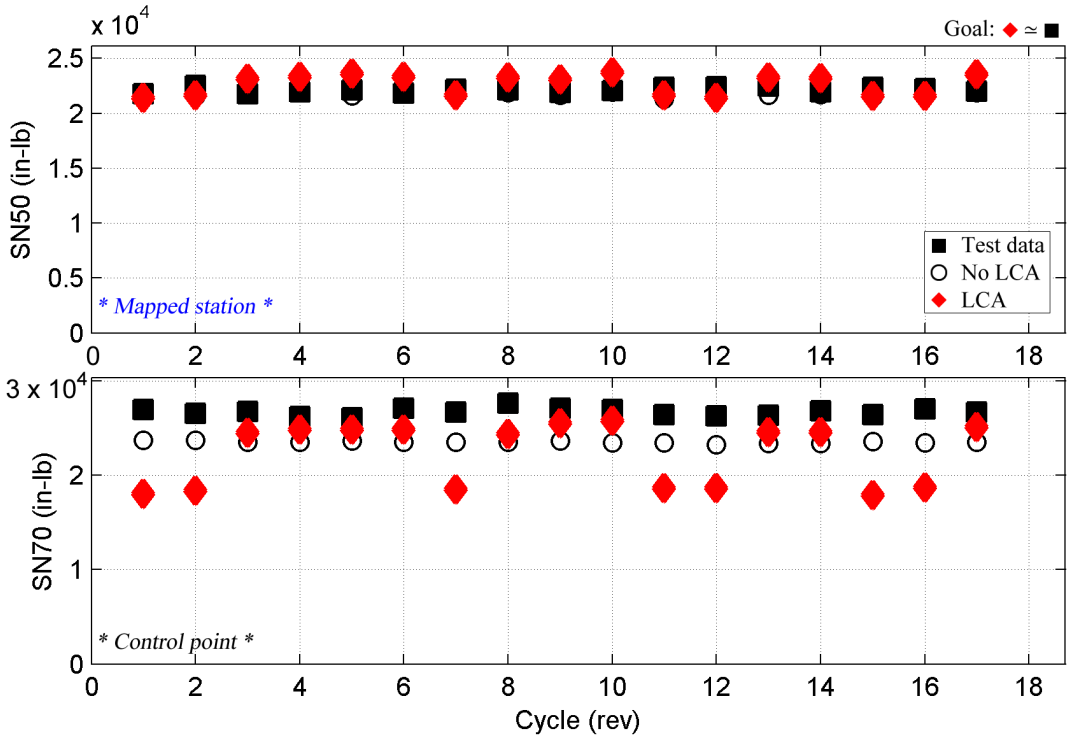

Figure 4.45: Peak-to-peak loads matching: all cycles of c8534: SN50, SN70.

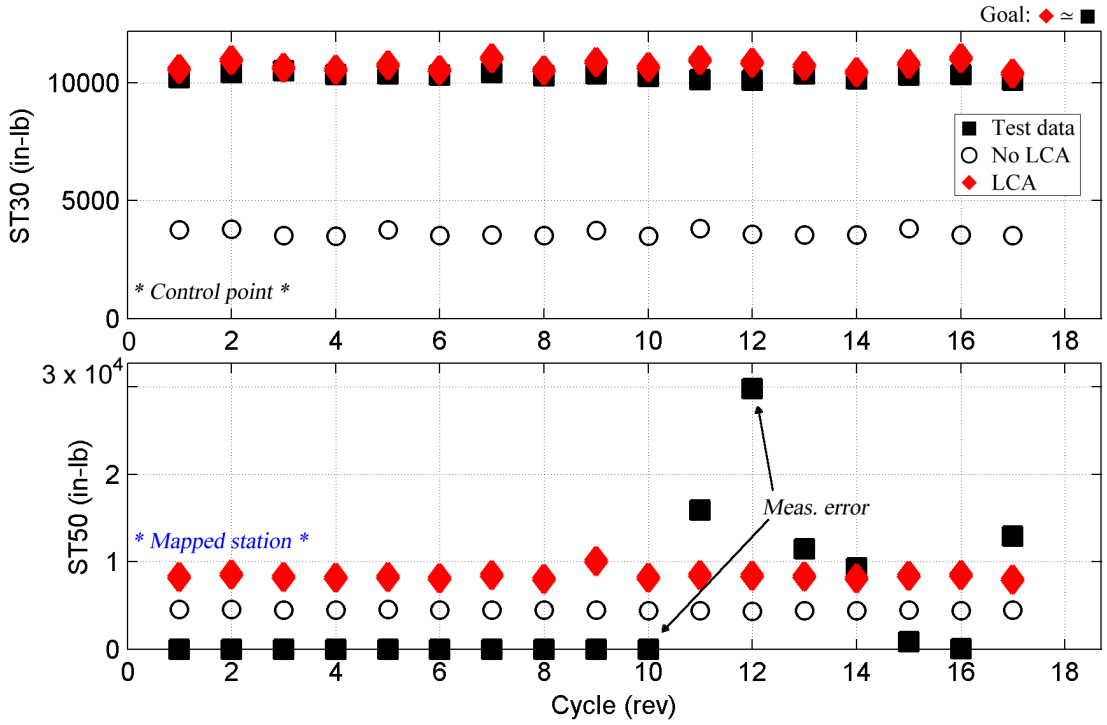

Figure 4.46: Peak-to-peak loads matching: all cycles of c8534: ST30, ST50.

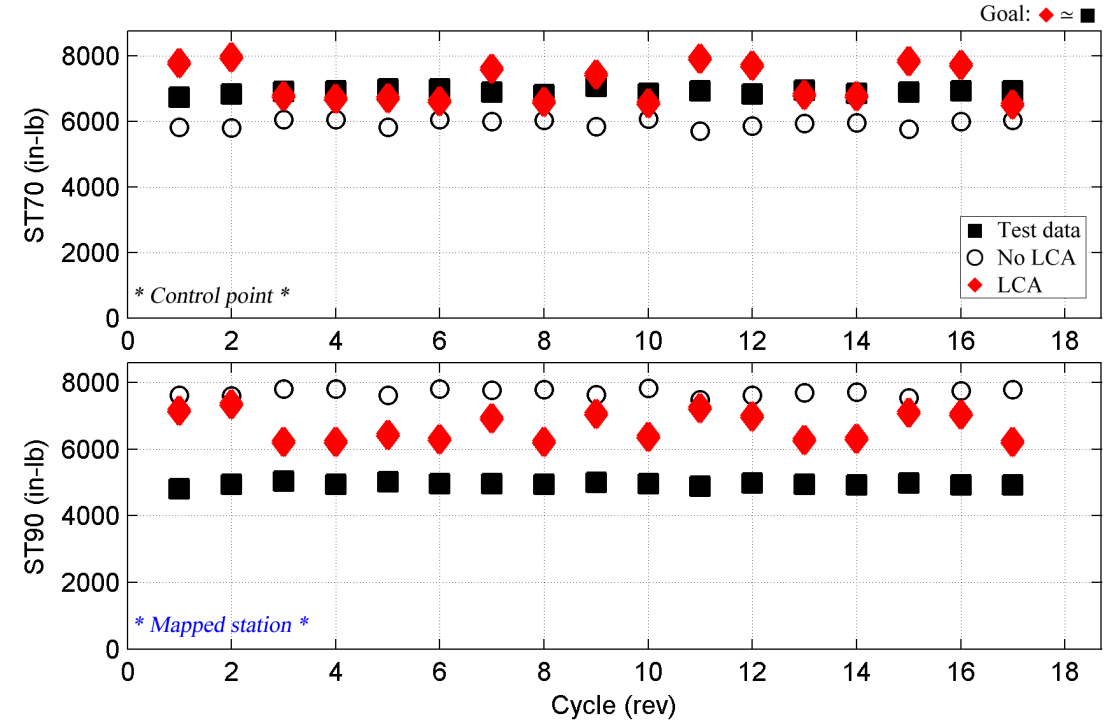

Figure 4.47: Peak-to-peak loads matching: all cycles of c8534: ST70, ST90.

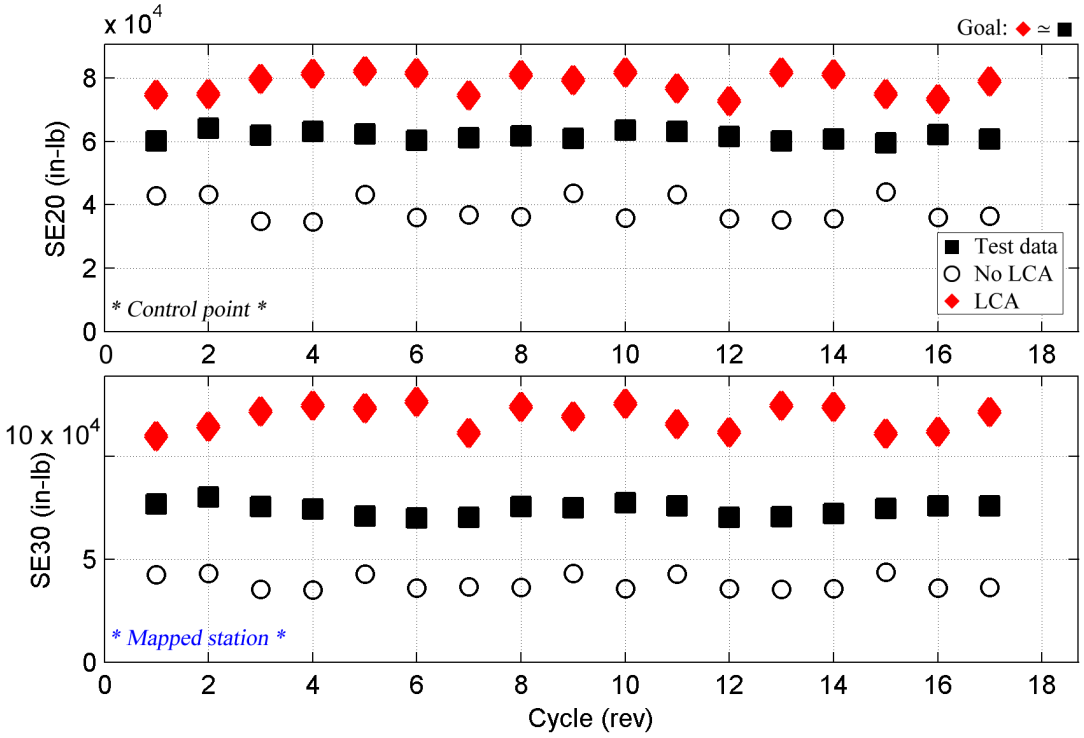

Figure 4.48: Peak-to-peak loads matching: all cycles of c8534: SE20, SE30.

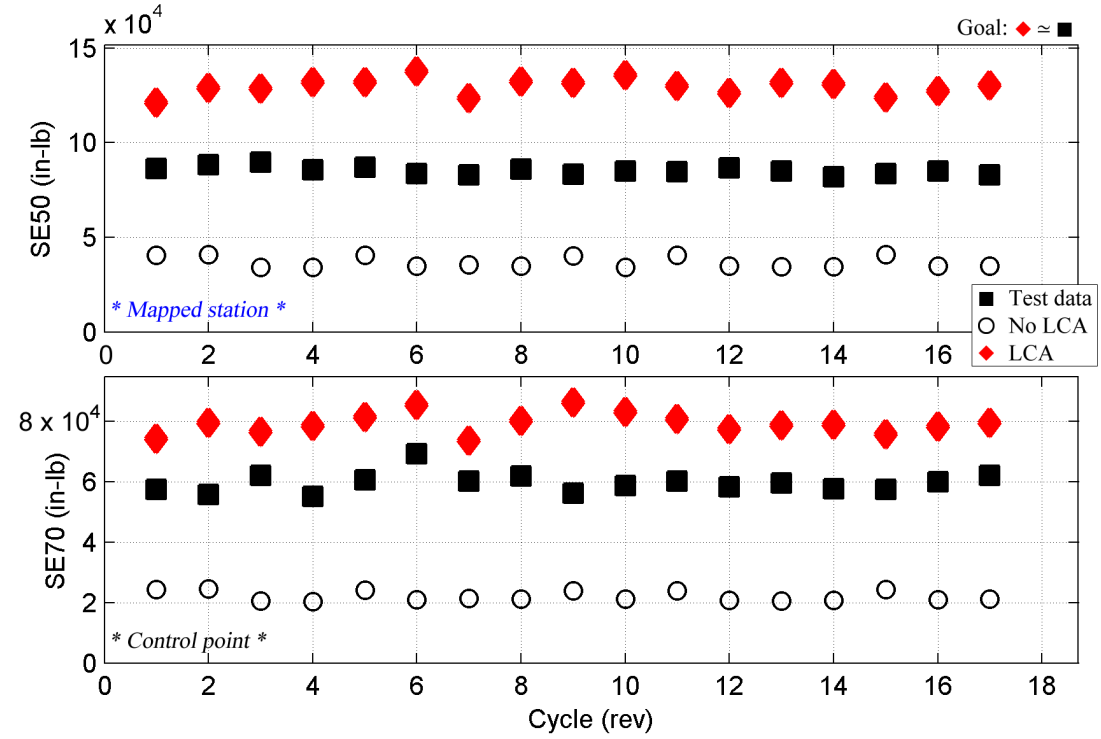

Figure 4.49: Peak-to-peak loads matching: all cycles of c8534: SE50, SE70.

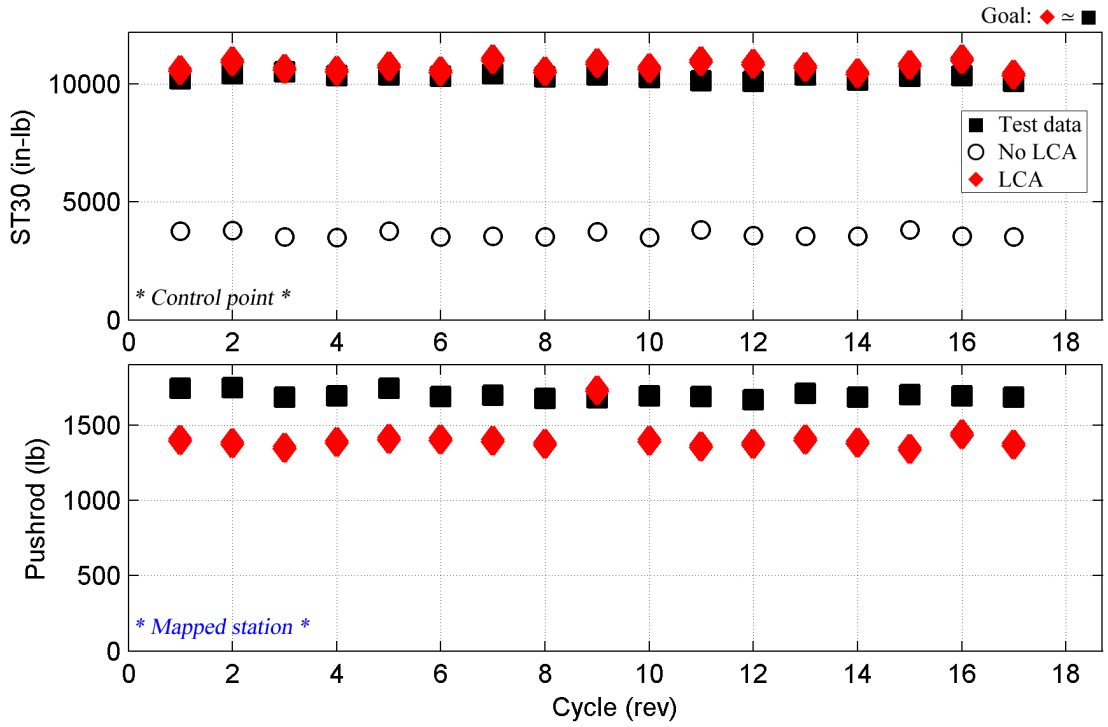

Figure 4.50: Peak-to-peak loads matching: all cycles of c8534: ST30, pushrod.

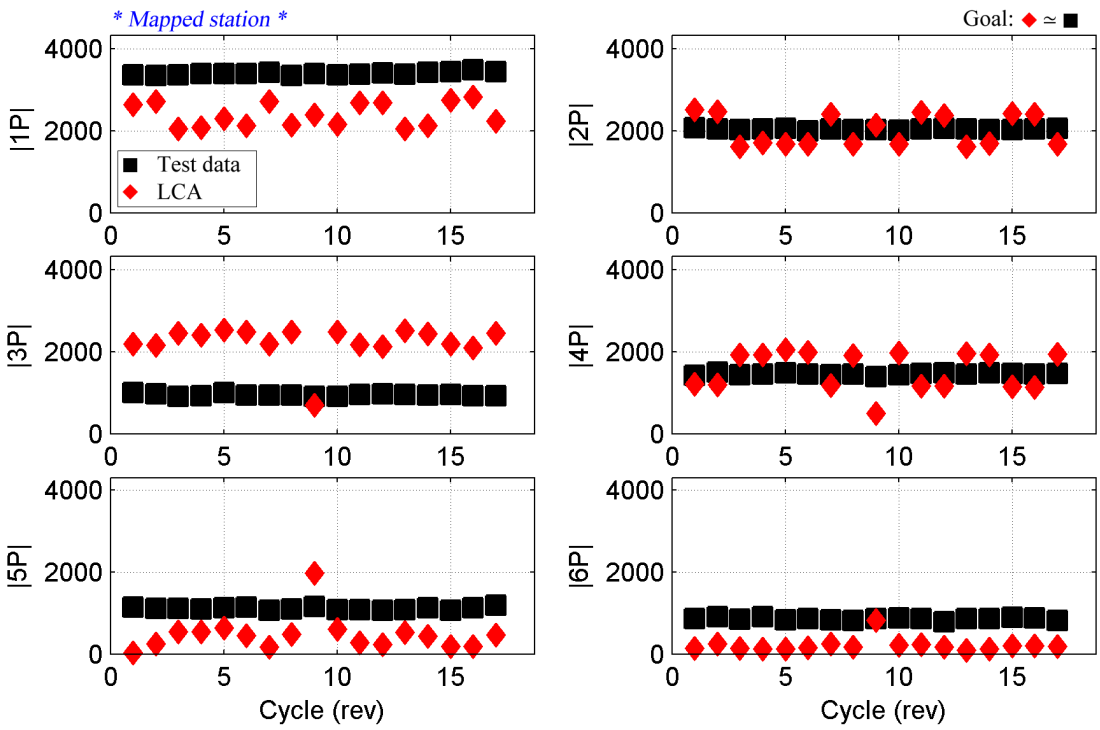

Figure 4.51: Loads matching by harmonic: all cycles of c8534: SN20 (in-lb).

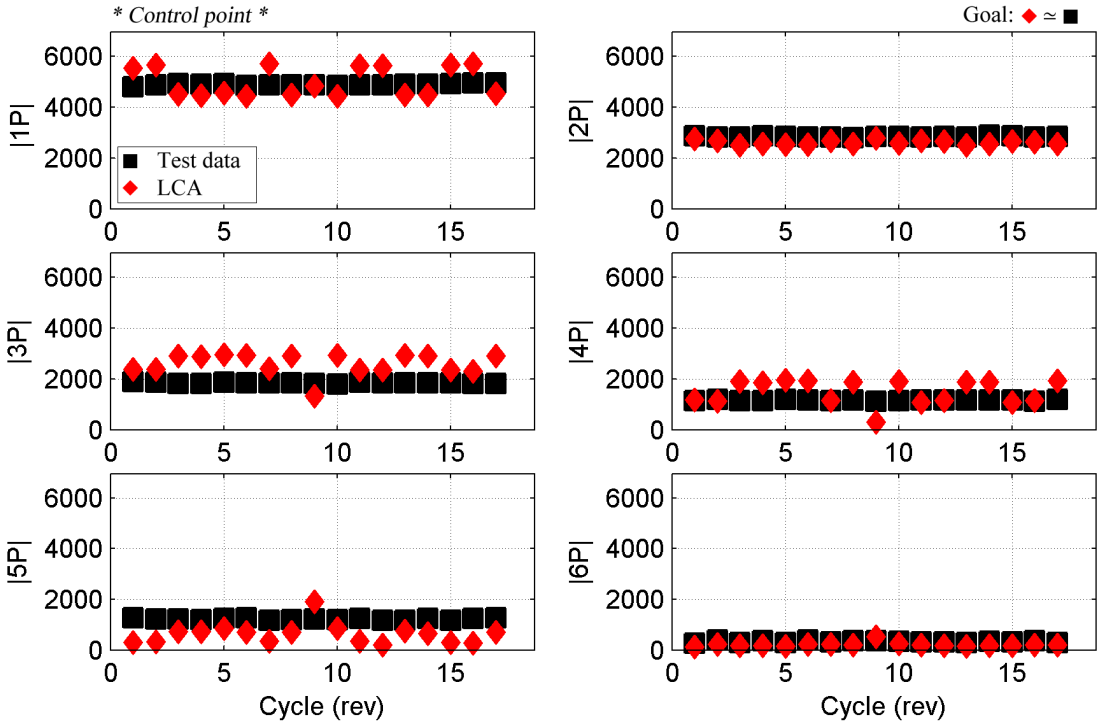

Figure 4.52: Loads matching by harmonic: all cycles of c8534: SN30 (in-lb).

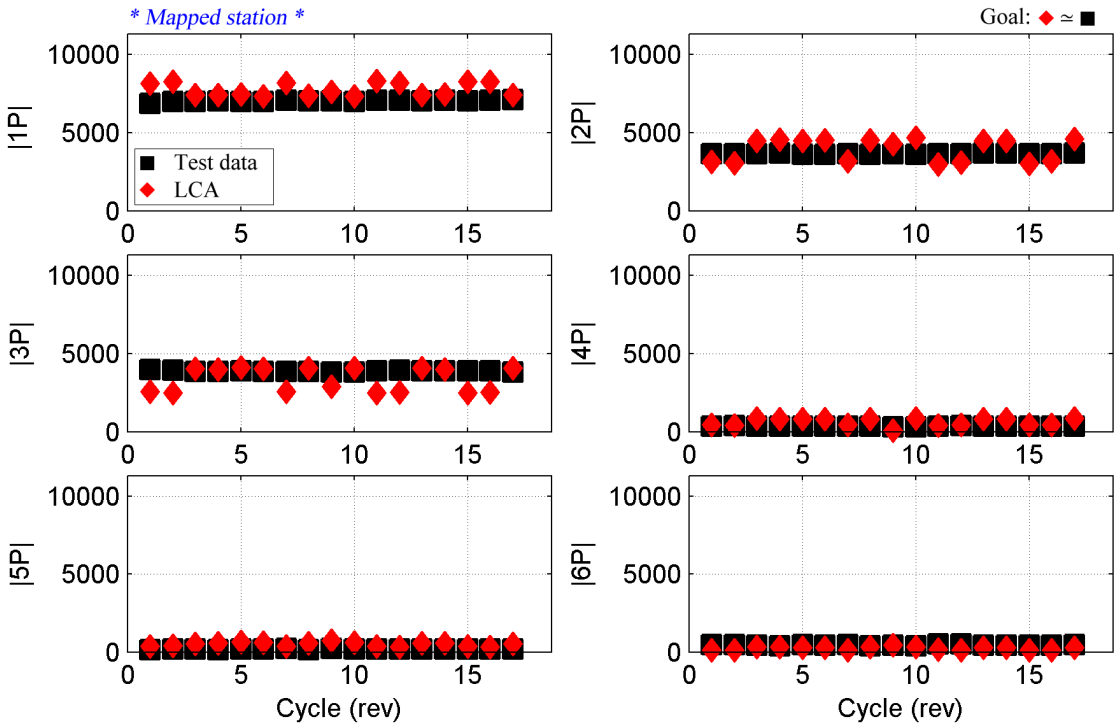

Figure 4.53: Loads matching by harmonic: all cycles of c8534: SN50 (in-lb).

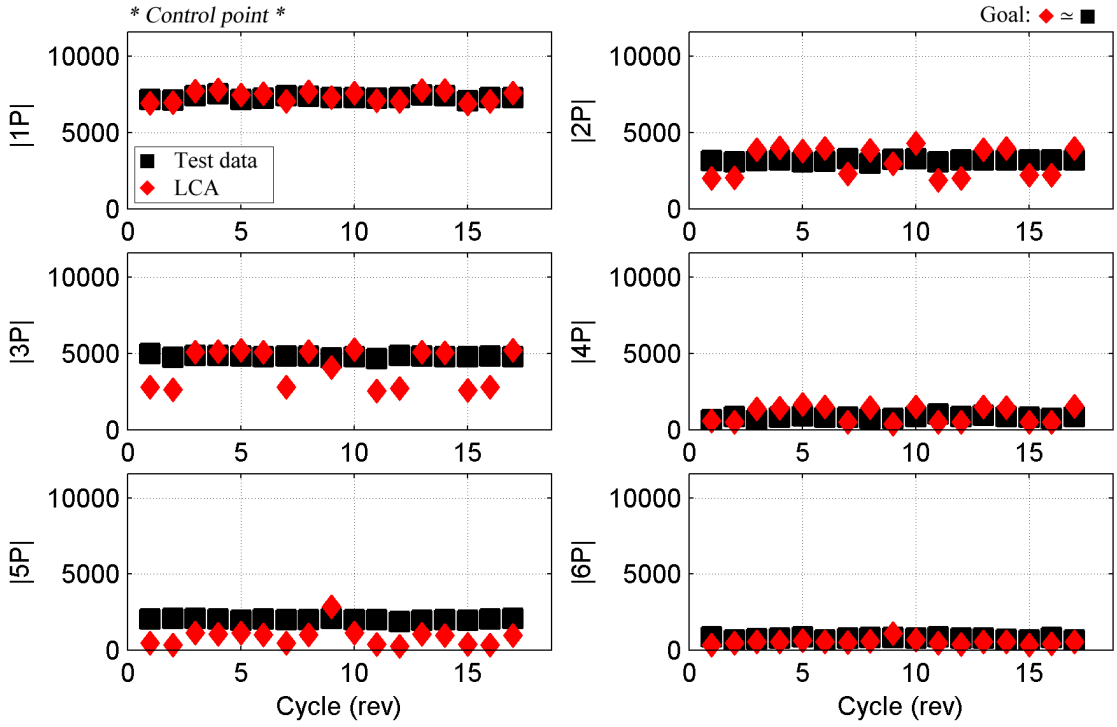

Figure 4.54: Loads matching by harmonic: all cycles of c8534: SN70 (in-lb).

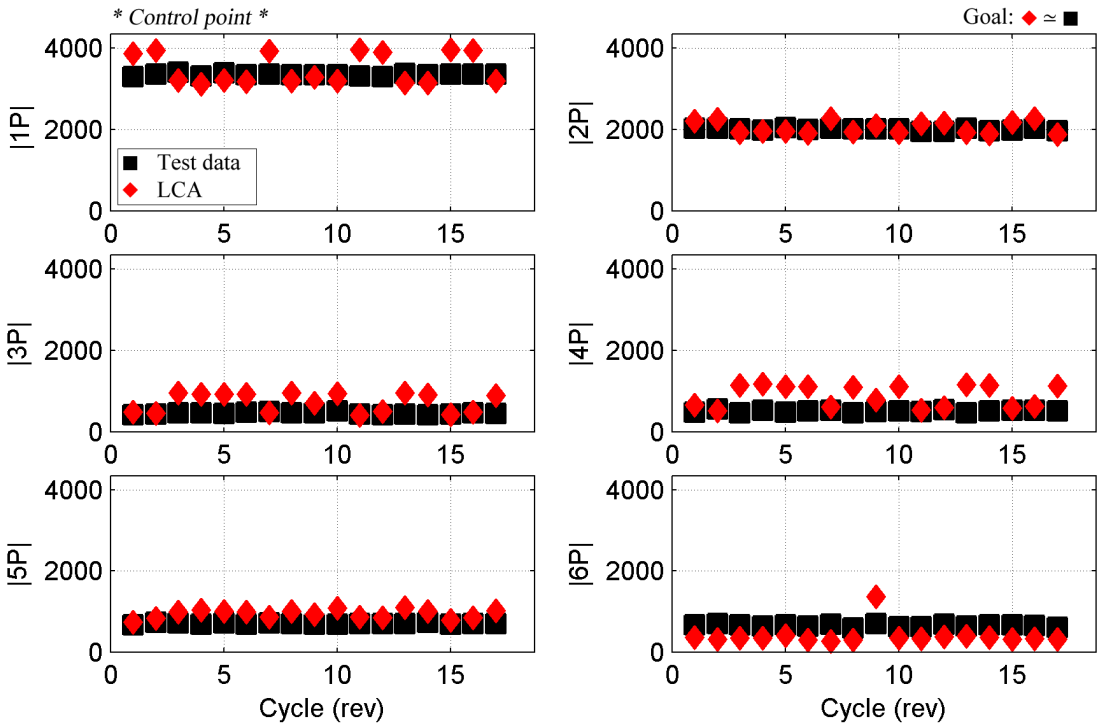

Figure 4.55: Loads matching by harmonic: all cycles of c8534: ST30 (in-lb).

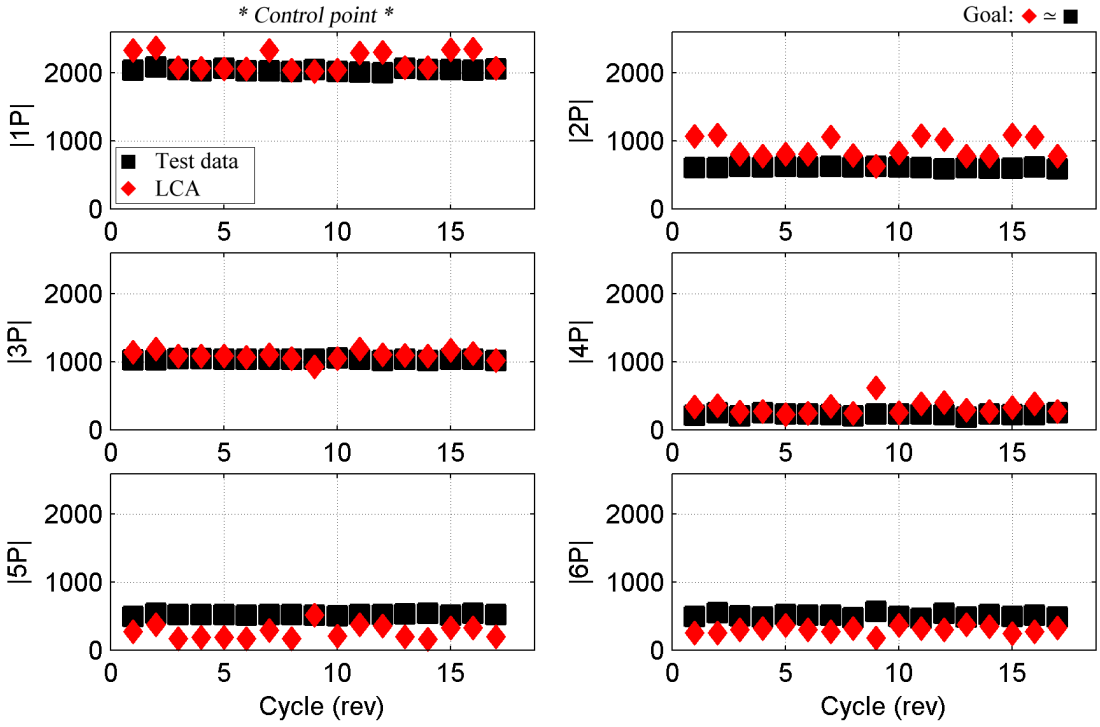

Figure 4.56: Loads matching by harmonic: all cycles of c8534: ST70 (in-lb).

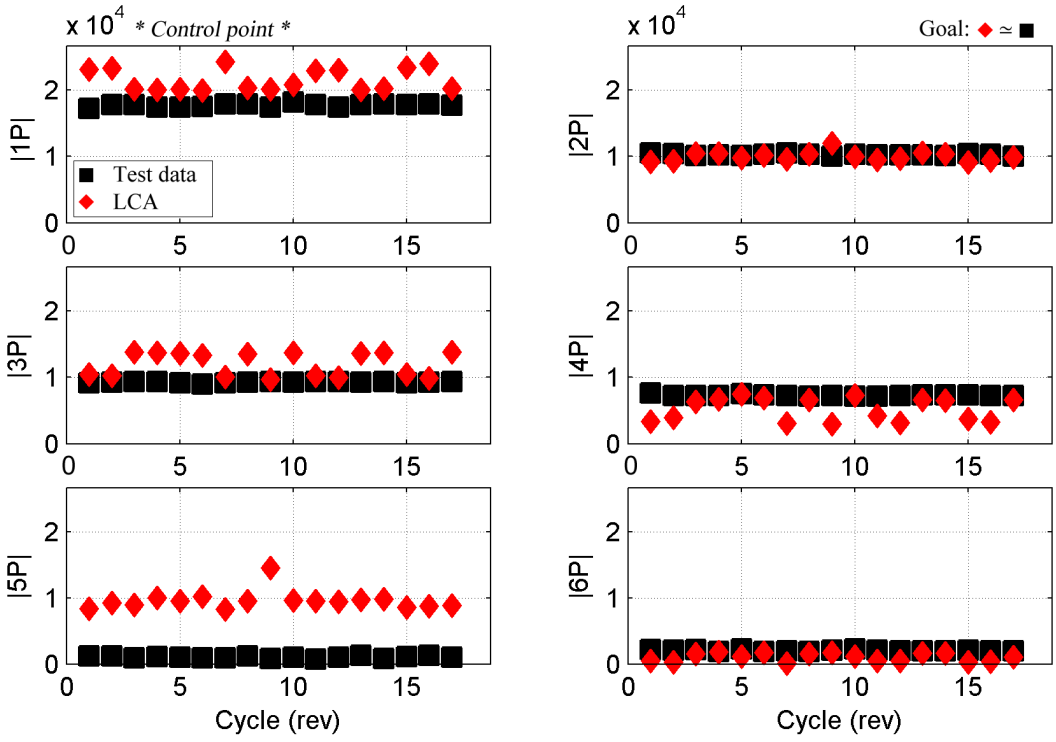

Figure 4.57: Loads matching by harmonic: all cycles of c8534: SE20 (in-lb).

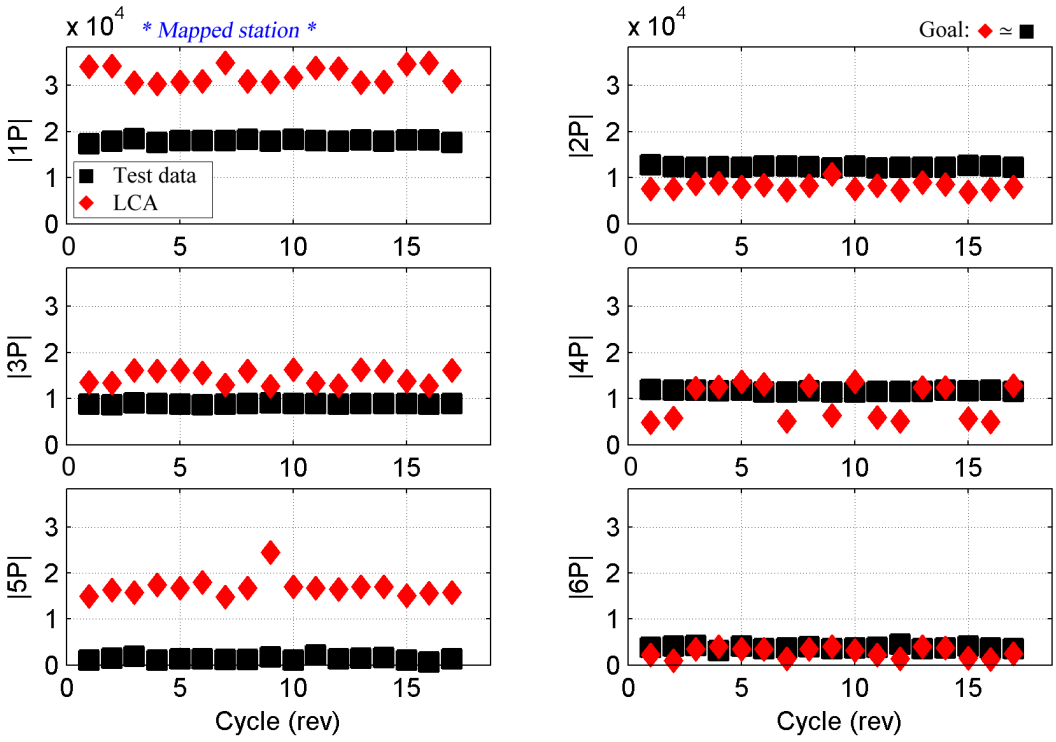

Figure 4.58: Loads matching by harmonic: all cycles of c8534: SE30 (in-lb).

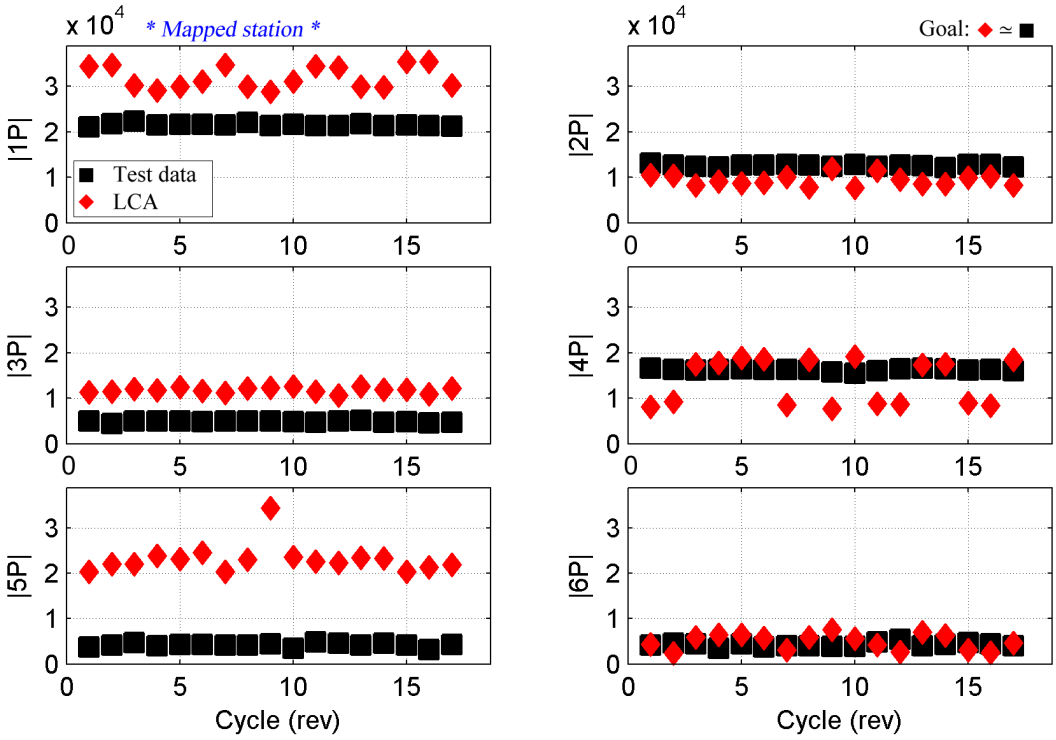

Figure 4.59: Loads matching by harmonic: all cycles of c8534: SE50 (in-lb).

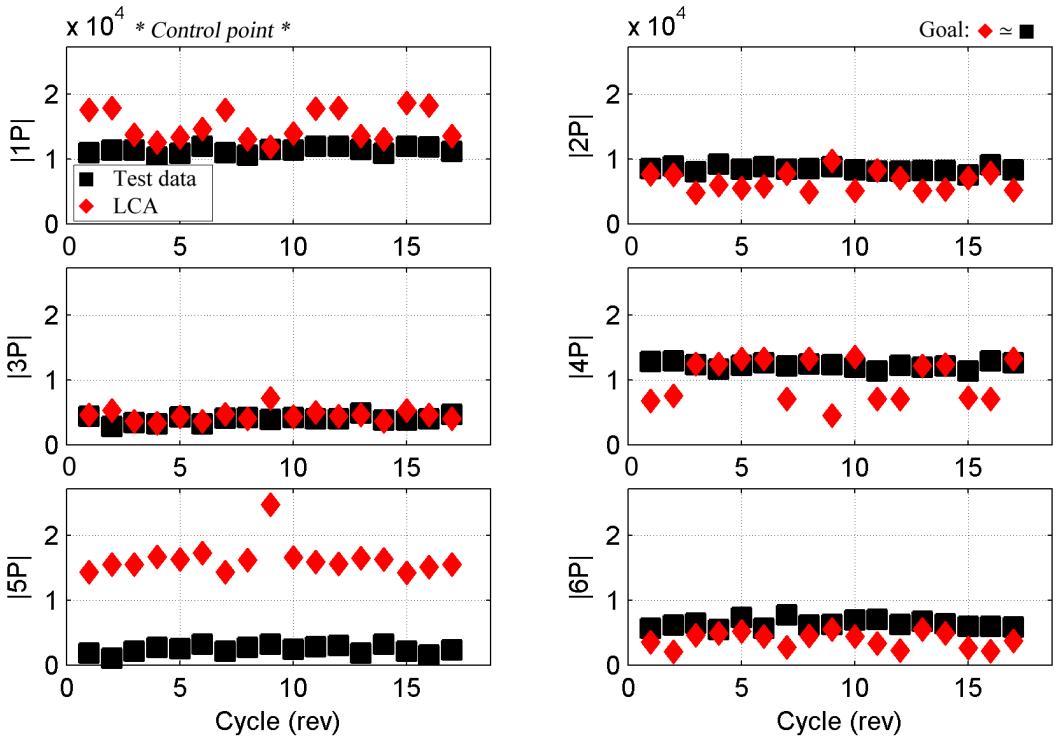

Figure 4.60: Loads matching by harmonic: all cycles of c8534: SE70 (in-lb).

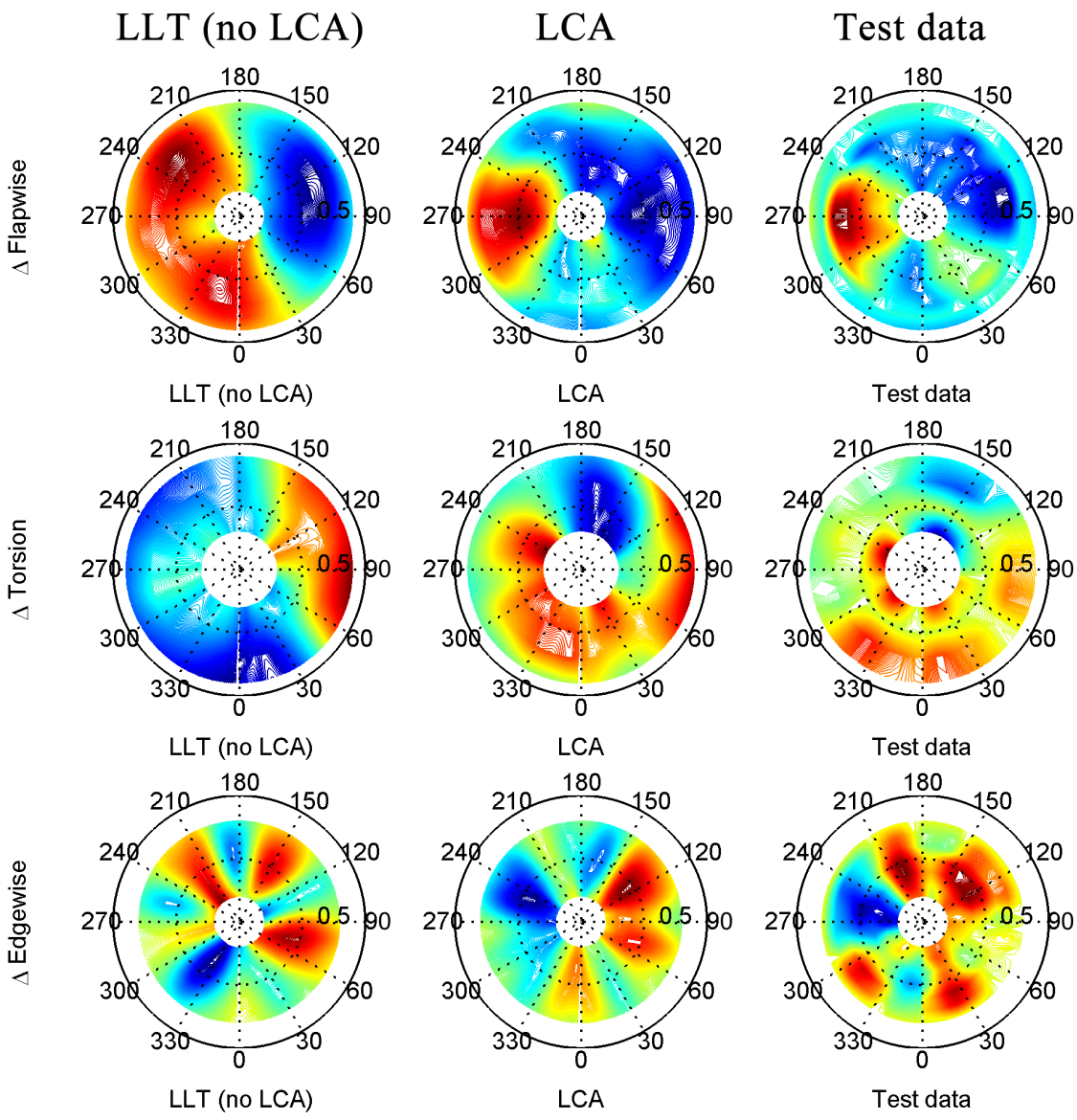

Figure 4.61: Flapwise, torsional, edgewise moments: radial, azimuthal distribution; cycle 1 [flight counter, μ] = [8534, 0.368] (top-to-bottom); red (peak), blue (valley).

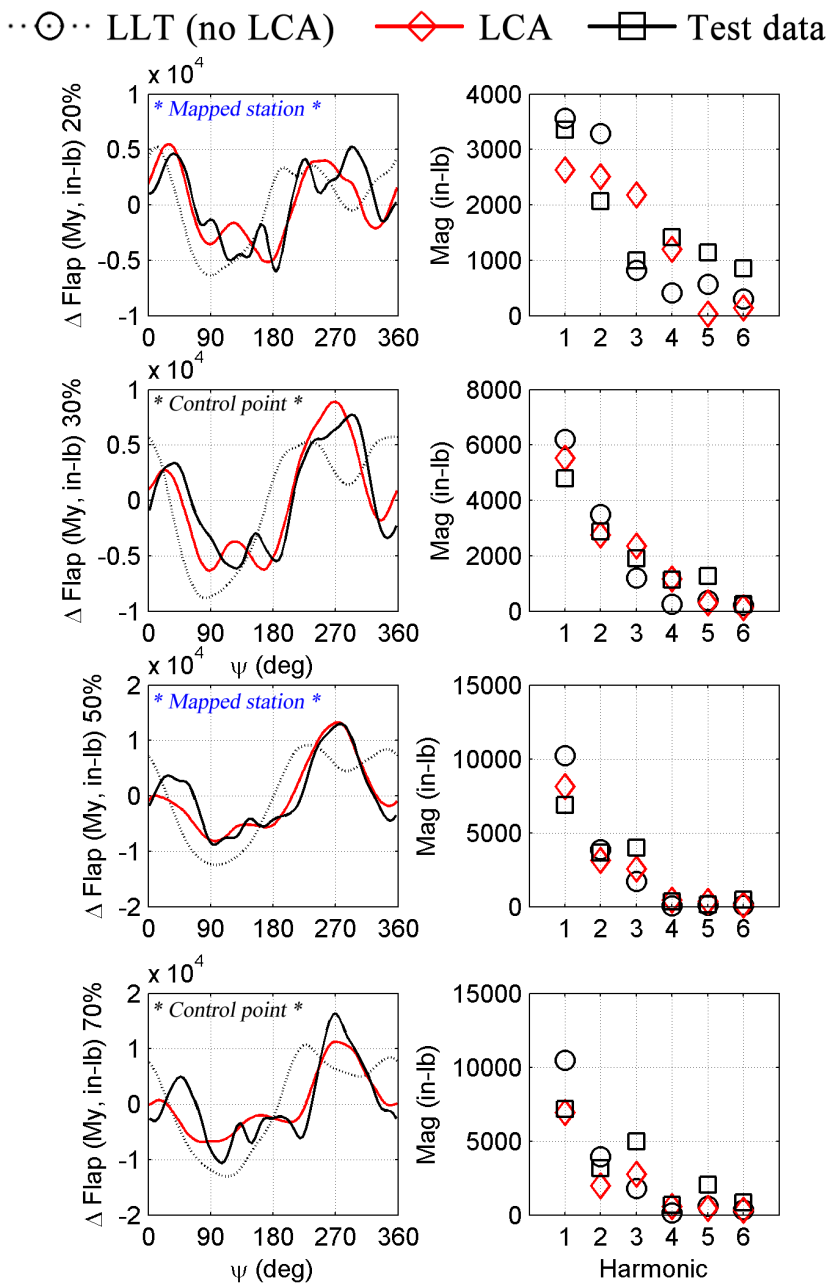

Figure 4.62: Flapwise bending moment: time history, load component by harmonic; cycle 1 [flight counter, μ] = [8534, 0.368]

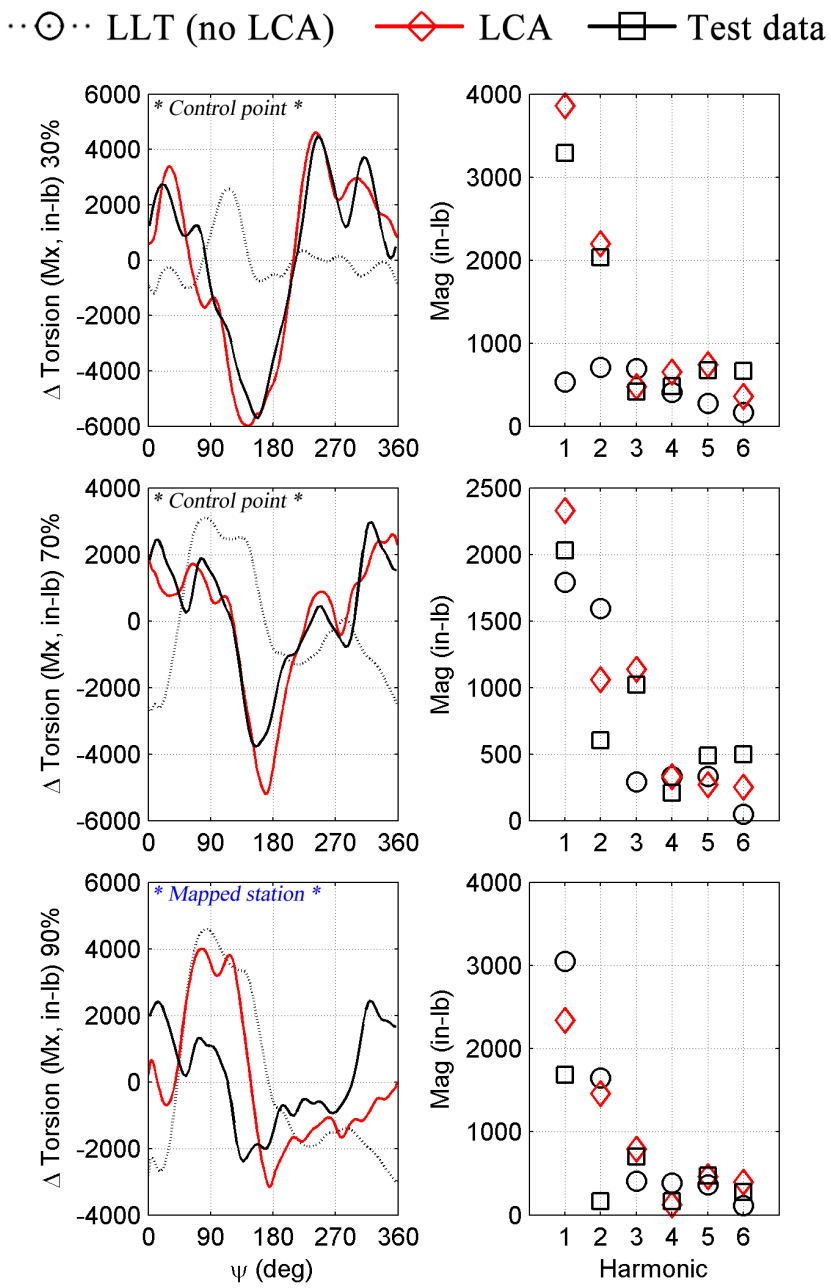

Figure 4.63: Torsional moment: time history, load component by harmonic; cycle 1 [flight counter, μ] = [8534, 0.368]

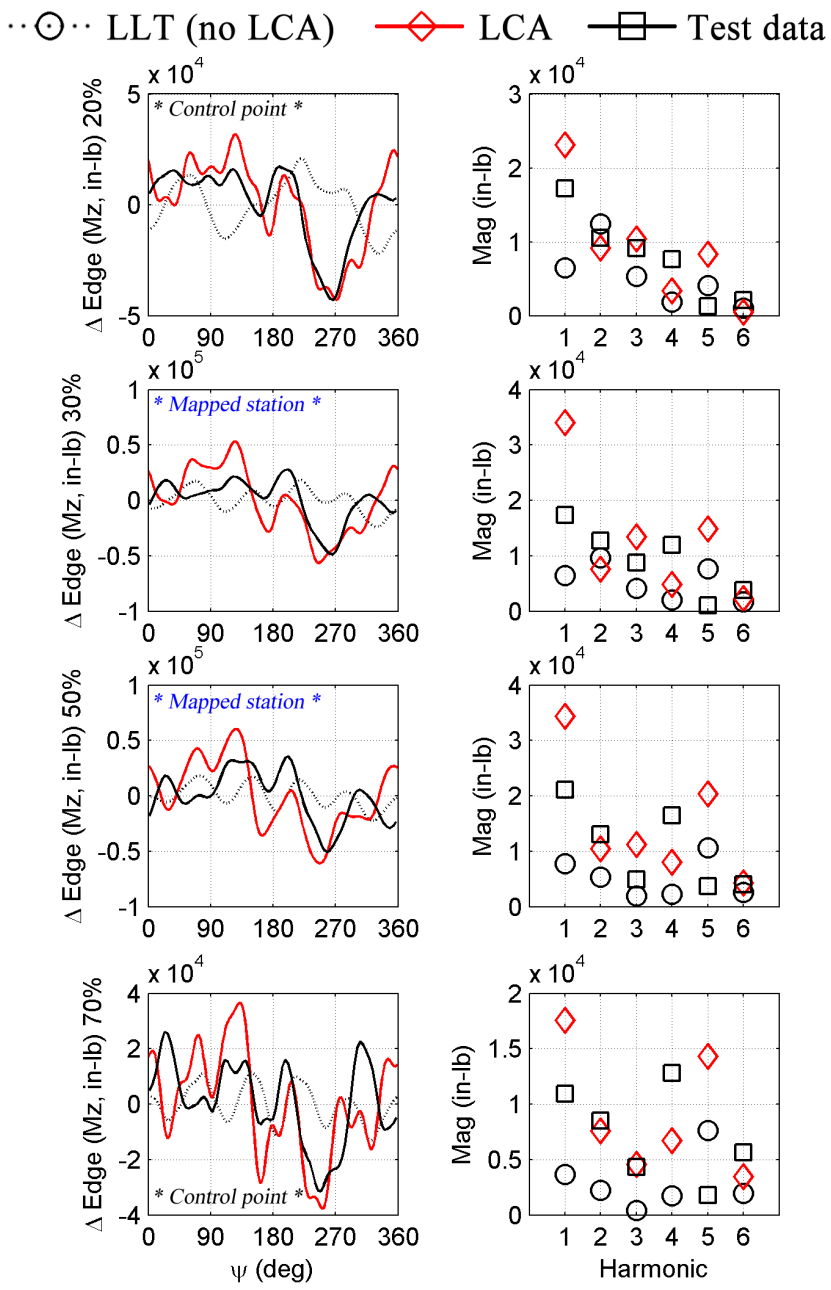

Figure 4.64: Edgewise bending moment: time history, load component by harmonic; cycle 1 [flight counter, μ] = [8534, 0.368]

4.6.4 Pull-up maneuver: c8927

c8927 was studied by Kufeld et al. [53]. This pull-up maneuver achieved 2g at 80 kias (rev 41). High BVI was observed, with the rotor flying through its own wake. All interactions occurred in the first and fourth quadrants, as noted above. These multiple vortex encounters manifest themselves as rapid fluctuations in pitching moment (i.e., high harmonic content) - mainly in Q1 and Q4. Also of note was that normal forces show much more unsteadiness at 2g in Q1 and Q2 than at level flight. The tip region carries a larger percentage of the blade load on the advancing side at 2g than at level flight.

Figures 4.65 through 4.71 show peak-to-peak loads for blade flapwise bending, torsional, and edgewise bending moments (as well as pushrod load) for the 78 cycles of this flight counter. Figures 4.72 through 4.81 show load magnitudes by harmonic for these cycles as well. The response varies with N_z, maximized at cycle 33, which is examined in detail (Figures 4.82 through 4.85).

The presence of the stall cycles is evident in Figures 4.82 and 4.84 for blade torsional moment, with peaks in Q1 and Q4 across the blade span.

The LCA provides a good loads match for this flight counter, with the following observations:

1. SN50, SE30, and SE50 measurements are erroneous.

2. An excellent match is achieved for SN30, SN70, and ST30 for all harmonics (as well as peak-to-peak).

3. SN20 under-predicts $1P$ load content (due to the lack of the rigid flapping mode in the LCA solution).

4. SE20 produces an excellent match for $1P$ but over-predicts for $5P$.

5. ST70 over-predicts $1P$ load content (due to the lack of the rigid flapping mode in the LCA solution).

6. There is an unusual response observed where the LLT solution (as well as the LCA for ST90) predicts the maximum loads to be at cycle 23, rather than at cycle 33. This is due to the embedded swashplate-to-blade root angle mapping in the algorithm showing deficiencies at this cycle. This leads to an out-of-phase blade flapping (and blade feathering) relative to the measured response. This mapping could be improved upon in future research efforts to handle such outlier cases.

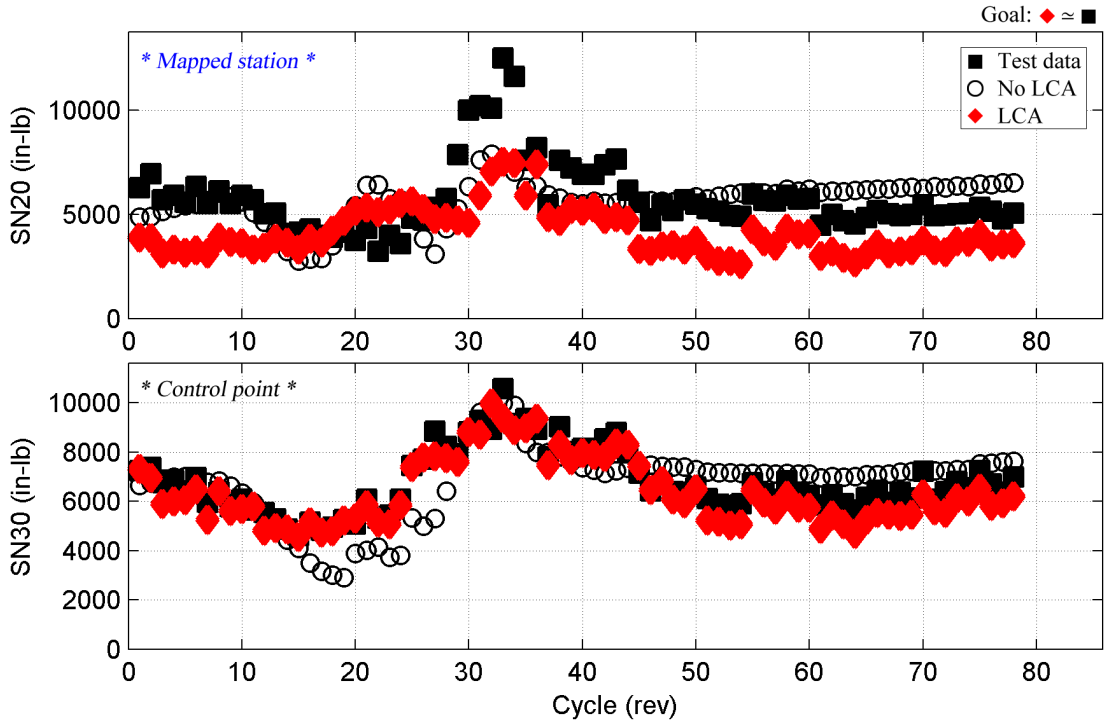

Figure 4.65: Peak-to-peak loads matching: all cycles of c8927: SN20, SN30.

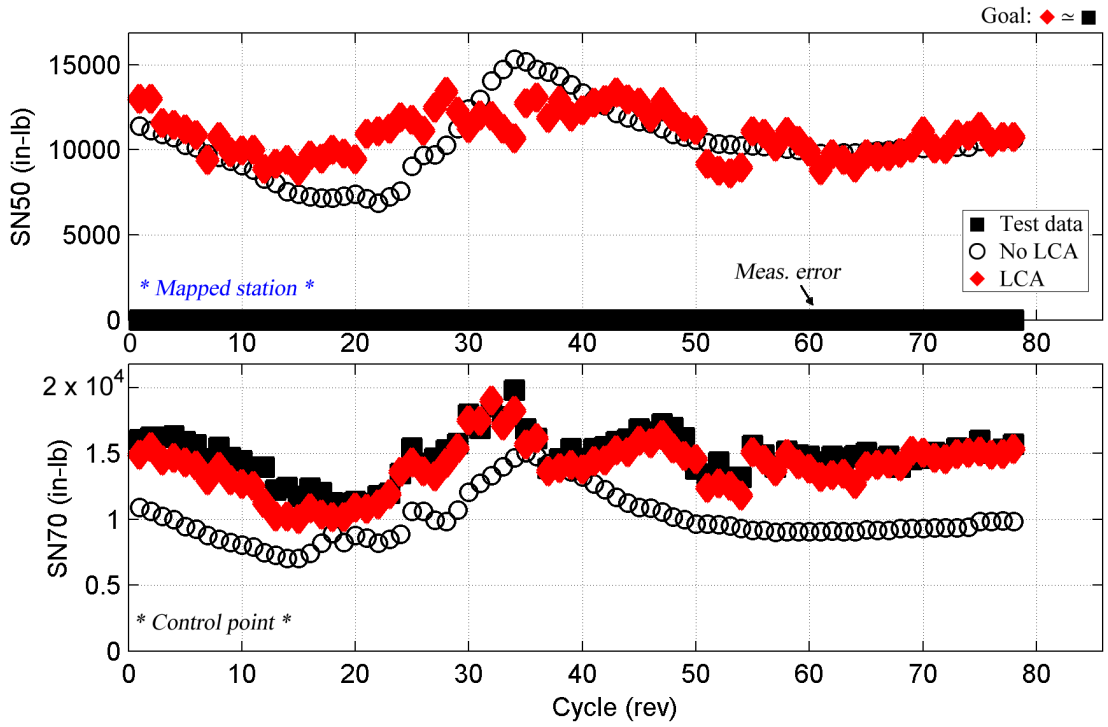

Figure 4.66: Peak-to-peak loads matching: all cycles of c8927: SN50, SN70.

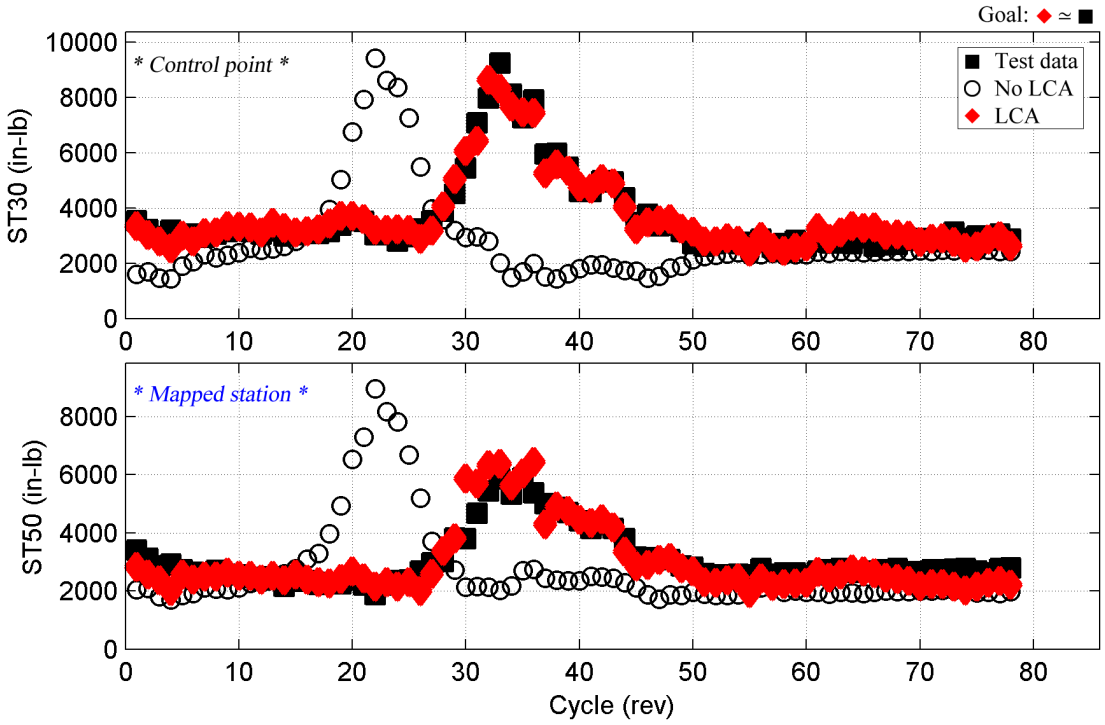

Figure 4.67: Peak-to-peak loads matching: all cycles of c8927: ST30, ST50.

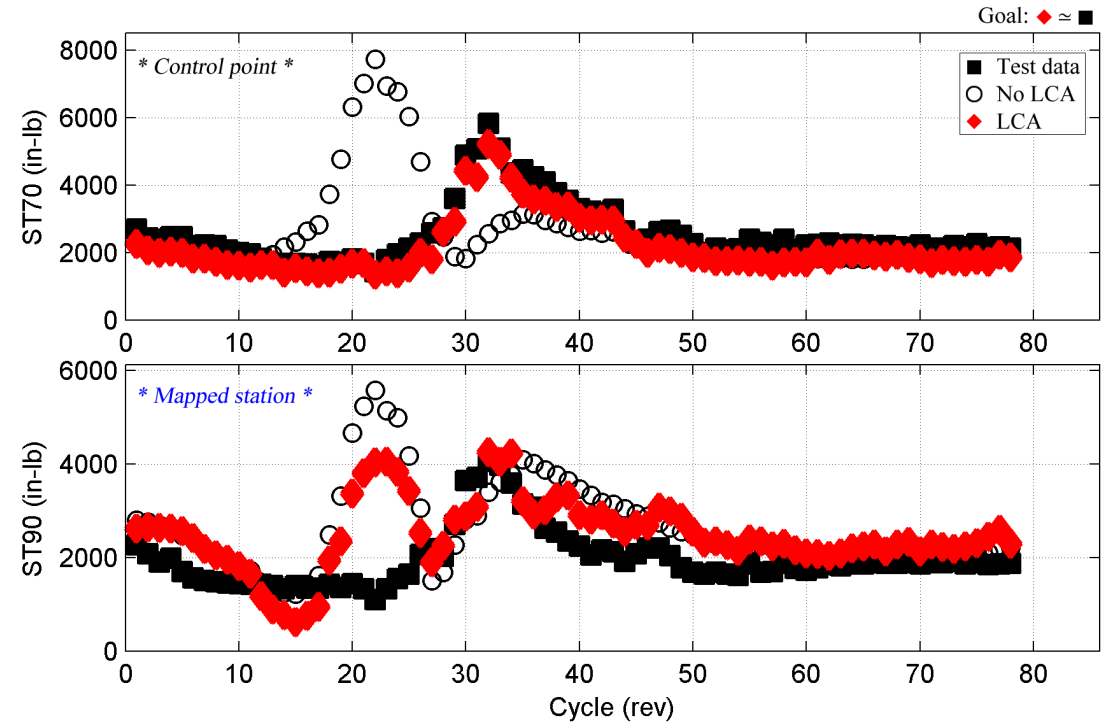

Figure 4.68: Peak-to-peak loads matching: all cycles of c8927: ST70, ST90.

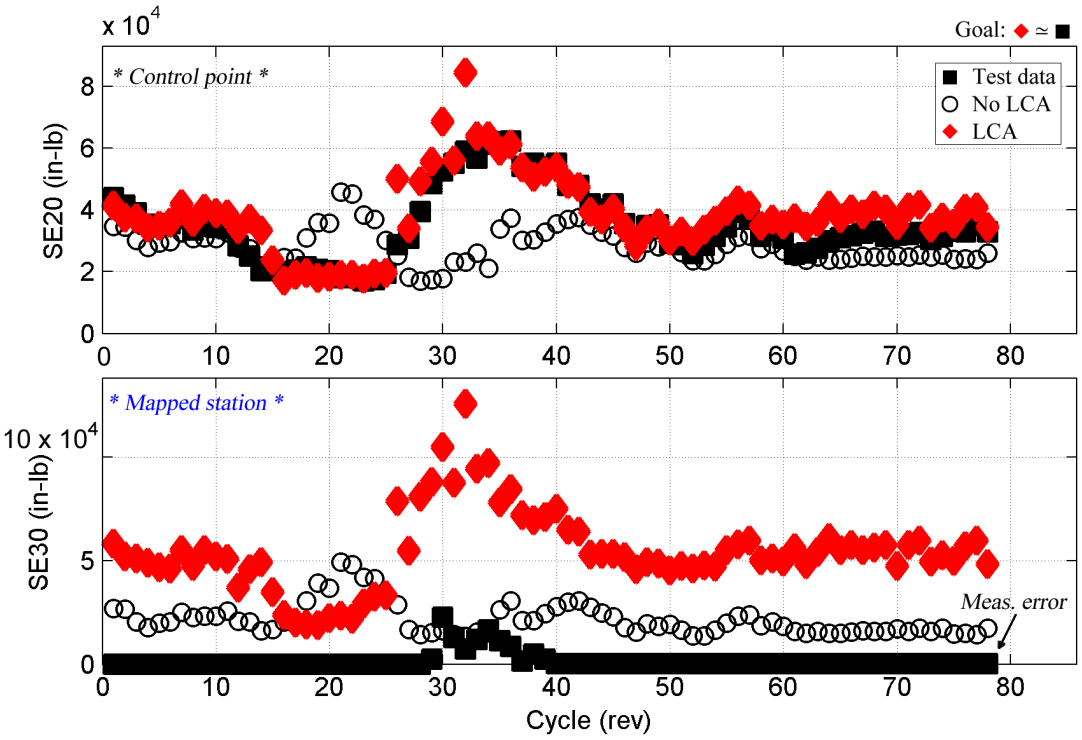

Figure 4.69: Peak-to-peak loads matching: all cycles of c8927: SE20, SE30.

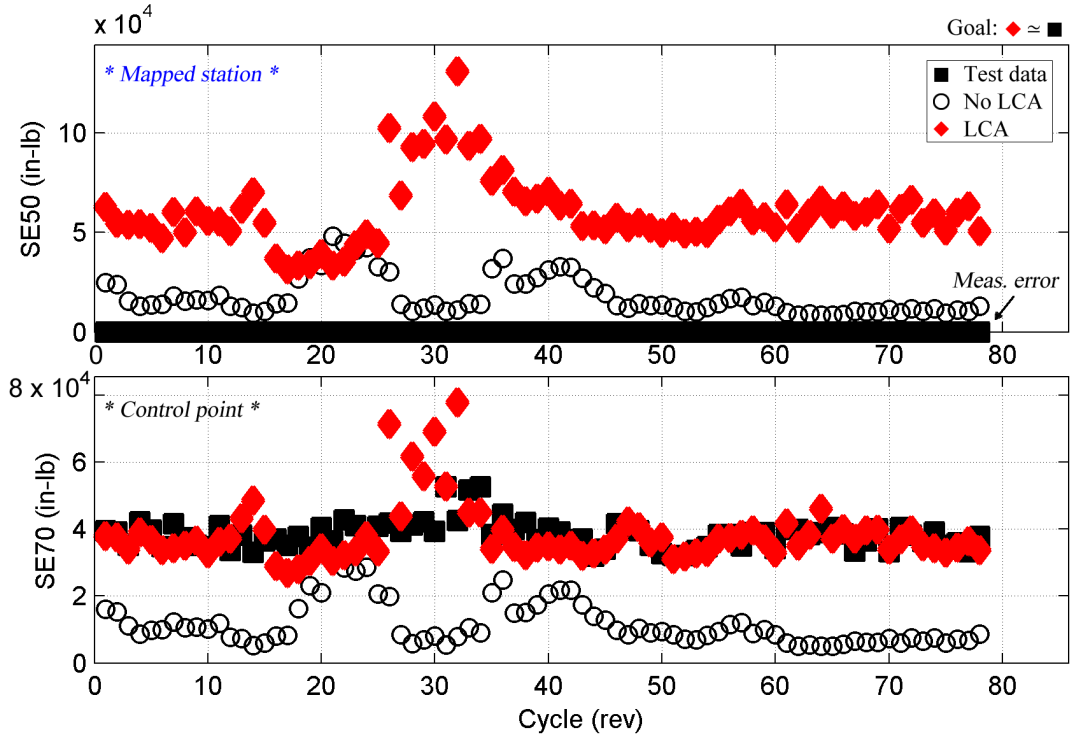

Figure 4.70: Peak-to-peak loads matching: all cycles of c8927: SE50, SE70.

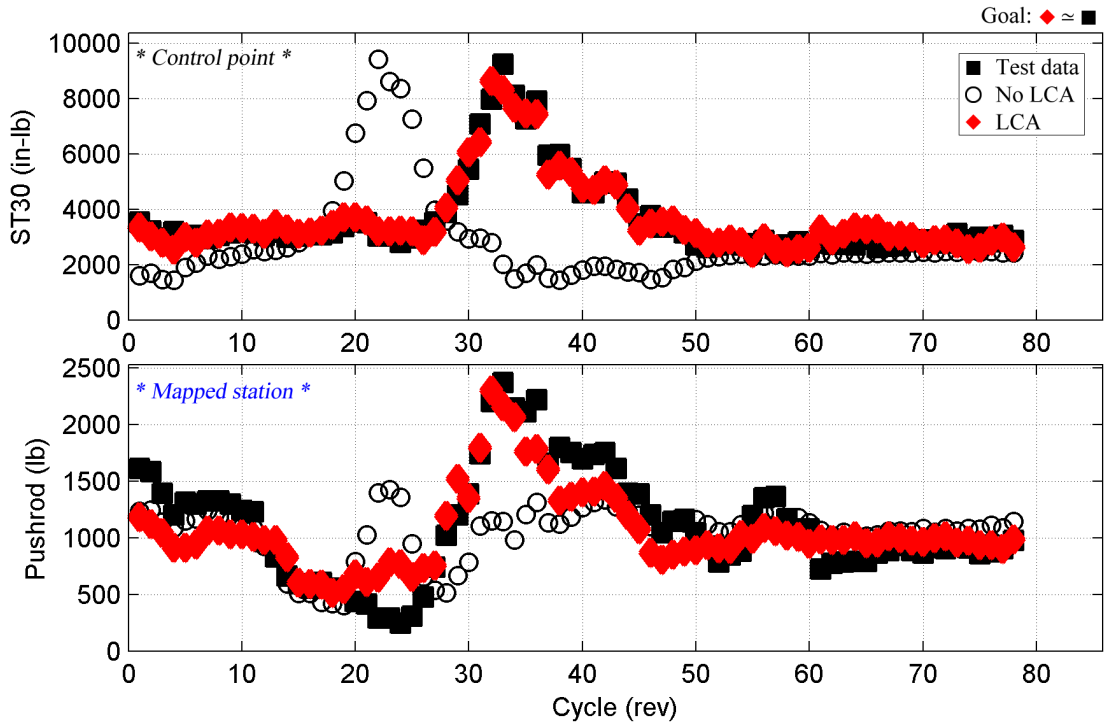

Figure 4.71: Peak-to-peak loads matching: all cycles of c8927: ST30, pushrod.

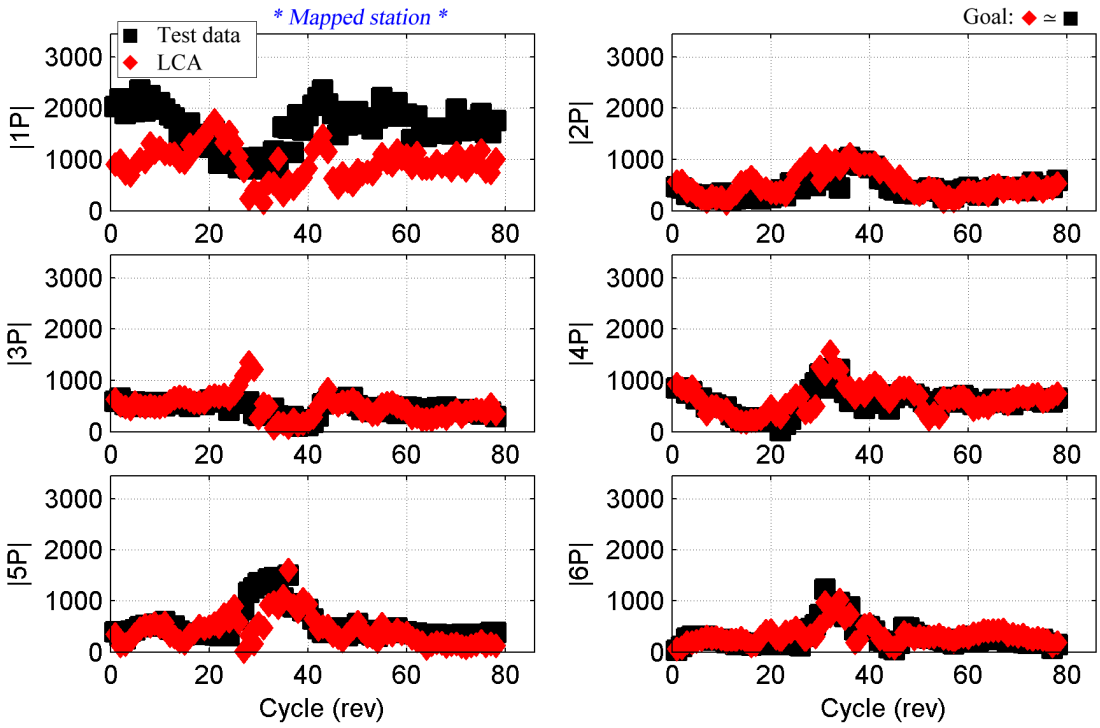

Figure 4.72: Loads matching by harmonic: all cycles of c8927: SN20 (in-lb).

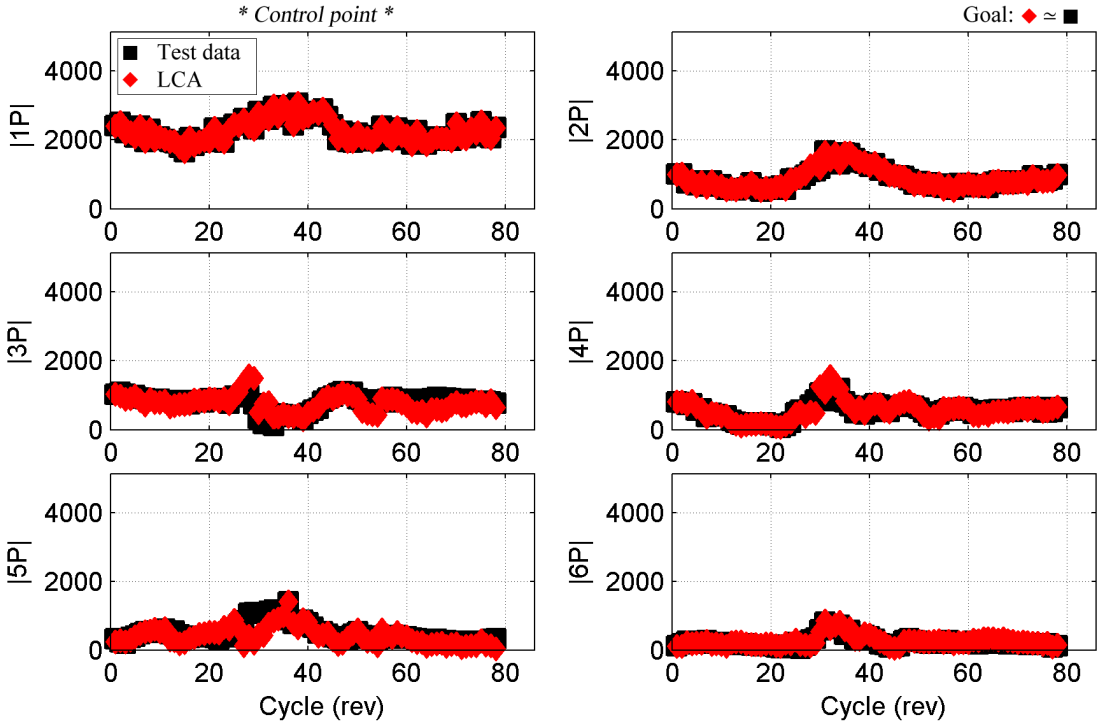

Figure 4.73: Loads matching by harmonic: all cycles of c8927: SN30 (in-lb).

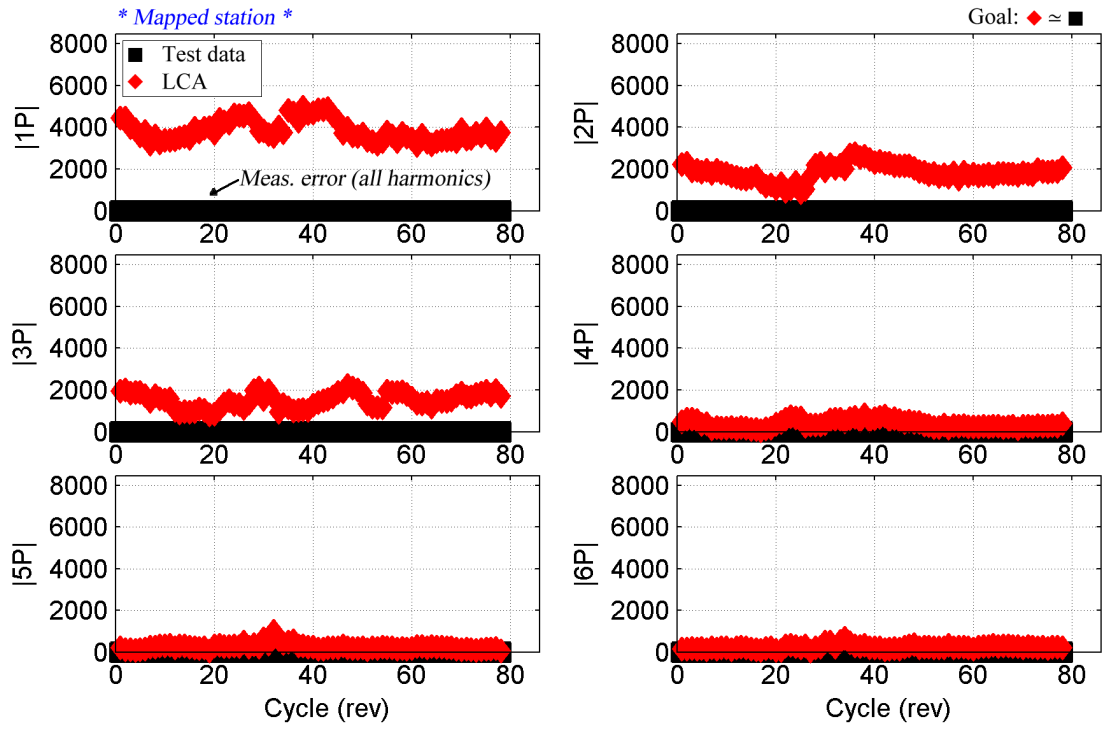

Figure 4.74: Loads matching by harmonic: all cycles of c8927: SN50 (in-lb).

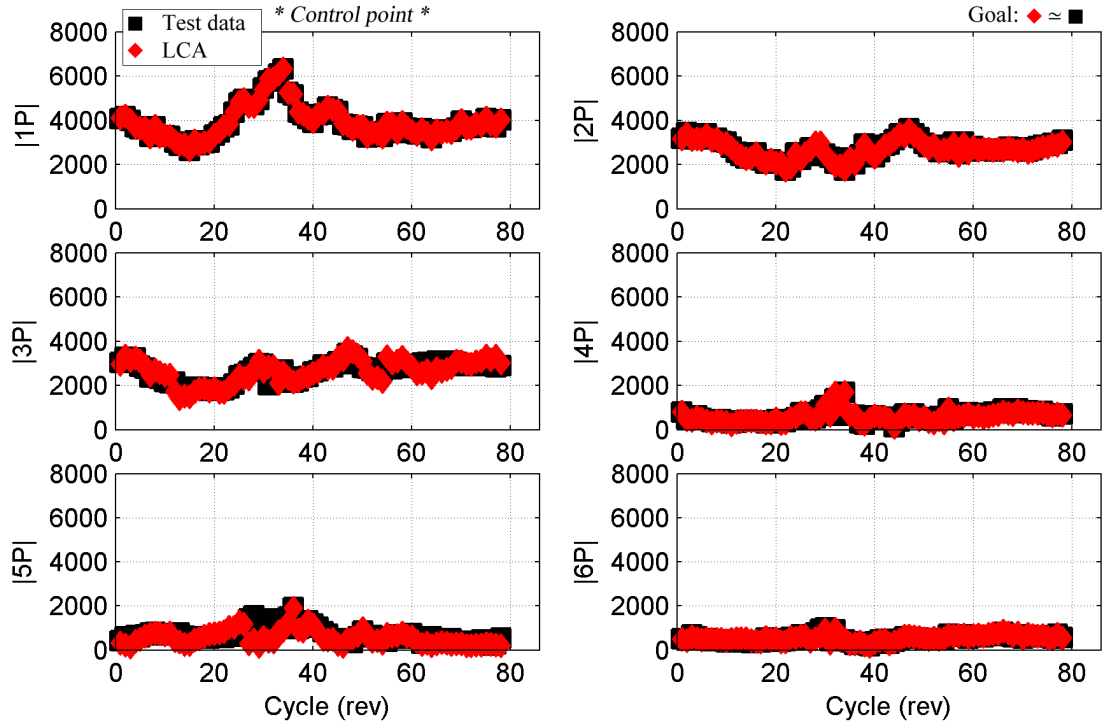

Figure 4.75: Loads matching by harmonic: all cycles of c8927: SN70 (in-lb).

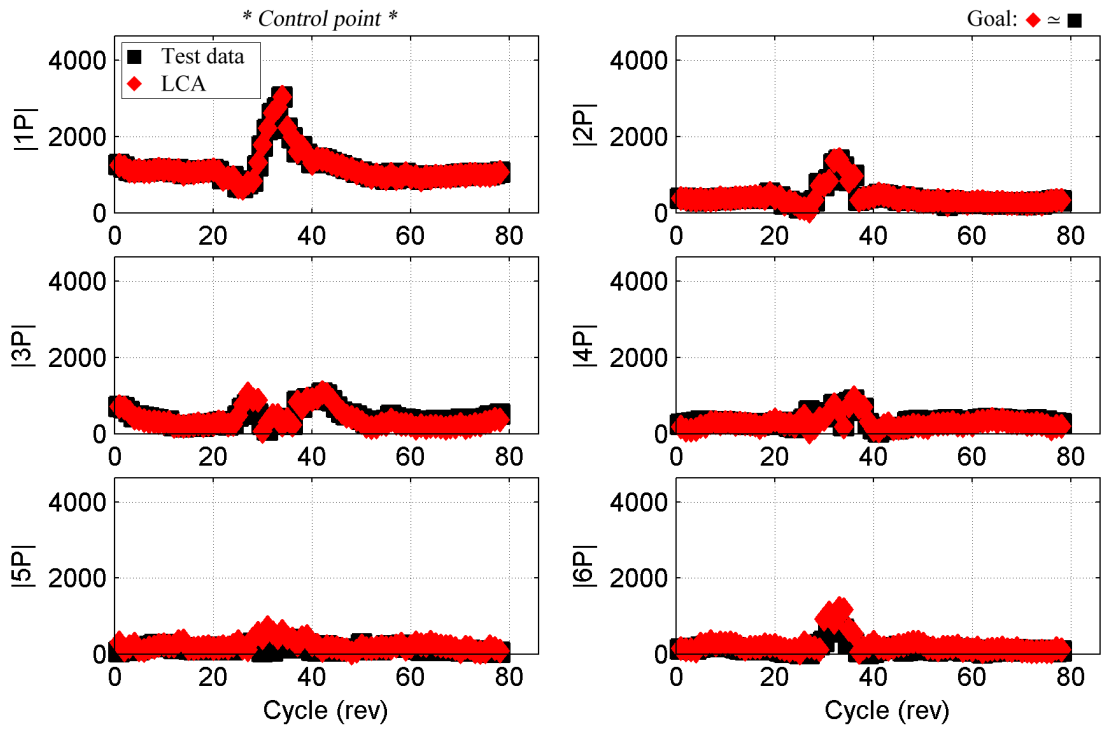

Figure 4.76: Loads matching by harmonic: all cycles of c8927: ST30 (in-lb).

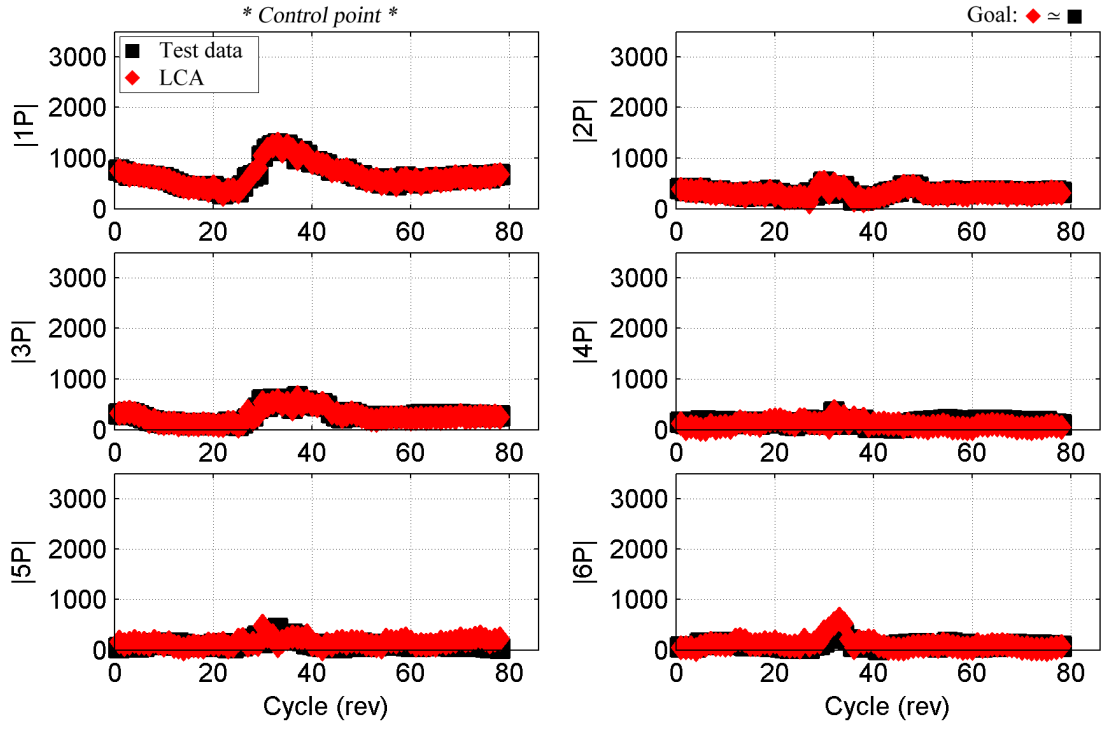

Figure 4.77: Loads matching by harmonic: all cycles of c8927: ST70 (in-lb).

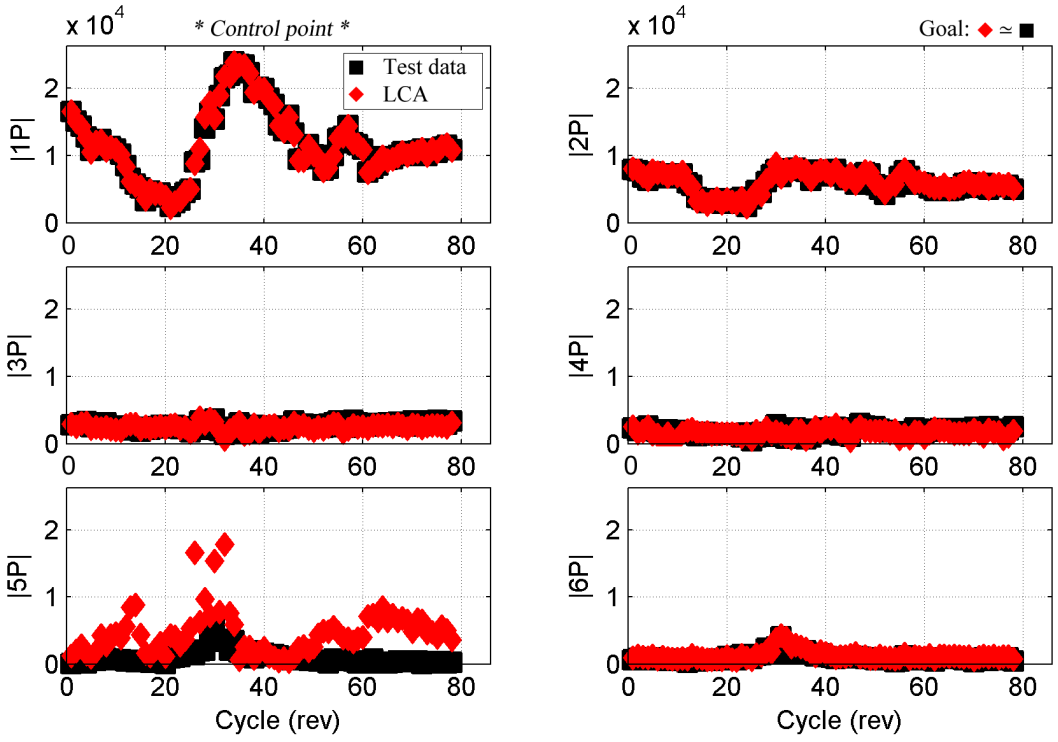

Figure 4.78: Loads matching by harmonic: all cycles of c8927: SE20 (in-lb).

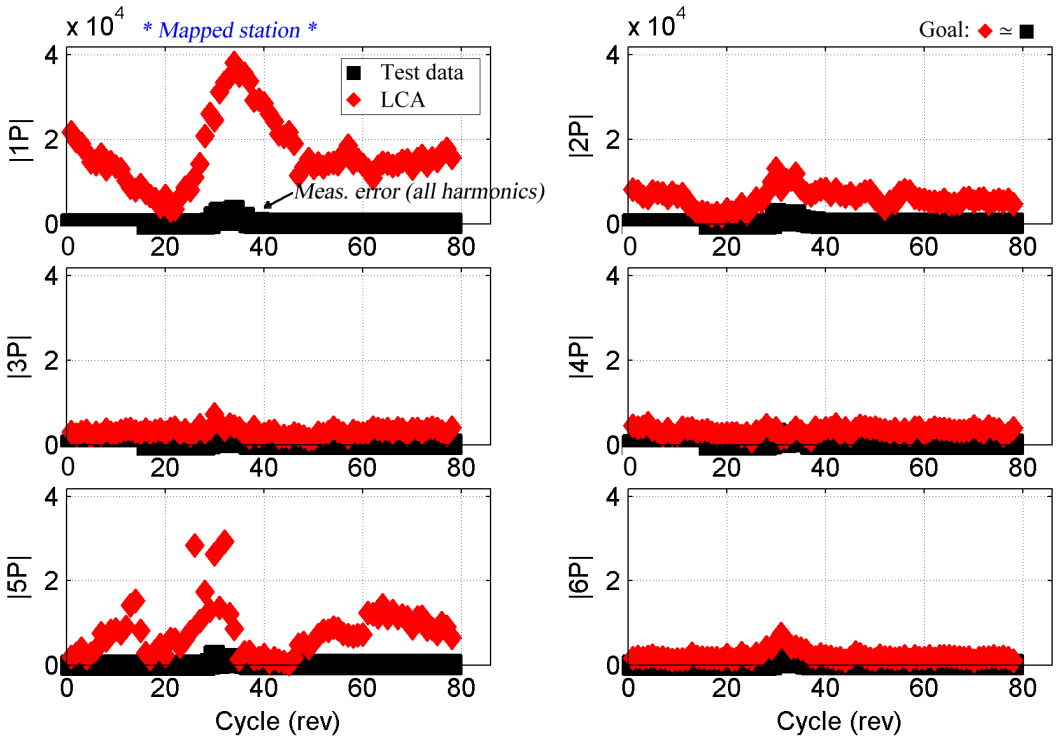

Figure 4.79: Loads matching by harmonic: all cycles of c8927: SE30 (in-lb).

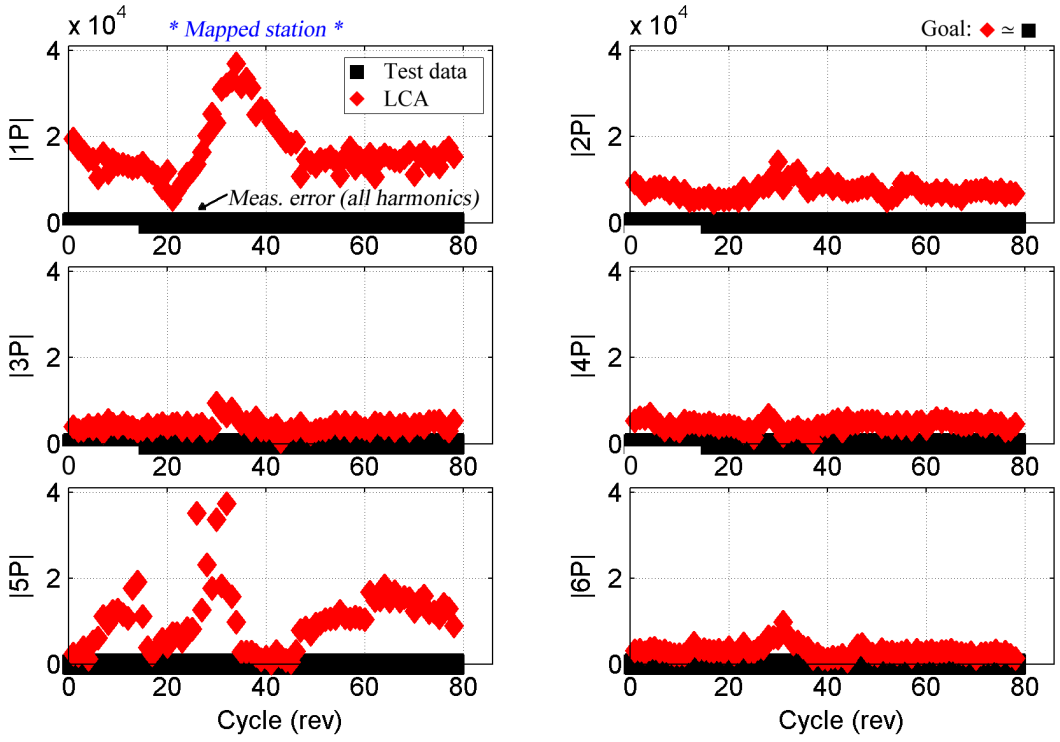

Figure 4.80: Loads matching by harmonic: all cycles of c8927: SE50 (in-lb).

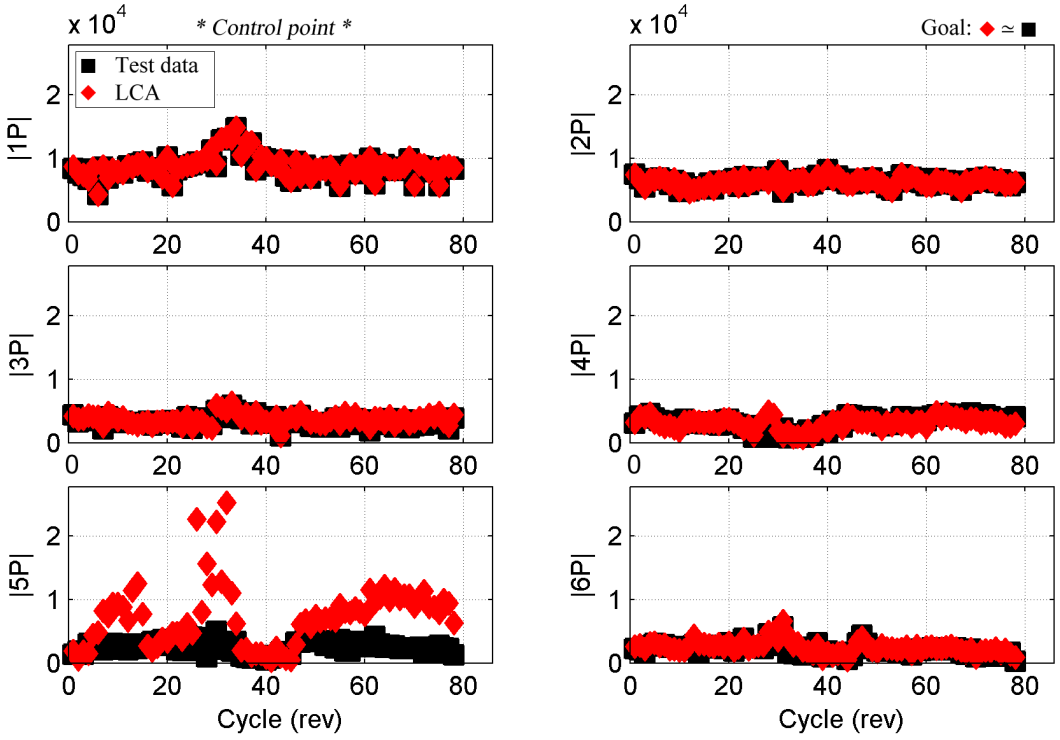

Figure 4.81: Loads matching by harmonic: all cycles of c8927: SE70 (in-lb).

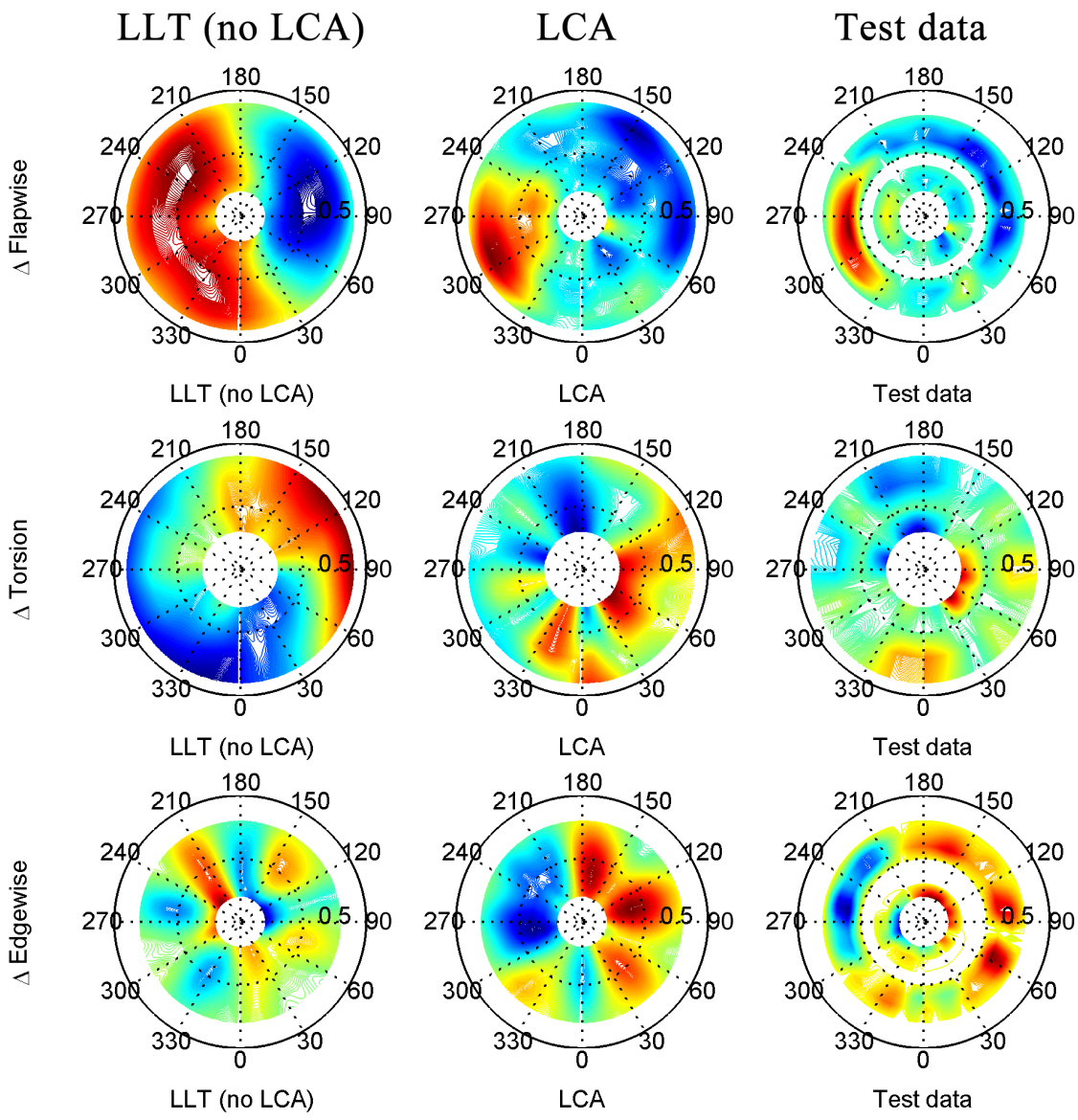

Figure 4.82: Flapwise, torsional, edgewise moments: radial, azimuthal distribution; cycle 33 [flight counter, μ] = [8927, 0.277] (top-to-bottom); red (peak), blue (valley).

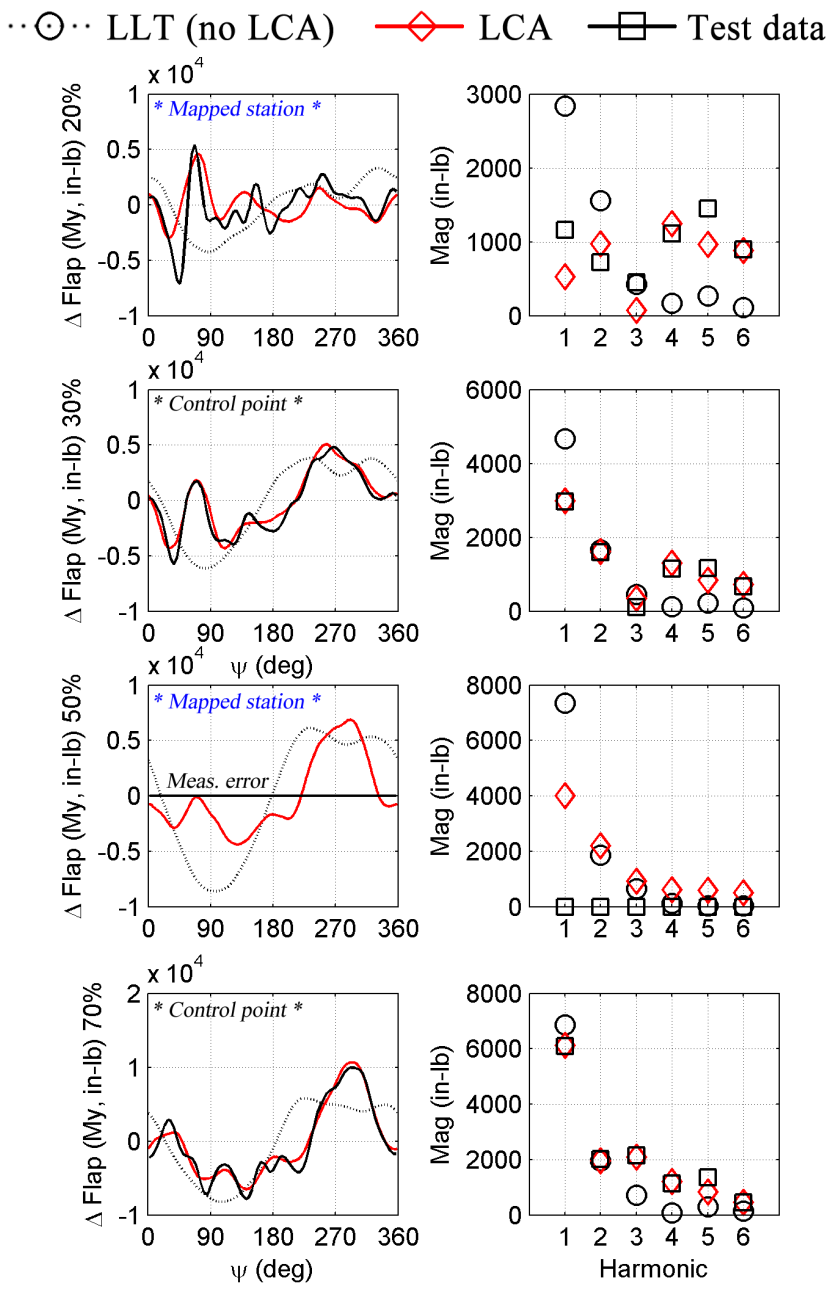

Figure 4.83: Flapwise bending moment: time history, load component by harmonic; cycle 33 [flight counter, μ] = [8927, 0.277]

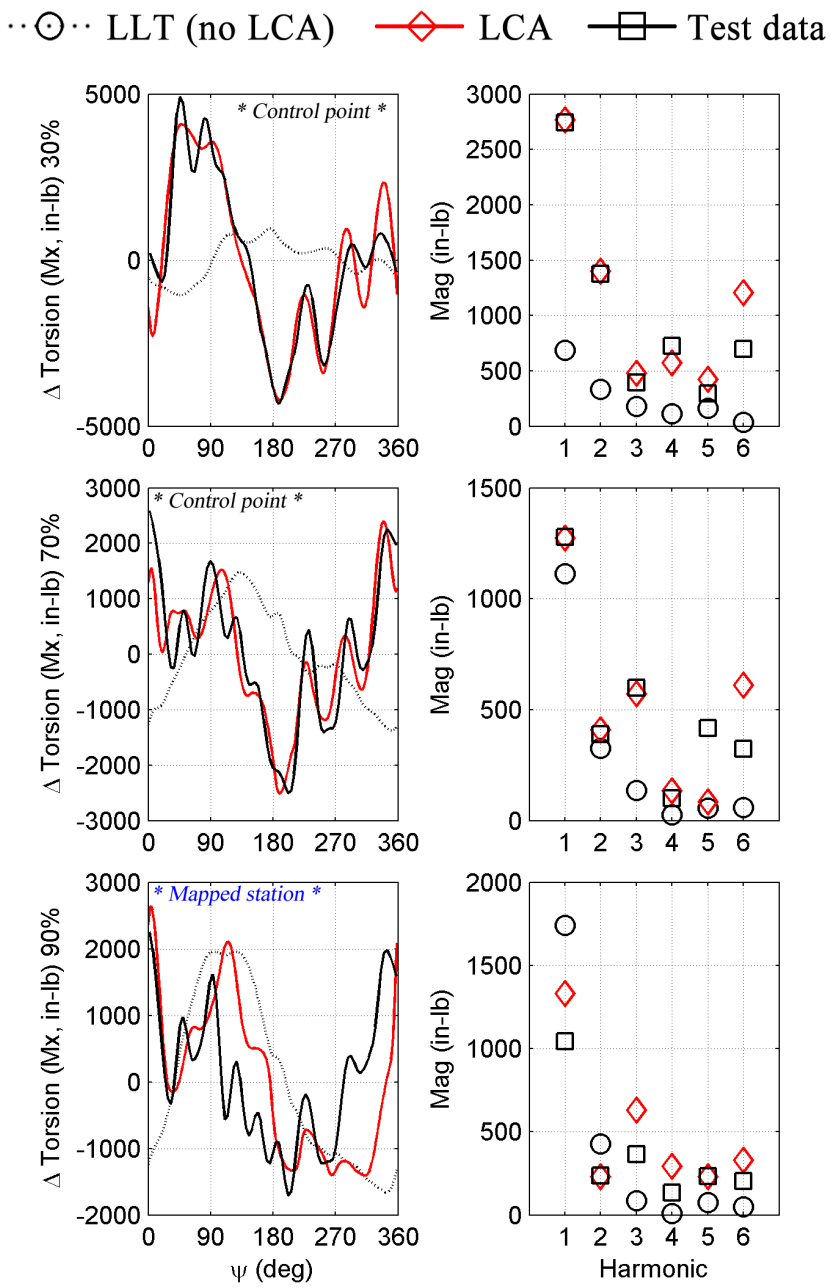

Figure 4.84: Torsional moment: time history, load component by harmonic; cycle 33 [flight counter, μ] = [8927, 0.277]

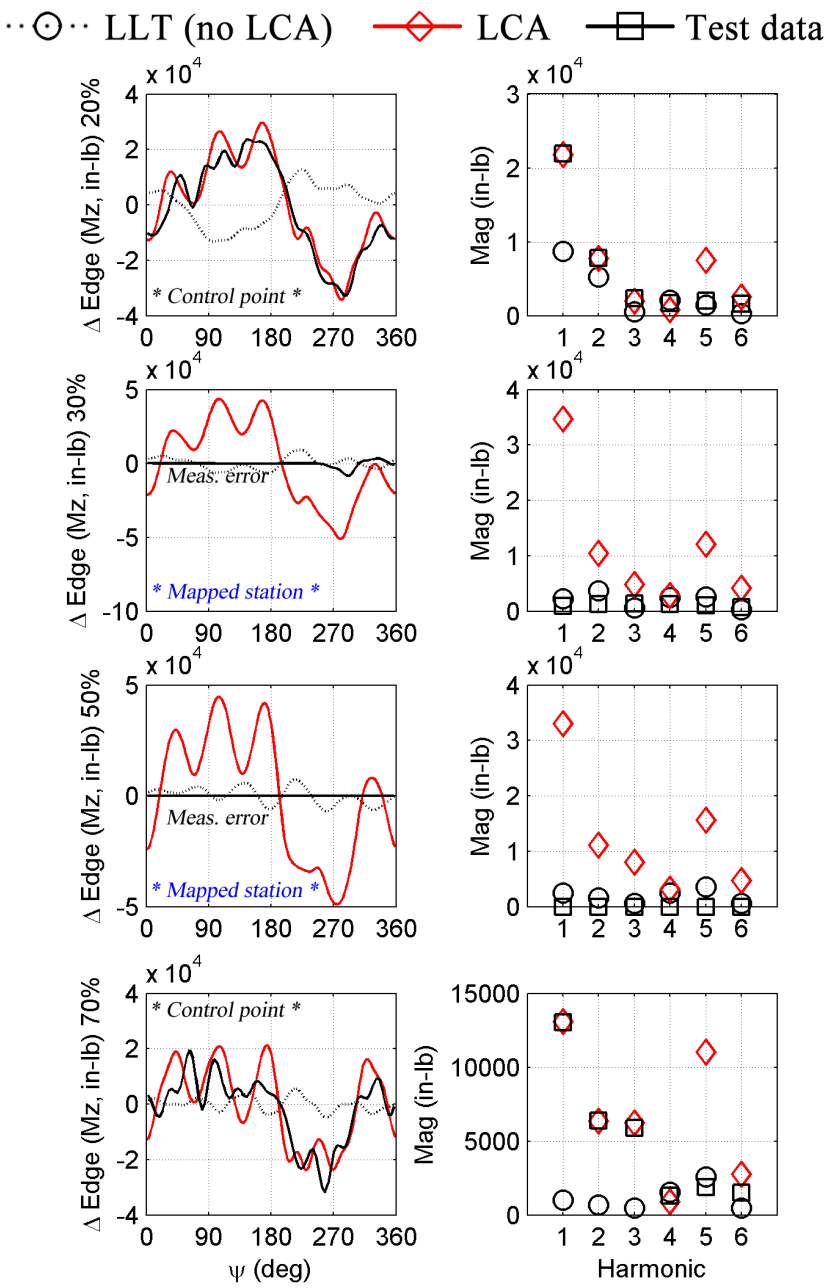

Figure 4.85: Edgewise bending moment: time history, load component by harmonic; cycle 33 [flight counter, μ] = [8927, 0.277]

4.6.5 Pushover maneuver: c8930

c8930 was studied by Kufeld et al. [53]. This pushover maneuver achieved 0.22g at 80 kias (rev 9). As in high-speed flight, there was a reduction in lift in Q2 near the blade tip. This was required for roll balance. The two stall cycles on the retreating side seen in level flight and diving turns were not present for pushover maneuvers. Lastly, pushrod loads were up to 60% higher relative to level flight due to large blade pitching motion.

4.6.6 Pull-up maneuver: c11029

Sitarama et al. [77] used a coupled CFD/CSD solution (UMTURNS/DYMORE) to study c11029, a pull-up maneuver quantified by Bousman as the second most severe maneuver in the UH-60A Airloads flight test program [19]. This dynamic pull-up reaches 2.12g at 139 knots, producing the highest root flap bending moment and the 3rd highest pushrod load. Observed effects are as follows. Large unsteadiness is seen in the flow through this pull-up maneuver due to vertical convection of the vortex wake and pass-through of the vortex wake through the rotor disk as the aircraft increases thrust, pitches up, reduces forward speed, and climbs. The two retreating side stall cycles are present, due to flow separation at high blade angles-of-attack (first stall cycle) and high frequency torsional motion out of phase with the control pitch, thus inducing a higher sectional angle of attack (second stall cycle). These two retreating side stall cycles are more severe at higher thrust settings.

A third stall cycle is also present (on the advancing side, due to transonic airflow), consistent with other maneuver cases described above. Again, this stall cycle is difficult to predict with CFD due to complex flow separation, flow reattachment, and shock-boundary layer interactions, all of which are more dominant during maneuvers than in steady, level flight.

c11029 was also studied by Abhishek et al. [1, 2]. They also observed two distinct

stalls on the retreating side and one on the advancing side, the latter being difficult to predict with CFD. An interesting observation from this reference is the large impact swashplate dynamics have on fixed system control servo loads. This is discussed further in Section 6.3.2.

4.6.7 Dynamic stall: c9017

Potsdam et al. [72] cite c9017 as a challenging and quintessential rotorcraft test case due to the wide variation of unsteady flow conditions present, ranging from transonic to stall, all with appreciable wake interactions. Datta et al. [29] used loose CFD/CSD coupling to predict UH-60A rotor loads under dynamic stall for c9017. Rotor dynamic stall differs from airfoil and 3D wing stall due to additional excitations caused by wake induced inflow and high frequency elastic twist deformations. This moderate speed (100 kias) is high enough to prevent strong tip vortices influencing the surrounding structures but low enough to prevent onset of strong transonic effects.

They note the presence of three stall cycles on the blades during maneuvers such as c9017:

1. The first stall cycle on the advancing side (due to transonic flow effects)
2. The second in Q3 due to high blade trim angles on the retreating blade
3. The third in Q4 due to elastic twist deformation

The presence of this last stall cycle excites the $5P$ torsion dynamics to produce a twist oscillation in Q4. The challenge with numerical simulations is capture of the magnitude (driven by accurate prediction of inflow) and location (driven by accurate prediction of elastic twist) of these stall cycles; i.e., the quality of the aerodynamic model determines whether this last stall cycle is triggered independently from the second trim angle-based stall cycle (and, if so, the magnitude of its response), while the quality of the structural model determines the azimuthal location of these stall

cycles. It was observed that the advancing side stall is not present in steady, level flight due to the lower angle of attack variations relative to maneuvering. Marpu et al. [57] add that accurate prediction of the retreating stall cycles is important for capturing the advancing side stall which is driven by the correct combination of control angles, elastic twist, and blade angle of attack.

Ho et al. [45] found that the correlation of pushrod load and blade torsional moments between predictions and measurements is worse for this high thrust case compared with c8534 and c8513 (moderate thrust). They attribute this difference to an over-prediction of $5P$ torsional moment and pushrod load content.

Figures 4.86 through 4.92 show peak-to-peak loads for blade flapwise bending, torsional, and edgewise bending moments (as well as pushrod load) for the 16 cycles of this flight counter. Figures 4.93 through 4.102 show load magnitudes by harmonic for these cycles as well. The response is fairly consistent throughout, so the first cycle is examined in detail (Figures 4.103 through 4.106).

The presence of the stall cycles is evident in Figures 4.103 and 4.105 for blade torsional moment, though, interestingly, three peaks are present outboard on the blade (e.g., ST70) on the advancing side and two on the retreating side (one in Q3 and one in Q4, as expected). These three peaks on the advancing side are likely one stall cycle with higher frequency ($6P$) vibratory content superimposed upon it.

The LCA provides a good loads match for this flight counter, with the following observations:

1. SE20 and SE70 measurements are suspect. From Figure 4.106, the data look too smooth from mid-Q1 to mid-Q3. Interestingly enough, the LCA matches this response quite well. This brings up a limitation of the LCA: it will match load response at control points, even if the measurement for a given control point is in error.

2. An excellent match is seen for peak-to-peak loads for SN20, SN30 (mapped),

SN70, ST30, SE20, and SE70 (even though the measured data for the latter looks to be in error).

3. SN20 $1P$ content is over-predicted; likely due to the lack of the rigid blade flapping mode in the LCA.

4. ST30 over-predicts $5P$ content; ST70 over-predicts $1P$ content (again, likely due to the lack of the rigid blade flapping mode in the LCA).

5. SE70 predictions have a wide variation in $5P$ response. The reasons for this are unknown, but this effect is consistent with the previously-formed hypothesis that the LCA's prediction of edgewise bending is highly sensitive to control point selection (number and location of sensors).

6. As before, the LCA over-predicts the response at ST90.

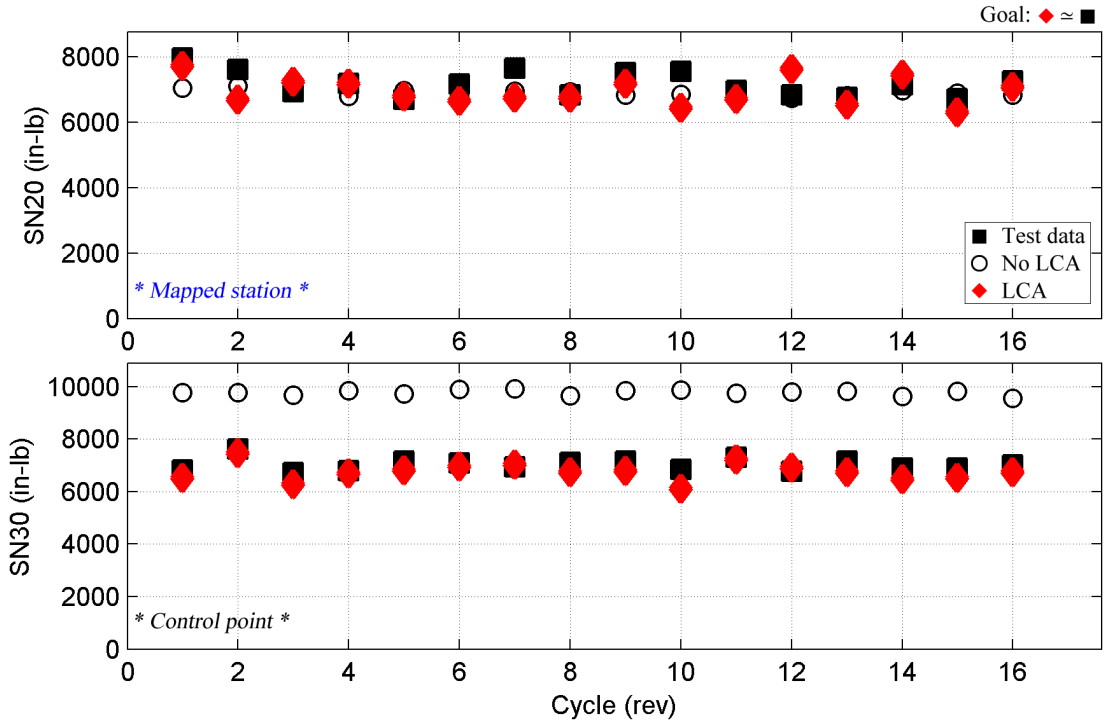

Figure 4.86: Peak-to-peak loads matching: all cycles of c9017: SN20, SN30.

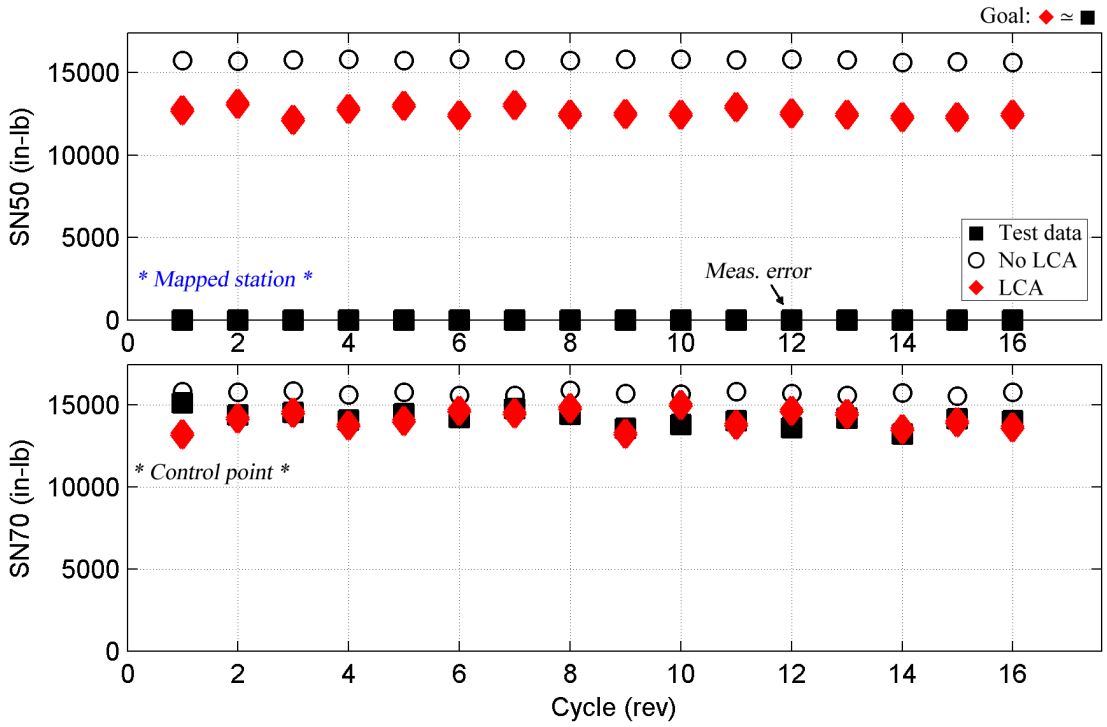

Figure 4.87: Peak-to-peak loads matching: all cycles of c9017: SN50, SN70.

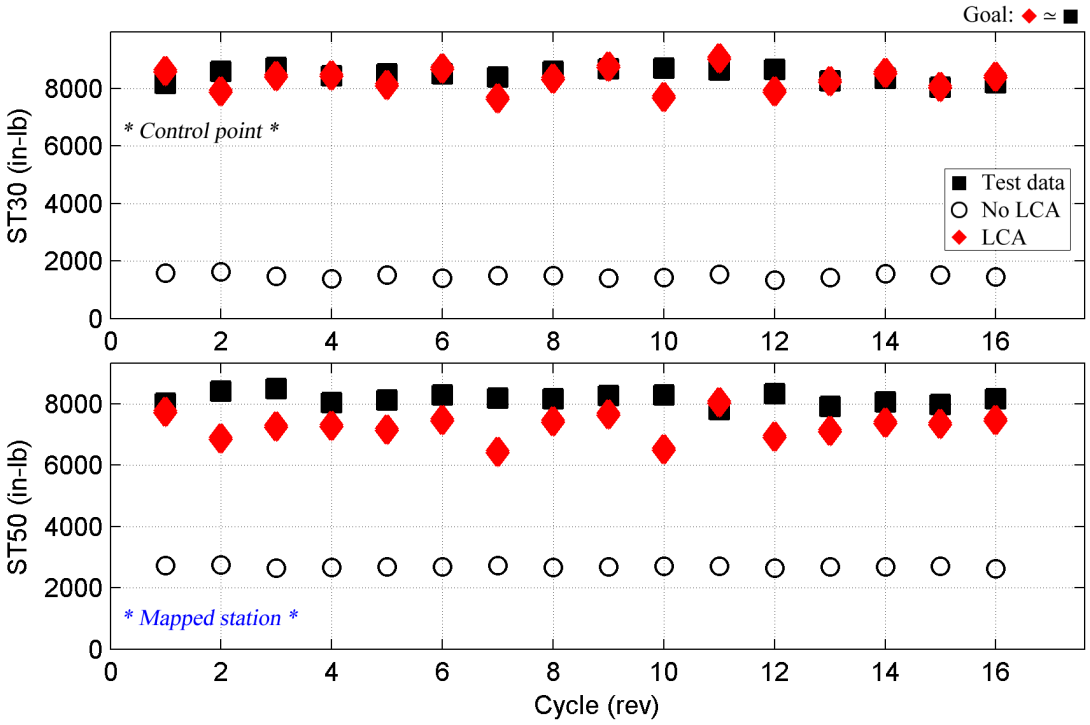

Figure 4.88: Peak-to-peak loads matching: all cycles of c9017: ST30, ST50.

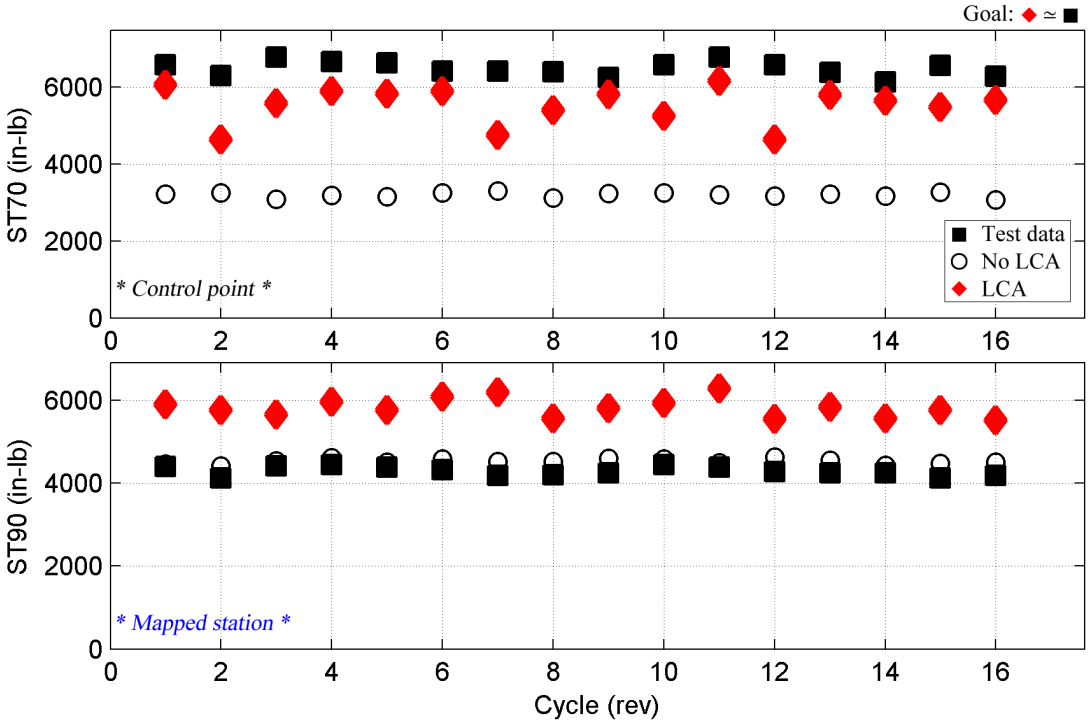

Figure 4.89: Peak-to-peak loads matching: all cycles of c9017: ST70, ST90.

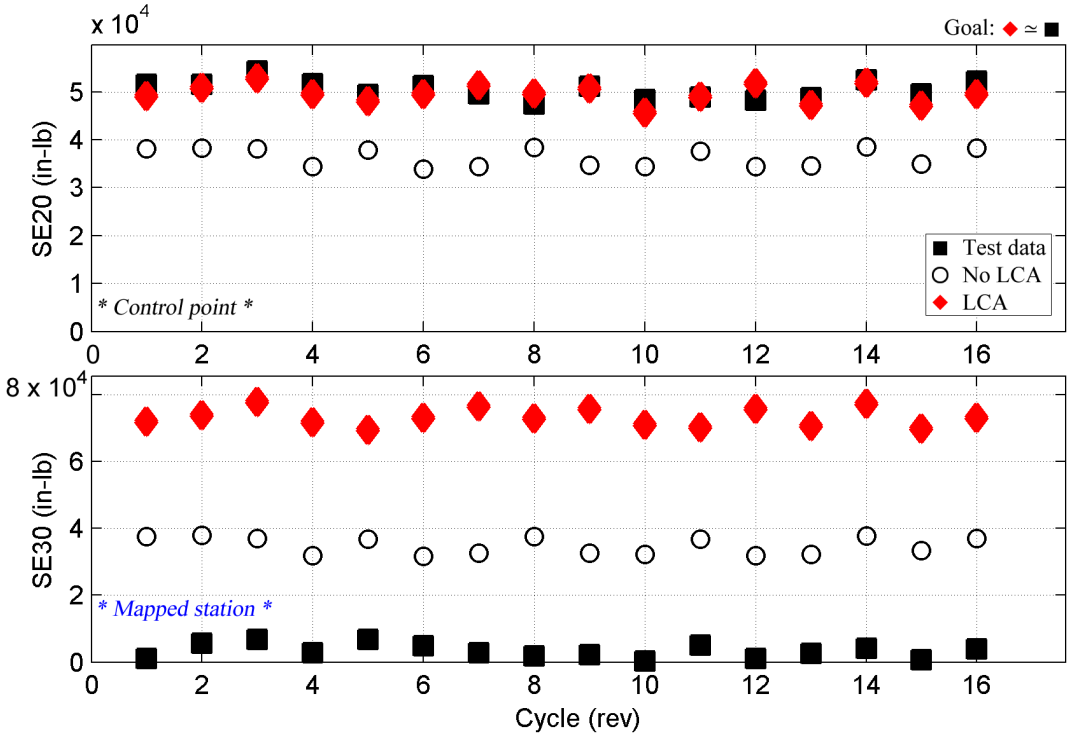

Figure 4.90: Peak-to-peak loads matching: all cycles of c9017: SE20, SE30.

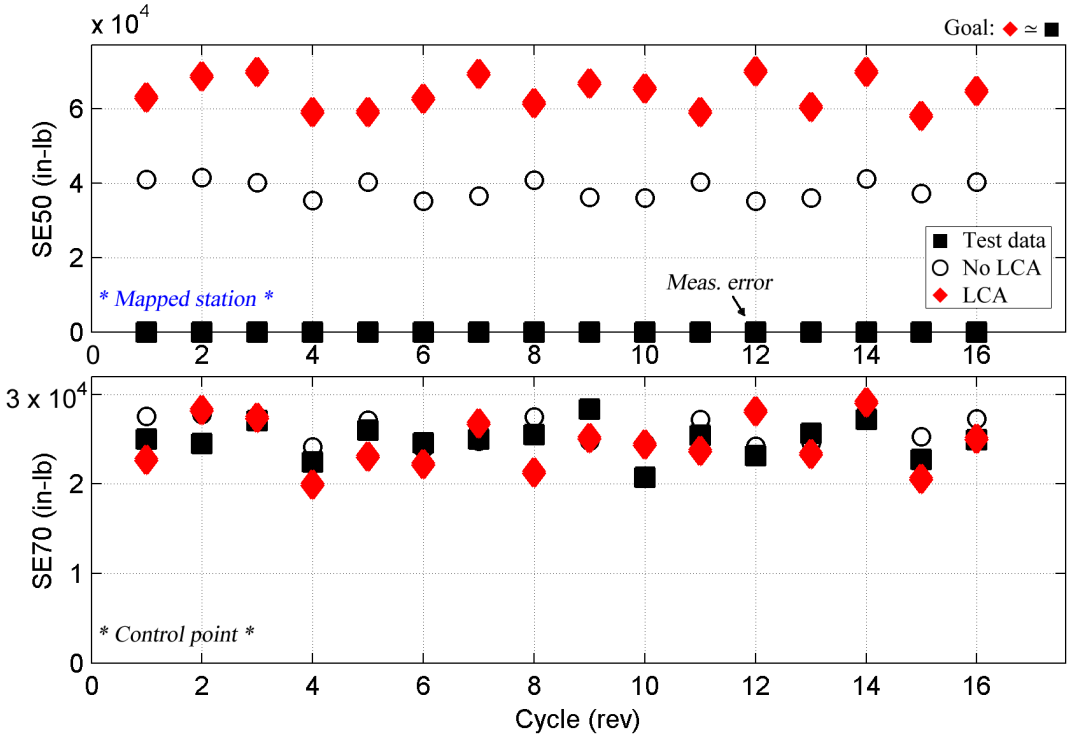

Figure 4.91: Peak-to-peak loads matching: all cycles of c9017: SE50, SE70.

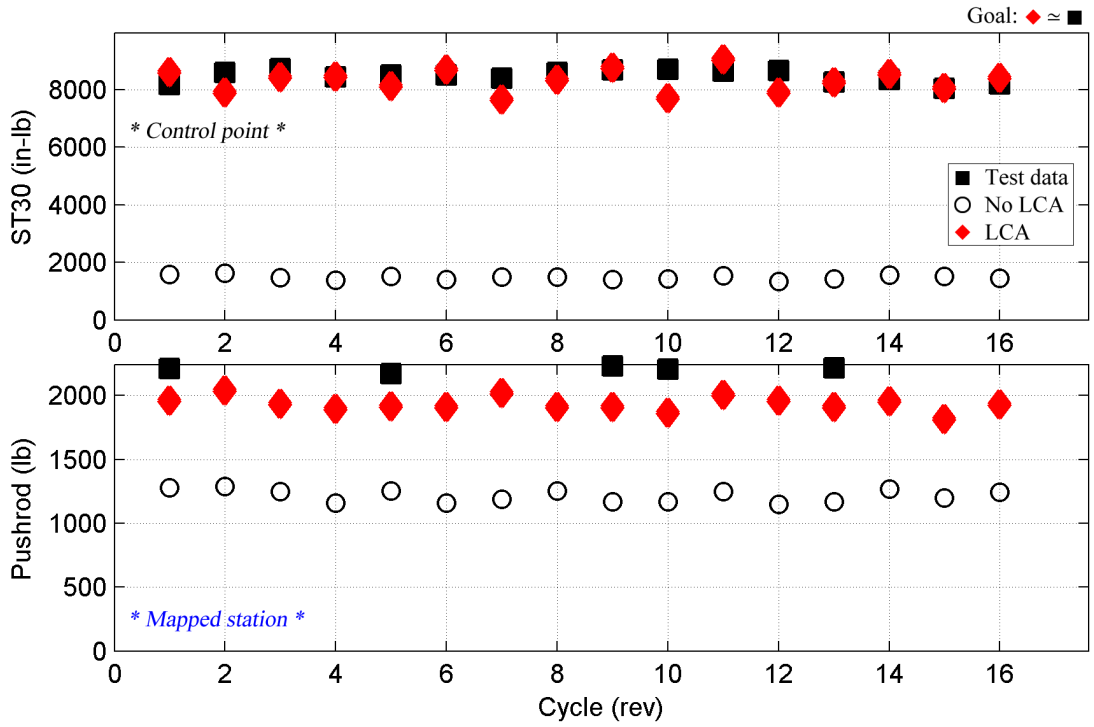

Figure 4.92: Peak-to-peak loads matching: all cycles of c9017: ST30, pushrod.

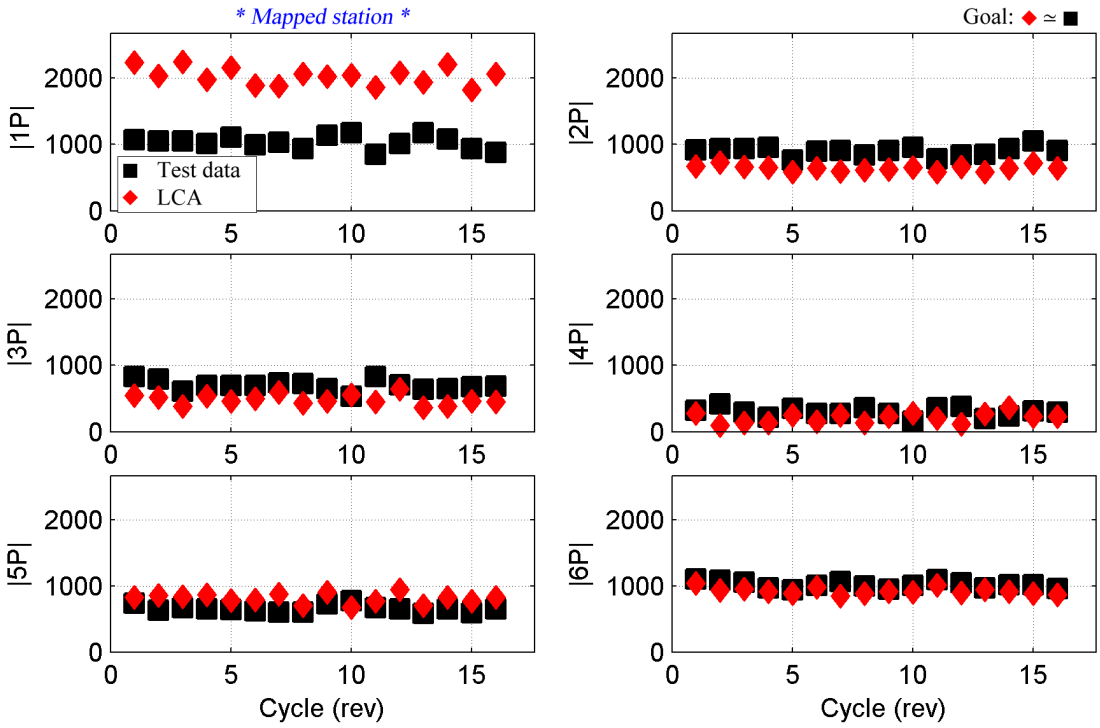

Figure 4.93: Loads matching by harmonic: all cycles of c9017: SN20 (in-lb).

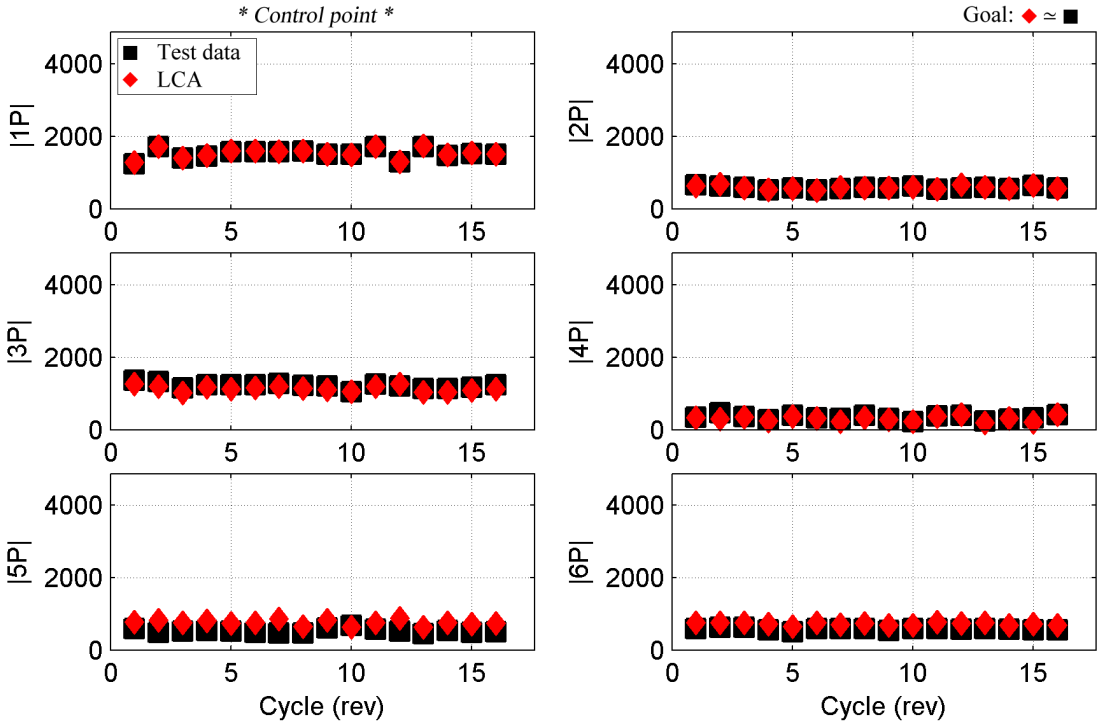

Figure 4.94: Loads matching by harmonic: all cycles of c9017: SN30 (in-lb).

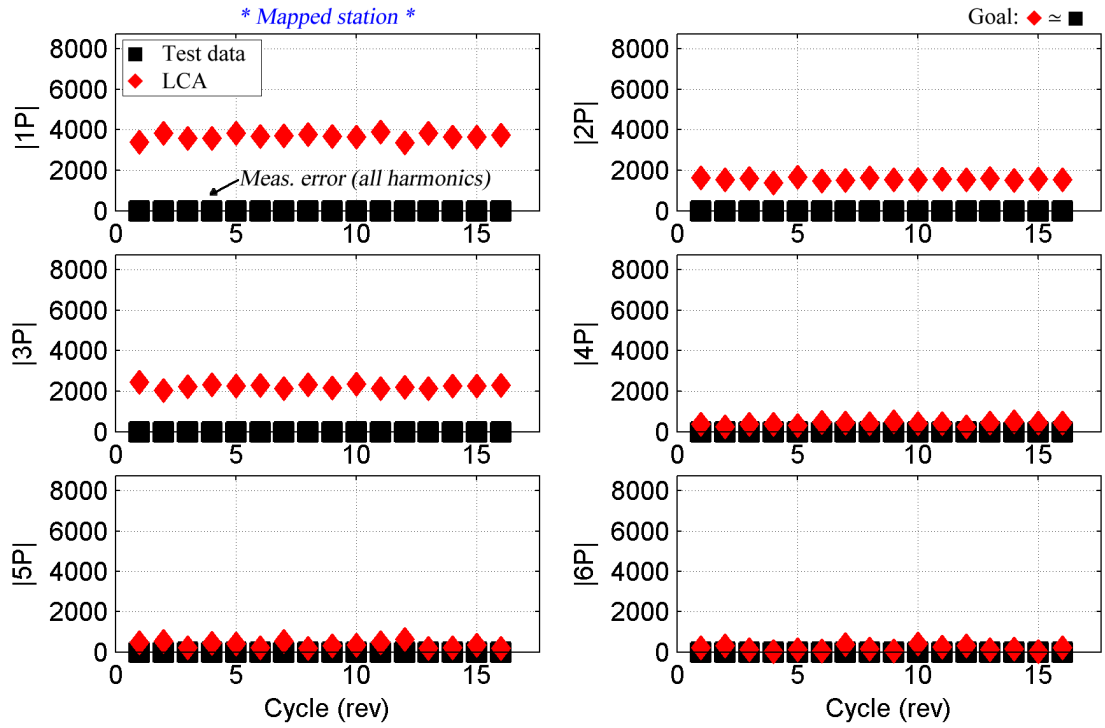

Figure 4.95: Loads matching by harmonic: all cycles of c9017: SN50 (in-lb).

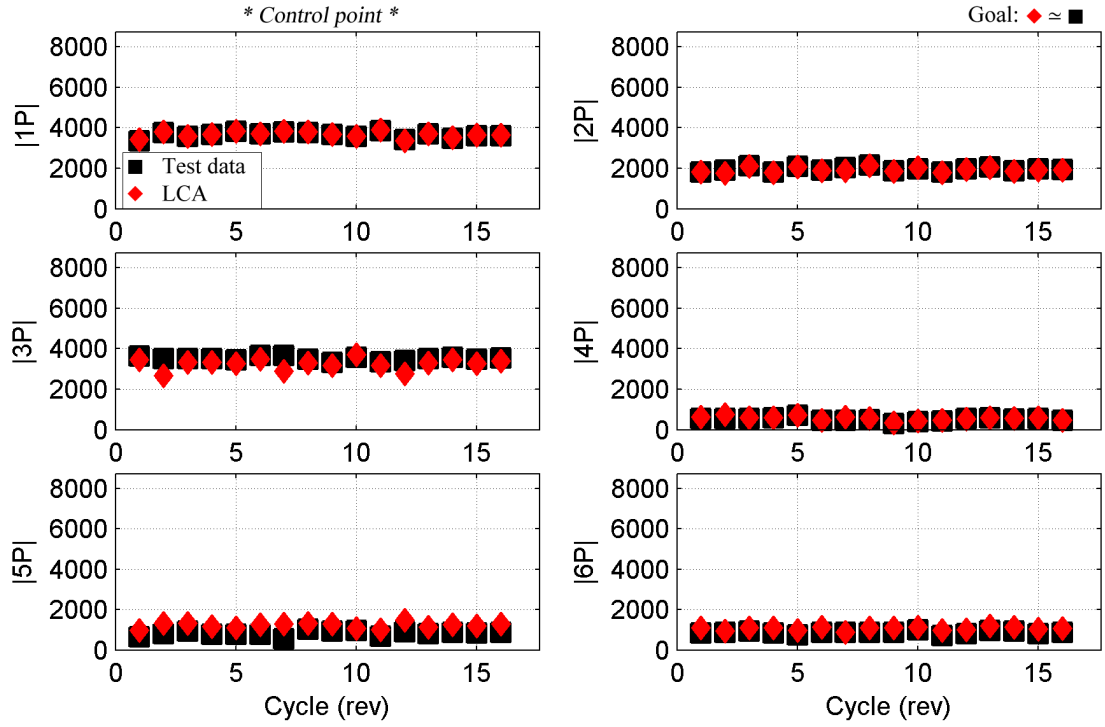

Figure 4.96: Loads matching by harmonic: all cycles of c9017: SN70 (in-lb).

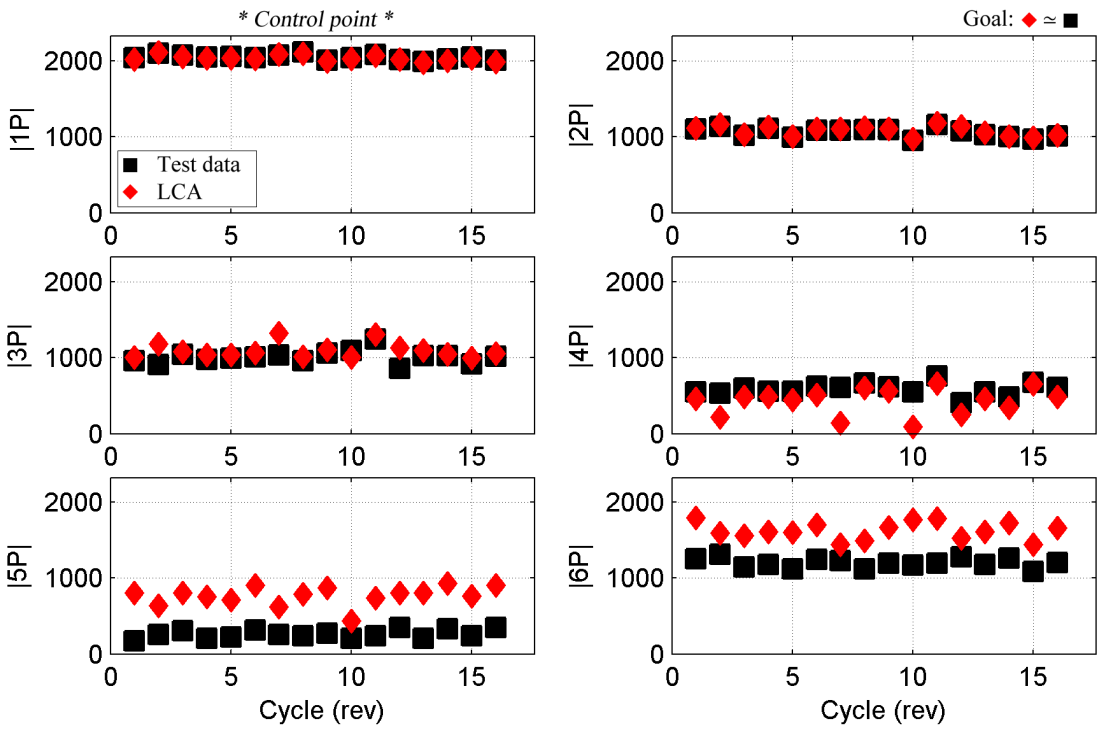

Figure 4.97: Loads matching by harmonic: all cycles of c9017: ST30 (in-lb).

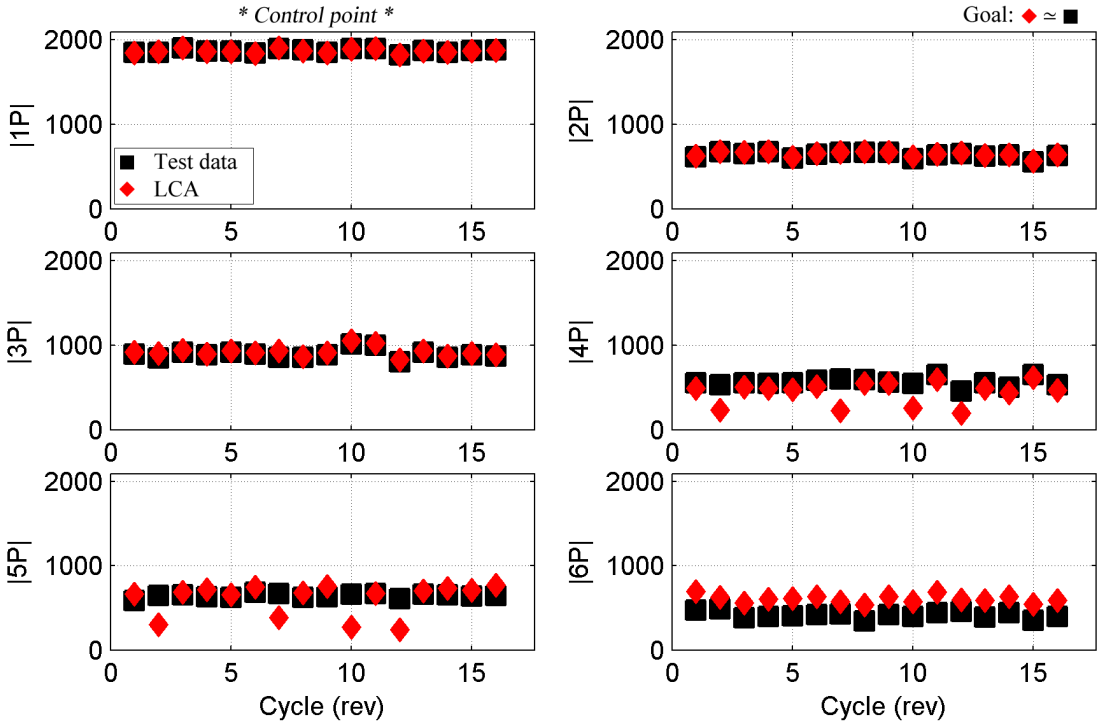

Figure 4.98: Loads matching by harmonic: all cycles of c9017: ST70 (in-lb).

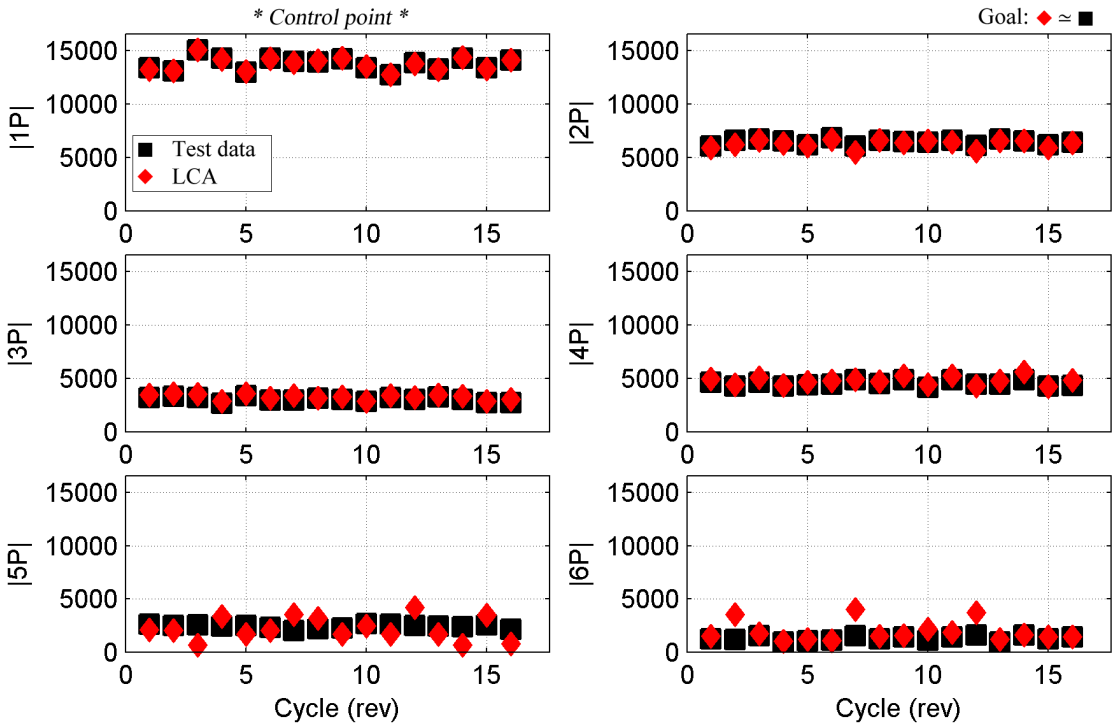

Figure 4.99: Loads matching by harmonic: all cycles of c9017: SE20 (in-lb).

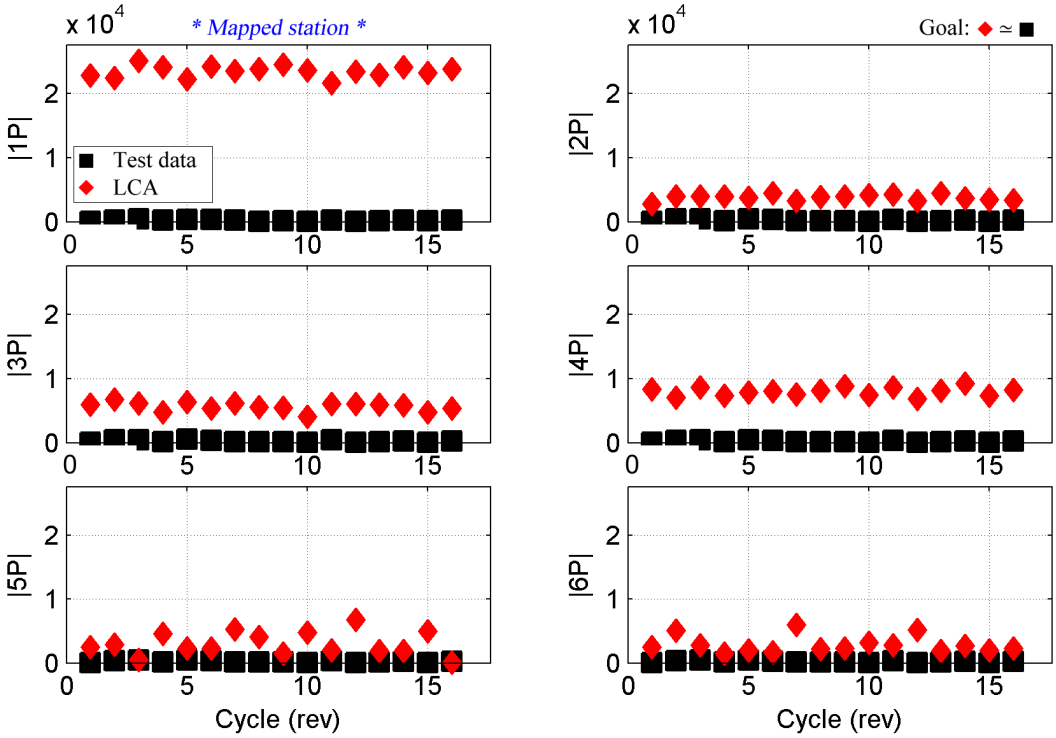

Figure 4.100: Loads matching by harmonic: all cycles of c9017: SE30 (in-lb).

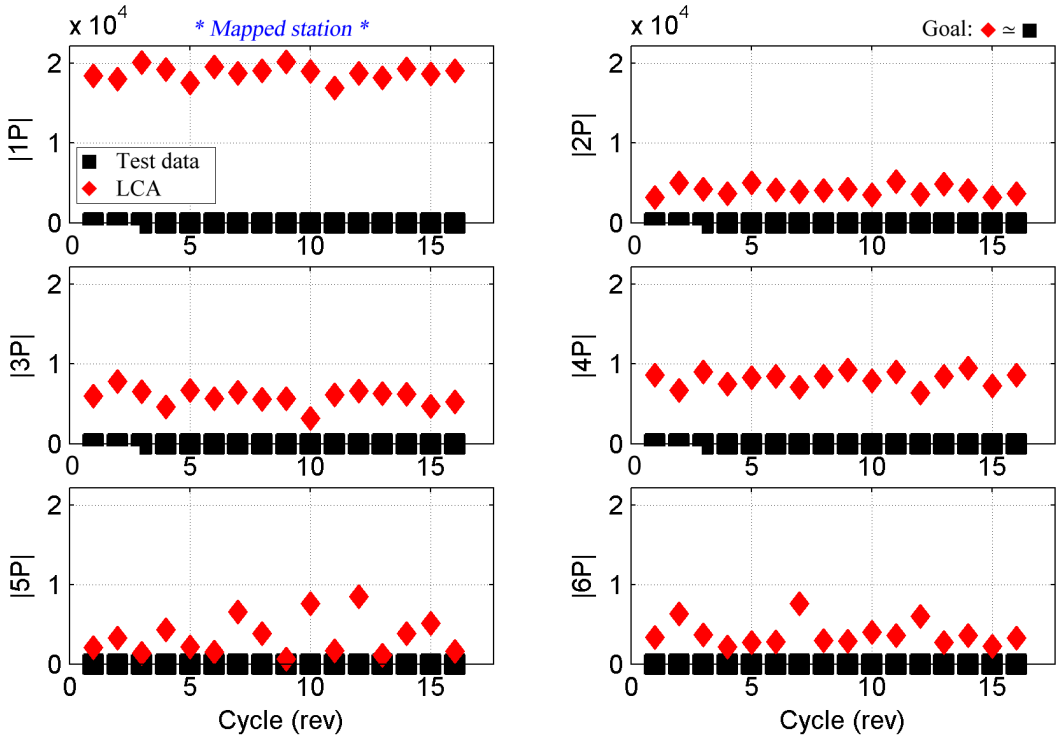

Figure 4.101: Loads matching by harmonic: all cycles of c9017: SE50 (in-lb).

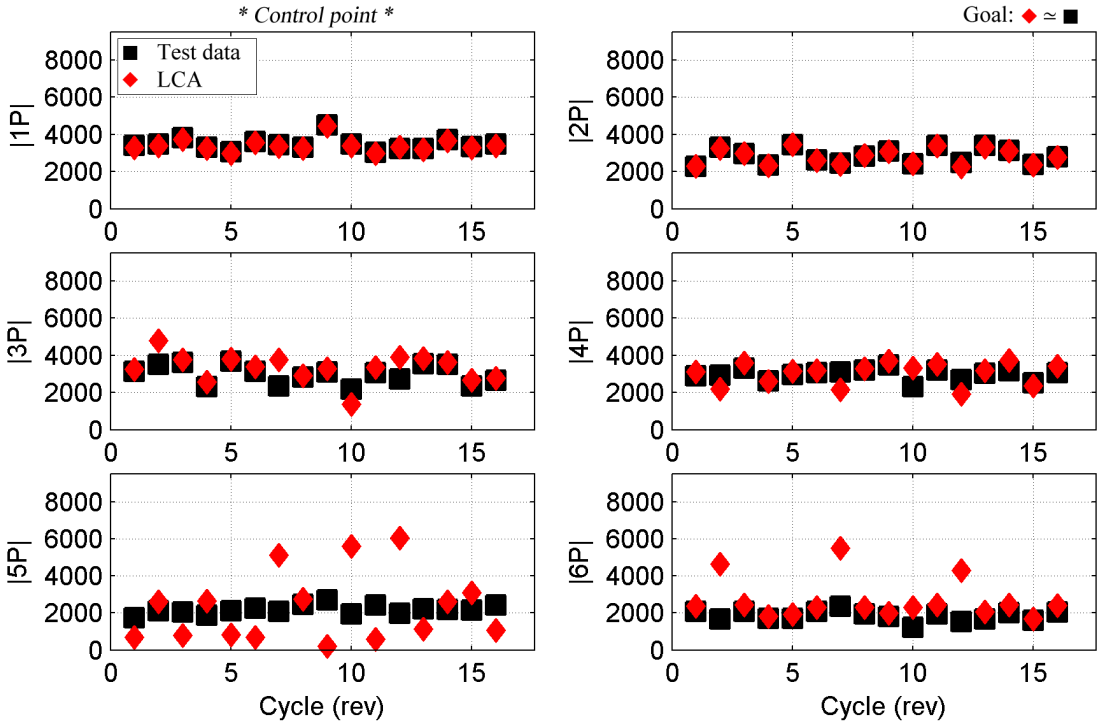

Figure 4.102: Loads matching by harmonic: all cycles of c9017: SE70 (in-lb).

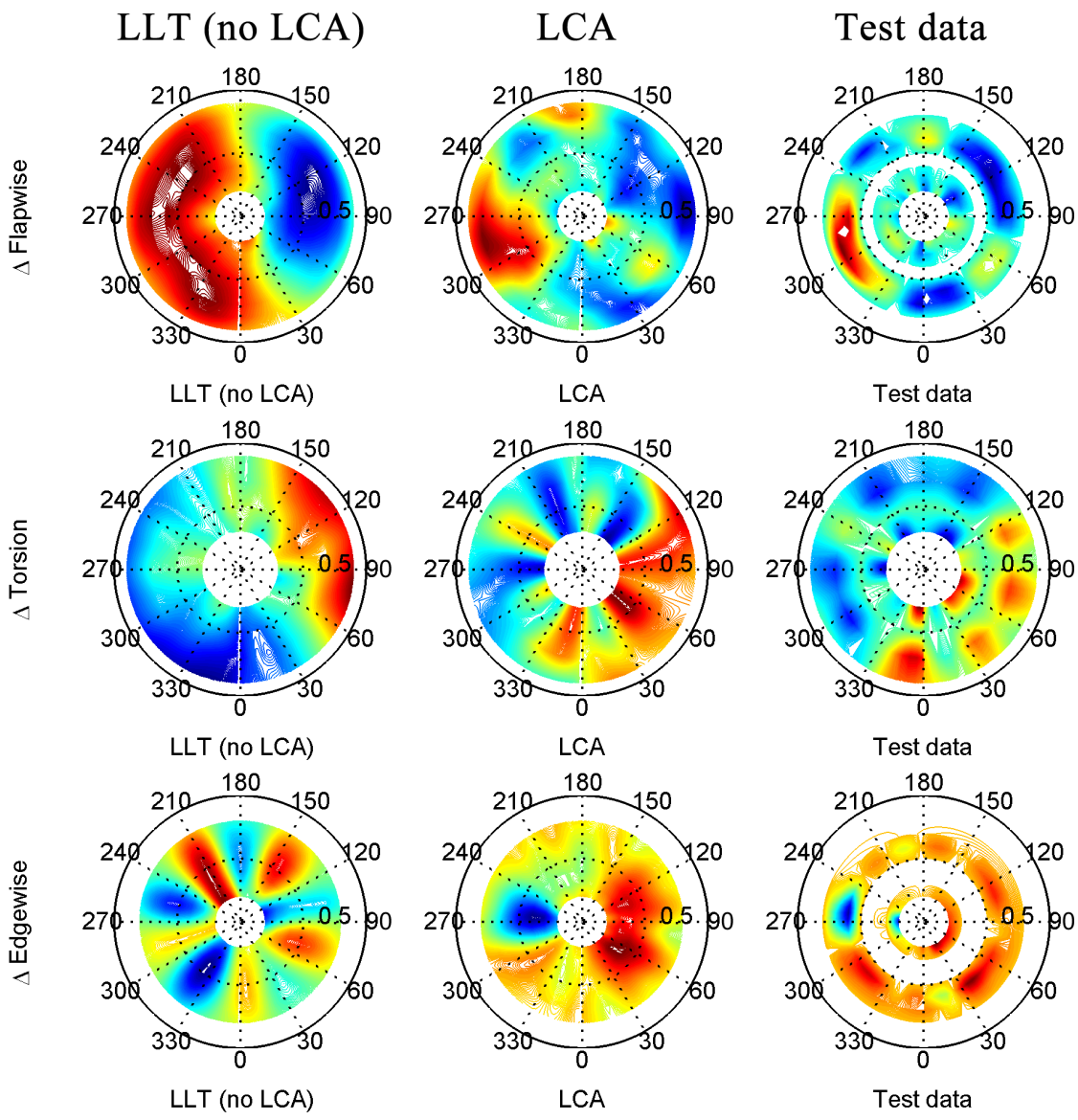

Figure 4.103: Flapwise, torsional, edgewise moments: radial, azimuthal distribution; cycle 1 [flight counter, μ] = [9017, 0.237] (top-to-bottom); red (peak), blue (valley).

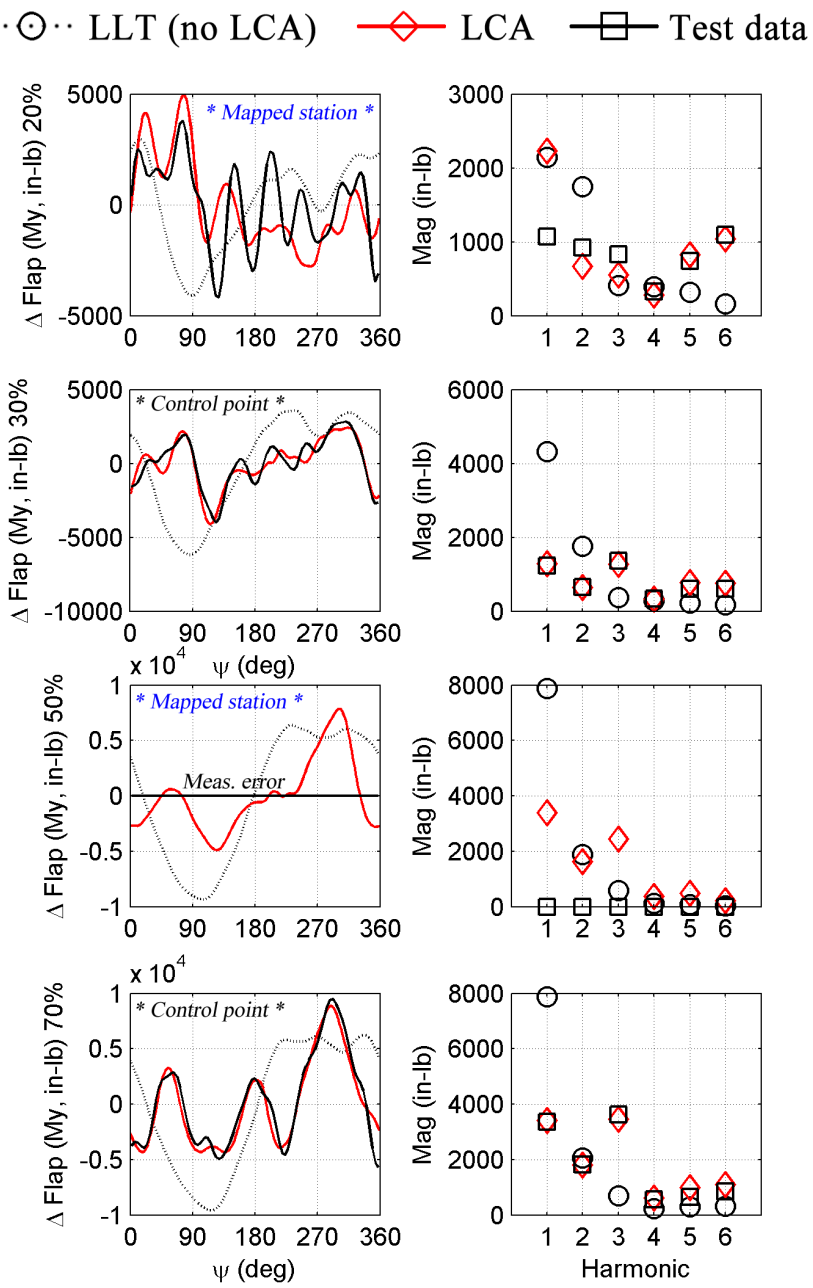

Figure 4.104: Flapwise bending moment: time history, load component by harmonic; cycle 1 [flight counter, μ] = [9017, 0.237]

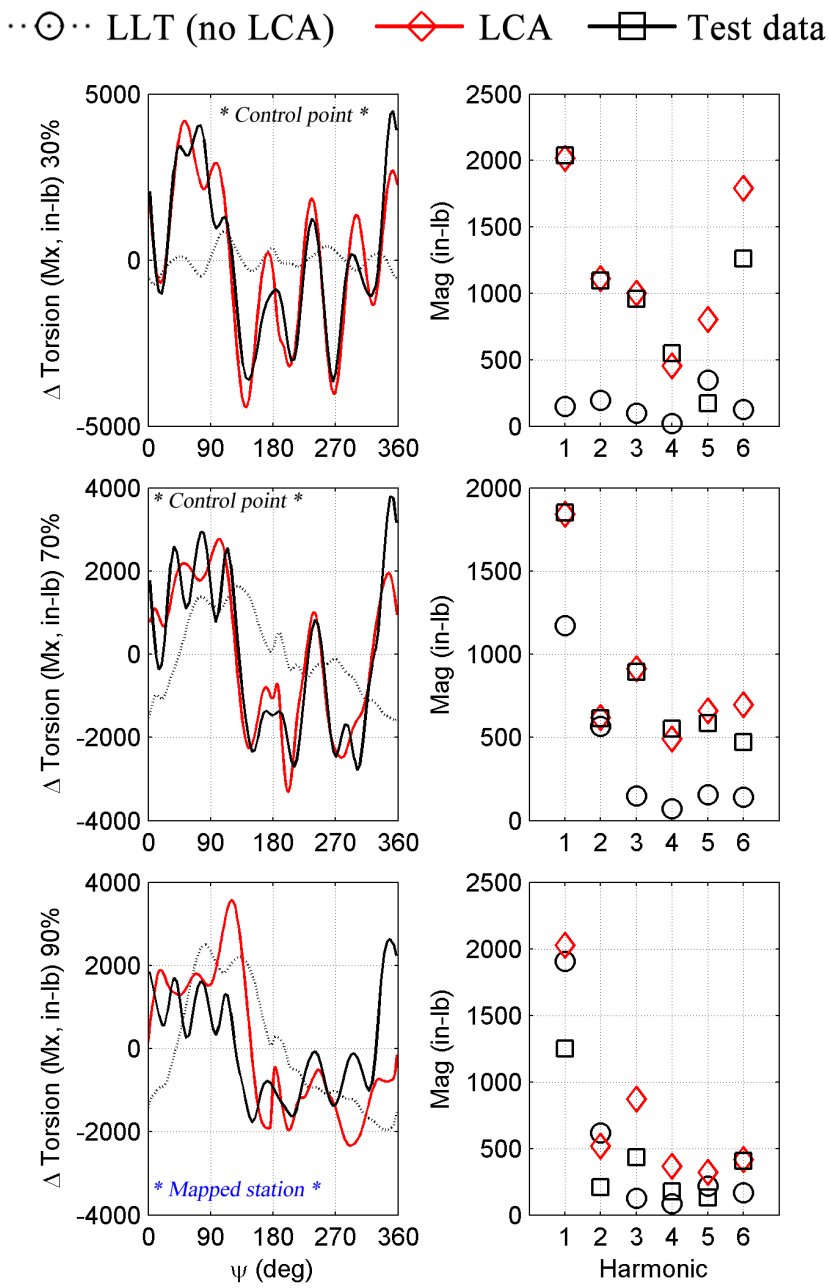

Figure 4.105: Torsional moment: time history, load component by harmonic; cycle 1 [flight counter, μ] = [9017, 0.237]

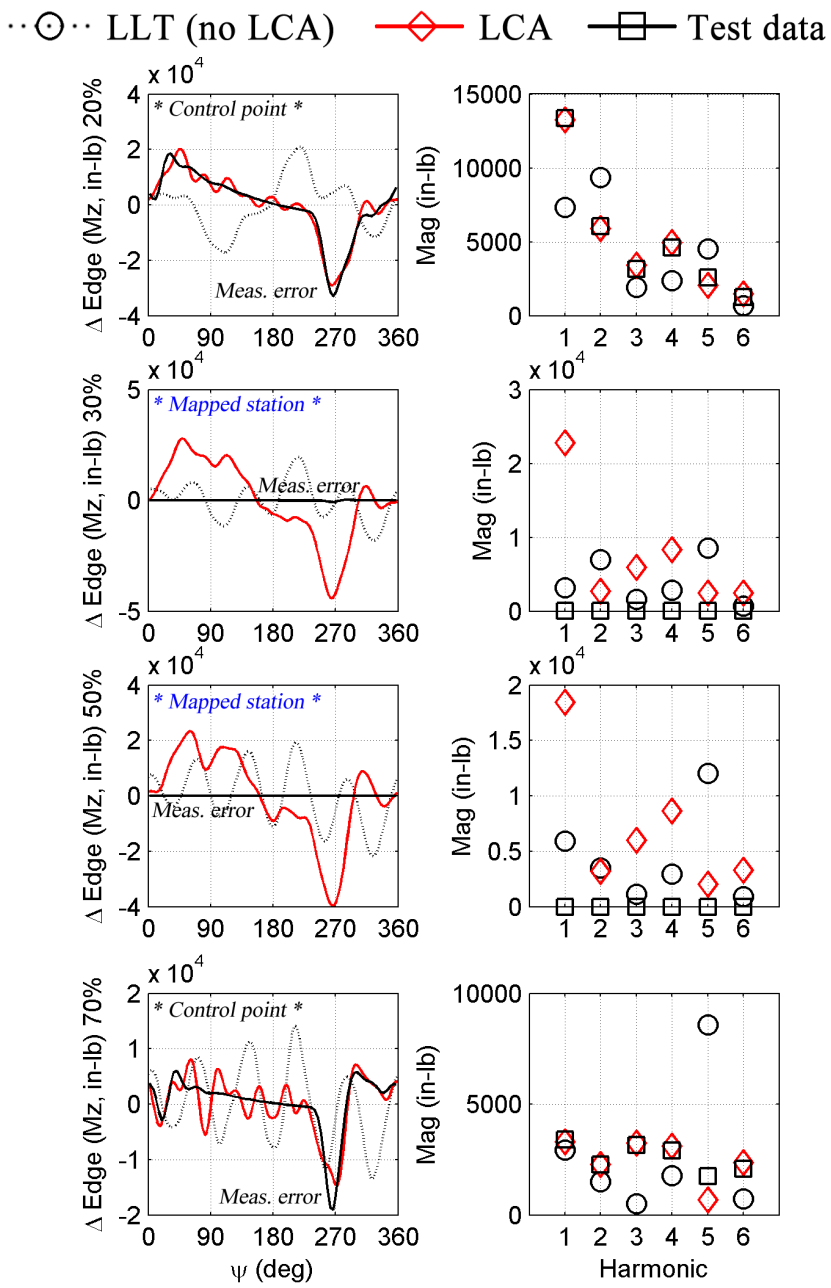

Figure 4.106: Edgewise bending moment: time history, load component by harmonic; cycle 1 [flight counter, μ] = [9017, 0.237]

4.6.8 Diving turn: c11679

Marpu et al. [57] studied c11679, a severe right turn diving maneuver (max N_z=1.69g). This condition - along with c11680 - produces critical blade and pushrod loads. Diving turns are characterized by high-speed and high-load factor. There is significant vibration in these flight conditions. The pushrod loads experienced during these severe maneuvers are about 2.5 times greater than the loads in maximum speed flight. For c11679, at the max N_z of 1.69g ($\approx$ cycle (rev) 20), the advancing side stall cycle mentioned above for c9017 (along with the two retreating side stall cycles) are observed.

Figures 4.107 through 4.113 show peak-to-peak loads for blade flapwise bending, torsional, and edgewise bending moments (as well as pushrod load) for the 34 cycles of this flight counter. Figures 4.114 through 4.123 show load magnitudes by harmonic for these cycles as well. The response varies with N_z, maximized at cycle 24, which is examined in detail, along with cycle 23 (Figures 4.124 through 4.131). Both cycles 23 and 24 are studied, because the first provides an excellent match (cycle 24); the second (cycle 23) is not as effective a match.

The presence of the stall cycles is evident in Figures 4.125 and 4.129 for blade torsional moment, with peaks in Q1 and Q4 across the blade span.

The LCA provides a good loads match for this flight counter, with the following observations:

1. SE is over-predicted throughout - all due to an over-prediction of $5P$ load content (see Figures 4.120 through 4.123). This could be remedied in the LCA by deactivating a correction by harmonic if the resulting response is too high.

2. ST70 over-predicts the $3P$ load content, more so at higher N_z.

3. An excellent match is seen for other load stations, including pushrod peak-to-peak load (Figure 4.112).

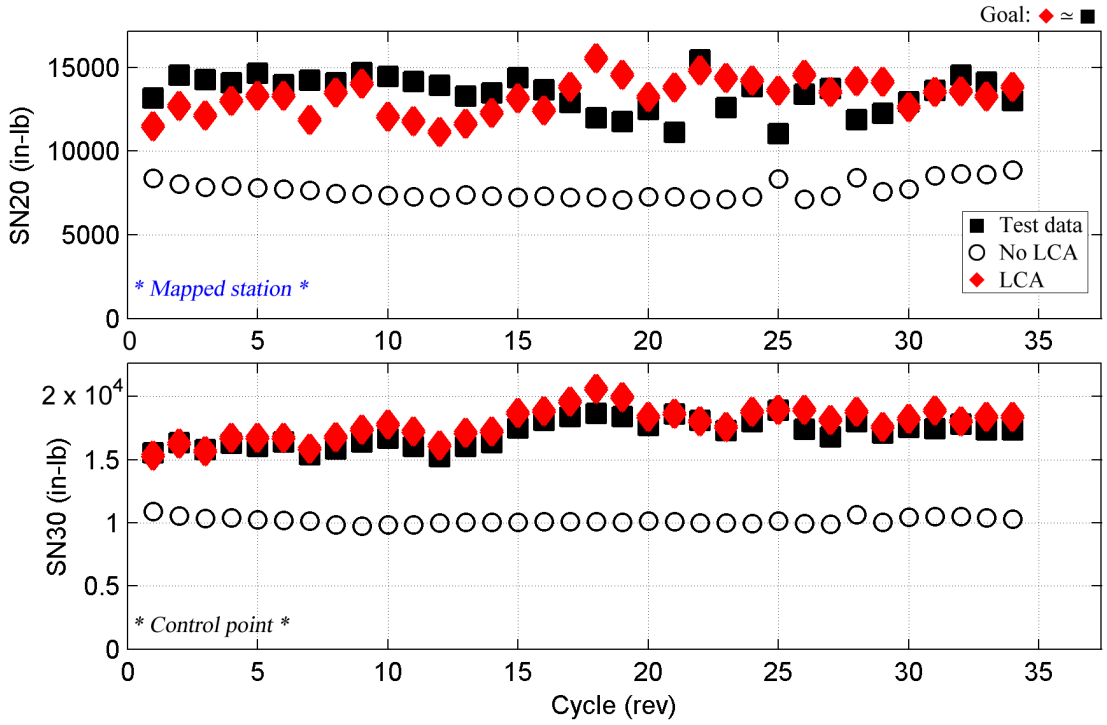

Figure 4.107: Peak-to-peak loads matching: all cycles of c11679: SN20, SN30.

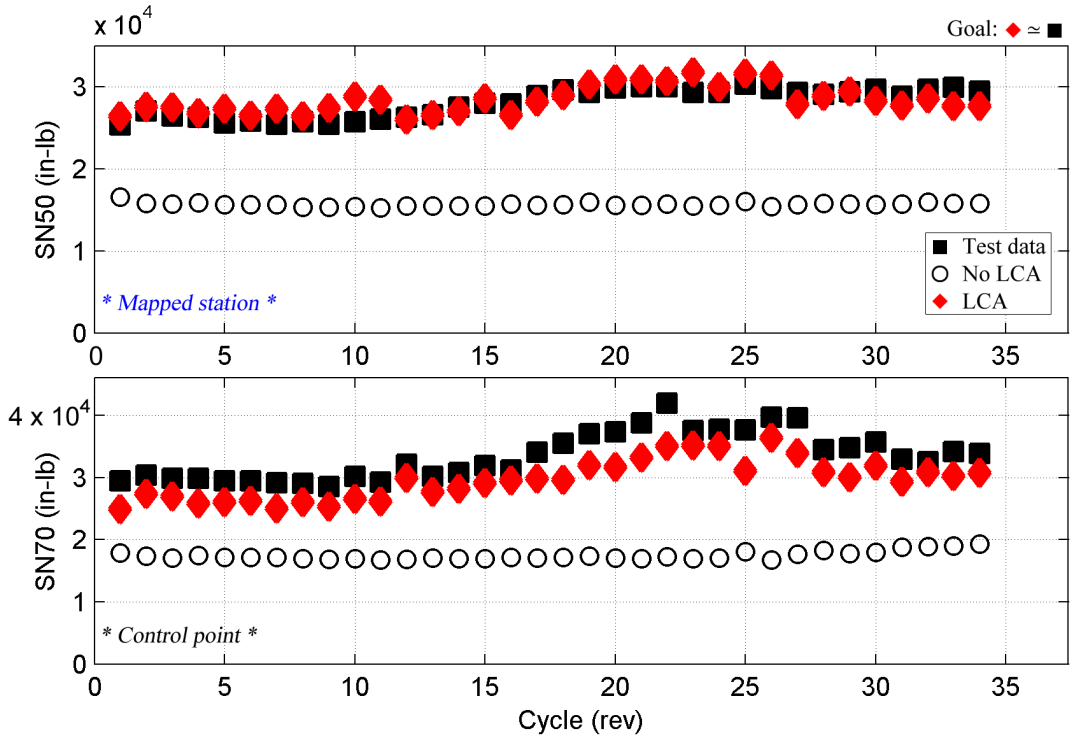

Figure 4.108: Peak-to-peak loads matching: all cycles of c11679: SN50, SN70.

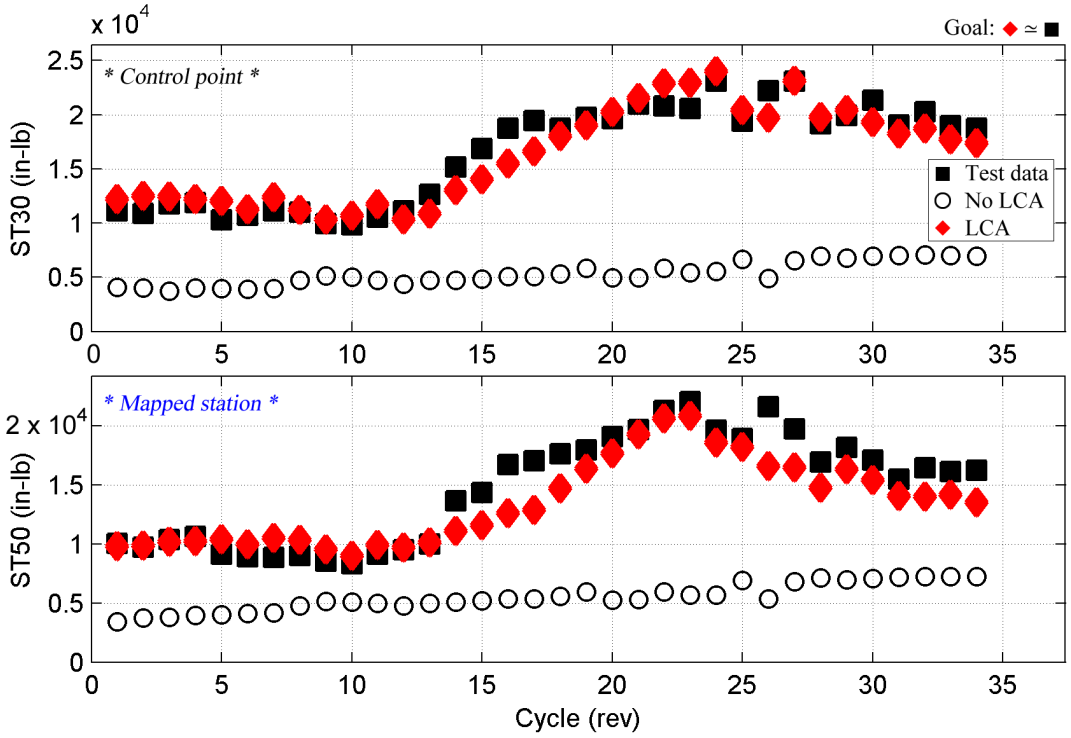

Figure 4.109: Peak-to-peak loads matching: all cycles of c11679: ST30, ST50.

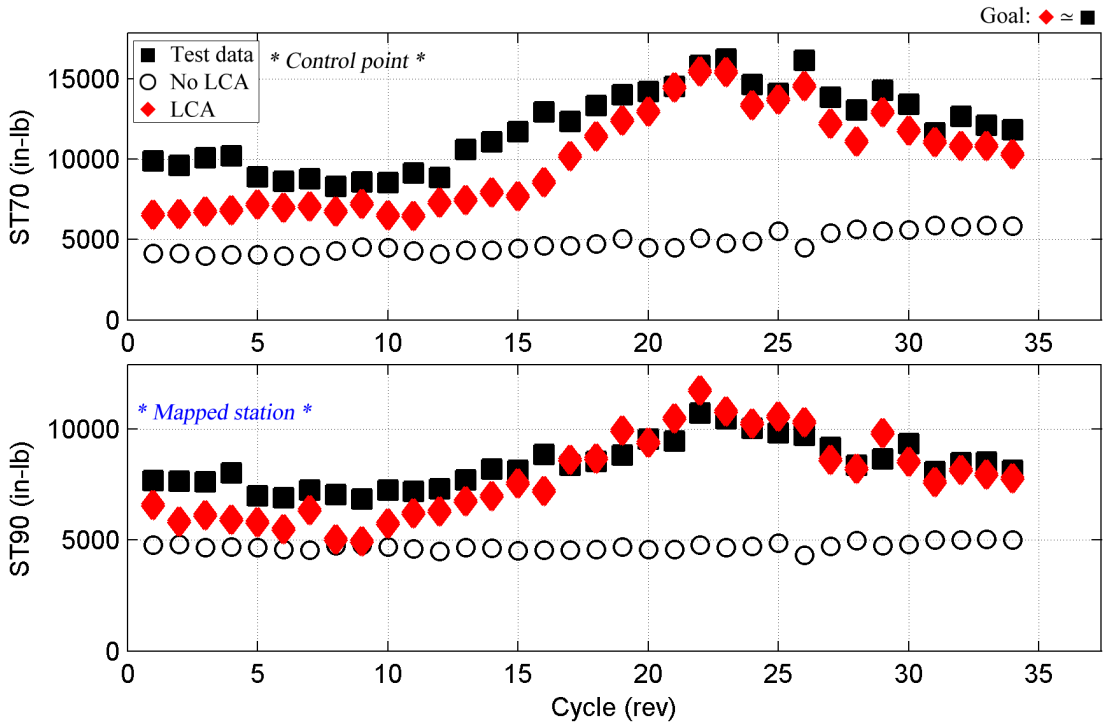

Figure 4.110: Peak-to-peak loads matching: all cycles of c11679: ST70, ST90.

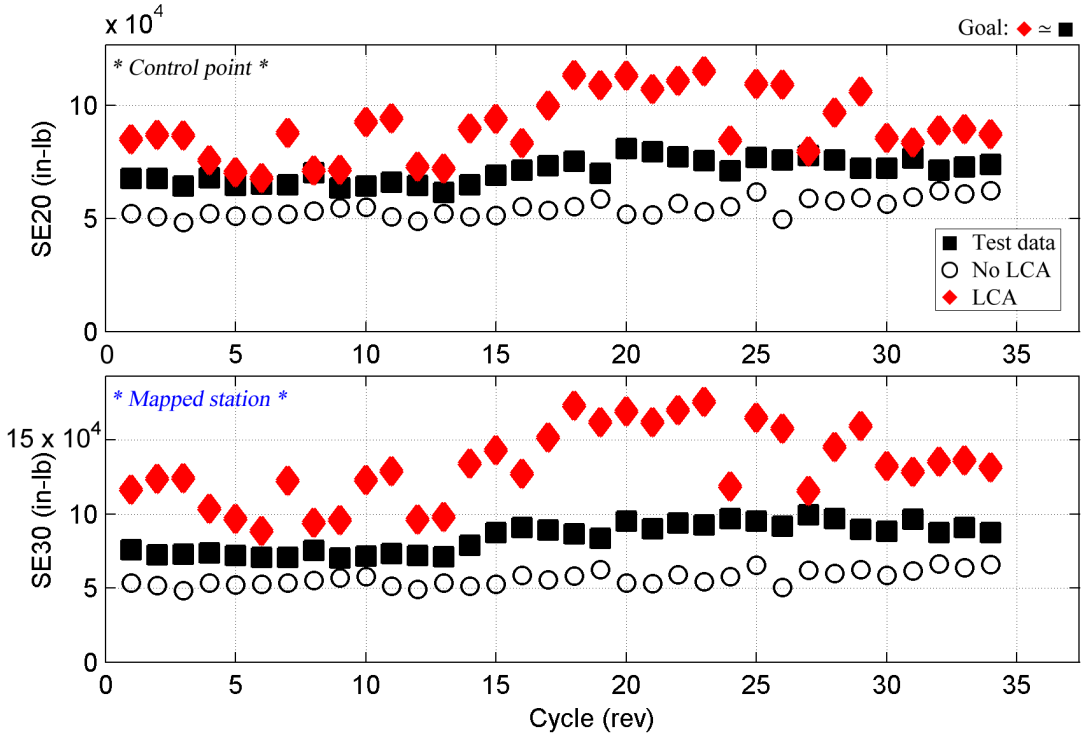

Figure 4.111: Peak-to-peak loads matching: all cycles of c11679: SE20, SE30.

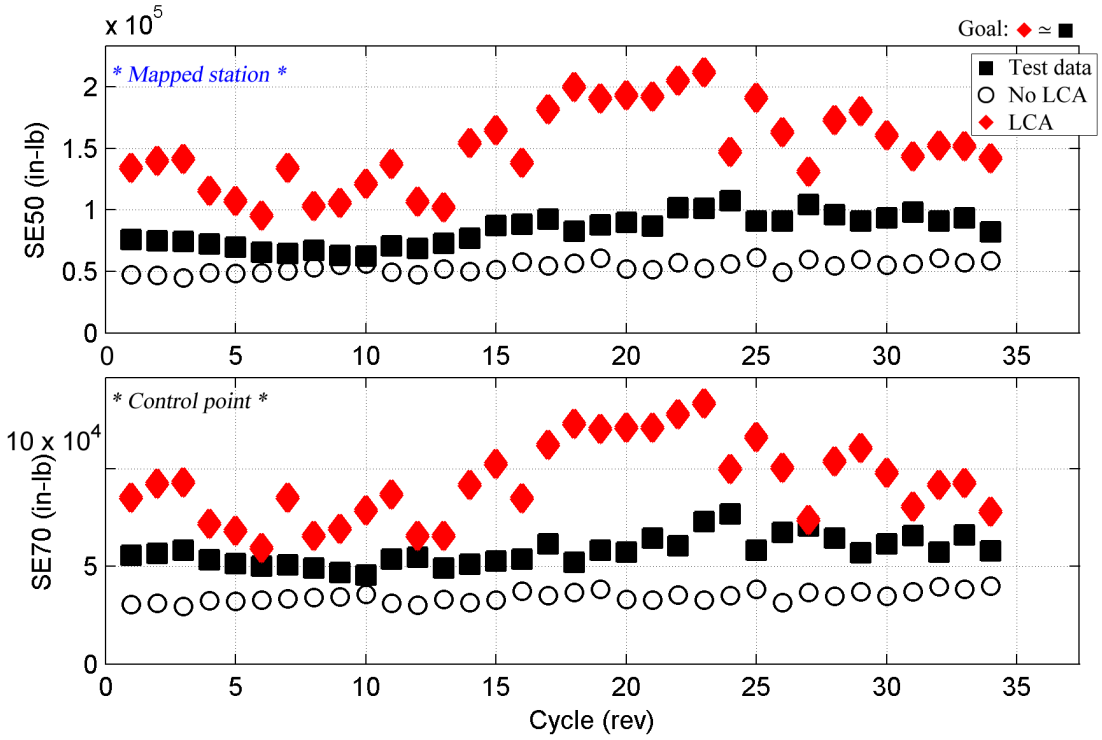

Figure 4.112: Peak-to-peak loads matching: all cycles of c11679: SE50, SE70.

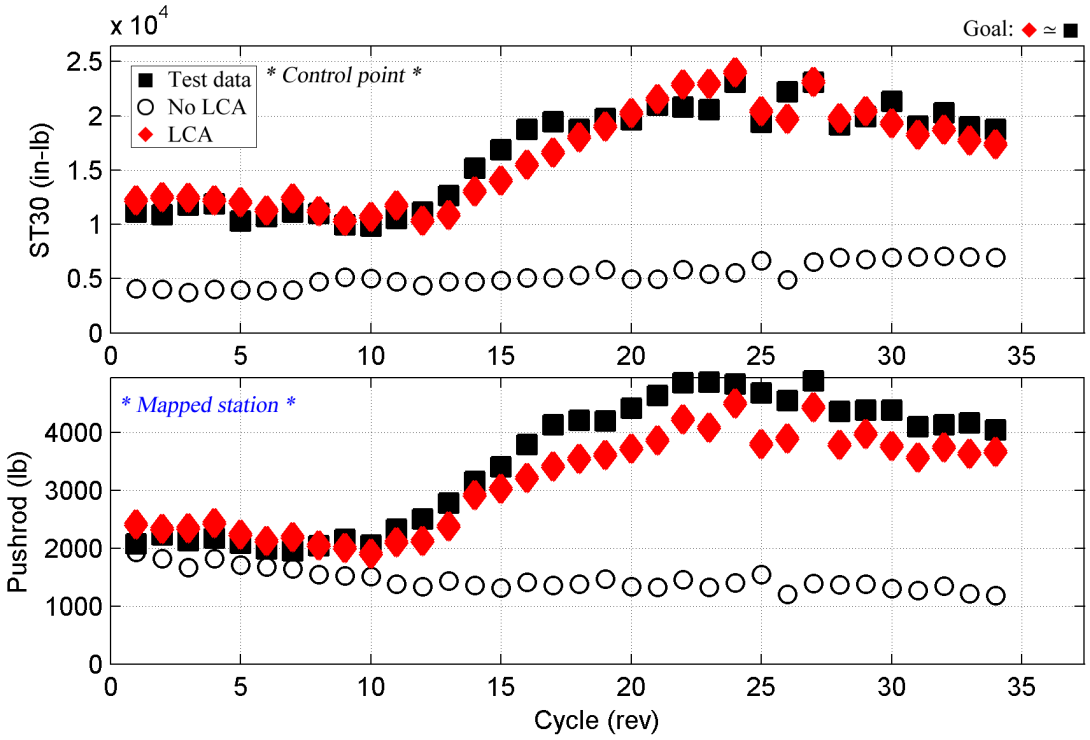

Figure 4.113: Peak-to-peak loads matching: all cycles of c11679: ST30, pushrod.

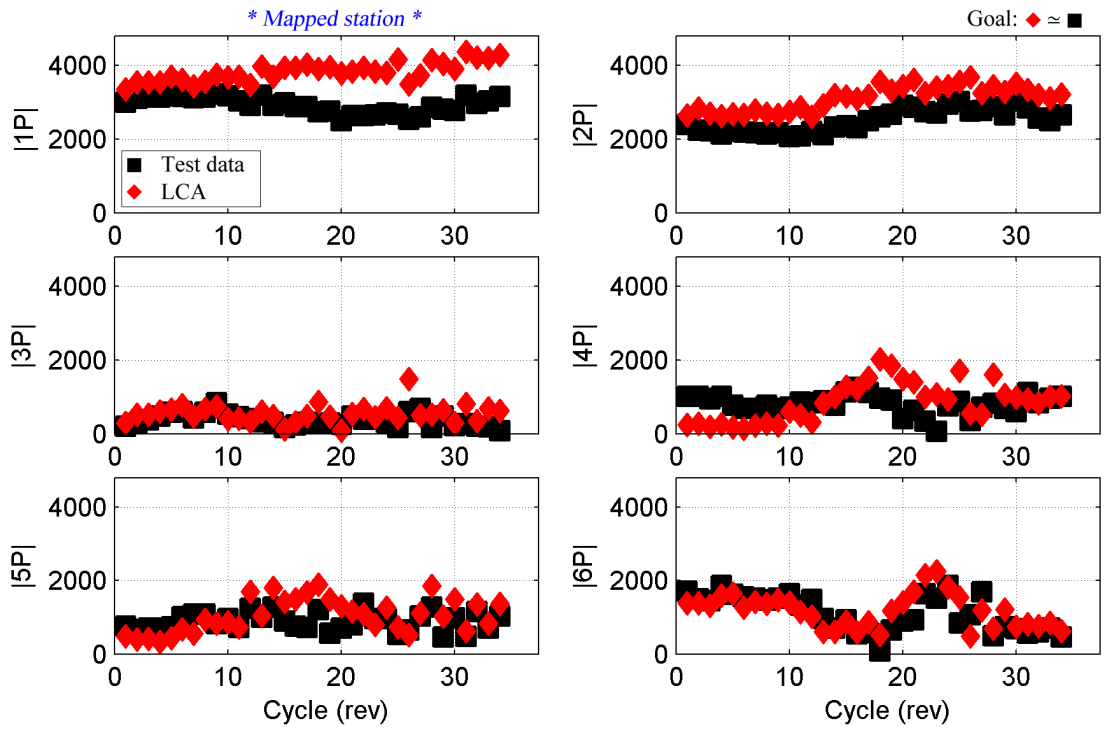

Figure 4.114: Loads matching by harmonic: all cycles of c11679: SN20 (in-lb).

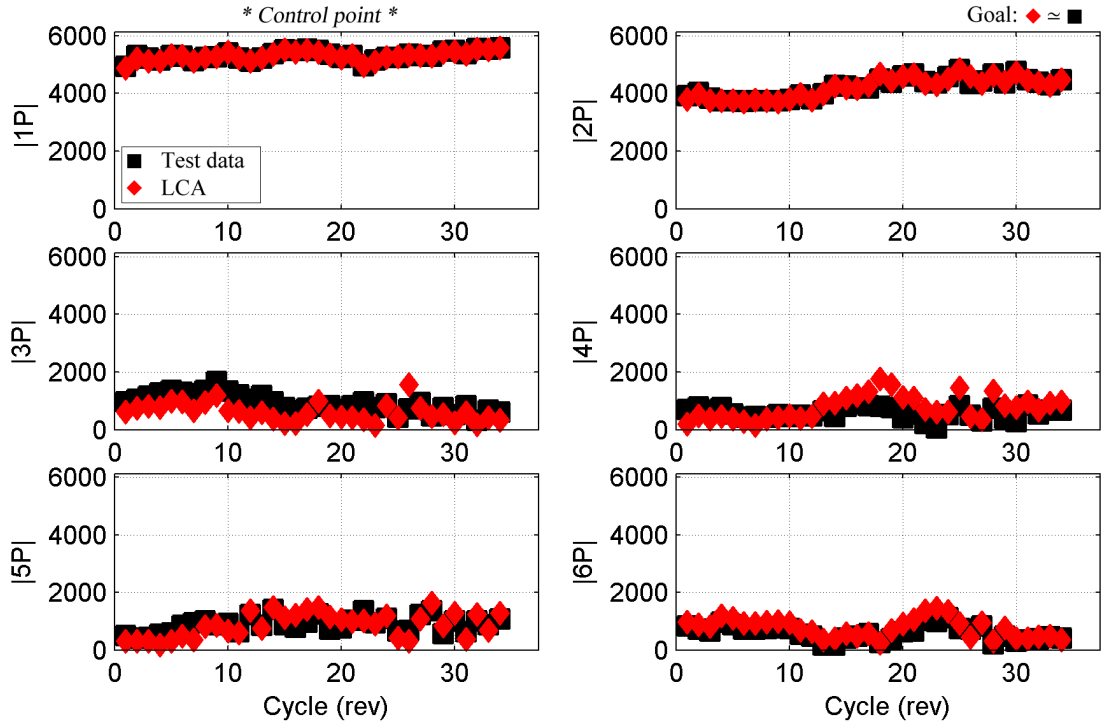

Figure 4.115: Loads matching by harmonic: all cycles of c11679: SN30 (in-lb).

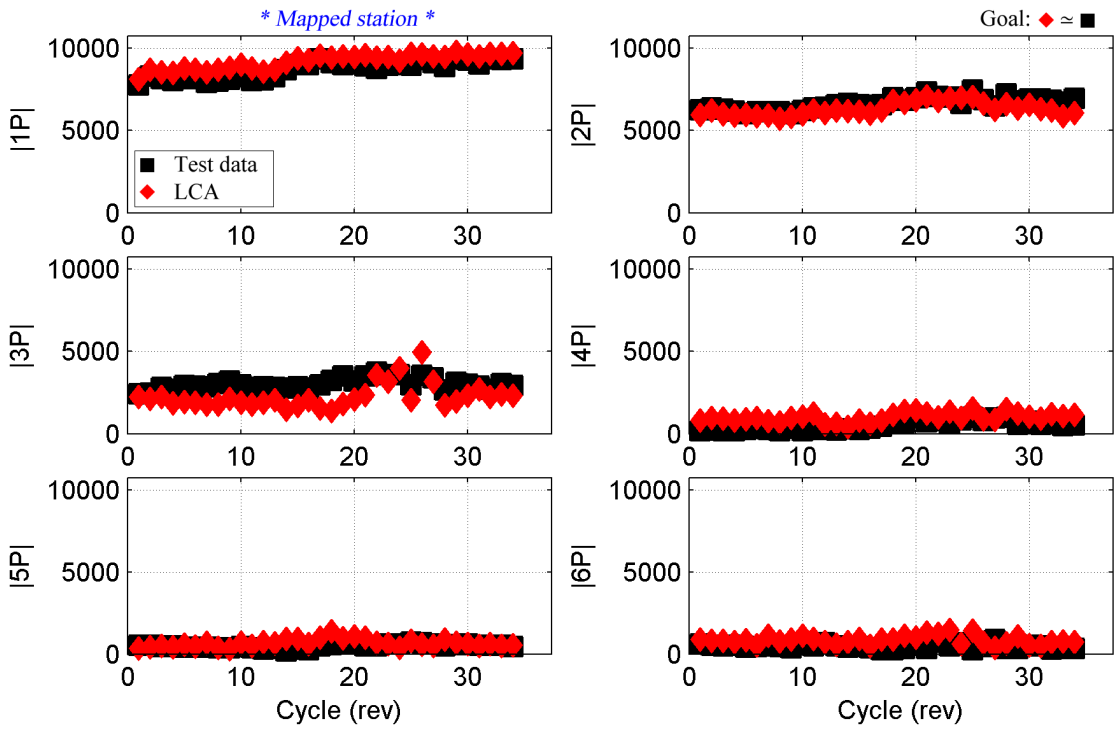

Figure 4.116: Loads matching by harmonic: all cycles of c11679: SN50 (in-lb).

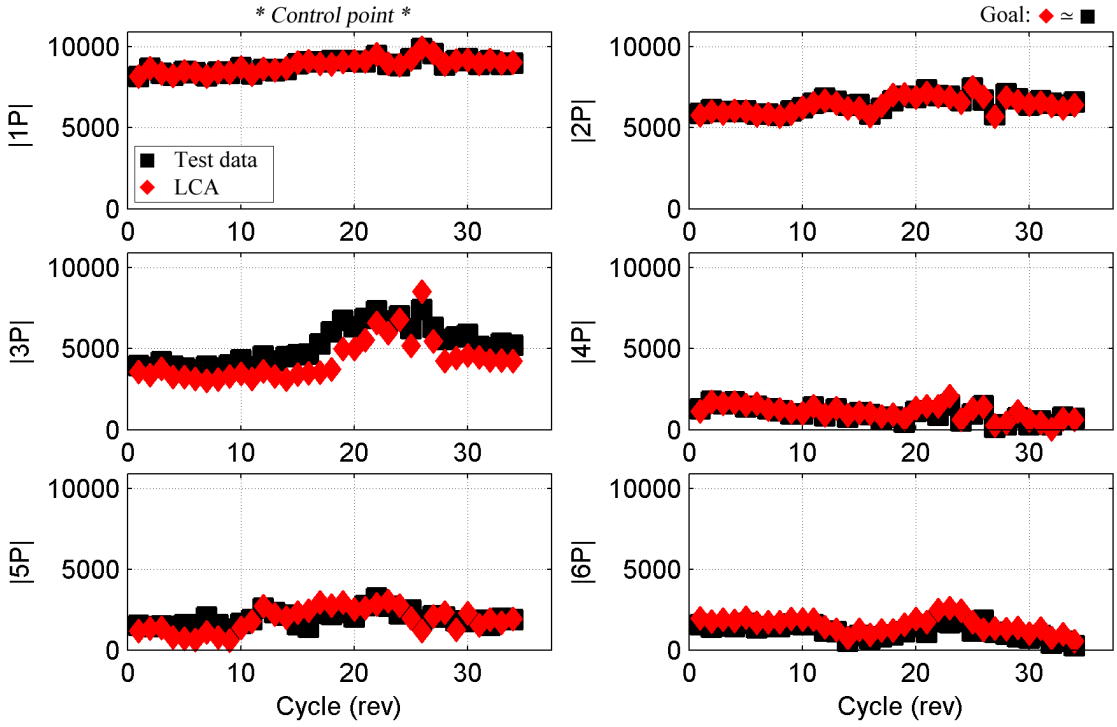

Figure 4.117: Loads matching by harmonic: all cycles of c11679: SN70 (in-lb).

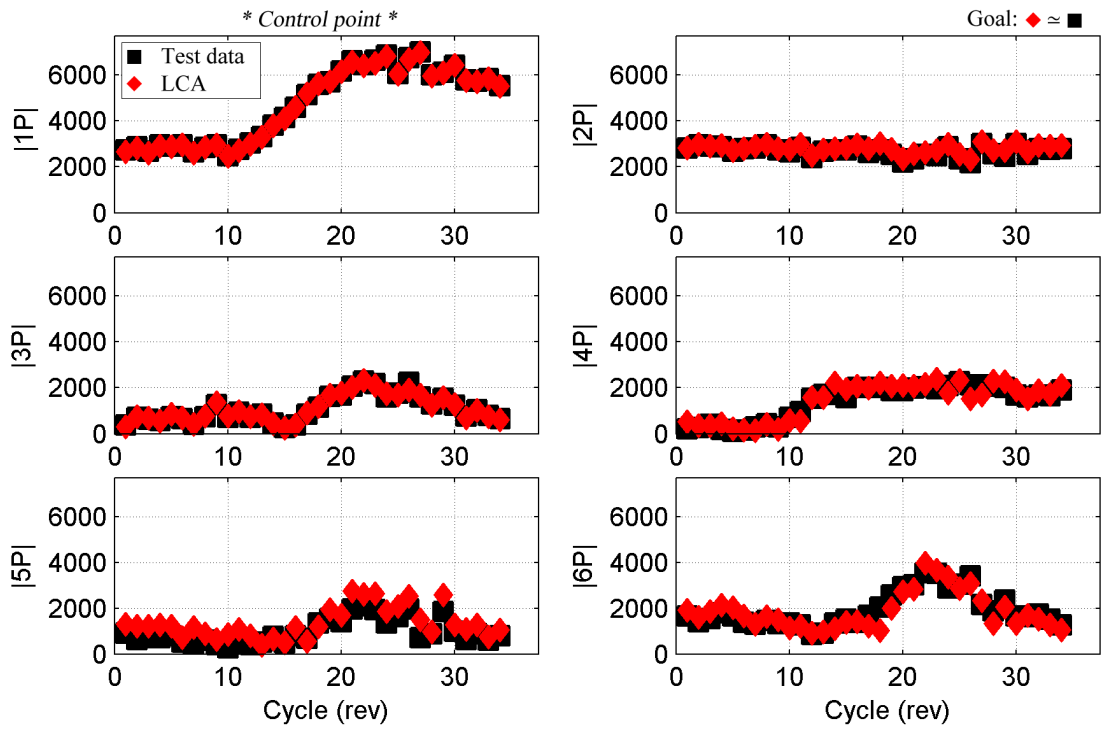

Figure 4.118: Loads matching by harmonic: all cycles of c11679: ST30 (in-lb).

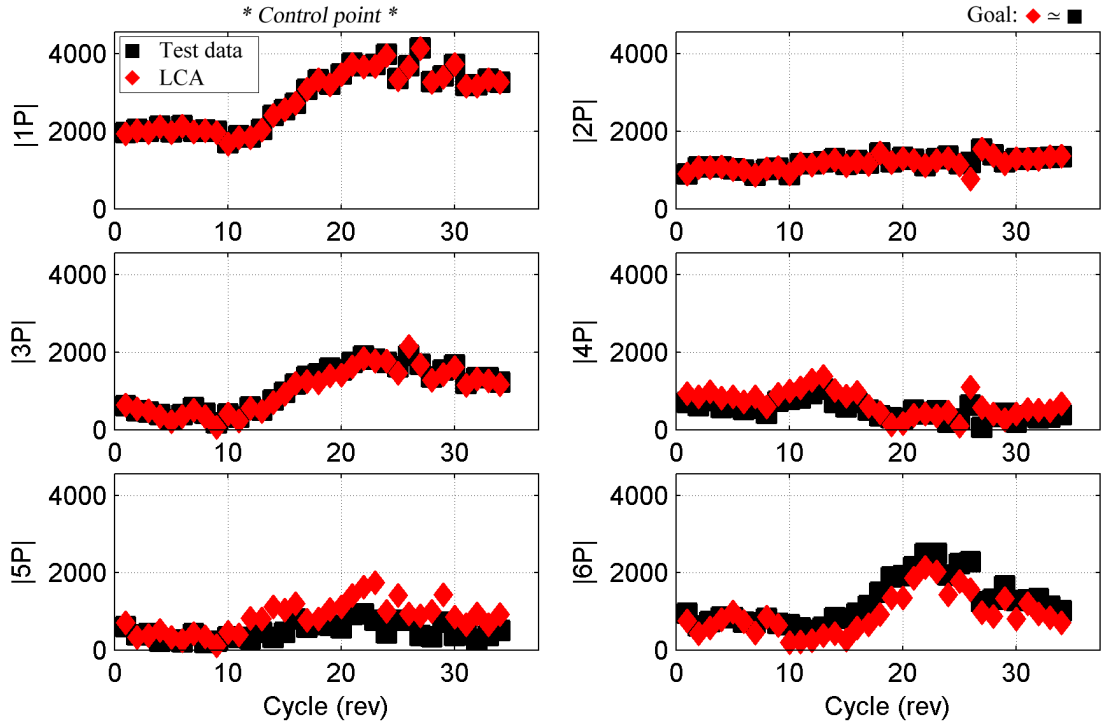

Figure 4.119: Loads matching by harmonic: all cycles of c11679: ST70 (in-lb).

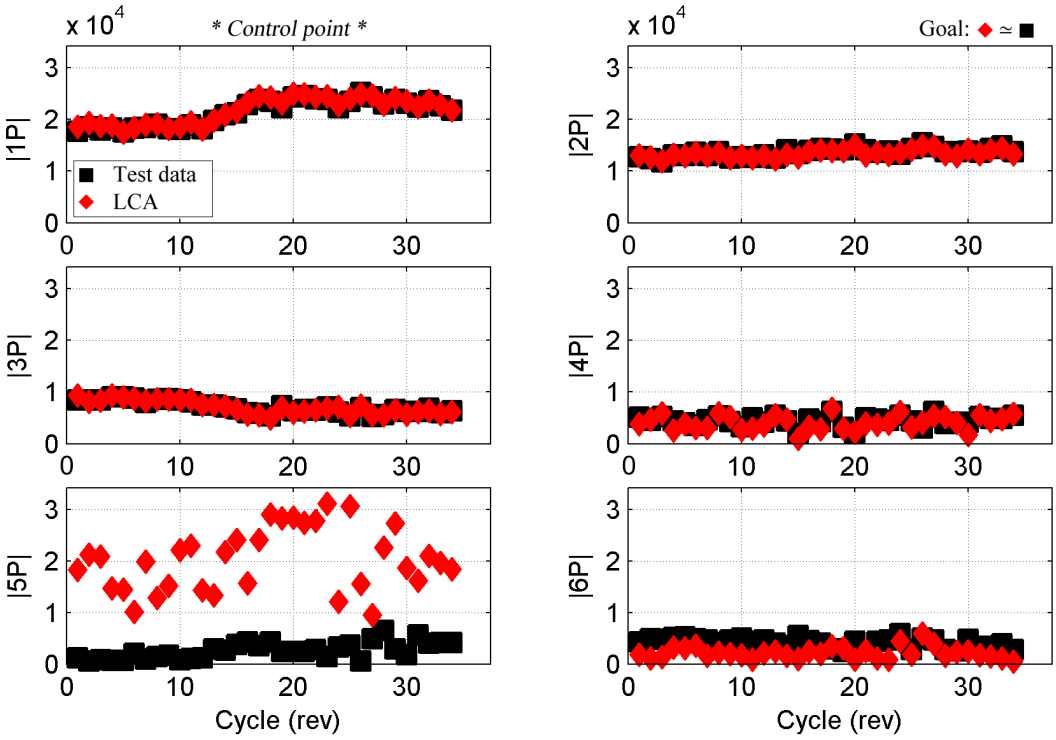

Figure 4.120: Loads matching by harmonic: all cycles of c11679: SE20 (in-lb).

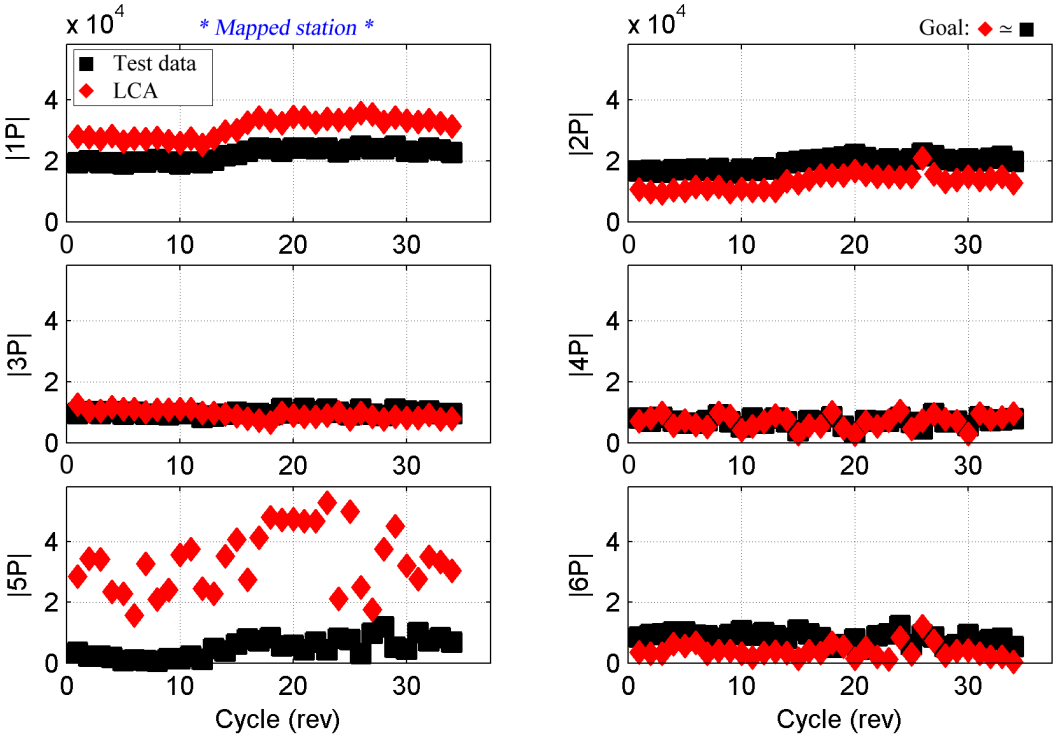

Figure 4.121: Loads matching by harmonic: all cycles of c11679: SE30 (in-lb).

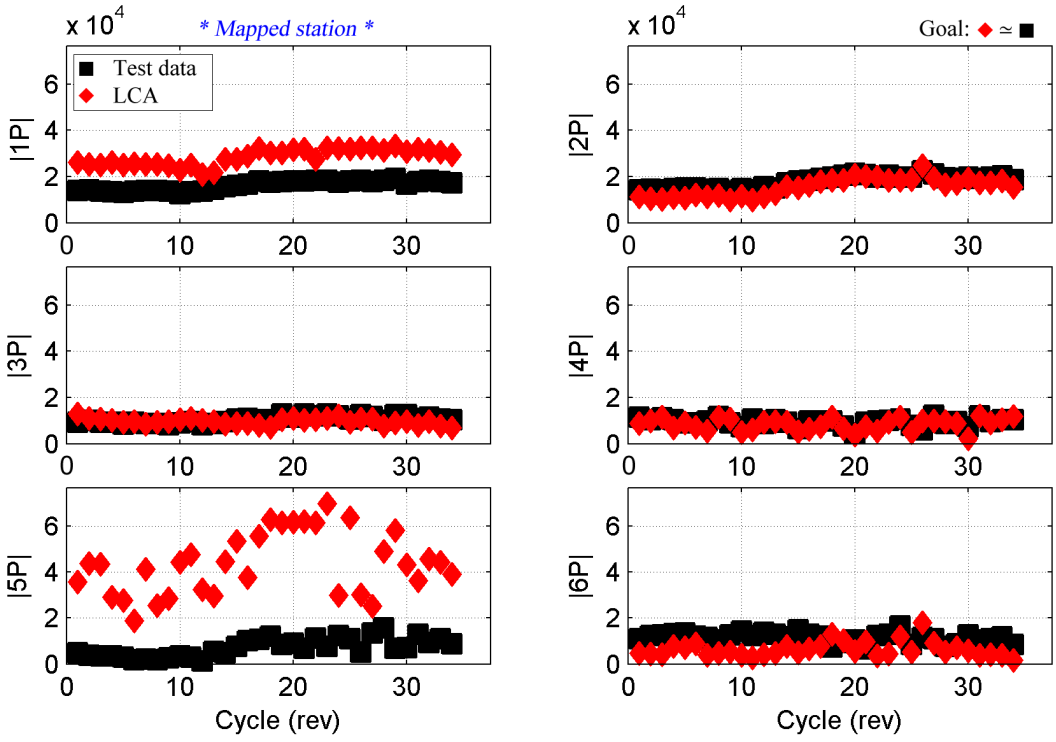

Figure 4.122: Loads matching by harmonic: all cycles of c11679: SE50 (in-lb).

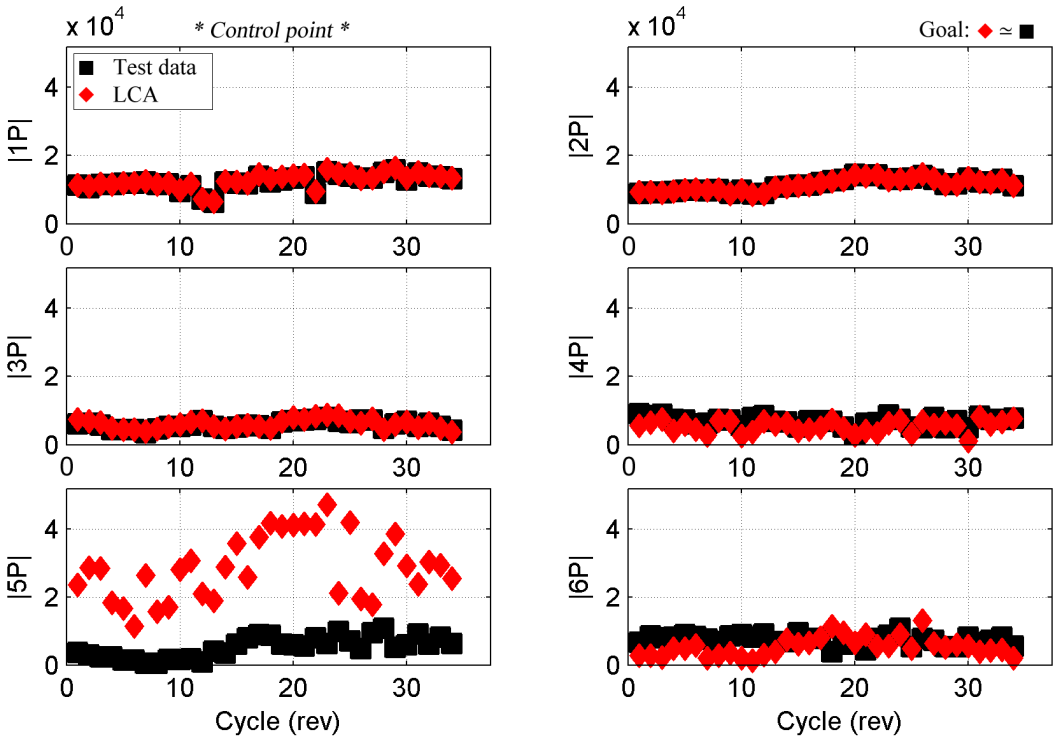

Figure 4.123: Loads matching by harmonic: all cycles of c11679: SE70 (in-lb).

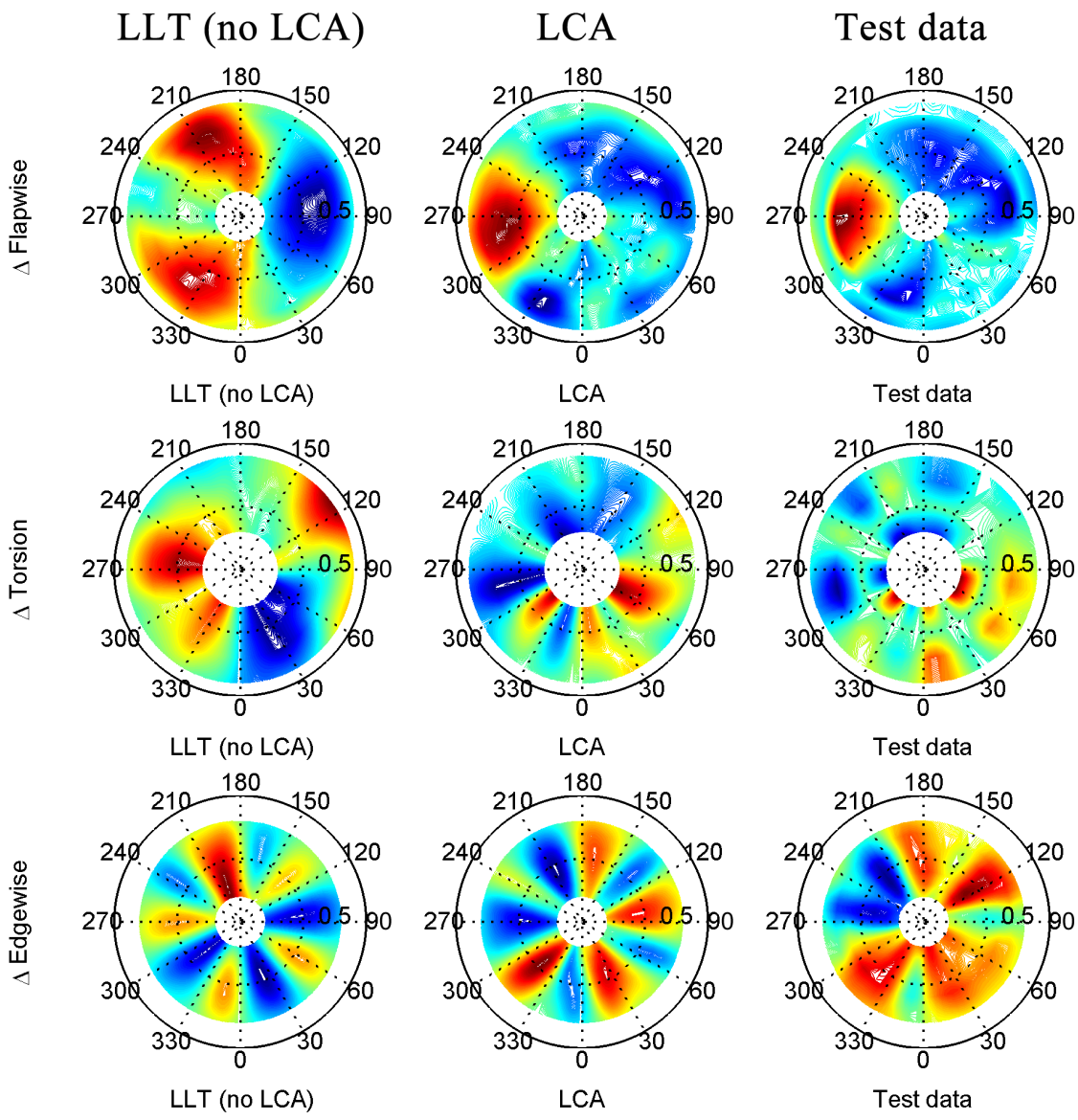

Figure 4.124: Flapwise, torsional, edgewise moments: radial, azimuthal distribution; cycle 23 [flight counter, μ] = [11679, 0.393] (top-to-bottom); red (peak), blue (valley).

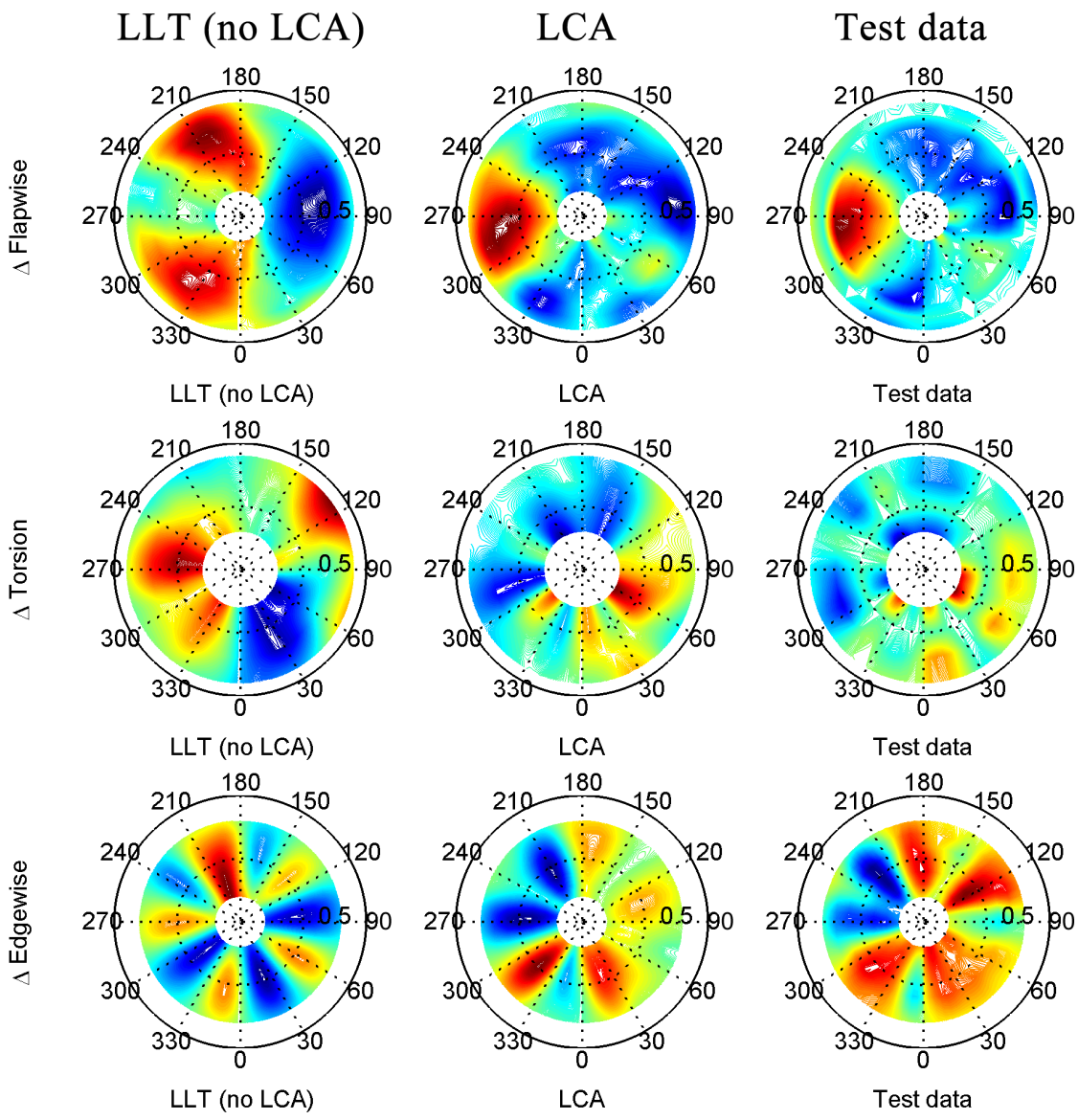

Figure 4.125: Flapwise, torsional, edgewise moments: radial, azimuthal distribution; cycle 24 [flight counter, μ] = [11679, 0.393] (top-to-bottom); red (peak), blue (valley).

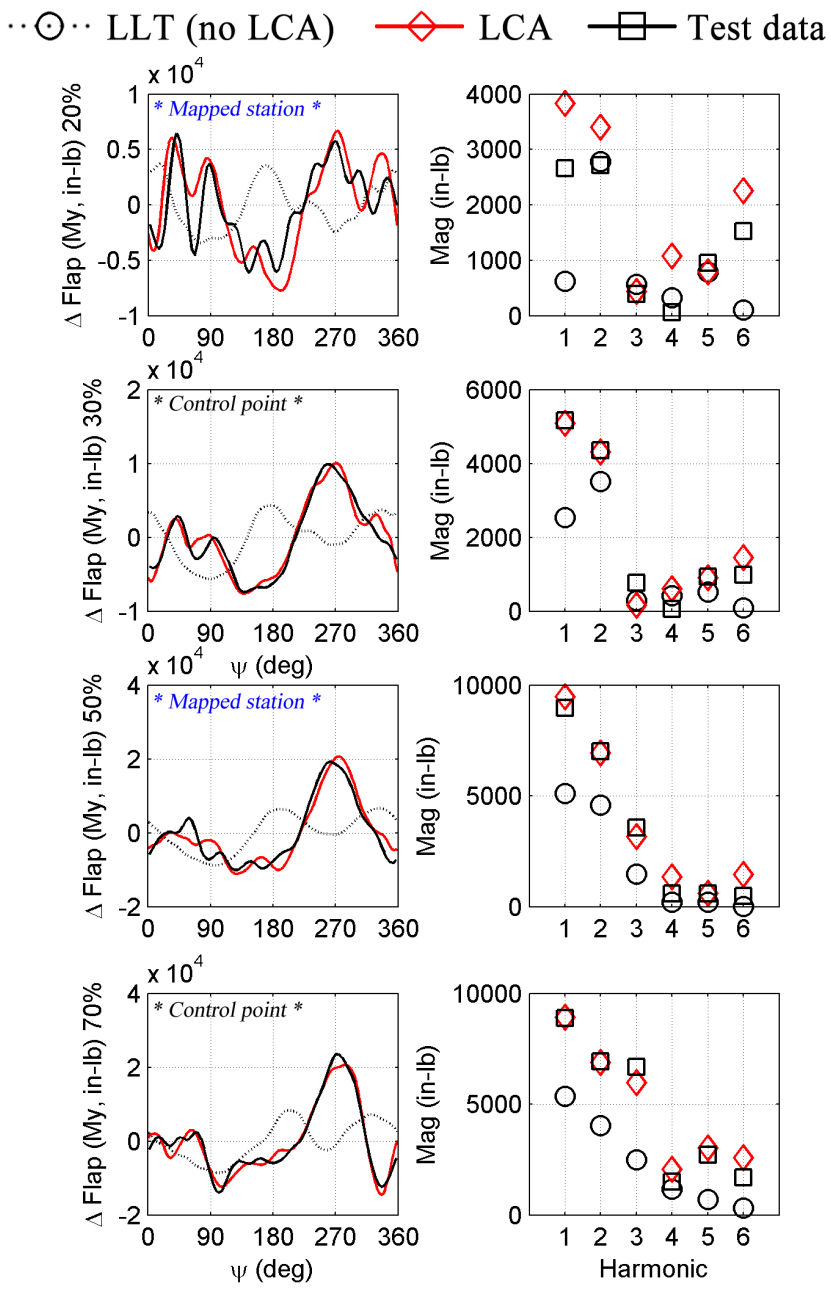

Figure 4.126: Flapwise bending moment: time history, load component by harmonic; cycle 23 [flight counter, μ] = [11679, 0.393]

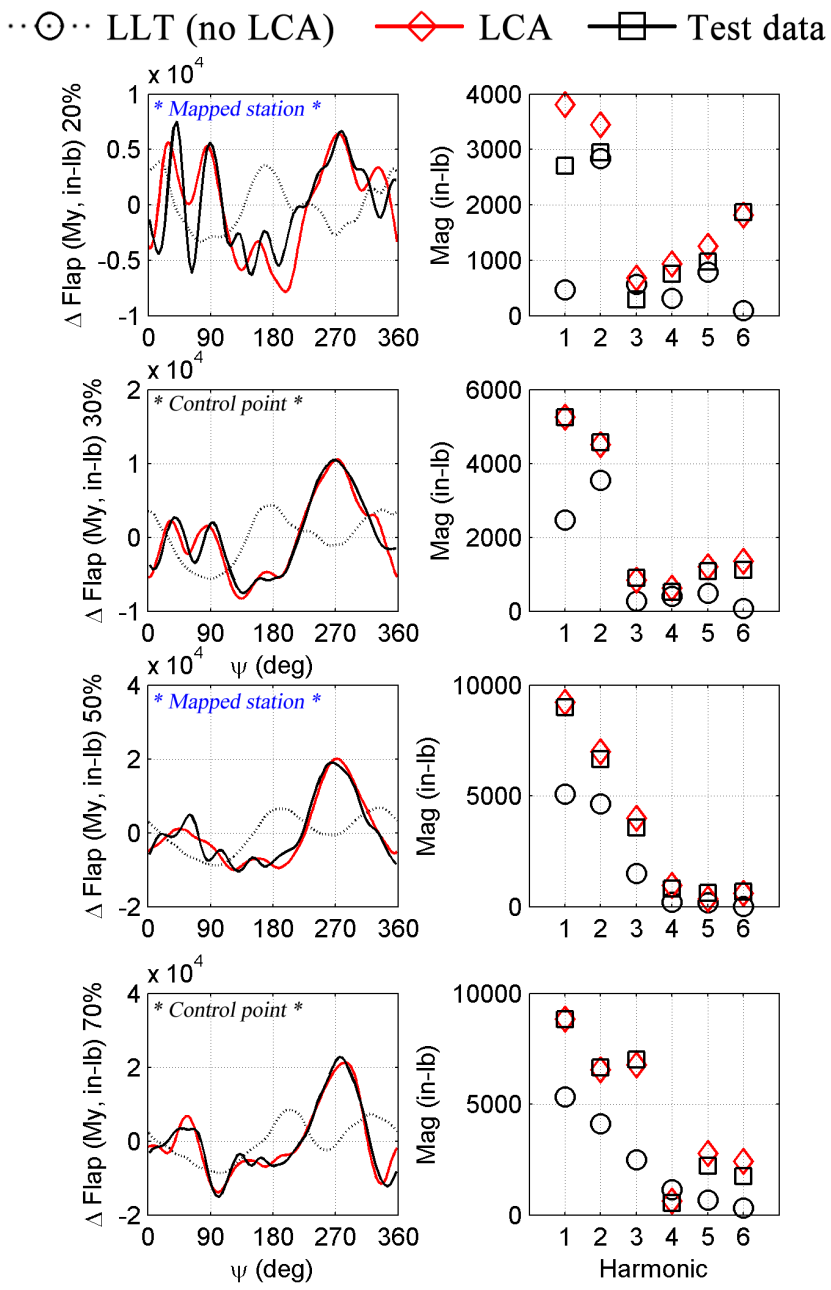

Figure 4.127: Flapwise bending moment: time history, load component by harmonic; cycle 24 [flight counter, μ] = [11679, 0.393]

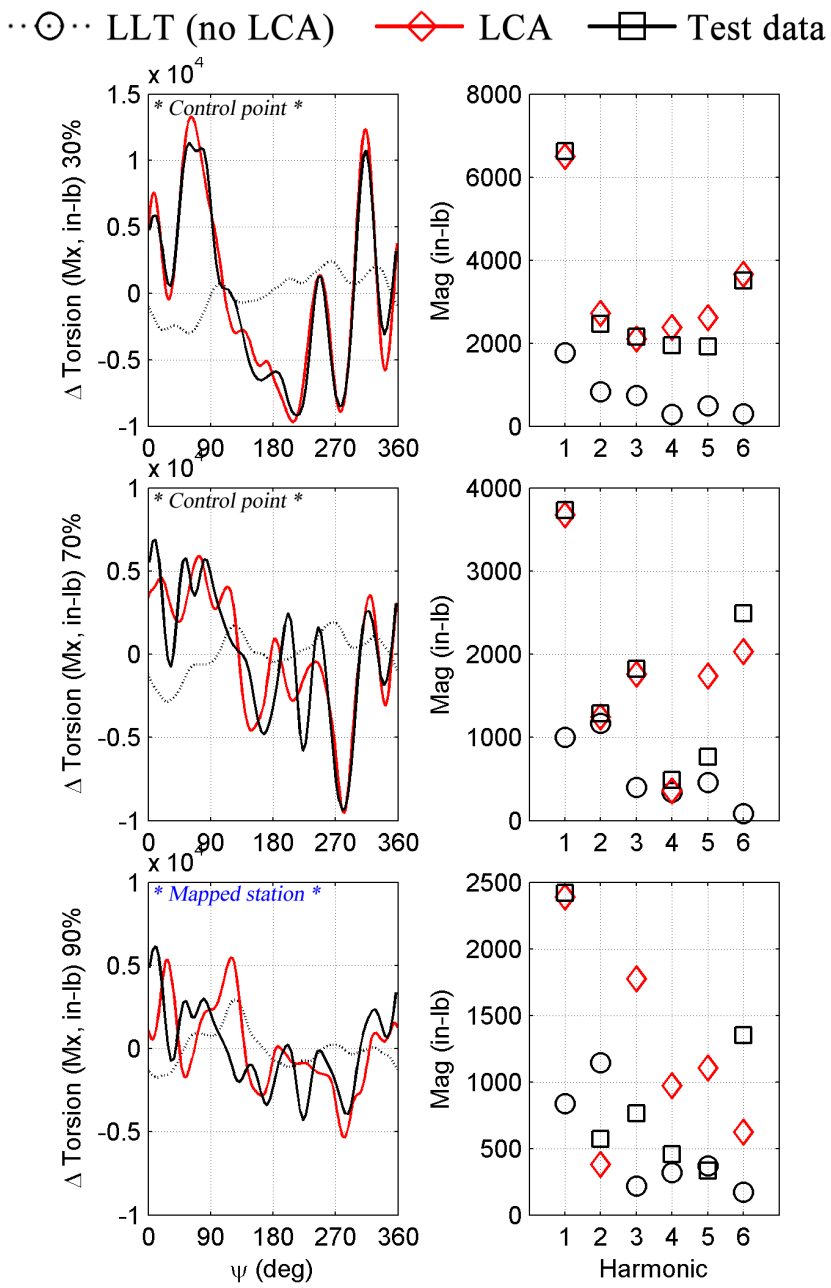

Figure 4.128: Torsional moment: time history, load component by harmonic; cycle 23 [flight counter, μ] = [11679, 0.393]

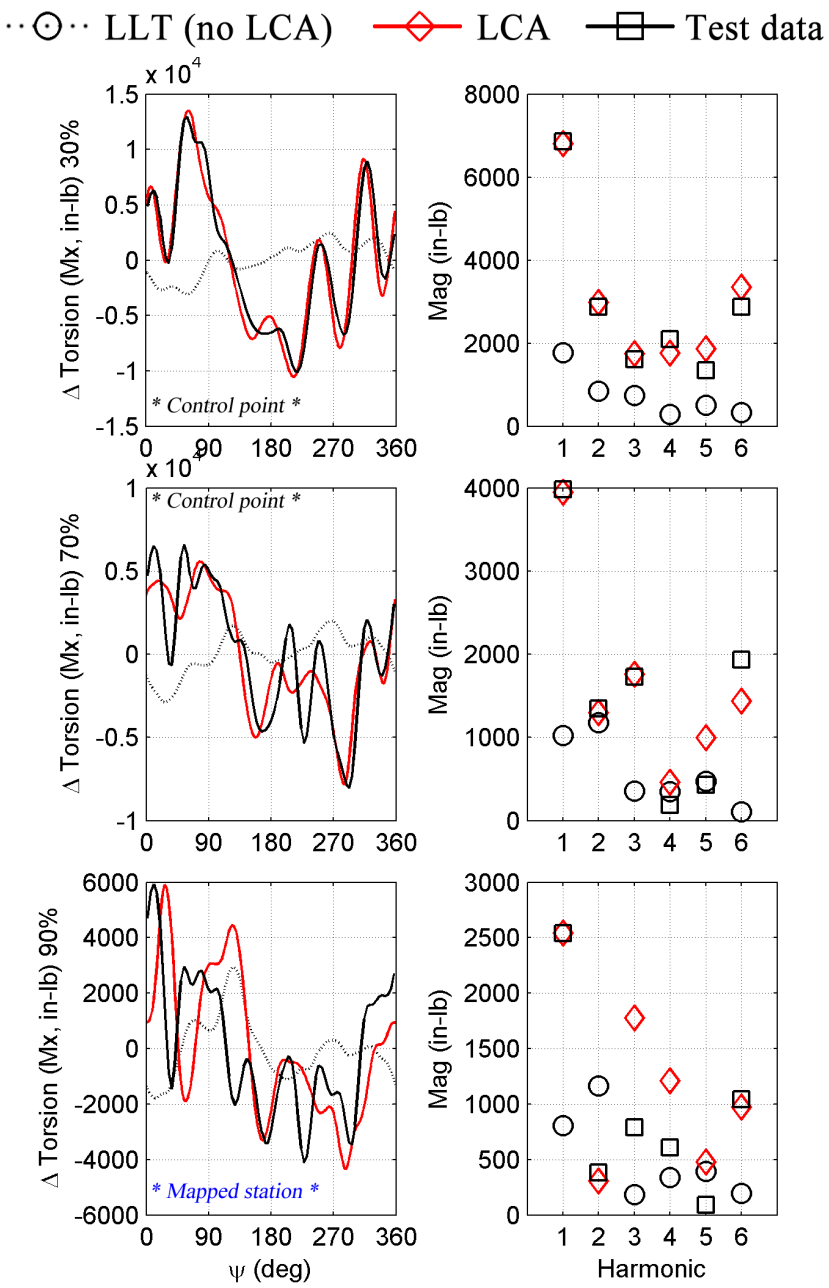

Figure 4.129: Torsional moment: time history, load component by harmonic; cycle 24 [flight counter, μ] = [11679, 0.393]

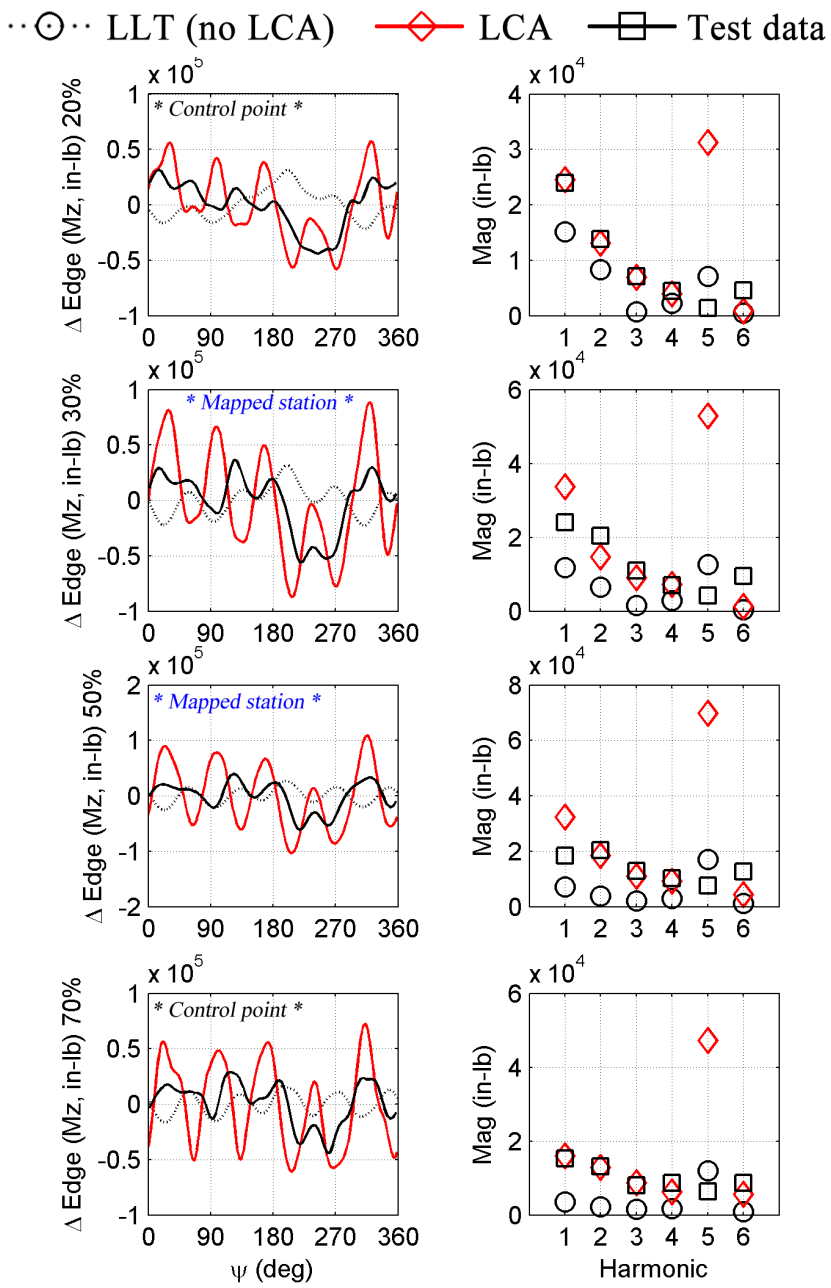

Figure 4.130: Edgewise bending moment: time history, load component by harmonic; cycle 23 [flight counter, μ] = [11679, 0.393]

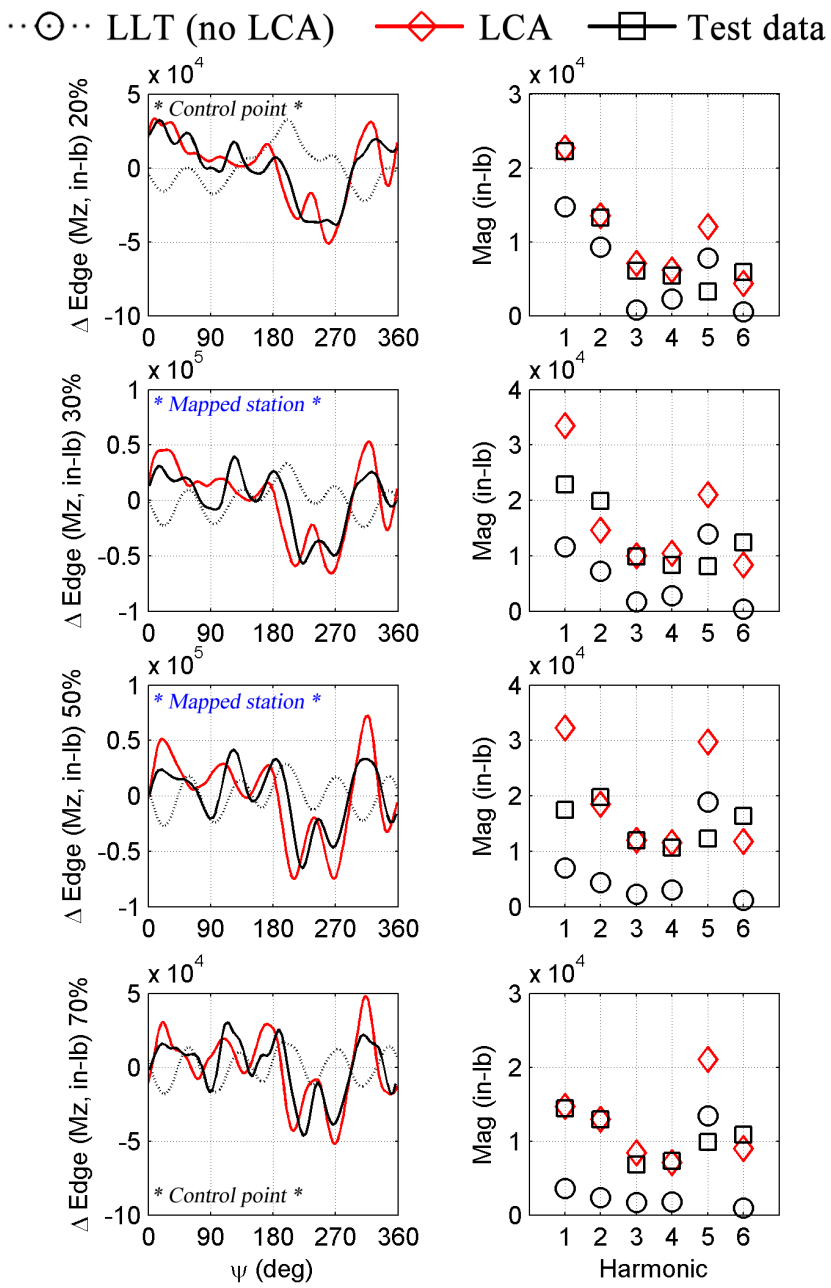

Figure 4.131: Edgewise bending moment: time history, load component by harmonic; cycle 24 [flight counter, μ] = [11679, 0.393]

4.6.9 Diving turn: c11680

Marpu et al. [57] also studied c11680 (max N_z=1.48g). This reference accurately predicts peak-to-peak, $1P$, $2P$, and $3P$ content for ST30. The $4P$ content is better captured at ST50 than at ST30. This is attributed to the quality of the blade root boundary conditions. For pushrod, $1P$, $2P$, and $3P$ are accurately predicted. $4P$, $5P$, and $6P$ pushrod loads are under-predicted.

Figures 4.132 through 4.138 show peak-to-peak loads for blade flapwise bending, torsional, and edgewise bending moments (as well as pushrod load) for the 34 cycles of this flight counter. Figures 4.139 through 4.148 show load magnitudes by harmonic for these cycles. The response varies with N_z, maximized at cycle 11, which is examined in detail in Figures 4.149 through 4.152.

The presence of the stall cycles is evident in Figures 4.149 and 4.151 for blade torsional moment, with peaks in Q1 and Q4 across the blade span.

The LCA provides a good loads match for this flight counter, with the following observations (the same as for c11679):

1. SE is over-predicted throughout - all due to an over-prediction of $5P$ load content (see Figures 4.145 through 4.148). This could be remedied in the LCA by deactivating a correction by harmonic if the resulting response is too high.

2. ST70 over-predicts the $3P$ load content, more so at higher N_z.

3. An excellent match is seen for other load stations, including pushrod peak-to-peak load (Figure 4.137).

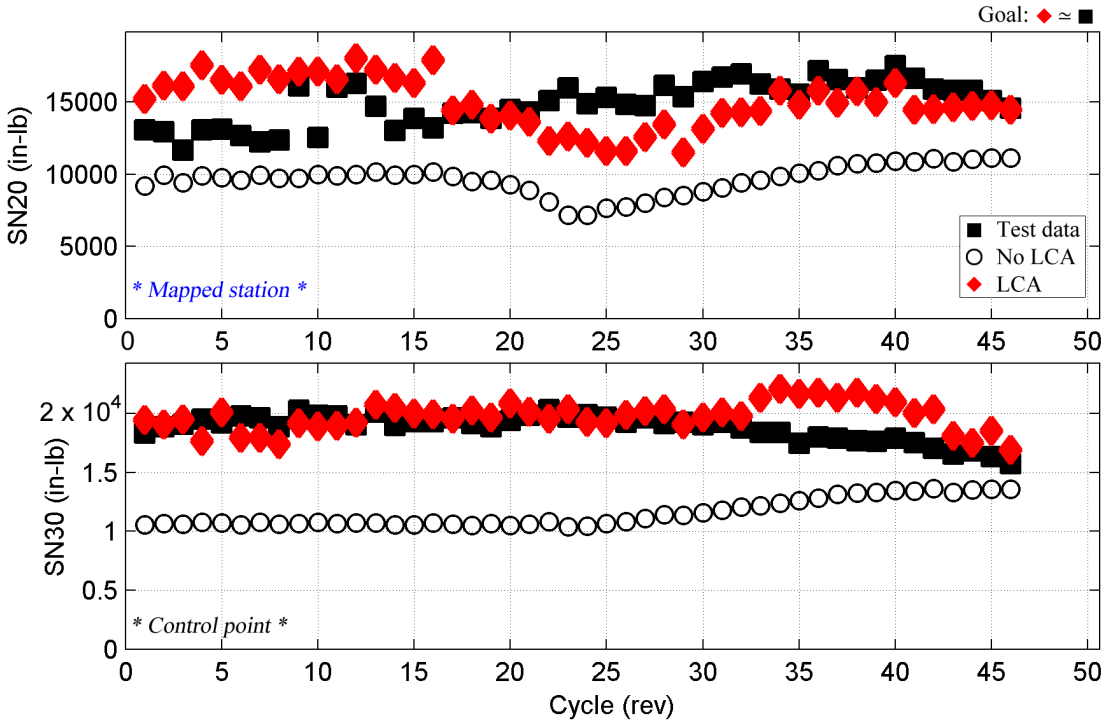

Figure 4.132: Peak-to-peak loads matching: all cycles of c11680: SN20, SN30.

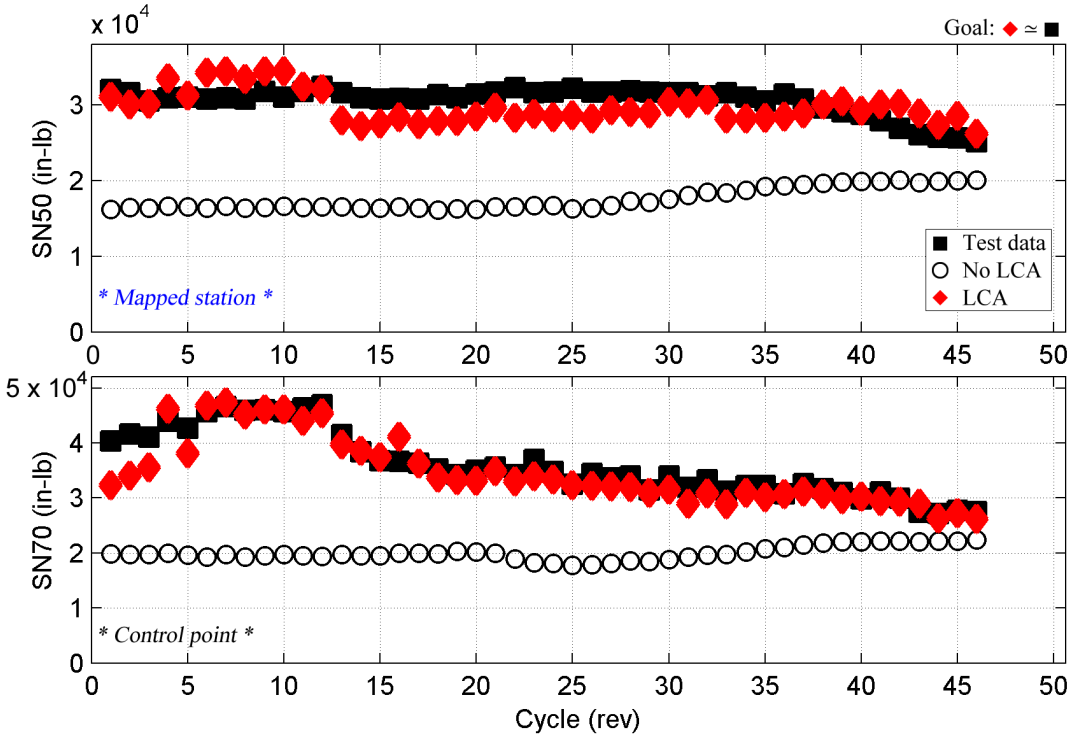

Figure 4.133: Peak-to-peak loads matching: all cycles of c11680: SN50, SN70.

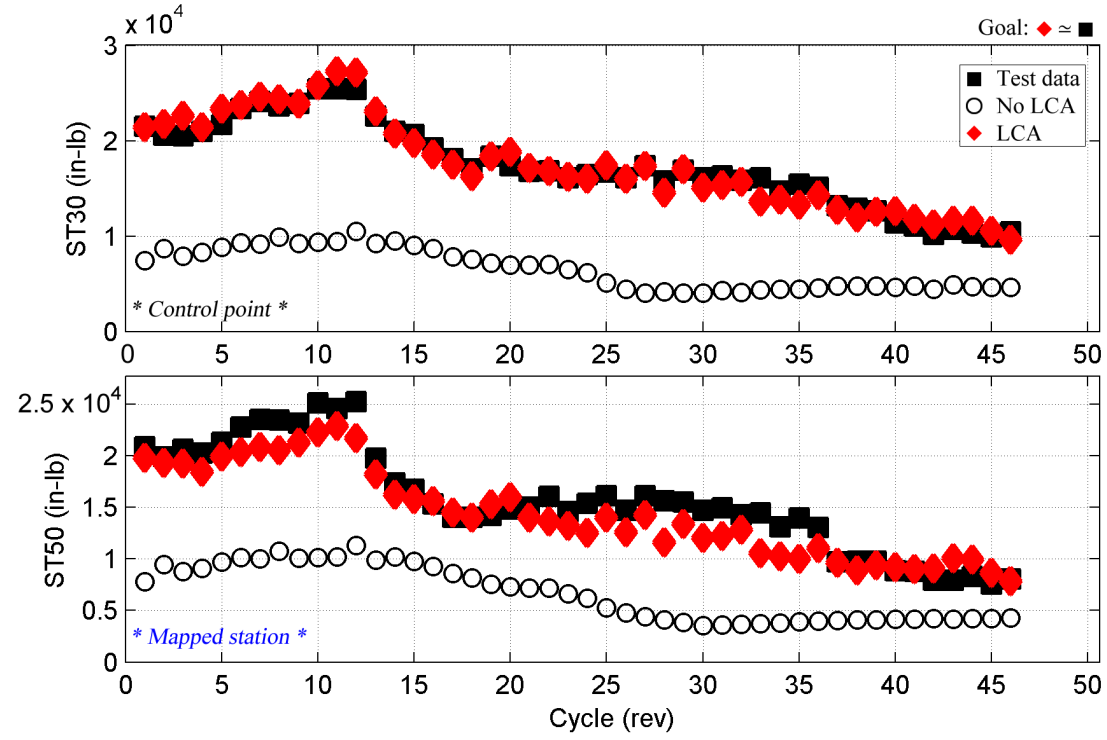

Figure 4.134: Peak-to-peak loads matching: all cycles of c11680: ST30, ST50.

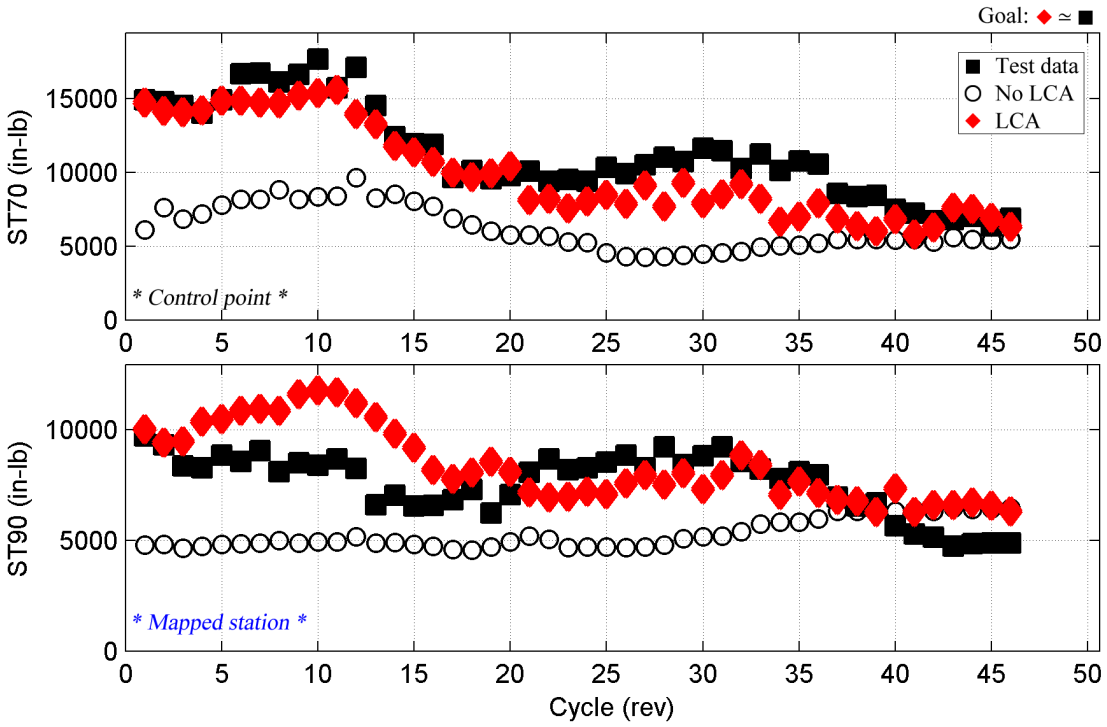

Figure 4.135: Peak-to-peak loads matching: all cycles of c11680: ST70, ST90.

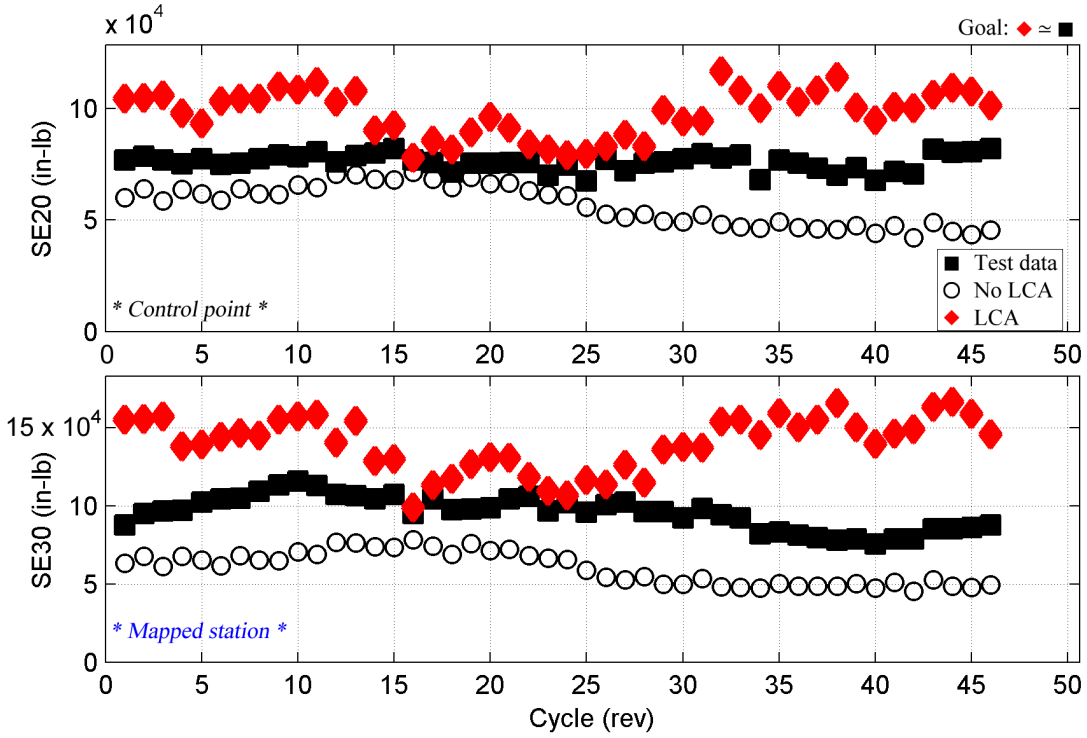

Figure 4.136: Peak-to-peak loads matching: all cycles of c11680: SE20, SE30.

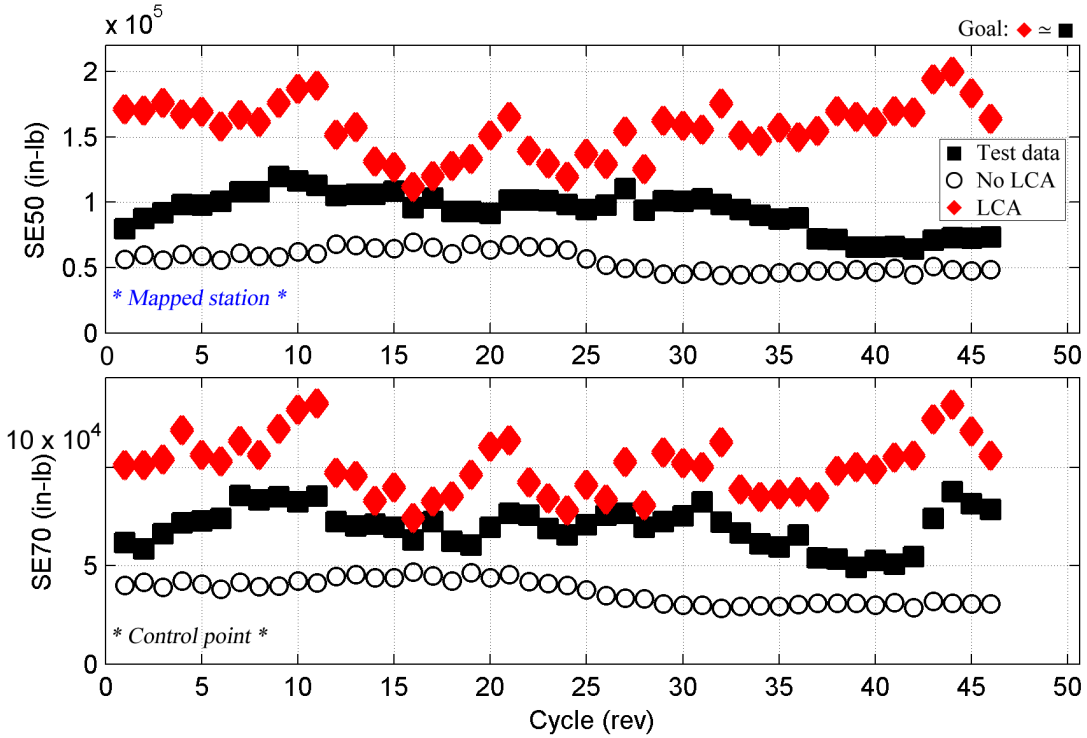

Figure 4.137: Peak-to-peak loads matching: all cycles of c11680: SE50, SE70.

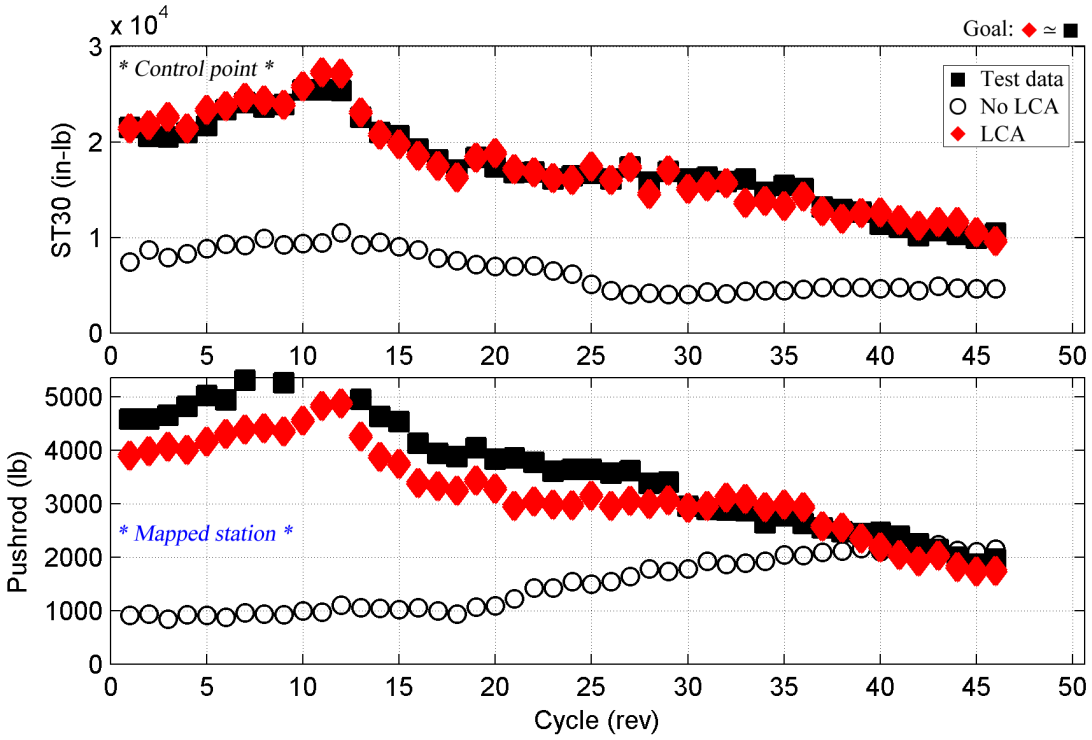

Figure 4.138: Peak-to-peak loads matching: all cycles of c11680: ST30, pushrod.

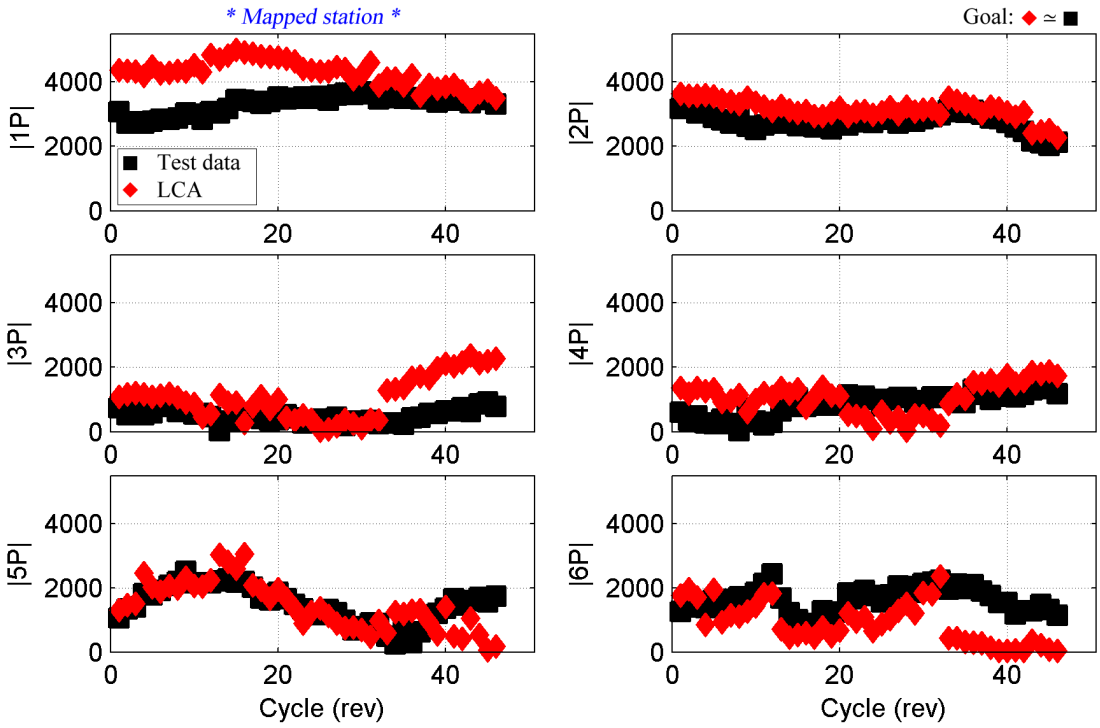

Figure 4.139: Loads matching by harmonic: all cycles of c11680: SN20 (in-lb).

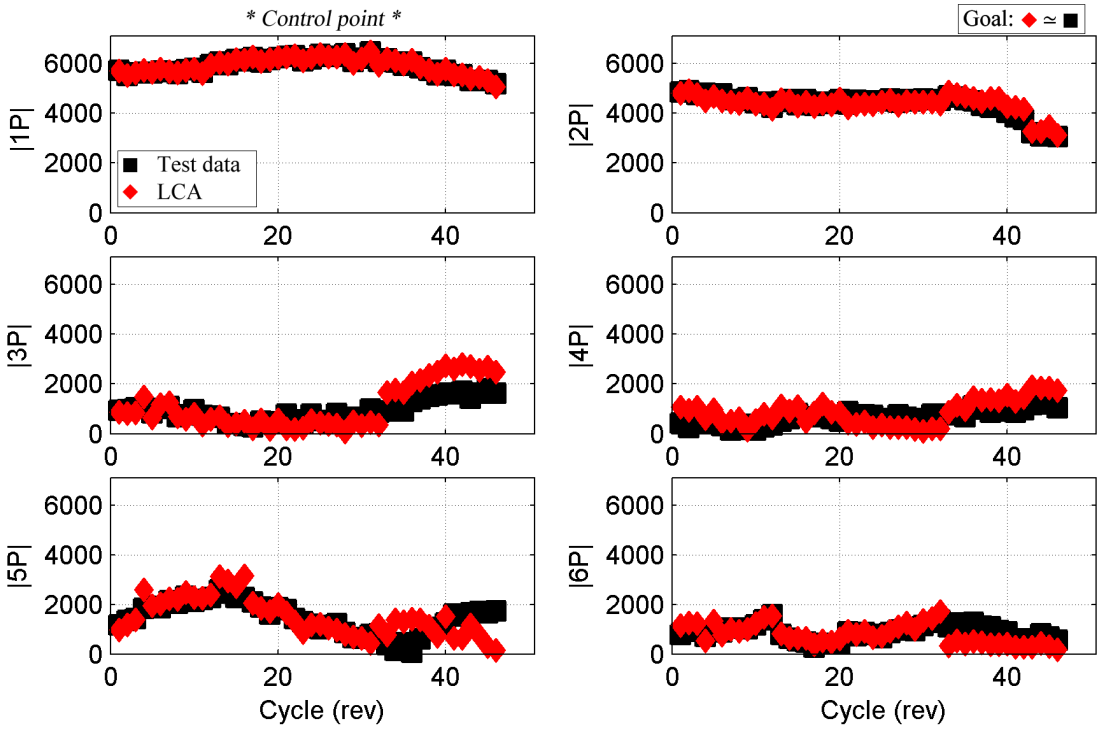

Figure 4.140: Loads matching by harmonic: all cycles of c11680: SN30 (in-lb).

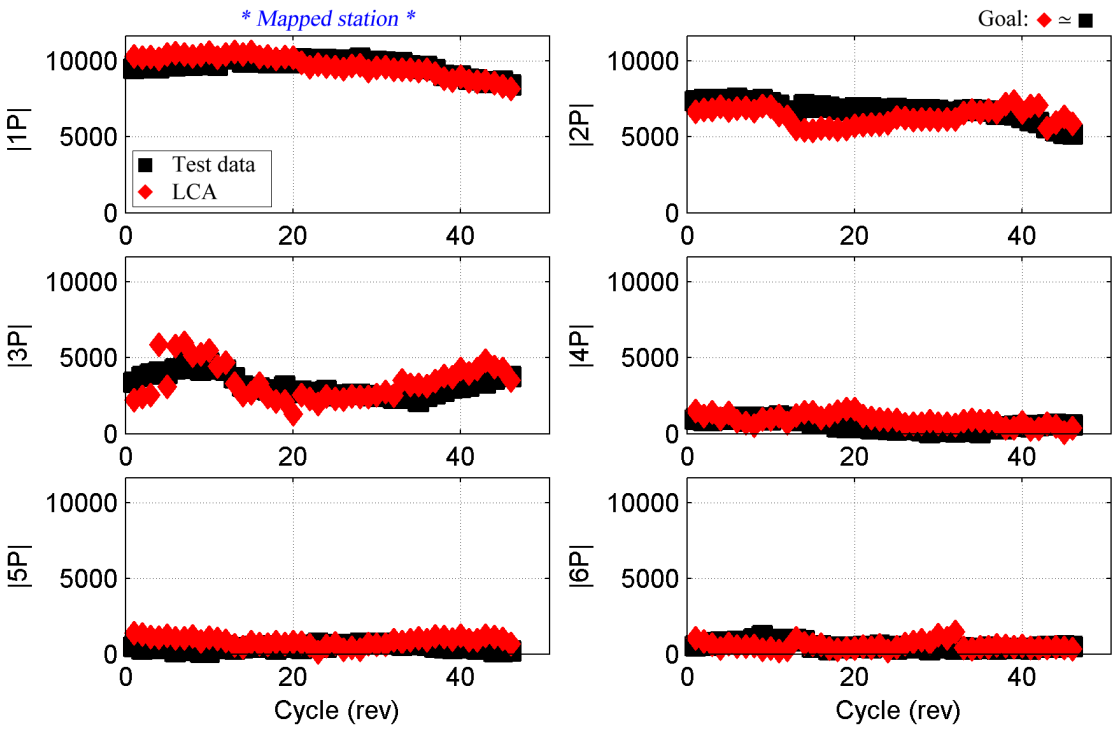

Figure 4.141: Loads matching by harmonic: all cycles of c11680: SN50 (in-lb).

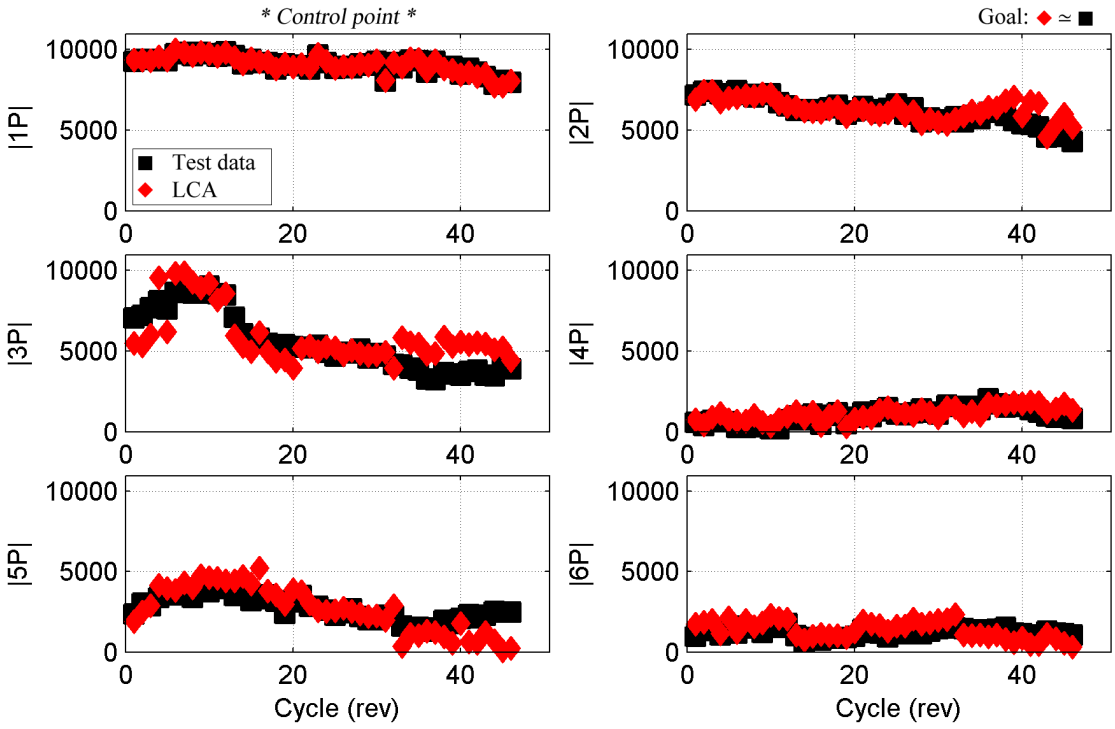

Figure 4.142: Loads matching by harmonic: all cycles of c11680: SN70 (in-lb).

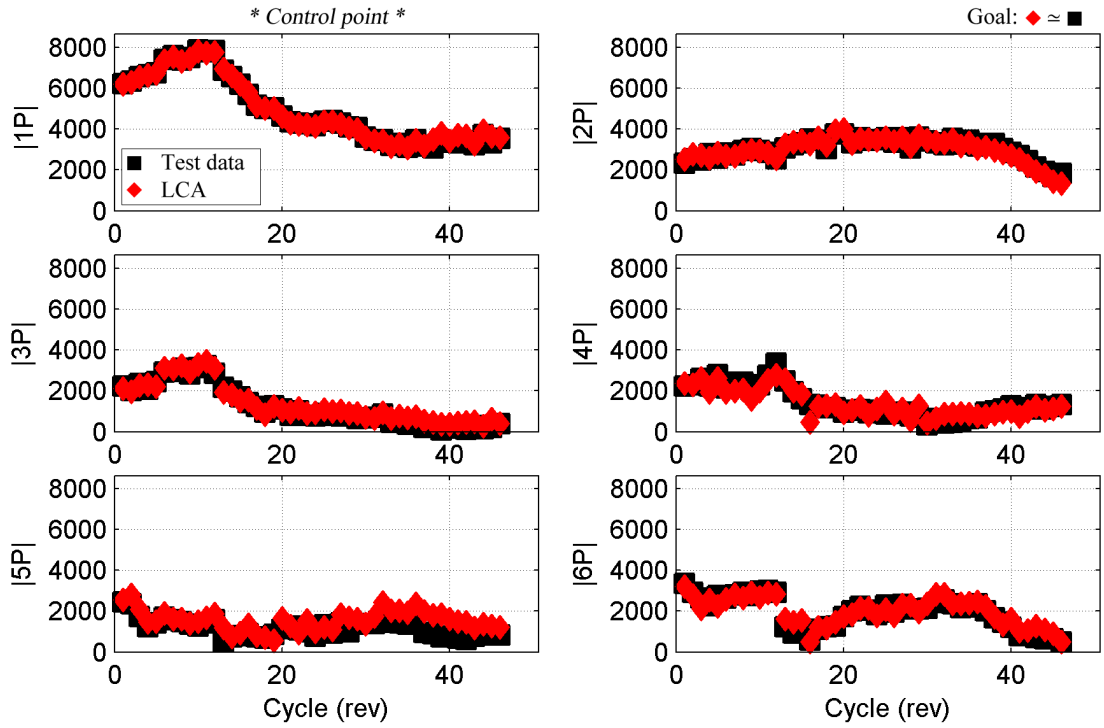

Figure 4.143: Loads matching by harmonic: all cycles of c11680: ST30 (in-lb).

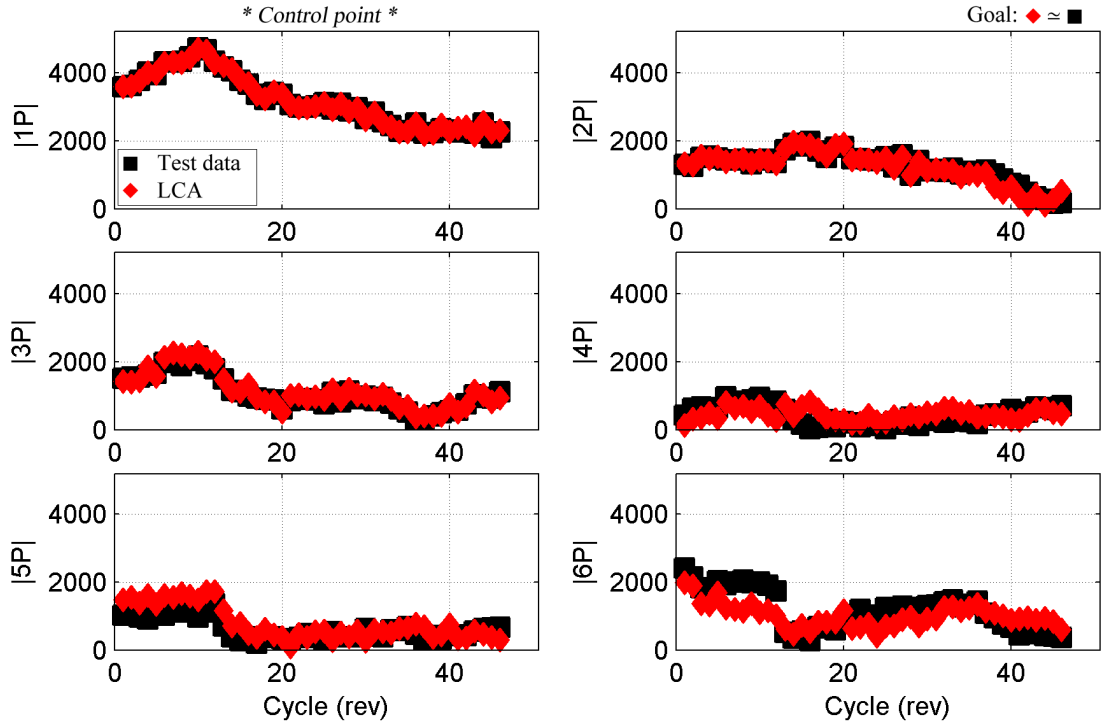

Figure 4.144: Loads matching by harmonic: all cycles of c11680: ST70 (in-lb).

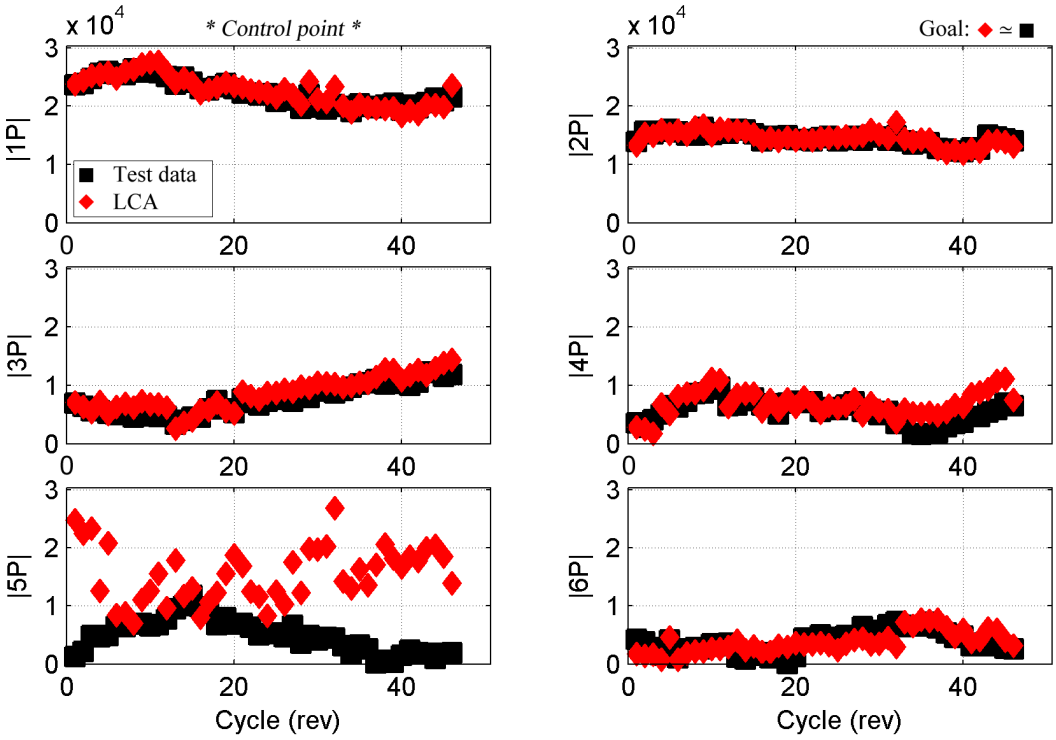

Figure 4.145: Loads matching by harmonic: all cycles of c11680: SE20 (in-lb).

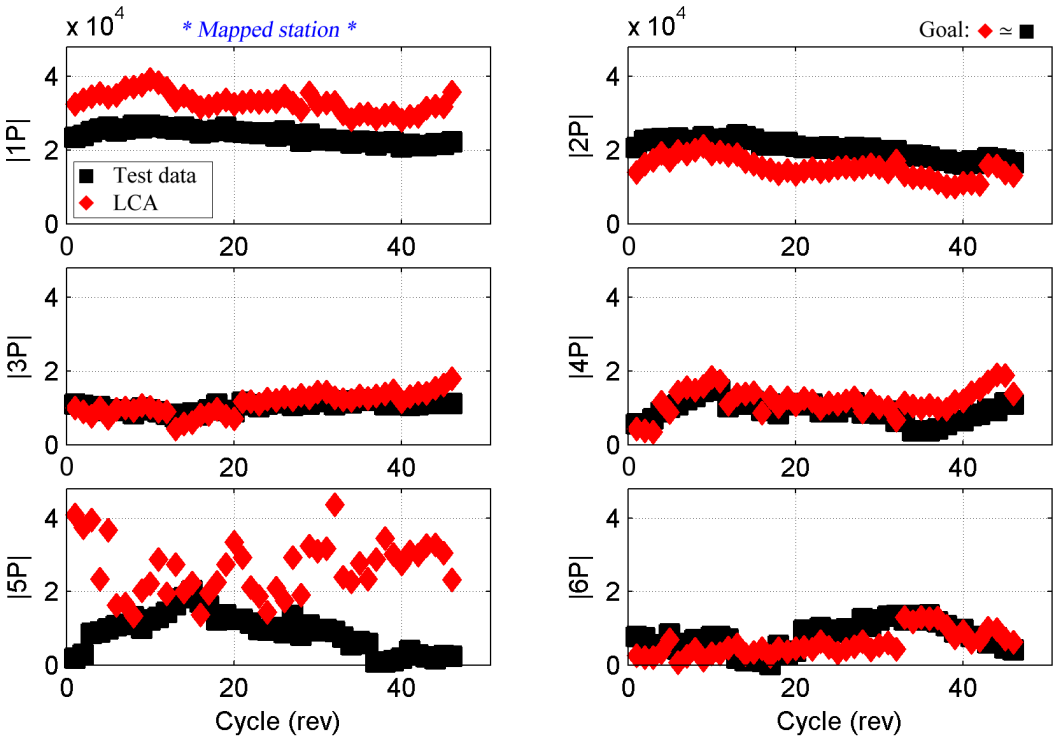

Figure 4.146: Loads matching by harmonic: all cycles of c11680: SE30 (in-lb).

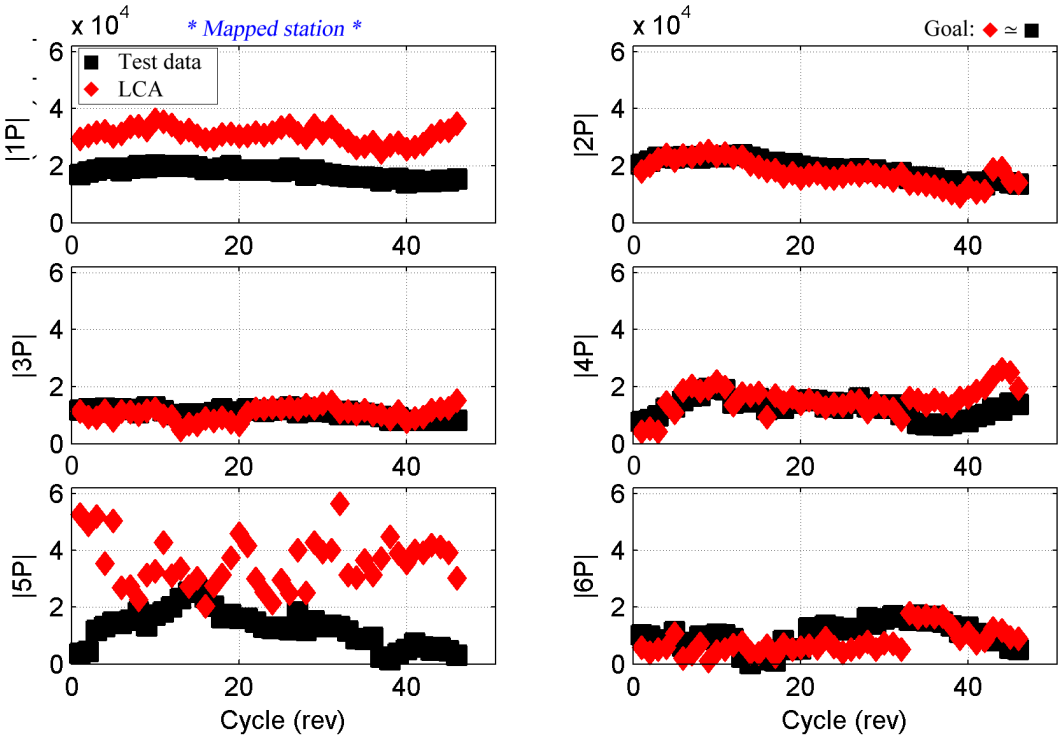

Figure 4.147: Loads matching by harmonic: all cycles of c11680: SE50 (in-lb).

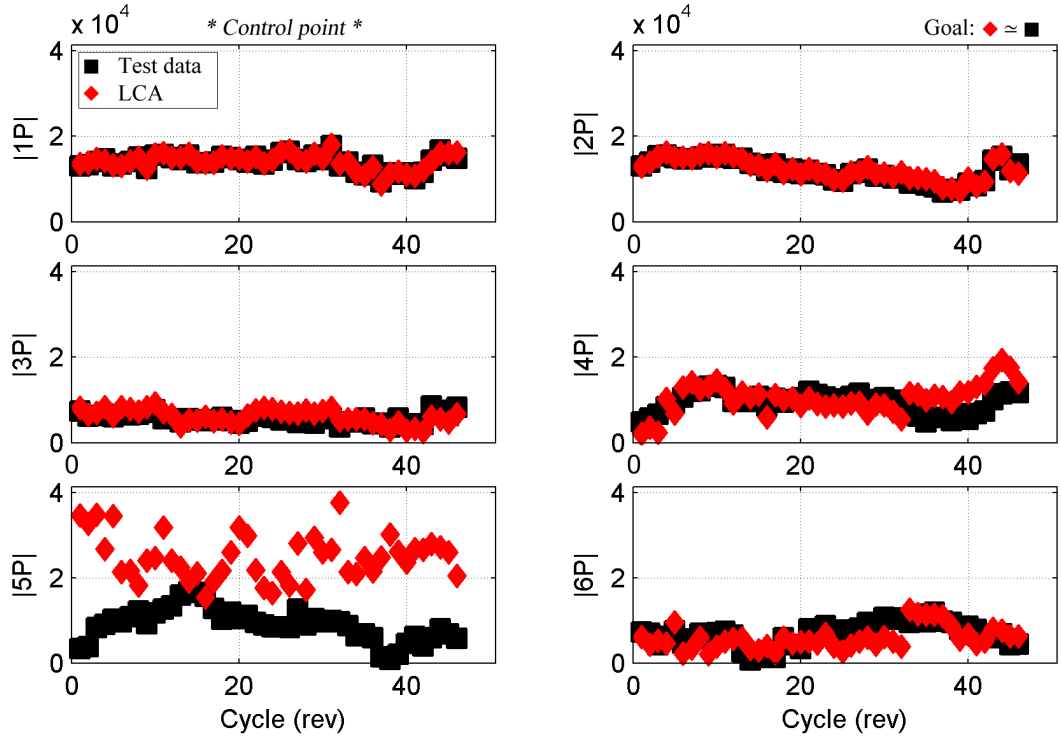

Figure 4.148: Loads matching by harmonic: all cycles of c11680: SE70 (in-lb).

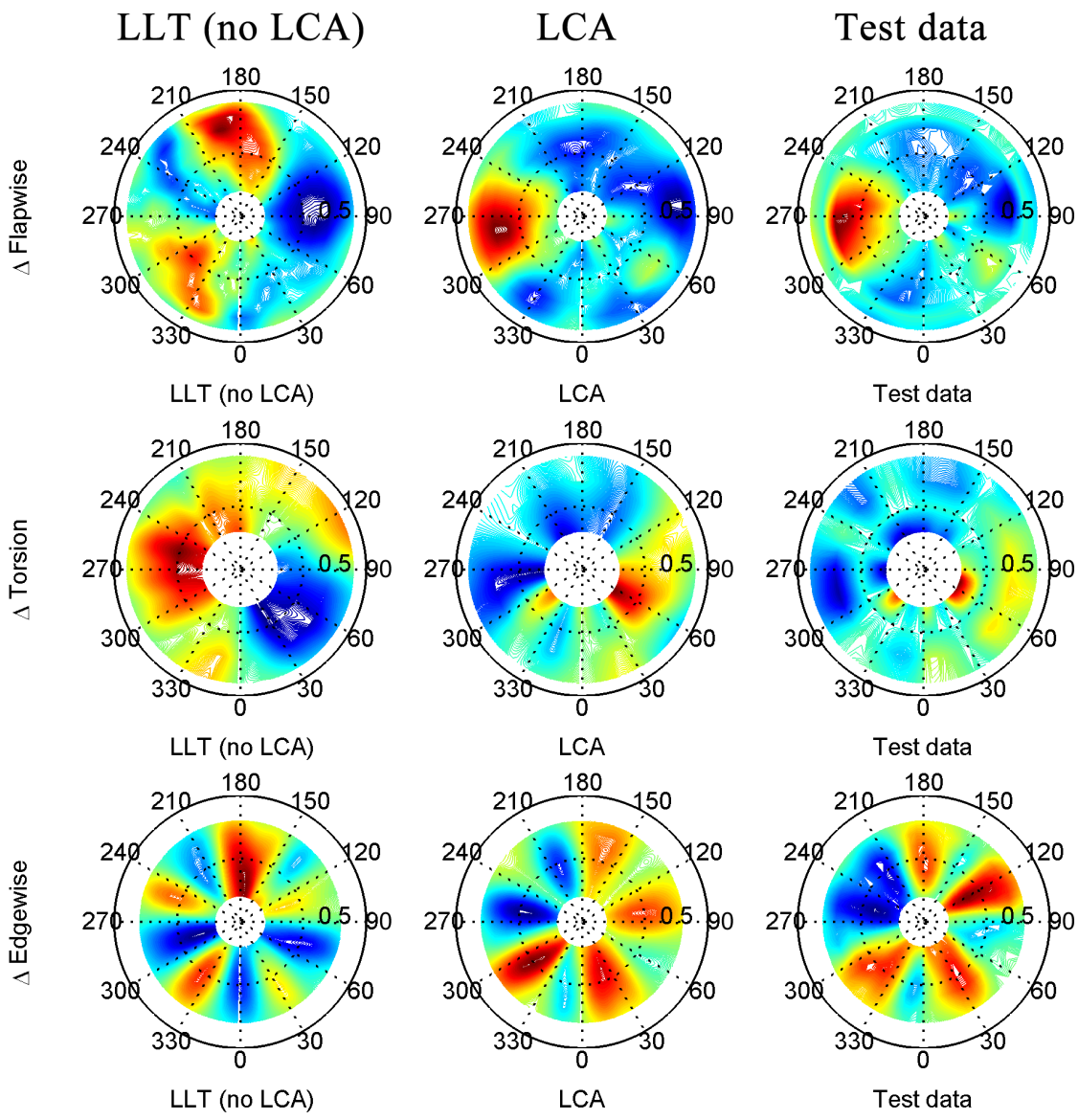

Figure 4.149: Flapwise, torsional, edgewise moments: radial, azimuthal distribution; cycle 11 [flight counter, μ] = [11680, 0.388] (top-to-bottom); red (peak), blue (valley).

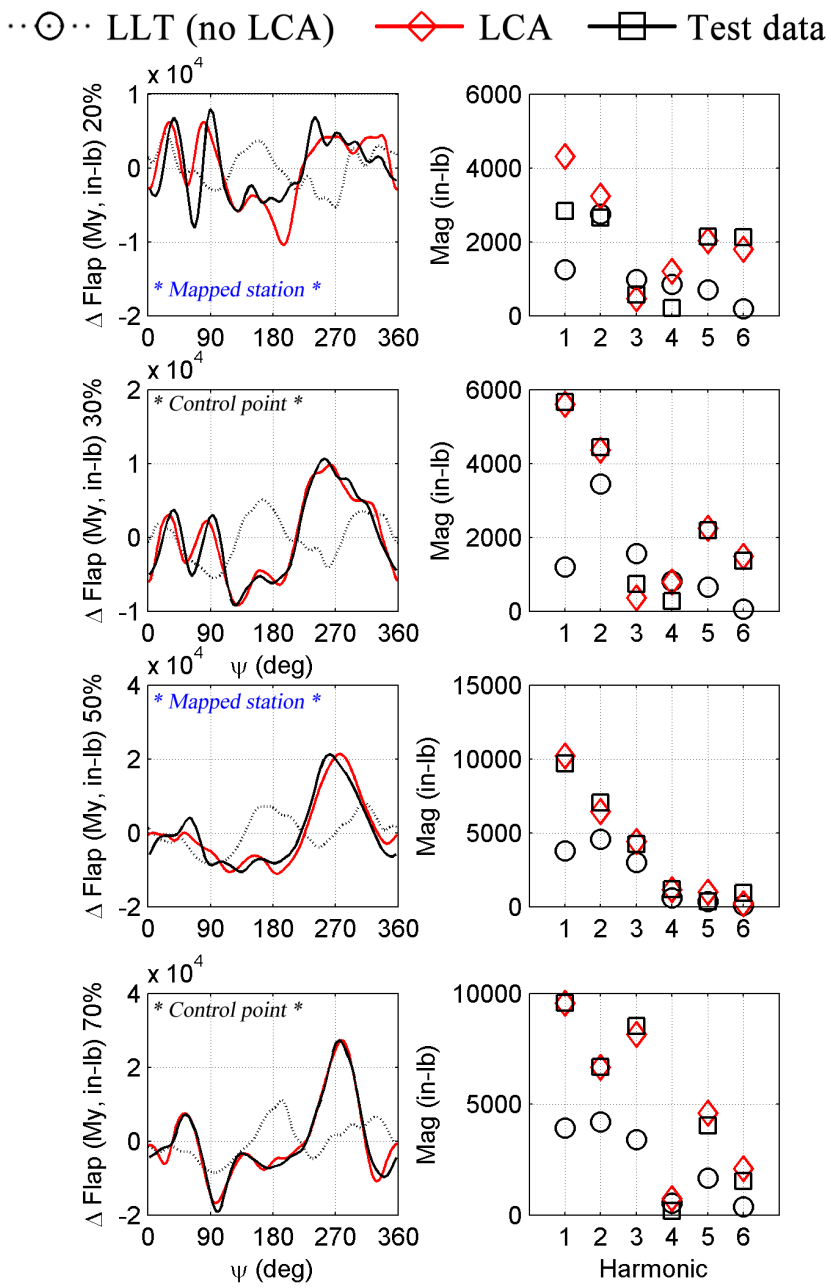

Figure 4.150: Flapwise bending moment: time history, load component by harmonic; cycle 11 [flight counter, μ] = [11680, 0.388]

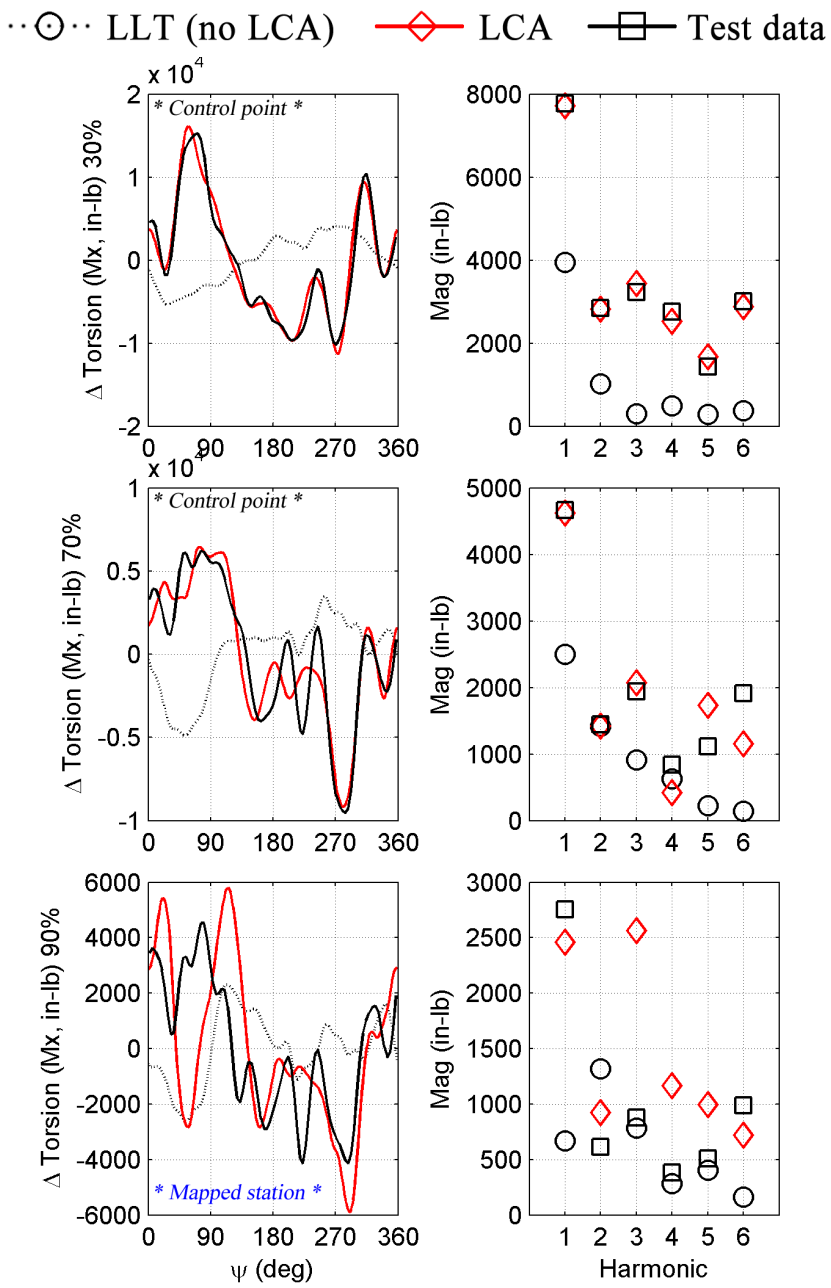

Figure 4.151: Torsional moment: time history, load component by harmonic; cycle 11 [flight counter, μ] = [11680, 0.388]

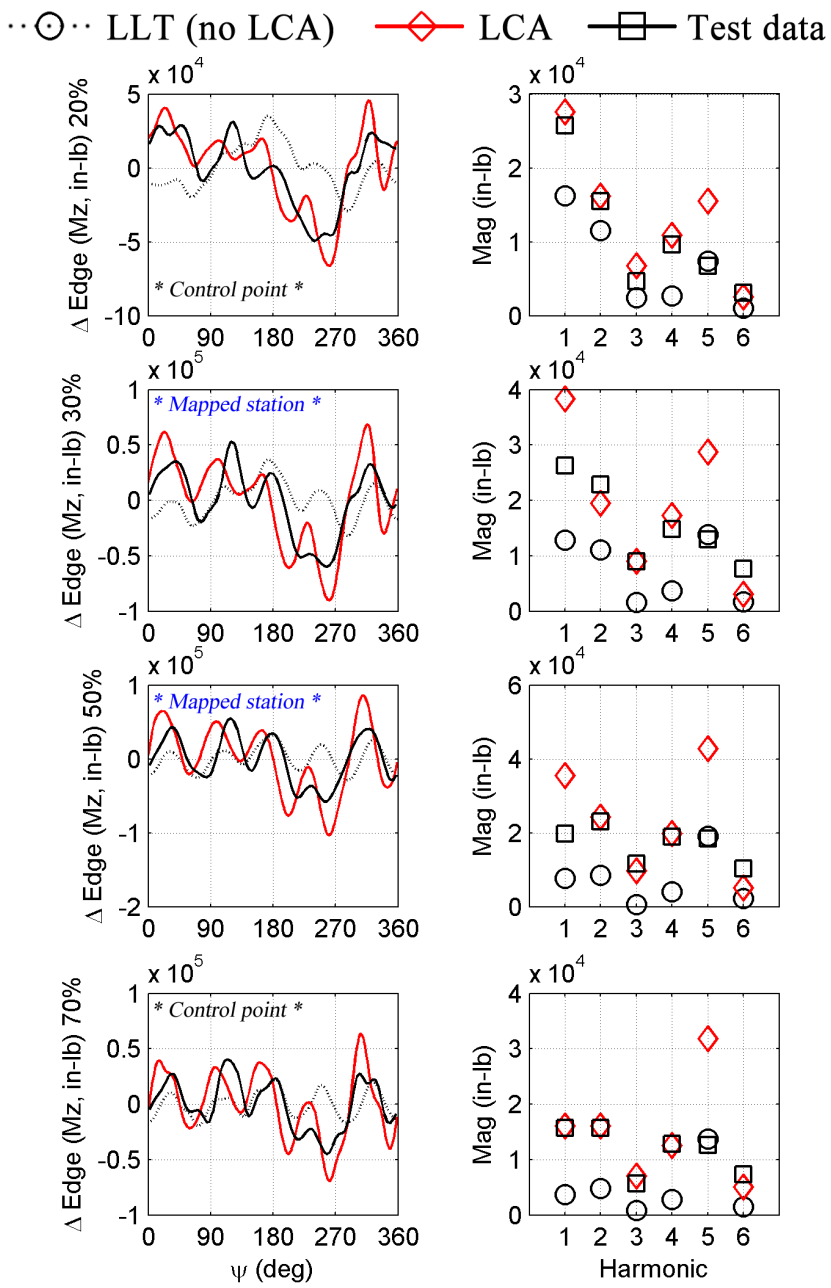

Figure 4.152: Edgewise bending moment: time history, load component by harmonic; cycle 11 [flight counter, μ] = [11680, 0.388]

4.7 All Flight Counters for Flights 84 Through 116

This final section of Chapter 4 analyzes the first cycle of all flight counters for flights 84 through 116 (601 total flight counters). The purpose is to show the robustness of the LCA across all flight regimes. The flights are listed in Table 4.5. Figure 4.153 shows the control points and mapped stations used in this simulation.

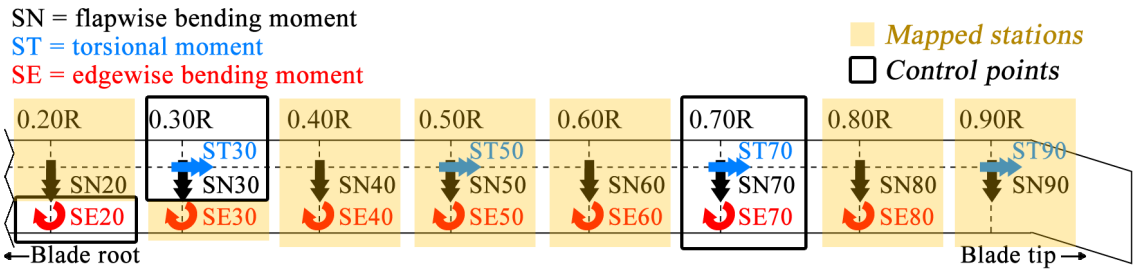

Figure 4.153: UH-60A blade control points and mapped stations.

Figures 4.154 through 4.160 show peak-to-peak loads for blade flapwise bending, torsional moment, and edgewise bending (as well as pushrod load) for the 34 cycles of this flight counter. Figures 4.161 through 4.167 show load magnitudes by harmonic for these cycles as well.

From a qualitative standpoint, application of the LCA across all flight counters provides an excellent load match. The largest deficiencies are seen in matching edgewise bending (especially at *mapped* load stations; e.g., SE30 and SE50), with the LCA over-predicting $1P$ and, more so, $5P$ response. This effect was observed before (e.g., c11679, above) and highlights the sensitivity of in-plane loads matching to the selection of control points.

Table 4.5: UH-60A flights used for analysis.

Flt #	Flt ctrs	Objective	Description
84	22	Steady, mnvr	Level flight; accel/decel; hover
85	29	Steady, mnvr	Level flight; steady turns; roll reversals
88	30	Steady, mnvr	Level flight; steady turns; decel
89	28	Steady, mnvr	Level flight; turns; roll reversals; pull-ups; pushovers
90	27	Steady, mnvr	Level flight; turns; climbs
91	34	Grd meas. acoustics	Level flt; ascents; descents
92	24	Grd meas. acoustics	Turns; ascents; descents
93	26	Grd meas. acoustics	Level flt; ascents; descents
94	29	Grd meas. acoustics	Hover; ascents; descents
95	24	Grd meas. acoustics	Ascents; descents
96	24	Grd meas. acoustics	Turns
97	23	Grd meas. acoustics	Turns
98	30	Grd meas. acoustics	Turns
99	23	Grd meas. acoustics	Turns
100	11	Airborne meas. acoustics	Descents
101	10	Airborne meas. acoustics	Descents
102	16	Airborne meas. acoustics	Descents
103	8	Airborne meas. acoustics	Descents
105	2	Flight dynamics	Control sweep
106		Flight dynamics	Response to turbulence
107	2	Flight dynamics	Frequency sweeps
108	3	Flight dynamics	Frequency sweeps
110	30	Maneuvers	Level flight; hover; dives; turns; roll rev.; pull-ups; pushovers
111	13	Flight dynamics	Freq. sweeps
112	22	Flight dynamics	Freq. sweeps
113	25	Airborne meas. acoustics	Descents
114	22	Airborne meas. acoustics	Descents
115	23	Maneuvers	Autorotations; climbs; turns; hover; level flight
116	24	Maneuvers	Wind-up turns; dives; hover; level flight
Total:	**601**		

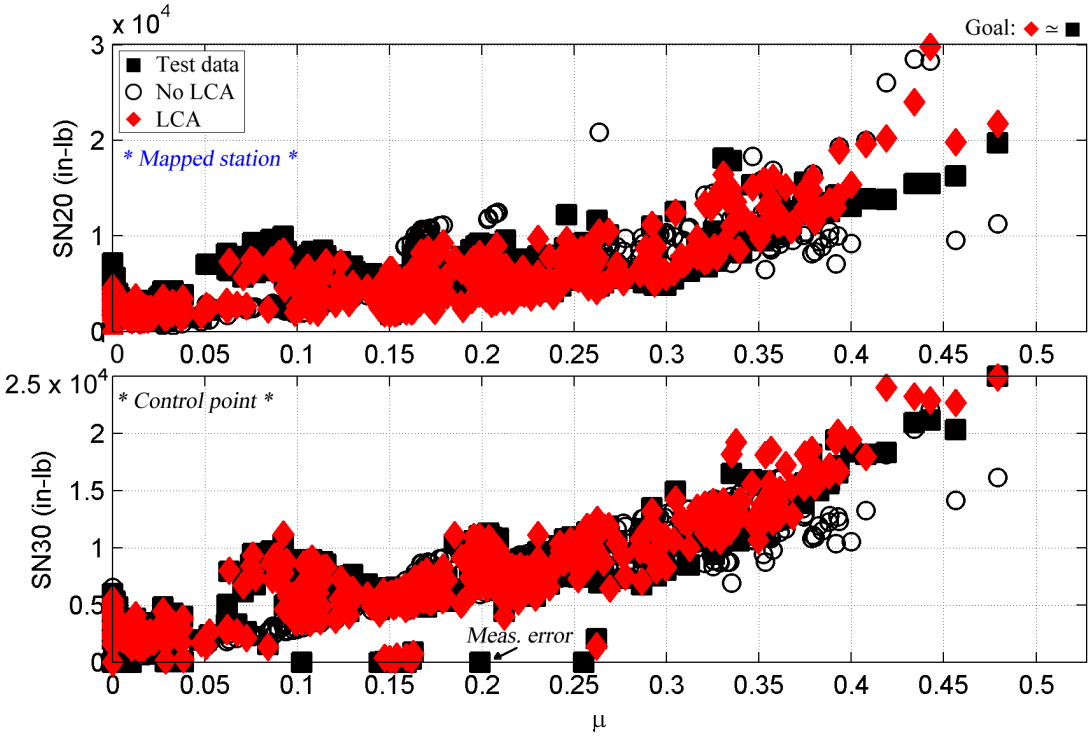

Figure 4.154: Peak-to-peak loads matching: all flight counters: SN20, SN30.

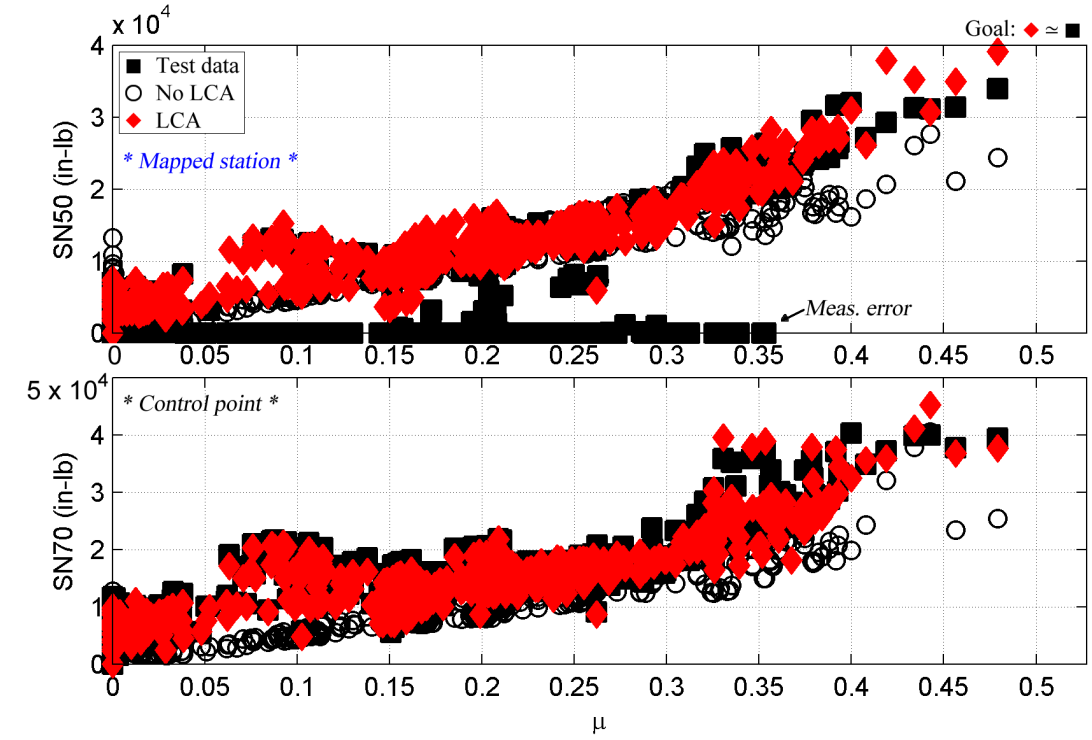

Figure 4.155: Peak-to-peak loads matching: all flight counters: SN50, SN70.

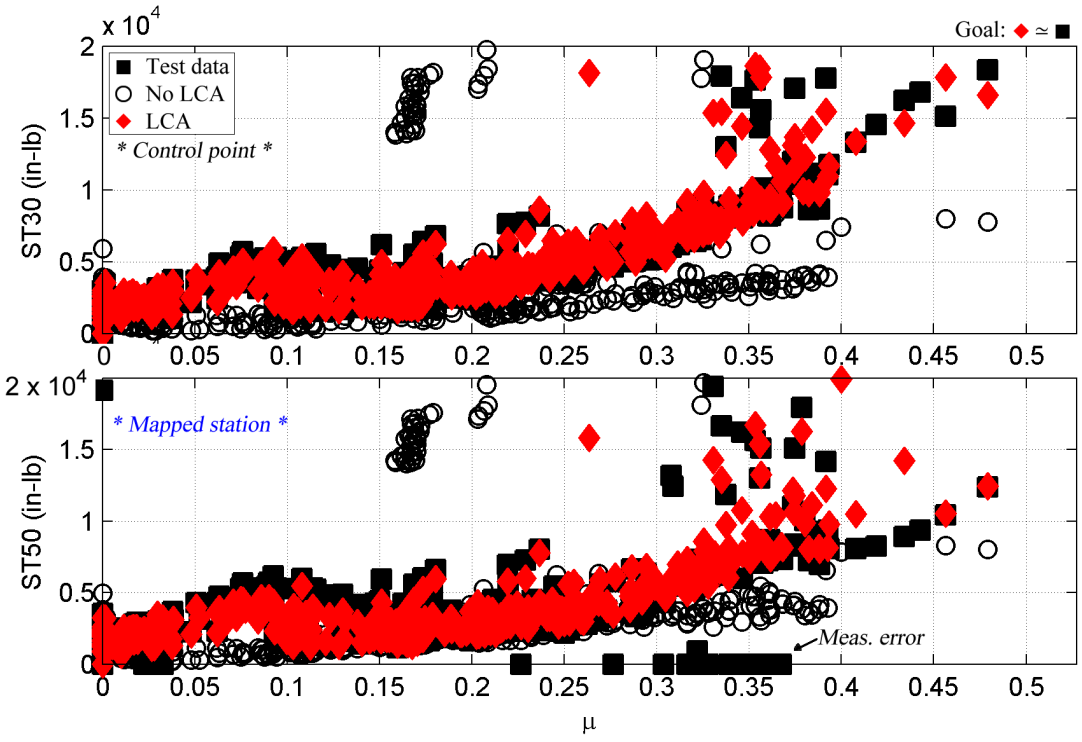

Figure 4.156: Peak-to-peak loads matching: all flight counters: ST30, ST50.

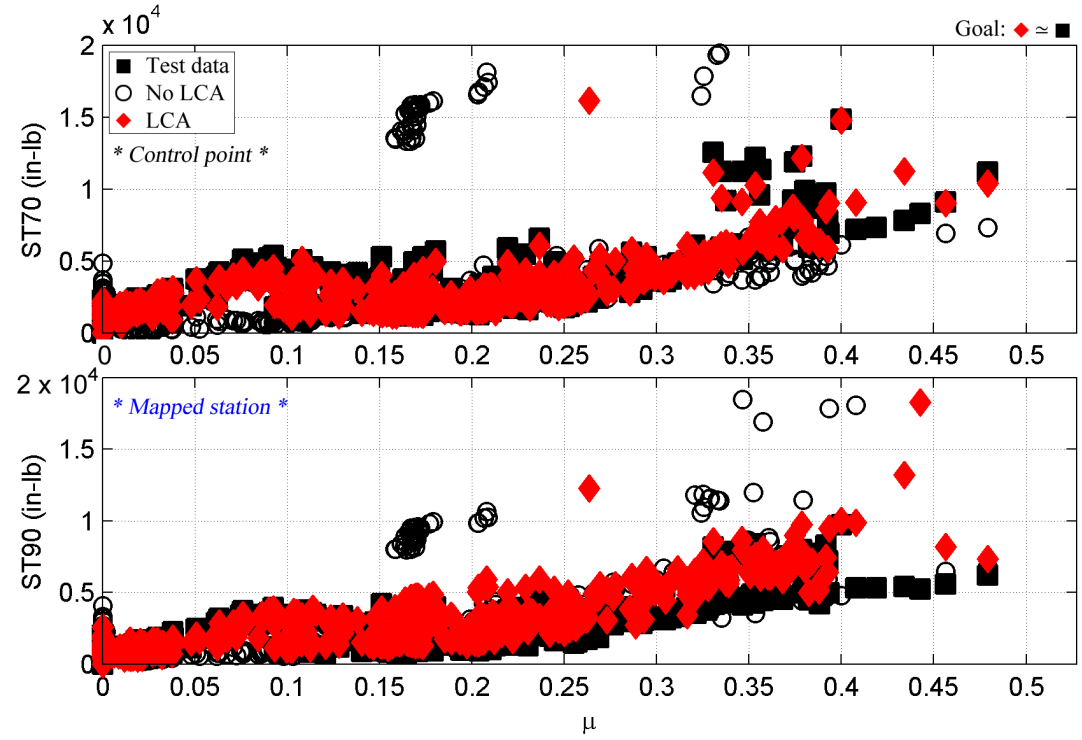

Figure 4.157: Peak-to-peak loads matching: all flight counters: ST70, ST90.

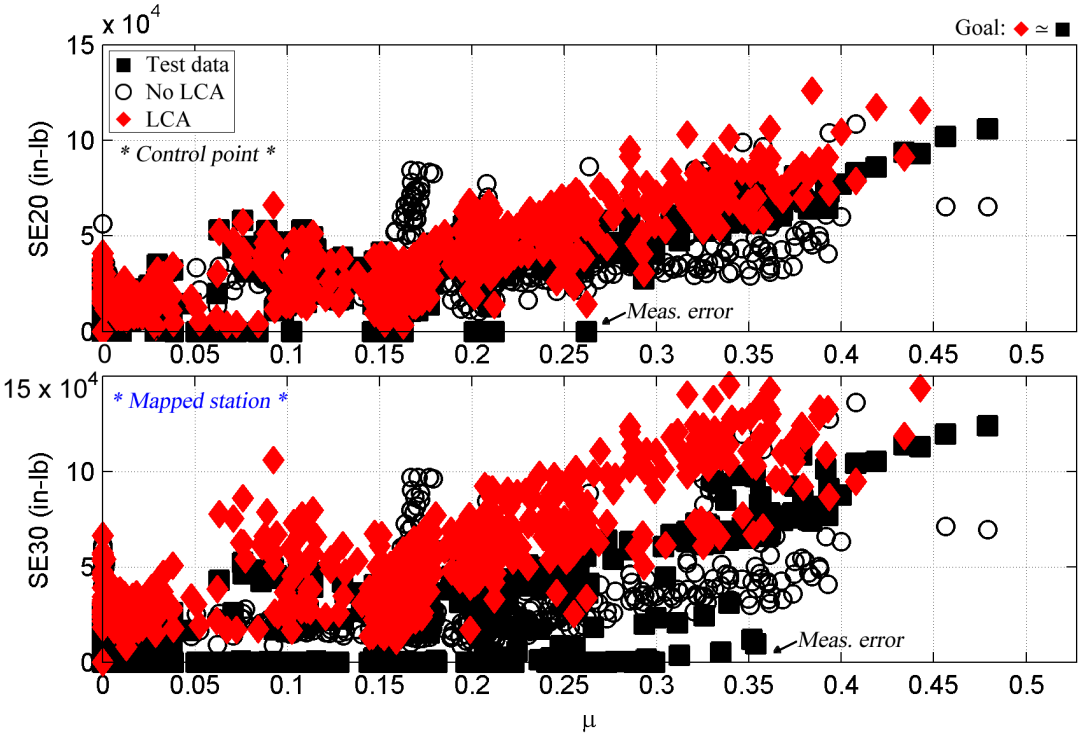

Figure 4.158: Peak-to-peak loads matching: all flight counters: SE20, SE30.

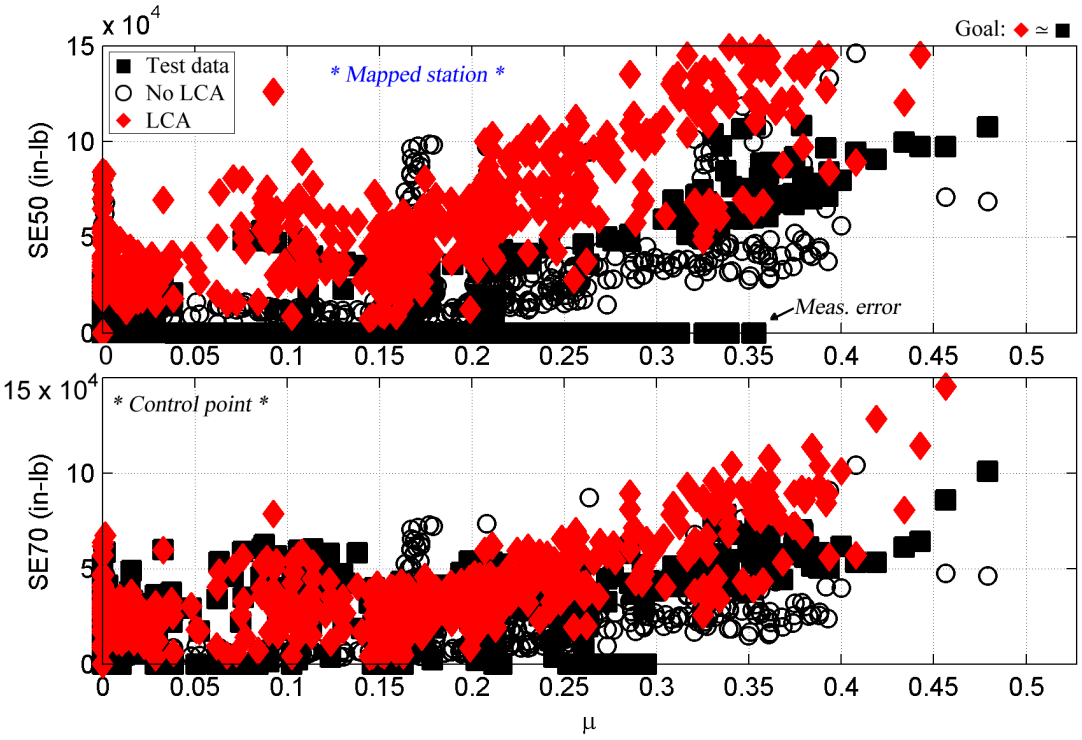

Figure 4.159: Peak-to-peak loads matching: all flight counters: SE50, SE70.

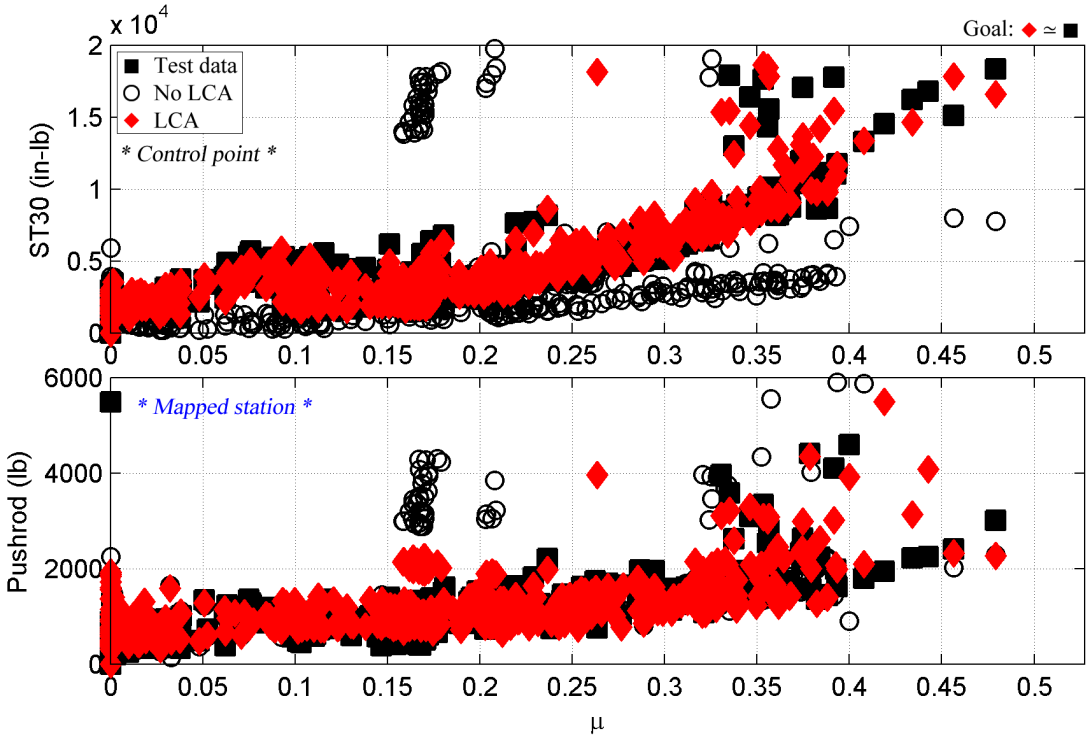

Figure 4.160: Peak-to-peak loads matching: all flight counters: ST30, pushrod.

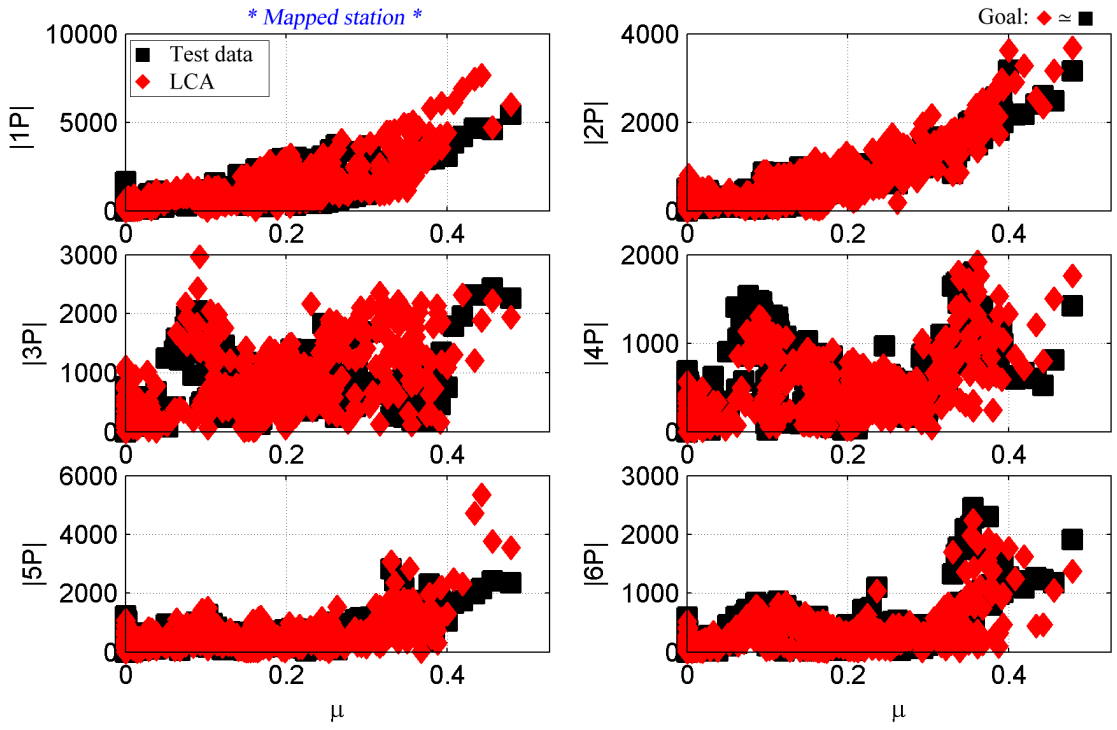

Figure 4.161: Loads matching by harmonic: all flight counters: SN20 (in-lb).

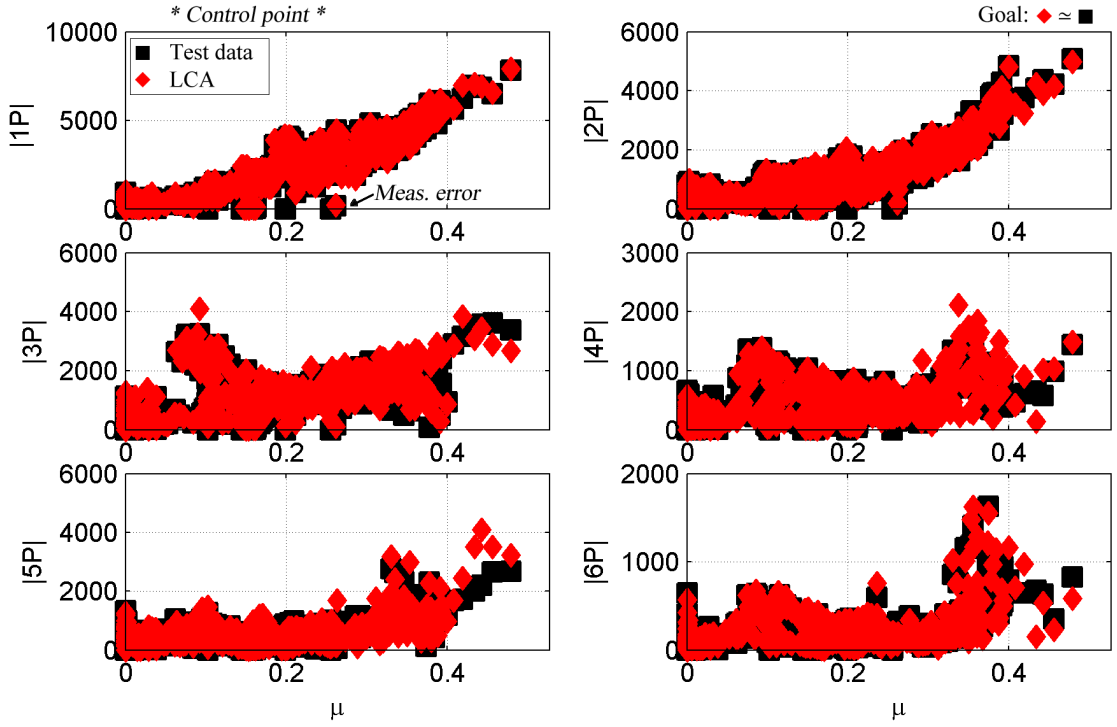

Figure 4.162: Loads matching by harmonic: all flight counters: SN30 (in-lb).

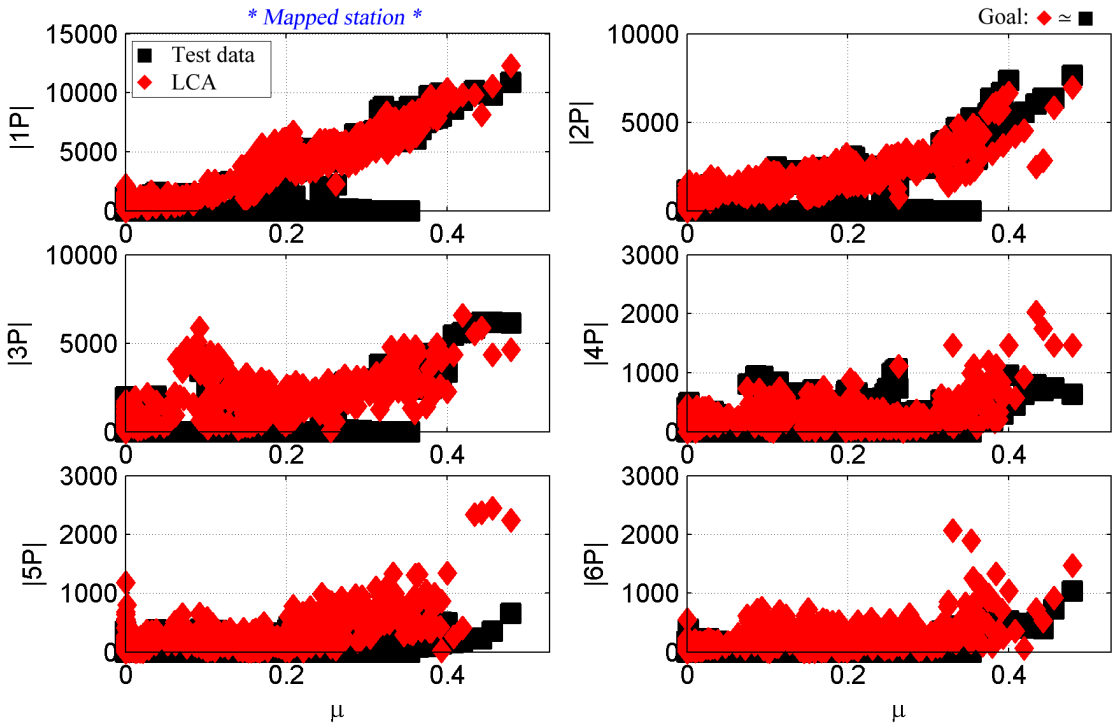

Figure 4.163: Loads matching by harmonic: all flight counters: SN50 (in-lb).

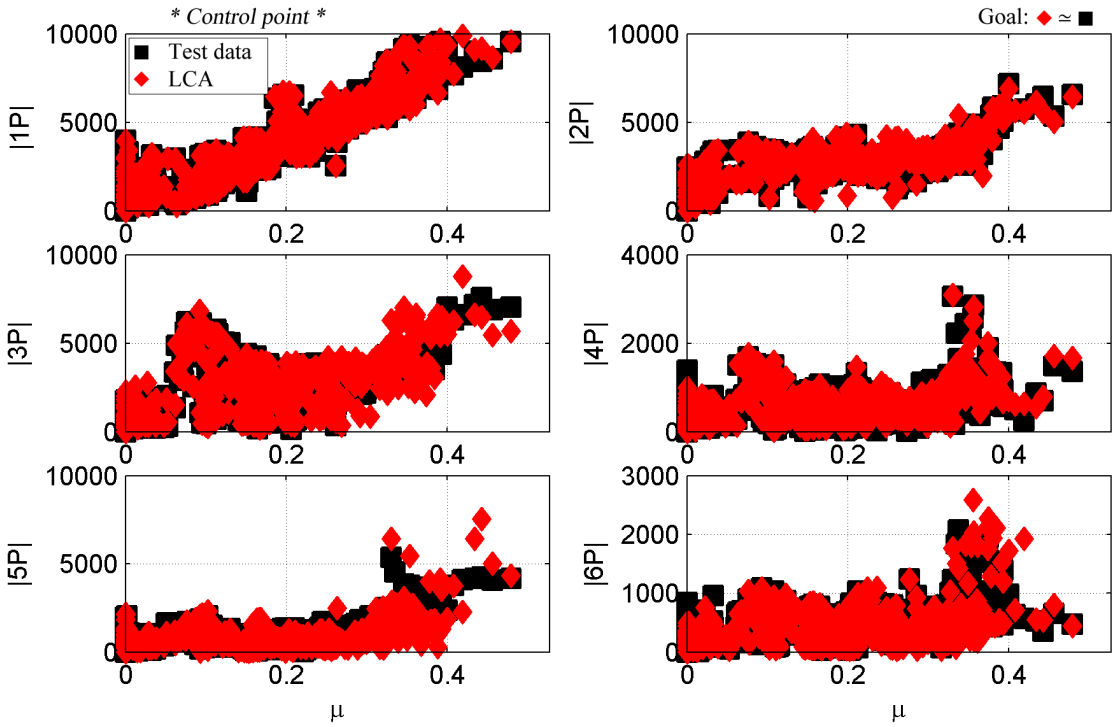

Figure 4.164: Loads matching by harmonic: all flight counters: SN70 (in-lb).

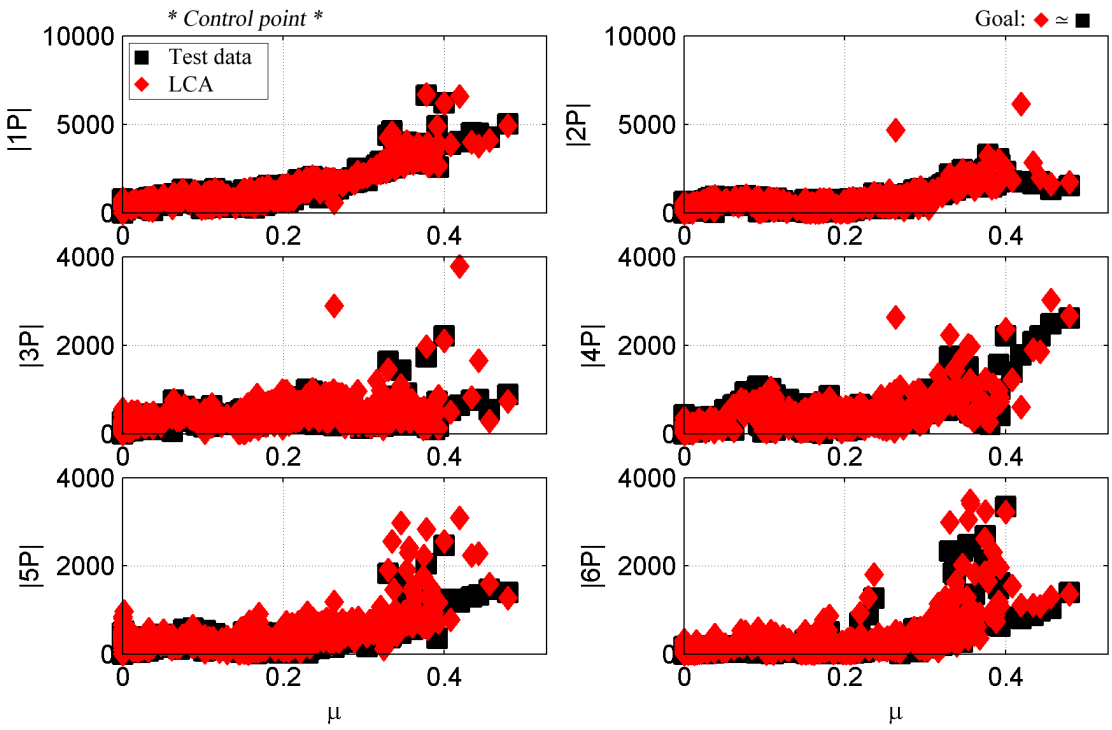

Figure 4.165: Loads matching by harmonic: all flight counters: ST30 (in-lb).

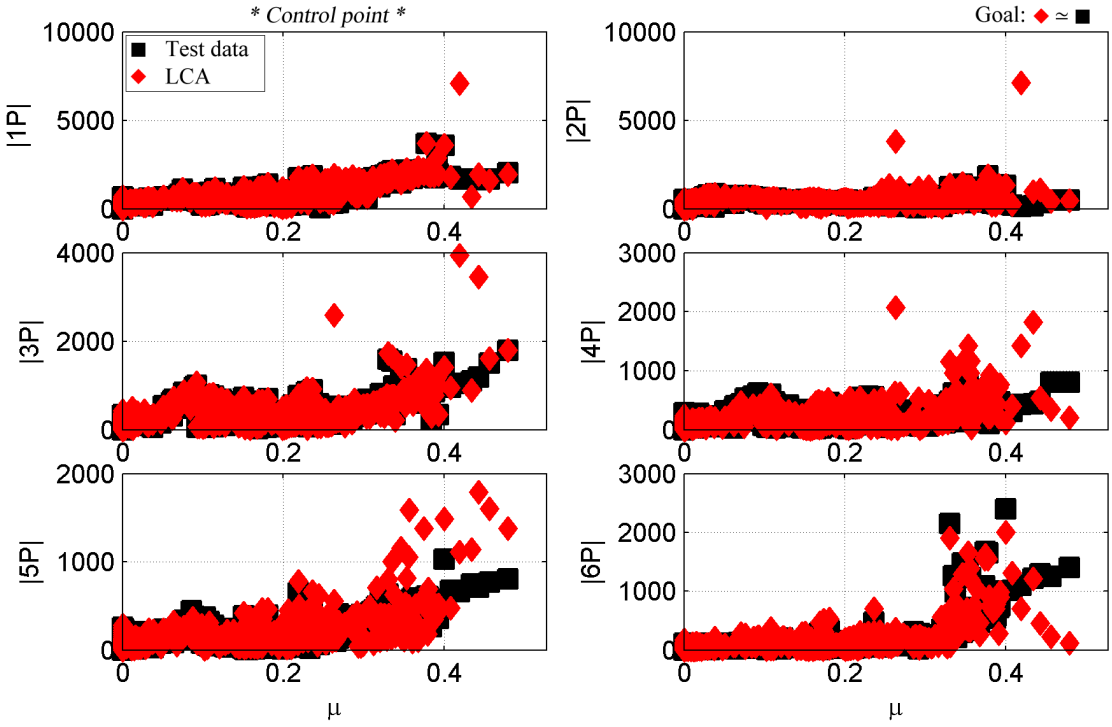

Figure 4.166: Loads matching by harmonic: all flight counters: ST70 (in-lb).

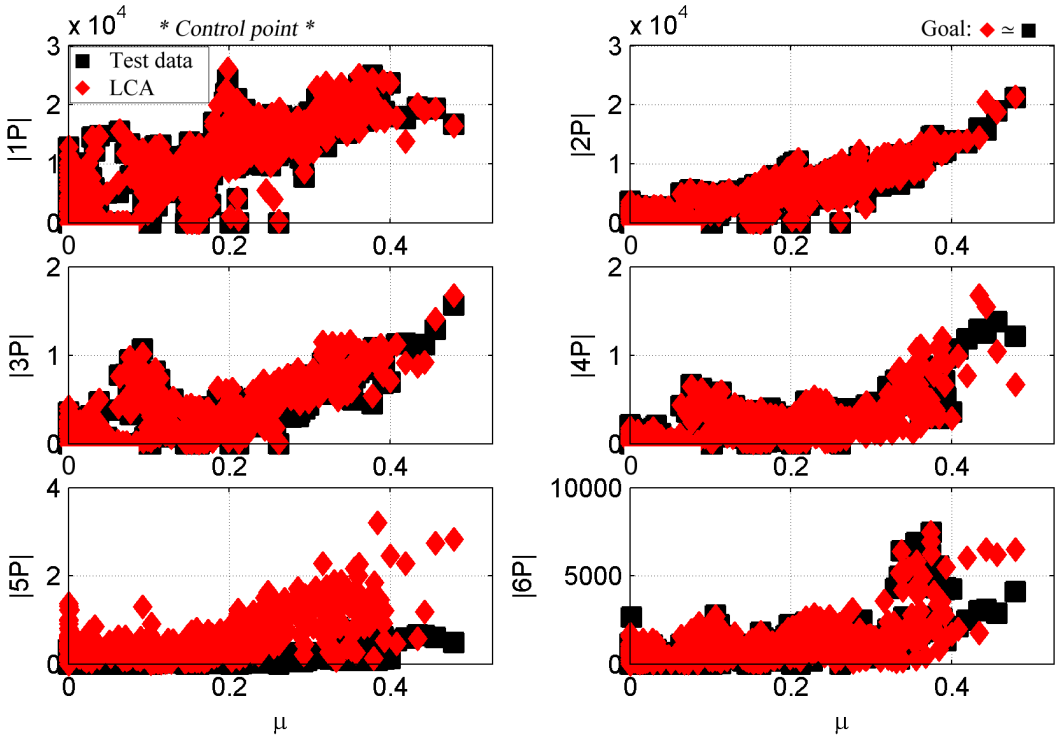

Figure 4.167: Loads matching by harmonic: all flight counters: SE20 (in-lb).

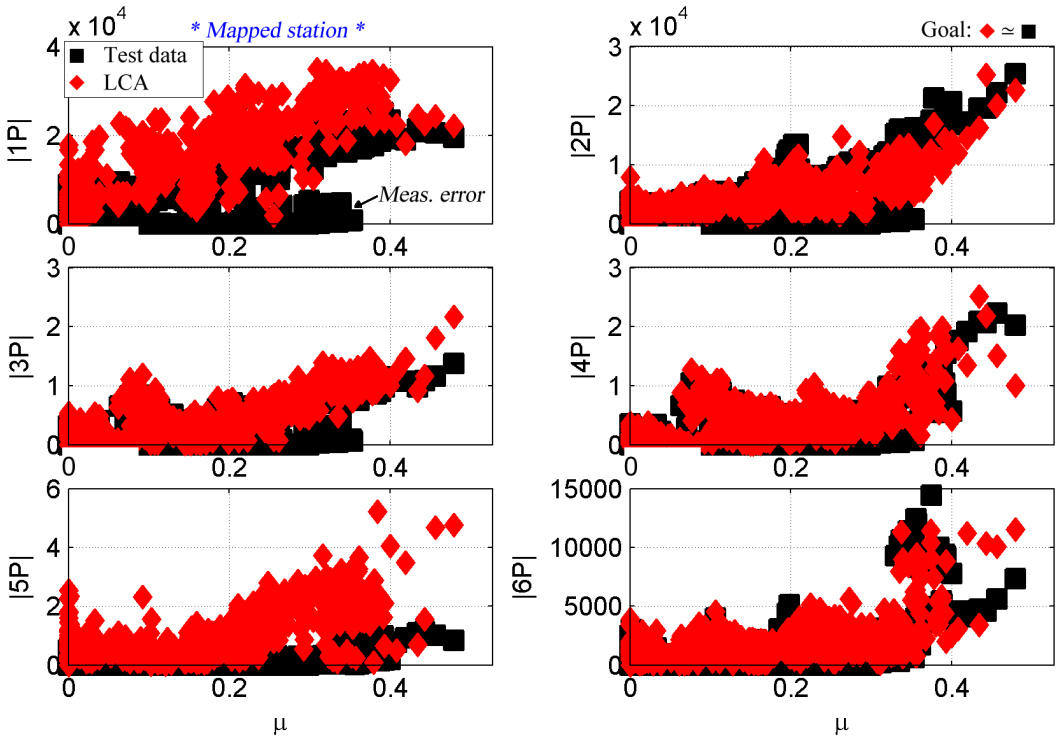

Figure 4.168: Loads matching by harmonic: all flight counters: SE30 (in-lb).

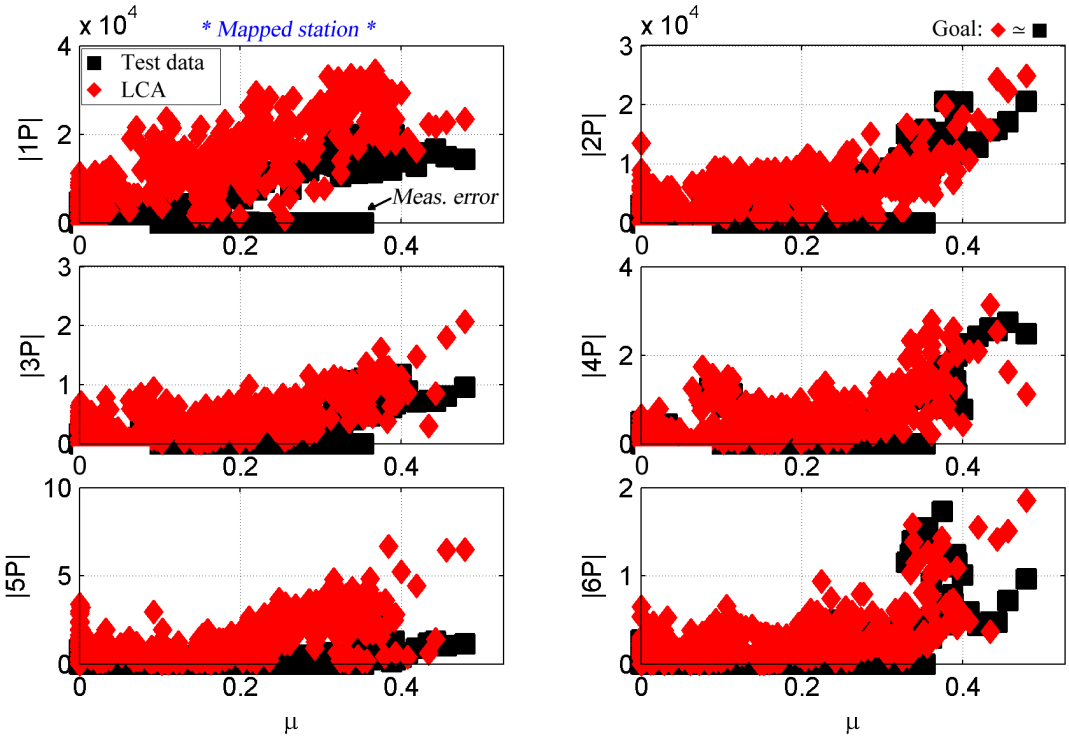

Figure 4.169: Loads matching by harmonic: all flight counters: SE50 (in-lb).

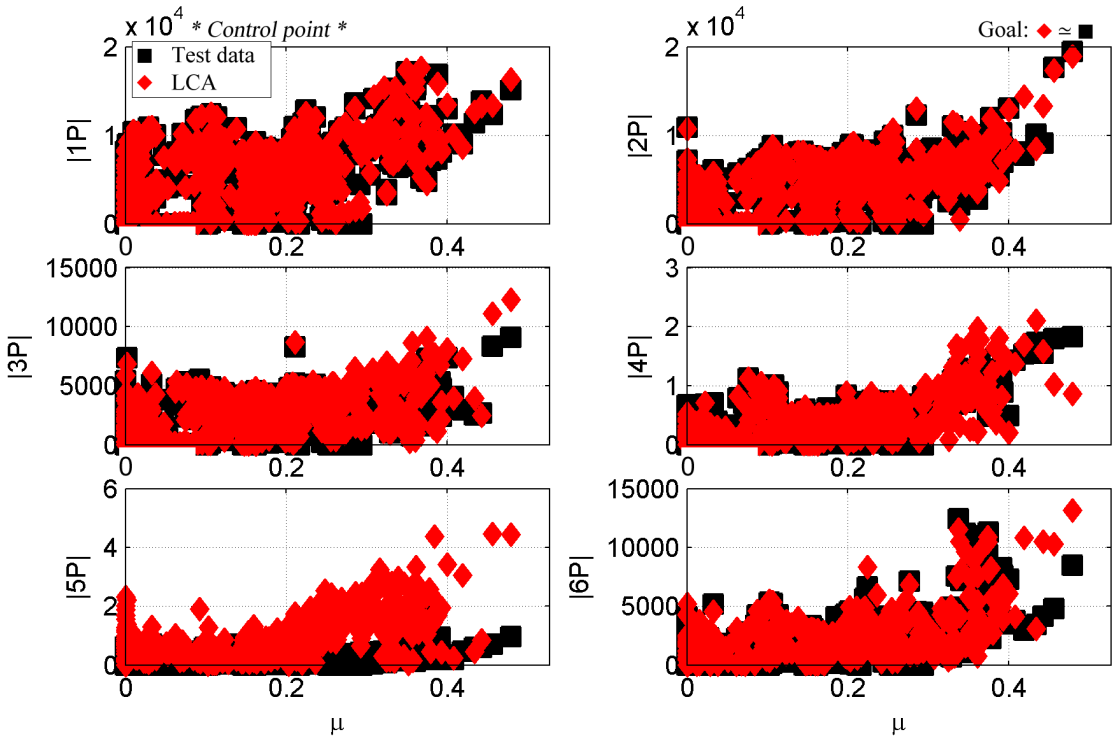

Figure 4.170: Loads matching by harmonic: all flight counters: SE70 (in-lb).

4.8 Lag Damper Loads

No direct lag damper sensors were applied as control points in this analysis. The hypothesis was that matching edgewise bending near the blade root would improve lag damper loads. Figure 4.171 shows peak-to-peak lag damper load (along with SE30) for the full sensor set for flights 84 and 85 (51 total flight counters). As shown, a dramatic improvement in SE30 does not influence lag damper response. In fact, in certain cases, application of the LCA worsens the loads match relative to LLT-generated loads. The reasons for this are not well understood at this time, but it is likely related to the fact that the LCA comprehensively corrects for flapwise bending moment, torsional moment, etc. Improvements to the external forcing function vector based on flapwise bending moment may in fact adversely impact torsional moment, and vice versa.

Two steps could be taken to remedy this poor lag damper loads match in future research efforts:

1. Add a lag damper sensor control point

2. Given the strong correlation between SE30 and lag damper load observed in Figure 4.171, develop an externally-applied lag damper load correction factor based on SE30

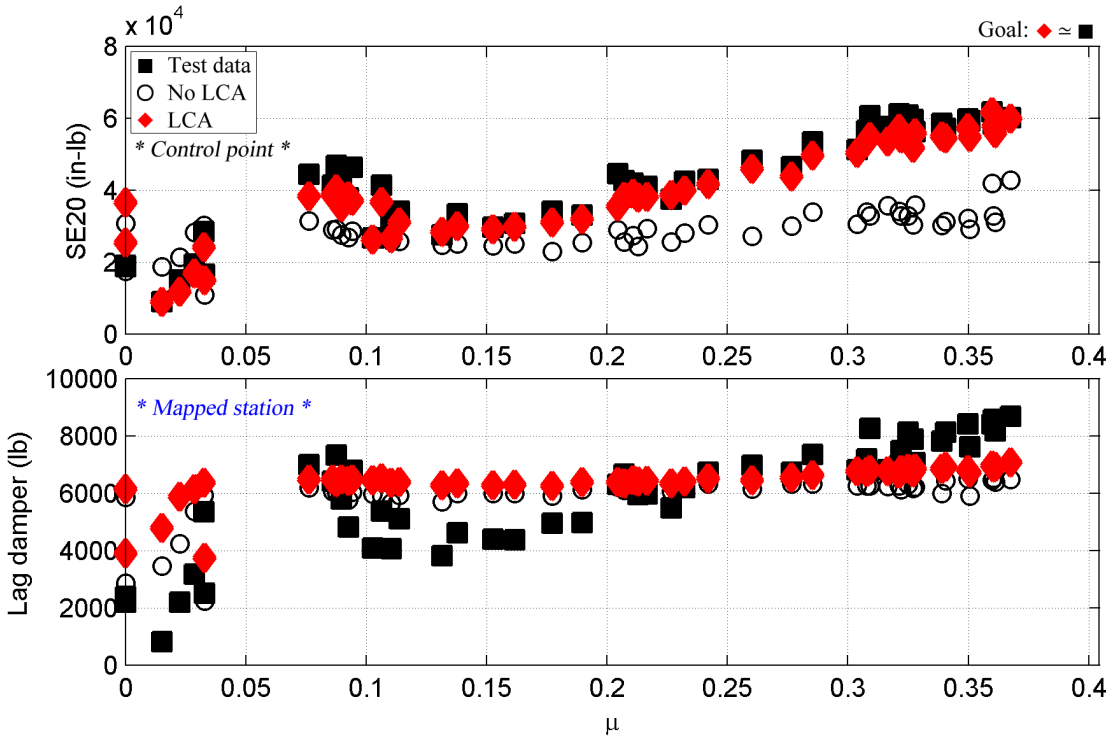

Figure 4.171: Peak-to-peak loads matching: sensor study: SE30, lead-lag damper load.

4.9 Summary

This chapter applied the LCA to a range of UH-60A test cases. The objective in each case was to match peak-to-peak load (per cycle) as well as magnitude and phase by harmonic It also defined the *LCA score*, an objective metric used to compare different loads results in order to determine the best match. The LCA was applied to the UH-60A flight test dataset, specifically the following cases:

1. Eight arbitrarily-selected flight counters from flight 84, covering hover to high-speed flight. LLT airloads were used. The effects due to two different control point sets were examined.

2. 51 flight counters (flights 84 and 85) for the *mechanical airloads* problem, where measured airloads from the UH-60A Airloads Program are fed into the DY-MORE LCA simulation.

3. Nine flight counters from legacy MDC-based analyses were discussed; five of these (c8534, c8927, c9017, c11679, and c11680) were examined in detail using the LCA.

4. The first cycle of all flight counters for flights 84 through 116 (601 total flight counters) were examined in order to show the robustness of the LCA across all flight regimes.

Chapter 5 examines the sensitivity of the LCA to input settings such as the duration of the simulation, the number of LCA applications, choice of control points, and the number of type of blade modes used in the simulation.

CHAPTER V

LCA PARAMETER SENSITIVITY STUDIES

5.1 Overview

This chapter examines the sensitivity of the LCA to the following parameters:

1. Starting timepoint for LCA application
2. Criteria for best fit solution
3. Duration of simulation; number of LCA applications
4. Choice of control points
5. Blade modes included in the simulation
6. Harmonic scalar (to be defined in Section 5.6)

Sensitivity is defined in terms of robustness of the LCA. Each of these parameters has been studied in detail. Based on experience and empirical studies, the settings provided in Section 4.2 have been defined. Each of the parameters listed above will be discussed and demonstrated in the following sections.

5.2 Starting Point for LCA Application

The LCA is applied every 6 rotor revolutions starting at 4 seconds into the simulation, giving the DYMORE simulation adequate time reach a periodic steady state. This holds true for all flight counters and all control points and is demonstrated in Figure 5.1 for c8534, blade torsional moment (mean removed) at $0.70R$ (ST70).

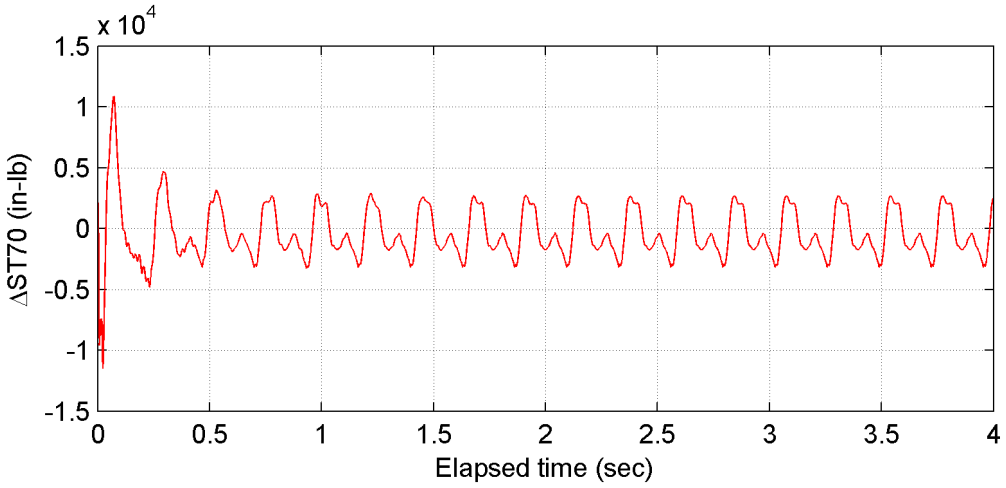

Figure 5.1: DYMORE solution convergence (c8534, ST70).

5.3 Criteria for Best Fit Solution

To ensure the best fit loads match, implementation of the LCA methodology includes the following. A time history simulation is performed for a full 36 seconds. This includes approximately 137 applications of the LCA ((36 - 4 sec) * 4.3 Hz). Then, in Matlab post-processing, a multi-objective optimization (MOO) is performed to construct a single aggregate objective function (AOF; effectively a weighted linear sum) as shown in equation 5.1. The minimum value of this AOF provides the timepoint at which the simulation is ended and the final load set is extracted. This AOF is based on the best aggregate match for SN30, ST30, and SE30. Given that it is computed in post-processing, this AOF could be based on the best aggregate match for any set of user-defined control points.

$$AOF(t_\tau) = \left(\frac{1}{S} \frac{1}{H} \sum_{s=1}^{S} \sum_{h=1}^{H} \left(\frac{\epsilon_{hj} - \epsilon^*_{hj}}{\epsilon^*_{hj}} \right)^2 \right)^{1/2} \tag{5.1}$$

where S is the number of LCA control points and H is the number of harmonics. The minimum value of this AOF is solved for using the Matlab *min()* function. An example of the timepoint selected for loads extraction is shown in Figure 5.3.

5.4 Simulation Duration; Effects on Convergence due to Simulation Runtime

The quality of the converged solution is a function of the duration of the simulation. The baseline case is a full 36 second time history simulation. A study was performed to see if this duration is adequate to provide a converged solution. For flights 84 and 85 (51 flight counters), simulations were run for both 36 seconds and 108 seconds. The control points were 16 blade sensors: [SN20/30/40/50/60/70/90, ST30/70/90, and SE20/30/40/50/60/70]. Figures 5.2 through 5.7 show a time history of the magnitudes of the blade bending load magnitudes by harmonic. The black solid line is the test data; the red line is the DYMORE solution with the LCA applied (starting at 4 seconds). The red diamond is the AOF-computed final timepoint (convergence point). These results are shown for six flight counters, in order of increasing advance ratio: (1) c8509 (hover), (2) c8521 ($\mu = 0.029$), (3) c8517 ($\mu = 0.090$), (4) c8513 ($\mu = 0.153$), (5) c8525 ($\mu = 0.232$), and (6) c8534 ($\mu = 0.368$). In these charts, load magnitude for the j^{th} harmonic is defined as follows:

$$|L_j| = \sqrt{c_j^2 + s_j^2} \tag{5.2}$$

These time histories highlight the fact that the DYMORE LCA implementation computes an on-line FFT for each control point for each timepoint. This on-line FFT computes an estimate of the magnitudes of the Fourier components of each signal at specific, given frequencies - each a multiple of the rotor angular speed, $\Omega = 4.3$ Hz. See Section 17.3 of Reference [9] for the full description of the on-line FFT calculation.

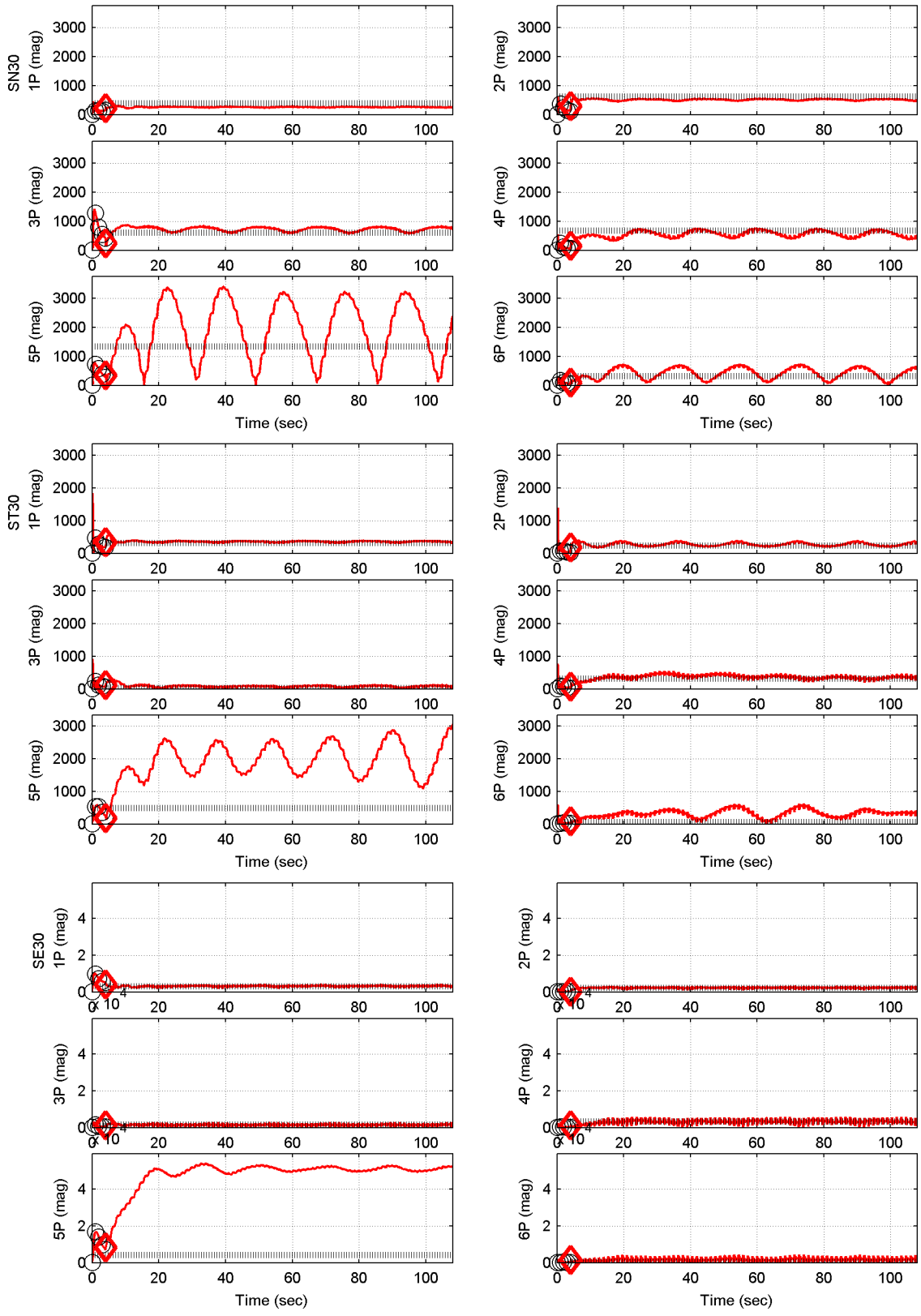

Figure 5.2: SN30, ST30, SE30: time history, load component by harmonic; [flight counter, μ] = [8509, 0.0]; LLT (no LCA; circle), LCA (red line), LCA convergence point (red diamond), test data (black line).

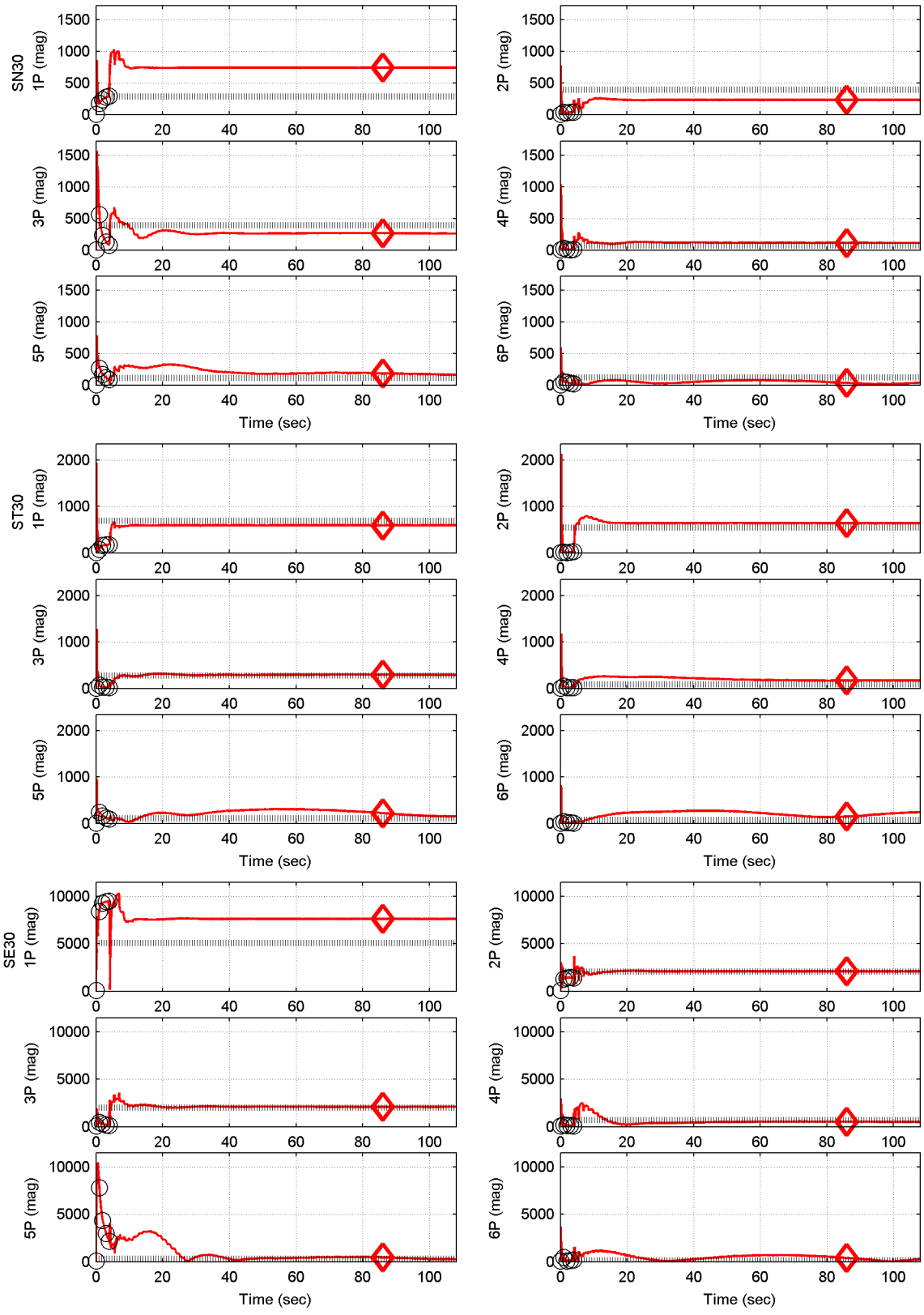

Figure 5.3: SN30, ST30, SE30: time history, load component by harmonic; [flight counter, μ] = [8521, 0.029]; LLT (no LCA; circle), LCA (red line), LCA convergence point (red diamond), test data (black line).

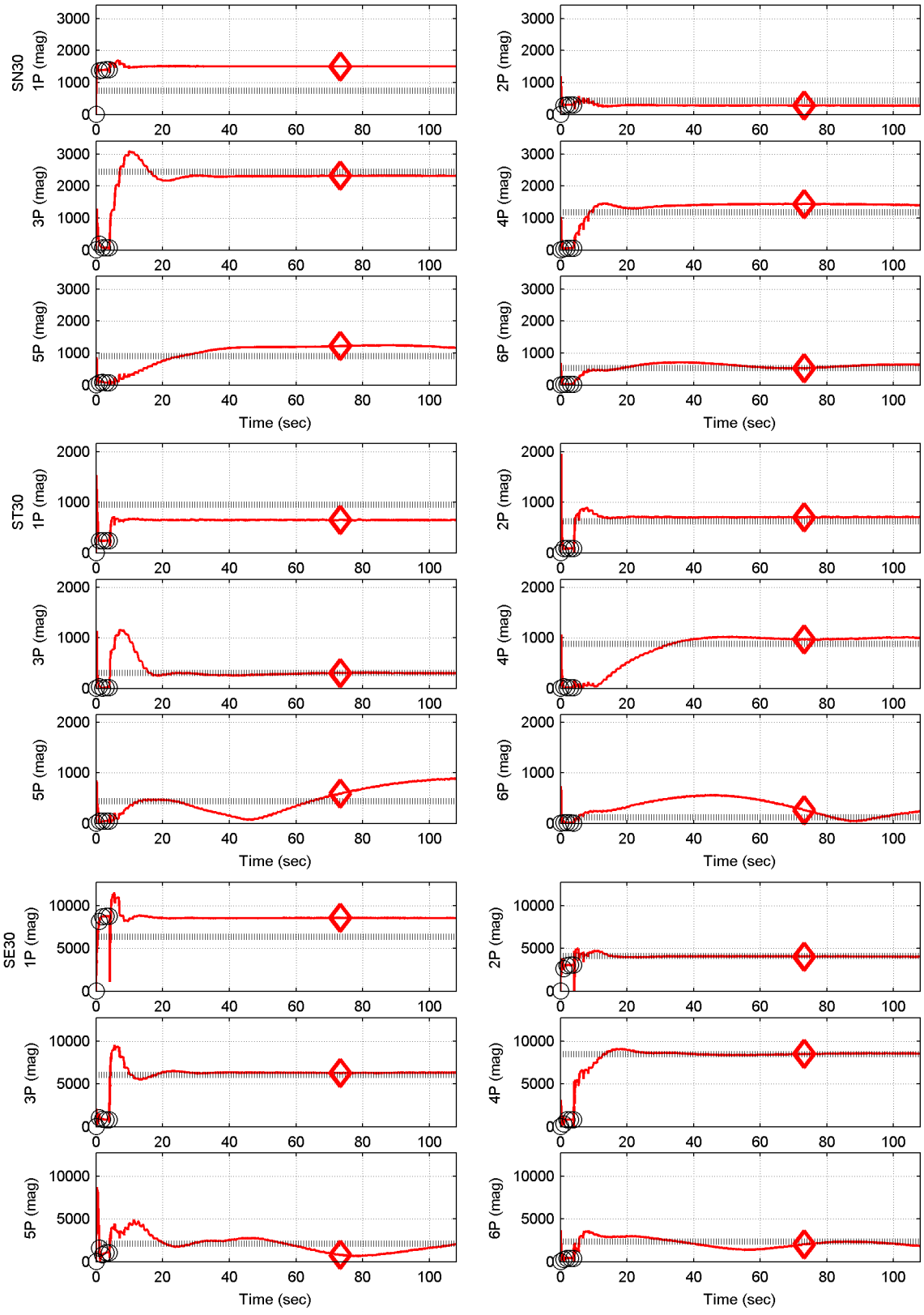

Figure 5.4: SN30, ST30, SE30: time history, load component by harmonic; [flight counter, μ] = [8517, 0.090]; LLT (no LCA; circle), LCA (red line), LCA convergence point (red diamond), test data (black line).

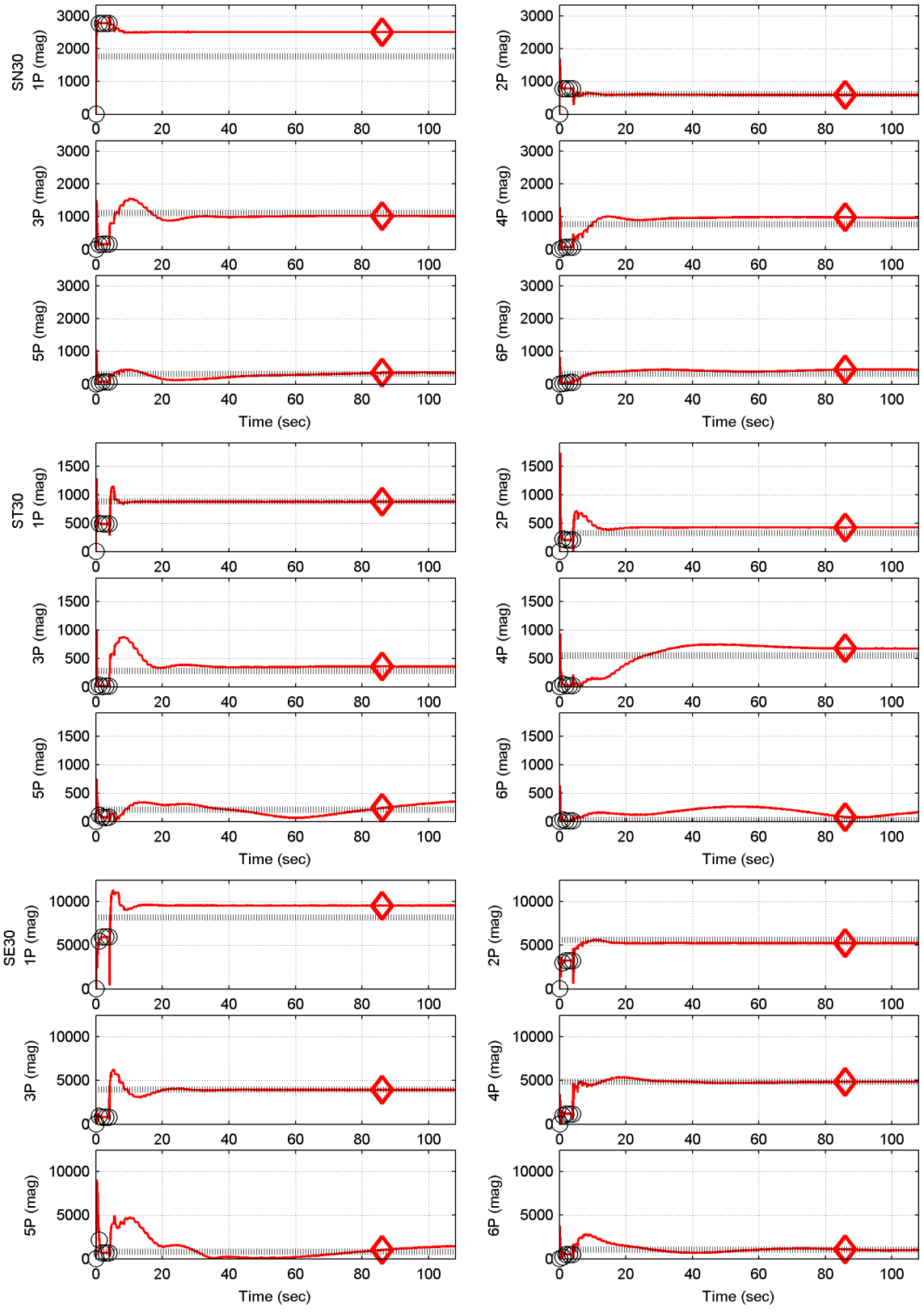

Figure 5.5: SN30, ST30, SE30: time history, load component by harmonic; [flight counter, μ] = [8513, 0.153]; LLT (no LCA; circle), LCA (red line), LCA convergence point (red diamond), test data (black line).

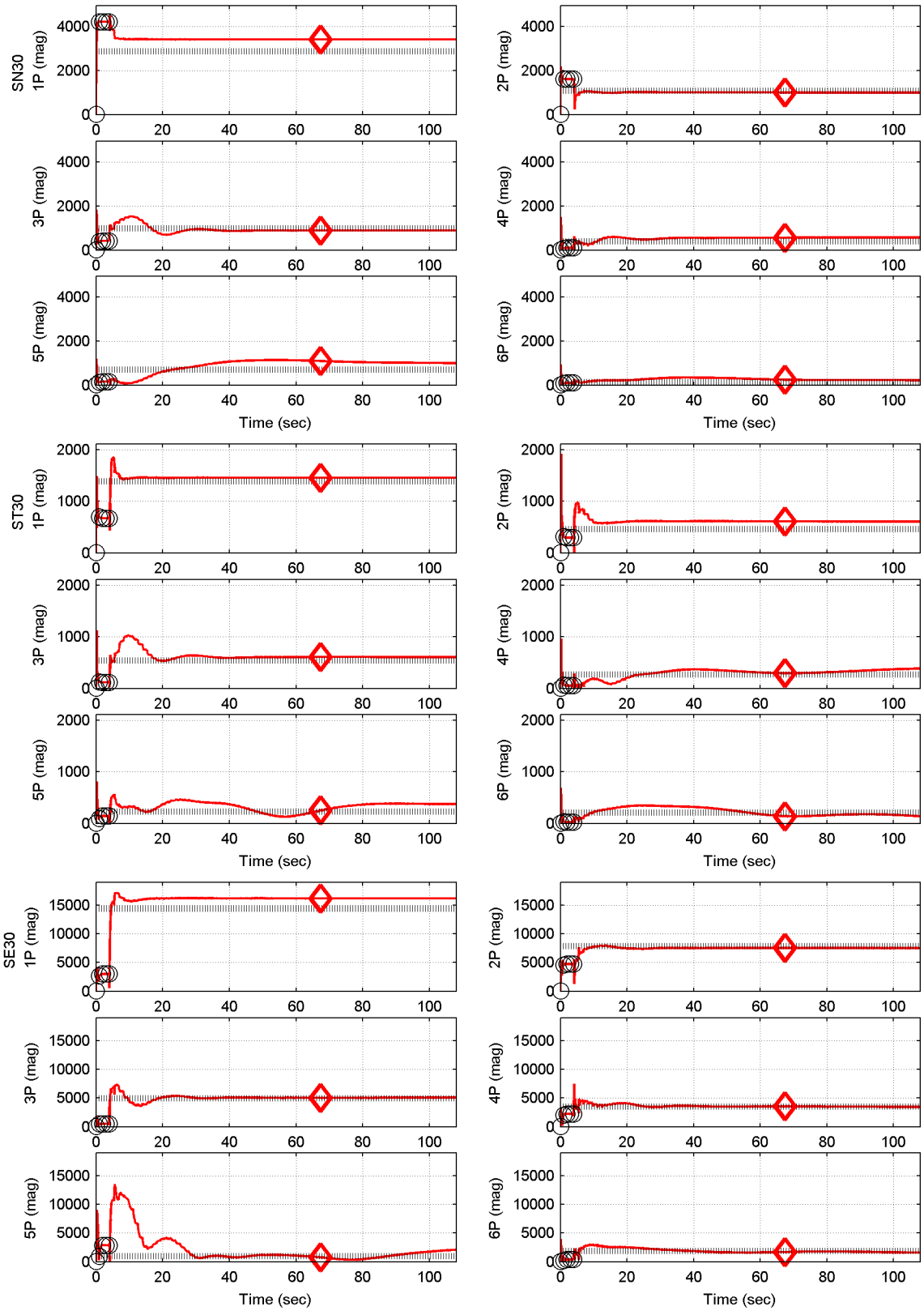

Figure 5.6: SN30, ST30, SE30: time history, load component by harmonic; [flight counter, μ] = [8524, 0.232]; LLT (no LCA; circle), LCA (red line), LCA convergence point (red diamond), test data (black line).

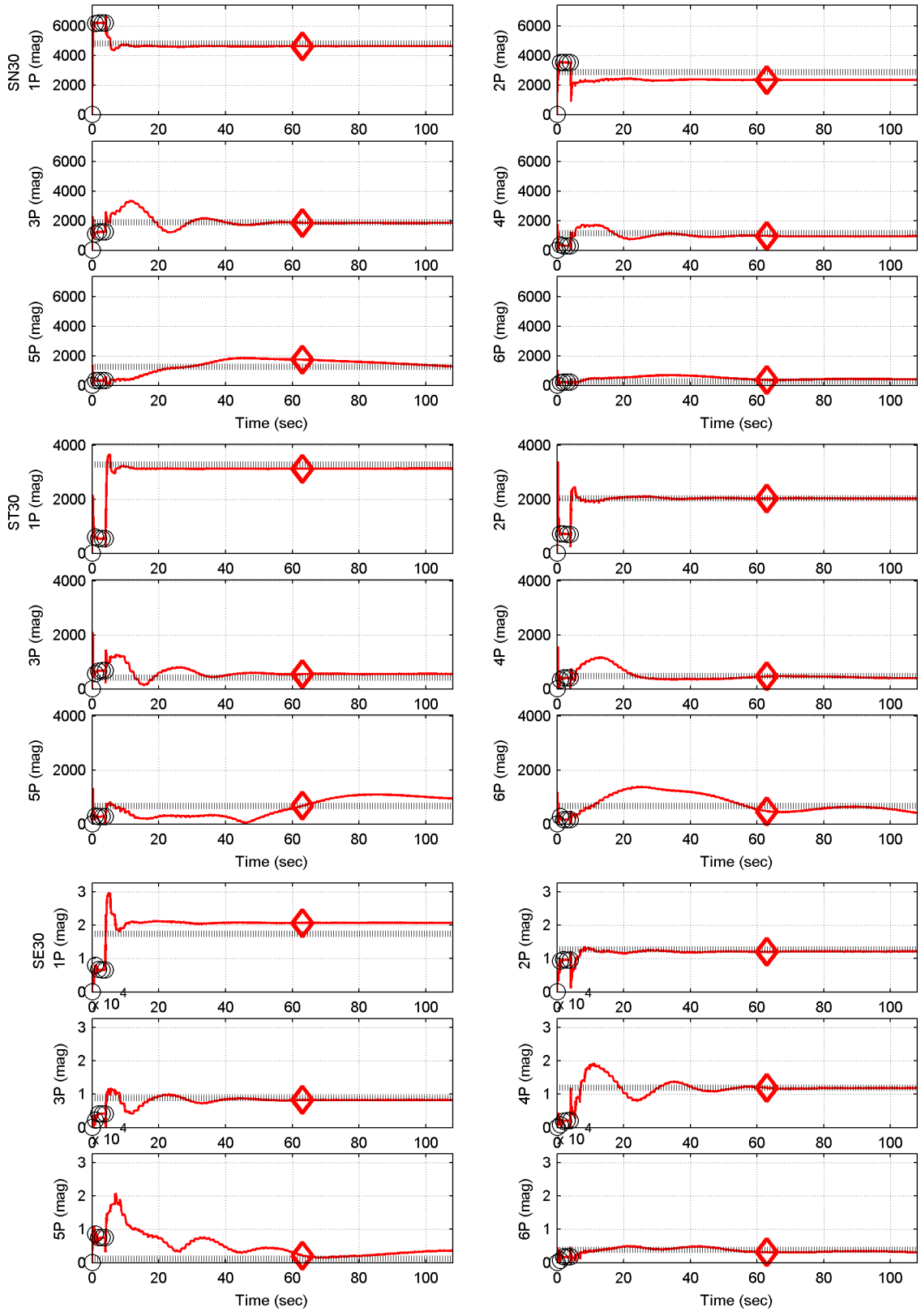

Figure 5.7: SN30, ST30, SE30: time history, load component by harmonic; [flight counter, μ] = [8534, 0.368]; LLT (no LCA; circle), LCA (red line), LCA convergence point (red diamond), test data (black line).

Several conclusions can be reached. First, for the hover case (c8509), there are both large divergences and dynamic instabilities in the $5P$ response. This will be discussed in greater detail in Section 5.4.1. For other cases, the minimum AOF is at a timepoint beyond 36 sec. For example, Figure 5.3 (c8521), with a stopping point of approximately 87 seconds. However, the solution is fairly stable beyond 40 seconds. Thus a truncated solution of 36 seconds is deemed to provide a best fit solution. In this case, computational time is a consideration. It takes approximately 8 minutes of CPU time on a standard i5 quad-core desktop PC with 16 GB RAM to perform a 36 second simulation; run time is approximately proportional to simulation time. The LCA adds approximately 10% runtime to a standard DYMORE simulation. The largest adverse computational effect is large I/O file writing to disk. Future research efforts could focus on file I/O optimization. The final conclusion is that an acceptable loads match is achieved for all harmonics (with some offset seen in $1P$) with a 36 second simulation, with little quantitative improvement by extending the simulation to 108 seconds. This $1P$ offset reduces with increasing advance ratio and is discussed in greater detail in Section 5.4.2.

As mentioned above, the 108 sec case does present a somewhat more robust loads match than the 36 sec case. However, as shown by the closeness of the *LCA scores* for each (Table 5.1) - as well as the sensitivity to the need for a faster computational solution - the 36 sec case has been used for all other simulations presented herein.

Table 5.1: Simulation runtime: scoring.

Case	**LCA score**
No LCA	0.150
108 sec simulation	0.117
36 sec simulation	0.128

5.4.1 Instability in 5P Response

Instability in $5P$ response (e.g., Figure 5.2) occurs in cases where $5P$ magnitude is largest relative to $1P$, $2P$, etc. The physical explanation is as follows. Dominant $5P$ response - and, more so, dominant *off-harmonic* response between $4P$ and $5P$ (e.g., Figure 5.8, bottom) - causes excitation of nearby blade modes. Specifically, dominant $5P$ response excites the $5.21P$ blade bending mode with some potential contributions from the neighboring $4.64P$ and $4.53P$ blade bending modes as well. These lightly damped modes produce a large system response, driven to a larger margin of instability by forcing function modifications at the $5P$ frequency via the LCA.

This phenomenon occurs primarily near hover (e.g., c8509, $\mu = 0.0$; Figure 5.9) but can occur at higher μ values as well, such as maneuvers providing strong $5P$ excitation due to multiple blade stalls presented in Q3 and Q4 (e.g., c11680, $\mu = 0.388$; Figure 5.10) or BVI excitation (e.g., c8431, $\mu = 0.103$; Figure 5.11). The impact at hover is more dramatic, given that $5P$ load content is much larger relative to lower harmonic load content. For higher-speed flight, the effect is reduced; although there can be non-negligible $5P$ content, the overall response is driven as much or more by $1P$, $2P$, etc.

This does, however, point out a deficiency in the LCA: it cannot necessarily match response at a given control point for a given harmonic if the measured response at that control point is appreciable enough to excite a lowly damped neighboring structural mode to the point of static divergence or dynamic instability (in this example, dominant $5P$ exciting the $5.21P$ blade bending mode). Two points should be mentioned that reduce the impact of this deficiency. First, the LCA attempts to recover from this deficiency by stopping the solution at the timepoint producing the minimum AOF (equation 5.1). Second, this appears to primarily be an issue near hover, where (1) there is more *off-harmonic* content in the data, and (2) load magnitudes

are much smaller in hover than for forward flight. This issue can occur at higher μ, but here the $5P$ response - though present - is dominated more by other harmonics. It also becomes less of an issue due to the relative purity of the response at $1P$, $2P$, ..., $6P$ (i.e., minimal *off-harmonic* content) at higher μ. To show this last point, see Figure 5.12. In this figure, all 601 flight counters from Section 4.7 were studied. The relative magnitude of the $5P$ response to the overall magnitude is examined for SN30. This *5P ratio* is defined as follows:

$$5P\ ratio = \frac{|5P|}{(|1P|^2 + |2P|^2 + |3P|^2 + |4P|^2 + |5P|^2 + |6P|^2)^{0.5}} \tag{5.3}$$

Part (a) of Figure 5.12 shows the maximum $5P$ ratio computed across the full 36 second DYMORE simulation plotted versus μ. - i.e., without the AOF-calculated simulation end time (equation 5.1). The general trend is that the $5P$ ratio reduces with increased μ, although there is non-negligible $5P$ content throughout. This is quantified in part (c), showing this DYMORE-computed $5P$ ratio versus the $5P$ ratio computed for the UH-60A test data. A perfect loads match between analysis and test would show results along the diagonal on this chart. As shown, most values are in the upper left half, showing an over-prediction of analysis-based $5P$ content. Part (e) of this chart simply overlays the two-dimensional parts (a) and (c), showing the general trend of lower $5P$ content with increased μ. Parts (b), (d), and (f) of this figure show the same results, but now with application of the AOF-computed simulation end time (equation 5.1). The same trends are seen, but with much better match with test data. This chart highlights the advantages of the use of the AOF-computed simulation end time.

In future studies, it is recommended that modal damping be considered as an option in application of the LCA, much as modal damping is used in the mechanical airloads solution, where an artificial damping coefficient of 0.02 is added to improve

convergence (see [9], Section 10.2). The other consideration would be to determine *a priori* the presence of these sensitive modes and reduce or eliminate LCA application to these modes' neighboring harmonics, as required.

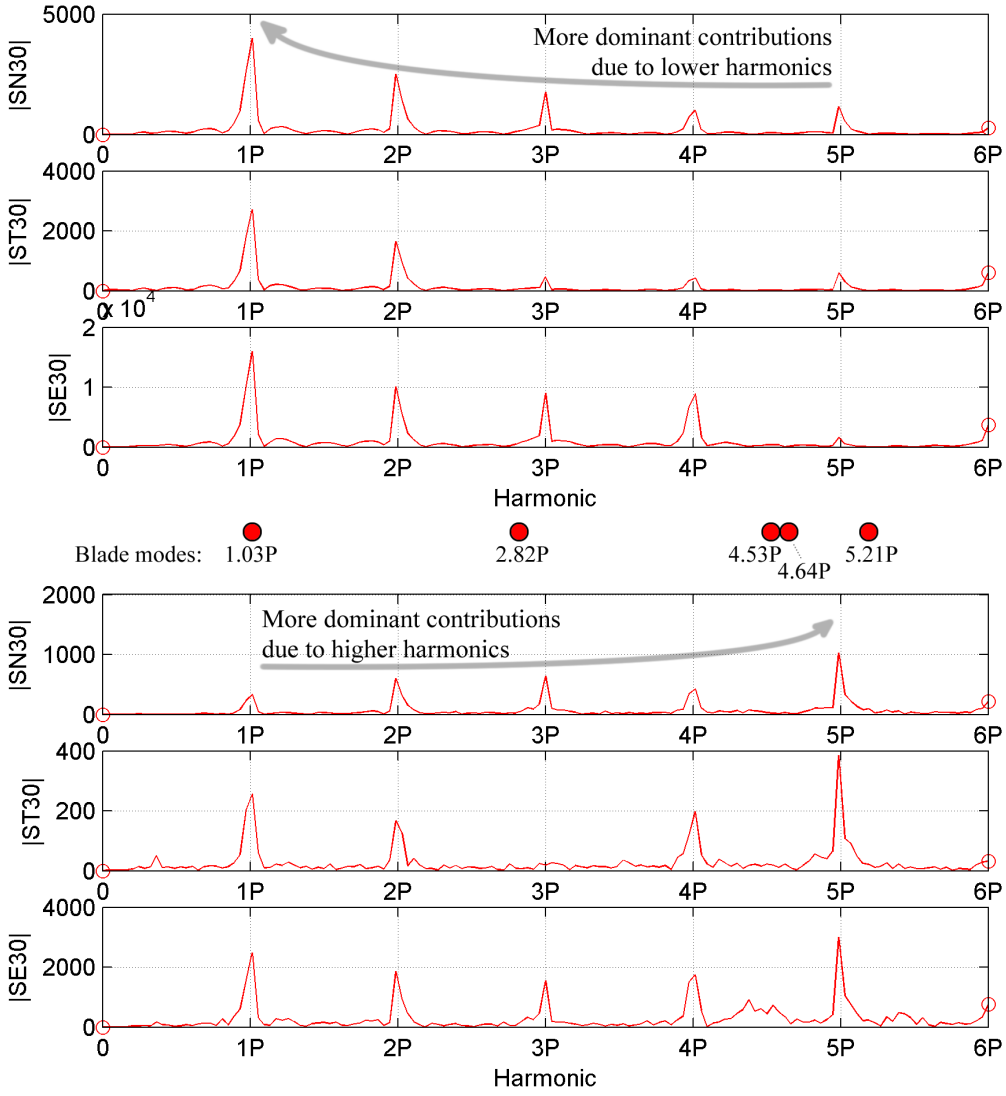

Figure 5.8: Blade bending, by harmonic: c8533, $\mu = 0.360$ (top); c8509, $\mu = 0.0$ (bottom).

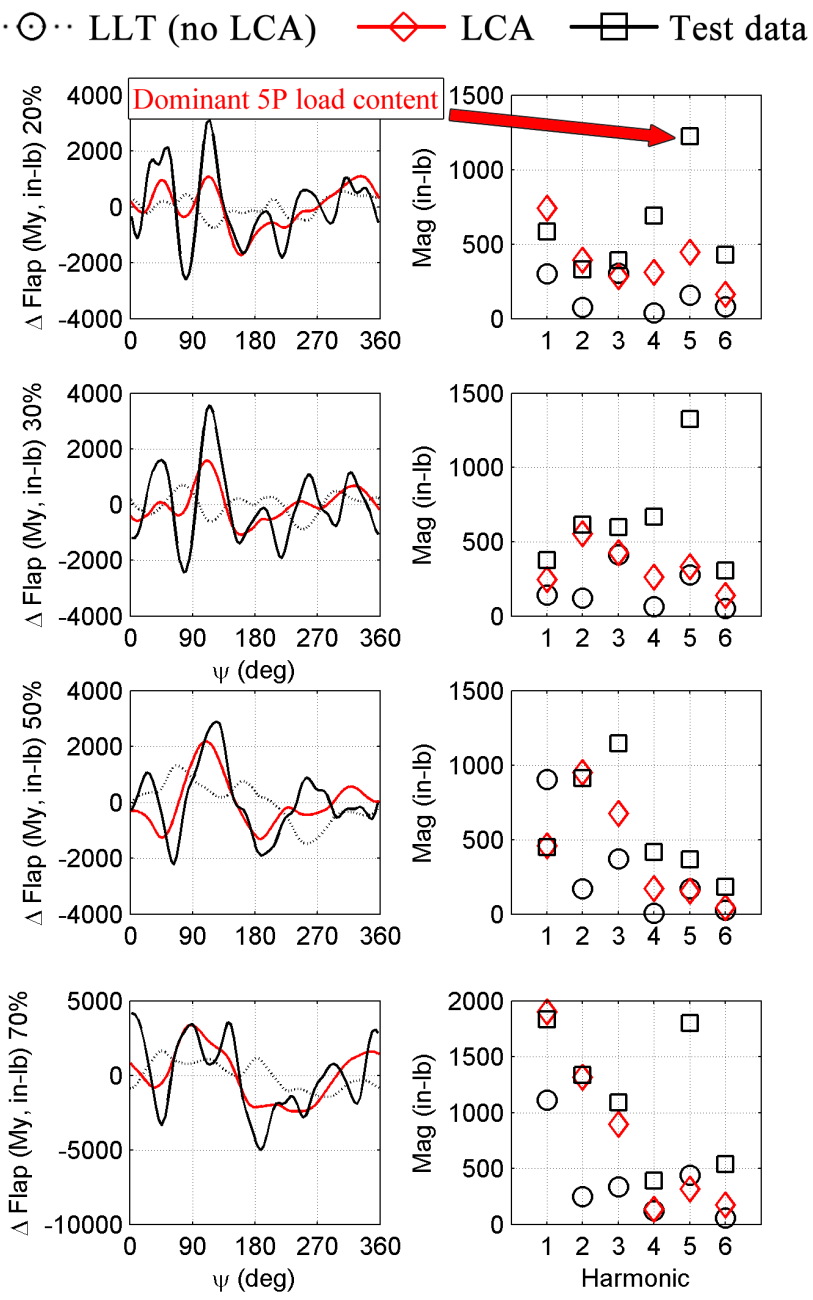

Figure 5.9: Flapwise bending moment: time history, load component by harmonic; [flight counter, μ] = [8509, 0.0]

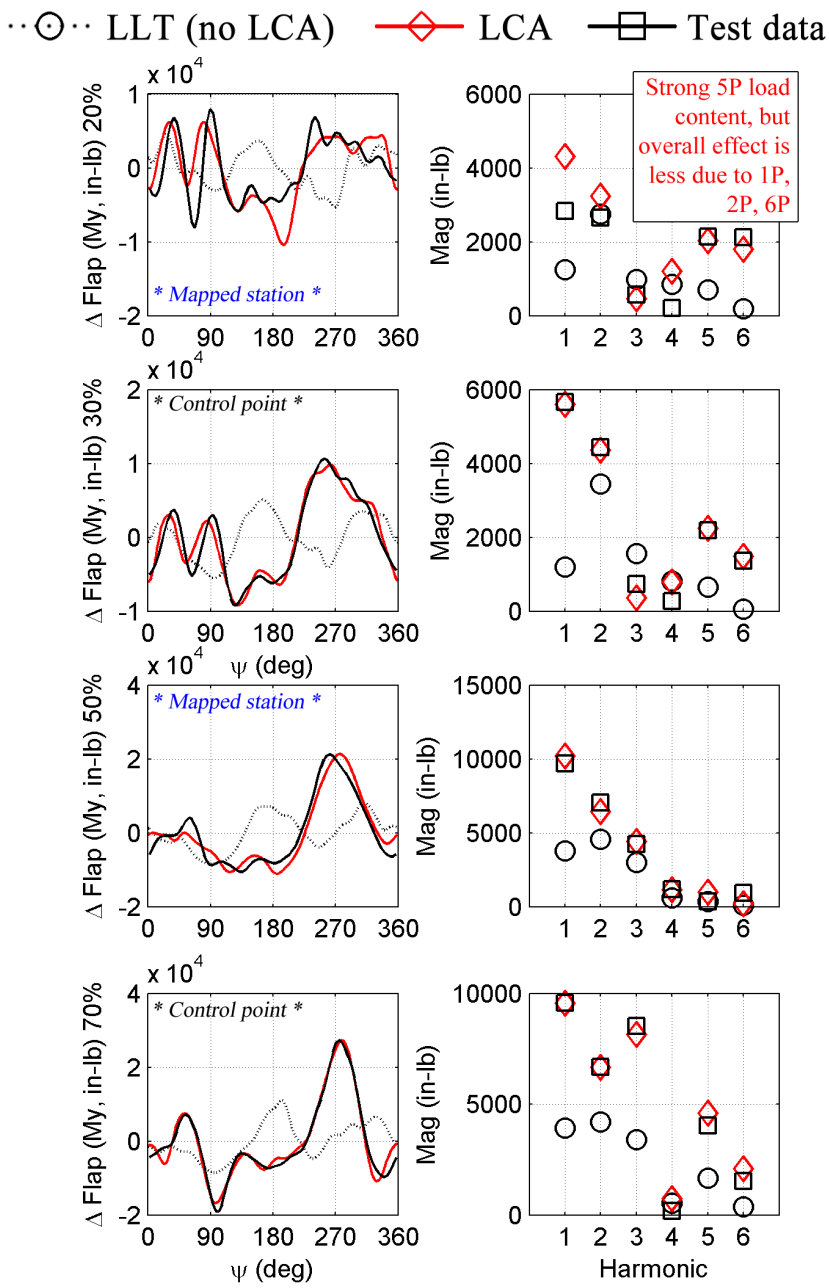

Figure 5.10: Flapwise bending moment: time history, load component by harmonic; cycle 11 [flight counter, μ] = [11680, 0.388]

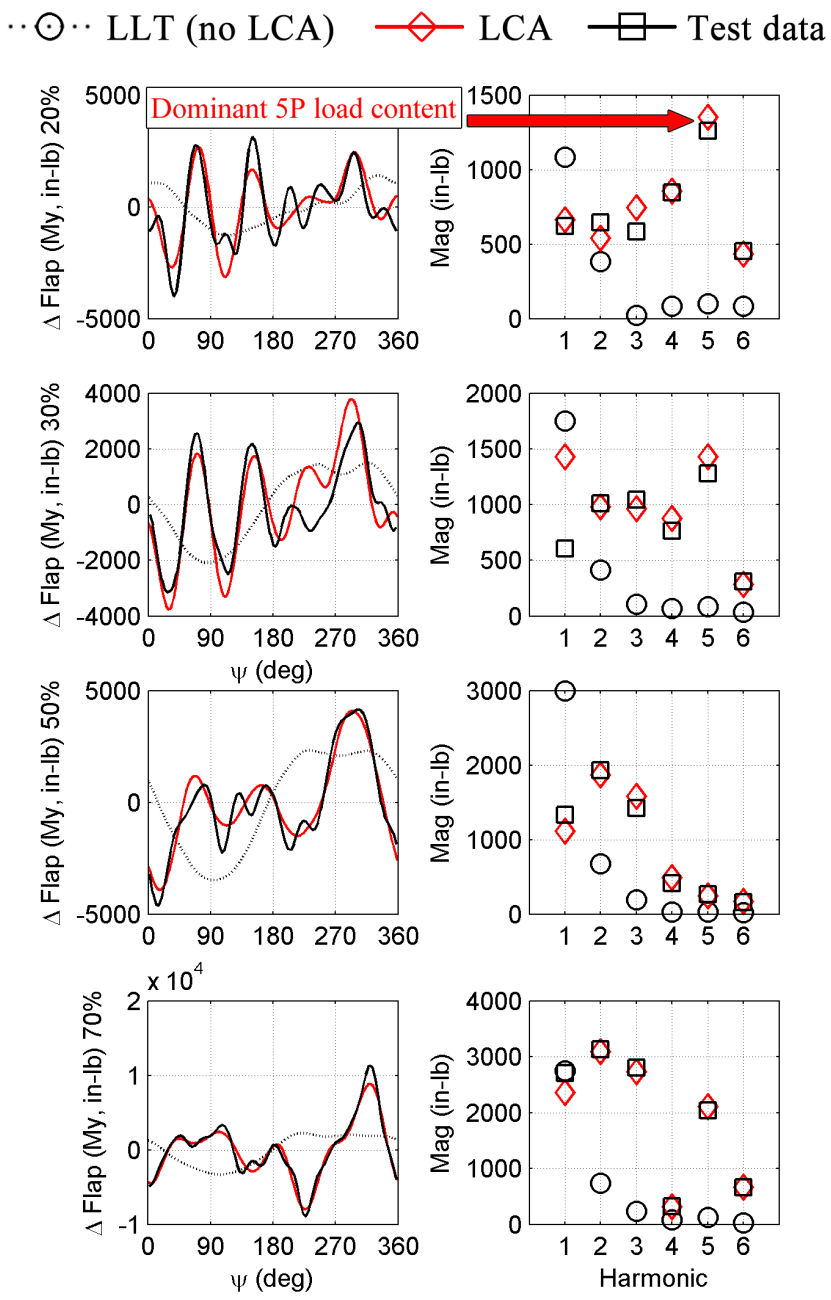

Figure 5.11: Flapwise bending moment: time history, load component by harmonic; [flight counter, μ] = [8431, 0.103]

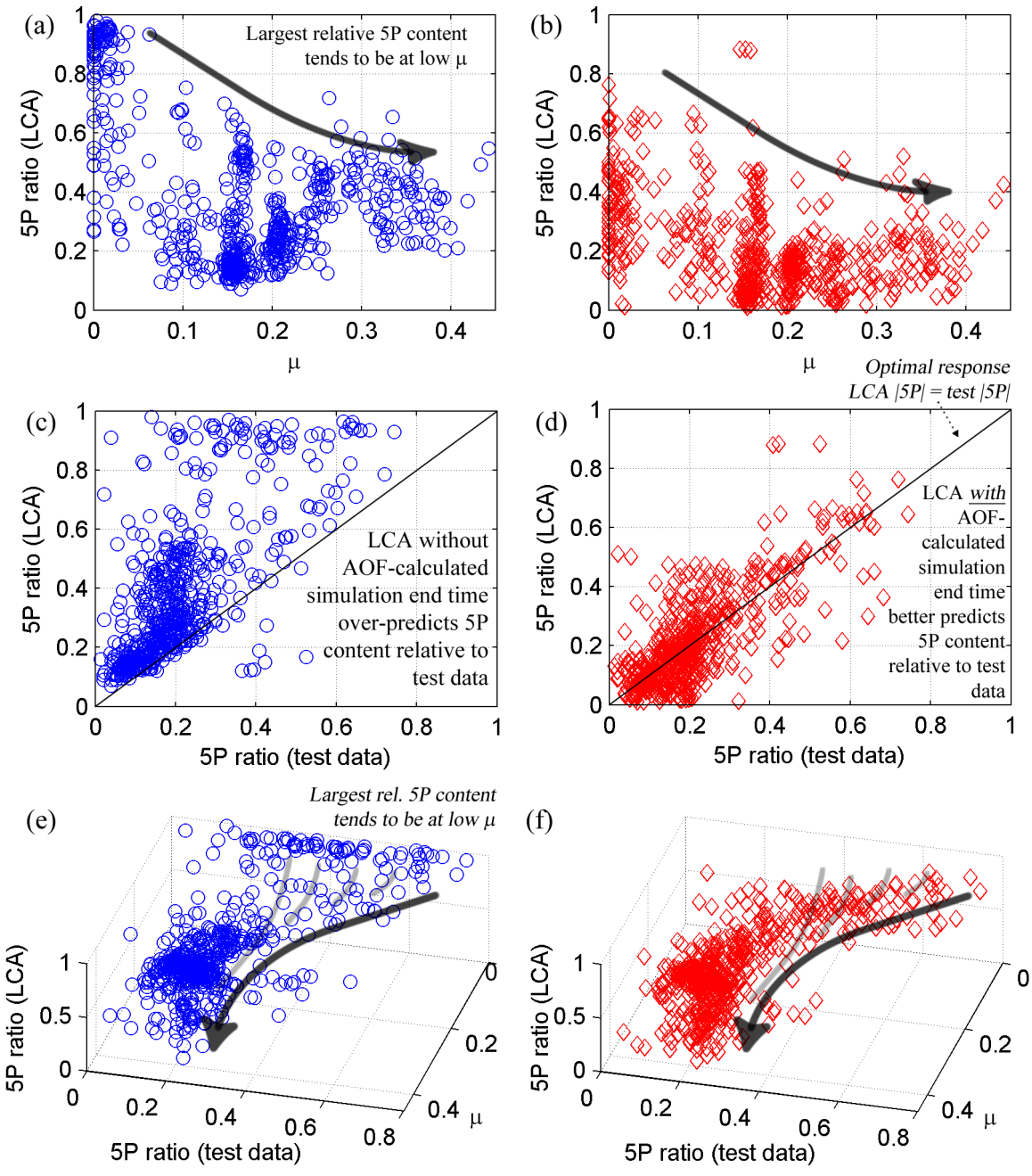

Max 5P ratio across full 36 sec simulation (i.e., without AOF-calculated simulation end time)

5P ratio at AOF-calculated simulation end time

Figure 5.12: 5P ratio: SN30.

5.4.2 1P Response Offset

The $1P$ offset seen in Figures 5.3 through 5.5 is due to the fact that only flexible modes (modes 3 and higher) are used in the LCA formulation. This is an important point. $1P$ is driven by rigid flapping (mode 2, $\approx$ 1.04P). The LCA is deficient at being able to support rigid modes in its numerical formulation (equation 2.2) for a complex problem such as a full-scale rotor. This is purely a numerical problem and not an issue with the underlying LCA formulation. This is not an issue for application of the LCA to simpler structures, such as the scale model rotor blade [22] and the plate structure [23] used to validate the LCA, as described in Section 2.5.

In Chapter 2, nodal forces/moments at the analysis *control points* ($\underline{\epsilon}$) were related to modal displacements ($\underline{q}$) by means of the force/moment-displacement matrix, $\mathbf{B}$ ($n \times m$), as follows:

$$\underline{\epsilon}(t) = \mathbf{B}\,\underline{q}(t) \tag{5.4}$$

Inversion of equation 5.4 via singular value decomposition (SVD) methods ([8], Section 18.9) yields the $\mathbf{B}^{+}$ matrix ($m \times n$), as follows.

$$\underline{q}(t) = \mathbf{B}^{+}\,\underline{\epsilon}(t) \tag{5.5}$$

For the current UH-60A solution, blade control points are all bending or torsional moments measured on the aircraft using strain gages. Blade bending moment (SN) is proportional to blade curvature [46]:

$$SN \propto EI\frac{\partial^2 z}{\partial x^2} \tag{5.6}$$

where SN is blade flapwise bending moment, z is the direction normal to the blade surface, x is the radial direction, and EI is the effective bending stiffness of the blade at a particular cross section. Rigid blade flapping (mode 2 for the UH-60A) produces effectively zero curvature and contributes to bending moment via its second time derivative weighted by blade mass and the appropriate moment arm. Therefore,

strain gages (e.g. SN20) will measure very little contribution due to this flapping acceleration. This means that, if q_2 - the rigid flapping mode - is included in the formulation, the associated column in the **B** matrix for each blade bending moment *control point* will be very small relative to the higher mode columns. Pseudo-inversion of **B** should subsequently yield very large terms in the row of the $\mathbf{B}^+$ matrix associated with q_2.

A simple example to demonstrate this issue is now provided. Look at a system with two control points (ϵ_1, ϵ_2) based on two modes (q_1, q_2). Let ϵ_1 be blade flapwise bending moment at station r, ϵ_2 be blade edgewise bending moment at station r, q_1 be rigid blade flapping, and q_2 be a blade bending mode (coupled flap and lag motion). Equation 5.4 may now be formulated as:

$$\begin{Bmatrix} \epsilon_1 \\ \epsilon_2 \end{Bmatrix} = \begin{bmatrix} B_{11} & B_{12} \\ B_{21} & B_{22} \end{bmatrix} \begin{Bmatrix} q_1 \\ q_2 \end{Bmatrix} \tag{5.7}$$

In this example, $\underline{\epsilon}$ should be dominated by blade bending; therefore B_{11} and B_{21} should each be $<<$ B_{12} and B_{22}. Also, ϵ_1 should be $<<$ ϵ_2 (e.g., Figures 4.37 and 4.41). The following values will be used to represent this case.

$$\begin{Bmatrix} \epsilon_1 \\ \epsilon_2 \end{Bmatrix} = \begin{bmatrix} 10^2 & 2 \times 10^4 \\ 2 \times 10^2 & 8 \times 10^4 \end{bmatrix} \begin{Bmatrix} q_1 \\ q_2 \end{Bmatrix} \tag{5.8}$$

Inversion yields the following:

$$\begin{Bmatrix} q_1 \\ q_2 \end{Bmatrix} = \begin{bmatrix} 2 \times 10^{-2} & -5 \times 10^{-3} \\ -5 \times 10^{-5} & 2.5 \times 10^{-5} \end{bmatrix} \begin{Bmatrix} \epsilon_1 \\ \epsilon_2 \end{Bmatrix} \tag{5.9}$$

If, in this example, $\epsilon_1 = 2e4$ in-lb and $\epsilon_2 = 8e4$ in-lb, the resulting values for $\underline{q}$ would be $q_1 = 0$ and $q_2 = 1$. If however, there were small offsets in $\underline{\epsilon}$, e.g., $\epsilon_1 = 2.2e4$ in-lb and $\epsilon_2 = 8e4$ in-lb, the resulting values for $\underline{q}$ would be $q_1 = 40$ and $q_2 = 0.9$. This is a dramatic difference in modal response.

For a problem as complex as a rotor system using real-world rotor loads measurements in the LCA formulation, these variations in $\underline{\epsilon}$ are present, and it results

in numerical ill-conditioning in the $\mathbf{B}^+$ matrix. Effectively, there is such a large differential in size between rigid and flexible modes in the $\mathbf{B}$ matrix, matrix inversion leads to an inability to converge in the numerical simulation. This could potentially be improved upon in the numerical simulation in future research efforts. Given that the LCA is only minimally affected by this, as has been shown throughout Chapter 4, peak-to-peak (and *by harmonic*) loads comparisons between analysis and test across all flight regimes, this issue is not addressed further in this research effort.

5.5 Number, Type, and Location of Control Points; Number of Blade Modes Used in Analysis

This section examines three control point sets, as shown in Table 5.2 and Figure 5.13. Also shown in this table are the modes used in each solution.

Table 5.2: LCA control points used in analysis.

Case	Number of points	LCA control points	Rationale	Blade modes
1	16	SE20/30/40/50/60/70, SN20/30/40/50/60/70/90, ST30/70/90	Full blade instrumentation set	3-10
2	6	SE30/70, SN30/70, ST30/70	Demonstration of LCA loads mapping capabilities (prediction of load at non-instrumented locations; e.g. SN50)	3-6,8,10
3	1	PL (pushrod)	Simplest instrumentation set (and easiest to implement)	10

Section 5.5.1 details the sensitivity of each of these three control point sets to choice of modes. Section 5.5.4 compares the results for these three control point sets.

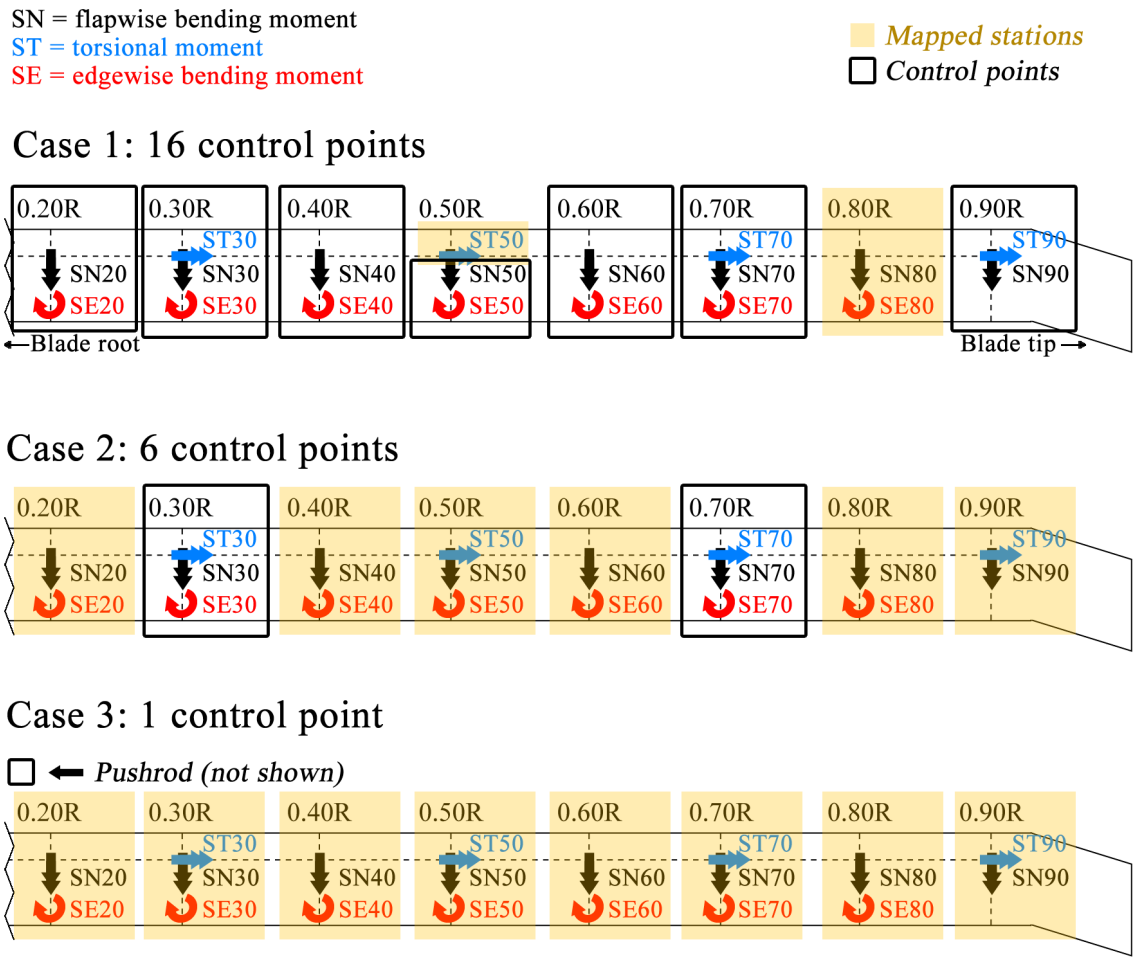

Figure 5.13: UH-60A blade control points and mapped stations.

5.5.1 Full Blade Control Point Set

For the full control point set (*Case 1* in Table 5.2), a range of mode sets have been examined (Table 5.3). These mode sets were selected to help determine the optimal mode combination required to provide the best fit loads match. Figures 5.14 through 5.20 show peak-to-peak loads comparisons for the first cycle of each flight counter for flights 84 and 85 (51 total flight counters) for the following cases: experimental (test) data, the DYMORE solution immediately prior to application of the LCA, modes 3-9, modes 3-10, and modes 3-11. All other cases from Table 5.3 were examined as well but are not included in the figures. They are, however, included in

the *LCA scores* listed in Table 5.3.

Table 5.3: Modes (all blade control points): scoring.

Case	Modes	LCA score
No LCA	-	0.150
1a	3-5	0.174
1b	3-6	0.248
1c	3-7	0.200
1d	3-8	0.157
1e	3-9	0.151
1f	**3-10**	**0.128**
1g	3-11	0.159

The first observation from these results is the inability of LLT airloads (run with no vortex model) to capture BVI effects (see, for example, Figure 5.14 at $\mu \approx 0.09$). LLT, as run with no vortex model, predicts flapwise bending as a monotonically increasing function with μ. To understand this in greater detail, Figures 5.21 through 5.24 show flapwise bending moment magnitude by harmonic versus advance ratio for the first cycle of each flight counter for flights 84 and 85 (51 total flight counters). LLT does a suitable job capturing $1P$ (cyclic) load content but is deficient at capturing $3P$ through $6P$ effects. As discussed in Section 1.5.1, forward flight has multiple stalls throughout a rotor rotation, resulting in $3P$ and higher content. Application of the LCA remedies this deficiency and suitably matches flapwise bending all μ across all radial stations.

For the blade torsional moment (Figures 5.16 and 5.17), LLT under-predicts load magnitude for $0.30R$ and $0.50R$, with improvements in peak-to-peak load matching outboard on the blade. Note that, as detailed in Section 3.3.4, ST50 contains significant erroneous measured test data; the y-axis is cropped appropriately in these

charts to show details of valid flight data. For application of the LCA, the presence of mode 11 leads to a dramatic over-prediction of blade torsional moment. Mode 11 - a 2nd torsional moment mode - appears to be similar in nature to mode 10. The LCA seems to work best with more distinct modes; the presence of multiple modes of similar content makes the LCA over-correct. The underlying physics behind this is not understood at this time.

Figures 5.25 and 5.26 show load content by harmonic for ST30 and ST70, respectively. Application of the LCA does an excellent job at matching peak-to-peak torsional moments, with some degradation in match at ST90. This is likely due to more dramatic unsteady airload effects present outboard on the blade, producing modal content well above the 2nd torsional moment mode included in the solution herein. The LCA does an excellent job of matching $1P$, $3P$, and $5P$ content, yet over-predicts $2P$, $4P$, and $6P$, more so at higher μ.

For blade edgewise bending, (Figures 5.18 and 5.19), LLT under-predicts load magnitude at all radial stations, more so with higher μ. Again this is heavily influenced by the lack of in-plane flow effects, including vortices (e.g., $3P$ content, as shown in Figure 5.27). Application of the LCA does a suitable job at matching both peak-to-peak load as well as load magnitude across all harmonics. Figure 5.27 is an excellent example of the value of the LCA at correcting the load response (in this case, at $3P$).

Figure 5.20 shows peak-to-peak loads for ST30 and pushrod. Both are shown because there is a strong correlation between the two. In this case, pushrod load is a *mapped* quantity, i.e., not applied as a control point in the algorithm. An interesting observation is that the LCA better predicts ST30 from a *pushrod control point* (Section 5.5.3) than pushrod load from an *ST30 control point* (Figure 5.20). The reason for this is not well understood at this time.

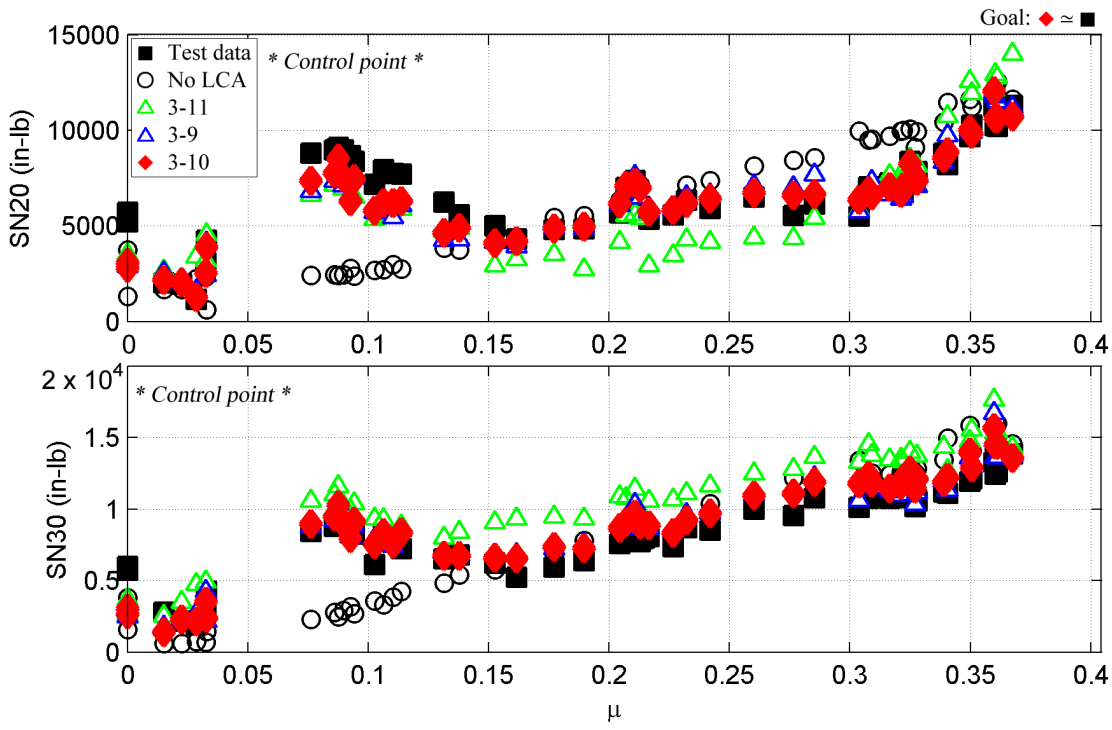

Figure 5.14: Peak-to-peak loads matching: effects of modes; all sensors: SN20, SN30.

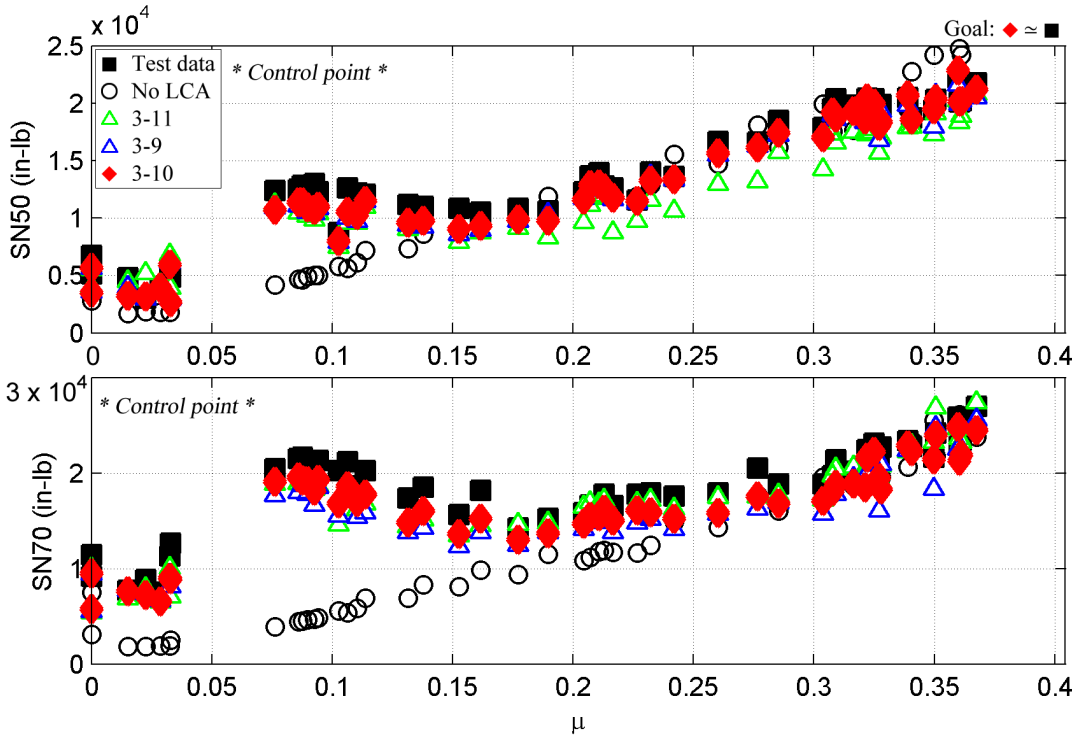

Figure 5.15: Peak-to-peak loads matching: effects of modes; all sensors: SN50, SN70.

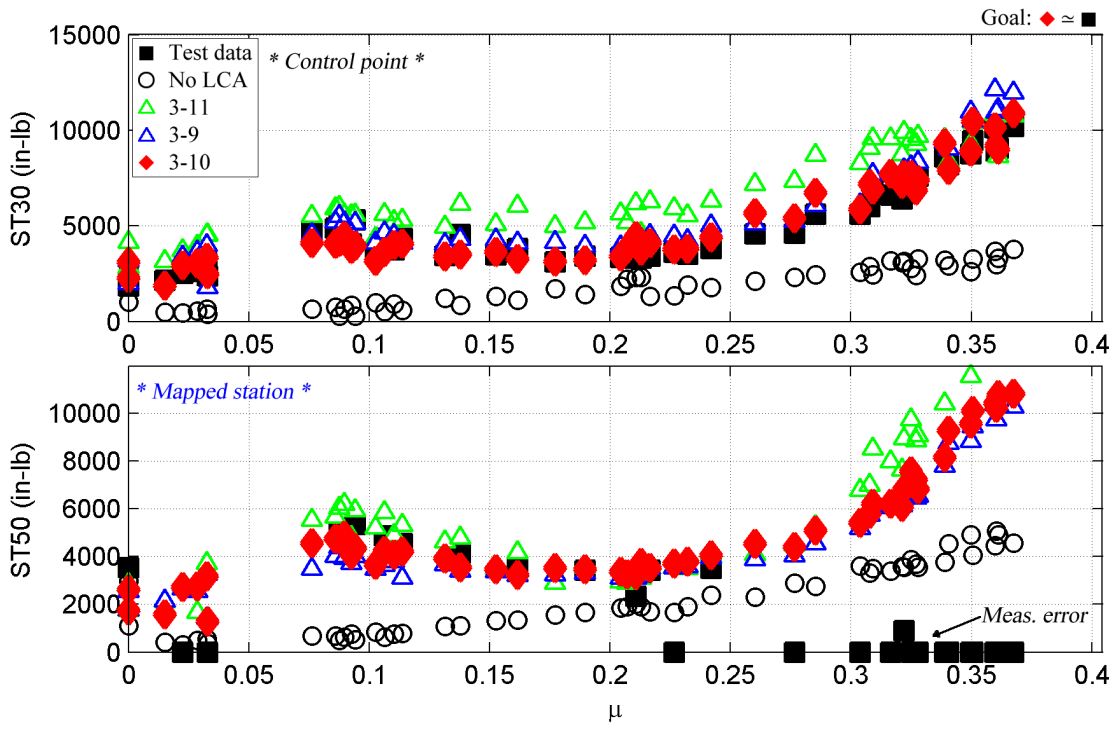

Figure 5.16: Peak-to-peak loads matching: effects of modes; all sensors: ST30, ST50.

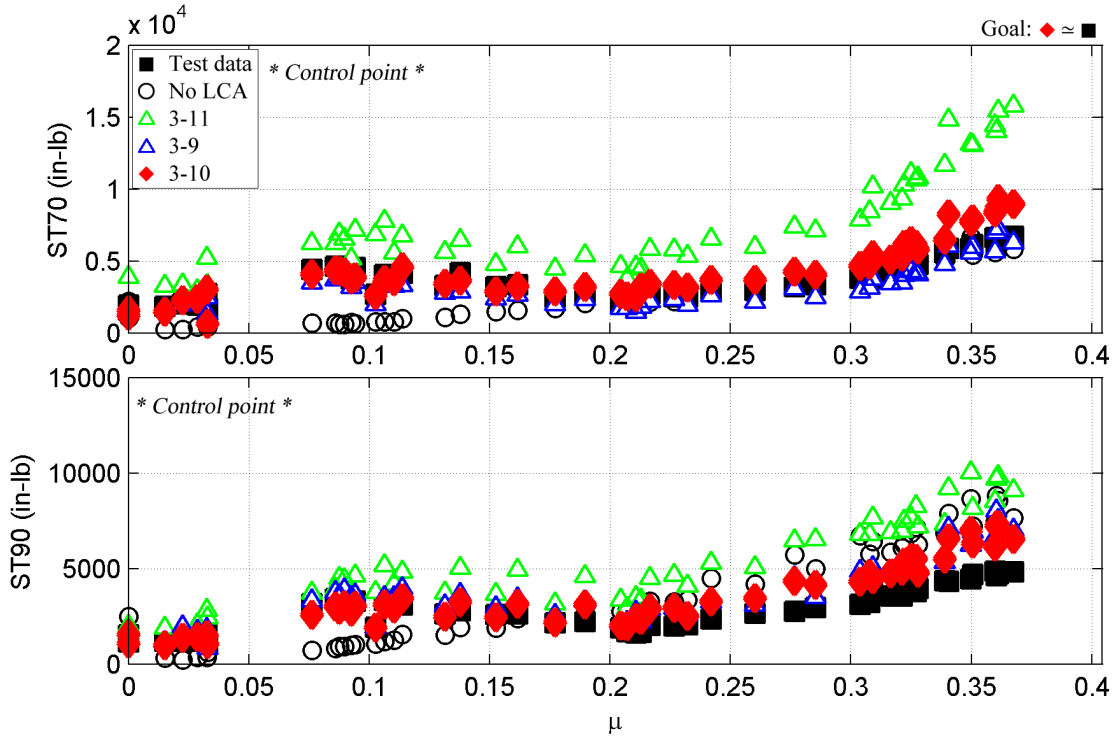

Figure 5.17: Peak-to-peak loads matching: effects of modes; all sensors: ST70, ST90.

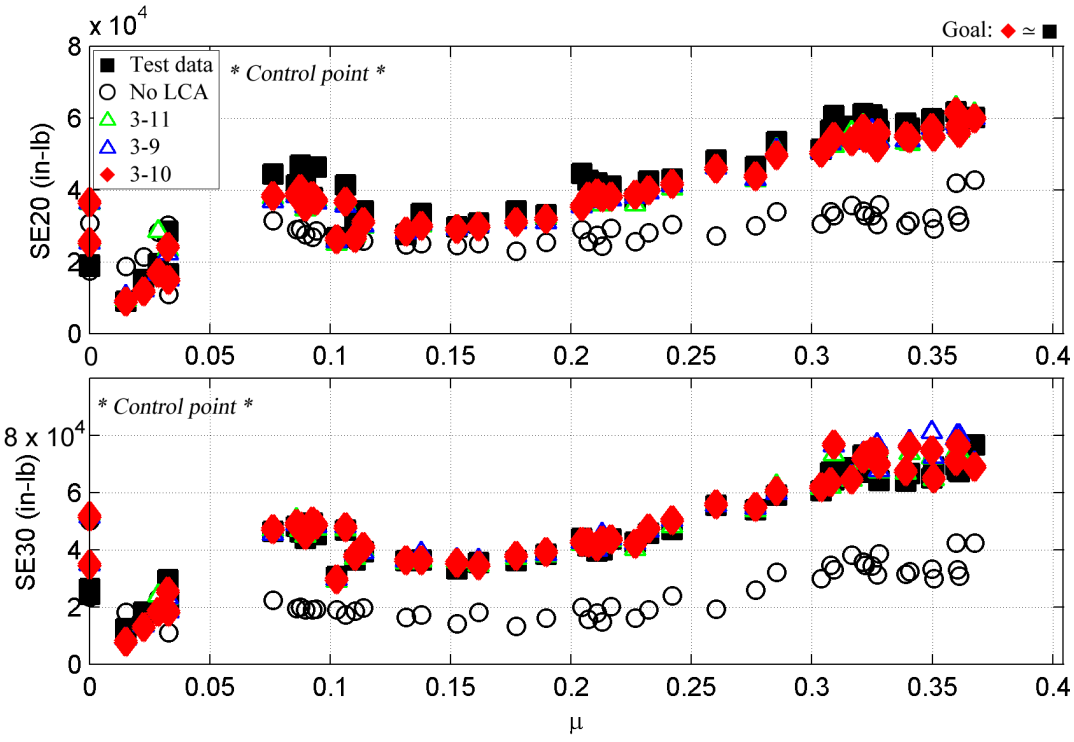

Figure 5.18: Peak-to-peak loads matching: effects of modes; all sensors: SE20, SE30.

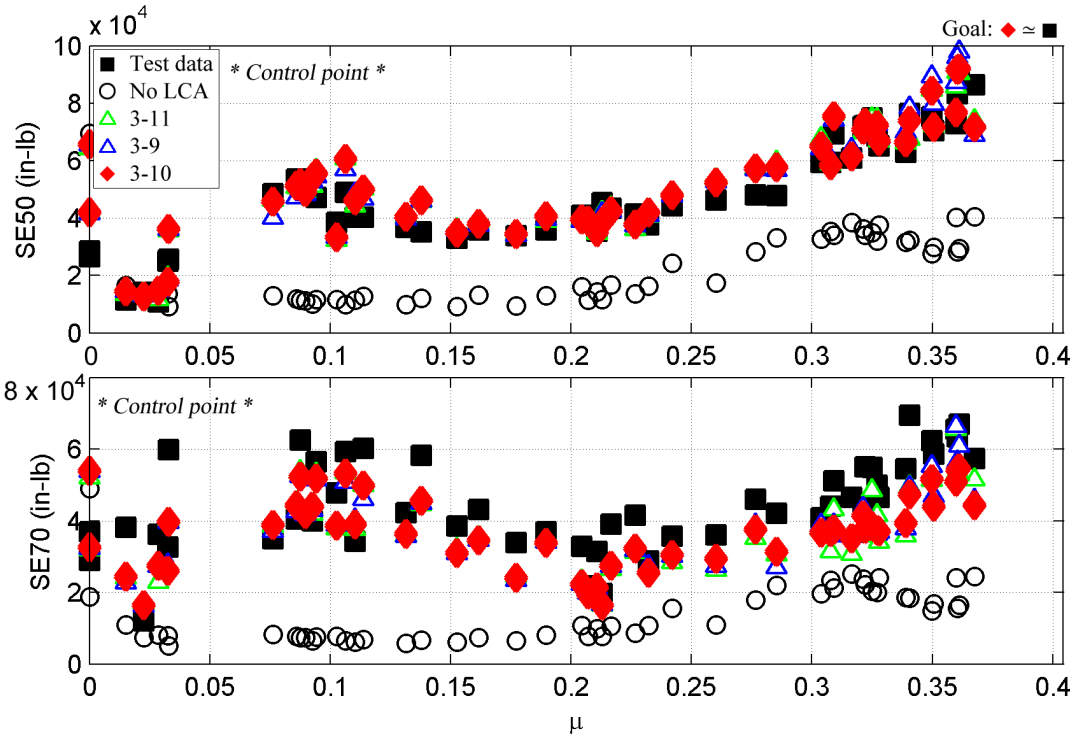

Figure 5.19: Peak-to-peak loads matching: effects of modes; all sensors: SE50, SE70.

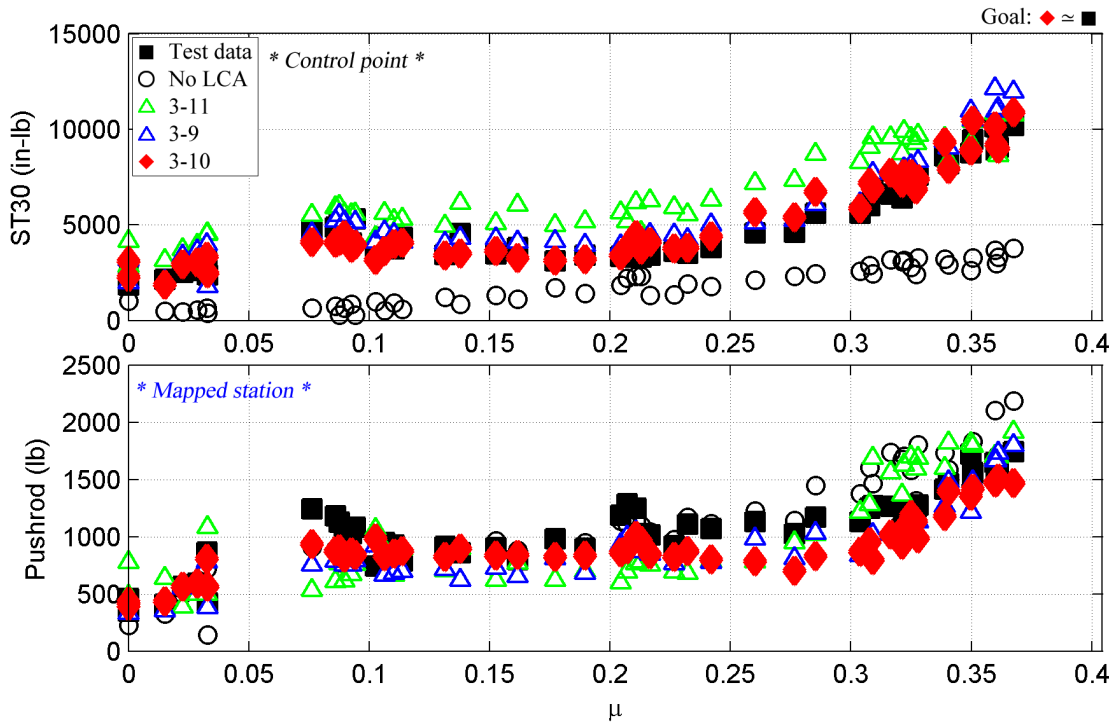

Figure 5.20: Peak-to-peak loads matching: effects of modes; all sensors: ST30, pushrod.

To further understand the application of the *LCA score* implemented for each case, the underlying loads match by harmonic is now examined. Figures 5.21 through 5.30 show load magnitude by harmonic versus advance ratio for the first cycle of each flight counter for flights 84 and 85 (51 total flight counters) for a subset of cases from Table 5.3.

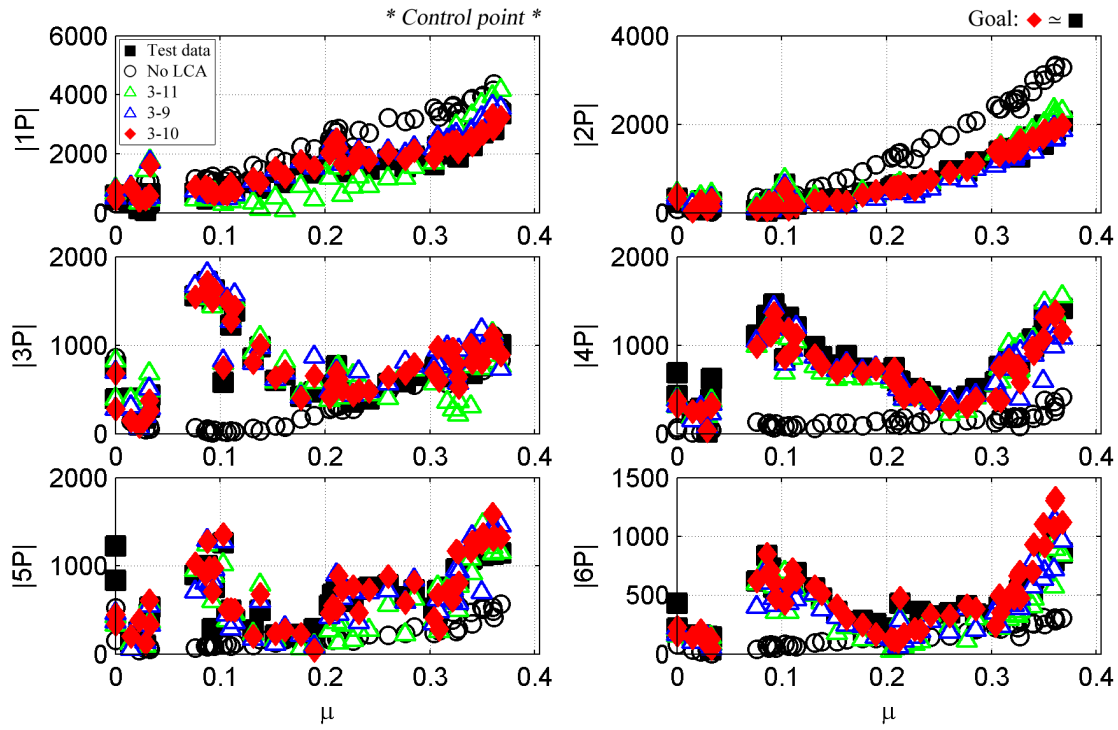

Figure 5.21: Loads matching by harmonic: effects of modes; all sensors: SN20 (in-lb).

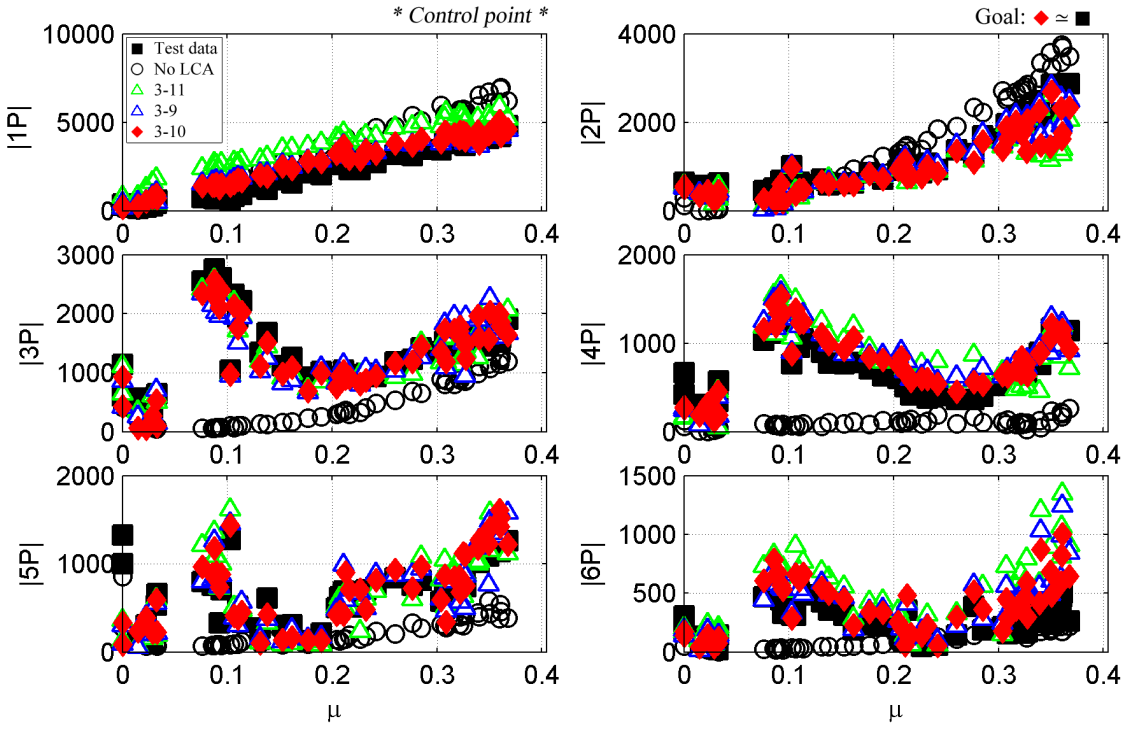

Figure 5.22: Loads matching by harmonic: effects of modes; all sensors: SN30 (in-lb).

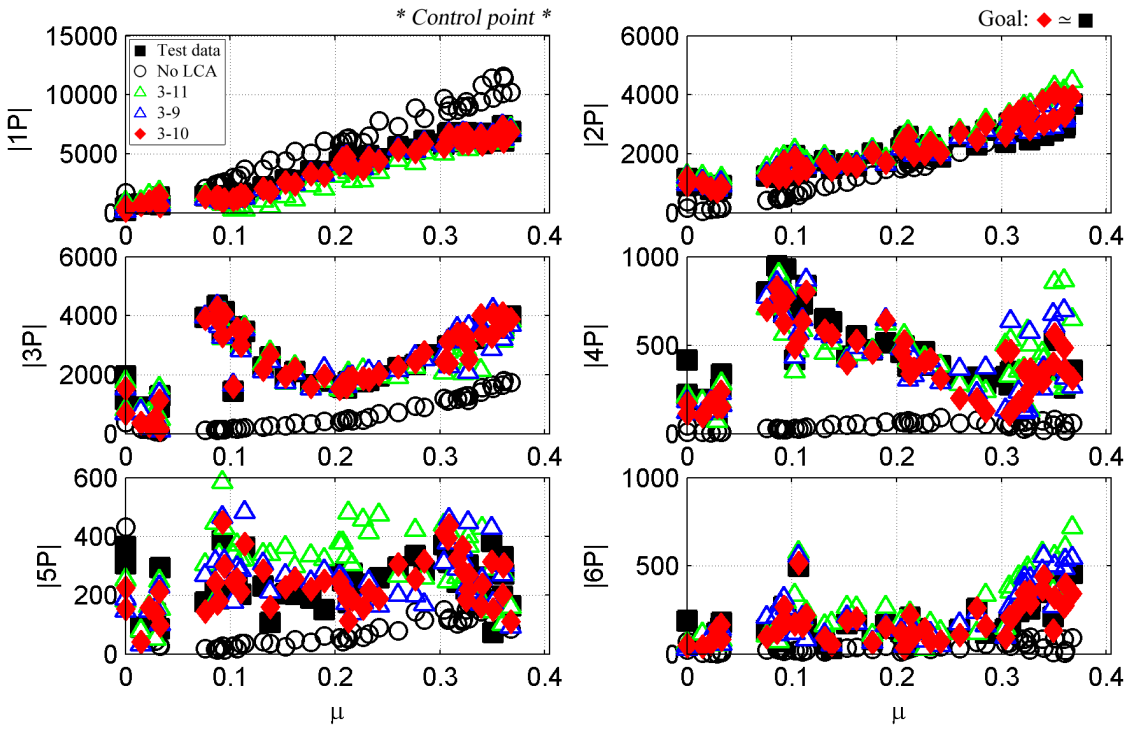

Figure 5.23: Loads matching by harmonic: effects of modes; all sensors: SN50 (in-lb).

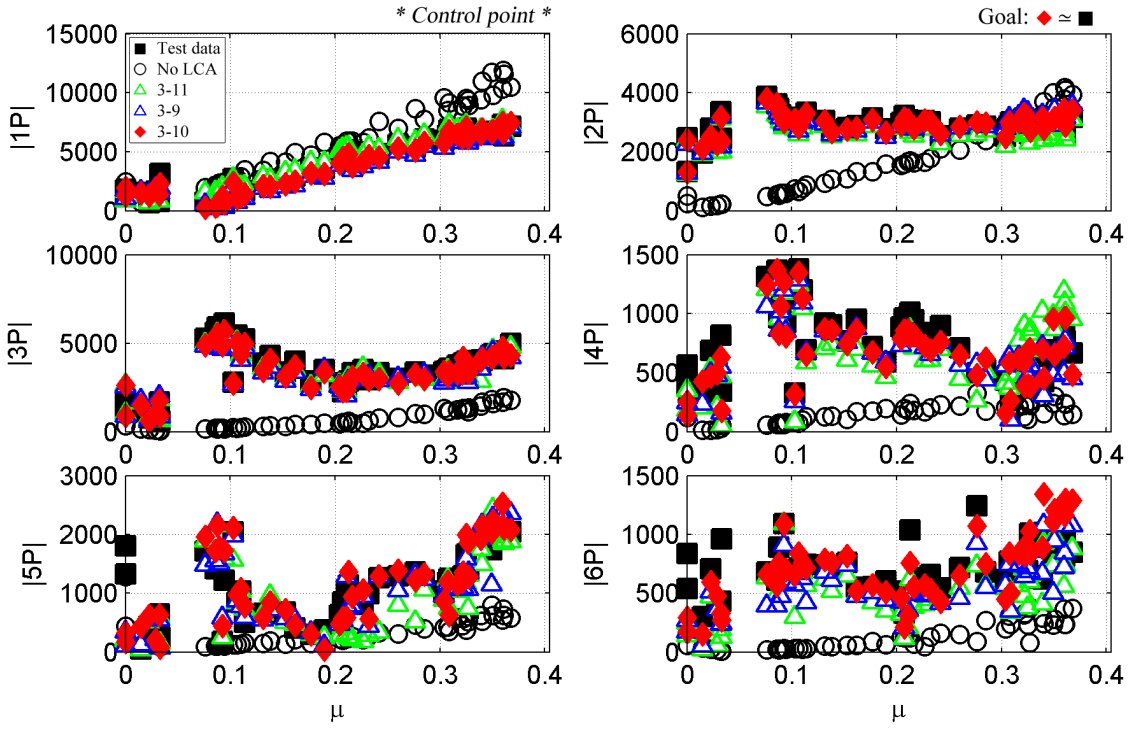

Figure 5.24: Loads matching by harmonic: effects of modes; all sensors: SN70 (in-lb).

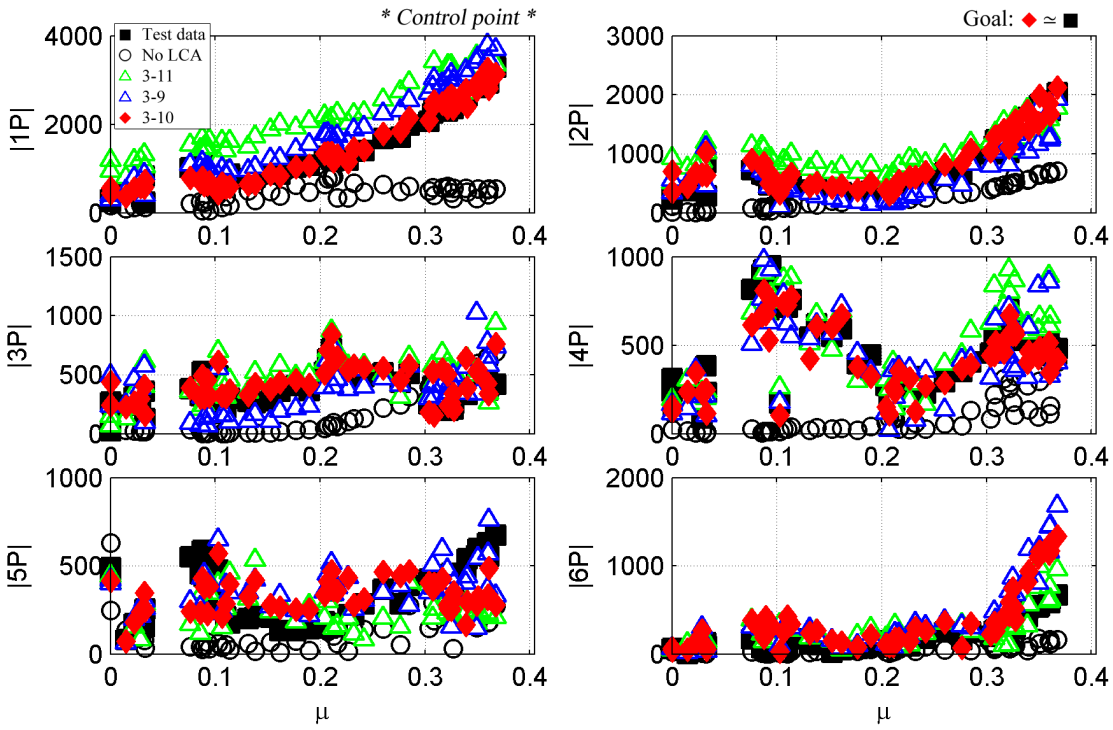

Figure 5.25: Loads matching by harmonic: effects of modes; all sensors: ST30 (in-lb).

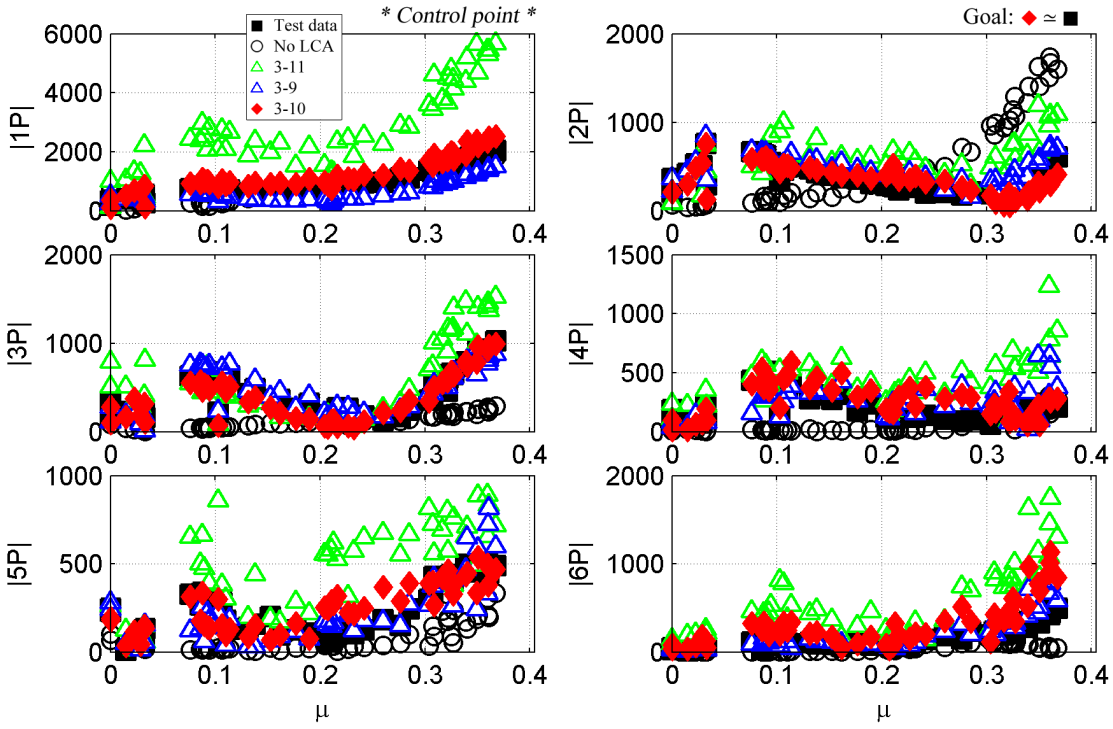

Figure 5.26: Loads matching by harmonic: effects of modes; all sensors: ST70 (in-lb).

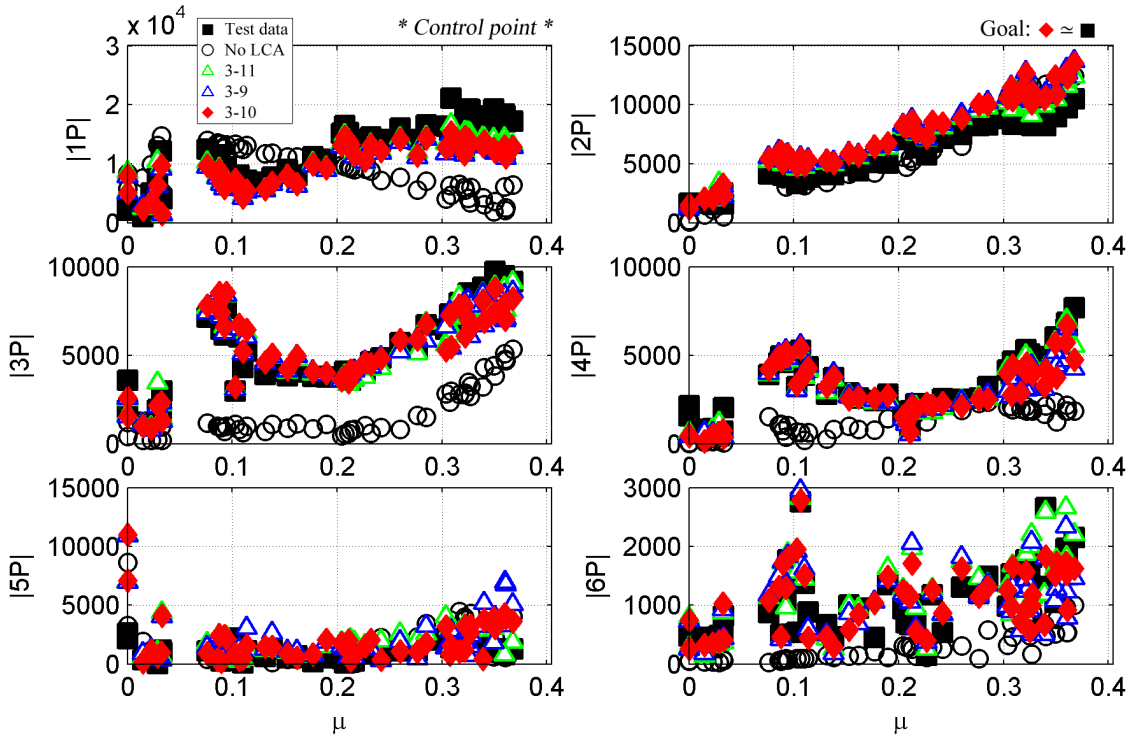

Figure 5.27: Loads matching by harmonic: effects of modes; all sensors: SE20 (in-lb).

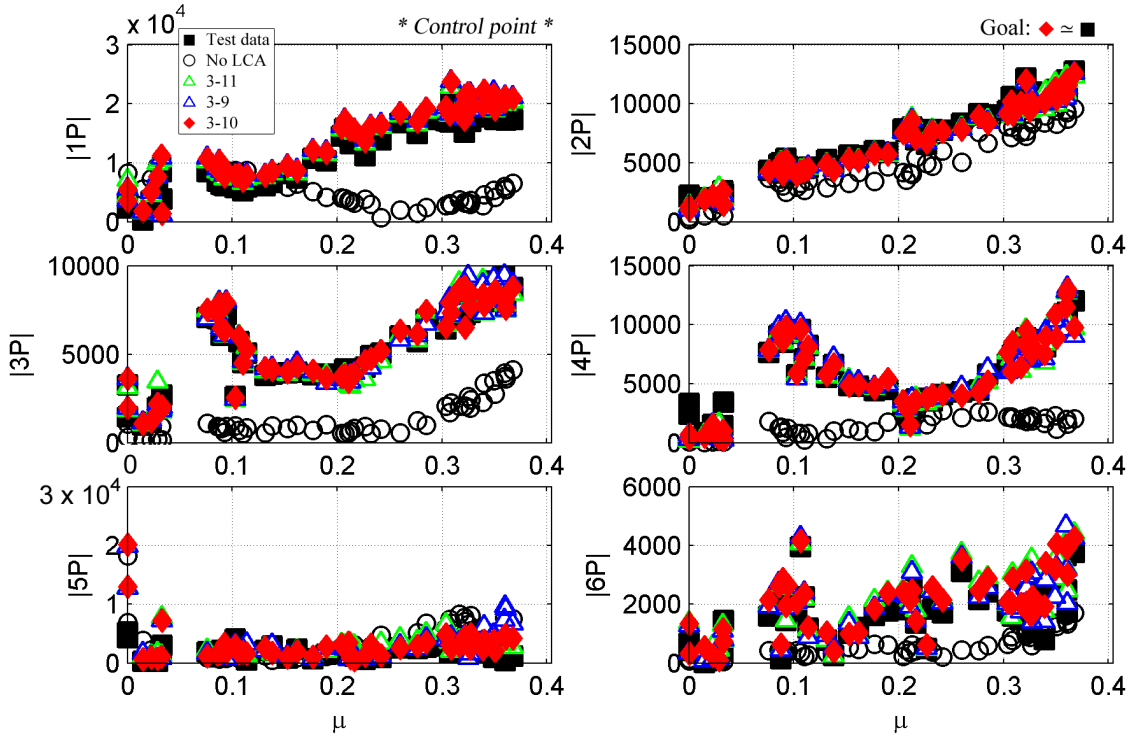

Figure 5.28: Loads matching by harmonic: effects of modes; all sensors: SE30 (in-lb).

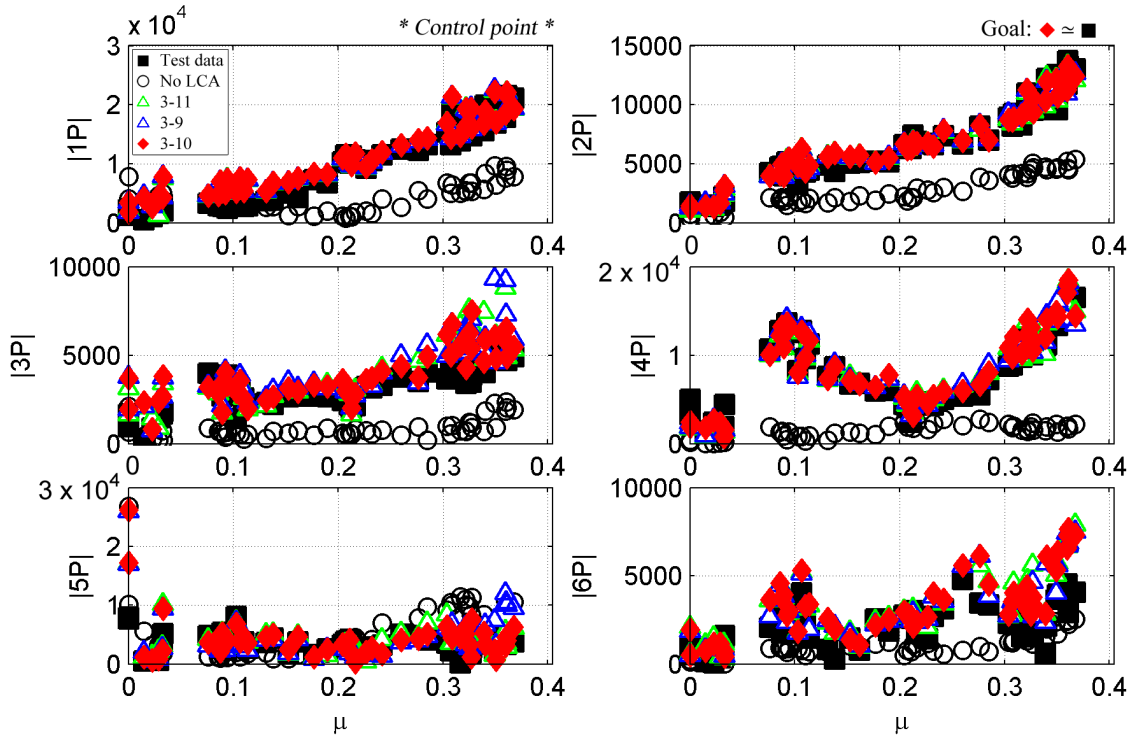

Figure 5.29: Loads matching by harmonic: effects of modes; all sensors: SE50 (in-lb).

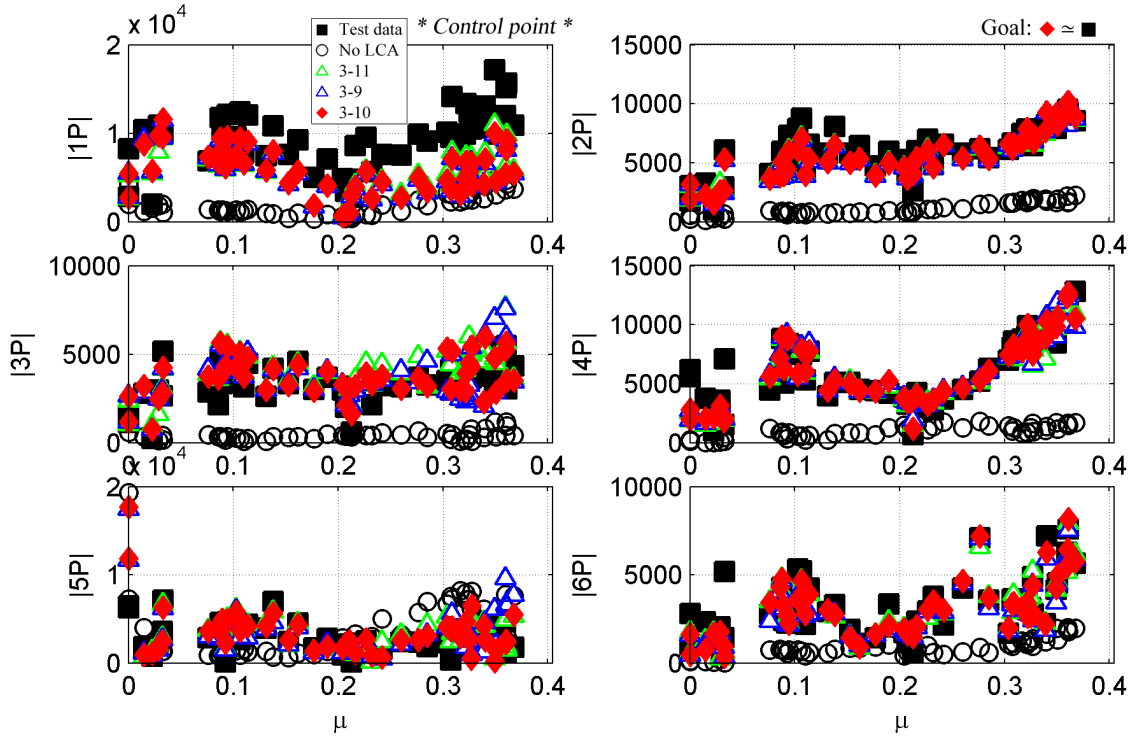

Figure 5.30: Loads matching by harmonic: effects of modes; all sensors: SE70 (in-lb).

5.5.2 Reduced Blade Control Point Set

For the control point set with two 3-axis sensors at $0.30R$ and $0.70R$ (*Case 2* in Table 5.2), a range of mode sets were examined (Table 5.4). Figures 5.31 through 5.37 show peak-to-peak loads comparisons for the first cycle of each flight counter for flights 84 and 85 (51 total flight counters) for the following cases: experimental (test) data, the DYMORE solution immediately prior to application of the LCA, modes 4-8, and modes 3,4,5,6,8,10. All other cases from Table 5.4 were examined as well but are not included in the charts. They are, however, included in the *LCA scores* listed in Table 5.4. In this table, *n/c* means no convergence was reached in the numerical simulation.

Table 5.4: Modes (SN/ST/SE 30/70 blade control points): scoring.

Case	**Modes**	**LCA score**
No LCA	-	0.150
2a	3-5	n/c
2b	3-6	0.319
2c	3-7	0.481
2d	3-8	n/c
2e	4-6	0.203
2f	4-7	0.309
2g	4-8	0.277
2h	4-9	0.346
2i	**3-6,8,10**	**0.212**

The LLT results are the same as in the previous section (since loads extracted prior to application of the LCA). This section highlights the strength of the LCA to accurately predict loads at non-control point locations (SN20/40/50/60/90, ST50/90, and SE20/40/50/60, in this case). For descriptive purposes, this will be labeled as

a *mapped station*. Figures 5.31 and 5.33 show excellent loads mapping for SN20 and SN50, respectively. For SN30, the case with modes 4-6 over-predicts the response, while under-predicting it for SN70. For SN30, this is due to over-compensation of the 3rd flap mode (mode 4, $4.53P$) to account for the lack of the 2nd flap mode (mode 3, $2.87P$) in the solution. For SN70, this is due to the inability to capture higher flapping modes. The solution with modes 3-6,8,10 accurately captures all relevant content for flapwise bending.

For torsional moment, the same issue is seen as the full control point set: an excellent match is seen up to $0.70R$, but over-predicts the response at ST90. For the edgewise bending moment, a worse match is seen relative to the full control point set, with an over-prediction of load with higher μ.

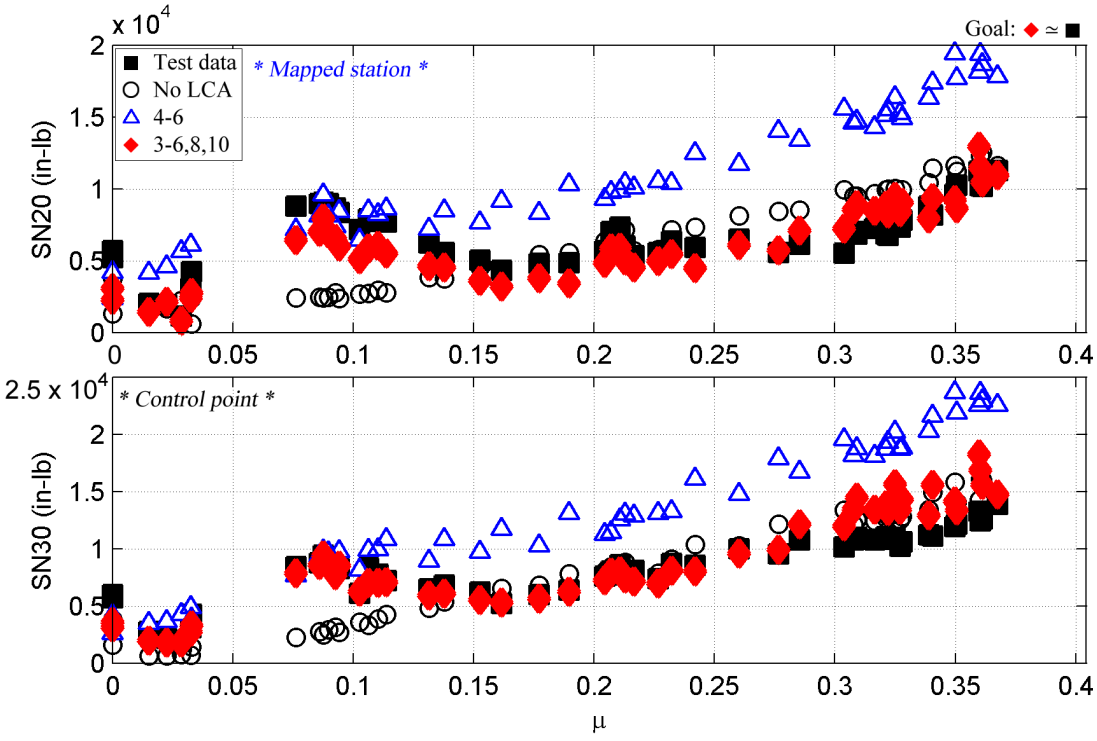

Figure 5.31: Peak-to-peak loads matching: effects of modes; 6 sensors: SN20, SN30.

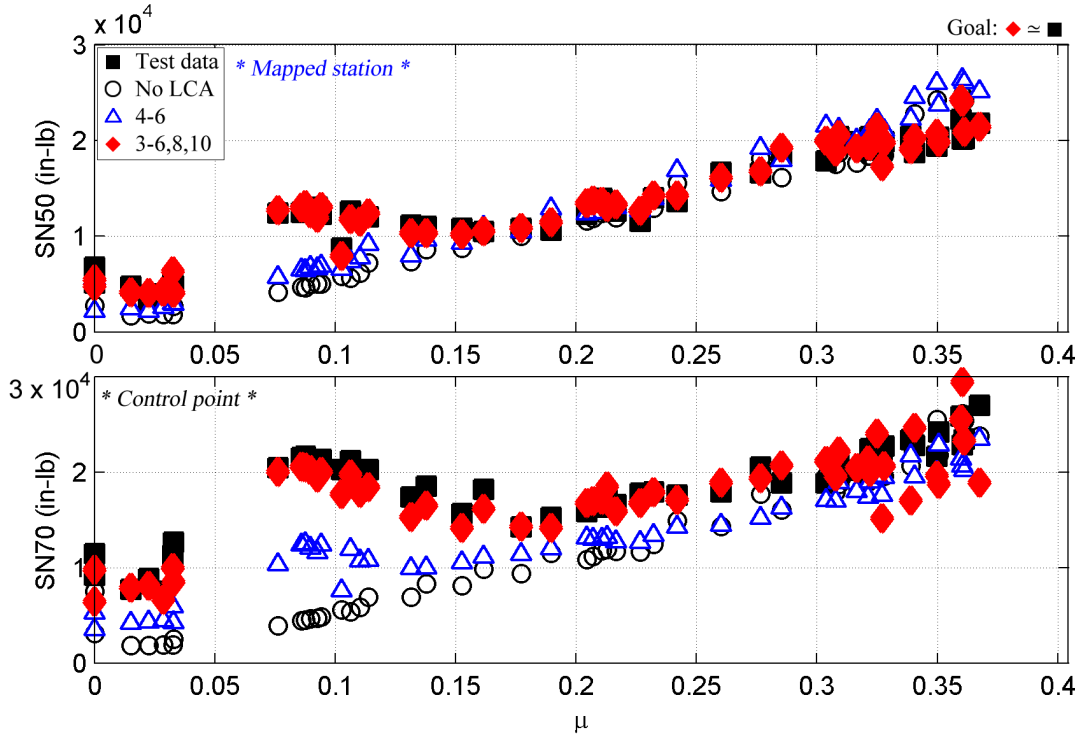

Figure 5.32: Peak-to-peak loads matching: effects of modes; 6 sensors: SN50, SN70.

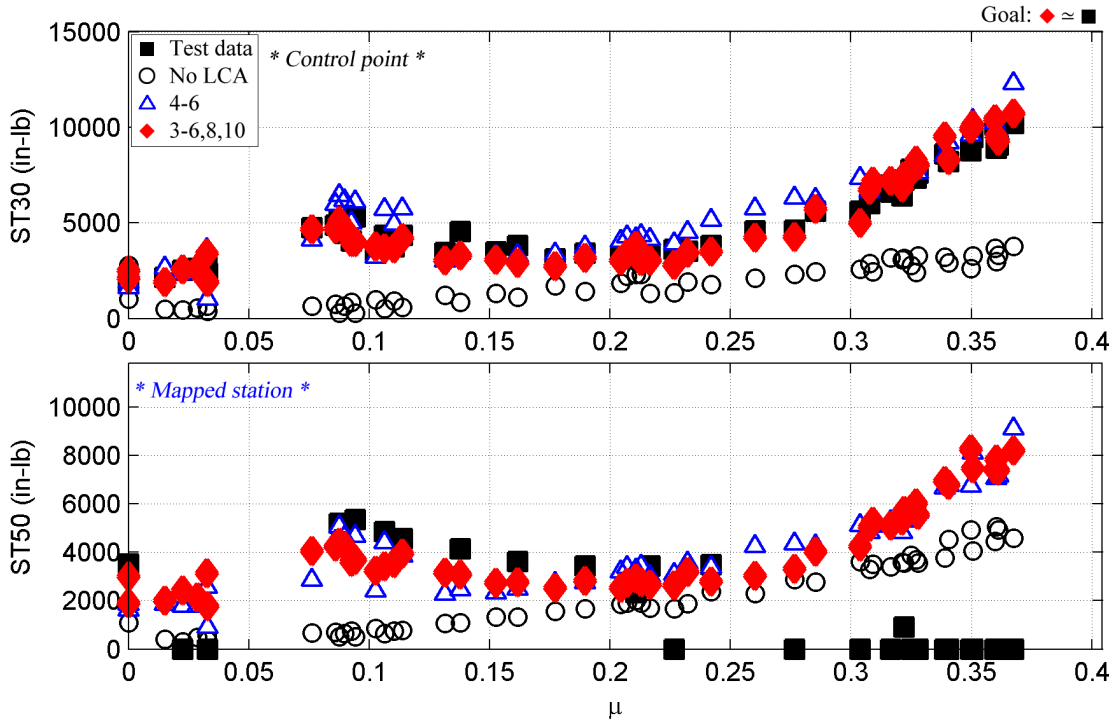

Figure 5.33: Peak-to-peak loads matching: effects of modes; 6 sensors: ST30, ST50.

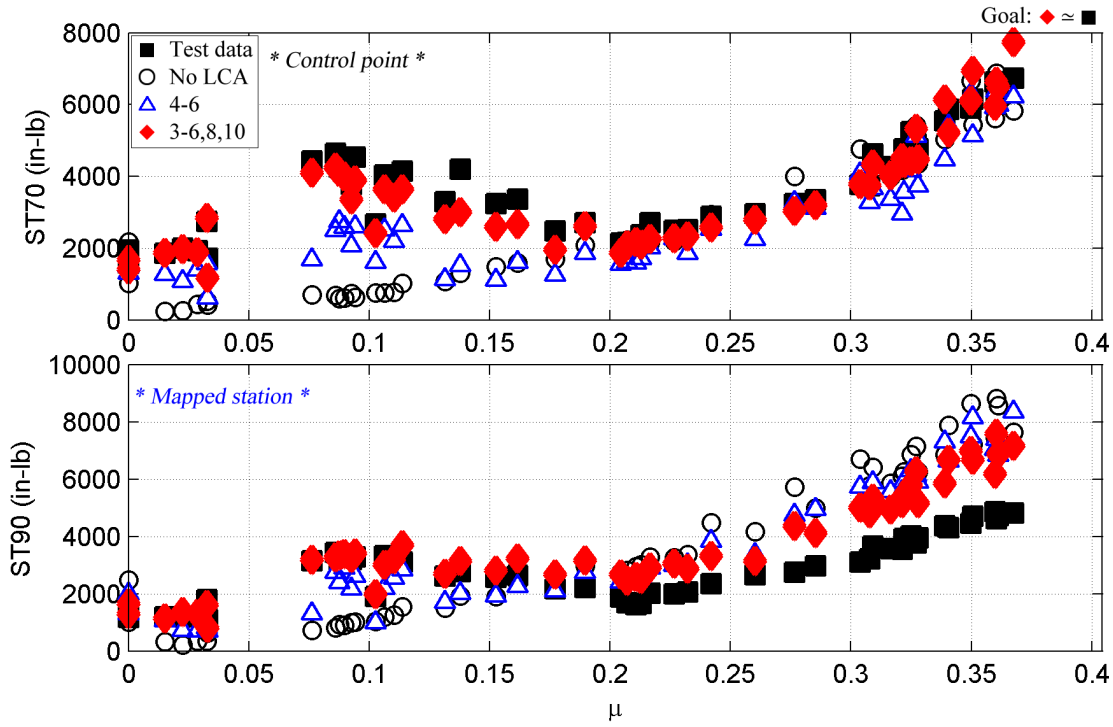

Figure 5.34: Peak-to-peak loads matching: effects of modes; 6 sensors: ST70, ST90.

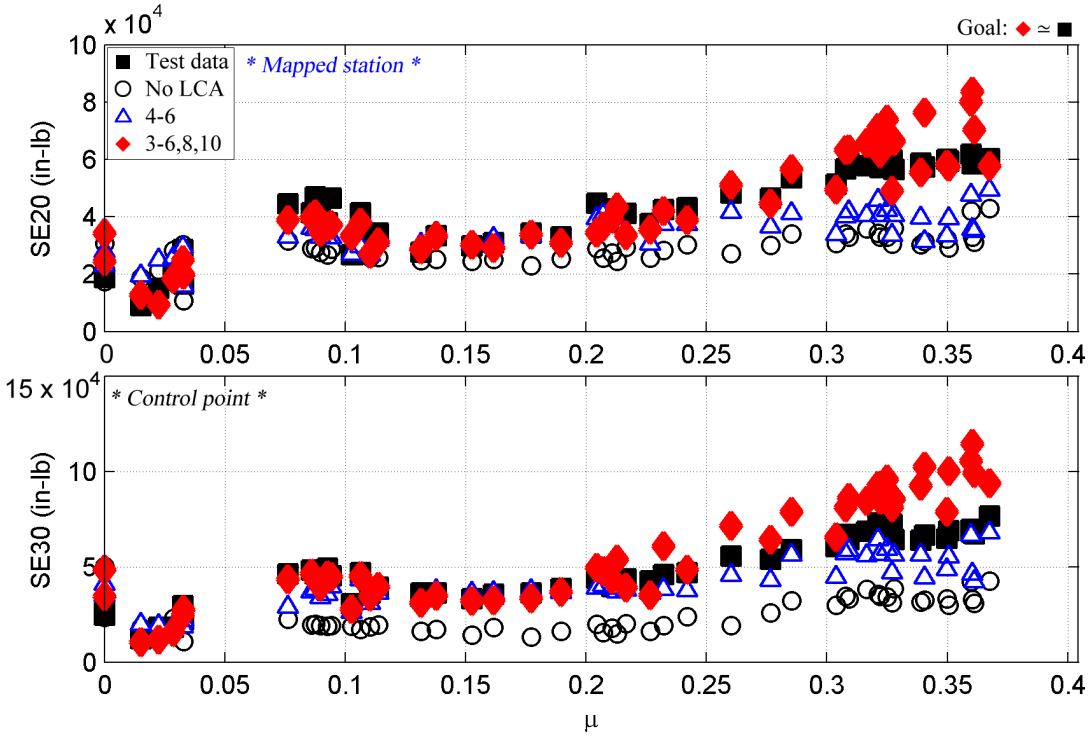

Figure 5.35: Peak-to-peak loads matching: effects of modes; 6 sensors: SE20, SE30.

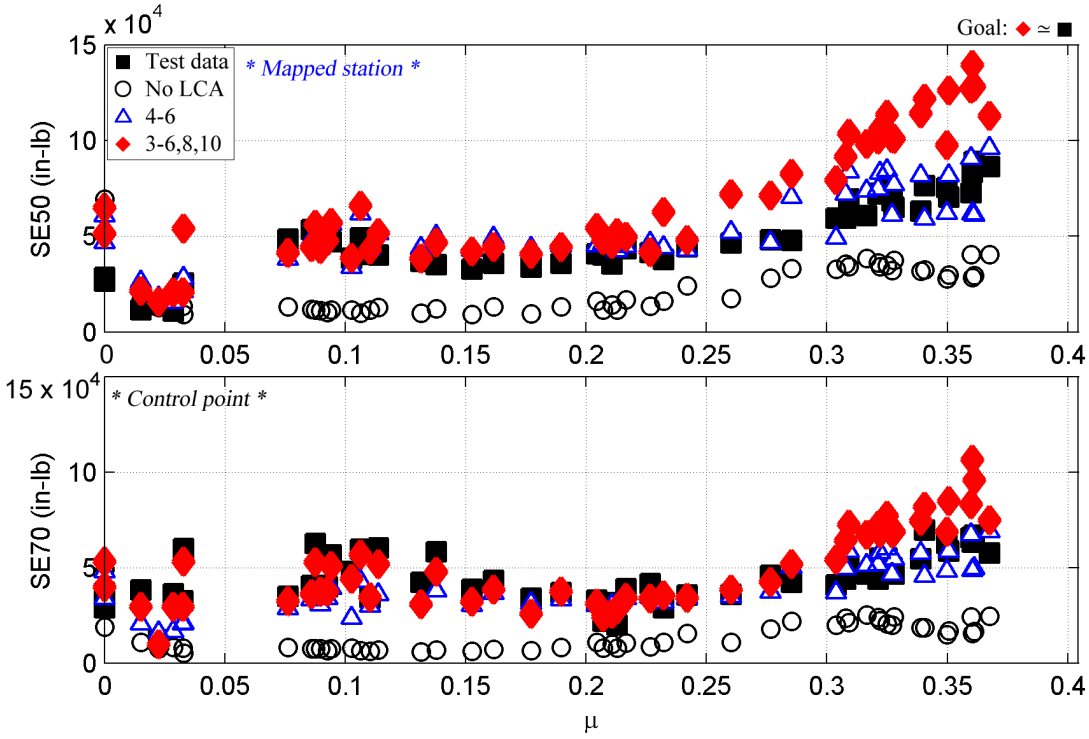

Figure 5.36: Peak-to-peak loads matching: effects of modes; 6 sensors: SE50, SE70.

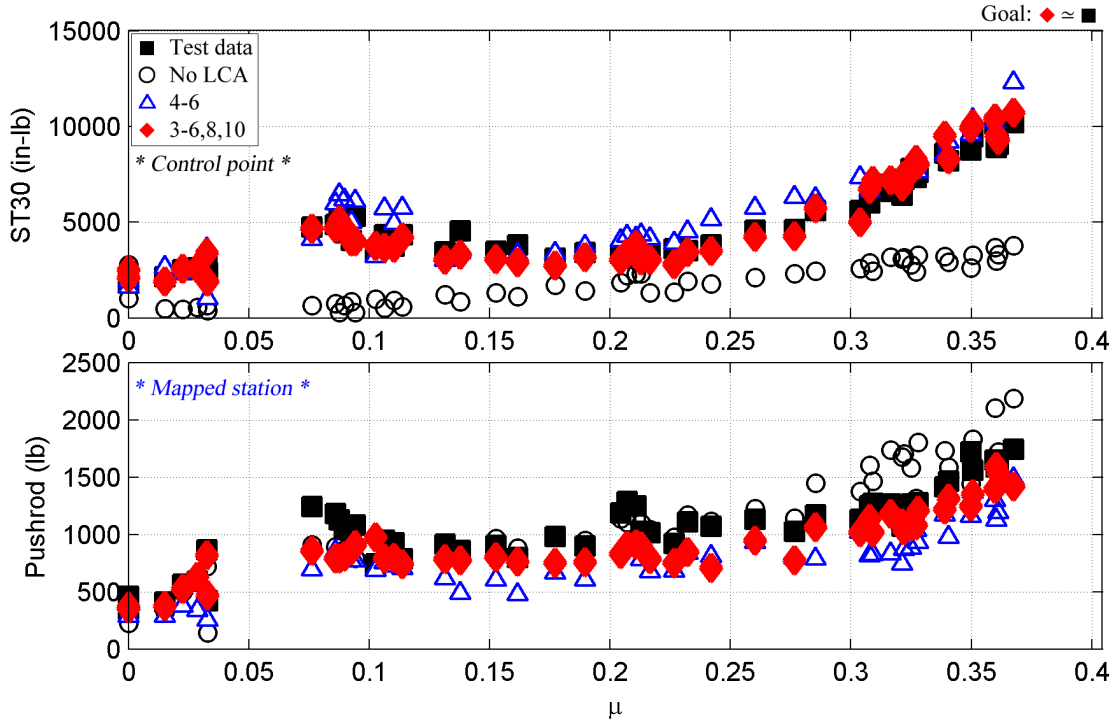

Figure 5.37: Peak-to-peak loads matching: effects of modes; 6 sensors: ST30, pushrod.

5.5.3 Pushrod Control Point

For the control point set with a single pushrod sensor (*Case 3* in Table 5.2), a range of mode sets were examined (Table 5.5). For this case - a single sensor located on the pushrod - a good prediction of blade loads is not necessarily expected (since, among other reasons, only a single mode may be included in the solution). However, pushrod is a critical load to match due to two reasons: (1) it is the easiest component in the rotating frame to instrument (a number of research efforts are focused on pushrods manufactured with (or altered to include) embedded load sensors; see Arms et al., [6]), and (2) it is most indicative of the loads being fed from the rotating system into the fixed frame. Given this expectation of poor blade loads matches (with the exception of blade torsional moment near the root), two new *LCA scores* have been created: one focused on how well ST30 is matched, and one focused on how well pushrod load is matched. Thus equation 4.1 becomes the following (for ST30 and blade 3 pushrod (P), respectively):

$$LCA\ score\ (ST30) = median\left[\left(\frac{1}{C}\frac{1}{H}\sum_{c=1}^{C}\sum_{h=1}^{H}\left(\frac{ST30_{ch} - ST30^{*}_{ch}}{ST30^{*}_{ch}}\right)^{2}\right)^{1/2}\right] \quad (5.10)$$

$$LCA\ score\ (pushrod) = median\left[\left(\frac{1}{C}\frac{1}{H}\sum_{c=1}^{C}\sum_{h=1}^{H}\left(\frac{P_{ch} - P^{*}_{ch}}{P^{*}_{ch}}\right)^{2}\right)^{1/2}\right] \quad (5.11)$$

Figures 5.38 through 5.44 show peak-to-peak load comparisons for the first cycle of each flight counter for flights 84 and 85 (51 total flight counters) for the following cases: experimental (test) data, the DYMORE solution immediately prior to application of the LCA, mode 5, and mode 10. All other cases from Table 5.5 were examined as well but are not included in the charts. They are, however, included in the *LCA scores* listed in Table 5.5.

The pushrod sensor set, as expected given its ability to only apply one mode (a torsion mode) in the LCA solution, has little impact on flapwise (Figures 5.38 and 5.39) or edgewise bending (Figures 5.42 and 5.43), with those results little changed from

Table 5.5: Modes (pushrod control point): scoring.

Case	Mode	LCA score (blade)	LCA score (ST30)	LCA score (pushrod)
No LCA	-	0.150	0.100	0.092
3a	3	n/c	n/c	n/c
3b	4	0.356	0.166	0.140
3c	5	0.253	0.158	0.041
3d	6	0.563	0.159	0.076
3e	7	n/c	n/c	n/c
3f	8	n/c	n/c	n/c
3g	9	0.735	0.207	0.035
3h	**10**	**0.201**	**0.075**	**0.007**

the LCA solution. The match on pushrod and ST30 are excellent (Figure 5.44). This single torsion mode dramatically over-predicts the blade torsional moment at $0.70R$ and $0.90R$.

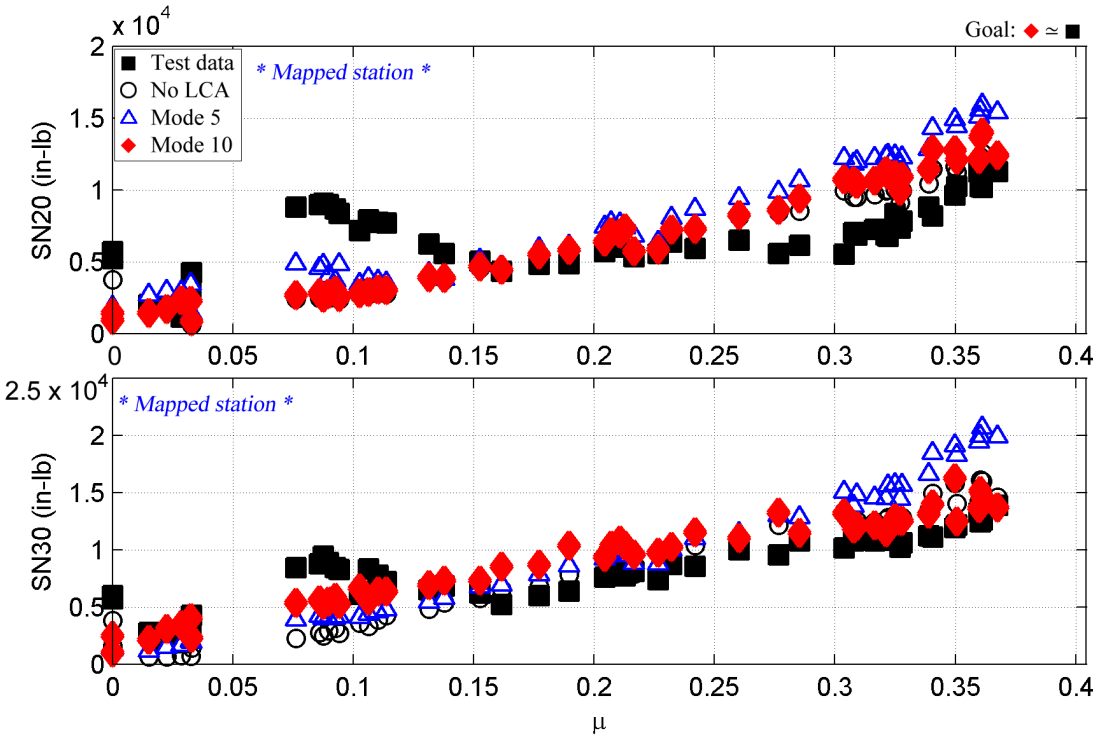

Figure 5.38: Peak-to-peak loads matching: effects of modes; 1 sensor: SN20, SN30.

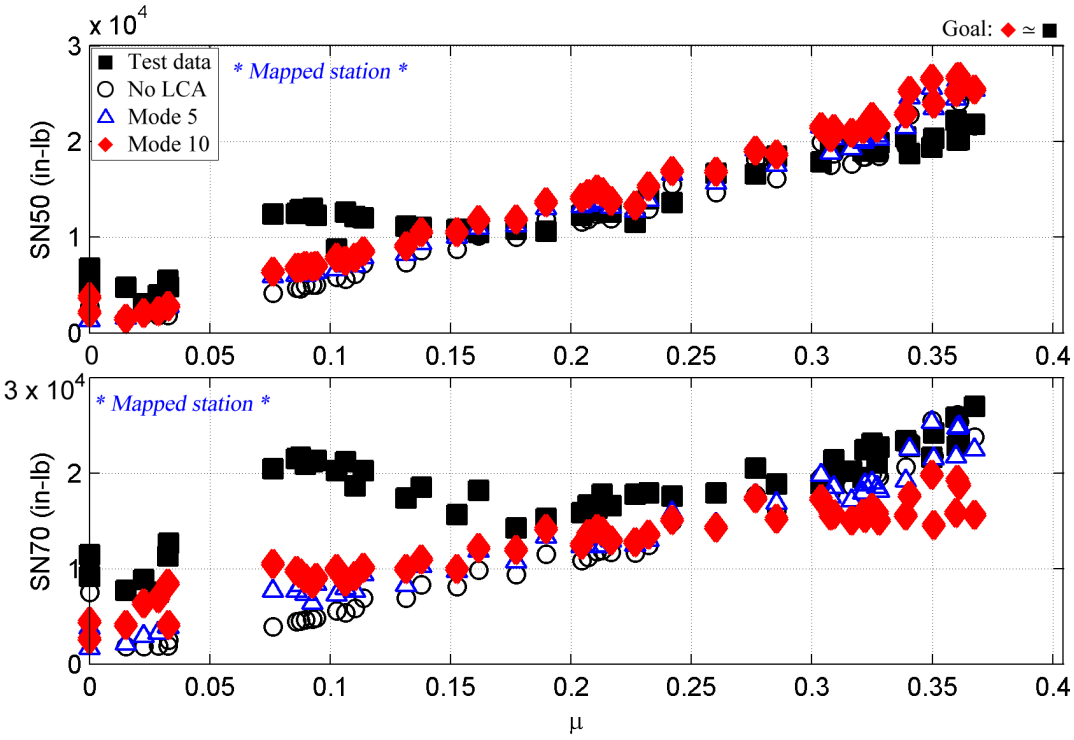

Figure 5.39: Peak-to-peak loads matching: effects of modes; 1 sensor: SN50, SN70.

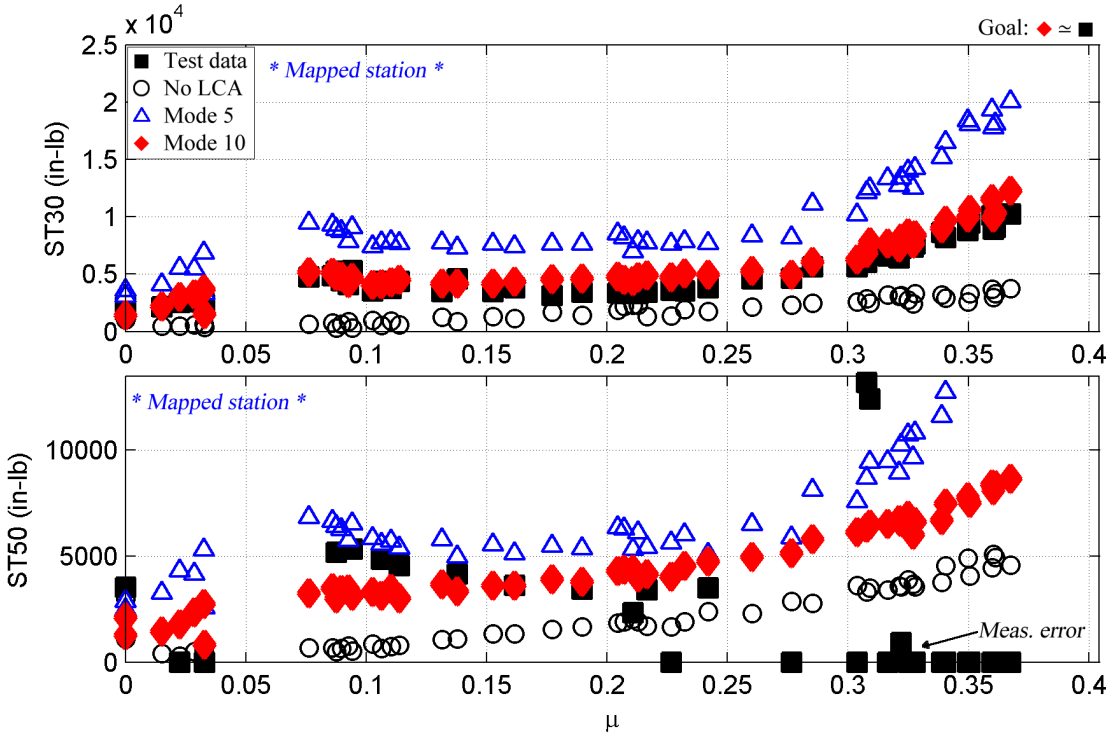

Figure 5.40: Peak-to-peak loads matching: effects of modes; 1 sensor: ST30, ST50.

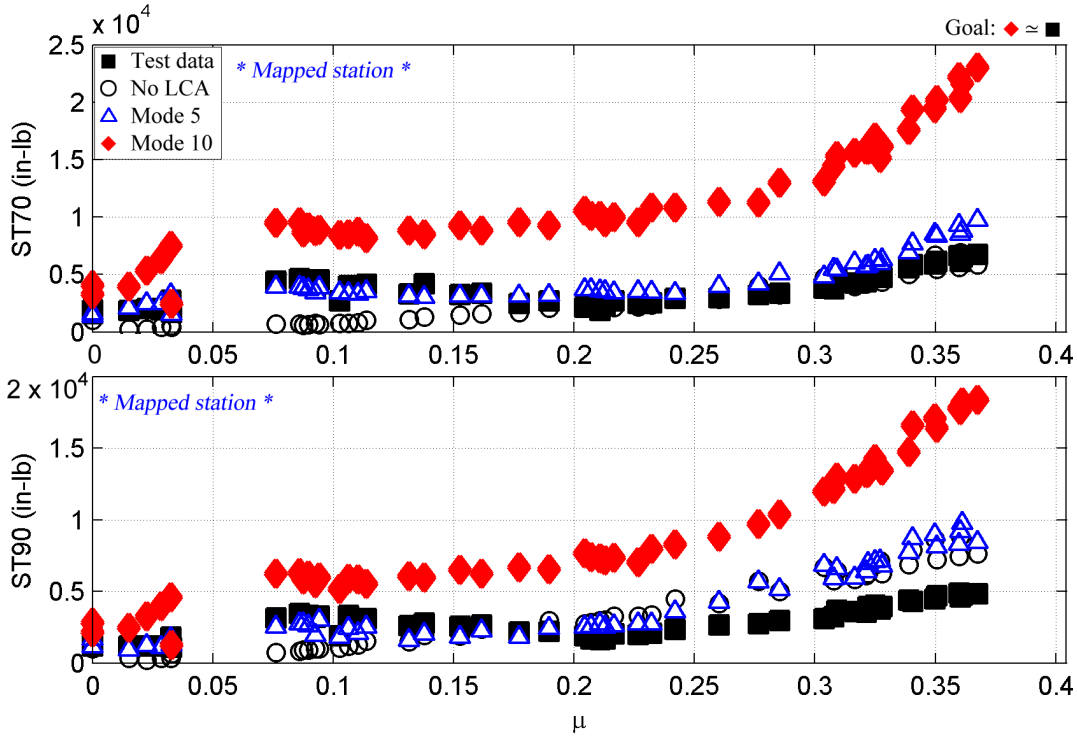

Figure 5.41: Peak-to-peak loads matching: effects of modes; 1 sensor: ST70, ST90.

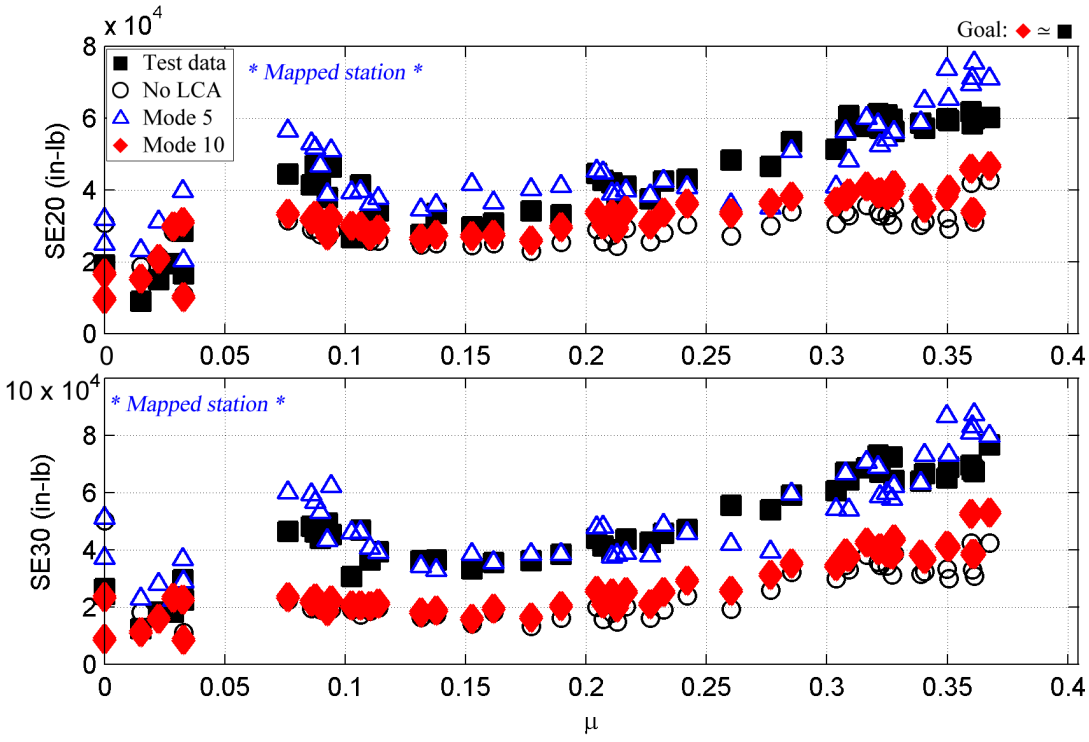

Figure 5.42: Peak-to-peak loads matching: effects of modes; 1 sensor: SE20, SE30.

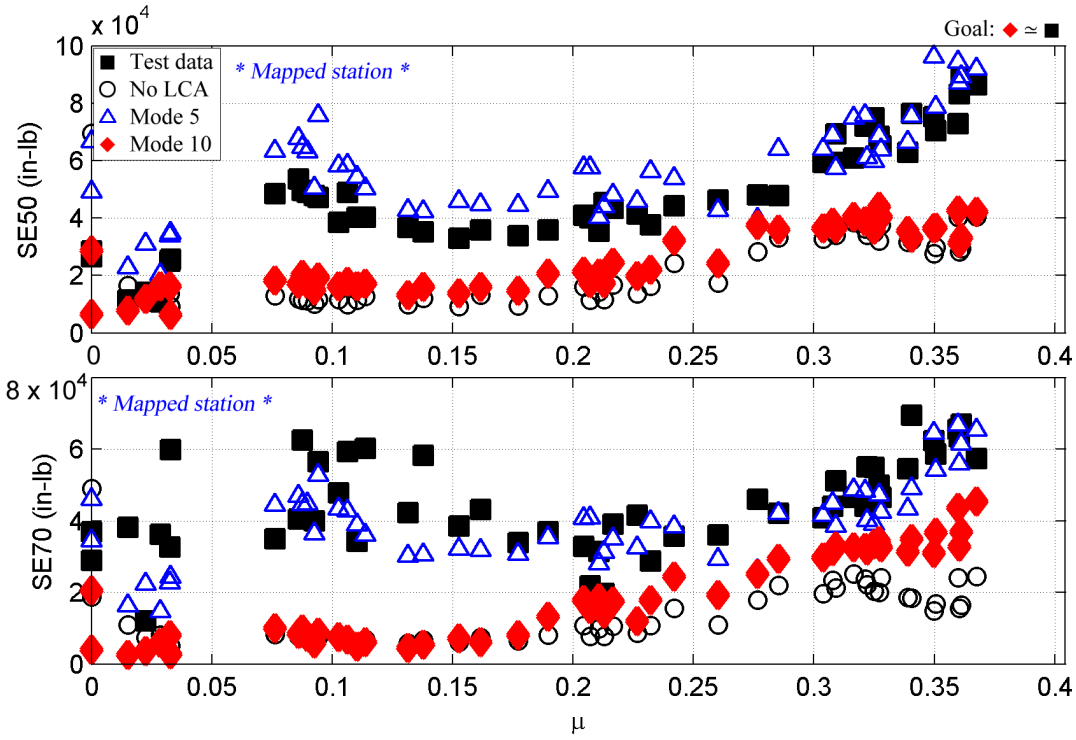

Figure 5.43: Peak-to-peak loads matching: effects of modes; 1 sensor: SE50, SE70.

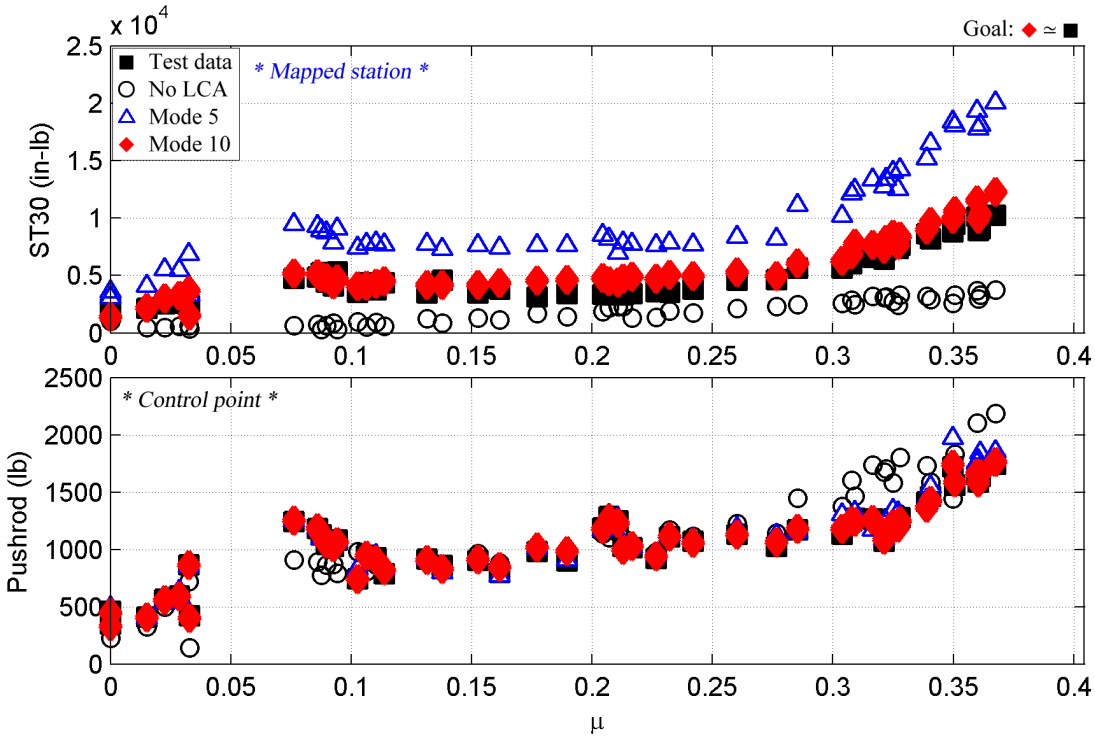

Figure 5.44: Peak-to-peak loads matching: effects of modes; 1 sensor: ST30, pushrod.

5.5.4 Control Point Sensitivity

Now the three control point sets defined above will be compared to each other. As expected the full sensor set is the most robust solution for all blade loads. However, the latter two are more practical for in-service application in a rotorcraft fleet. A recommended approach would be to use a subset of blade sensors as control points for mapping the full loads field in the blades and use a pushrod control point - even multiple pushrods - for blade root pitch, pitch control horn, swashplate, hub, and fixed-system loads field mapping.

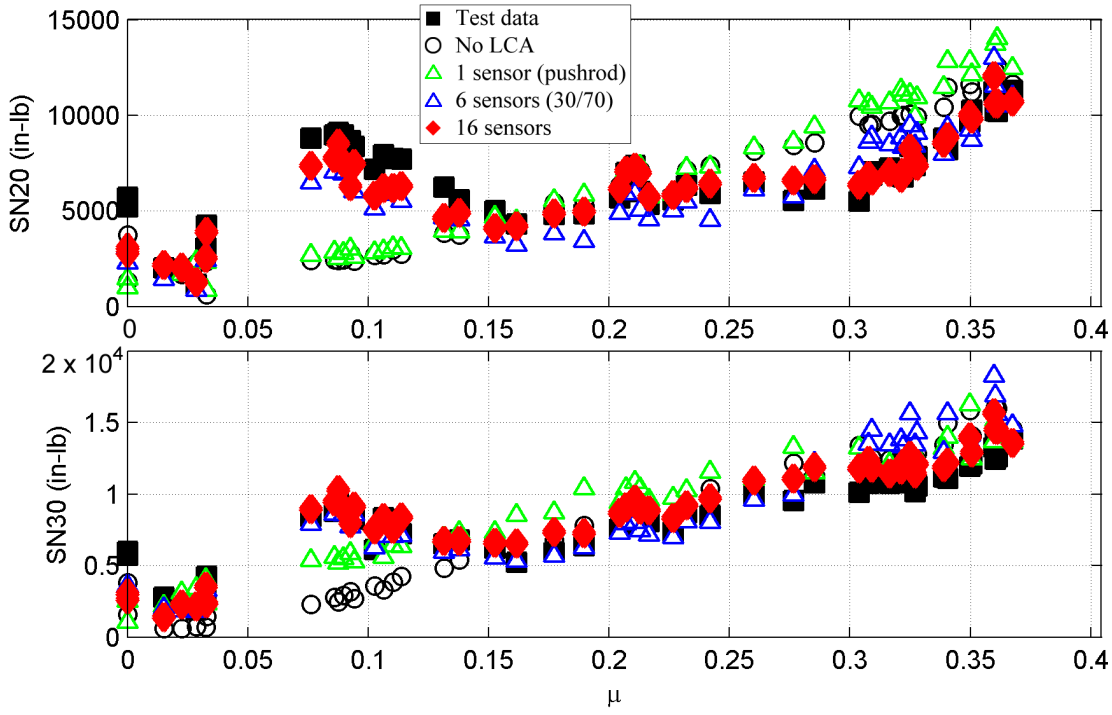

Figure 5.45: Peak-to-peak loads matching: sensor study: SN20, SN30.

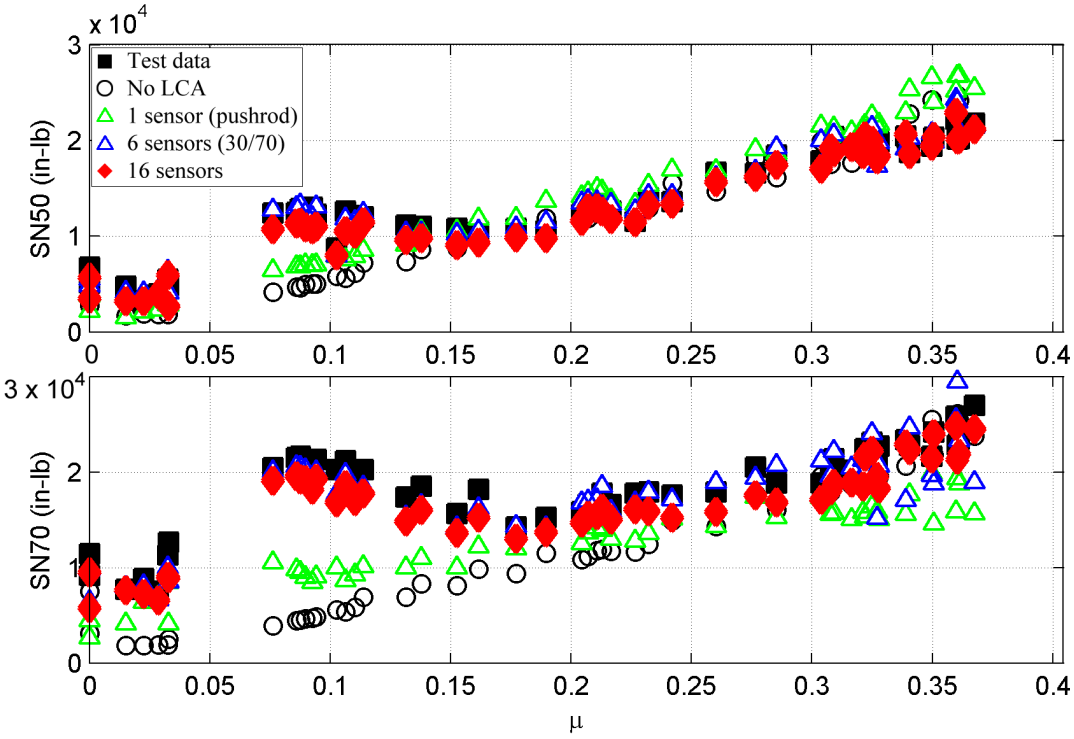

Figure 5.46: Peak-to-peak loads matching: sensor study: SN50, SN70.

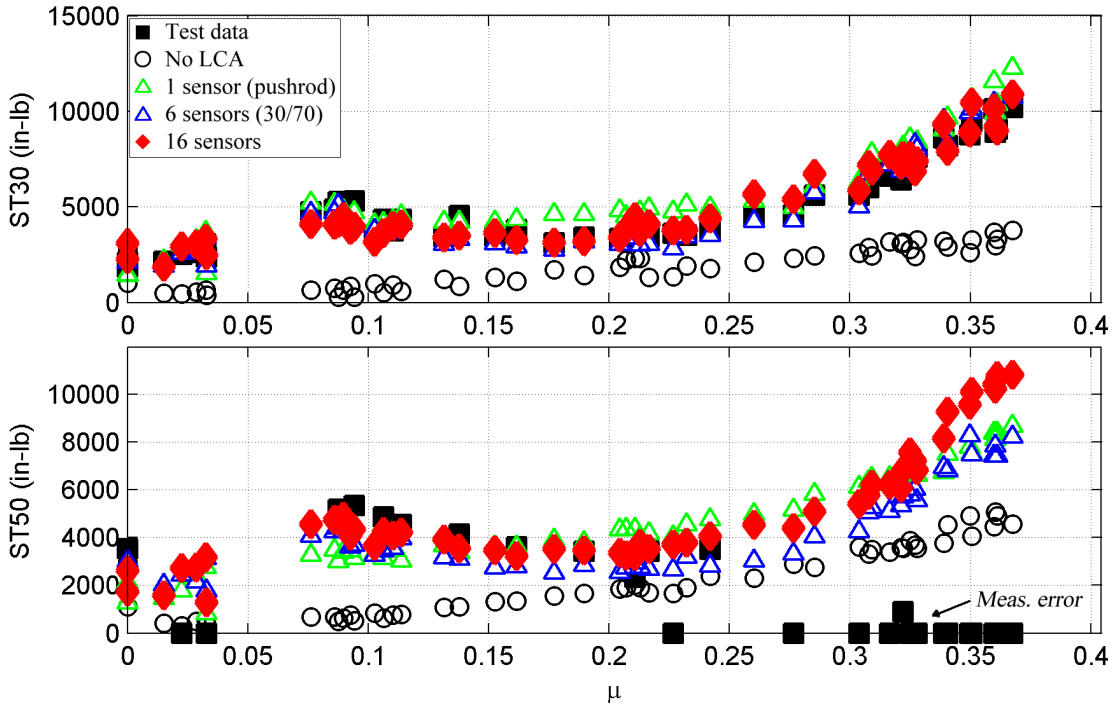

Figure 5.47: Peak-to-peak loads matching: sensor study: ST30, ST50.

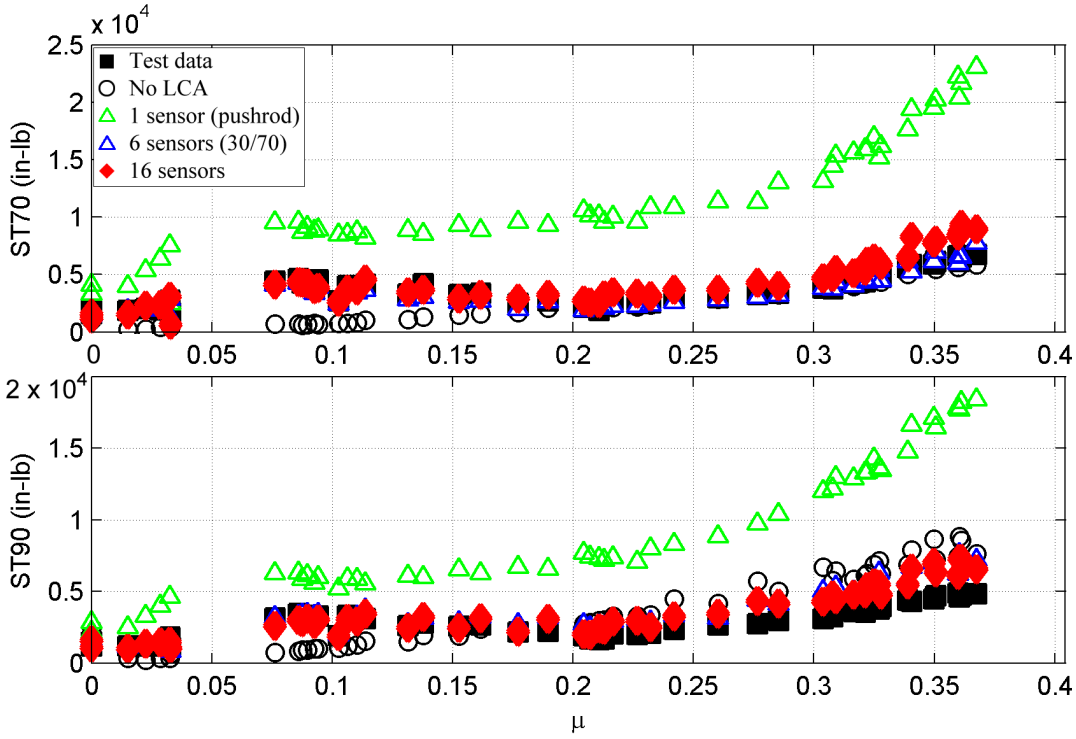

Figure 5.48: Peak-to-peak loads matching: sensor study: ST70, ST90.

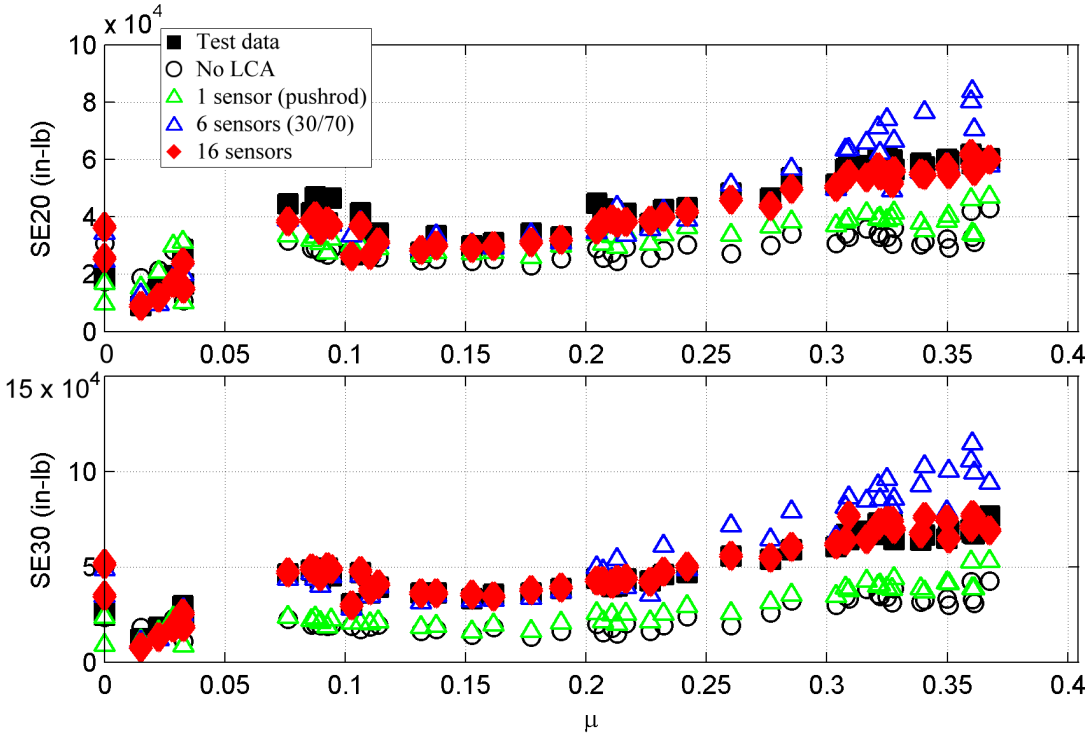

Figure 5.49: Peak-to-peak loads matching: sensor study: SE20, SE30.

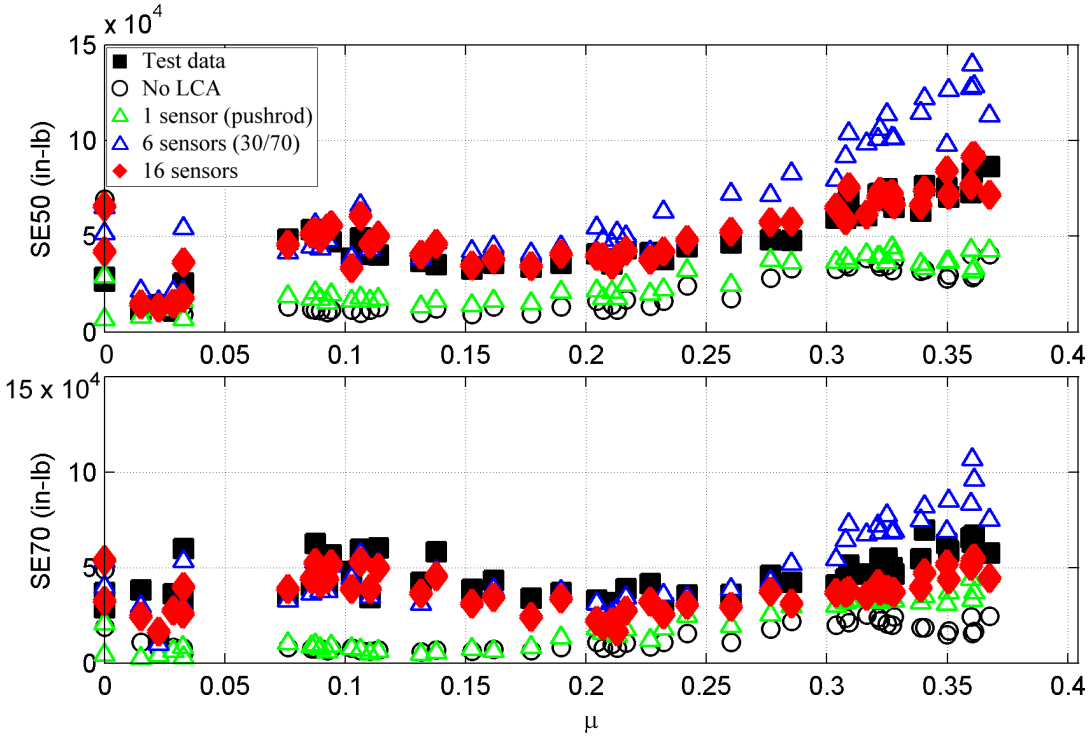

Figure 5.50: Peak-to-peak loads matching: sensor study: SE50, SE70.

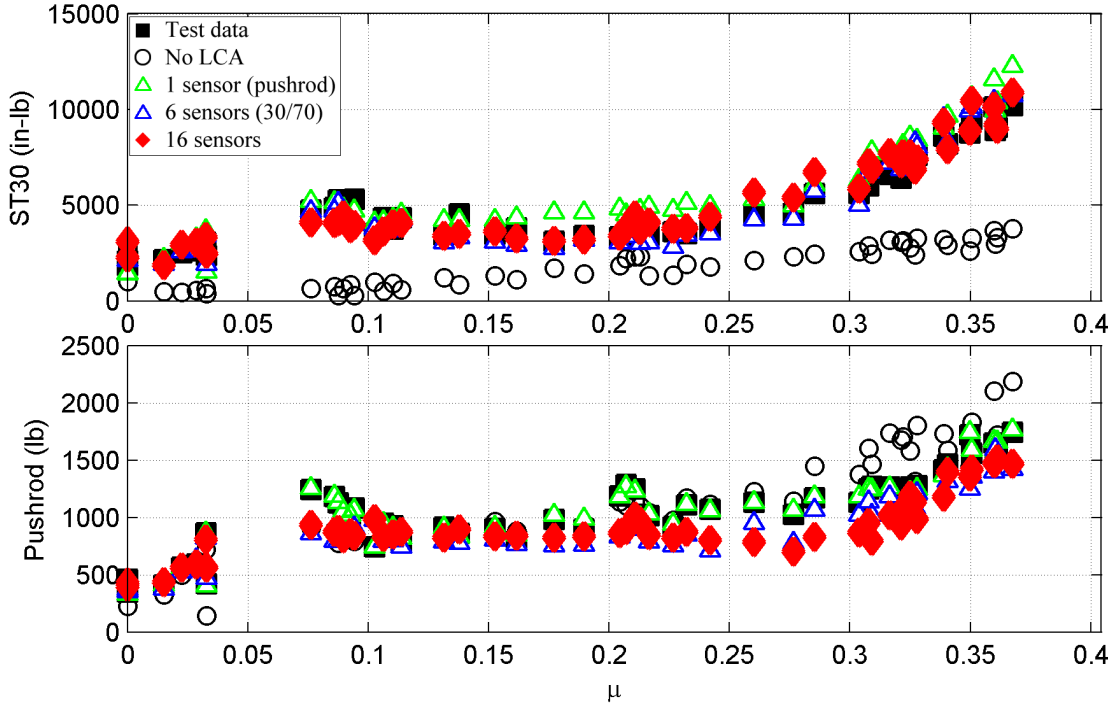

Figure 5.51: Peak-to-peak loads matching: sensor study: ST30, pushrod.

5.6 Scalar by Harmonic

Equation 2.25 defined the following difference between analysis and experiment for a given load quantity:

$$\Delta\underline{\epsilon} = \underline{\epsilon} - \underline{\epsilon}^* \tag{5.12}$$

From here $\Delta\underline{\lambda}$ was computed and, thus, $\Delta\underline{F}$, which yielded the change in external nodal loads required to produce the desired change in strain. Numerically, it was found that the solution was sensitive to the abruptness with which the external nodal force was modified in the time domain. Therefore, 2.25 was implemented as:

$$\Delta\underline{\epsilon} = \kappa\,(\underline{\epsilon} - \underline{\epsilon}^*) \tag{5.13}$$

where κ is defined as a *harmonic scalar*. Table 5.6 details the cases that were examined, as well as the *LCA score* for each case. The final cases used for all subsequent analyses is defined in the final row of this table. Loads comparison charts for this study are provided in Appendix B.

Table 5.6: Harmonic scalars: scoring.

Case *(scalar by harmonic)*	**LCA score**
No LCA	0.150
1.0 *(all harmonics)*	0.360
0.5 *(all harmonics)*	0.129
Baseline *(1.0, 1.0, 1.0, 0.5, 0.3, 0.3)*	**0.128**

5.7 Summary

This chapter examined the robustness of the LCA and the influence user settings has on quality of the loads match. A metric was defined - a single aggregate objective function (AOF) - to determine the best fit loads match between experimental data

and numerical simulation. Two particular issues with the LCA were examined: instability in $5P$ response due to blade bending mode excitation and $1P$ response offset due to rigid blade flapping. Both issues were addressed and found to be serviceable in the context of UH-60A rotor loads analysis. However, there are opportunities with both for improvements in future research efforts.

CHAPTER VI

ANALYSIS OF ROTOR LOAD HARMONIC COMPOSITION AND LOAD TRANSFERENCE BETWEEN FRAMES

6.1 Overview

This chapter examines rotor load content by harmonic. Accurate rotor loads prediction is driven by a clear understanding of the underlying physics of the problem. This understanding is important for several reasons. First, additive effects of multiple load components fed from the rotating frame to the fixed frame influence the vibratory response of the hub and fuselage; e.g., pushrod-to-control servo loads transfer. Second, structural fatigue life is driven by load magnitude as well as the number of applications of each load. Accurate fatigue life estimation requires accurate modeling of both the load magnitude and its frequency of occurrence. This latter point is elaborated and demonstrated via example in Chapter 7.

6.2 Rotor Load Harmonic Composition

Rotor control is primarily achieved by the placement of the swashplate. Swashplate position and orientation (driven by collective and cyclic control inputs, respectively) dictate the magnitude and direction of the rotor thrust vector, thus providing the mechanism through which the aircraft's velocity vector (and, thus, aircraft motion) is defined. For an n_b-bladed rotor rotating at angular speed Ω, in the local coordinate system of a given blade (blade 1, with the x-axis oriented along the blade span, positive outboard), the in-plane velocity at radial station r (at blade azimuth ψ) can

be idealized as follows [81].

$$V = \Omega r + V_\infty sin\psi \tag{6.1}$$

where V_∞ is the forward speed of the aircraft. The lift due to the motion of the blade as a function of azimuth can be idealized as:

$$L(\psi) = \frac{1}{2}\rho S C_L(\psi) V^2(\psi) \tag{6.2}$$

C_L accounts for the increased local blade velocity on the advancing side and the reduction in local blade velocity on the retreating side. For a given blade, C_L as a function of azimuth is:

$$C_L(\psi) = C_{L0} - \Delta C_L \sin\psi \tag{6.3}$$

C_{L0} is the lift at zero α and ΔC_L is some positive constant. The important concept is that C_L reduces on the advancing side and increases on the retreating side to ensure comparable lift magnitudes for both; i.e., for steady, level flight, no resulting pitching or rolling moment:

$$L(0^\circ) = L(180^\circ) \tag{6.4}$$

$$L(90^\circ) = L(270^\circ) \tag{6.5}$$

Plugging 6.1 and 6.3 into 6.2 yields the following, upon trigonometric manipulation.

$$\begin{aligned} L = 0.5\rho S[&-\Delta C_L \Omega r V_\infty + C_{L0}((\Omega r)^2 + 0.5V_\infty^2) \\ &+(2C_{L0}\Omega r V_\infty - \Delta C_L((\Omega r)^2 + 0.75V_\infty^2))\sin\psi \\ &+(\Delta C_L \Omega r V_\infty - 0.5C_{L0}V_\infty^2)\cos(2\psi) \\ &+0.5\Delta C_L V_\infty^2 \sin(3\psi)] \end{aligned} \tag{6.6}$$

Normalizing 6.6 by $(\Omega R)^2$ leads to:

$$L = 0.5\rho S(\Omega R)^2 \Bigg\{ -\Delta C_L \left(\frac{r}{R}\right)\mu + C_{L0}\Big[\left(\frac{r}{R}\right)^2 + 0.5\mu^2\Big] + [2C_{L0}\left(\frac{r}{R}\right)\mu - \Delta C_L(\left(\frac{r}{R}\right)^2 + 0.75\mu^2)]\sin\psi + \Big[\Delta C_L\left(\frac{r}{R}\right)\mu - 0.5C_{L0}\mu^2\Big]\cos(2\psi) + 0.5\Delta C_L\mu^2\sin(3\psi)\Bigg\} \tag{6.7}$$

The resulting expression of the lift contains $0P$, $1P$, $2P$, and $3P$ contributions. Assuming dominance in the response due to ΔC_L, the $1P$ airload is proportional to $((\frac{r}{R})^2 + 0.75\mu^2)$, the $2P$ to $(r/R)\mu$, and the $3P$ to $0.5\mu^2$. Thus, as one moves outboard on the blade, one expects the $1P$ airload to be much larger than the $2P$ and the $2P$, in turn, much larger than the $3P$ airload. Figure 6.1 shows experimentally-measured UH-60A blade normal force (per unit span) for radial station $0.225R$ and $0.775R$ versus μ for each flight counter of flight 85. This simplified representation of blade airloads does seem to hold true for the inboard station ($0.225R$), showing $1P > 2P > 3P$ response. However, this representation does not hold for airloads outboard on the blade. This is due to the unsteady airloads effects present outboard, such as negative lift on the advancing side, stall due to high blade angle-of-attack on the retreating sides (with higher μ), and excitation of the first elastic flapping mode ($2.87P$, close to $3P$).

6.2.1 Main Rotor Shaft Bending

Next rotor shaft bending is examined. The rotor shaft is typically a fatigue critical component. The UH-60A dataset contains bending for an upper and a lower location on the shaft. The upper bending location (RQ12) is located below and centered with blade 2. Conceptually, this shaft bending due to blade lift should be equal to the net lift of blade 2 minus the net lift of blade 4 (positive bending in tension), multiplied by the appropriate moment arm (treating the blade lift as acting at some station ($x_s R$)

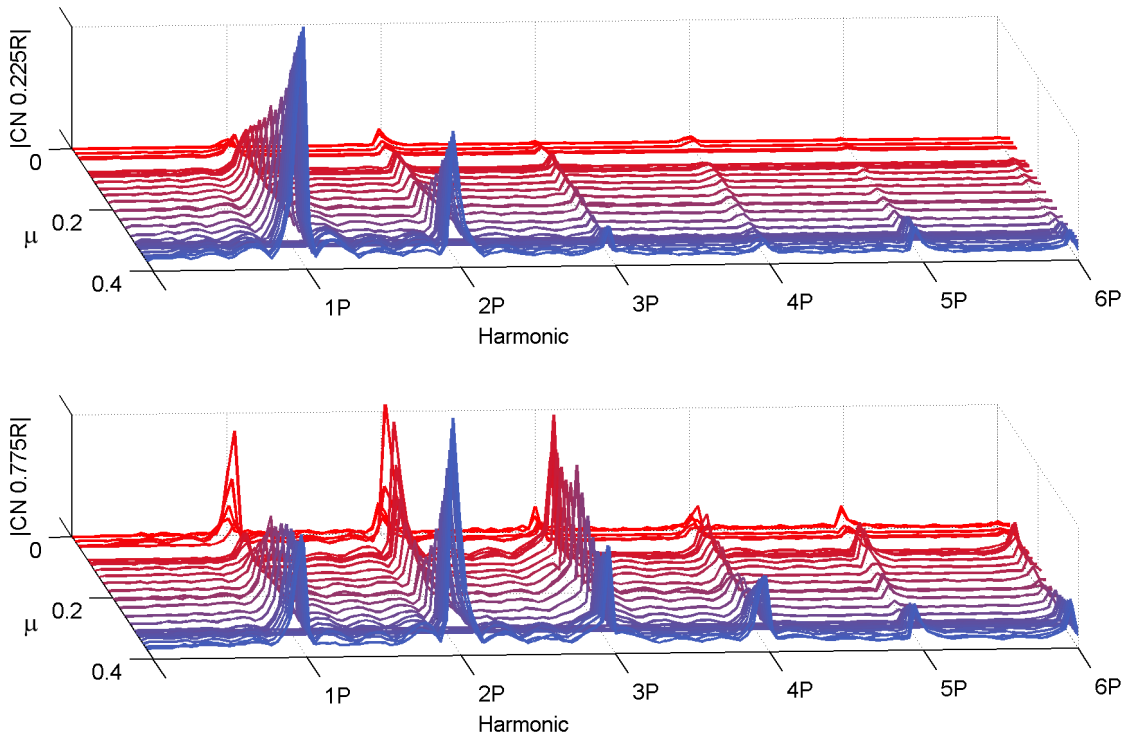

Figure 6.1: UH-60A measured blade normal force (per unit length; lb/in) by harmonic, v. advance ratio (each flight counter in flight 85).

on the blade), which can be shown to be equal to:

$$M_{shaft} = \rho S x_s R(\Omega R)^2[(-2C_{L0}x_s\mu + \Delta C_L({x_s}^2 + 0.75\mu^2))\cos\psi$$
$$+0.25\Delta C_L\mu^2\cos(3\psi)] \qquad (6.8)$$

This formulation contains $1P$ and $3P$ content, with $1P$ proportional to $({x_s}^2 + 0.75\mu^2)$ and $3P$ proportional to $0.25\mu^2$. Since the lift on a rotor blade is maximum outboard on the blade (say $x_s \approx 0.7$), the former term is much larger than the latter across typical operational UH-60A advance ratios ($\mu = 0$ to 0.4). Figure 6.2 shows experimentally-

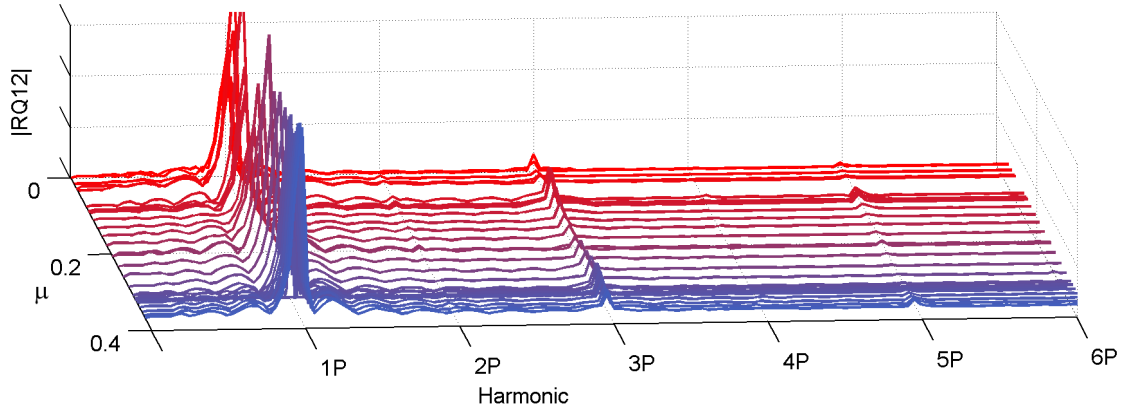

Figure 6.2: UH-60A measured upper shaft bending (bending in direction of blade 2 flapping; in-lb), by harmonic, v. advance ratio (each flight counter in flight 85).

measured UH-60A shaft upper bending moment versus azimuth for each flight counter in flight 85. These data are consistent with the formulation presented in equation 6.8, dominated by $1P$ content, with minor $3P$ content.

The intent of the above examples was not to derive closed form solutions for rotor loads harmonic content, but, rather, to explain the fundamental physical principles behind higher harmonic content.

6.3 Load Transference Between the Rotating and Fixed Frames

A number of research efforts have focused on vibratory response and load transference between the fixed and rotating frames [28, 35, 38, 39]. Traditionally, these efforts have addressed rotating loads prediction based on fixed-system measurements. This is a reasonable objective, given that fixed-system components are easier to instrument than rotating system components. This section will explain the challenges and limitations of these approaches.

The pushrod load P (for a given blade) may be written via Fourier expansion as a function of rotor speed Ω as follows.

$$P(\psi) = P_0 + \sum_{j=1}^{H} (c_j \cos(j\psi) + s_j \sin(j\psi)) \tag{6.9}$$

Where azimuth is related to the time domain as:

$$\psi = \Omega t \tag{6.10}$$

6.3.1 4-bladed Rotor

Figures 6.3 through 6.10 show the additive *load shape* of the pushrod loads for a 4-bladed rotor as a function of blade azimuth for eight harmonics. From here it is easy to visualize the net effect on fixed system forces and moments. Figure 6.3 shows the relative position of the four pushrods' $1P$ content ($c_1 \cos\psi + s_1 \sin\psi$) throughout a single rotation at rate Ω. At any given position, the sum of the vertical forces due to the four pushrods is zero. For non-zero longitudinal (s_1) and lateral (c_1) pushrod response, $1P$ bending moments are transferred to the fixed frame. The same holds true for $5P$ (Figure 6.7), $9P$, ..., $(jn_b+1)P$. This is known as a cyclic mode - or whirl mode, in the context of harmonics above $1P$.

Figure 6.4 shows the relative position of the four pushrods' $2P$ content ($c_2 \cos(2\psi) + s_2 \sin(2\psi)$) throughout a single rotation at rate Ω. At any given position, both the

sum of the vertical forces and the sum of the bending moments are zero. The same holds true for $6P$ (Figure 6.8), $10P$, ... $(jn_b+2)P$. This is known as a reactionless (or warp) mode. An interesting observation of the reactionless mode is that any attempt at using fixed system components to estimate the pushrod load will be unable to capture its $2P$ content, which can be a non-negligible component (Figure 6.14).

Figure 6.5 shows the relative position of the four pushrods' $3P$ content ($c_3\cos(3\psi)+ s_3\sin(3\psi)$) throughout a single rotation at rate Ω. At any given position, the sum of the vertical forces is zero. For non-zero longitudinal (s_3) and lateral (c_3) pushrod response, $3P$ bending moments are transferred to the fixed frame. It has the same net effect as $1P$, $5P$, etc., but with a difference in sign on the longitudinal component. The same holds true for $7P$ (Figure 6.9), $11P$, ... $(jn_b+3)P$. This is known as a whirl mode.

Figure 6.6 shows the relative position of the four pushrods' $4P$ content ($c_4\cos(4\psi)+ s_4\sin(4\psi)$) throughout a single rotation at rate Ω. At any given position, the sum of bending moments is zero, but the sum of the vertical forces can be non-zero, with all pushrod $4P$ components acting in the same direction. The same holds true for $8P$ (Figure 6.10), $12P$, ... $(jn_b)P$. This is known as a collective mode.

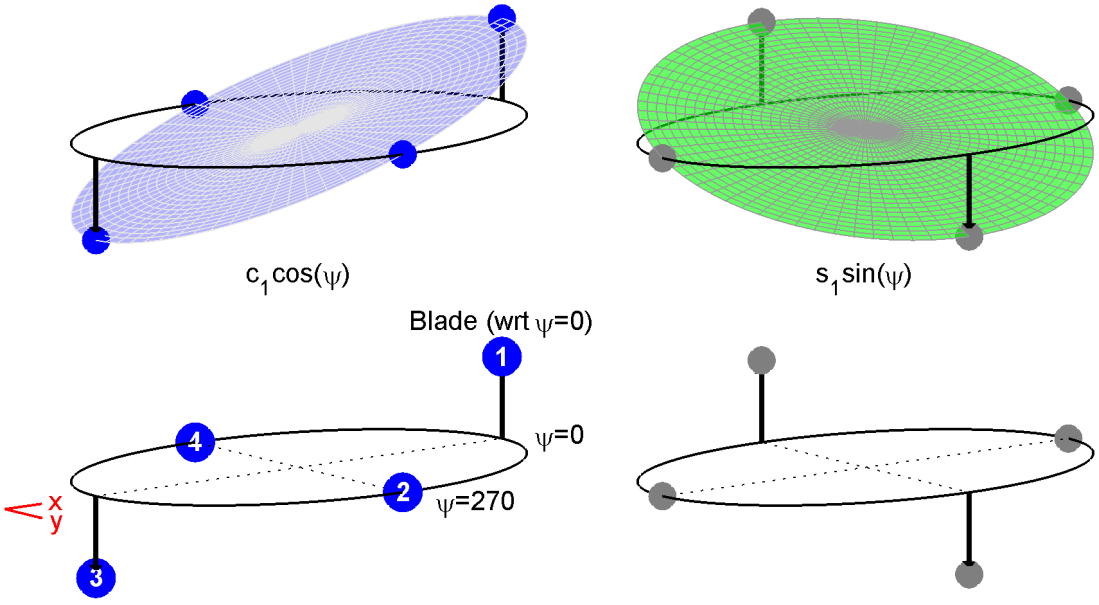

Figure 6.3: 4-bladed rotor fixed swashplate forces/moments (as a function of azimuth) due to pushrod axial loads: $1P$ harmonic (cyclic mode). Net result: zero ΣF_z; non-zero ΣM_y (left), ΣM_x (right).

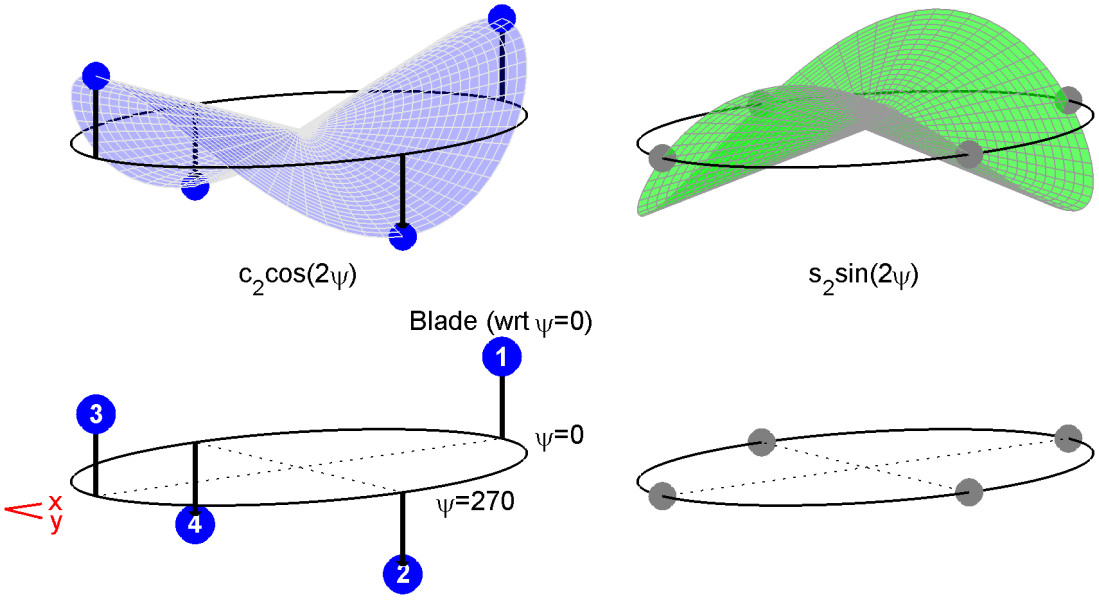

Figure 6.4: 4-bladed rotor fixed swashplate forces/moments (as a function of azimuth) due to pushrod axial loads: $2P$ harmonic (reactionless/warp mode). Net result: zero ΣF_z, ΣM_y (left), ΣM_x (right).

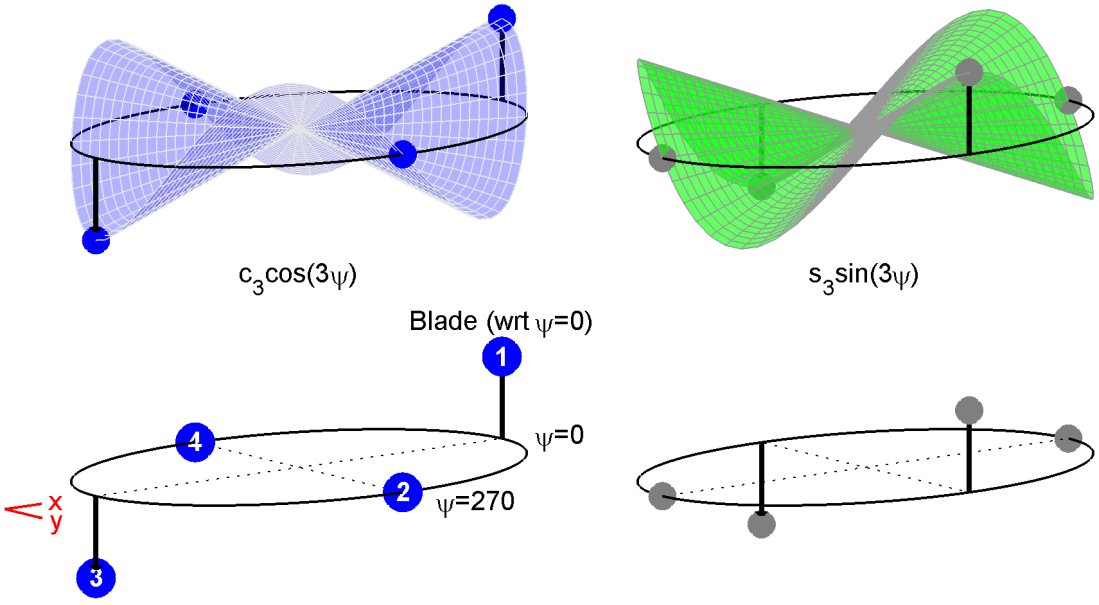

Figure 6.5: 4-bladed rotor fixed swashplate forces/moments (as a function of azimuth) due to pushrod axial loads: $3P$ harmonic (cyclic/whirl mode). Net result: zero ΣF_z; non-zero ΣM_y (left), ΣM_x (right).

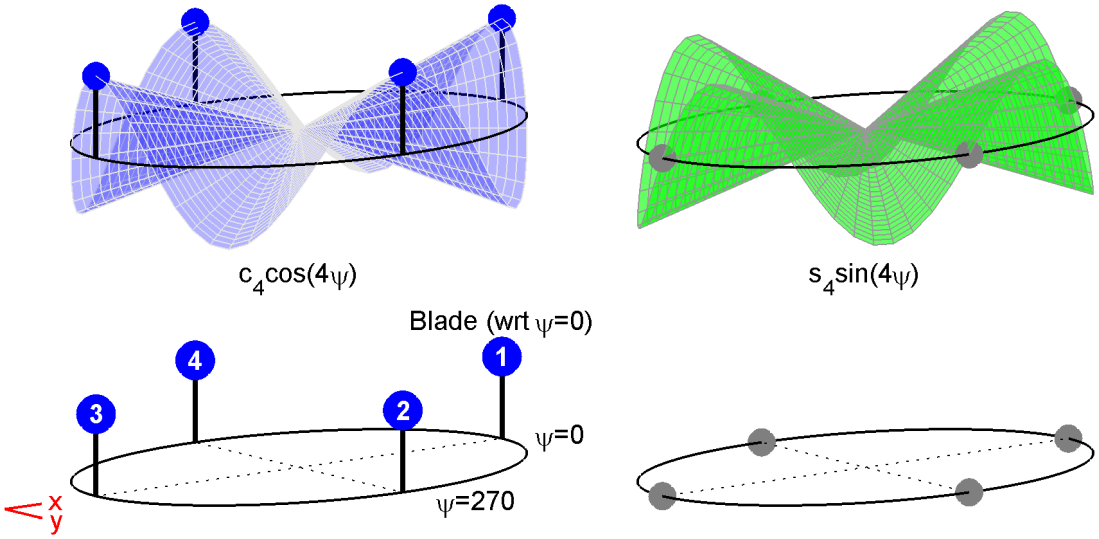

Figure 6.6: 4-bladed rotor fixed swashplate forces/moments (as a function of azimuth) due to pushrod axial loads: $4P$ harmonic (collective mode). Net result: non-zero ΣF_z; zero ΣM_y (left), ΣM_x (right).

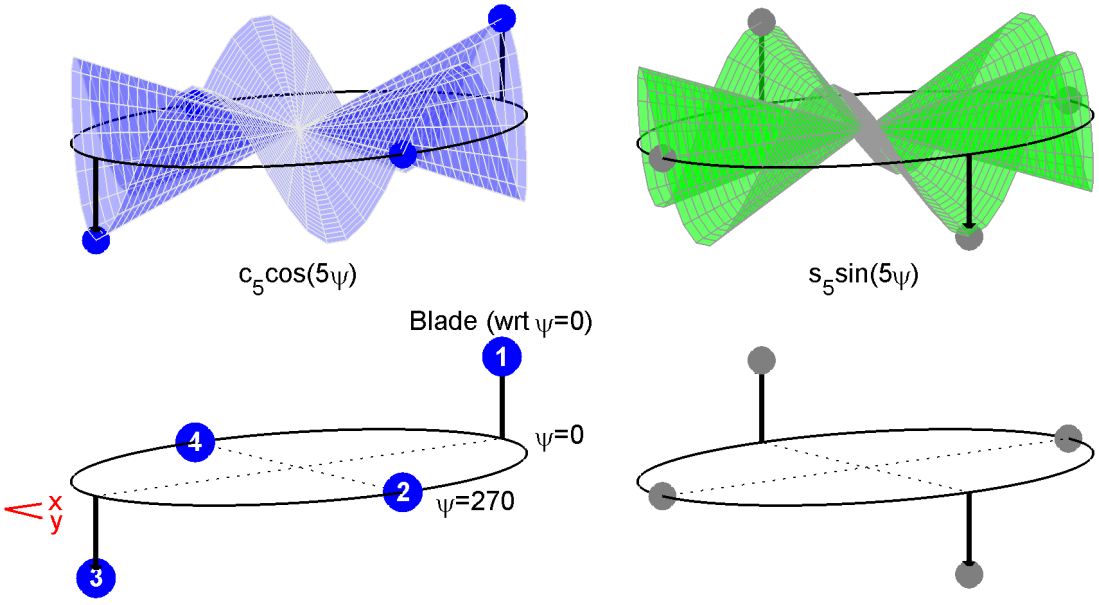

Figure 6.7: 4-bladed rotor fixed swashplate forces/moments (as a function of azimuth) due to pushrod axial loads: $5P$ harmonic (cyclic/whirl mode). Net result: zero ΣF_z; non-zero ΣM_y (left), ΣM_x (right).

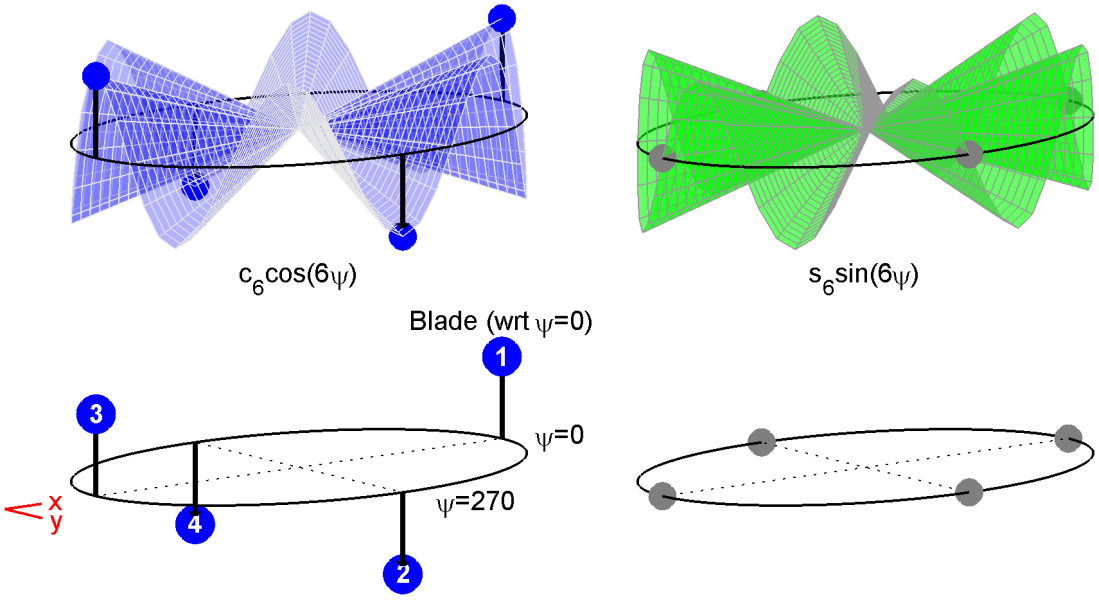

Figure 6.8: 4-bladed rotor fixed swashplate forces/moments (as a function of azimuth) due to pushrod axial loads: $6P$ harmonic (reactionless/warp mode). Net result: zero ΣF_z, ΣM_y (left), ΣM_x (right).

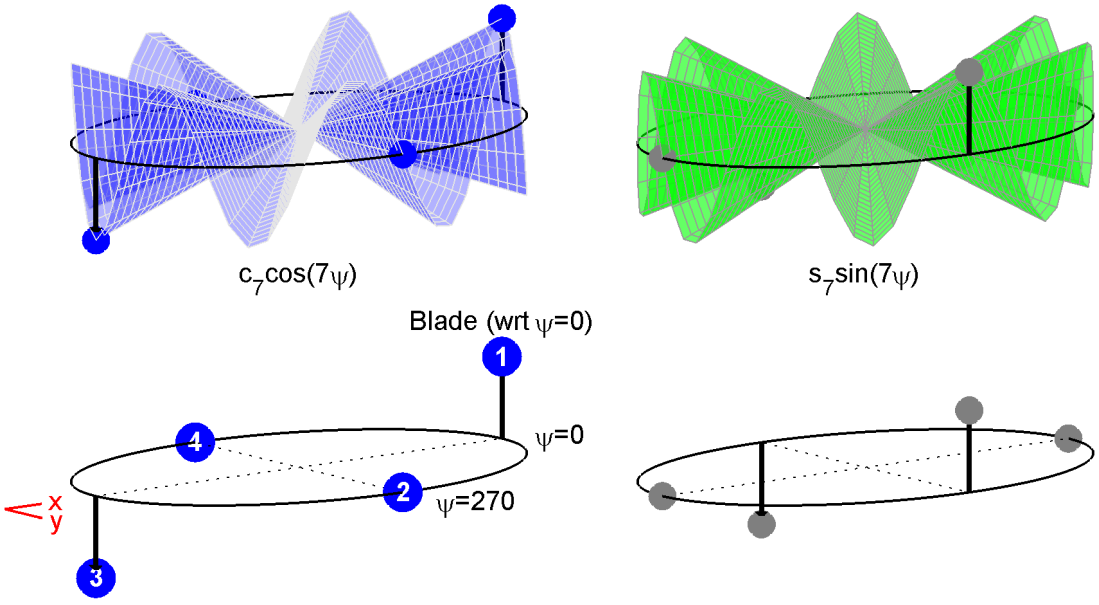

Figure 6.9: 4-bladed rotor fixed swashplate forces/moments (as a function of azimuth) due to pushrod axial loads: 7P harmonic (cyclic/whirl mode). Net result: zero ΣF_z; non-zero ΣM_y (left), ΣM_x (right).

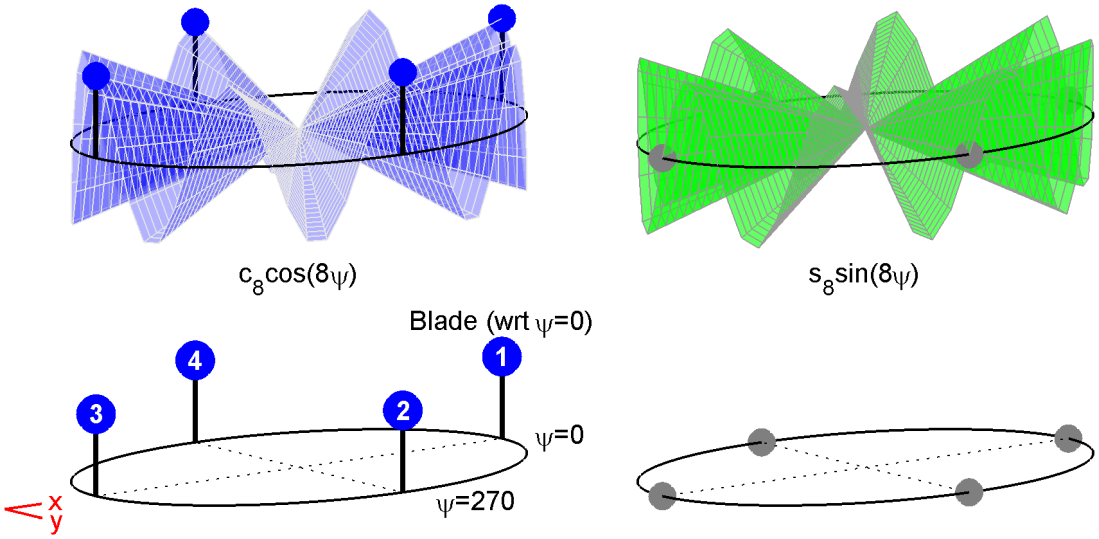

Figure 6.10: 4-bladed rotor fixed swashplate forces/moments (as a function of azimuth) due to pushrod axial loads: 8P harmonic (collective mode). Net result: non-zero ΣF_z; zero ΣM_y (left), ΣM_x (right).

Now that the pushrod force and moment transfer has been explained visually, the underlying physics will now be examined. The UH-60A will be used as an example. The pushrod load for blade 1, P_1, will be idealized as follows:

$$P_1(\psi) = P_0 + \sum_{j=1}^{H} \left[c_j \cos(j\psi) + s_j \sin(j\psi) \right] \tag{6.11}$$

Blade 2 through 4 pushrod loads will be idealized as azimuth-lagged distributions of P_1 with a zero frequency error/noise term, ϵ_i.

$$P_2(\psi) = P_1\left(\psi - \frac{1}{2}\pi\right) + \epsilon_2 \tag{6.12}$$

$$P_3(\psi) = P_1(\psi - \pi) + \epsilon_3 \tag{6.13}$$

$$P_4(\psi) = P_1\left(\psi - \frac{3}{2}\pi\right) + \epsilon_4 \tag{6.14}$$

Figure 6.11 shows the locations of the four UH-60A pushrod loads (P_1, P_2, P_3, and P_4) relative to the fixed-system servo loads (forward servo (FS), lateral servo (LS), and aft servo (AS)) [54]. Summing the forces in the vertical direction - treating pushrod loads and servo loads as carrying pure axial loads acting along the vertical axis - is formulated as follows.

$$FS + LS + AS + P_1 + P_2 + P_3 + P_4 = 0 \tag{6.15}$$

Plugging 6.12 through 6.14 into 6.15 yields:

$$-(FS + LS + AS) = \sum_{k=2}^{4} \epsilon_k + P_1(\psi) + P_1\left(\psi - \frac{1}{2}\pi\right) + P_1(\psi - \pi) + P_1\left(\psi - \frac{3}{2}\pi\right) \tag{6.16}$$

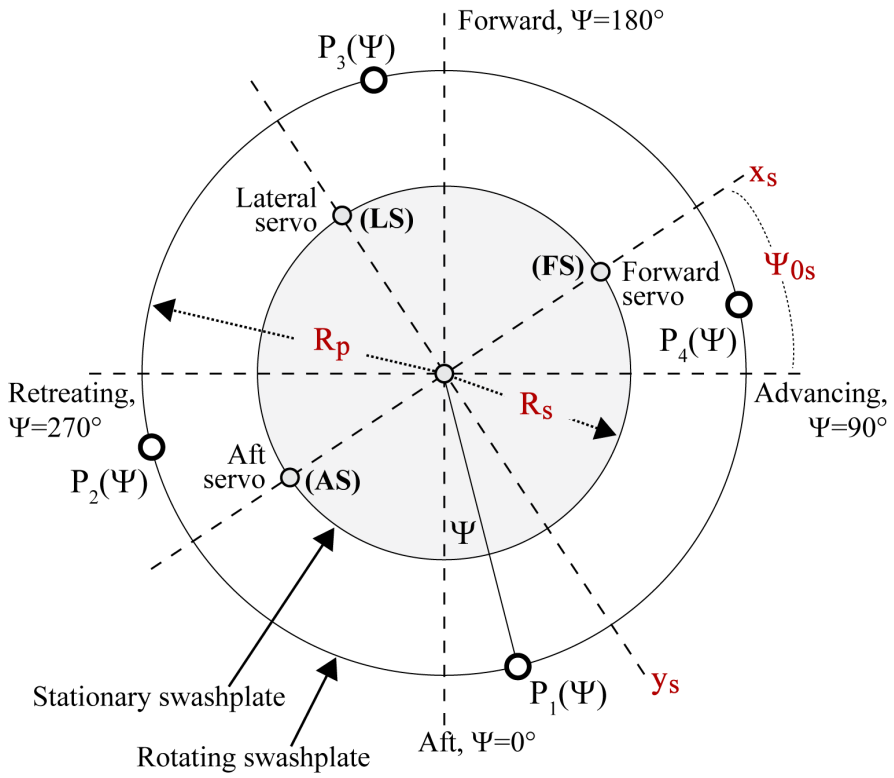

Figure 6.11: UH-60A pushrod, swashplate, and servo configuration.

Plugging 6.11 into 6.16 yields:

$$\begin{aligned}-(FS+LS+AS) = 4P_0 + \sum_{k=2}^{4}\epsilon_k + \sum_{j=1}^{H}[c_j\cos(j\psi) + s_j\sin(j\psi)] \\ + \sum_{j=1}^{H}\{c_j\cos[j(\psi-\frac{1}{2}\pi)] + s_j\sin[j(\psi-\frac{1}{2}\pi)]\} \\ + \sum_{j=1}^{H}\{c_j\cos[j(\psi-\pi)] + s_j\sin[j(\psi-\pi)]\} \\ + \sum_{j=1}^{H}\{c_j\cos[j(\psi-\frac{3}{2}\pi)] + s_j\sin[j(\psi-\frac{3}{2}\pi)]\} \qquad (6.17)\end{aligned}$$

Using trigonometric identities, 6.17 may be reduced to:

$$-(FS+LS+AS) = 4P_0 + \sum_{k=2}^{4}\epsilon_k + 4\sum_{j=4,8,12,\ldots}^{H}[c_j\cos(j\psi) + s_j\sin(j\psi)] \qquad (6.18)$$

Therefore, the sum of the three servo loads is a zero frequency term plus 4, 8, 12/rev, ... from the pushrod loads (plus noise). All other pushrod content ($1P$, $2P$, $3P$, $5P$,

$\dots$) are not directly present. These harmonics either cancel out ($2P$, $6P$, $\dots$) or combine into other frequencies ($3P + 5P$ into $4P$, $7P + 9P$ into $8P$, $\dots$). Thus, in the context of this idealization of pushrod response, only jn_bP force components ($j = 0, 1, 2, \dots$) are fed from the rotating frame into the fixed frame, where n_b is the number of blades. Note that the above idealization ignores swashplate dynamics (see Section 6.3.2).

Alternatively, it could be phrased that the sum of all pushrod loads is composed of jn_bP force components' ($j = 0, 1, 2, \dots$) content (e.g., $0P + 4P + 8P + ...$). This is shown in Figure 6.12, where pushrod and control servo load FTs are plotted v. advance ratio for flight 84. Note the equivalence between the summed servo loads and the summed pushrod loads. This is also shown in Figures 6.6 and 6.10, where the four pushrod loads additively produce a non-zero net F_z at $4P$ and $8P$, respectively (with zero F_z at $1P$, $2P$, $3P$, $5P$, etc.; see Figures 6.3, 6.4, 6.5, and 6.7, respectively).

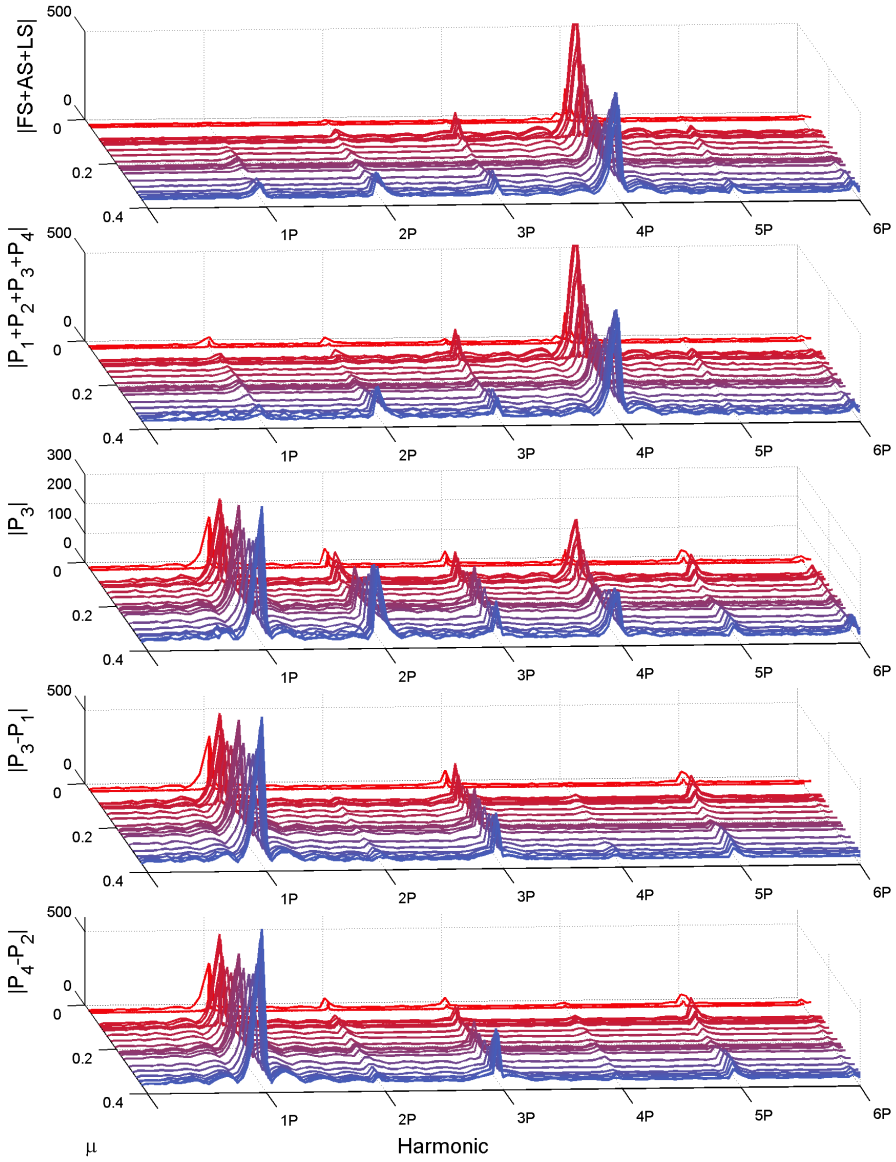

Figure 6.12: Pushrod, control servo loads, by harmonic, v. advance ratio (flight 84).

Now moments are examined. From Figure 6.11, the moments summed about x_s and y_s should each be zero, since no external moments are applied. The moment summed about x_s is then written as:

$$(LS)R_s + (P_3 - P_1)R_p \cos(\psi - \psi_{0s}) + (P_4 - P_2)R_p \sin(\psi - \psi_{0s}) = 0 \tag{6.19}$$

The moment summed about y_s is then written as:

$$(FS - AS)R_s - (P_3 - P_1)R_p \sin(\psi - \psi_{0s}) + (P_4 - P_2)R_p \cos(\psi - \psi_{0s}) = 0 \tag{6.20}$$

These two moment equations are of interest in that they each difference opposing pushrod loads ($P_3 - P_1$ and $P_4 - P_2$). These two differenced terms are expanded as follows.

$$(P_3 - P_1) = \epsilon_3 - 2 \sum_{j=1,3,5,\ldots}^{H} \left[c_j \cos(j\psi) + s_j \sin(j\psi)\right] \tag{6.21}$$

$$(P_4 - P_2) = \epsilon_4 - \epsilon_2 - 2 \sum_{j=1,3,5,\ldots}^{H} \left\{(-1)^{\frac{j+3}{2}} \left[c_j \sin(j\psi) - s_j \cos(j\psi)\right]\right\} \tag{6.22}$$

This shows that the differenced opposing pushrod loads ($P_3 - P_1$ and $P_4 - P_2$) are driven by odd harmonics ($1P$, $3P$, $5P$, etc.). This is verified with UH-60A flight test data in Figure 6.12. $1P$ dominates, but there is relevant content at $3P$ and, to a lesser degree, $5P$ as well. This was demonstrated visually in Figures 6.3 through 6.10. Opposing pushrod loads have the same sign for even harmonics but opposite sign for odd harmonics (same magnitude in both cases), thus differencing opposing pushrod loads cancels the even harmonic effects but adds the odd harmonic effects.

Plugging 6.21 and 6.22 into 6.19 yields the closed form solution for the lateral servo load, LS.

$$\begin{aligned} LS = \frac{R_p}{R_s}\{&2c_1 \cos\psi_{0s} + 2s_1 \sin\psi_{0s} \\ &-\epsilon_3 \cos(\psi - \psi_{0s}) + (\epsilon_2 - \epsilon_4)\sin(\psi - \psi_{0s}) \\ +2 \sum_{j=4,8,12,\ldots}^{H} &[c_{j-1}\cos(j\psi - \psi_{0s}) + c_{j+1}\cos(j\psi + \psi_{0s}) \\ &+s_{j-1}\sin(j\psi - \psi_{0s}) + s_{j+1}\sin(j\psi + \psi_{0s})]\} \end{aligned} \tag{6.23}$$

Now 6.18, 6.20, and 6.23 can be used to solve for the forward servo (FS) and aft servo (AS) loads, as shown in equations 6.24 and 6.25, respectively. These results (equations 6.23, 6.24, and 6.25) show that the control servo loads in the fixed system have a zero frequency term combined with dominant effects due to $4P$ content. The $1P$ content is present as a function of the noise in the system (ϵ_k), causing zero frequency offset (i.e., *bias*) between the four pushrod loads. Figure 6.13 shows the actual frequency content of the control servo loads. As shown, $4P$ is dominant, with some observable $1P$ content, along with $2P$ and $3P$ contributions, close in magnitude to the $1P$ response. This actual $2P$ and $3P$ content is due to this idealization's incorrect assumption that pushrods 2 and 4 would share identical $2P$ content, as would pushrods 1 and 3.

Figure 6.14 shows a time history and FFT for the four pushrod loads for flight counter c8534 ($\mu = 0.368$). As shown, there is some difference in magnitude, phasing, as well as frequency content between pushrods. Kufeld et al. [50] attribute some of the differences seen between pushrods at higher harmonics to blade-to-blade differences. However, given the dominance of $4P$ in the control servo loads, the above idealization is adequate for the goal of conceptual understanding of fixed and rotating system harmonic content addressed herein.

The next step is to use equations 6.23, 6.24, and 6.25 to formulate control servo loads based on measured UH-60A pushrod loads for blades 1 through 4 and compare to the measured control servo loads. Figures 6.15 and 6.16 show this comparison for flight counters c8418 ($\mu = 0.094$) and c8534 ($\mu = 0.368$), respectively. In the former, there is an under-prediction of $2P$, $3P$, and $4P$ for FS, an over-prediction of $2P$ and $4P$ for AS, and an under-prediction in LS. For the latter, a better match is seen, though still with some under-prediction in $2P$ and $4P$ for FS. Overall, however, a

reasonable approximation is obtained.

$$
\begin{aligned}
AS = -2P_0 - \frac{1}{2}\sum_{k=2}^{4}\epsilon_k \\
+\frac{R_p}{R_s}[-c_1(\cos\psi_{0s} + \sin\psi_{0s}) + s_1(\cos\psi_{0s} - \sin\psi_{0s})] \\
+\frac{1}{2}\frac{R_p}{R_s}[(-\epsilon_2 + \epsilon_3 + \epsilon_4)\cos(\psi - \psi_{0s}) - (\epsilon_2 + \epsilon_3 - \epsilon_4)\sin(\psi - \psi_{0s})] \\
-2\sum_{j=4,8,12,\ldots}^{H}[c_j\cos(j\psi) + s_j\sin(j\psi)] \\
-\sum_{j=4,8,12,\ldots}^{H}\{c_{j-1}[\cos(j\psi - \psi_{0s}) - \sin(j\psi - \psi_{0s})] \\
+c_{j+1}[\cos(j\psi + \psi_{0s}) + \sin(j\psi + \psi_{0s})] \\
+s_{j-1}[\cos(j\psi - \psi_{0s}) + \sin(j\psi - \psi_{0s})] \\
-s_{j+1}[\cos(j\psi + \psi_{0s}) + \sin(j\psi + \psi_{0s})]\}
\end{aligned}
\tag{6.24}
$$

$$
\begin{aligned}
FS = -2P_0 - \frac{1}{2}\sum_{k=2}^{4}\epsilon_k \\
+\frac{R_p}{R_s}[-c_1(\cos\psi_{0s} - \sin\psi_{0s}) - s_1(\cos\psi_{0s} + \sin\psi_{0s})] \\
+\frac{1}{2}\frac{R_p}{R_s}[(\epsilon_2 + \epsilon_3 - \epsilon_4)\cos(\psi - \psi_{0s}) - (\epsilon_2 - \epsilon_3 - \epsilon_4)\sin(\psi - \psi_{0s})] \\
-2\sum_{j=4,8,12,\ldots}^{H}[c_j\cos(j\psi) + s_j\sin(j\psi)] \\
-\sum_{j=4,8,12,\ldots}^{H}\{c_{j-1}[\cos(j\psi - \psi_{0s}) + \sin(j\psi - \psi_{0s})] \\
+c_{j+1}[\cos(j\psi + \psi_{0s}) - \sin(j\psi + \psi_{0s})] \\
+s_{j-1}[-\cos(j\psi - \psi_{0s}) + \sin(j\psi - \psi_{0s})] \\
+s_{j+1}[\cos(j\psi + \psi_{0s}) + \sin(j\psi + \psi_{0s})]\}
\end{aligned}
\tag{6.25}
$$

The relevance of this is as follows. If the objective was to model pushrod response based on measured servo loads, it would be impossible to predict any pushrod loads' $2P$ content (for a 4-bladed rotor) based on these measured servo loads. Additionally,

this would lead to an under-determined system, given that there are four unknowns, i.e., the four pushrod loads, but only three equations: $\sum F_z$, $\sum M_{xs}$, and $\sum M_{ys}$.

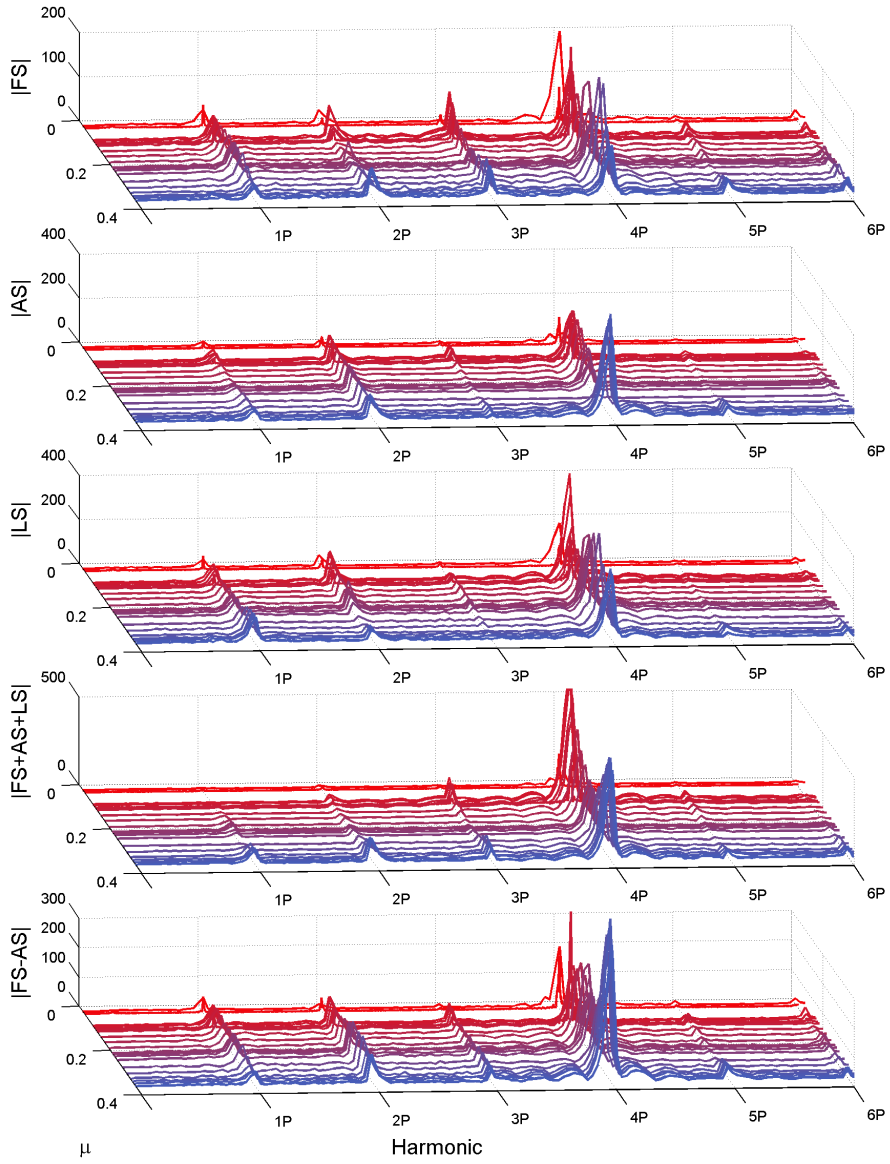

Figure 6.13: Control servo loads, by harmonic, v. advance ratio (flight 84).

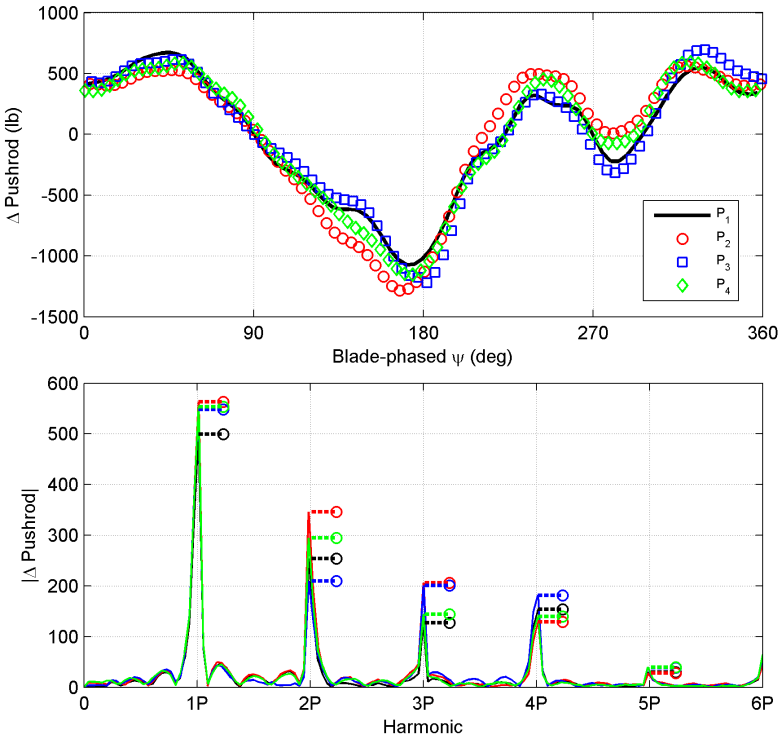

Figure 6.14: UH-60 measured pushrod loads, blades 1 through 4, c8534, $\mu = 0.368$.

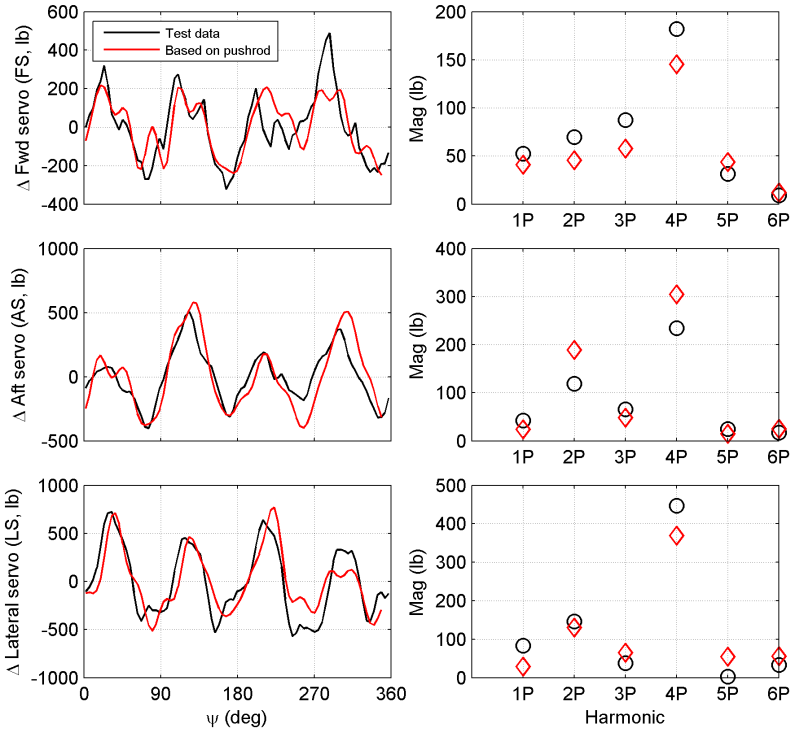

Figure 6.15: UH-60 measured v. computed servo loads, c8418, $\mu = 0.094$.

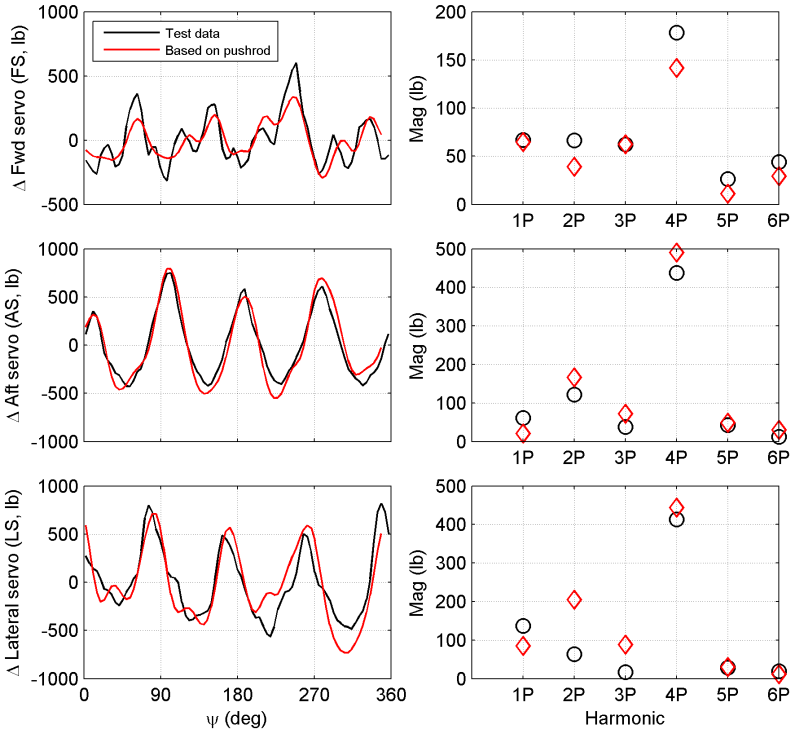

Figure 6.16: UH-60 measured v. computed servo loads, c8534, $\mu = 0.368$.

6.3.2 Swashplate Dynamics

Research by Abhishek et al. [3] has shown that the non-zero swashplate mass (m_{sp}) modifies equation 6.15 to the following:

$$FS + LS + AS + P_1 + P_2 + P_3 + P_4 = m_{sp} a_{sp} \tag{6.26}$$

This was shown to have appreciable effect on 4/rev servo loads (up to 25% variation in peak-to-peak load) but minimal effect on blade loads. These effects were not included herein. They could, perhaps, describe some of the differences seen in Figures 6.15 and 6.16.

6.3.3 7-bladed Rotor

Figures 6.17 through 6.24 show the additive *load shape* of the pushrod loads for a 7-bladed rotor as a function of blade azimuth for 8 harmonics. From here it is easy to visualize the net effect on fixed system forces and moments. Figure 6.17 shows the

relative position of the seven pushrods' $1P$ content ($c_1 \cos\psi + s_1 \sin\psi$) throughout a single rotation at angular speed Ω. At any given position, the sum of the vertical forces is zero. For non-zero longitudinal (s_1) and lateral (c_1) pushrod response, $1P$ bending moments are transferred to the fixed frame. The same holds true for $8P$ (Figure 6.24), $15P$, ... $(jn_b + 1)P$. This is known as a cyclic mode.

Figures 6.18 through 6.21 show the relative position of the seven pushrods' $2P$, $3P$, $4P$, and $5P$ content ($c_j \cos(j\psi) + s_j \sin(j\psi)$; j=2,3,4,5) throughout a single rotation at rate Ω. At any given position, the sum of the vertical forces is zero. For non-zero longitudinal (s_j) and lateral (c_j) pushrod response, jP bending moments are transferred to the fixed frame. The same holds true for $9P$ through $12P$. These are known as reactionless/warp modes.

Figure 6.22 shows the relative position of the seven pushrods' $6P$ content ($c_6 \cos\psi +$ $s_6 \sin\psi$) throughout a single rotation at rate Ω. At any given position, the sum of the vertical forces is zero. For non-zero longitudinal (s_6) and lateral (c_6) pushrod response, $6P$ bending moments are transferred to the fixed frame. The same holds true for $13P$, $20P$, ... $(jn_b + 1)P$. This is known as a whirl mode.

Figure 6.23 shows the relative position of the seven pushrods' $7P$ content ($c_7 \cos(7\psi) +$ $s_7 \sin(7\psi)$) throughout a single rotation at rate Ω. At any given position, the sum of the bending moments is zero, but the sum of the vertical forces can be non-zero, with all pushrod $7P$ components acting in the same direction. The same holds true for $14P$, $21P$, ... $(jn_b)P$. This is known as a collective mode.

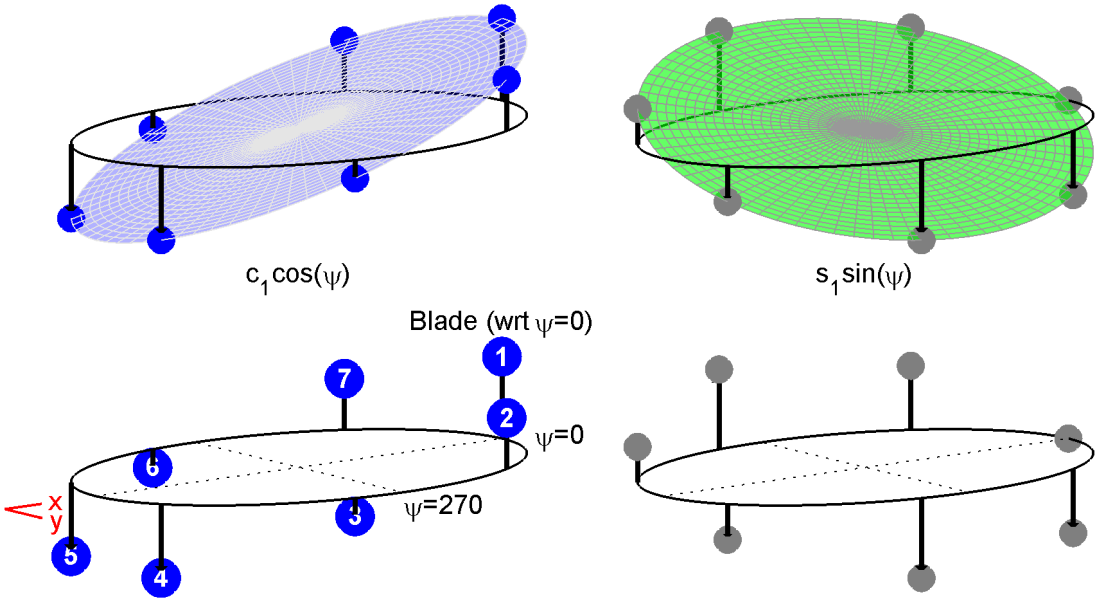

Figure 6.17: 7-bladed rotor fixed swashplate forces/moments (as a function of azimuth) due to pushrod axial loads: $1P$ harmonic (cyclic mode). Net result: zero ΣF_z; non-zero ΣM_y (left), ΣM_x (right).

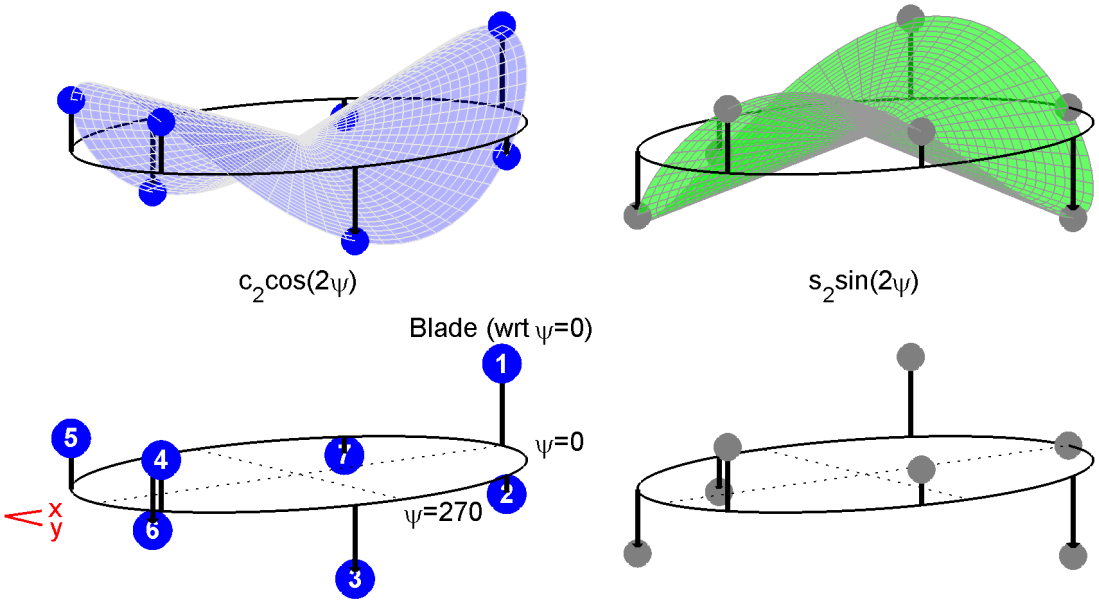

Figure 6.18: 7-bladed rotor fixed swashplate forces/moments (as a function of azimuth) due to pushrod axial loads: $2P$ harmonic (reactionless/warp mode). Net result: non-zero ΣF_z; zero ΣM_y (left), ΣM_x (right).

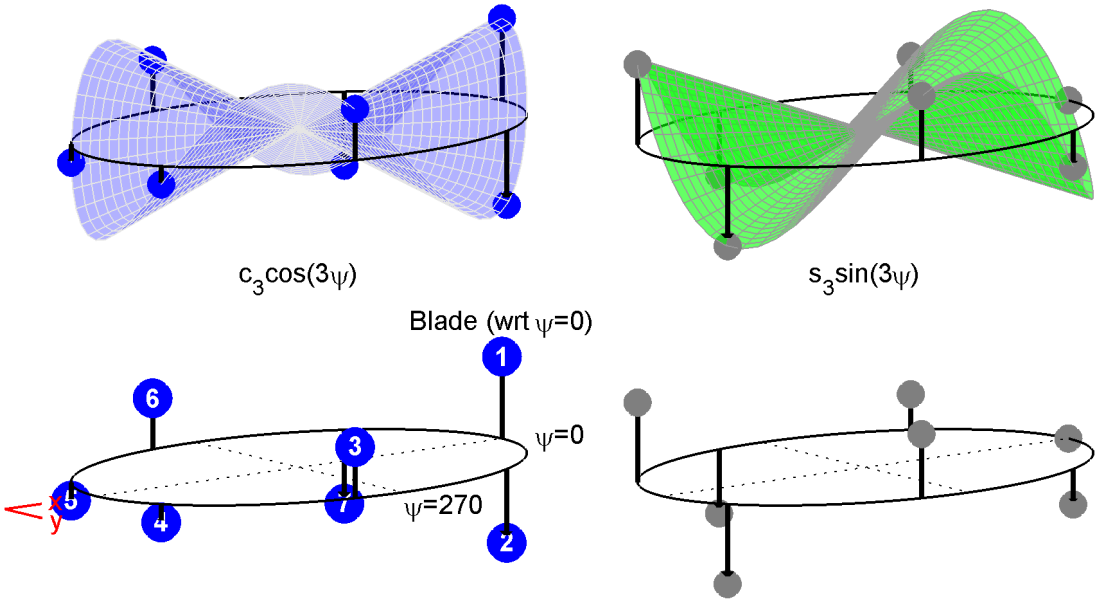

Figure 6.19: 7-bladed rotor fixed swashplate forces/moments (as a function of azimuth) due to pushrod axial loads: $3P$ harmonic (reactionless/warp mode). Net result: non-zero ΣF_z; zero ΣM_y (left), ΣM_x (right).

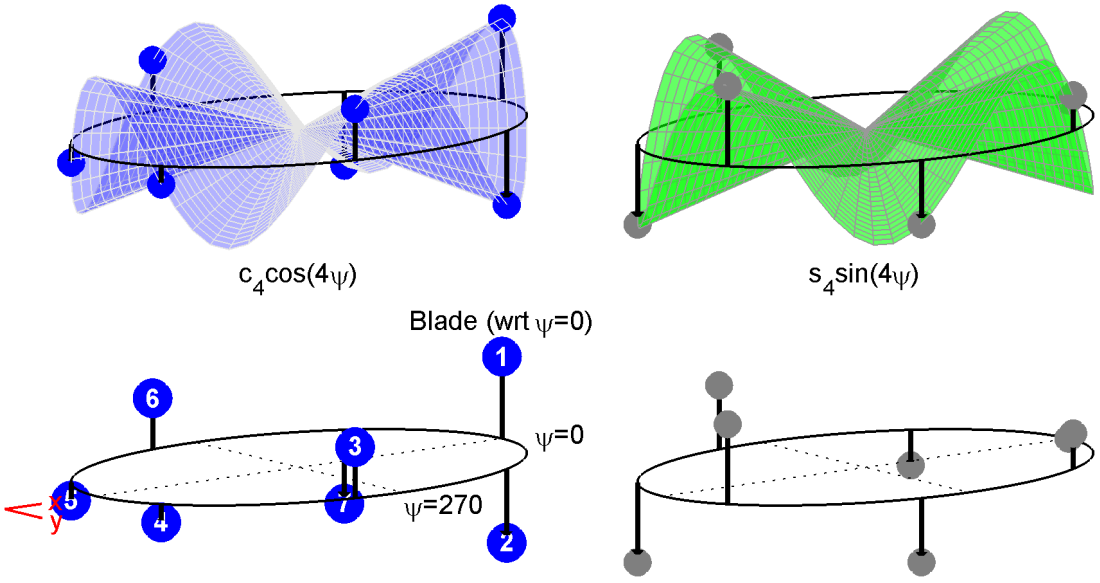

Figure 6.20: 7-bladed rotor fixed swashplate forces/moments (as a function of azimuth) due to pushrod axial loads: $4P$ harmonic (reactionless/warp mode). Net result: non-zero ΣF_z; zero ΣM_y (left), ΣM_x (right).

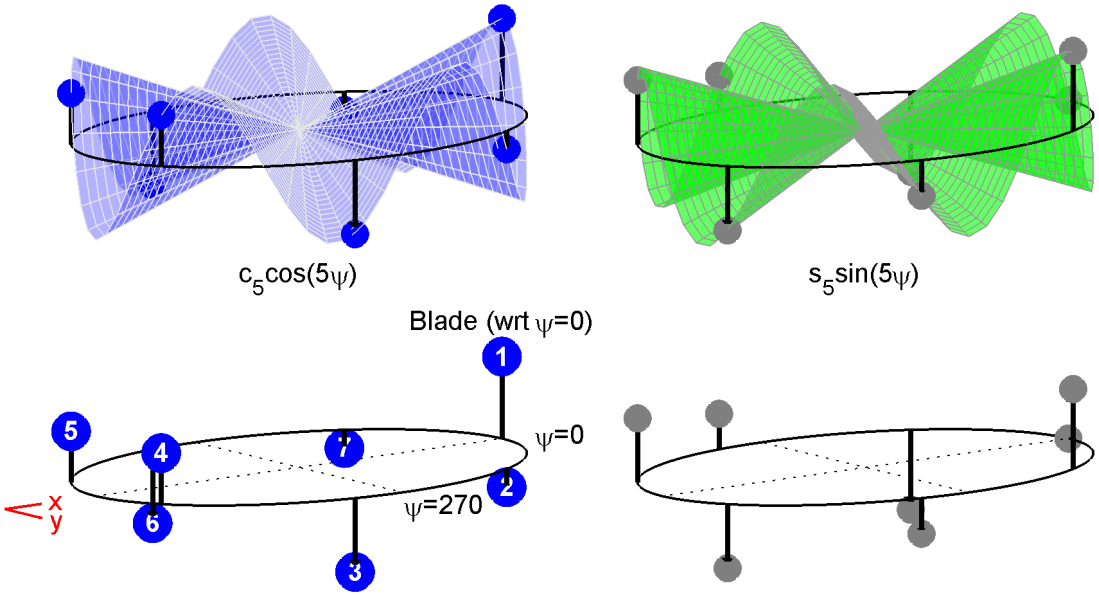

Figure 6.21: 7-bladed rotor fixed swashplate forces/moments (as a function of azimuth) due to pushrod axial loads: $5P$ harmonic (reactionless/warp mode). Net result: non-zero ΣF_z; zero ΣM_y (left), ΣM_x (right).

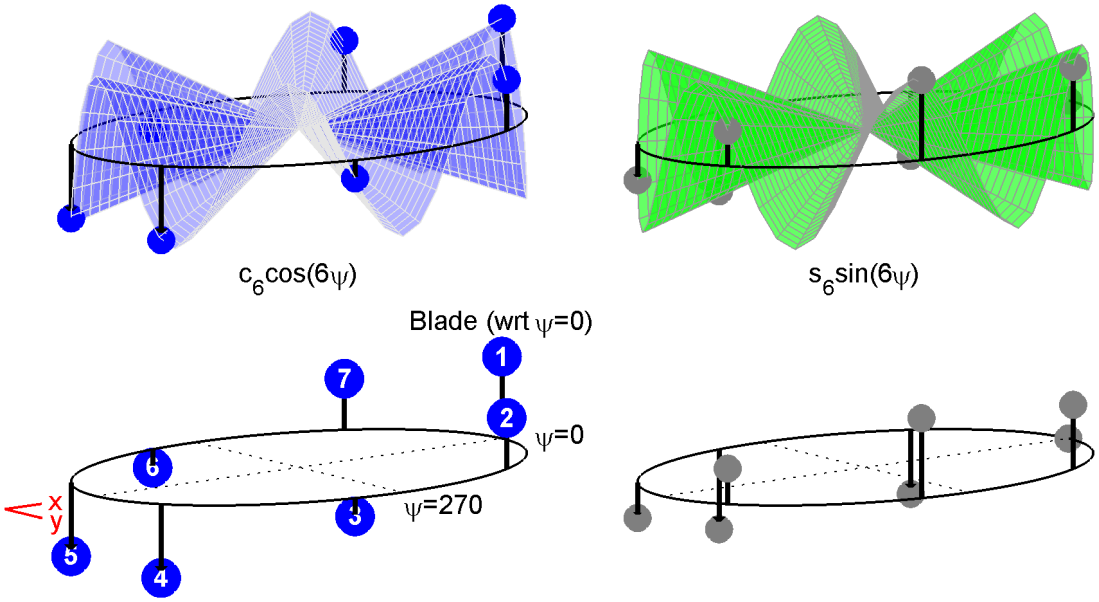

Figure 6.22: 7-bladed rotor fixed swashplate forces/moments (as a function of azimuth) due to pushrod axial loads: $6P$ harmonic (cyclic/whirl mode). Net result: zero ΣF_z; non-zero ΣM_y (left), ΣM_x (right).

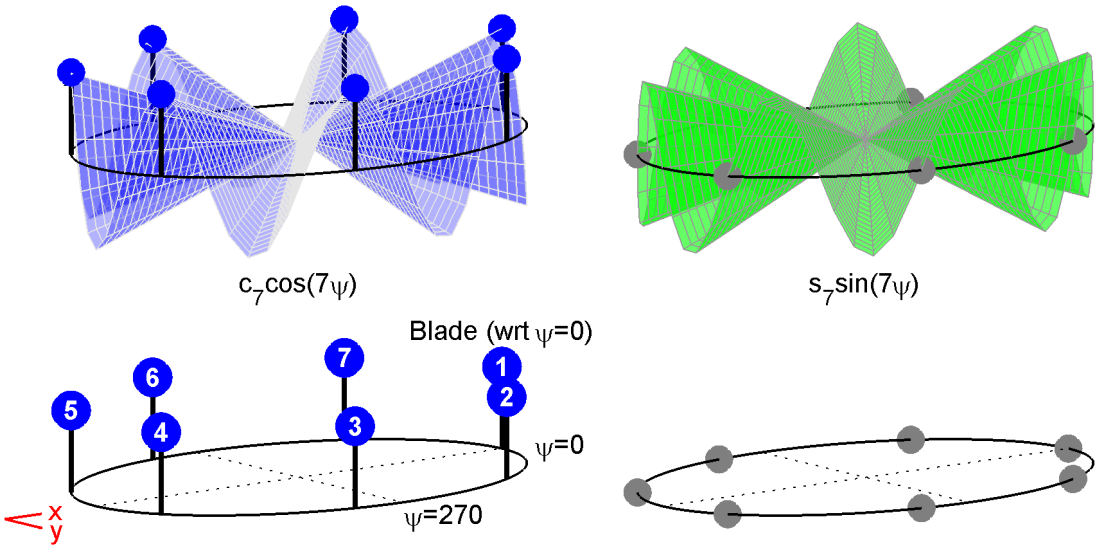

Figure 6.23: 7-bladed rotor fixed swashplate forces/moments (as a function of azimuth) due to pushrod axial loads: $7P$ harmonic (collective mode). Net result: non-zero ΣF_z; zero ΣM_y (left), ΣM_x (right).

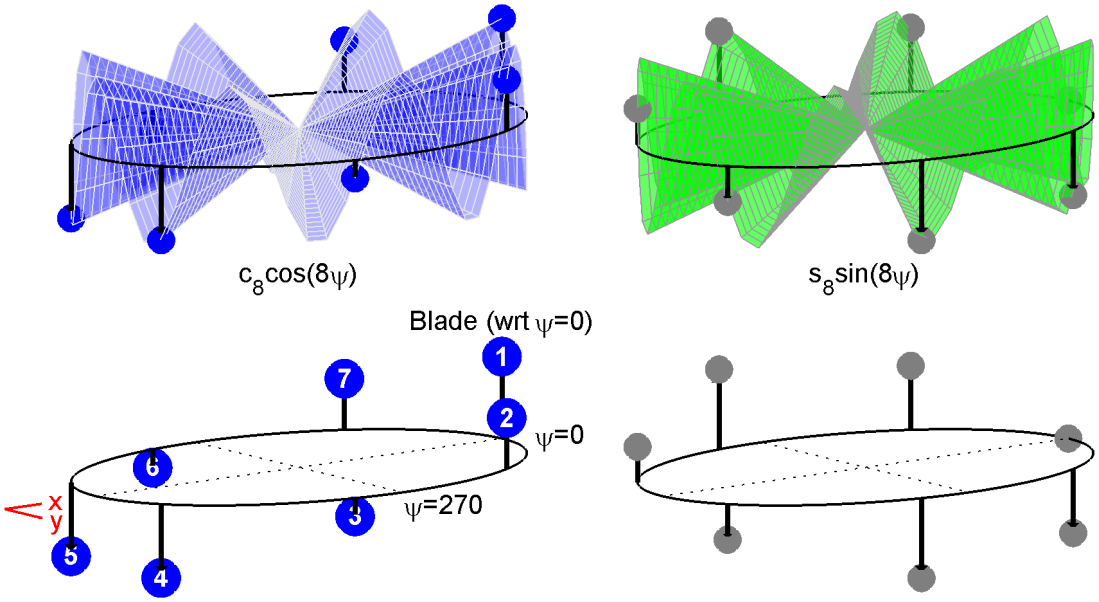

Figure 6.24: 7-bladed rotor fixed swashplate forces/moments (as a function of azimuth) due to pushrod axial loads: $8P$ harmonic (cyclic/whirl mode). Net result: zero ΣF_z; non-zero ΣM_y (left), ΣM_x (right).

6.4 Summary

This chapter examined rotor load content by harmonic. For a 4-bladed rotor system, blade lift due to simplified aerodynamics was derived and compared with measured UH-60A results. Inboard response of the blade followed the experimental trends. Outboard blade response did not, due to unsteady airloads effects.

The mechanics of load transference between the rotating and fixed frames were also examined. For the UH-60A, it was shown how the sum of all pushrod loads is composed of jn_bP force components' ($j = 0, 1, 2, \ldots$) content (e.g., $0P + 4P + 8P + \ldots$). Closed form expressions for the three UH-60A servo loads were derived as well. It was shown how, if the objective was to model pushrod response based on measured servo loads, it would be impossible to predict any pushrod loads' $2P$ content (for a 4-bladed rotor) based on these measured servo loads.

A generic 7-bladed rotor was also examined. For both the 4- and 7-bladed rotors, cyclic/whirl, reactionless/warp, and collective modes were defined and illustrated. The following generalizations may be applied to an n_b-bladed rotor (where $j = 1, 2, \ldots$):

1. 1, $(jn_b - 1)$, and $(jn_b + 1)$ are rotor cyclic/whirl modes
2. jn_b are collective modes
3. All others are reactionless/warp modes

This research thus far has focused on understanding and improving the accuracy of loads predictions for rotorcraft components, specifically those in the rotating frame (e.g., blade and pushrod loads). Chapter 7 will look at the impact of the accuracy of rotor loads prediction on component fatigue life.

CHAPTER VII

IMPACT ON FATIGUE LIFE ESTIMATION

7.1 Overview

This research has focused thus far on improving the accuracy of loads predictions for rotorcraft components, specifically those in the rotating frame (e.g., blade and pushrod loads). This chapter extends this by quantifying the effects of these improvements on rotorcraft component fatigue life.

Metallic components in rotorcraft are typically designed using a *safe life* methodology [33]. Safe life design is intended to ensure the structure has a damage-free service life for a period of two to four (or more) times that actually intended in service. This requirement is generally conservative and likely to result in design penalties (e.g., added weight). In the context of fixed wing aircraft (e.g., P-3C Orion, though also applicable to rotary wing aircraft [33, 60]), Iyyer and Sarkar, et al. [47] state that, for safe life design, service or retirement life of a component is defined by crack initiation time derived from a full-scale, component, or element fatigue test. In practice, however, the component is retired before the formation of a fatigue crack by using safety factors on calculated crack initiation time. This is due to inherent variability in both static and fatigue material properties as well as assumptions made in analytical models used to calculate crack initiation time. Safe life analysis is also referred to as *fatigue analysis*. It stands in contrast to *damage tolerance* (*crack growth*) analysis, which assumes some inherent flaws will be present in a given component. The damage tolerant approach recognizes this inherent damage and seeks to predict the rate of growth of such damage (as well as incorporate design features to delay the propagation of cracks) An integral part of the damage tolerant approach is establishing

inspection intervals to monitor damage from an *inspectable* crack size (dependent on the inspection or NDI technique) to its critical value.

7.2 Fatigue Analysis Methodology

For fatigue analysis, the concept for quantification of damage is based on the Palmgren-Miner Linear Damage Accumulation Hypothesis [63, 68], also known as *Miner's Rule* or the *Palmgren-Miner Rule*. In this hypothesis, crack onset (or the end of useful component life) is expected when life fractions sum to unity:

$$\frac{n_1}{N_{f1}} + \frac{n_2}{N_{f2}} + ... = \sum_j \frac{n_j}{N_{fj}} = 1.0 \tag{7.1}$$

Each n_j is the number of cycles seen at a given stress level in the usage block and N_{fj} is the number to cycles to failure at that stress level. These N_{fj} values are typically determined via cyclic testing and can be expressed graphically via a constant-life diagram (a series of stress-to-number of cycles to failure, or *S-N curves*), each for a different mean stress or stress ratio (see Figure 7.2).

This linear damage accumulation model was first introduced in the 1920s (A. Palmgren [68]) and gained wide acceptance in the mid-1940s (M. Miner [63]).

7.3 Application to a Rotorcraft Component

This linear damage accumulation model will now be applied to a rotorcraft component. Due to the lack of publicly-available usage and fatigue data for the UH-60A, a hypothetical component will be analyzed. Usage data includes definitions of flight profiles (speed, altitude, gross weight/cg, maneuvers flown, etc.) as well as the number of occurrences of each flight profile within a given usage block. Fatigue data includes component life target values (in terms of allowable cycles or flight hours to failure) as well as the component's S-N curve, as defined in Section 7.2.The intent of this analysis is to show the *relative effects* that errors in loads' predictions have on fatigue life - not to predict actual failure times for a given UH-60A component.

7.3.1 Assumptions

The following simplifying assumptions are made.

1. The component is a UH-60A pitch control horn (Figure 7.1), where the critical stresses are assumed to be driven purely by pushrod load.

2. Assume a 10,000 hour component life, which is typical for an H-60 aircraft rotor component [5].

3. Load sequencing effects are not considered; rather, a standard rainflow cycle counting procedure (ASTM E 1049-85 [7]) is used in the life calculation.

   (a) Crack growth analysis of metallic structures (and, to a lesser degree, durability or fatigue without cracks) can be highly sensitive to the placement of large amplitude cycles within the underlying stress sequence (McColl and Phan [59]).

   (b) Large amplitude cycles occurring near the beginning of a tensile-dominated stress sequence can potentially result in large residual stresses and, subsequently, slower crack growth or even crack retardation. Conversely, large amplitude cycles occurring near the end of the stress sequence can result in faster crack growth due to the absence of large residual stresses earlier in the spectrum.

   (c) A variety of intermediate effects can be achieved by more uniform distributions of large amplitude cycles throughout the stress sequence.

   (d) These effects are not considered herein.

4. The aircraft usage (mission profiles and mission mix) are based on the Helix sequence [31, 32], discussed below.

5. The S-N curves used herein (Figure 7.2) were derived based on fatigue tests performed on a lug component representative of one found in rotors [31, 32].

6. This analysis is a stress-life method - as opposed to strain-life, which more accurately models cracks initiated near notches with significant stress concentrations.

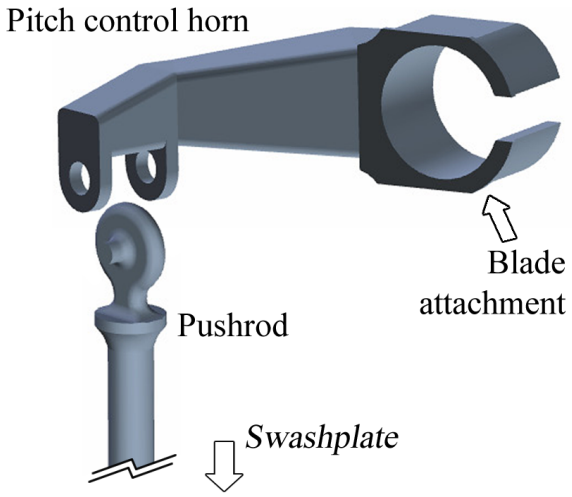

Figure 7.1: UH-60A pitch control horn, pushrod (CAD model elements copyright Brooke Strause).

7.3.2 Helix Loading Sequence

Helix [31, 32] is a standard loading sequence which relates to the main rotors of helicopters with articulated rotors (*Felix* is a similar sequence for semi-rigid rotors). The primary purpose of the loading standard is to provide a convenient tool for providing comparative fatigue spectra for different usage or loading scenarios.

The Helix sequence is based on an aggregate block of 140 mission occurrences (190.5 flight hours), comprised of prescribed sequences of four mission profiles: training (TNG), transport (TPT), anti-submarine warfare (ASW), and search-and-rescue (SAR). Each mission follows the same standard mission segment sequence, with different durations for each. Table 7.1 gives the mission profiles along with the mean

stress for each segment. All Helix stresses are given in *Helix units* (units normalized for a min/max stress of -20/100 in the spectrum). The mission profiles differ in length from 0.75 to 2.25 to 3.75 hours. This 190.5 hour flight block is then repeated approximately 52 times to represent the desired 10,000 hour block. Each segment is then applied a sequenced set of alternating stresses with values of (±) 20, 24, 28, 32, 36, or 40 *Helix units*, starting with the mean, then adding or subtracting (alternating peaks and valleys) the prescribed number of cycles and magnitude of alternating stress. Any intermediate stresses are then removed to ensure a true peak-valley sequence.

7.3.3 Rainflow Counted Sequence

The stress sequence is then rainflow counted, following ASTM E 1049-85 [7]. This rearranges the peak-valley pairings prior to computing damage. Table 7.2 shows the rainflow counted block set. The 190.5 hour values (column 2 of the table) are the truncated cycles (so-called *Helix32* cycles) from Reference [32]. These cycle counts were then scaled to produce a 10,000 hour block. The stress quantities (S) shown in Table 7.2 are defined as follows. S_{mean} are the distinct mean stresses occurring in the spectrum, while S_{min} and S_{max} are the associated min and max stresses, respectively. Also, S_a is the alternating stress, ΔS is the delta stress, and R is the stress ratio, as defined in equations 7.2, 7.3, and 7.4, respectively. Note that $R = -1$ for a *fully reversed* cycle, one with zero mean stress, resulting in $S_{min} = -S_{max}$. n_j are the number of cycles (peak-valley pairs, or mean level crossings with positive slope) for each distinct mean stress event in the spectrum.

$$S_a = \frac{S_{max} - S_{min}}{2} \tag{7.2}$$

$$\Delta S = 2S_a = S_{max} - S_{min} \tag{7.3}$$

$$R = \frac{S_{min}}{S_{max}} \tag{7.4}$$

The S-N curve from Reference [31] (Figure 31; Table 30) is for a lug tested under a series of constant amplitude axial loadings. This was selected as the basis for this

analysis given that the test was performed at a wide range of R values (-0.33 to 0.55). The experimental data from this test is shown in Figure 7.2, along with exponential curve fits for each dataset. Note that two changes have been made to this S-N data prior to application in this analysis: (1) the curve fits differ somewhat from the reference. An exponential curve fit was applied to the test data points. Equations and R^2 values are shown in Figure 7.2. The author is satisfied with the degree of matching shown herein. (2) the stress magnitudes (y-axis) are applied in *Helix units* (not psi or MPa) and are scaled to provide a damage of 1.0 for the above baseline spectrum (10,000 hour block).

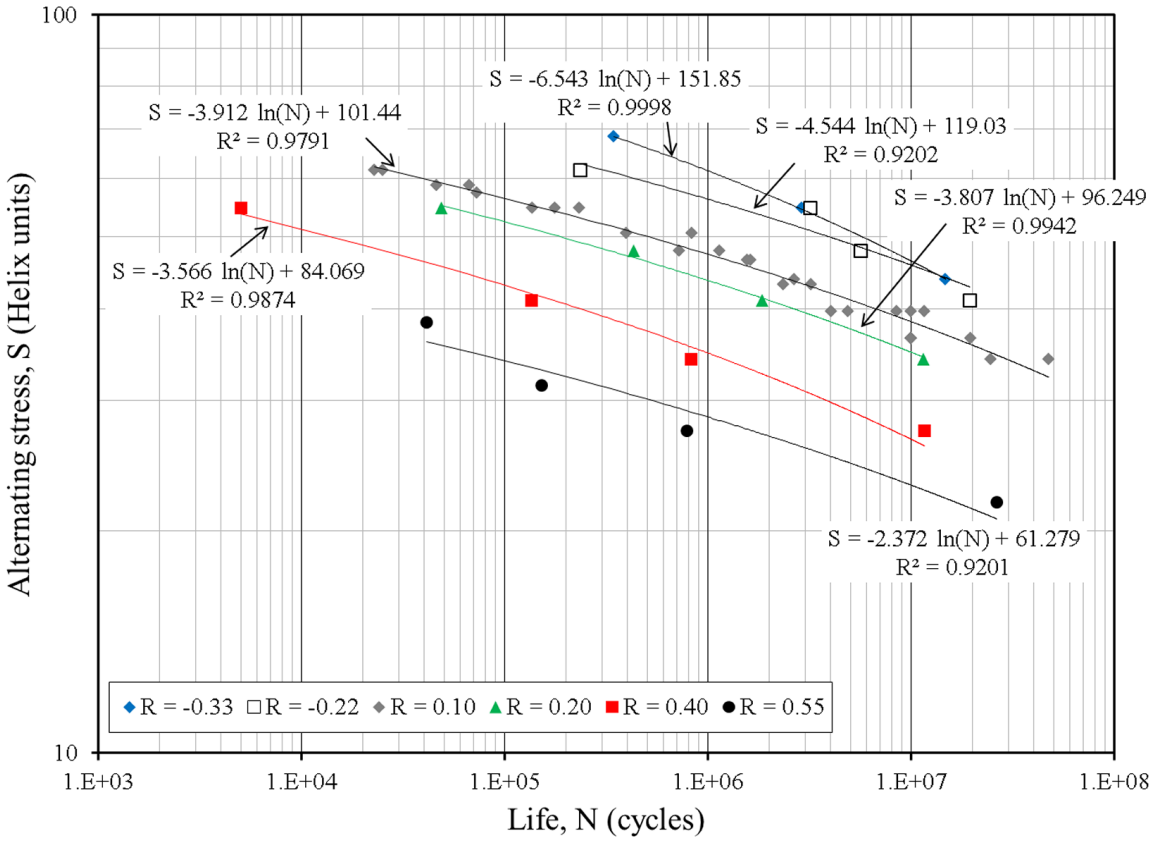

Figure 7.2: S-N curve, sample rotor component.

Table 7.1: Helix profiles.

Segment	Description	Mission				Mean stress*
		TNG	TPT	ASW	SAR	
1	Takeoff	0.27%	0.27%	0.13%	0.20%	44.0
2	Fwd flight, speed 1	2.34%	0.39%	2.79%	0.24%	72.0
3	Fwd flight, speed 2	1.69%	0.40%	2.80%	0.22%	68.0
4	Fwd flight, speed 3	1.60%	0.41%	2.79%	0.24%	60.0
5	Fwd flight, speed 4	3.17%	8.56%	5.96%	25.93%	60.0
6	Fwd flight, speed 5	63.04%	82.67%	35.89%	64.99%	64.0
7	Max power climb	0.51%	0.44%	1.33%	0.44%	68.0
8	Shallow appr. to hover	0.07%	0.19%	0.00%	0.00%	56.0
9	Normal appr. to hover	0.71%	0.00%	1.39%	0.09%	60.0
10	Hover	19.24%	2.86%	32.83%	4.88%	0.0
11	Bank turn, port	2.22%	0.80%	5.47%	0.44%	68.0
12	Bank turn, starboard	1.78%	0.81%	5.48%	0.44%	68.0
13	Sideways flight, port	0.18%	0.24%	0.24%	0.24%	56.0
14	Recovery from 13	0.15%	0.07%	0.07%	0.07%	52.0
15	Sideways flight, starbd	0.21%	0.23%	0.23%	0.23%	60.0
16	Recovery from 15	0.11%	0.07%	0.07%	0.07%	52.0
17	Rearwards flight	0.30%	0.22%	0.22%	0.22%	68.0
18	Recovery from 17	0.22%	0.09%	0.09%	0.09%	60.0
19	Spot turn, port	0.67%	0.13%	0.13%	0.13%	64.0
20	Spot turn, starbd	0.40%	0.13%	0.13%	0.13%	68.0
21	Autorotation	0.44%	0.44%	0.44%	0.00%	60.0
22	Recovery from 21	0.04%	0.04%	0.04%	0.00%	60.0
23	Descent	0.52%	0.26%	1.33%	0.56%	60.0
24	Landing	0.13%	0.27%	0.13%	0.13%	72.0
25	Ground**					-20.0

** Stress is given in* Helix units *(units normalized for a min/max of -20/100)*

*** Each mission is followed by a ground segment with a set mean stress of -20*

Table 7.2: Helix rainflow counted stress cycles (stresses (S) are given in *Helix units*).

ΔS	$2n_j$ **(190.5 hrs)**	$2n_j$ **(1e5 hrs)**	$\sum 2n_j$ **(1e5 hrs)**	S_{mean}	S_{min}	S_{max}	S_a	**R**
4.0	5.988e3	3.143e5	1.531e7	65.5	63.5	67.5	2.0	0.94
8.0	1.312e3	6.887e4	1.500e7	62.3	58.3	66.3	4.0	0.88
12.0	5.540e2	2.908e4	1.493e7	66.0	60.0	72.0	6.0	0.83
16.0	1.380e2	7.244e3	1.490e7	64.0	56.0	72.0	8.0	0.78
20.0	0.000e0	0.000e0	1.489e7	62.0	52.0	72.0	10.0	0.72
28.0	2.800e2	1.470e4	1.489e7	66.0	52.0	80.0	14.0	0.65
36.0	1.380e2	7.244e3	1.488e7	59.2	41.2	77.2	18.0	0.53
40.0	1.527e4	8.016e5	1.487e7	62.2	42.2	82.2	20.0	0.51
48.0	4.088e4	2.146e6	1.407e7	63.6	39.6	87.6	24.0	0.45
52.0	7.320e2	3.843e4	1.192e7	65.4	39.4	91.4	26.0	0.43
56.0	1.905e5	1.000e7	1.189e7	64.2	36.2	92.2	28.0	0.39
60.0	1.420e2	7.454e3	1.885e6	65.7	35.7	95.7	30.0	0.37
64.0	2.013e4	1.057e6	1.877e6	61.8	29.8	93.8	32.0	0.32
68.0	5.420e2	2.845e4	8.207e5	57.2	23.2	91.2	34.0	0.25
72.0	1.180e4	6.192e5	7.922e5	57.7	21.7	93.7	36.0	0.23
76.0	8.300e2	4.357e4	1.730e5	58.4	20.4	96.4	38.0	0.21
80.0	1.884e3	9.890e4	1.294e5	58.5	18.5	98.5	40.0	0.19
84.0	2.000e1	1.050e3	3.055e4	58.0	16.0	100.0	42.0	0.16
88.0	2.820e2	1.480e4	2.950e4	56.0	12.0	100.0	44.0	0.12
120.0	2.800e2	1.470e4	1.470e4	40.0	-20.0	100.0	60.0	-0.20

7.3.4 Damage Sensitivity to Load Magnitude

Once the baseline damage was established (1.0 at 10,000 hours), the following cases were examined to examine the sensitivity of damage due to load magnitude. Note that in all cases, the mean stress is unchanged; only S_a is modified. The cumulative rainflow counted cycles for each case are plotted in Figure 7.3.

1. S_a reduced by 25%
2. S_a reduced by 10%
3. S_a increased by 10%
4. S_a increased by 25%

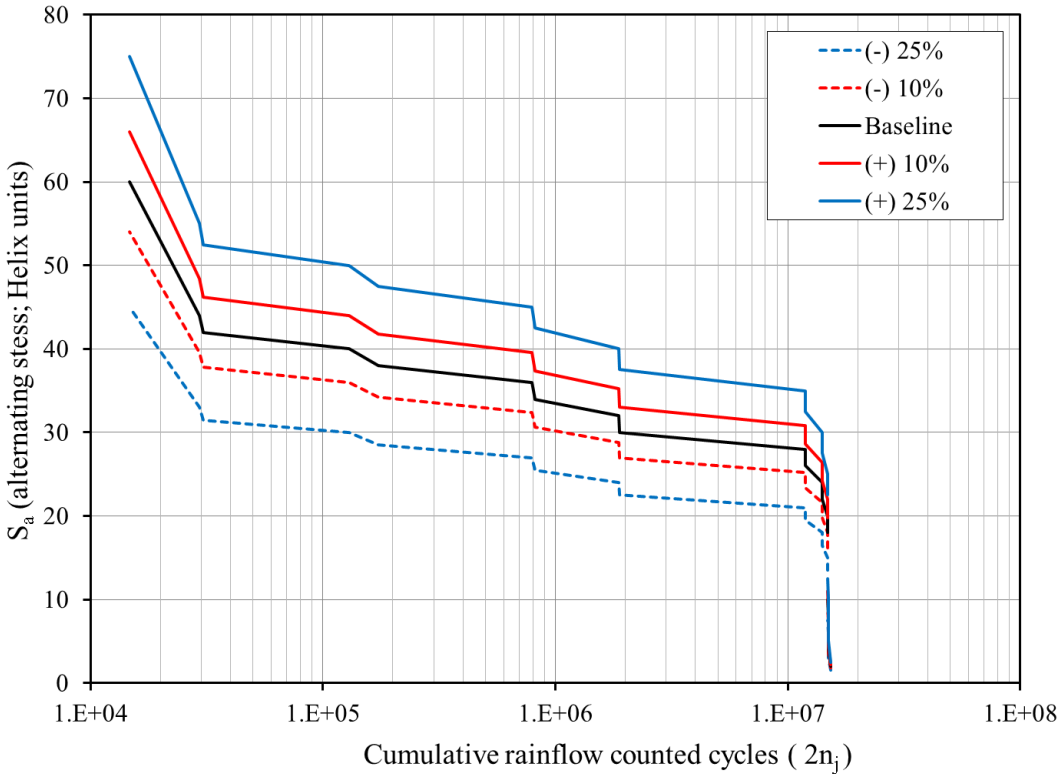

Figure 7.3: Cumulative rainflow counted cycles.

Table 7.3 and Figure 7.4 give the damage by load case. Results show that load magnitude has a tremendous influence on damage, with a 25% over-estimation of vibratory load resulting in a damage factor of nearly 3. These dramatic differences can be explained pictorially in Figure 7.3, where it is seen that a 25% increase in stress magnitude (vertical axis) equates to an approximate increase of 3-to-5 times the number of allowable cycles (horizontal axis).

Table 7.3: Fatigue damage results.

Case	**Damage**
Baseline	1.00
S_a reduced by 25%	0.51
S_a reduced by 10%	0.74
S_a increased by 10%	1.50
S_a increased by 25%	2.99

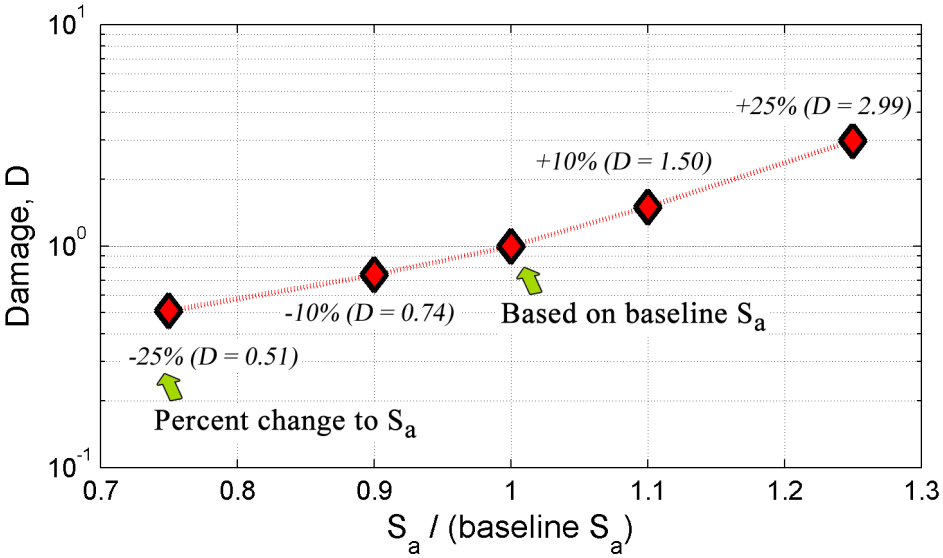

Figure 7.4: Fatigue damage results.

7.3.5 Damage Sensitivity to the Number of Applied Load Cycles

In addition to sensitivity to load magnitude, fatigue damage is also sensitive to the number of applied load cycles. From equation 7.1, damage is directly proportional to the number of applied load cycles. Therefore, for the same load magnitude, *twice* the number of applied load cycles would result in *twice* the damage - or *half* the component life; *half* the number of applied load cycles would result in *half* the damage - or *twice* the component life. This sensitivity to load cycles will now be examined.

Spectral centroid frequency (SCF) is the centroid of the FFT of a signal. It can be thought of as the *mean frequency* of a signal. It is commonly used in audio applications [49, 74], but is an effective metric to employ herein to quantify the differences in frequency content - and, thus, the number of applied load cycles - between numerical and experimental rotor loads predictions. The SCF for a discrete signal is defined as follows:

$$SCF = \frac{\sum_{k=1}^{K} (f_k \, m_k)}{\sum_{k=1}^{K} (m_k)} \tag{7.5}$$

where f_k is the k^{th} discrete frequency in the signal and m_k is the magnitude of the signal at that frequency. Specific application of the SCF to rotor loads (based on the first six harmonics of rotor angular speed, Ω) is defined in equation 7.6.

$$SCF = \Omega \left[\frac{1\,|1P| + 2\,|2P| + 3\,|3P| + 4\,|4P| + 5\,|5P| + 6\,|6P|}{|1P| + |2P| + |3P| + |4P| + |5P| + |6P|} \right] \tag{7.6}$$

Equation 7.6 is now applied to UH-60A pushrod loads. Figure 7.5 shows the SCF calculation for pushrod load for the 601 flight counters analyzed in Section 4.7. This calculation is performed for both the experimentally-measured and LLT-predicted pushrod loads. Results show that the SCF for the experimentally-measured data is

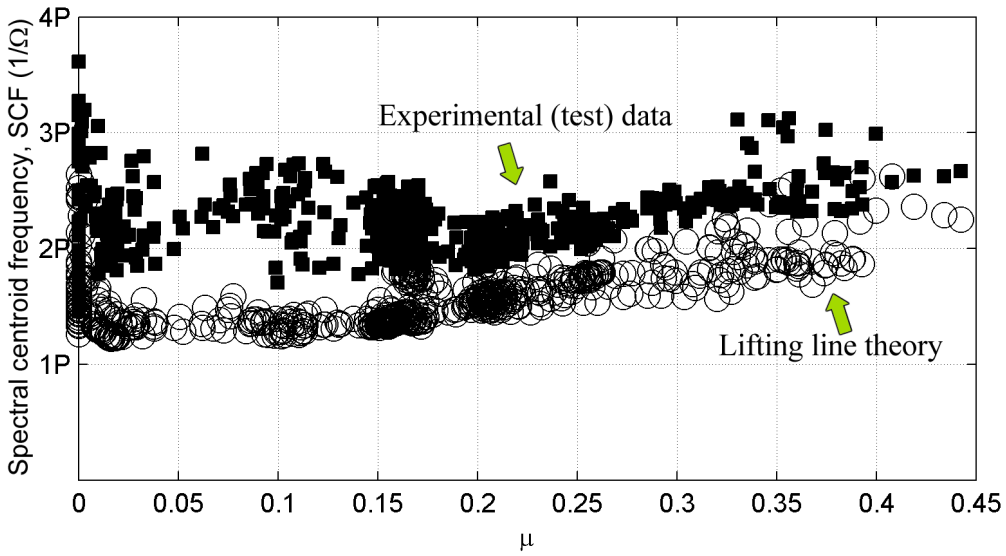

Figure 7.5: Spectral centroid frequency (SCF): UH-60A pushrod load.

generally higher than the LLT-predicted values. The mean ratio of experimental-to-LLT predicted SCF is 1.45, with a standard deviation of 0.25. Therefore, on average, experimentally-measured pushrod loads contain 1.45 applied cycles for each cycle predicted in LLT-based numerical simulation. From equation 7.1, damage is directly proportional to the number of applied load cycles. Let this 10,000 hour UH-60A pitch control horn fatigue analysis be based on experimentally-measured pushrod loads. Therefore, a baseline damage of 1.0 is reached at 10,000 hours. LLT-based analysis predicts a damage of 0.69 (1/1.45), resulting in a component life of 14,500 hours. Accounting for a $\mu \pm 1\,\sigma$ variation in the experimental-to-LLT predicted SCF would result in an LLT-based component life range from 12,000 to 16,900 hours. This could result in a very unconservative solution, meaning an under-designed component, one resulting in the requirement for application of large factors of safety to the design to compensate for this deficiency in loads prediction.

7.4 Conclusions

These results highlight the importance of accurate loads prediction for a rotorcraft life tracking program. Small inaccuracies in load magnitude lead to dramatic errors in damage assessment, resulting in a roughly order-of-magnitude ratio between load error and damage. Fundamental errors in the predicted frequency content of a load can also lead to errors in damage assessment, resulting in a one-to-one ratio between cycle error and damage. Given these ratios, load magnitude is the larger effect between the two, but the two effects are closely coupled in analysis.

CHAPTER VIII

CONCLUSIONS AND FUTURE WORK

This research focused on the development of a loads prediction method, known as the Load Confluence Algorithm (LCA), and its application to the analysis of a large flight test dataset. The LCA combines measured response at a prescribed set of locations with a numerical model of the rotor system. For a given flight condition (steady flight, maneuvers, etc.), the numerically-predicted loads distribution is iteratively incremented (by harmonic) until convergence with measured loads is reached at the prescribed locations (control points). Predicted loads response at non-instrumented locations was shown to be improved as well, thus enhancing fatigue lifing methods for these components. This effort also expanded on the physical understanding of rotor loads harmonic content, as well as the relationships between rotating and fixed-system responses. Lastly, better loads prediction supports and enables more realistic structural component life assessments. The quantification of the improvement in life assessment accuracy as a function of load calculation error offers opportunities to further expand the rotorcraft industry's ability to design, operate, and manage aircraft.

8.1 Summary of Findings

The UH-60A Airloads Program flight test dataset was comprehensively analyzed, with over 600 flight counters examined. The quality of the measured airloads was assessed for each flight counter. These are useful for future research efforts requiring UH-60A measured airloads. A systematic method with which this dataset is to be used for rotor loads analysis was defined. The DYMORE structural and aerodynamic model development processes were outlined. The *LCA score* was defined, offering an

objective metric for comparison of different loads results in order to determine the best match. The LCA was applied to the UH-60A flight test dataset, specifically the following cases:

1. Eight arbitrarily-selected flight counters from flight 84, covering hover to high-speed flight. LLT airloads were used. The effects due to two different control point sets were examined.

2. 51 flight counters (flights 84 and 85) for the *mechanical airloads* problem, where measured airloads from the UH-60A Airloads Program are fed into the DY-MORE LCA simulation.

3. Nine flight counters from legacy MDC-based analyses were discussed; five of these (c8534, c8927, c9017, c11679, and c11680) were examined in detail using the LCA.

4. The first cycle of all flight counters for flights 84 through 116 (601 total flight counters) were examined in order to show the robustness of the LCA across all flight regimes.

The robustness of the LCA and the influence user settings has on the quality of the loads match were also examined. A metric was defined - a single aggregate objective function (AOF) - to determine the best fit loads match between experimental data and numerical simulation.

Two particular issues with the LCA were examined: instability in $5P$ response due to blade bending mode excitation and $1P$ response offset due to rigid blade flapping. For the UH-60A, the $5P$ response instability occurs in cases where $5P$ magnitude is largest relative to $1P$, $2P$, etc. Dominant $5P$ response - and, more so, dominant *off-harmonic* response between $4P$ and $5P$ - causes excitation of nearby blade modes. Specifically, dominant $5P$ response was shown to excite the $5.21P$ blade bending

mode with some potential contributions from the neighboring 4.64P and 4.53P blade bending modes as well. These low damped modes produced a large system response, driven more unstable by forcing function modifications at the $5P$ frequency via the LCA. This phenomenon was shown to occur primarily at low speed, but can occur at higher airspeeds as well, such as maneuvers providing strong $5P$ excitation due to multiple blade stalls or BVI excitation. The impact in hover is more dramatic, given that $5P$ load content is much larger relative to lower harmonic load content. For higher-speed flight, the effect is reduced.

The $1P$ response offset issue is due to the fact that only flexible modes (modes 3 and higher) were used in the LCA formulation for the UH-60A. This is an important point. $1P$ is driven by rigid flapping (mode 2, $\approx 1.04P$). The LCA is deficient at being able to support rigid modes in its numerical formulation for a complex problem such as a full-scale rotor. This is purely a numerical problem and not an issue with the underlying LCA formulation. Both issues were addressed and found to be serviceable in the context of UH-60A rotor loads analysis. However, these each present opportunities for improvements in future research efforts.

This research effort also examined rotor load content by harmonic. For a 4-bladed rotor system, blade lift due to simplified aerodynamics was derived and compared with measured UH-60A results. Inboard response of the blade followed the experimental trends. Outboard blade response did not, due to unsteady airloads effects.

The mechanics of load transference between the rotating and fixed frames were also examined. For the UH-60A, it was shown how the sum of all pushrod loads is composed of jn_bP force components' (j=0,1,2,...) content (e.g., $0P + 4P + 8P +$ ...). Closed form expressions for the three UH-60A servo loads were derived as well. It was shown how, if the objective was to model pushrod response based on measured servo loads, it would be impossible to predict any pushrod loads' $2P$ content (for a 4-bladed rotor) based on these measured servo loads.

A generic 7-bladed rotor was also examined. For both the 4- and 7-bladed rotors, cyclic/whirl, reactionless/warp, and collective modes were defined and illustrated. Response for an n_b-bladed rotor were defined as well.

Finally, the research was extended by quantifying the effects of improved loads prediction accuracy on rotorcraft component fatigue life. These results highlighted the importance of accurate loads prediction for a rotorcraft life tracking program. Small inaccuracies in load magnitude lead to dramatic errors in damage assessment, resulting in a roughly order-of-magnitude ratio between load error and damage. Fundamental errors in the predicted frequency content of a load can also lead to errors in damage assessment, resulting in a one-to-one ratio between cycle error and damage. Given these ratios, load magnitude is the larger effect between the two, but the two effects are closely coupled in analysis.

The strengths of the LCA can be summarized as follows:

1. A suitable match of peak-to-peak and by-harmonic loads has been achieved for blade flapwise bending, edgewise bending, torsional moment, and pushrod for a full range of flight conditions, including hover, BVI, high-speed flight, and maneuvers. This would be supportive of a rotor component tracking program

2. Application of the LCA bypasses the problems associated with uncertainty in the aircraft operating environment. Whereas overall flight parameters, such as airspeed, altitude, and gross weight, are recorded, many other parameters are not. Among them are gust speed and direction, turbulence levels, instantaneous weight and center-of-gravity location, pilot inputs, etc. The LCA automatically corrects for these factors, because it is based on actual measurements in the rotating system.

3. The LCA seems to work best with more distinct modes; the presence of multiple modes of similar content makes the LCA over-correct. The underlying physics

behind this is not understood at this time.

4. Edgewise bending loads can be predicted, but the quality of the match seems most sensitive to the number of control points.

The deficiencies of the LCA can be summarized as follows:

1. No direct lag damper sensors were applied as control points in this analysis. The hypothesis was that matching edgewise bending near the blade root would improve lag damper loads. It was shown that improvement in SE30 loads match does not influence lag damper response.

2. The LCA is not an accurate predictor of high frequency (greater than $6P$) aerodynamic effects that may be dominant near the blade tip. This solution may be best left for CFD - or a CFD-based LCA analysis.

3. The LCA will attempt to match load response at control points, even if the measurement for a given control point is in error. In other words, *a priori* knowledge of the quality of a given measurement may be required to ensure the integrity of the LCA solution.

4. The LCA cannot necessarily match response at a given control point for a given harmonic if the measured response at that control point is appreciable enough to excite a lightly damped neighboring structural mode to the point of divergent motion or dynamic instability.

   (a) Several points should be mentioned that reduce the impact of this deficiency. First, the LCA attempts to recover from this deficiency by stopping the solution at the timepoint producing the minimum AOF.

   (b) Second, this appears to be more of an issue during hover, where (1) there is more *off-harmonic* content in the data, and (2) load magnitudes are much

smaller than for forward flight. This issue can occur at higher μ, but here the $5P$ response - though present - is dominated more by other harmonics. It also becomes less of an issue due to the relative purity of the response at $1P$, $2P$, ..., $6P$ (i.e., minimal *off-harmonic* content) at higher μ.

(c) In cases where the LCA-corrected response is over-predicted throughout (for a given harmonic: e.g., $5P$ for edgewise bending for c11679), the LCA should be configured (in a future effort) to deactivate that given correction.

5. For a problem as complex as a rotor system using real-world rotor loads measurements in the LCA formulation, these variations in $\underline{\epsilon}$ are present and it results in numerical ill-conditioning in the $\mathbf{B}^+$ matrix. Effectively, there is such a large differential in size between rigid and flexible modes in the $\mathbf{B}$ matrix, matrix inversion leads to an inability to converge. This could potentially be improved upon by detailed numerical analysis of the $\mathbf{B}$ matrix, and optimization of its entries (ie., number, type, and locations of transducers). However, as shown, the LCA is only minimally affected by this, in terms of peak-to-peak (and *by harmonic*) loads comparisons between analysis and test across all flight regimes.

6. In certain cases, application of the LCA worsens the loads match relative to LLT-generated loads. The reasons for this are not well understood at this time, but it is likely related to the fact that the LCA comprehensively corrects for flapwise bending moment, torsional moment, etc. Improvements to the external forcing function vector based on flapwise bending moment may in fact adversely impact torsional moment, and vice versa.

8.2 Summary of Contributions

The following is a list of innovative contributions generated from this research.

1. Development of the Load Confluence Algorithm (LCA)

2. Systematic application of the LCA to UH-60A flight test data

3. Assessment, derivation, and understanding of rotor loads harmonic content as well as load transference between the rotating and fixed frames

4. Enhanced application and advancement of the use of real-world measurement for numerical simulation loads correction and matching

5. Advancing the knowledge base for rotor component fatigue lifing

8.3 Future Work

Opportunities for further work in this area include the following. Effects due to rigid flap and lag modes could be incorporated. Also, effects due to multiple instrumented blades (e.g., both blade 1 and blade 2), pushrods, or lag dampers could be addressed. This would better capture rotating-to-fixed frame effects when there are differences in response between blades. Accurate lag damper loads matching could be pursued by either adding a lag damper sensor control point or, given the strong correlation between SE30 and lag damper load, developing an externally-applied lag damper load correction factor based on SE30. The swashplate could be modeled to better capture its effects on servo loads. The model could be even further extended by modeling the coupled rotor-hub-fuselage system. Also, high frequency (greater than $6P$) aerodynamic effects that may be dominant near the blade tip could be addressed based on a coupled CFD/CSD/LCA solution. The structural model itself could be improved to include periodic coefficients (i.e., structural properties with time or azimuthal variation). Lastly, the starting formulation (equation 2.1) could be expanded beyond a linear second order system to include damping and/or basic nonlinearities. This may improve the LCA's ability to correct loads differences driven by damping forces or nonlinear system behavior.

APPENDIX A

UH-60A MEASURED LOADS' HARMONIC CONTENT (FLIGHTS 88, 89, 90, 110, 115, 116)

This appendix supplements the UH-60A measured loads' harmonic content discussed in Section 3.3.4 by adding results for flights 88, 89, 90, 110, 115, and 116.

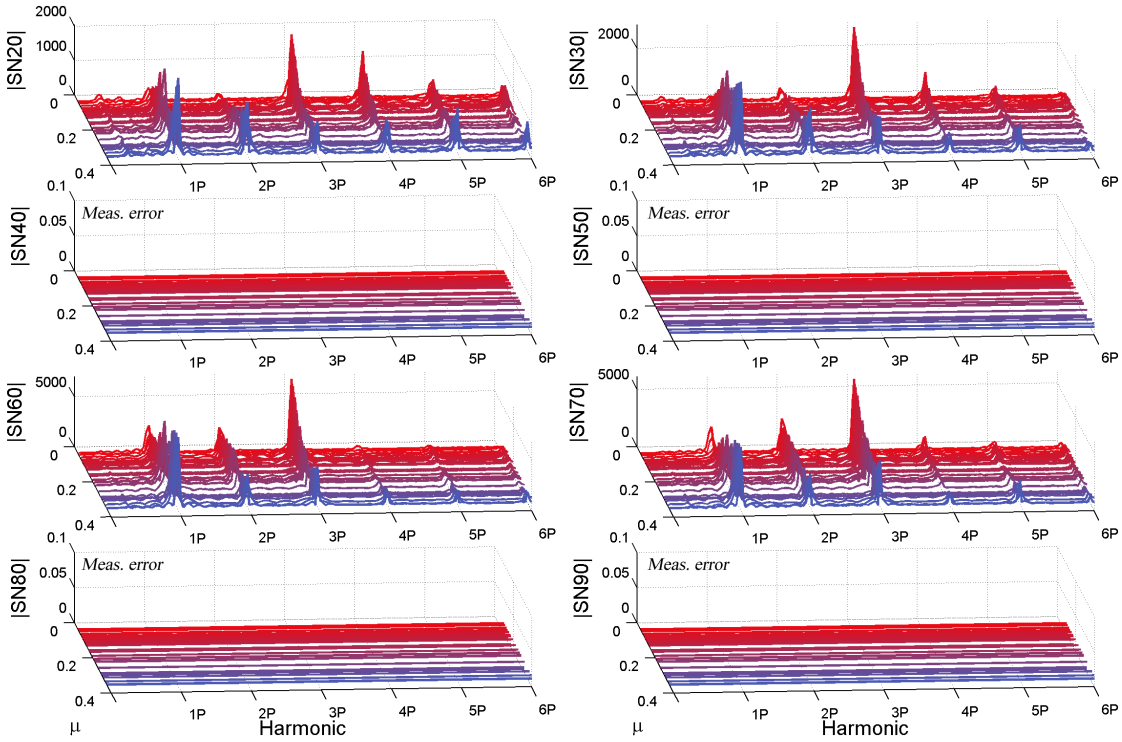

Figure A.1: Blade flapwise bending moment v. advance ratio (flight 88).

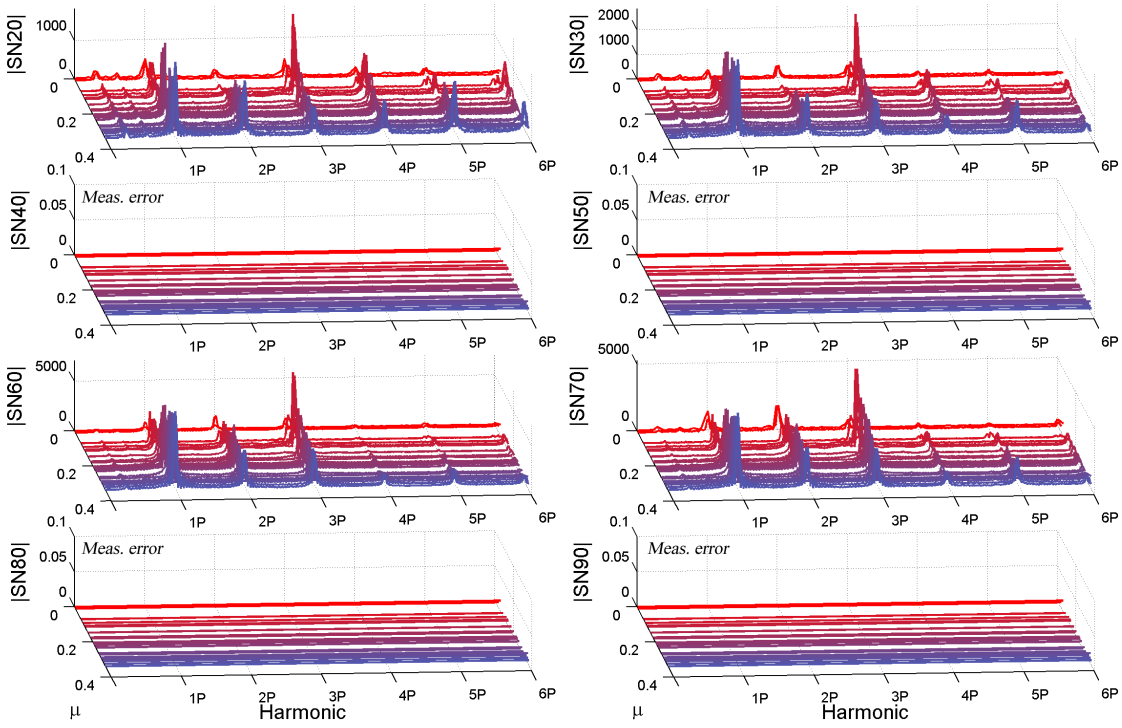

Figure A.2: Blade flapwise bending moment v. advance ratio (flight 89).

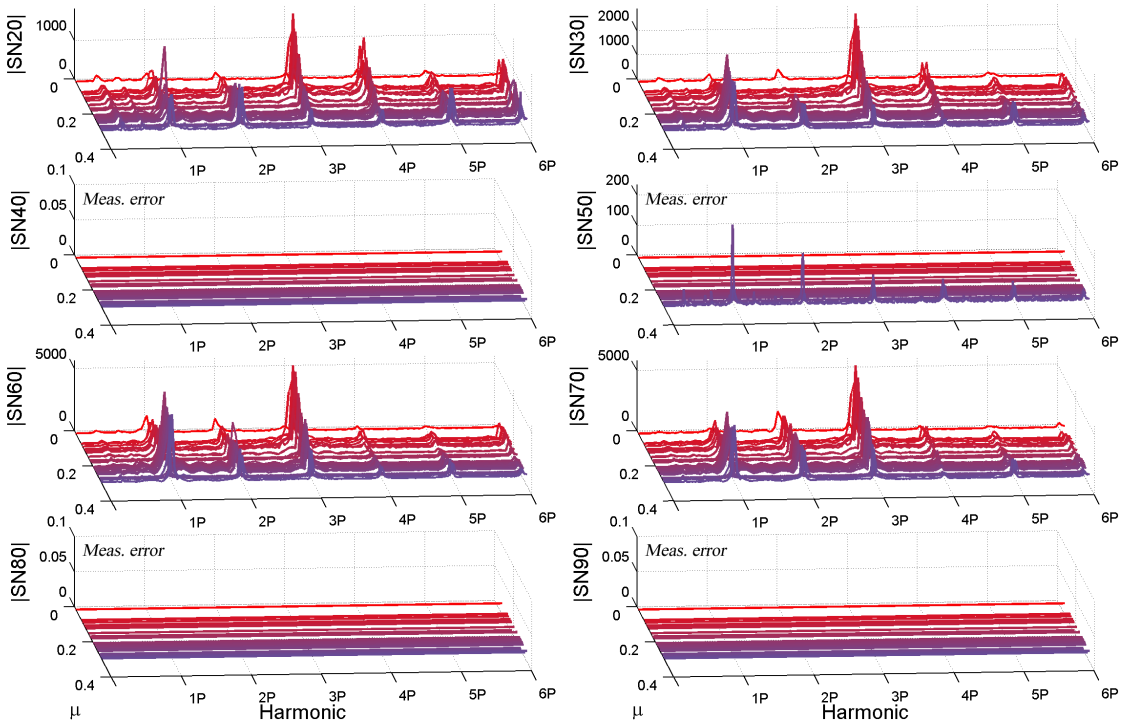

Figure A.3: Blade flapwise bending moment v. advance ratio (flight 90).

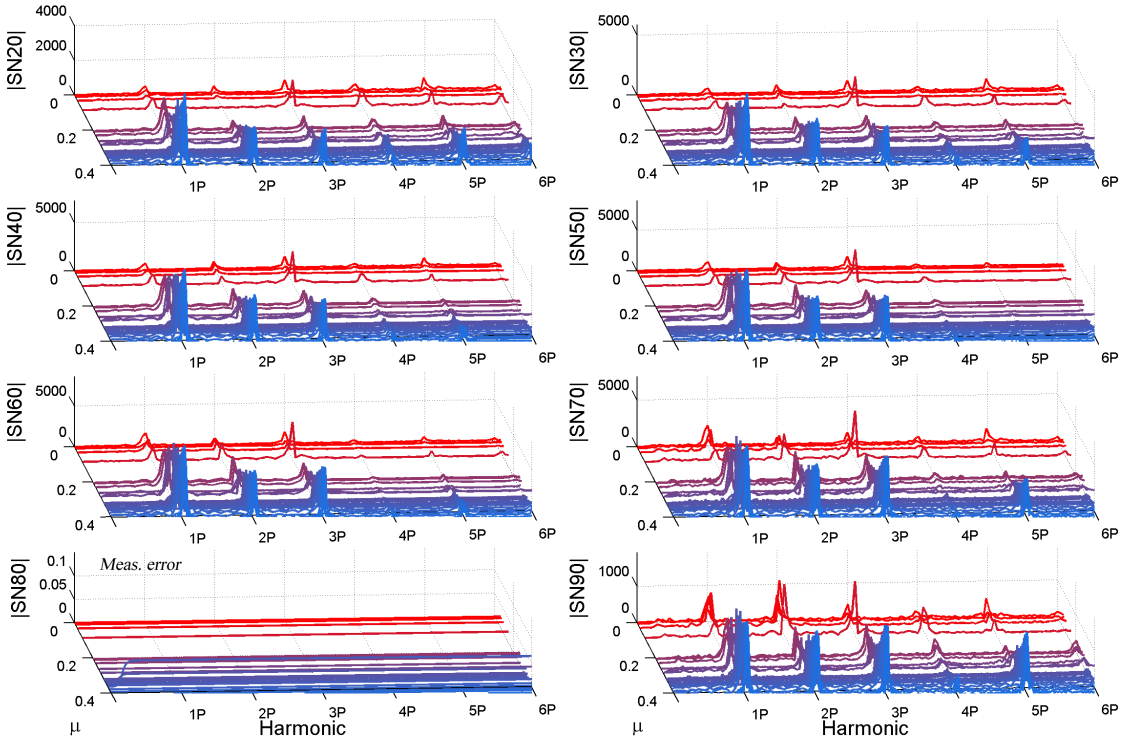

Figure A.4: Blade flapwise bending moment v. advance ratio (flight 110).

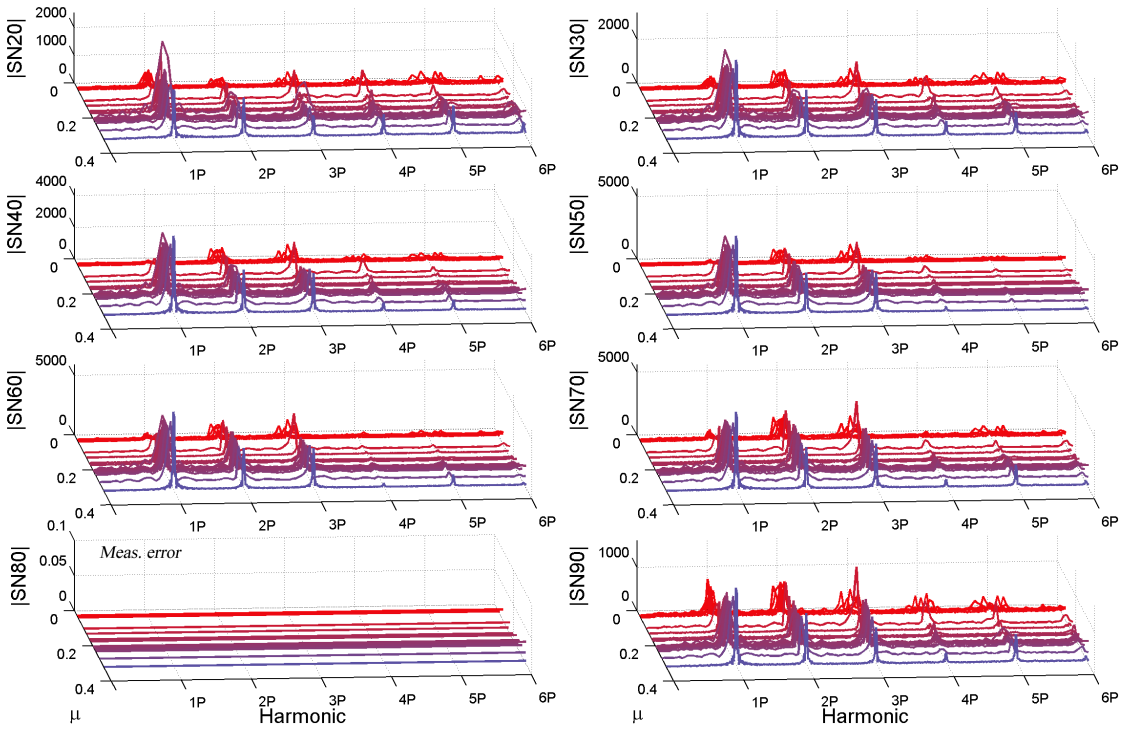

Figure A.5: Blade flapwise bending moment v. advance ratio (flight 115).

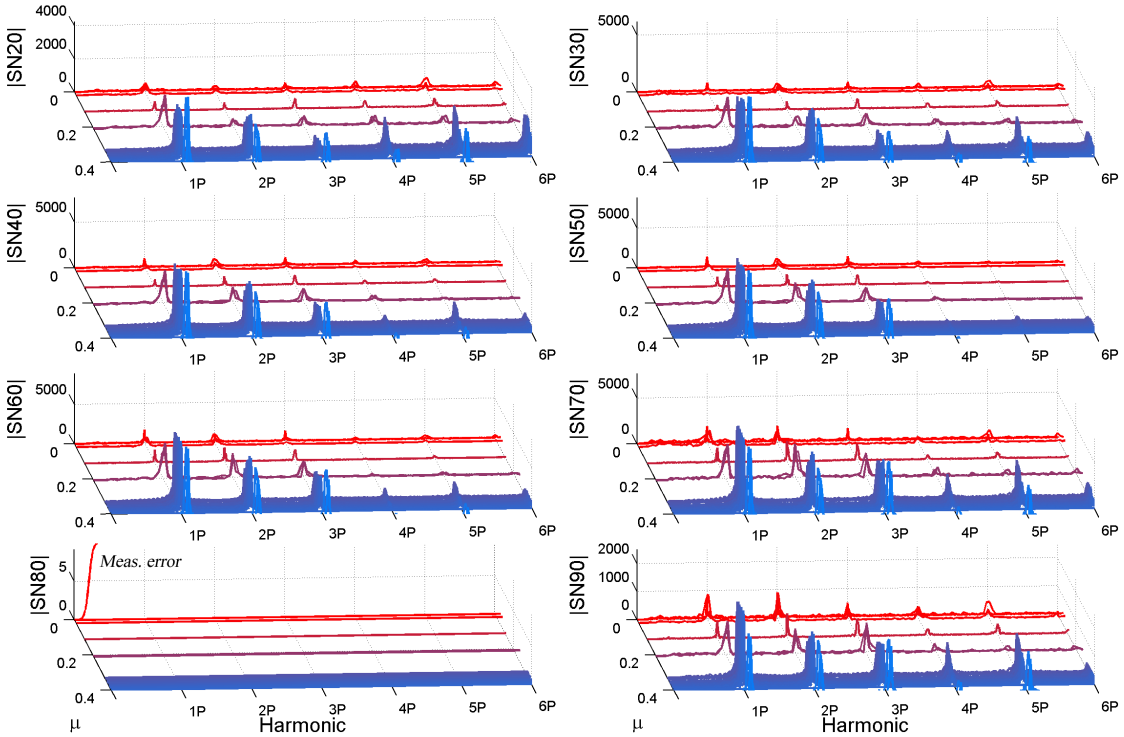

Figure A.6: Blade flapwise bending moment v. advance ratio (flight 116).

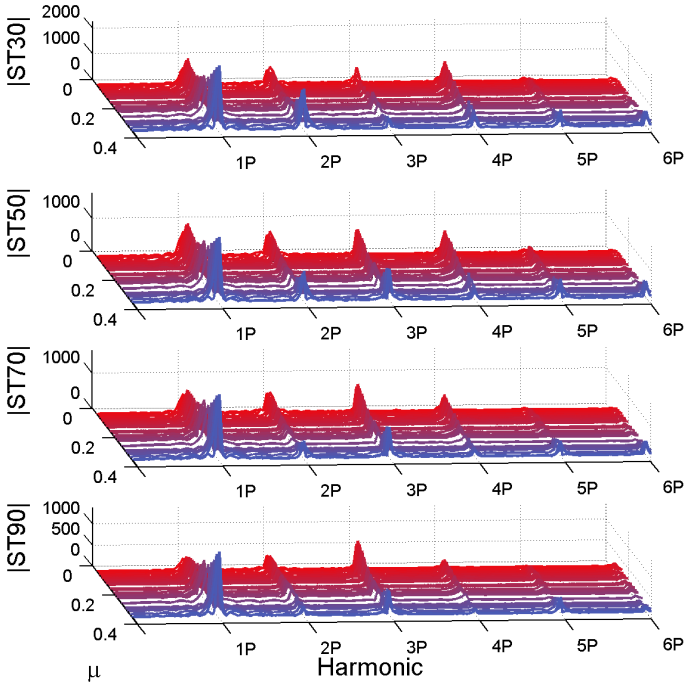

Figure A.7: Blade torsional moment v. advance ratio (flight 88).

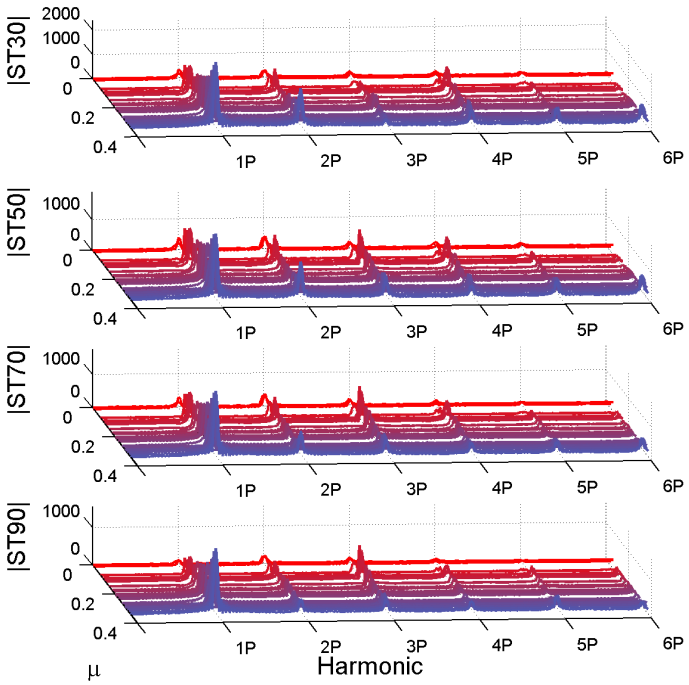

Figure A.8: Blade torsional moment v. advance ratio (flight 89).

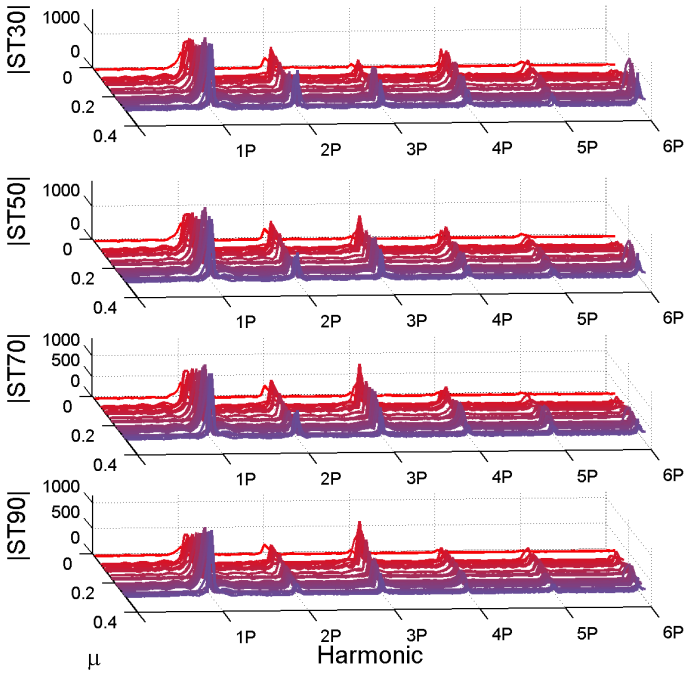

Figure A.9: Blade torsional moment v. advance ratio (flight 90).

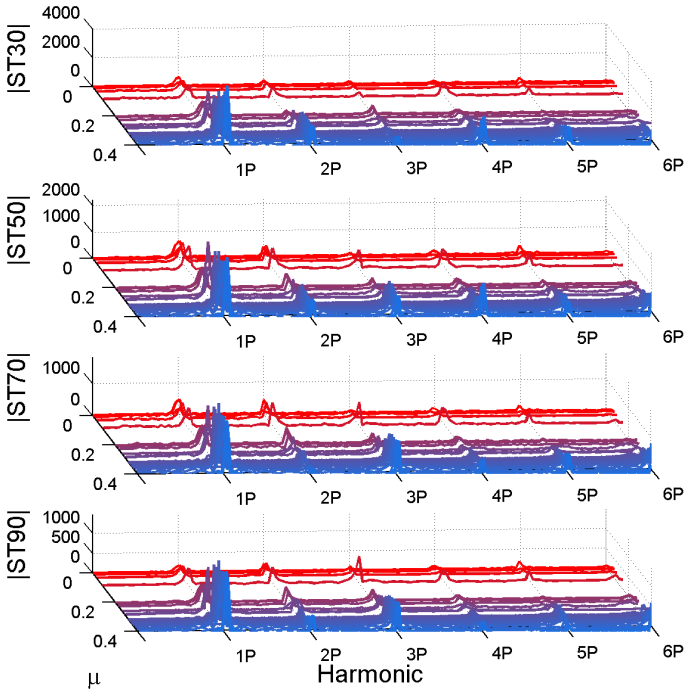

Figure A.10: Blade torsional moment v. advance ratio (flight 110).

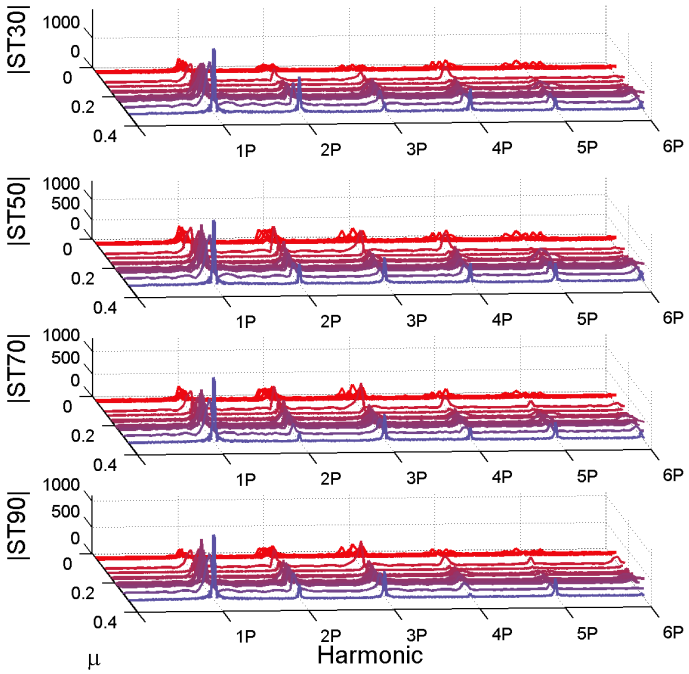

Figure A.11: Blade torsional moment v. advance ratio (flight 115).

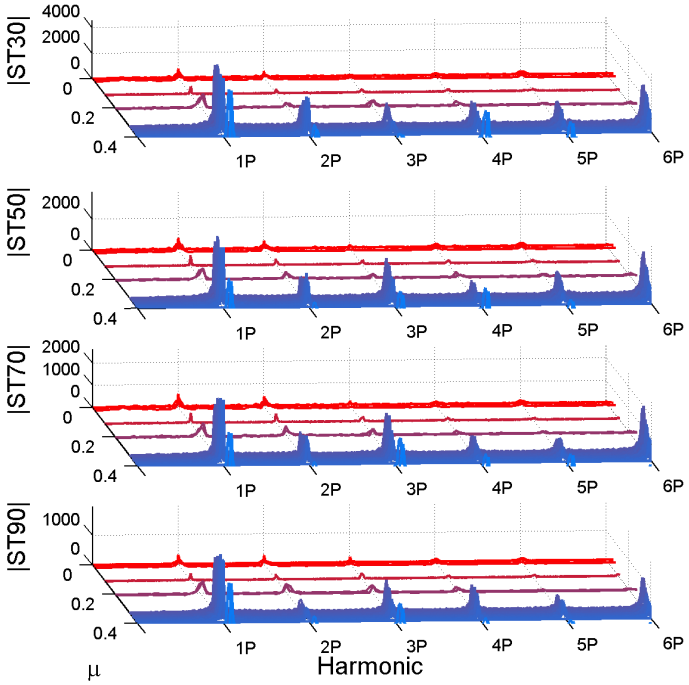

Figure A.12: Blade torsional moment v. advance ratio (flight 116).

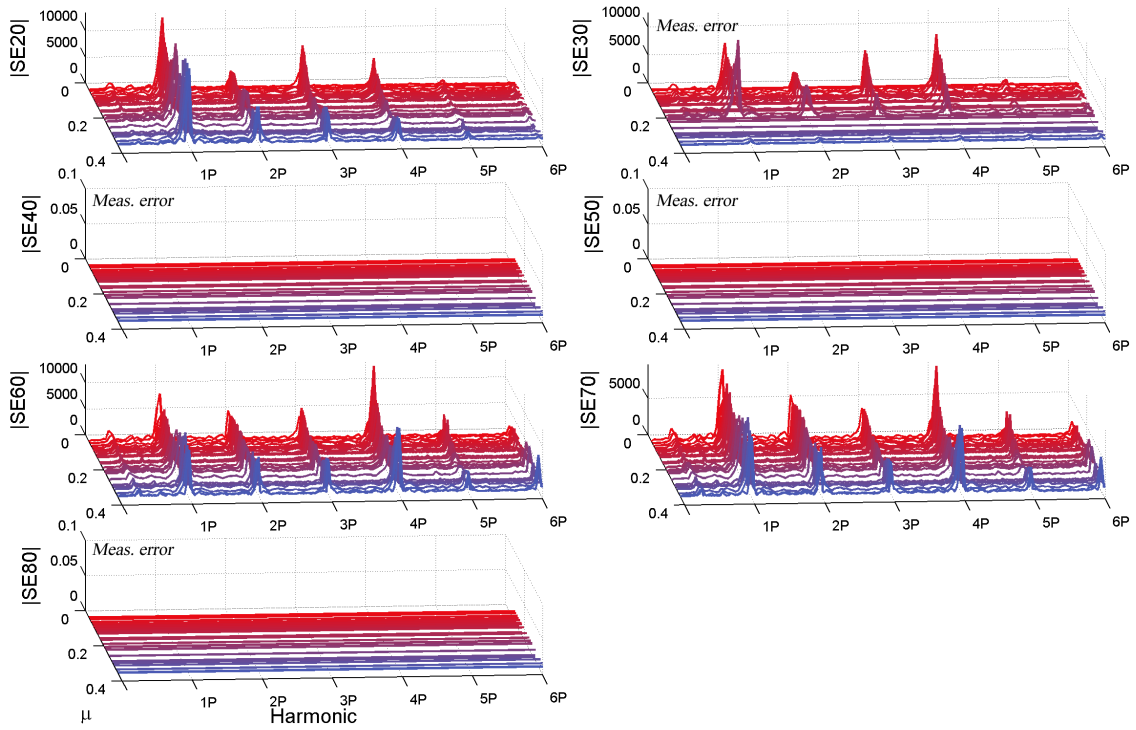

Figure A.13: Blade edgewise bending moment, v. advance ratio (flight 88).

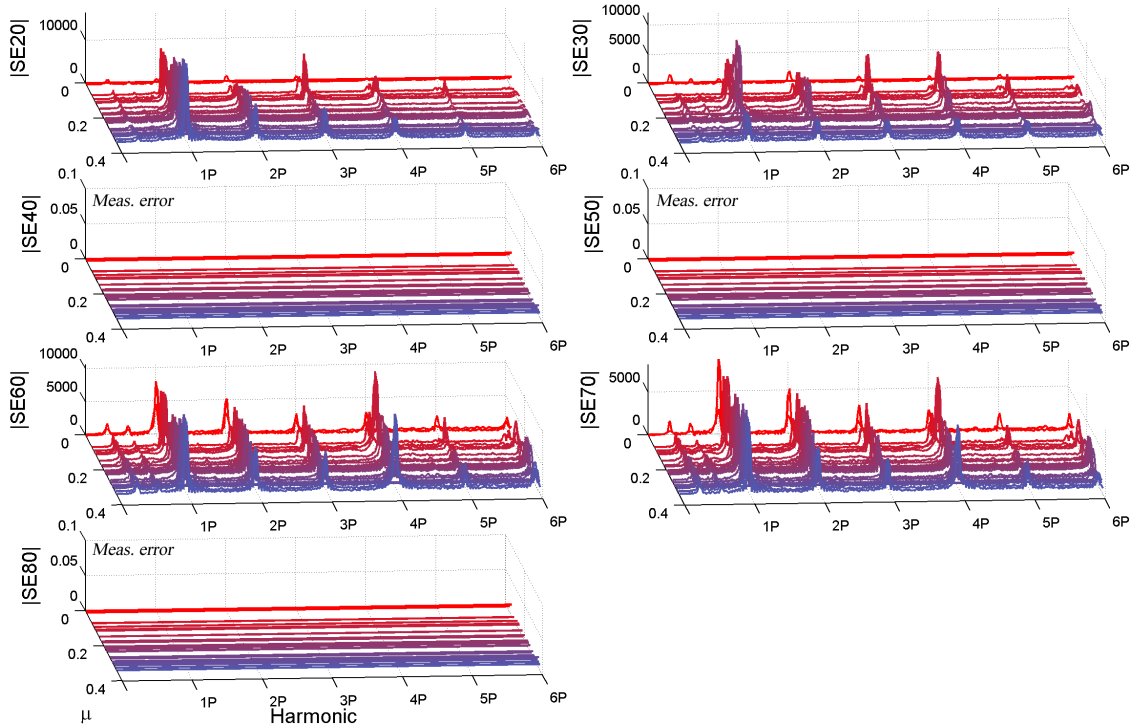

Figure A.14: Blade edgewise bending moment v. advance ratio (flight 89).

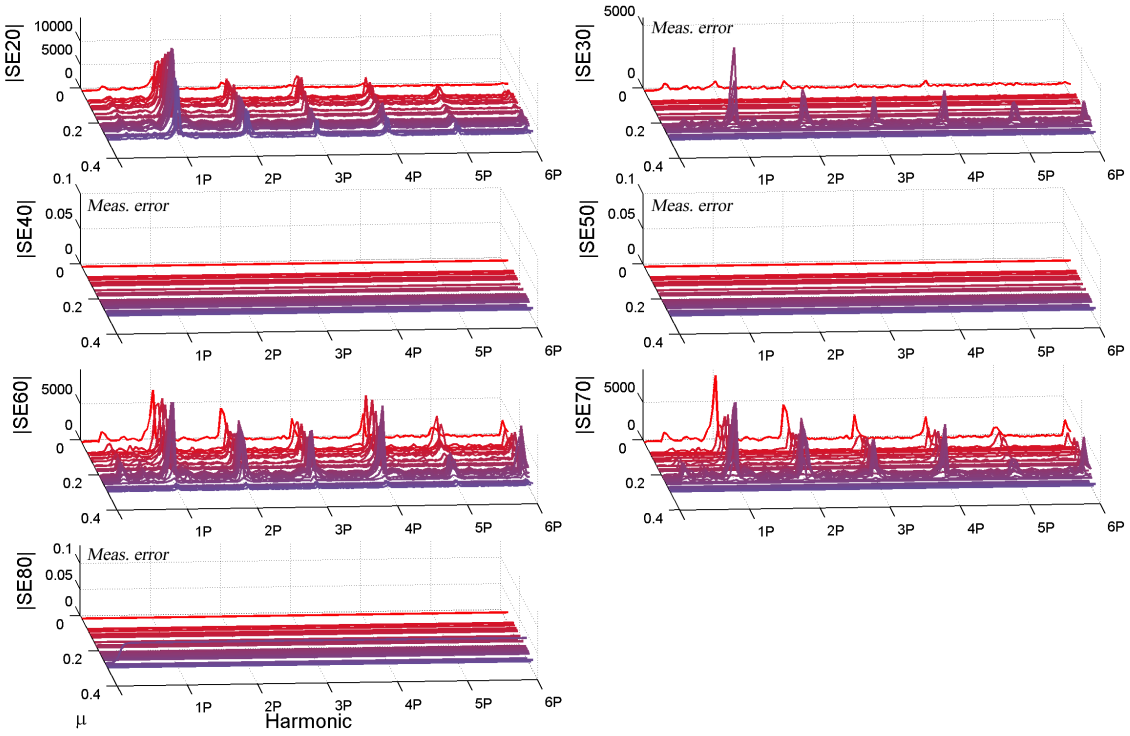

Figure A.15: Blade edgewise bending moment v. advance ratio (flight 90).

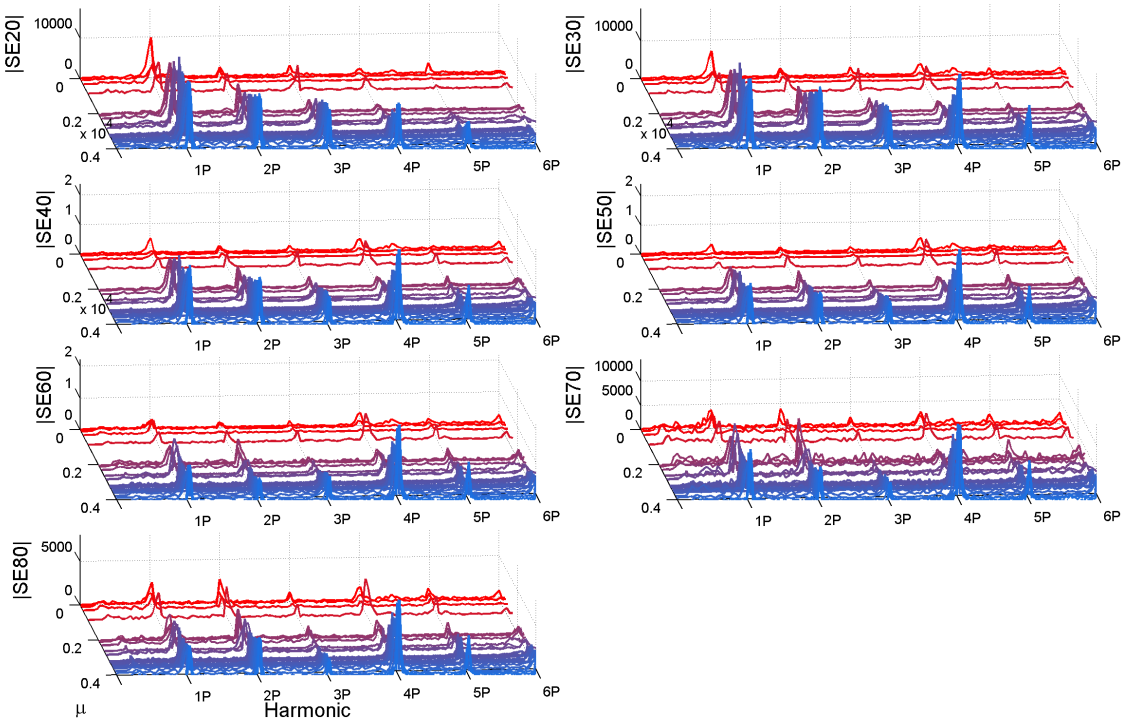

Figure A.16: Blade edgewise bending moment v. advance ratio (flight 110).

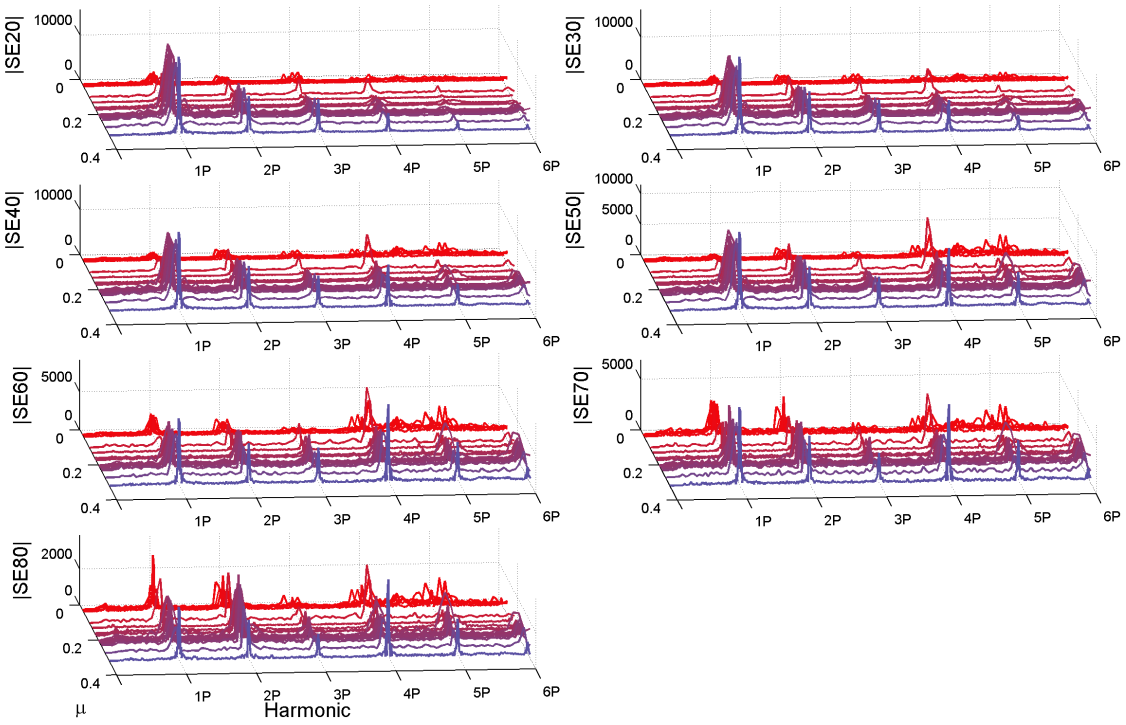

Figure A.17: Blade edgewise bending moment v. advance ratio (flight 115).

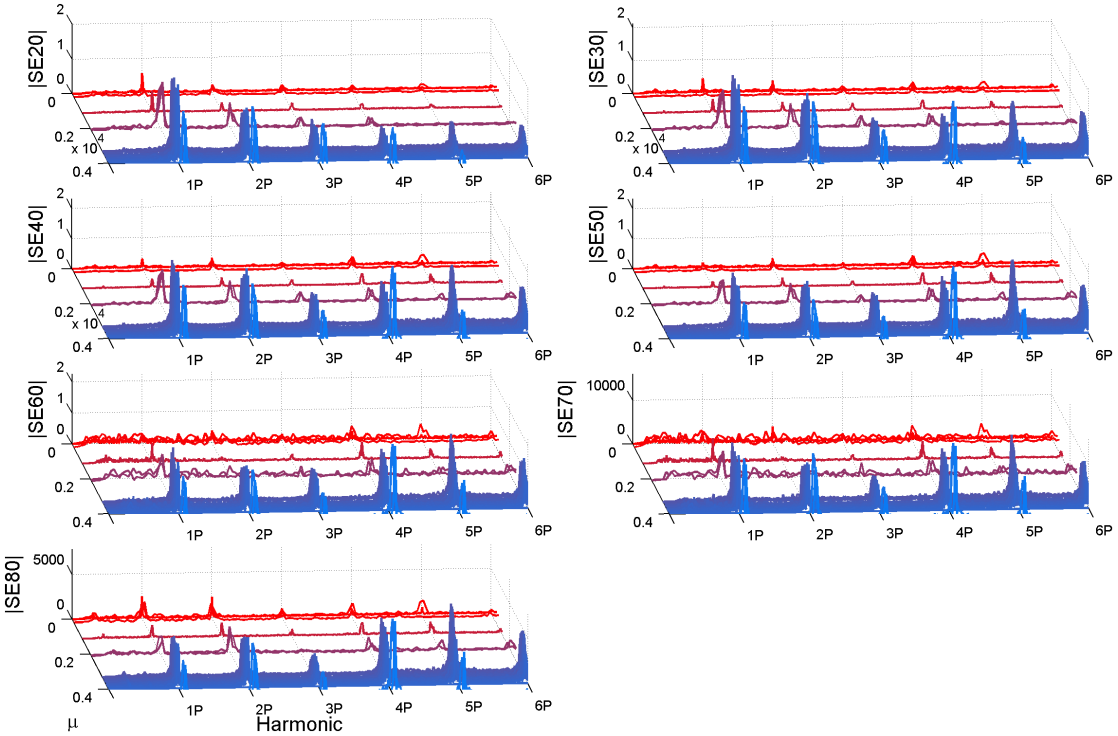

Figure A.18: Blade edgewise bending moment v. advance ratio (flight 116).

APPENDIX B

LOADS COMPARISON CHARTS: EFFECTS OF SCALARS BY HARMONIC

This appendix supplements Section 5.6 by adding the peak-to-peak loads results (flights 84 and 85, totaling 51 flight counters) for the different harmonic scalars (κ) listed in Table 5.6.

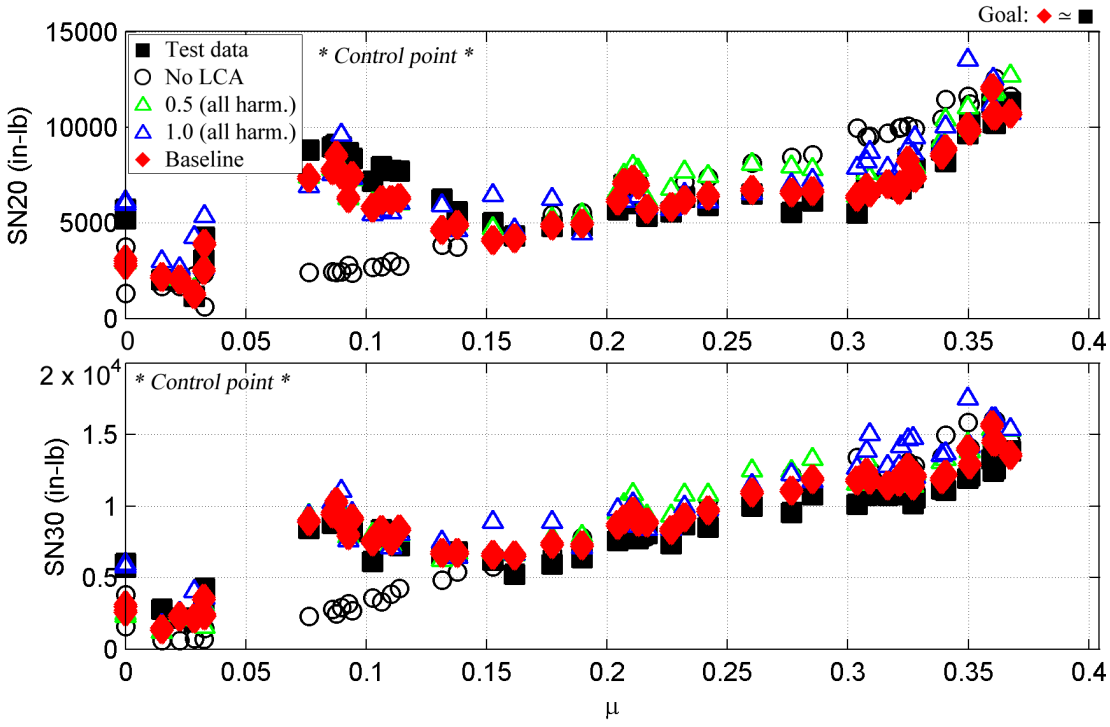

Figure B.1: Peak-to-peak loads matching: effects of κ; all sensors: SN20, SN30.

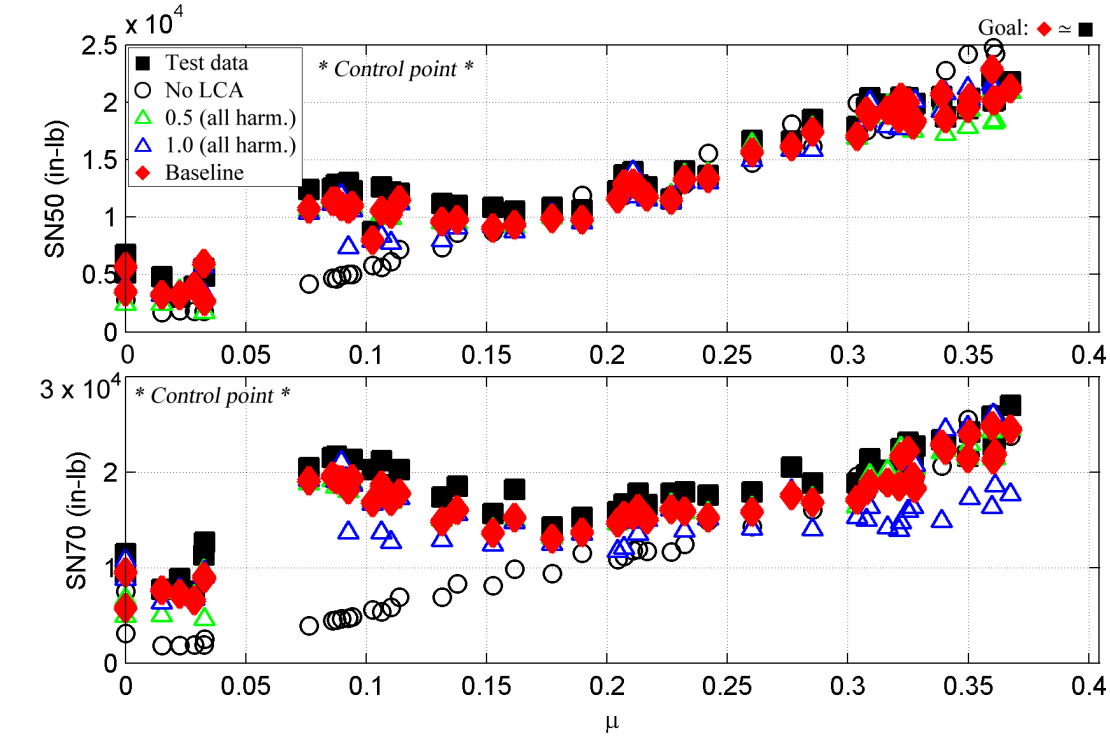

Figure B.2: Peak-to-peak loads matching: effects of κ; all sensors: SN50, SN70.

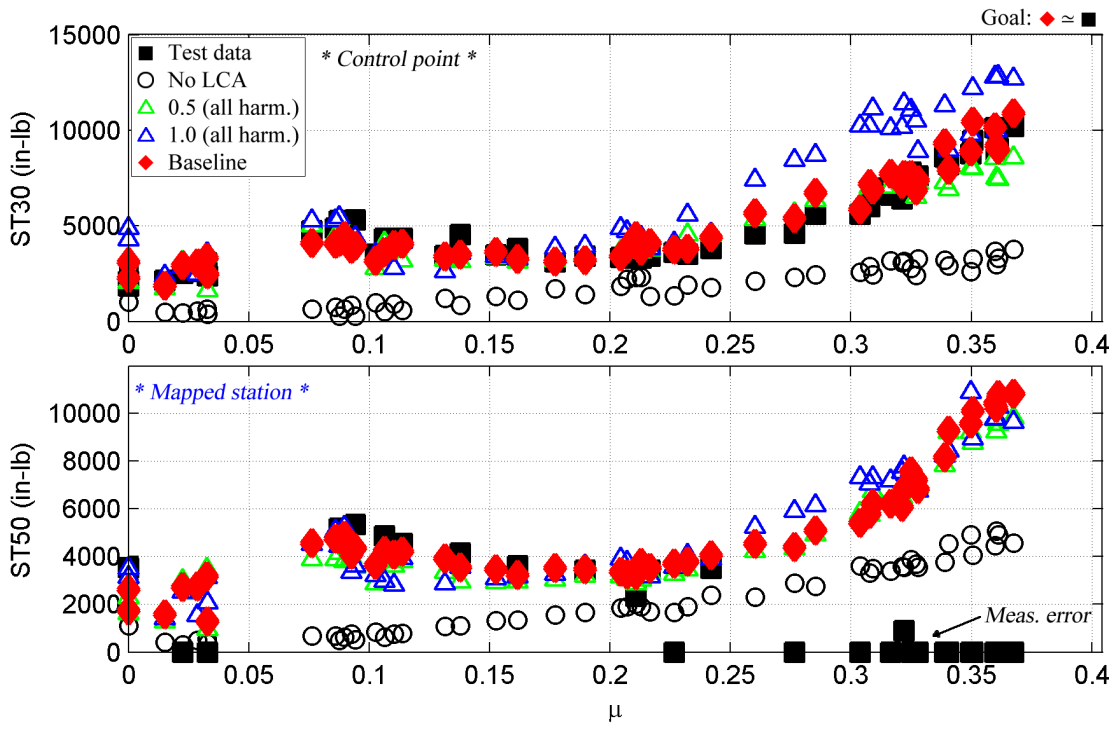

Figure B.3: Peak-to-peak loads matching: effects of κ; all sensors: ST30, ST50.

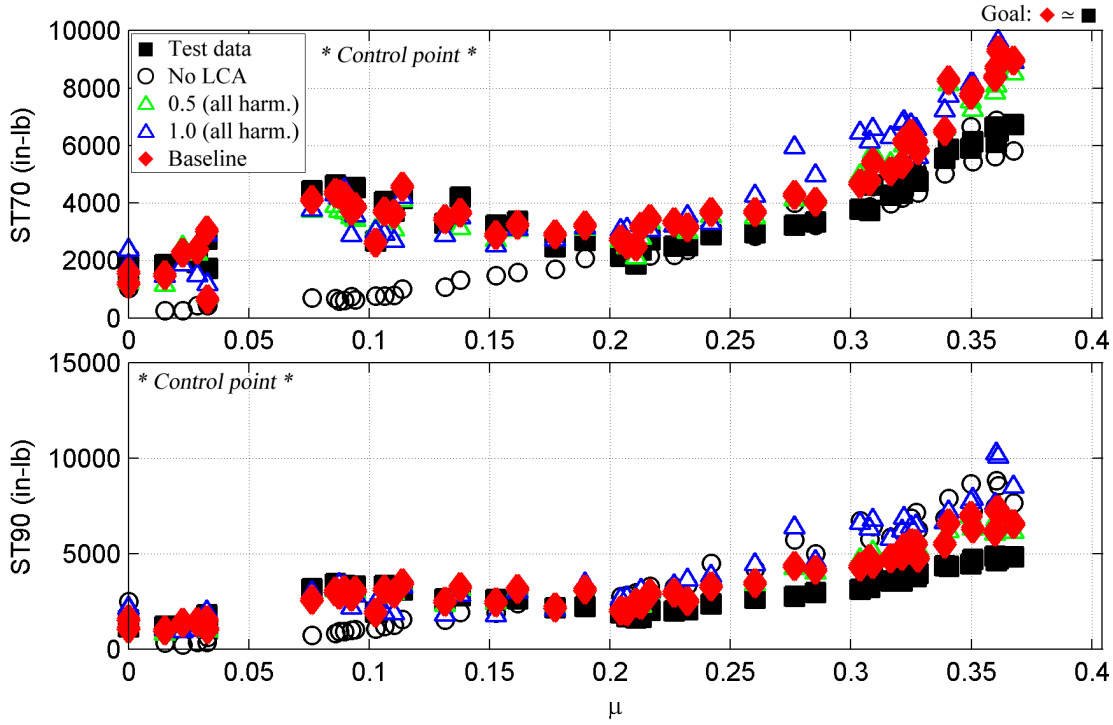

Figure B.4: Peak-to-peak loads matching: effects of κ; all sensors: ST70, ST90.

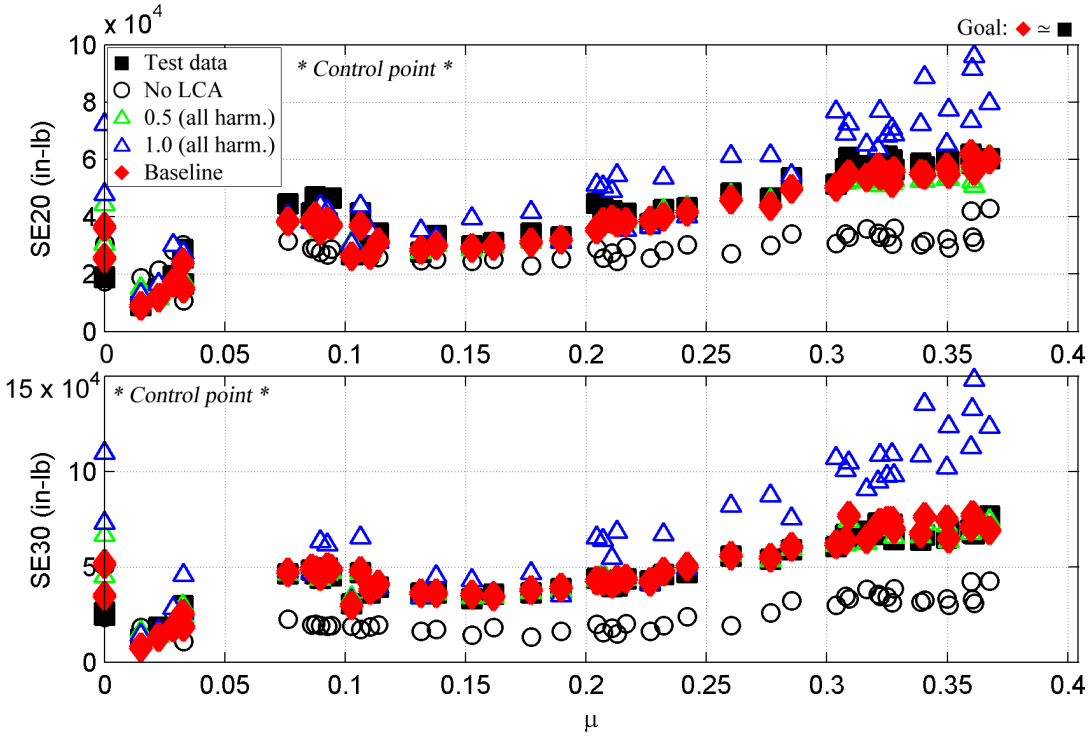

Figure B.5: Peak-to-peak loads matching: effects of κ; all sensors: SE20, SE30.

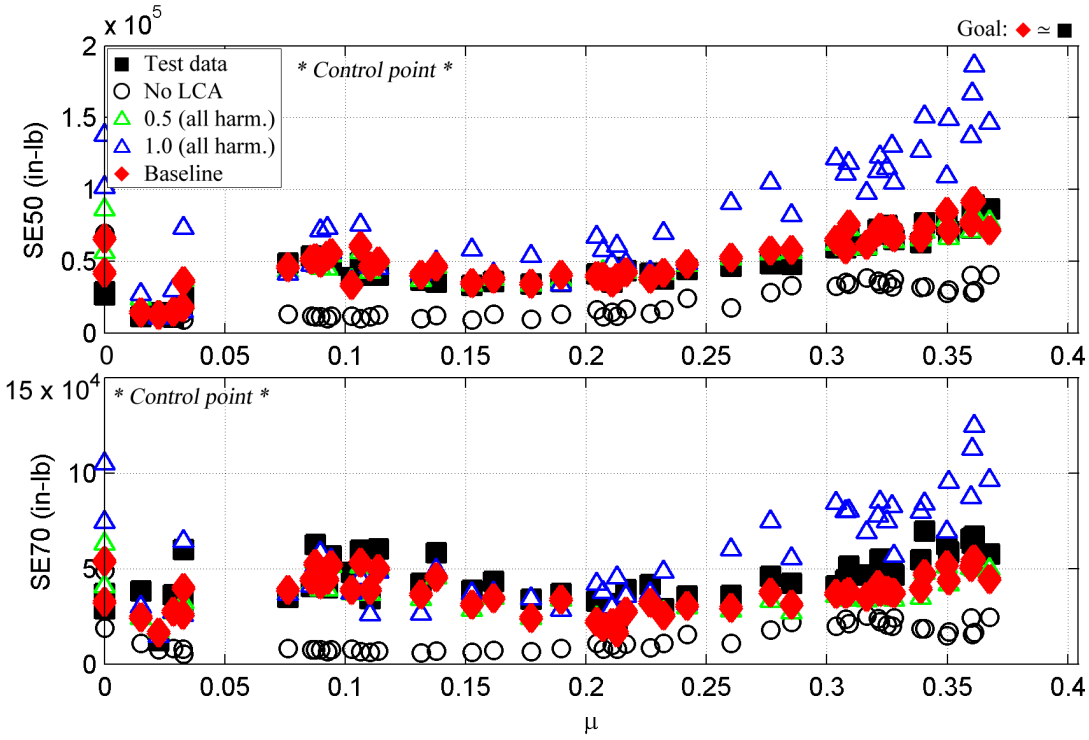

Figure B.6: Peak-to-peak loads matching: effects of κ; all sensors: SE50, SE70.

REFERENCES

[1] Abhishek, A., Ananthan, S., Baeder, J., and Chopra, I., "Prediction of and Fundamental Understanding of Stall Loads in a UH-60A Pull-up Maneuver," *Journal of the American Helicopter Society*, vol. 56, Oct. 2011.

[2] Abhishek, A., Datta, A., Ananthan, S., and Chopra, I., "Prediction, Analysis, and Validation of Main Rotor Blade Loads in a Prescribed Pull-Up Maneuver," (Palm Springs, CA), 50th AIAA/ASME/ASCE/AHS/ASC Structures, Structural Dynamics, and Materials Conference, May 2009.

[3] Abhishek, A., Datta, A., and Chopra, I., "Prediction of UH-60A Structural Loads Using Multibody Analysis and Swashplate Dynamics," *Journal of Aircraft*, vol. 46, Mar. 2009.

[4] Abras, J., Lynch, C., and Smith, M., "Computational Fluid Dynamics-Computational Structural Dynamics Rotor Coupling Using an Unstructured Reynolds-Averaged Navier-Stokes Methodology," *Journal of the American Helicopter Society*, vol. 57, Jan. 2012.

[5] Algera, D., Iyyer, N., Hong, C., Sarkar, S., Singh, A., and Bradfield, S., "Rotary Wing Structural Life Tracking Architecture," (Phoenix, AZ), 66th American Helicopter Society Annual Forum, May 2010.

[6] Arms, S., Townsend, C., and Churchill, D., "Tracking Pitch Link Dynamic Loads with Energy Harvesting Wireless Sensors," (Virginia Beach, VA), 63rd American Helicopter Society Annual Forum, May 2007.

[7] ASTM International, "Standard Practices for Cycle Counting in Fatigue Analysis (ASTM E 1049-85)," June 2005.

[8] Bauchau, O., "DYMORE: A Finite Element Based Tool for the Analysis of Nonlinear Flexible Multibody Systems," *http://www.ae.gatech.edu/people/obauchau/dymore.pdf*.

[9] Bauchau, O., *DYMORE User's Manual*. June 2010.

[10] Bauchau, O., Bottasso, C., and Nikishkov, Y., "Modeling Rotorcraft Dynamics with Finite Element Multibody Procedures," *Mathematical and Computer Modeling*, vol. 33, no. 10, 2001.

[11] Bauchau, O., Rodriguez, J., and Chen, S., "Coupled Rotor-Fuselage Analysis with Finite Motions Using Component Mode Synthesis," *Journal of the American Helicopter Society*, vol. 49, no. 2, 2004.

[12] Bauchau, O. and Wang, J., "Stability Analysis of Complex Multibody Systems," *Journal of Computational and Nonlinear Dynamics*, vol. 1, no. 1, 2006.

[13] Bogert, P., Haugse, E., and Gehrki, R., "Structural Shape Identification from Experimental Strains Using a Modal Transformational Technique," (Norfolk, VA), 44th AIAA/ASME/ASCE/AHS Structures, Structural Dynamics, and Materials Conference, Apr. 2003.

[14] Bousman, W., "Estimation of Blade Airloads from Rotor Blade Bending Moments (NASA TM 100020)," Aug. 1987.

[15] Bousman, W., "Putting the Aero Back into Aeroelasticity," 8th ARO Workshop on Aeroelasticity of Rotorcraft Systems, Oct. 1999.

[16] Bousman, W., "UH-60A Airloads Program Occasional Note 1999-01: UH-60A Airloads Program (1984-1994)," Mar. 1999.

[17] Bousman, W., "UH-60A Airloads Program Occasional Note 1999-02: Data Base Description," May 1999.

[18] Bousman, W., "UH-60A Airloads Program Occasional Note 2001-02: Counter 8534 Steadiness," Oct. 2001.

[19] Bousman, W. and Kufeld, R., "UH-60A Airloads Catalog (NASA TM 212827," Aug. 2005.

[20] Bousman, W. and Maier, T., "An Investigation of Helicopter Rotor Blade Flap Vibratory Loads," 48th American Helicopter Society Annual Forum, June 1992.

[21] Chierichetti, M., D.Palmer, Ruzzene, M., McColl, C., and Bauchau, O., "Prediction of UH-60 Blade Loads: An Insight on the Confluence Algorithm to Correct Internally Generated Airloads," (Virginia Beach, VA), 67th American Helicopter Society Annual Forum, May 2011.

[22] Chierichetti, M., McColl, C., Palmer, D., Ruzzene, M., and Bauchau, O., "Combined Analytical and Experimental Approaches to Rotor Component Stress Predictions," *Journal of Multi-body Dynamics*, vol. 225, Apr. 2011.

[23] Chierichetti, M., Ruzzene, M., and Bauchau, O., "Dynamic Displacement Field Reconstruction Through a Limited Set of Measurements: Application to Plates," *Journal of Sound and Vibration*, 2012.

[24] Choi, S., Datta, A., and Alonso, J., "Prediction of Helicopter Rotor Loads Using Time-Spectral Computational Fluid Dynamics and an Exact Fluid-Structure Interface," *Journal of the American Helicopter Society*, vol. 56, Oct. 2011.

[25] Coates, C. and Thamburaj, P., "Inverse Method Using Finite Strain Measurements to Determine Flight Load Distribution Functions," *Journal of Aircraft*, Mar. 2008.

[26] Coates, C., Thamburaj, P., and Kim, C., "An Inverse Method for Selection of Fourier Coefficients for Flight Load Identification," (Reston, VA), 46th AIAA/ASME/ASCE/AHS Structures, Structural Dynamics, and Mechanics Conference, Apr. 2005.

[27] Coleman, C. and Bousman, W., "Aerodynamic Limitations of the UH-60A Rotor (NASA TM 110396)," Aug. 1996.

[28] Cook, A., Fuller, C., O'Brien, W., and Cabell, R., "Artificial Neural Networks for Predicting Nonlinear Dynamic Helicopter Loads," *AIAA Journal*, vol. 32, Mar. 1994.

[29] Datta, A. and Chopra, I., "Prediction of UH-60A Dynamic Stall Loads in High Altitude Level Flight using CFD/CSD Coupling," (Grapevine, TX), 61st Annual AHS Forum, June 2005.

[30] Davies, B., *Integral Transforms and Their Applications*. Springer, 2005.

[31] Edwards, P. and Darts, J., "Standardized Fatigue Loading Sequences for Helicopter Rotors (Helix and Felix) - Part 1: Background and Fatigue Evaluation (TR 84084)," Aug. 1984.

[32] Edwards, P. and Darts, J., "Standardized Fatigue Loading Sequences for Helicopter Rotors (Helix and Felix) - Part 2: Final Definition of Helix and Felix (TR 84085)," Aug. 1984.

[33] Everett, R., "A Comparison of Fatigue Life Prediction Methodologies for Rotorcraft (NASA TM 102759)," Dec. 1990.

[34] Everett, R., Bartlett, F., and Elber, W., "Probabilistic Fatigue Methodology for Six Nines Reliability (NASA TM 102757)," Dec. 1990.

[35] Flitter, L., McCool, K., and Haas, D., "Rotor System Load Monitoring Using a Neural Network Based Approach," *AIAA Journal*, 1997.

[36] Foss, G. and Haugse, E., "Using Modal Test Results to Develop Strain to Displacement Transformations," 13th International Modal Analysis Conference, Feb. 1995.

[37] Gopinath, A. and Jameson, A., "Time Spectral Method for Periodic Unsteady Computations over Two- and Three- Dimensional Bodies," (Reno, NV), 43rd AIAA Aerospace Sciences Meeting and Exhibit, Jan. 2005.

[38] Haas, D., "Determination of Helicopter Flight Loads from Fixed System Measurements," AIAA 32nd Structures, Structural Dynamics, and Materials Conference, Apr. 1991.

[39] Haas, D. and Imber, R., "Identification of Helicopter Component Loads Using Multiple Regression," *Journal of Aircraft*, vol. 31, July 1994.

[40] Hall, K., Thomas, J., and Clark, W., "Computation of Unsteady Nonlinear Flows in Cascades Using a Harmonic Balance Technique," *AIAA Journal*, vol. 40, May 2002.

[41] Hamade, K. and Kufeld, R., "Modal Analysis of UH-60A Instrumented Rotor Blades (NASA TM 4239)," 1990.

[42] Hansford, R. and Vorwald, J., "Dynamics Workshop On Rotor Vibratory Loads Prediction," (Washington, DC), June 1996.

[43] Hilbert, K., "A Mathematical Model of the UH-60 Helicopter (NASA TM 85890)," 1984.

[44] Hines, W. and Montgomery, D., *Probability and Statistics in Engineering and Management Science (3rd Ed.)*. John Wiley and Sons, 1990.

[45] Ho, J., Yeo, H., and Ormiston, R., "Investigation of Rotor Blade Structural Dynamics and Modeling Based on Measured Airloads," *Journal of Aircraft*, vol. 45, Sept. 2008.

[46] Hodges, D. and Pierce, G., *Introduction to Structural Dynamics and Aeroelasticity*. Cambridge Aerospace Series, 2002.

[47] Iyyer, N., Sarkar, S., Merrill, R., and Phan, N., "Aircraft Life Management Using Crack Initiation and Crack Growth Models - P-3C Aircraft Experience," *International Journal of Fatigue*, vol. 29, 2007.

[48] Khosrovaneh, A. and Dowling, N., "Fatigue Life Estimates for Helicopter Loading Spectra (NASA CR 181941)," Dec. 1989.

[49] Kua, J., Thiruvaran, T., Nosratighods, M., Ambikairajah, E., and Epps, J., "Investigation of Spectral Centroid Magnitude and Frequency for Speaker Recognition," (Brno, Czech Republic), Odyssey 2010: The Speaker and Language Recognition Workshop, June 2010.

[50] Kufeld, R., Balough, D., Cross, J., Studebaker, K., Jennison, C., and Bousman, W., "Flight Testing the UH-60A Airloads Aircraft," (Washington, DC), 50th American Helicopter Society Annual Forum, May 1994.

[51] Kufeld, R. and Bousman, W., "UH-60A Helicopter Rotor Airloads Measured in Flight," *The Aeronautical Journal*, pp. 217–227, May 1997.

[52] Kufeld, R. and Bousman, W., "Technical Note: UH-60A Airloads Program Azimuth Reference Correction," *Journal of the American Helicopter Society*, vol. 50, Apr. 2005.

[53] Kufeld, R., Cross, J., and Bousman, W., "A Survey of Rotor Loads Distribution in Maneuvering Flight," AHS Aeromechanics Specialists Conference, Jan. 1994.

[54] Kufeld, R. and Johnson, W., "The Effects of Control System Stiffness Models on the Dynamic Stall Behavior of a Helicopter," (Washington, DC), 54th American Helicopter Society Annual Forum, May 1998.

[55] Leishman, J., *Principles of Helicopter Aerodynamics (2nd Ed.)*. Cambridge University Press, 2000.

[56] Maley, S., Plets, J., and Phan, N., "US Navy Roadmap to Structural Health and Usage Monitoring - The Present and Future," (Virginia Beach, VA), 63rd American Helicopter Society Annual Forum, May 2007.

[57] Marpu, R., Sankar, L., Makinen, S., and Baeder, J., "Computational Modeling of Diving-turn Maneuvers using Hybrid Methodology," 68th American Helicopter Society Annual Forum, May 2012.

[58] McColl, C., Palmer, D., Chierichetti, M., Bauchau, O., and Ruzzene, M., "Comprehensive UH-60 Loads Model Validation," (Phoenix, AZ), 66th American Helicopter Society Annual Forum, May 2010.

[59] McColl, C. and Phan, N., "Measured Gust Cycle Clustering Effects and the Implications on Aircraft Fatigue and Damage Tolerance," (Palm Springs, CA), 10th Joint FAA/DoD/NASA Conference on Aging Aircraft, Apr. 2007.

[60] McFalls, M., White, D., and Jackson, A., "Fatigue Life Analysis of Helicopter Components Based on Usage Monitoring," (Phoenix, AZ), 60th American Helicopter Society Annual Forum, June 2004.

[61] McFarland, J. and Riha, D., "Uncertainty Quantification Methods for Helicopter Fatigue Reliability Analysis," (Grapevine, TX), 65th American Helicopter Society Annual Forum, May 2009.

[62] Meirovitch, L., *Analytical Methods in Vibrations*. Macmillan Publishing Co., Inc., 1967.

[63] Miner, M., "Cumulative Damage in Fatigue," *ASME Journal of Applied Mechanics*, vol. 12, Sept. 1945.

[64] Ormiston, R., "Comparison of Several Methods for Predicting Loads on a Hypothetical Helicopter Rotor," *Journal of the American Helicopter Society*, Oct. 1974.

[65] Ormiston, R., "An Investigation of the Mechanical Airloads Problem for Evaluating Rotor Blade Structural Dynamics Analysis," (San Francisco, CA), American Helicopter Society 4th Decennial Specialists Conference on Aeromechanics, Jan. 2004.

[66] Ormiston, R., "NRTC/RITA Rotorcraft Airloads Workshop: UH-60 Rotor Airloads/Blade Loads - Comments," Sept. 2004.

[67] Ormiston, R. and Martin, P., "Rotor Blade Stall Flutter, Stable or Unstable? An Exploratory Investigation of Nonlinear Aeroelasticity," (Virginia Beach, VA), 63rd American Helicopter Society Annual Forum, May 2007.

[68] Palmgren, A., "The Service Life of Ball Bearings," *NASA Technical Translation TT F-13460 (Mar 1971)*, Apr. 1924.

[69] Penrose, R., "A Generalized Inverse for Matrices," July 1954.

[70] Peters, D., Karunamoorthy, S., and Cao, W., "Finite State Induced Flow Models. Part I: Two-dimensional Thin Airfoil," *Journal of Aircraft (32(2))*, pp. 313–322, 1995.

[71] Potsdam, M., Yeo, H., and Johnson, W., "Rotor Airloads Prediction Using Loose Aerodynamic/Structural Coupling," 61st American Helicopter Society Annual Forum, June 2004.

[72] Potsdam, M., Yeo, H., and Johnson, W., "Rotor Airloads Prediction Using Multidisciplinary Coupling," IEEE Users Group Conference, 2005.

[73] Potsdam, M., Yeo, M., and Johnson, W., "Rotor Airloads Comparison using Multidisciplinary Coupling," *IEEE, Computer Society - Proceedings of the Users Group Conference*, 2005.

[74] Schubert, E., Wolfe, J., and Tarnopolsky, A., "Spectral Centroid and Timbre in Complex, Multiple Instrumental Textures," (Evanston, IL), Proceedings of the 8th International Conference on Music Perception and Cognition, 2004.

[75] Shkarayev, S., Krashantisa, R., and Tessler, A., "An Inverse Interpolation Method Utilizing In-flight Strain Measurements for Determining Loads and Structural Response of Aerospace Vehicles (NASA TR 31WSHM)," 2011.

[76] Sicot, S., Dufour, G., and Gourdain, N., "A Time-domain Harmonic Balance Method for Rotor/Stator Interactions," *Journal of Turbomachinery*, vol. 134, Jan. 2012.

[77] Sitarama, J. and Roget, B., "Prediction of Helicopter Maneuver Loads Using a Coupled CFD/CSD Analysis," 26th International Congress of the Aeronautical Sciences, 2008.

[78] Theodore, C., "Helicopter Flight Dynamics Simulation with Refined Aerodynamic Modeling (Ph.D. Dissertation)," 2000.

[79] Tiong, U., Jones, R., and Molent, L., "Damage Tolerance Analysis of a Helicopter Component," *International Journal of Fatigue*, pp. 1046–1053, June 2009.

[80] Totah, J., "A Critical Assessment of UH-60 Main Rotor Blade Airfoil Data (AIAA-93-3413-CP)," 1993.

[81] Watkinson, J., *The Art of the Helicopter*. Elsevier Butterworth-Heinemann, 2004.

VITA

Chance McColl obtained a Bachelor of Science degree in Aerospace Engineering Sciences from the University of Colorado at Boulder in May 1992. He obtained a Master of Science degree in Aerospace Engineering from The Georgia Institute of Technology in December 1993. In January 1994, he began his career with The Boeing Company in Renton, WA as an aircraft loads engineer in the Loads and Dynamics Group. Mr. McColl developed flight and ground loads for the 737-600/700/800 aircraft before becoming Lead Engineer for Dynamic Flight Loads for the 757-200/300 aircraft. In October 1998, Mr. McColl went to work for Lockheed Martin Corporation in Marietta, GA, serving as Lead Engineer for Loads and Spectra Development for the P-3C Orion Service Live Assessment Program. Mr. McColl worked in software development for Aelera Corporation in Alpharetta, GA from December 2000 through August 2001, at which point he went to work for Technical Data Analysis, Inc. (TDA) in Marietta, GA. Mr. McColl currently serves as Director of Engineering (Marietta) for TDA where he has extensive experience in fixed- and rotary-wing aircraft loads, spectra, and fatigue, supporting organizations including the US Navy, the Royal Australian Air Force, the Canadian Forces, the Royal Norwegian Air Force, the Royal Netherlands Navy, the Hellenic Navy, NASA, and NOAA. Mr. McColl is a member of the American Helicopter Society and the American Institute of Aeronautics and Astronautics and has served as Co-chair of the Georgia Aerospace Policy Working Group.

Selected publications

[1] Chierichetti, M., D.Palmer, Ruzzene, M., McColl, C., and Bauchau, O., "Prediction of UH-60 Blade Loads: An Insight on the Confluence Algorithm to Correct Internally Generated Airloads," (Virginia Beach, VA), 67th AHS Conference, May 2011.

[2] Chierichetti, M., McColl, C., Palmer, D., Ruzzene, M., and Bauchau,

O., "Combined Analytical and Experimental Approaches to Rotor Component Stress Predictions," *Journal of Multi-body Dynamics*, vol. 225, Apr. 2011.

[3] Chierichetti, M., McColl, C., Palmer, D., Bauchau, O., and Ruzzene, M., "Combined Analytical and Experimental Approaches to Rotor Components Stress Predictions", (Lappeenranta, Finland), 1st Joint International Conference on Multi-body System Dynamics, May 2010.

[4] McColl, C., Palmer, D., Chierichetti, M., Bauchau, O., and Ruzzene, M., "Comprehensive UH-60 Loads Model Validation," (Phoenix, AZ), 66th AHS Conference, May 2010.

[5] Iyyer, N., Bradfield, S., Sarkar, S., McColl, C., Algera, D., Flores, E., and Phan, N., "Architecture for Dynamic Component Life Tracking in an Advanced HUMS, RFID, and Direct Load Sensor Environment," (Melbourne, Australia), 13th Australian International Aerospace Congress, Mar. 2009.

[6] Palmer, D., Higa, R., McColl, C., and Crosby, T., "The Effects of Air Vehicle Health Monitoring System Fidelity on Fatigue and Damage Tolerance Assessments," (Kansas City, MO), 12th Joint FAA/DoD/NASA Conference on Aging Aircraft, May 2009.

[7] McColl, C., "A Template for Successful Development and Implementation of an Aircraft Life Tracking Program," (Phoenix, AZ), 11th Joint FAA/DoD/NASA Conference on Aging Aircraft, Apr. 2008.

[8] McColl, C. and Phan, N., "Measured Gust Cycle Clustering Effects and the Implications on Aircraft Fatigue and Damage Tolerance," (Palm Springs, CA), 10th Joint FAA/DoD/NASA Conference on Aging Aircraft, Apr. 2007.

[9] Moon, S., McColl, C., and Phan, N., "C-130 Usage/Environmental Criteria Analysis and Gust Loads Assessment," (San Antonio, TX), 2006 USAF Aircraft Structural Integrity Program Conference, November 2006.

[10] McColl, C. and Bradfield, S., "The Effects of Extreme Weather Environments/ Severe Flight Loads Spectra on the Aging Fleet of NOAA's WP-3D Hurricane Hunter Aircraft," (Atlanta, GA), 9th Joint DoD/FAA/NASA Conference on Aging Aircraft, Mar. 2006.

A Matched-Harmonic Confluence Approach to Rotor Loads Prediction With Comprehensive Application to Flight Test

Chance C. McColl

314 Pages

Directed by Professor Massimo Ruzzene

Future management of helicopter fleets will be more heavily based on individual component damage tracking and less on legacy usage monitoring (flight parameter-based) methods. This enhances health assessment capabilities by taking into account the actual loads on a component-by-component basis. However, accurate loads prediction in rotating frame components remains a challenge. Even with advanced computational fluid dynamics (CFD) techniques, prediction of the unsteady aerodynamic loads acting on the rotor blades is computationally intensive and problematic in terms of accurate loads prediction across the entire flight regime of the helicopter. High-speed flight can potentially introduce both shock and near-stall effects within a given rotor rotation. Low-speed flight can include blade-vortex interaction effects, wherein flow from a given blade (vorticity loading from tip vortices) impinges upon the preceding blade, causing unsteady aerodynamic loading that is difficult to quantity and predict numerically. Vehicle maneuvering can produce significantly higher blade pitching moments than steady flight. All of these regimes combine to represent the loading history of the rotor system. Therefore, accurate loads prediction methods, in terms of matching peak-to-peak, magnitude, phase, as well as vibratory/harmonic content, are required that capture all flight regimes for all critical structural components.

This research focuses on the development of a loads prediction method, known as the Load Confluence Algorithm (LCA), and its application to the analysis of a large set of flight test data from the NASA/US Army UH-60A Airloads Program. The LCA combines measured response at a prescribed set of locations with a numerical

model of the rotor system. For a given flight condition (steady flight, maneuvers, etc.) the numerical simulation's predicted loads distribution is iteratively incremented (by harmonic) until convergence with measured loads is reached at the prescribed locations (control points). Predicted loads response at non-instrumented locations is shown to be improved as well, thus enhancing fatigue lifing methods for these components.

The procedure specifically investigates the harmonic content of the applied loads and the improved prediction of the harmonic components. The impact of the enhanced accuracy on loads predictions on component structural fatigue is illustrated by way of an example.

Results show that, for a limited sensor set (two 3-axis sensors per blade), blade loads are accurately predicted across a full range of flight regimes. Hub loads are best modeled using the pushrod as the control point. Results also show that load magnitude has a tremendous influence on damage, with a 25% over-estimation of vibratory load resulting in a damage factor of nearly 3. This research highlights the importance of accurate loads prediction for a rotorcraft life tracking program. Small inaccuracies in loads lead to dramatic errors in damage assessment.